

AGARD-R-780

AGARD-R-780



AD-A230 761

AGARD REPORT No.780

Special Course
on
**Inverse Methods for Airfoil Design
for Aeronautical and Turbomachinery
Applications**

DTIC
ELECTE
JAN 24 1991

(Méthodes Inverses pour la Conception des Profils
Porteurs pour des Applications dans les Domaines
de l'Aéronautique et des Turbomachines)

NORTH ATLANTIC TREATY ORGANIZATION



DISTRIBUTION AND AVAILABILITY
ON BACK COVER

91

DISTRIBUTION STATEMENT A

Approved for public release
Distribution Unlimited

NORTH ATLANTIC TREATY ORGANIZATION
ADVISORY GROUP FOR AEROSPACE RESEARCH AND DEVELOPMENT
(ORGANISATION DU TRAITE DE L'ATLANTIQUE NORD)

AGARD Report No.780

Special Course
on
Inverse Methods for Airfoil Design for Aeronautical
and Turbomachinery Applications

(Méthodes Inverses pour la Conception des Profils Porteurs pour des Applications
dans les Domaines de l'Aéronautique et des Turbomachines)

Accession For	
NTIS GRA&I	<input checked="" type="checkbox"/>
DTIC TAB	<input type="checkbox"/>
Unannounced	<input type="checkbox"/>
Justification	
By _____	
Distribution/ _____	
Availability Codes	
Dist	Avail and/or Special
A-1	



The material assembled in this book was prepared under the combined sponsorship of the Fluid Dynamics Panel, the von Kármán Institute and the Consultant and Exchange Program of AGARD and was presented as an AGARD Special Course at the von Kármán Institute, Rhode-Saint-Genèse, Belgium on 14th—18th May 1990.

The Mission of AGARD

According to its Charter, the mission of AGARD is to bring together the leading personalities of the NATO nations in the fields of science and technology relating to aerospace for the following purposes:

- Recommending effective ways for the member nations to use their research and development capabilities for the common benefit of the NATO community;
- Providing scientific and technical advice and assistance to the Military Committee in the field of aerospace research and development (with particular regard to its military application);
- Continuously stimulating advances in the aerospace sciences relevant to strengthening the common defence posture;
- Improving the co-operation among member nations in aerospace research and development;
- Exchange of scientific and technical information;
- Providing assistance to member nations for the purpose of increasing their scientific and technical potential;
- Rendering scientific and technical assistance, as requested, to other NATO bodies and to member nations in connection with research and development problems in the aerospace field.

The highest authority within AGARD is the National Delegates Board consisting of officially appointed senior representatives from each member nation. The mission of AGARD is carried out through the Panels which are composed of experts appointed by the National Delegates, the Consultant and Exchange Programme and the Aerospace Applications Studies Programme. The results of AGARD work are reported to the member nations and the NATO Authorities through the AGARD series of publications of which this is one.

Participation in AGARD activities is by invitation only and is normally limited to citizens of the NATO nations.

The content of this publication has been reproduced
directly from material supplied by AGARD or the authors.

Published November 1990

Copyright © AGARD 1990
All Rights Reserved

ISBN 92-835-0591-3



Printed by Specialised Printing Services Limited
40 Chigwell Lane, Loughton, Essex IG10 3TZ

Introduction

The demands for higher performance and a more flexible design system require the airfoil and turbomachinery blade designer to be more innovative and to design beyond the limits of experimental data. Iterative procedures in which an optimum is obtained by a comparison between the results of different designs are being replaced by new computational methods in which the objective is defined by a direct calculation. Such methods use a minimum of empiricism, are better suited to profit from modern computational tools, and are more easily integrated into modern manufacturing systems.

Blade or airfoil designs are normally made in two steps, and the lectures are accordingly grouped into two parts.

In the first part, optimisation of the target pressure and velocity distributions are discussed taking into account the required performance and the loss mechanisms in the boundary layer. Both direct optimisation resulting from an inverse boundary layer calculation, and an iterative optimisation by minimisation of the losses are presented. It is clear from both procedures that inclusion of off-design operation is one of the greatest difficulties involved in blade or airfoil optimisation.

The second part of the course gives an overview of the numerous inverse blade design methods that have been developed both for turbomachinery and aeronautical applications. This ranges from simple parameter definitions of two-dimensional cross-sections to the full three-dimensional definition of wings and blade channels. The more academic interest of a detailed numerical definition of arbitrary shapes conflicts here with the mechanical constraints imposed by the industrial manufacturer.

The methodology to account for a large number of constraints, as required in inverse designs and optimisations, is also discussed and is illustrated by results from numerous applications discussed in the last group of lectures.

One of the objectives of this short course is to exchange views and to promote a discussion between turbomachinery and aeronautical designers. Most designers are active only in one field of application and are not aware of publications by the other group. However, boundary layer calculation methods, potential flow and Euler solvers are almost directly applicable to both single blades and multiple blade rows. It is therefore surprising that this kind of discussion is not more frequent.

R.Van den Braembussche
Lecture Series Director

*Course on Optimising Turbine blades
by R. Van den Braembussche
Aerojet General Corporation*

Introduction

Face à la volonté des constructeurs d'améliorer les performances des profils aérodynamiques et des aubes des turbomachines, et d'adopter une méthodologie de conception plus souple, le concepteur devient plus innovateur, en placant le concept de son prototype au-delà des limites des données expérimentales.

Les procédures itératives, où le résultat optimal est obtenu par comparaison entre les résultats de différentes projets, cède la place à de nouvelles méthodes informatiques, où l'objectif est défini par calcul direct. De telles méthodes, qui ne font appel qu'à un minimum d'empirisme, sont plus susceptibles de bénéficier des outils informatiques modernes et de s'intégrer aux systèmes de fabrication modernes.

Les profils aérodynamiques et les aubes des turbomachines sont généralement définis en deux étapes et le cours est, par conséquent, divisé en deux parties.

La première partie examine l'optimisation de la répartition des pressions et des vitesses, en tenant compte des performances souhaitées et du processus des pertes au niveau de la couche limite. L'optimisation directe qui résulte du calcul inverse de la couche limite est décrite, ainsi que l'optimisation itérative obtenue par minimalisation des pertes. Les deux approches démontrent clairement que la prise en compte du fonctionnement hors-étude reste l'une des plus grandes difficultés à surmonter pour réussir l'optimisation des profils aérodynamiques et des aubes des turbomachines.

La deuxième partie du cours est consacrée à un exposé des différentes méthodes inverses qui ont été développées pour la conception des aubes des turbomachines et pour d'autres applications aéronautiques. Ceci va des simples définitions paramétriques de coupes bidimensionnelles à la définition complète d'aubes et de canaux d'aube. L'intérêt plutôt spéculatif présenté par des définitions numériques détaillées, se heurte, ici, aux contraintes mécaniques imposées par l'industriel.

Une méthodologie qui tient compte d'un grand nombre de contraintes, comme c'est le cas pour l'optimisation et la conception à l'aide des méthodes inverses, est examinée et mise en lumière par les résultats de nombreuses applications qui sont traitées lors de la dernière session de cours.

L'un des objectifs de ce cours est de permettre un échange de vues et de développer le débat entre concepteurs de turbomachines et concepteurs d'aéronefs. La plupart des concepteurs travaille dans un seul domaine d'application et ne sont pas informés des communications publiées par leurs confrères actifs dans d'autres domaines. Cependant, les méthodes de calcul de la couche limite, les résolveurs d'écoulements à potentiel, et les résolveurs d'Euler s'appliquent plus ou moins directement aux grilles d'aubes simples et multiples. Il est donc surprenant que ce type de débat n'ait pas lieu plus souvent.

R.Van den Braembussche
Directeur de Cycle de Conférences

Special Course Staff

Special Course Director: Prof. R. Van den Braembussche
von Kármán Institute for Fluid Dynamics
Chaussée de Waterloo, 72
B-1640 Rhode-St-Genèse
Belgium

Ir O.Leonard
VKI
Chaussée de Waterloo, 72
1640 Rhode-Saint-Genèse
Belgium

Mr J.J.Thibert
Div. Aérodynamique Appl.
ONERA
B.P. 72
92322 Châtillon
France

Mr B.Bouras
Nat. Techn. Univ. of Athens
Dept. of Mechanical Engineering
Lab. Thermal Turbomachines
P.O. Box 64069
15710 Athens
Greece

Prof. L.Papailiou
Nat. Techn. Univ. of Athens
Dept. of Mechanical Engineering
Lab. Thermal Turbomachines
P.O. Box 64069
15710 Athens
Greece

Mr F.Larocca
Fiat Aviazione
Direzione Progettazione
Corso Ferrucci, 112
10138 Torino
Italy

Prof. L.Zannetti
Politecnico di Torino
Corso Duca degli Abruzzi 24
Torino
Italy

Ir R.Evan den Dam
National Aerospace Lab. NLR
Anthony Fokkerweg 2
1059 Amsterdam
Netherlands

Ir J.A.van Egmond
National Aerospace Lab. NLR
Anthony Fokkerweg 2
1059 Amsterdam
Netherlands

Prof. Ir J.W.Slooff
National Aerospace Lab. NLR
Anthony Fokkerweg 2
1059 CM Amsterdam
Netherlands

Prof. M.Drela
M.I.T.
Dept. of Aeronautics and Astronautic
Cambridge, MA 02139
Massachusetts
United States

Prof. G.S.Dulikravich
Dept. of Aerospace Engineering
Penn State University
233 Hammond Bldg
University Park, PA 16802
United States

Dr M.H.Rizk
Sverdrup Technology, Inc.
TEAS Group
Building 260
P.O. Box 1935
Eglin Air Force, FL 32542
United States

Dr G.Volpe
Grumman Aerospace Corp.
Res. Dev. Center
Bethpage, NY 11714
United States

AGARD Representative

Dr W.D.Goodrich
Fluid Dynamics Panel Executive
AGARD, 7 rue Ancelle
92200 Neuilly-sur-Seine

Contents

	Page
Introduction (Eng.)	iii
Introduction (Fr.)	iv
Special Course Staff	v
	Reference
Aerodynamic Shape Design by G.S.Dulikravich	1
Arbitrary Blade Section Design Based on Viscous Considerations by K.D.Papailiou and B.Bouras	2
Optimization of Target Pressure Distributions by R.F.van den Dam, J.A.van Egmond and J.W.Slooff	3
Geometric and Surface Pressure Restrictions in Airfoil Design by G.Volpe	4
Transonic Shock Free Wing Design by G.Volpe	5
A Stream-Function-Coordinate (SFC) Concept in Aerodynamic Shape Design by G.S.Dulikravich	6
Subsonic and Transonic Cascade Design by O.L'andonard	7
Inverse Methods for 3D Internal Flows by L.Zannetti and F.Larocca	8
Viscous and Inviscid Inverse Schemes Using Newton's Method by M.Drela	9
One Point and Multi-Point Design Optimization for Airplane and Helicopter Application by J.J.Thibert	10
Constrained Spanload Optimization for Minimum Drag of Multi-Lifting-Surface Configurations by R.F.van den Dam	11
Aerodynamic Optimization by Simultaneously Updating Flow Variables and Design Parameters by M.H.Rizk	12

AERODYNAMIC SHAPE DESIGN

George S. Dulikravich
 Department of Aerospace Engineering
 Pennsylvania State University
 University Park, PA 16802, USA

1. SUMMARY

Design of aerodynamic shapes can be accomplished by using the methodologies from computational fluid dynamics and optimization. Two basic categories of the inverse (design) formulations are surface flow design and flow field design. A number of methods in both categories have been discussed and critically evaluated. Open questions remain to be specification of a more appropriate surface pressure, acceleration of iterative algorithms, increased versatility of the design methods, direct use of the existing and future flow field analysis software.

2. PREFACE

The field of aerodynamic shape design involves the ability to determine the geometry of an aerodynamic object that will satisfy the governing flow field equations and specified boundary conditions. For example, it is possible to determine the coordinates of an airfoil if a surface pressure distribution is specified. The resulting designs can be subject to certain specified constraints. Examples include finding aerodynamic configurations compatible with entirely shock-free transonic flow fields, obtaining shapes of objects that produce flow fields with minimum entropy generation, minimum noise generation, etc.

One of the first meetings on the general topic of shape design was the International Conferences on Inverse Design Concepts and Optimization in Engineering Sciences (ICIDES). The first ICIDES was organized and held October 17-18, 1984, at the University of Texas at Austin, while ICIDES-II was held October 26-28, 1988, at the Pennsylvania State University. They were followed by an AGARD Specialists' Meeting on Computational Methods for Aerodynamic Design (Inverse) and Optimization held in Loen, Norway, on May 22-23, 1989.

In the general field of aerodynamics as well as in any other field theory, we are basically faced with two problems: analysis and design. In the case of an analysis (direct problem) we are asked to predict the details of a flow field if the

geometry of the flying object is given. In the case of a design (inverse problem) we are asked to predict the detailed geometry of the flying object so that it is compatible with specified features of the flow field.

Depending on the prescribed desired features of the flow field, the design (inverse) can be divided into two general categories: surface flow design and the flow field design [5,6]. Surface flow design is achieved by specifying a certain flow parameter (pressure, Mach number, etc.) on the surface of the flying object and finding the shape that will generate these surface conditions without regard for the rest of the flow field. The flow field design, on the other hand, enforces certain global flow field features (shock-free flow, minimal entropy generation, etc.) at every point of the flow field by finding the shape that will satisfy these global constraints at every point of the flow field. A large number of methods for performing the surface flow design have been developed, while only a few methods for the flow field design are known to exist.

Mathematical models used in the design are based on partial differential equations, integral equations, and algebraic equations. For example, Zhukovski conformal mapping is actually a technique for designing a class of airfoil shapes having specified surface distribution of pressure that corresponds to a flow around a rotating circle. Although we are dealing here with a simple algebraic expression, it is based on an integral equation formulation (a point-dipole and a point vortex) which resulted from the Laplace operator (a partial differential equation) governing the flow field. Thus, any global conformal mapping can be viewed as a very special method for designing certain simple shapes in a steady, planar, irrotational, inviscid flow field. Moreover, global conformal mapping is the only example that comes to mind as a method which combines the surface flow design concept and the flow field design concept by guaranteeing that the resulting shapes will have the specified surface distribution of the flow parameters while the flow field will be irrotational.

In a more general situation, arbitrary distribution of the surface flow parameters or the flow field distribution of the flow parameters could result in shapes that do not have to be physically meaningful and manufacturable. For example, the lower surface and upper surface of an airfoil could either cross over ("fish tail shapes") or never meet (open trailing edge shapes) although these solutions are mathematically acceptable (Fig. 1). Obviously, the problem is in choosing an appropriate surface distribution of the flow parameters. On the other hand, when performing the flow field design by minimizing the entropy generation at every point in the field, the resulting shape will most likely have zero thickness and no stagnation points, that is, the optimal shape will most likely be a flat plate. Certain constraints on

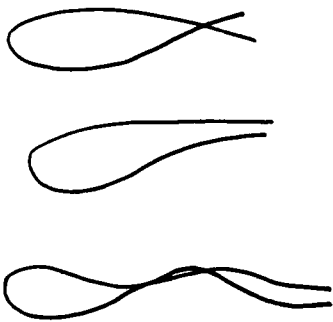


Fig. 1 Different configurations resulting from the unconstrained surface flow design

the acceptable final geometry are needed especially since the final aerodynamic design is often incompatible with the minimum acceptability criteria posed by heat transfer, structural dynamics and vibrations, acoustics, and manufacturing, just to name a few [5,6].

The main objection raised by the designers when discussing the inverse (design) methodologies is that these methods create strictly point-designs

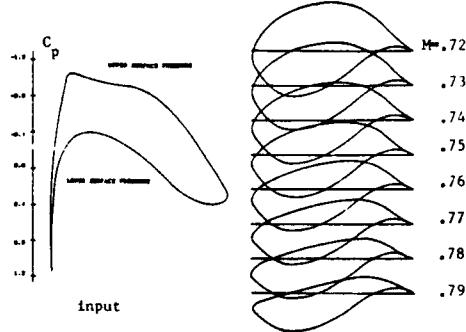


Fig. 2 Shock-free airfoil shapes having same surface pressure distribution; [7] vertical axis magnified five times

rather than range-designs. In other words, an aerodynamic shape (Fig. 2) designed by using a surface flow design method will have the desired [7] characteristics only at the design conditions. If the operating conditions (angle of attack, free stream Mach number, etc.) are changed, the performance of the designed configuration can deteriorate rapidly. Moreover, when designing transonic shock-free shapes with any of the surface flow design methods, the resulting configuration could have a mildly concave surface (Fig. 3) that is covered by the supersonic

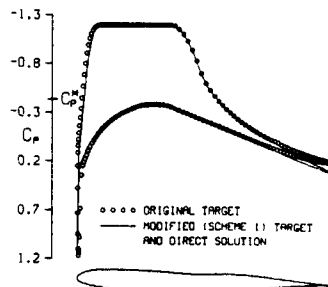


Fig. 3 An example of a "shock-free" surface pressure distribution with a concave suction surface [8]

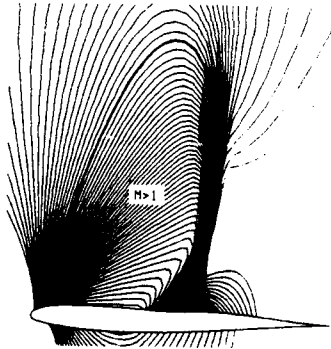


Fig. 4 Iso-Mach distribution for the shock-free surface designed airfoil; notice the hanging shock [8]

flow. As a result, a "hanging shock" or a "loose-foot shock" will form (Fig. 4) even at the design conditions [8]. The aerodynamic efficiency of such a configuration will not be satisfactory even at the design operating point. At off-design values for the Mach number or the angle of attack, the hanging shock will violently re-attach itself to the airfoil surface thus causing rapid increase in drag due to the boundary layer separation. Consequently, it is more appropriate to design an almost shock-free shape even at the design conditions. Such shapes would have a weak family [9] of shocks that would not

increase in strength appreciably at the off-design.

3. SURFACE DATA SPECIFICATION

This brings us to the question of what is the appropriate surface pressure distribution. The most desired feature of an aerodynamic design is to prevent flow separation over a wider range of angles of attack, Mach numbers, and Reynolds numbers. The answer to the question as to what is the optimal surface pressure distribution is not known. It might be an altogether wrong question to ask in light of the fact that the surface pressure distribution alone is not indicative of potentially hazardous flow field features as is the case of an unexpected hanging shock. Nevertheless, a number of researchers [10-14] have entertained this problem by using a classical approach based on the information from the boundary layer. A somewhat speculative approach using a concept of minimal kinetic energy rate [15] has been reported recently. A fast method capable of detecting laminar and turbulent flow separation from the prescribed surface pressure distribution would certainly be very useful. These relatively simple methods can help eliminate those surface pressure distributions that would separate the flow. Besides, these methods leave the designer with a psychologically important feeling that he is still in command, although knowing that all of his experience is still inadequate when compared to a true mathematical optimization.

Among a large number of publications using various surface flow designs, applications have been reported to single airfoils [16-24], multi-component airfoils [25], cascades of airfoils [26-32], ducts [34], rotors [35-46], isolated wings [47-48], wing-body combinations [49-50], nozzles and inlets [51-52], and axisymmetric bodies [53]. Some of the methods have received wider acceptance than the others. The general conclusion is that these methods which are more versatile, easy to comprehend and implement, are the more widely used. Since a number of flow field analysis codes are quite reliable, versatile, and efficient, most designers would like to make use of this software directly in the design process.

4. MODIFIED GARABEDIAN'S METHOD

Methods like Garabedian [19] and the modified Garabedian [20] are becoming quite popular since they require an extremely simple master code which can call any available flow field analysis code simply as a subroutine. Thus, as more sophisticated analysis codes become available, they can be directly substituted in the master code that computes corrections (Fig. 5) to the input geometry. The main drawback of the method is that it converges relatively slowly. The iterative motion of the surface which is

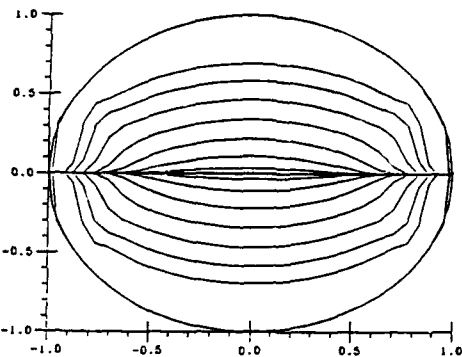


Fig. 5 Convergence history from a slit to a circle using panel code

undergoing design can become irregular very quickly if some sort of control over the motion of surface points is not enforced. The concept of treating such a surface as an elastic membrane which moves according to a simple linear time dependent damped model [19] is quite effective in enforcing a relatively smooth convergence of the surface geometry. A more thorough study on the stability of the surface motion model is necessary, since the choice of coefficients in the model [19,20] can seriously affect the convergence rate and the stability of the entire iterative process.

5. STREAM FUNCTION BASED METHODS

A very interesting concept, termed Stream-Function-as-a-Coordinate (SFC), is based on a transformed flow field governing equations where the vertical coordinate of each stream line is treated as an unknown. Thus, the SFC formulation [32-33] solves directly for the unknown geometric coordinate which is the coordinate of a stream line (Fig. 6). A similar concept derived from the boundary element integral method [18] gives a fully converged solution in 10-20 iterations.

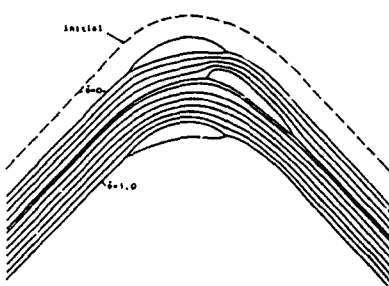


Fig. 6 Design of a tandem cascade using SFC formulation [32]

Another method that is based on the interplay of stream function and potential function in irrotational subsonic inviscid flows is due to Stanitz [34]. He has obtained fascinating configurations of channels and ducts subject to specified surface pressure along the duct walls (Fig. 7).

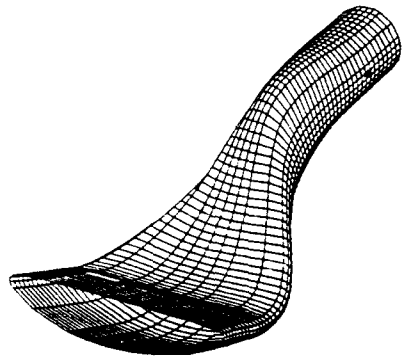


Fig. 7 Air intake scoop designed using Stanitz method [34]

6. TAYLOR SERIES EXPANSION METHOD

An extremely efficient and simple, although approximate method has been developed in China [37-39] and can be reportedly used on a pocket programmable calculator. The method is based on prescribing, say, Mach number distribution along the mid-passage streamline and then deducing values of the Mach number on the top and the bottom of the passage by expanding the prescribed data in the vertical direction using Taylor series. With more terms in the Taylor series, the larger gap-to-chord cascade can be designed. Since the analyticity is carried to an extreme, very little work needs to be performed iteratively. As a consequence, the method converges very fast. Errors in this method will be rapidly increasing towards the stagnation points especially if they are blunt. The method is applicable to radial turbomachinery as well (Fig. 8).

7. NEW THREE-DIMENSIONAL FORMULATIONS

Highly sophisticated and computational complex computer codes have been developed and successfully applied in the design of three-dimensional coaxial nozzles [40] and turbomachinery blading [41]. The governing model is a complete set of three-dimensional Euler equations of gas dynamics.

Analytically novel and interesting are several new formulations [42-46] for quasi three-dimensional and fully three-dimensional

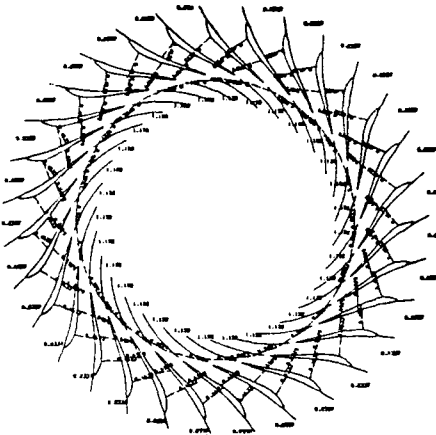


Fig. 8 Radial diffuser vanes designed using Taylor series expansion

turbomachinery inviscid flow field design. The main drawback of these approaches is the absence of viscosity and turbulence in the basic model.

The general concept of having a small master code and being able to utilize any available analysis code as a subroutine in the process of surface flow design has been successfully applied by Takanashi [47] in transonic wing design. The method converges extremely fast since he used a small perturbation integral formulation to evaluate geometry corrections of the wing surface.

Surface flow inverse designs of wings [48,50] and a wing-body combination [49] have been successfully accomplished recently using full potential transonic equation solvers [48,49] or higher order surface panel method [50] and fictitious surface transpiration concept.

Inverse designs of supersonic nozzles [51], supercritical jet engine inlets [52], and axisymmetric bodies in incompressible potential flow [53] have been accomplished. The approach of Ives [52] is especially innovative and unique.

8. TRANSONIC SHOCK-FREE DESIGN

Probably the best known method for the flow field design is a hodograph based method [54-57] for designing transonic shock-free shapes. Actually, the method is a unique combination of both surface flow design (surface Mach number can be specified on a point-by point basis) and flow field design formulations (no shocks are guaranteed to occur in the flow field). Consequently, the method suffers from the known problems (open trailing edges and fish-tail shapes) associated with both general approaches to design. The method has been well publicized in the seventies and the resulting

software [18] found its use in industry. Nevertheless, any method based on the hodograph transformation is inapplicable to three dimensions. Since Garabedian's method is based on elliptic continuation approach [56] it requires two real and two imaginary characteristics. Needless to say, it is a highly complicated method and the resulting software is not easy to modify. The entire method is well described in a textbook by Schrier [57].

An alternative method is known in the West as Sobieczky's [58,59] fictitious gas or as Nakamura's gas [60] in Japan, since both researchers have developed and published the method independently. The concept is based on the basic fact that the shocks can form only if there is a supersonic flow, that is, if the governing partial differential equation is locally of a hyperbolic type. Consequently, if the conditions for possible shock formations are to be eliminated, the governing partial differential equation should never be allowed to become hyperbolic. Sobieczky and Nakamura accomplished this by switching from an isentropic expression for density to an appropriate analytical fictitious density relation at every point in the field and on the boundary where the flow would like to become supersonic. The resulting computations are acceptable in the subsonic regions (where the isentropic relations were used), but are not acceptable in the supersonic regions (where the fictitious gas relations were used). Nevertheless, the resulting sonic line which now separates the two regions is acceptable by both the isentropic and by the fictitious gas relations (Fig. 9). If we now decide to use the isentropic relations in the previously fictitious gas domain, the governing equations will be locally strictly hyperbolic. Hence, the sonic line values of the stream function can be used as initial data for a straight forward integration of the locally hyperbolic system.

Moreover, the system becomes linear if transformed to a rheograph plane characterized by the Prandtl-Meyer function and the local velocity vector angle. The new shape coordinates will be determined from the condition that the stream function should maintain its constant value at every point of the airfoil surface. This method is fairly simple to comprehend and implement in the existing full potential codes. Nevertheless, the fictitious gas method does not give us freedom to specify surface values of flow parameters. It only guarantees that if our choice for the fictitious gas density - Mach number relation is not too restrictive, the supersonic bubble will become shallow and stretched along the surface (Fig. 9) resulting in an entirely shock-free flow field. The method is suitable for redesigning of the existing airfoils [58-62], cascades (Fig. 10) of airfoils [63-65], quasi three-dimensional rotors [66], wings [67-69] without having to worry about surface cross-over, fish-tail shapes, and hanging shocks.

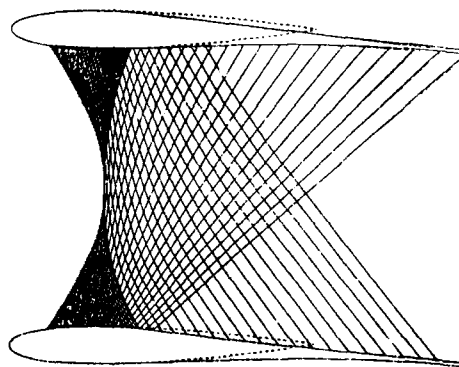


Fig. 10 Lifting choked shock-free cascade designed using fictitious gas [64]

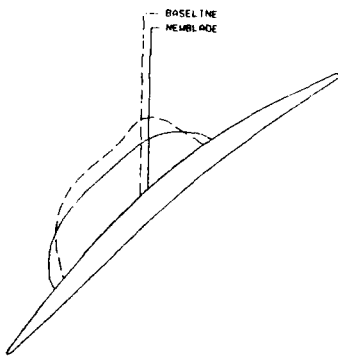


Fig. 9 Sonic line shape before and after the use of fictitious gas [66]

9. OPTIMIZATION

Due to the fact that aerodynamic shape design represents only a part of the overall design of a flying vehicle, the need for an interdisciplinary optimization is arising [4-6]. Simultaneously, the optimization algorithms are finding a rapidly growing applicability in the pure aerodynamic design [70-84]. The optimization algorithms are presently used mainly to minimize a difference between the specified and the computed surface flow data. This is obviously not a very imaginative use of the computational resources, since optimization codes are known to require a large number of flow field analysis solutions. Since the present use of the optimizers is largely not to minimize certain global measure of aerodynamic inefficiency but to enforce the surface flow data, such use of an optimizer has

nothing to do with actually optimizing the shape. The noteworthy exceptions involve maximizing lift-to-drag ratio for a multicomponent airfoil [74], minimization of the total pressure loss across the shock waves in a supersonic inlet [77], minimization of the total pressure loss in an S-shaped duct [78], and optimization over a range of operating conditions [79]. Recent publication [80] exposes an interesting and potentially promising new formulation for the fast evaluation and optimization of off-design conditions. The approach of Rizk [81-83] is especially welcome since it allows for a stable iterative algorithm where an optimizer is used on each updated configuration even before the flow field has converged on the new geometry. As a consequence, a typical airfoil design involves the equivalent of 5-10 fully converged solutions (Fig. 11).

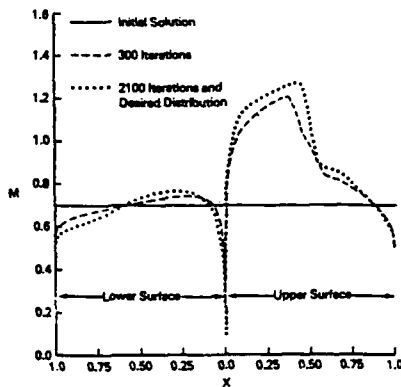


Fig. 11 Convergence history of a surface design using Rizk optimization [81]

10. EMERGING CONCEPTS

Recently, several researchers have looked into using control theory concepts [84-87] in order to achieve an inverse (design) algorithm. The approach is certainly novel and mathematically challenging since most of the fluid flow theory is based on partial differential equations, while the control theory is usually formulated via ordinary differential equations. Preliminary formulations [87] reconfirm earlier observations [84] that this type of formulation might not be efficient.

11. CONCLUSIONS

A survey of a vast number of different inverse (design) concepts and algorithms has been performed with an attempt to classify them. Positive and known negative characteristics of each of the more prominent methods have been outlined. Future research should concentrate on the use of Navier-Stokes equations and three-dimensionality of the problem. Optimization and

especially interdisciplinary optimization should play a more prominent role in the near future.

12. ACKNOWLEDGMENTS

I would like to express my deep appreciation to Prof. Helmut Sobieczky whose pioneering research on transonic shock-free flow field design has sparked my interest in the general field of aerodynamic shape design. Mr. Robert Kampia and Ms. Suzanne Condon have helped me generously during the final preparation of the manuscript. My thanks to them and to Apple Computer, Inc., for the donated equipment that we used.

13. REFERENCES

1. Proceedings of the International Conference on Inverse Design Concepts in Engineering Sciences (ICIDES-I), ed. G.S. Dulikravich, Aero. Eng. Dept., Univ. of Texas, Austin, TX, Oct. 17-18, 1984.
2. Proceedings of the International Conference on Inverse Design Concepts and Optimization in Engineering Sciences (ICIDES-II), ed. G. S. Dulikravich, Aero. Eng. Dept., Penn State Univ., University Park, PA, Oct. 26-28, 1987.
3. Proceedings of the AGARD Specialist's Meeting on Computational Methods for Aerodynamic Design (Inverse) and Optimization, ed. J.W. Sloof, Loen, Norway, May 24-25, 1989.
4. Voigt, R. G., "Requirements for Multidisciplinary Design of Aerospace Vehicles on High Performance Computers," ICASE Report No. 89-70, Sept. 1989.
5. Slooff, J. W., "Computational Methods for Subsonic and Transonic Aerodynamic Design," Proceedings of ICIDES-I, ed. G.S. Dulikravich, Univ. of Texas, Austin, TX, Oct. 17-18, 1984, pp. 1-68.
6. Sobieczky, H., "Research on Inverse Design and Optimization in Germany", Appl. Mech. Rev., vol. 41, no. 6, June 1988, pp. 217-238.
7. Chin, W. C., "Class of Shock-Free Airfoils Producing the Same Surface Pressure", AIAA J. of Aircraft, Vol.17, No. 4, April 1980, pp. 286-288.
8. Volpe, G. and Melnik, R.E. "A Method for Designing Closed Airfoils", AIAA paper 85-5023 presented at the 3rd Applied Aerodynamics Conference, Colorado Springs, CO, Oct. 14-16, 1985.
9. Zhu, Z. and Sobieczky, H., "An Engineering Approach for Nearly Shock-Free Wing Design", Proceedings of the Internat. Conf. on Fluid Mech., Beijing, China, July 1987.

10. Ives, D. C., "Inverse and Hybrid Compressor Cascade Design Methods", Proceedings of ICIDES-I, ed. G.S. Dulikravich, Univ. of Texas, Austin, TX, Oct. 17-18, 1984, pp. 555-572.
11. Papailiou, K., "An Investigation on Le Foll's Method used for Blade Optimization Based on Boundary Layer Concepts," paper presented at the XXth International Astronautical Congress, August 1969.
12. Citavy, J., "Two-Dimensional Compressor Cascades With Optimum Velocity Distribution Over the Blade," Journal of Engineering for Power, January 1975, pp. 101-110.
13. Lekoudis, S.G., Sankar, N.L., and Radwan, S.F., "A Method for Designing Three-Dimensional Configurations With Prescribed Skin Friction," Journal of Aircraft, Vol. 21, No. 11, Nov. 1984, pp. 924-926.
14. Lekoudis, S.G., Sankar, N.L., and Malone, J.B., "The Application of Inverse Boundary Layer Methods to the Three-Dimensional Viscous Design Problem," Commun. in Appl. Num. Meth., Vol. 2, No. 1, Jan.-Feb. 1986, pp. 57-61.
15. Dulikravich, G. S., "A Criteria for Surface Pressure Specification in Aerodynamic Shape Design," AIAA paper 90-0124 presented at the 28th Aerospace Sciences Meeting, Reno, Nevada, January 8-11, 1990.
16. Taverna, F., "Advanced Airfoil Design for General Aviation Propellers," AIAA paper 83-1791 presented at the AIAA Applied Aerodynamics Conference, Danvers, MA, July 13-15, 1983.
17. Tranen, T., "A Rapid Computer Aided Transonic Airfoil Design Method," McDonnell Douglas Corporation Report No. MDC A2584, Dec. 31, 1973.
18. Soinne, E., and Laine, S., "An Inverse Boundary Element Method for Single Component Airfoil Design," Journal of Aircraft, Vol. 22, No. 6, June 1985, pp. 541-543.
19. Garabedian, P., and McFadden, G., "Design of Supercritical Swept Wings," AIAA Journal, Vol. 20, No. 3, March 1982, pp. 289-291.
20. Malone, J. B., Narramore, J. C., and Sankar, L. N., "An Efficient Airfoil Design Method Using the Navier-Stokes Equations," AGARD Specialists' Meeting on Computational Methods for Aerodynamic Design (Inverse) and Optimization, Loen, Norway, May 22-23, 1989.
21. Fray, J. M. J., Slooff, J. W., Boerstoel, J. W., and Kassies, A., "Design of Transonic Airfoils with Given Pressure, Subject to Geometric Constraints," National Aerospace Laboratory NLR, Amsterdam, The Netherlands, July 13, 1984.
22. Giles, M. B., and Drela, M., "Two-Dimensional Transonic Aerodynamic Design Method," AIAA Journal, Vol. 25, No. 9, September 1987, pp. 1199-1206.
23. Hassan, A. A., "A Viscous-Inviscid Coupling Method for the Design of Low Reynolds Number Airfoil Sections," Proceedings of the Conference on Low Reynolds Number Airfoil Aerodynamics, June 1985, pp. 53-63.
24. Hirose, N., Takanashi, S., and Kawai, N., "Transonic Airfoil Design Procedure Utilizing a Navier-Stokes Analysis Code," AIAA Journal, Vol. 25, No. 3, March 1987, pp. 353-359.
25. Kennedy, J. L., and Marsden, D. J., "A Potential Flow Design Method for Multicomponent Airfoil Sections," Journal of Aircraft, Vol. 15, No. 1, January 1978, pp. 47-52.
26. Jacquotte, O.-P., "A Finite Element Inverse Method for the Design of Turbomachinery Blades," presented at the 7th International Conference "Finite Element Methods in Flow Problems," Huntsville, Alabama, April 3-7, 1988.
27. Gelder, T. F., Moore, R. D., Sanz, J. M., and McFarland, E. R., "Wind Tunnel Turning Vanes of Modern Design," AIAA paper 86-0044 prepared for the Twenty-fourth Aerospace Sciences Meeting, Reno, Nevada, January 6-8, 1986.
28. Tong, S. S., and Thompkins, Jr., W. T., "A Design Calculation Procedure for Shock-free or Strong Passage Shock Turbomachinery Cascades," ASME 27th Gas Turbine Conference, London, England, April 18-22, 1982.
29. Miton, H. H., "Properties of a Space-wise Periodic Flow Application to Flow Computation and Design for Blade Cascades," Communications in Applied Numerical Methods, Vol. 2, No. 1, Jan.-Feb. 1986, pp. 101-112.
30. Meauze, G., "An Inverse Time Marching Method for the Definition of Cascade Geometry," ASME paper 81-GT-167 presented at the International Gas Turbine Conference and Products Show, Houston, Texas, March 9-12, 1981.
31. Meauze, G., "On the Use of Inverse Modes of Calculation in Two-dimensional Cascades and Ducts," Communications in Applied Numerical Methods, Vol. 2, no. 1, Jan.-Feb. 1986, pp. 73-81.
32. Chen, N.-X. and Zhang, F.-X., "A Generalized Numerical Method for Solving Direct, Inverse and Hybrid Problems of Blade Cascade Flow by Using Streamline-Coordinate Equation", ASME paper 87-GT-29, Anaheim, CA, June 1987.
33. Huang, C.-Y. and Dulikravich, G.S., "Stream Function and Stream-Function-Coordinate (SFC) Formulation for Inviscid Flow Field Calculations".

- Computer Meth. in Appl. Mech. and Eng., Vol. 59, 1986, pp.155-177.
34. Stanitz, J.D., "A Review of Certain Inverse Methods for the Design of Ducts With 2- or 3-Dimensional Potential Flow", Appl. Mech. Rev., Vol. 41, no. 6, June 1988, pp. 217-238.
35. Cedar, R. D., and Stow, P., "The Role of a Mixed Design and Analysis Method in a Turbomachinery Blade Design System," Communications in Applied Numerical Methods, Vol. 2, No. 1, Jan.-Feb. 1986, pp. 91-99.
36. Ribaut, M., and Martin, D., "A Quasi Three-dimensional Inverse Design Method Using Source and Vortex Integral Equations," Communications in Applied Numerical Methods, Vol. 2, No. 1, Jan.-Feb. 1986, pp. 63-72.
37. Zhengming, W., "A Method of Aerodynamic Design of Blades in Quasi-Three-Dimensional Calculation of Turbomachine," ASME paper 86-GT-192 presented at the International Gas Turbine Conference and Exhibit, Dusseldorf, West Germany, June 8-12, 1986.
38. Xiaolu, Zhao, and Lisen, Qin, "An Approximate 3-D Aerodynamic Design Method for Centrifugal Impeller Blades," ASME paper 89-GT-73 presented at the Gas Turbine and Aeroengine Congress and Exposition, Toronto, Canada, June 4-8, 1989.
39. Gong, Yifang, and Cai, Ruixian, "3D Mean-Stream-Line Method--A New Engineering Approach to the Inverse Problem of 3D Cascade," ASME paper 89-GT-48 presented at the Gas Turbine and Aeroengine Congress and Exposition, Toronto, Canada, June 4-8, 1989.
40. Couaillier, V. and Veuillot, J.P., "Inverse Method for the Euler Equations", Proceedings of ICIDES-II, ed. G.S. Dulikravich, Penn State Univ., University Park, PA, Oct. 26-28, 1987, pp. 131-146.
41. Zannetti, L., di Torino, P., and Ayele, T. T., "Time Dependent Computation of the Euler Equations for Designing Fully 3D Turbomachinery Blade Rows, Including the Case of Transonic Shock Free Design," AIAA paper 87-0007 presented at the 25th Aerospace Sciences Meeting, Reno, Nevada, January 12-15, 1987.
42. Miyazaki, T., and Hirayama, N., "A Theoretical Solution of Three-Dimensional Flows in Subsonic, Transonic and Supersonic Turbomachines: An Exact Solution and Its Numerical Method," ASME paper 86-GT-111 presented at the 31st Internat. Gas Turbine Conf. and Exhibit, Dusseldorf, Germany, June 1986.
43. Borges, J. E., "A Three Dimensional Inverse Method in Turbomachinery; Part 1--Theory," ASME paper 89-GT-136 presented at the Gas Turbine and Aeroengine Congress and Exposition, Toronto, Canada, June 4-8, 1989.
44. Borges, J. E., "A Three Dimensional Inverse Method in Turbomachinery; Part 2--Experimental Verification," ASME paper 89-GT-137 presented at the Gas Turbine and Aeroengine Congress and Exposition, Toronto, Canada, June 4-8, 1989.
45. Hawthorne, W.R. and Tan, C.S., "Design of Turbomachinery Blading in Three-Dimensional Flow by the Circulation Method; A Progress Report", Proceedings of ICIDES-II, ed. G.S. Dulikravich, Penn State Univ., University Park, PA, Oct. 26-28, 1987, pp. 207-226.
46. Ghaly, W. S., "A Design Method for Turbomachinery Blading in Three-Dimensional Flow," International Journal for Numerical Methods in Fluids, Vol. 10, 1990, pp. 179-197.
47. Takanashi, S., "Iterative Three-Dimensional Transonic Wing Design Using Integral Equations," Journal of Aircraft, Vol. 22, No. 8, August 1985, pp. 655-660.
48. Gally, T. A., and Carlson, L. A., "Transonic Wing Design Using Inverse Methods in Curvilinear Coordinates," Journal of Aircraft, Vol. 25, No. 11, November 1988, pp. 1009-1017.
49. Hazarika, N., "An Efficient Inverse Method for the Design of Blended Wing-Body Configurations," Ph.D. thesis, Aero. Eng. Dept., Georgia Institute of Technology, June 1988.
50. Fornasier, L., "An Iterative Procedure for the Design of Pressure-Specified Three-Dimensional Configurations at Subsonic and Supersonic Speeds by Means of a Higher-Order Panel Method", AGARD Specialists' Meeting on Computational Methods for Aerodynamic Design (Inverse) and Optimization, Loen, Norway, May 22-23, 1989.
51. Meauze, G., and Fourmaux, A., "A Coupled Inverse-Inverse Method for Over-Expanded Supersonic Nozzles," paper 109 presented at the 7th ISABE International Symposium on Air Breathing Engines, Beijing, People's Republic of China, September 2-6, 1985.
52. Ives, D. C., "Supercritical Inlet Design," AIAA paper 83-1866 presented at the AIAA Applied Aerodynamics Conference, Danvers, Massachusetts, July 13-15, 1983.
53. Zedan, M. F., and Dalton, C., "The Inverse Method Applied to a Body of Revolution with an

- Extended Favourable Pressure Gradient Forebody," Communications in Applied Numerical Methods, Vol. 2, No. 1, Jan.-Feb. 1986, pp. 113-119.**
54. Boerstoel, J.W. and Huizing, G.H., "Transonic Airfoil Design by an Analytic Hodograph Method", AIAA paper 74-539, 1974.
55. Hobson, D.E., "Shock-Free Transonic Flow in Turbomachinery Cascades", Univ. of Cambridge, UK, CUED/A Turbo/TR 65, 1974.
56. Bauer,F., Garabedian, P., Korn, D. and Jameson, A., "Supercritical Wing Sections 1,2,3", Lecture Notes in Economics, Math. Syst., No. 66, 108, 150, Springer Verlag, Berlin, 1972, 1975, 1977.
57. Schrier, S., "Compressible Flow", John Wiley & Sons, New York, 1982.
58. Sobieczky, H., Fung, K.-Y., Seebass, R.A., Yu, N.J., "New Method for Designing Shock-Free Transonic Configurations", AIAA Journal, Vol.17, No. 7, 1979.
59. Sobieczky, H., "Related Analytical, Analog and Numerical Methods in Transonic Airfoil Design", AIAA paper 79-1980, Williamsburg, VA, June 1979.
60. Nakamura, M., "A Method for Obtaining Shockless Transonic Flows past Two-Dimensional Airfoils whose Profiles are Partially Modified from a Given Arbitrary Profile," Trans. Japan Soc. Aero. Space Sci., Vol. 23, No. 62, Feb. 1981, pp. 195-213.
61. Hassan, A., Sobieczky, H., and Seebass, A. R., "Subsonic Airfoils with a Given Pressure Distribution," AIAA Journal, Vol. 22, No. 9, September 1984, pp. 1185-1191.
62. Dulikravich, D. S., and Sobieczky, H., "Shockless Design and Analysis of Transonic Cascade Shapes," AIAA Journal, Vol. 20, No. 11, November 1982, pp. 1572-1578.
63. Dulikravich, G.S. and Sobieczky, H., "CAS22-FORTRAN Program for Fast Design and Analysis of Shock-Free Airfoil Cascades", NASA CR 165596, 1982.
64. Sobieczky, H. and Dulikravich, G.S., "A Computational Design Method for Turbomachinery Cascades", ASME paper 82-GT-117, London, UK, April, 1982.
65. Dulikravich, G.S. and Sobieczky, H., "Design of Shock-free Compressor Cascades Including Viscous Boundary Layer Effects", ASME paper 83-GT-134, Phoenix, AZ, March 27-31, 1983.
66. Prince, T. C., and Beauchamp, P. P., "Shock-free Transonic Rotor Design," Communications in Applied Numerical Methods, Vol. 2, No. 1, Jan.-Feb. 1986, pp. 21-27.
67. Fung, K.-Y., Sobieczky, H., and Seebass, R., "Shock-Free Wing Design," AIAA Journal, Vol. 18, No. 10, October 1980, pp. 1153-1158.
68. Yu, N. J., "Efficient Transonic Shock-Free Wing Redesign Procedure Using a Fictitious Gas Method," AIAA Journal, Vol. 18, No. 2, February 1980, pp. 143-148.
69. Raj, P., and Miranda, L. R., "A Cost-Effective Method for Shock-Free Supercritical Wing Design," Journal of Aircraft, Vol. 19, No. 4, April 1982, pp. 283-289.
70. Silver, B., and Ashley, H., "Optimization Techniques in Aircraft Configuration Design," Department of Aeronautics and Astronautics, Stanford University, SUDAAR No. 406, June 1970.
71. Reneaux, J., and Thibert, J.-J., "The Use of Numerical Optimization for Airfoil Design," AIAA paper 85-5026 presented at the AIAA 3rd Applied Aerodynamics Conference, Colorado Springs, CO, October 14-16, 1985.
72. Sanger, N. L., "The Use of Optimization Techniques to Design Controlled Diffusion Compressor Blading," NASA Technical Memorandum 82763, April 1982.
73. Ormsbee, A. I., and Chen, A. W., "Multiple Element Airfoils Optimized for Maximum Lift Coefficient," AIAA J., Vol. 10, No. 12, Dec. 1972, pp. 1620-1624.
74. Misegades, K. P., "Optimization of Multi-Element Airfoils," Von Karman Institute for Fluid Dynamics, Belgium, Project Report 1980-5, June 1980.
75. Cosentino, G. B., "Numerical Optimization Design of Advanced Transonic Wing Configurations," AIAA paper 85-0424 presented at the AIAA 23rd Aerospace Sciences Meeting, Reno, NV, January 14-17, 1985.
76. Lock, R. C., "Comment on 'Numerical Optimization Design of Advanced Transonic Wing Configurations'," Journal of Aircraft, Vol. 24, No. 8, August 1987, pp. 575-576.
77. Huddleston, D. H., and Mastin, C. W., "Optimization of Aerodynamic Designs Using Computational Fluid Dynamics," Proceedings of the 7th International Conference on Finite Element Methods in Flow Problems, ed. Chung, T.J. and Karr, G.R., Univ. of Alabama in Huntsville Press, April 3-7, 1989, pp. 899-907.

78. Madabhushi, R.K., Levy, R. and Pinkus, S.M., "Design of Optimum Ducts Using an Efficient 3-D Viscous Computational Flow Analysis", Proceedings of ICIDES-II, ed. G.S. Dulikravich, Penn State Univ., University Park, PA, Oct. 26-28, 1987, pp.147-166.
79. Ghielmi, L., Marazzi, R. and Baron, A., "A Tool for Automatic Design of Airfoils in Different Operating Conditions", AGARD Specialists' Meeting on Computational Methods for Aerodynamic Design (Inverse) and Optimization, Loen, Norway, May 22-23, 1989.
80. Sharp, H. T., and Sirovich, L., "Constructing a Continuous Parameter Range of Computational Flows," AIAA Journal, Vol. 27, No. 10, 1989, pp. 1326-1331.
81. Rizk, M. H., "The Single-Cycle Scheme: A New Approach to Numerical Optimization," AIAA Journal, Vol. 21, No. 12, Dec. 1983, pp. 1640-1647.
82. Rizk, M. H., "A New Approach to Optimization for Aerodynamic Applications," Journal of Aircraft, Vol. 20, No. 1, Jan. 1983, pp. 94-96.
83. Rizk, M. H., "Application of the Single-Cycle Optimization Approach to Aerodynamic Design," Jour. of Aircraft, Vol. 22, No. 6, June 1985, pp. 509-515.
84. Angrand, F., "Optimum Design for Potential Flows," International Journal for Numerical Methods in Fluids, Vol. 3, 1983, pp. 265-282.
85. Gu, Chuan-gang, and Miao, Yong-miao, "Blade Design of Axial-Flow Compressors by the Method of Optimal Control Theory--Physical Model and Mathematical Expression," ASME paper 86-GT-183 presented at the 31st Internat. Gas Turbine Conf. and Exhibit, Dusseldorf, Germany, June 1986.
86. Gu, Chuan-gang, and Miao, Yong-miao, "Blade Design of Axial-Flow Compressors by the Method of Optimal Control Theory--Application of Pontryagin's Maximum Principles, a Sample Calculation and Its Results," ASME paper 86-GT-182 presented at the 31st Internat. Gas Turbine Conf. and Exhibit, Dusseldorf, Germany, June 1986.
87. Jameson, A., "Aerodynamic Design Via Control Theory," ICASE Report No. 88-64, 1988.

ARBITRARY BLADE SECTION DESIGN BASED ON VISCOUS CONSIDERATIONS

by

K.D.Papailiou and B.Bouras
Thermal Turbomachinery Lab.
National Technical University of Athens
PO. Box 64069, 15710 Athens
Greece

1. Introduction

The material presented in this work can be used for different types of design. Furthermore, a design process is one full of constraints and compromises, so that one cannot pretend that any one of the present day theories may produce the optimum optimorum. What the designer desires to possess, however, is a reliable and flexible tool, which can help him evaluate the situation at hand. In addition, it is necessary that this tool be rapid enough with a reasonably fast response, when an interactive computing procedure is used.

The objective of the work presented here, was to create a tool for optimizing the viscous behaviour of the flow, particularly in view of designing arbitrary compressor and turbine blade sections for Mach numbers, which may reach the transonic regime.

The requirement of computing speed rules out for the moment design tools, which compute directly unsteady flow. On the other hand, although inverse methods utilizing the Navier-Stokes equations start making their appearance, still the two-zone hypothesis, which divides the flow into an inviscid (external) and a viscous part, is by far the most practical. This fact will be made more explicit and explained further in the present lecture. The two-zone hypothesis will be employed here and the flow will be considered for a purely two-dimensional case, as presented schematically in figure (1.1). In addition, it will be considered steady and the approximation presented in Lock, Firmin and East's [1.1], [1.2], [1.3] papers will be adopted. This approximation seems to be a good compromise, allowing the computation of relatively extended separated flow regions, without important additional computational labor. Details may be found in the cited references. A general description will be presented in Chapter 2 and some details will be given, when the equations will be presented.

The importance of centrifugal and Coriolis force effects on turbulence is vital in turbomachinery applications. The same goes for the variation of the streamtube width along meridional distance. The corresponding effects will be taken into account in the present theory. In addition, one may remark that not taking into account these effects, would rule out application of this methodology to radial machines, while, for axial machines, there would be too much room left for interpretation.

Regardless of how the optimization problem is set and what constraints are imposed, two parameters are playing the most important role. The section circulation (or the peripheral force) and the total pressure losses. Then,

constraints such as a desired low loss incidence interval (in order to ensure enough margin for stall) or an adequate blade thickness in the proper places and a convenient position of the center of gravity of the blade section (in order to ensure the desired mechanical properties) are considered separately, once a blade section shape is established. Consequently, two different computing tools are necessary, in order to do the job. One, which deals with the viscous effects and another one which deals with the inviscid external flow.

People are familiar with the inviscid external flow computational tool. We shall adopt here an inverse one, which produces the blade section shape, given the velocity distribution along the two blade surfaces. Contrary to other practices, we shall adopt an inverse viscous flow methodology. It will give us, as we shall see, the possibility to optimize, at the same time, the viscous behaviour.

The inverse procedures will allow us a maximum possible flexibility. However, it is necessary to stress that a direct (analysis) method is necessary, in order to complete an optimization procedure, both inviscid and viscous. In fact, coupling of the two (inverse and direct) gives, in our opinion, the best results.

Considering the viscous flow problem, it is essential to state from the very beginning that the inverse procedure relies heavily upon the capability of the corresponding direct, in order to reproduce accurately the various practical situations. In addition, all semi-empirical information required to ensure the mathematical closure of the computational procedure is common to both the "direct" and "inverse" viscous calculations.

Unfortunately, because of space limitations, it is impossible to give all the details of the method. However, an extended version has been, fortunately, presented in ref.[3.23]. Reference will be continuously made there. Only more recent developments will be mentioned as extensively as possible. These developments, although other people from the Lab have assisted as well, have been essentially achieved by Kallas[3.30] and, especially, Bouras[3.32].

Finally, for economy of space, all explaining of symbols is presented in the corresponding list, in Appendix A1.

2. Description of the Two-Zone Model

The separation of the flow into an inviscid and a viscous part will follow the model described, as said above, in the paper of Lock and Firmin[1.1]. This model relies heavily on the theoretical development performed by East[1.1]. A

short description of the model follows.

The model is schematically presented in figure (2.1a). The coordinate system used (s, n) is the one described in the same figure. The external inviscid flow (it is called Equivalent Inviscid Flow by Lock and Firmin) quantities are allowed to vary across the shear layer (see figures (2.1b) and (2.1c)). This variation is caused by both the solid wall curvature K_w and the additional curvature due to the shear layer presence.

Within this model, there exist two possibilities for obtaining at distance δ the matching of the External Inviscid (EIF) and the Real Viscous Flow (RVF). The first one consists of displacing the solid surface by δ_{1B} , when δ_{1B} is defined by the equation

$$\int_{\delta_1}^{\delta} \rho_e W_{se} dn = \int_0^{\delta} \rho W_s dn \quad (2.1)$$

The line $n=\delta_{1B}$ is, then, a streamline. The second one stems from distributing sources along the solid surface, of strength

$$\rho_e W_{ne} = \frac{d}{ds} (\rho_e W_{se} \delta_1) \quad (2.2)$$

The definition of the corresponding displacement thickness δ_{1A} is

$$\rho_e W_{se} \delta_{1A} = \int_0^{\delta} (\rho_e W_{se} - \rho W_s) dn \quad (2.3)$$

In practice the difference between δ_{1A} and δ_{1B} is negligible, expressed by the following relation

$$\frac{\delta_{1A} - \delta_1}{\delta_{1B}} = \frac{1}{2} (1 - M_w^2) K^* \delta_1 \quad (2.4)$$

where K^* is the total (effective) curvature due to both the solid wall and the shear layer presence. It is expressed as

$$K^* = K_w + \frac{d^2 \delta_1}{ds^2} = K_w + \frac{d}{ds} \left(\frac{W_n}{W_s} \right) \quad (2.5)$$

In the following, we shall use only δ_{1A} , adopting the second flow model and we shall drop the suffix A.

Looking at figure (2.1c), it is possible to express the various static pressure differences, appearing there, utilizing the flow equations. The accepted approximate expressions for these differences [1.2] are listed below

$$\frac{P_w - P}{\rho_e W_{se}^2} = K^*(\delta_1 + \delta_2) \quad (2.6)$$

$$\frac{P_e - P_w}{\rho_e W_{se}^2} = K^* \delta \quad (2.7)$$

from equations (2.6) and (2.7) follows that

$$\frac{P_w - P_e}{\rho_e W_{se}^2} = K^*(\delta_1 - \delta_2) \quad (2.8)$$

The viscous shear layer computational procedure, which will be described later, utilizes as external velocity distribution the one given by $W_{se}(s)$. What the present flow model tells us, up to now, is that, in order to obtain $W_{se}(s)$, we have to perform the external inviscid flow calculation, introducing at the wall a normal velocity component W_{new} expressed by equation (2.2). Once the computation has converged, then comparison with experimental results will be made using the pressure distribution $P_w(s)$, which will be issued from $P_w(s)$ utilizing equation (2.6). On the other hand, the model tells us that, in order to compare the results of a shear layer calculation method with experiment, one has to deduce $W_{new}(s)$ starting from P_w and P_{te} , deduce P_{new} from equation (2.6) and utilize W_{new} in order to deduce from P_{te} , P_{ew} , T_{te} and W_{new} the value of W_{se} .

To the above remarks one has to add that terms containing the curvature K^* appear in the equations, as we shall see later, and that the corresponding expression for the integral

$$\int (P_w - P) dn \text{ is given as} \\ 0 \\ \int_0^{\delta} (P_w - P) dn = \frac{1}{2} \rho_e W_{se}^2 K^* (\delta_1 + \delta_2)^2 + \\ 0 \\ + \int_0^{\delta} \rho W_n^2 dn \quad (2.9)$$

noting that its influence is of lesser significance to that due to the pressure differences introduced above.

A second and equally important effect is introduced, when the present model is applied to the wake, as well as in the region of the trailing edge. This effect is described below, considering the schematic representation of figure

(2.1d). We shall apply our model, now, considering the dividing streamline, which is issued by the inviscid flow field. In the theoretical development underlying the model it was only assumed that $W_{aw}=0$, so that the same expressions are valid when the dividing streamline is considered. Applying equation (2.2) for the upper and lower part of the dividing streamline, one can get the following simplified expression for the jump in W_{se} across it

$$\Delta W_{se} = \frac{1}{\rho_e} \frac{d}{ds} (\rho_e W_{se} \delta_1)$$

where

$$\begin{aligned} W_{se} &= \frac{1}{2} (W_{se_u} + W_{se_l}); \quad \rho_e = (\rho_{eu} + \rho_{el}) \\ \delta_1 &= \delta_{eu} + \delta_{el} \end{aligned} \quad (2.10)$$

The suffix w here denotes conditions at the diving streamline. Applying the situation described in figure (2.1c) to the wake region, we get a static pressure distribution presented schematically in figure (2.1e). Following the same reasoning one can get the jump in the velocity component W_{sew} across the dividing streamline as

$$\begin{aligned} \Delta W_{se} &= [K_w W_{se} (\delta_{eu} + \delta_{el}) + K_l W_{se} (\delta_{el} + \delta_{eu})] = \\ &= -K_w W_{se} (\delta_{eu} + \delta_{el}) \end{aligned} \quad (2.11)$$

or, for the static pressure,

$$\begin{aligned} \Delta p_e &= p_{eu} - p_{el} = [K_w p_{eu} W_{se}^2 (\delta_{eu} + \delta_{el}) + \\ &+ K_l p_{el} W_{se}^2 (\delta_{el} + \delta_{eu})] \end{aligned} \quad (2.12)$$

The above wake analysis tells us that the inviscid calculation used must be capable of introducing combined source and vortex sheets along the dividing streamline. It also provides the corresponding jump conditions in static pressure and velocity components, as well.

On the other hand, at the trailing edge itself, provided that it is not rounded, the static pressure of the RVP must be the same for both the upper and lower surfaces, or the upper and lower sides of the dividing streamline (that is whether the trailing edge is approached from upstream or from downstream). This situation presented schematically in figure (2.1f) and implied, also, in figure (2.1e), results in a smaller circulation value, than the one which corresponds to the equality of inviscid static pressures (and velocities) at the trailing edge, applied usually. In fact, this replaces

the Kutta condition for viscous flow.

An alternative way of imposing the Kutta condition is to respect the following equality

$$[P_{e,u}]_{n=\delta_1+\delta_2} = [P_{e,l}]_{n=\delta_1+\delta_2} \quad (2.13)$$

This condition is more convenient when the displaced by δ_1 surface is utilized during the inviscid calculation. In this last case, when the inviscid static pressure must be imposed at distance δ_1 from the solid surface, the following equation may be used

$$P_w = P_{eu} - K^* p_{eu} \frac{W_{se}^2}{\delta_1} \delta_2 \quad (2.14)$$

Having related the inviscid external flow field with the viscous part, we shall now proceed in describing the methods used for calculating each one of them. When these calculations have been established, we shall return back to examine how the matching together is done, utilizing what has been said in this section.

3. The Development of the Canonical Equations

The basic equations are the same for both direct and inverse computations. The additional relations, which take the form of a semi-empirical frame and ensure the mathematical closure of the problem, are, as well, the same for both direct and inverse formulations.

In this Chapter a brief description of the development of the equations will be presented. Details may be found for the development of the method upto 1981 in references [3.1] to [3.23]. The last reference summarizes the work performed until then. Additional work that has been done since 1981 may be found in references [3.24] to [3.32].

The basic equations are considered in a rotating frame of reference. It is, then, easy to deduce from them the equations valid for a stationary frame. They will be considered for turbulent flow. For laminar flow, Stewartson's transformation^[3.35] is used in order to place the problem on an equivalent incompressible plane. It can be proved that this transformation is valid for a rotating frame of reference, as well.

An axially symmetric orthogonal curvilinear system of coordinates is used (see figure (3.1)). It is assumed that the m -lines of the system coincide with the streamlines of the real flow. The continuity equation, the two momentum equations and the energy equation are written in this system. In addition to those, the turbulent kinetic energy equation is written, in order to be used for turbulent flow.

The above mentioned equations are simplified in the following way: (a) The stress terms containing the coordinate system curvatures, as well as the terms

containing the derivatives of stresses in the m -direction (parabolization) are neglected. However, all normal fluctuation terms are conserved.

(b) Some simplifications are applied, concerning the inertia terms of the normal momentum equation. However, the main effect of these terms which contributes to the variation of the static pressure in the normal to the flow direction is retained.

(c) Following Lock and Firmin^[1,2] a representative curvature is taken into account for each position (m). It is partly to this curvature that the variation of the static pressure along a normal to the flow direction is accounted for. (d) The pressure term in the turbulent kinetic energy equation is neglected.

At this level, the production term in the streamwise momentum equation for turbulent flow is substituted by the corresponding terms appearing in the turbulent kinetic energy equation. This last equation is not used any further.

When these simplifications are performed, the equations are written for the external inviscid and the real flow. They are then subtracted from each other, forming the corresponding deficit equations and are integrated along the normal to the streamwise direction.

After some rearrangement, the following equations are formulated:

(a) The streamwise momentum integral equation

$$\frac{d}{ds} \left(\rho_e R_w W_{se} \delta_2 \right) + \rho_e R_w W_{se} \delta_1 = \frac{dW_{se}}{ds} - \frac{\omega^2 R_w}{2} \frac{R_w}{2} \frac{d}{ds} \left[\frac{\rho_e W_{se} K^* (\delta_1 + \delta_2)^2}{w} \right] + \frac{d}{ds} \left[\frac{\rho_e R_w W_{se}}{w} \int_0^\delta \frac{\rho W_b^2 - \rho W_n^2}{\rho_e W_{se}^2} dn \right] + R_w \tau_{se} + H.O.T.'s \quad (3.1)$$

(b) The energy integral equation

$$\frac{d}{ds} \left(\rho_e R_w W_{se} \delta_3 \right) + \rho_e R_w W_{se} (\delta_1 - \delta_{1k}) = \frac{dW_{se}}{ds} - 2 \rho_e R_w W_{se} \left(\delta_1 - \delta_{1k} \right) \frac{d}{ds} \left(\frac{\omega^2 R_w}{2} \right) = 2 R_w \int_0^\delta Ddn + \frac{d}{ds} \left[\frac{\rho_e R_w W_{se}}{w} \int_0^\delta \frac{\rho W_b (3W_b^2 - W_n^2 + W_u^2)}{\rho_e W_{se}^3} dn \right] + H.O.T.'s \quad (3.2)$$

In the above $\int_0^\delta Ddn$ is the dissipation integral.

During the development, the following relation has been deduced from the normal momentum equation, which describes, the difference between the real and inviscid static pressures

$$\begin{aligned} & \int_0^\delta (\rho_e - \rho) dn = \frac{1}{2} \frac{\rho_e}{w} \frac{W_{se}^2}{w} K^* (\delta_1 + \delta_2)^2 + \\ & \int_0^\delta \rho W_b^2 dn + H.O.T.'s \end{aligned} \quad (3.3)$$

The above relation was introduced into the streamwise momentum equation in order to render it in the form of equation (3.1). The same goes for equation (2.2), which was used and accounts, as well, for the coupling of the external inviscid and the real viscous flow.

We shall introduce now the dissipation factor C_D

$$C_D = \frac{1}{\frac{1}{2} \frac{\rho_e}{w} \frac{W_{se}^2}{w} K^* (\delta_1 + \delta_2)^2} \int_0^\delta Ddn \quad (3.4)$$

and the skin friction coefficient

$$C_f = \frac{2 \tau_{se}}{\rho_e W_{se}} \quad (3.5)$$

We shall incorporate, as well, for convenience, the normal fluctuation terms in the shear layer thicknesses in the following way

$$\delta_2^* = \delta_2 - \int_0^\delta \frac{\rho W_b^2 - \rho W_n^2}{\rho_e W_{se}^2} dn \quad (3.6)$$

$$\delta_3^* = \delta_3 - \int_0^\delta \frac{\rho W_b (3W_b^2 - W_n^2 + W_u^2)}{\rho_e W_{se}^2} dn \quad (3.7)$$

Consequently, our equations, leaving out the Higher Order Terms (H.O.T.'s) become for compressible flow

$$\begin{aligned} & \frac{1}{\rho_e R_w W_{se}} \frac{d}{ds} \left(\frac{\rho_e R_w W_{se}}{w} \delta_2^* \right) + \frac{\delta_1}{W_{se}} \frac{dW_{se}}{ds} = \\ & \frac{\delta \rho}{w^2} \frac{d}{ds} \left(\frac{\omega^2 R_w}{2} \right) + \frac{C_f}{2} - \frac{1}{2 \rho_e W_{se}^2} \\ & \frac{d}{ds} \left[\frac{\rho_e W_{se}}{w} K^* (\delta_1 + \delta_2)^2 \right] \end{aligned} \quad (3.8)$$

$$\begin{aligned} & \frac{1}{\rho_e R_e W_{se}} \frac{d}{ds} (\rho_e R_e W_{se} \delta_3^*) + \\ & + \frac{(\delta_1 - \delta_{ik})}{W_{se}} \frac{d^2 W_{se}}{ds^2} = \\ & = \frac{2(\delta_1 - \delta_{ik})}{W_{se}} \frac{d}{ds} \left(\frac{\omega^2 R_e}{2} \right) + C_D \quad (3.9) \end{aligned}$$

and for the incompressible flow

$$\begin{aligned} & \frac{1}{R_e W_{se}} \frac{d}{ds} (R_e W_{se} \delta_2^*) + \frac{\delta_{ik}}{W_{se}} \frac{d W_{se}}{ds} = \\ & = \frac{C_f}{2} - \frac{1}{2 W_{se}} \frac{d}{ds} [W_{se} K^* (\delta_1 + \delta_2)^2] \quad (3.10) \\ & \frac{1}{R_e W_{se}} \frac{d}{ds} (R_e W_{se} \delta_3^*) = C_D \quad (3.11) \end{aligned}$$

The above equations hold for turbulent flow. The corresponding equations for laminar flow are derived easily by dropping the normal fluctuation terms and considering that C_f corresponds to the laminar shear stress. Note, that the inviscid pressure at the wall is given by the following equation:

$$\begin{aligned} & W_{se} \frac{d W_{se}}{ds} + W_{se} \frac{d W_{se}}{dn} = \frac{1}{\rho_e} \frac{dp_w}{ds} + \\ & + \frac{d(\omega^2 R^2/2)}{ds} + \text{Curvature Terms} \quad (3.12) \end{aligned}$$

We are ready, now, to develop the equations in their final form. To conserve printing space without losing the steps of this development, we shall describe below in some detail the development of the equations for the incompressible attached case. Then, we shall give the results for the general compressible case. Details of how these developments are realized may be found in reference [3.23].

The Development of the Attached Incompressible Boundary Layer Equations

We shall formulate our development neglecting the last term of equation (3.10). For this development new variables will be introduced and certain

assumptions will be made. The reason for introducing these new variables will be seen clearly later, while the assumptions will be justified when discussing the semi-empirical frame.

Our starting point will be equations (3.10) and (3.11) with the last term neglected in equation (3.10). We may introduce as a first step the kinetic energy dissipation

$$E = \rho \delta_3 \frac{W_{se}^3}{K} = \rho v R_e \frac{W_{se}^2}{2} \quad (3.13)$$

The part $\rho \delta_3 W_{se}^2/2$ of the above variable is an increasing function of distance, as the losses are increasing, when the shear layer is developing. Then, the energy integral equation (3.11) becomes

$$\frac{dE}{ds} = C_D \frac{ds}{\delta_3^*} \quad (3.14)$$

Taking $\delta_3 K = H_{32k} \delta_{2k}$ and introducing it to equation (3.13), differentiating and combining with the momentum integral equation (3.10) and using the definition $H_{12}^* = \delta_1^*/\delta_2^*$, one gets

$$\begin{aligned} & \frac{1}{H_{12}^* - 1} \frac{d H_{32k}^*}{ds} = \frac{1}{H_{12}^* - 1} \left[1 - \frac{C_f}{2 C_D} \right] \\ & \frac{d W_{se}}{E} = \frac{d W_{se}}{W_{se}} \quad (3.15) \end{aligned}$$

For unseparated shear layers the normal fluctuation terms influence in the energy equation can be neglected so the $H_{32k} = H_{32f}$. On the other hand, for unseparated flow the ratio $(H_{12k}-1)/(H_{12f}-1)$ can be taken constant and will be denoted as K . Finally, with a very good approximation H_{32k} will be taken to be a unique function of H_{2k} (the influence of the Reynolds number is neglected), so that one may introduce a new form factor L_k , as

$$dL_k = \frac{1}{H_{12k}-1} \frac{d H_{32k}}{H_{32k}} \quad (3.16)$$

remarking that the right hand side of equation (3.16) with the above mentioned assumption becomes a total differential. We shall introduce a new Reynolds number Re_4 as

$$Re_4 = Re_3 e^{2 L_k} \quad (3.17)$$

and its neperian logarithm

$$X = \ln Re_4 = \ln Re_3 + 2 L_k \quad (3.18)$$

We shall introduce, as well, the velocity logarithm q instead of the velocity as

$$q = \ln \frac{w_{\text{new}}}{w_{\text{ref}}} \quad (3.19)$$

and the position Reynolds number ϕ , instead of the arc length s , as

$$\phi = \int_0^s \frac{w_{\text{new}} ds}{v} \quad (3.20)$$

We shall, finally, introduce a grouping coefficient M , as

$$M = \frac{1}{H_{12k}-1} [1 - \frac{H_{12k} C_f}{2C_D}] \quad (3.21)$$

and, with the above definitions and assumptions, we shall rewrite equations (3.15) and (3.14) in the following form

$$KdL_k = +dq + KM \frac{dE}{E} \quad (3.22)$$

$$\frac{dE}{E} = C_D \frac{d\phi}{Re_3} \quad (3.23)$$

Differentiating equation (3.13) and using equation (3.22) in order to eliminate dq , one gets

$$(1+2KM) \frac{dE}{E} = \frac{dRe_3}{Re_3} + 2dL_k \quad (3.24)$$

Using the definition (3.18), one finally gets

$$(1+2KM) \frac{dE}{E} = dX \quad (3.25)$$

We have developed above various forms of equations, which will be used later in order to reveal some general properties of the shear layers. Before obtaining the final form of the equations, called sometimes canonical, it will be helpful to make some additional remarks. In the next Chapter the semi-empirical frame will be examined briefly. It is important to note that the semi-empirical frame will provide us not only with expressions for the variables appearing in our equations, but, also, with enough information to obtain closure. That is to say, as we have two equations available, the independent variables of our problem must be, as well, two. From the development made above it is apparent that the two independent variables chosen (for reasons which will be clear later) to characterize each shear layer section are L_k (as a form factor) and X (as a Reynolds number). Then $M=M(L_k, X)$ and $C_D=C_D(L_k, X)$, so that eliminating dE/E between equations (3.22) and (3.25) and between (3.23) and (3.25) we get the following two equations

$$dq = KdL_k - \frac{KM(L_k, X)}{1+2KM(L_k, X)} dX \quad (3.26)$$

$$d\phi = \frac{1}{(1+2KM)C_D L_k} dRe_3 \quad (3.27)$$

which relate the physical variables (q, ϕ) to the intrinsc variables (L_k, X) . Of course for laminar flows $K=1$. These are the canonic equations.

We shall regroup the shear layer properties in a slightly different manner for laminar and turbulent flows and we shall have:

(a) For the laminar case

$$\beta_l(L_k) = - \frac{M_l(L_k, X)}{1+2M_l(L_k, X)} \quad (3.28)$$

$$C_l(L_k) = C_{Dl}(L_k, X) e^{2L_k} \quad (3.29)$$

The corresponding equations will be

$$dq = dL_k + \beta_l dX \quad (3.30)$$

$$d\phi = \frac{d(Re_3)}{2C_l}$$

(b) For the turbulent case

$$\beta_t(L_k, X) = - \frac{kM_t(L_k, X)}{1+2kM_t(L_k, X)} \quad (3.31)$$

$$C_t(L_k, X) = C_{Dt}(L_k, X) e^{2L_k} \quad (3.32)$$

The corresponding equations will be

$$dq = dL_k + \beta_t dX$$

$$d\phi = \frac{dRe_3}{C_t} \quad (3.33)$$

The advantage of this formulation for laminar shear layers is that the coefficients depend upon only the form factor L_k , as follows from the semi-empirical frame. An attractive feature of equations (3.26), (3.27), (3.30) and (3.33) is that for the case of the inverse problem, for which $q(\phi)$ is calculated when $L_k(X)$ is given, the integration procedure is reduced to two quadratures.

The Form of the General Compressible Shear Layer Equations for the Calculation of the Attached and Detached Shear Layers

The same analysis can be performed for compressible turbulent flow (for laminar flow the equations for incompressible flow are sufficient, as Stewartson's transformation is utilized). The corresponding equations are derived following a similar development as the one presented in reference [3.23]. They are

$$F_1 dL_k - F_2 dq + \frac{C_D M}{Re_3} d\phi +$$

$$+ \frac{F_{33}}{W\epsilon^2} d\left(\frac{\omega^2 R_w}{2}\right) - A_\epsilon = 0 \quad (3.34)$$

$$dX - 2dL_k + F_{44}dq - \frac{C_D d\phi}{Re_3} +$$

$$+ \frac{F_{55}}{W\epsilon^2} d\left(\frac{\omega^2 R_w}{2}\right) - A_\epsilon = 0 \quad (3.35)$$

where

$$F_1 = \frac{H_{12k-1}}{(H_{12}-1)-r(\gamma-1/2)M_{ew}^2} \quad (3.36)$$

$$F_2 = 1 - \frac{(1+(\gamma-1/2)M_{ew}^2)(2K_1 M_{ew}^2 + 3K_2 M_{ew})M_{ew}}{(H_{12}-1)-r(\gamma-1/2)M_{ew}^2(1+K_1 M_{ew}^2 + K_2 M_{ew}^3)} \quad (3.37)$$

$$F_3 = \frac{r(\gamma-1)M_{ew} - H_{p2}}{(H_{12}-1)-r(\gamma-1/2)M_{ew}^2} \quad (3.38)$$

$$F_4 = 2[1+(r-\omega)\frac{\gamma-1}{2}M_{ew}^2] \quad (3.39)$$

$$F_5 = (r-\omega)(\gamma-1)M_{ew} \quad (3.40)$$

$$F_{22} = F_2 + \frac{1}{(H_{12}-1)-r(\gamma-1/2)M_{ew}^2} [(2-\omega(\gamma-1)M_{ew}) \quad (3.41)$$

$$\frac{Re_{\infty}}{Re_3} - (1-\omega(\gamma-1)M_{ew}) \frac{Re_{\infty}}{Re_2}] \quad (3.41)$$

$$F_{33} = F_3 + [\frac{Re_{\infty}}{Re_3} - \frac{Re_{\infty}}{Re_2}] \omega(\gamma-1)M_{ew} \quad (3.42)$$

$$F_{44} = F_4 - [2-\omega(\gamma-1)M_{ew}] \frac{Re_{\infty}}{Re_3} \quad (3.43)$$

$$F_{55} = F_5 + \omega(\gamma-1) \frac{Re_{\infty}}{Re_3} M_{ew}^2 \quad (3.44)$$

$$A_\epsilon = \frac{dRe_{\infty}}{Re_3} - \frac{dRe_{\infty}}{Re_2} \frac{Re_{\infty}}{Re_3} - \frac{Re_{\infty}}{Re_2} \frac{dR_w}{R_w} \quad (3.45)$$

$$A_\epsilon = \frac{dRe_{\infty}}{Re_3} + (1 + \frac{Re_{\infty}}{Re_3}) \frac{dR_w}{R_w} \quad (3.46)$$

In the above equations note the K_1 and K_2 are constants and that F_1 and F_2 are function of the Mach number reducing to unity for $M_\infty=0$.

The above equations differ from those presented in ref. [3.23]. A restructuring was performed, when it was realized what was needed in order to march more deeply (than it was done in refs [3.12] and [3.13]) into the separated flow region, as well as when

it was realized that, when strong flow separation exists, the value of K reflecting the normal fluctuation terms presence, was not constant.

4. The Semi-Empirical Frame

In order to obtain closure of the system of integral equations used for the calculation of the development of a shear layer, it is necessary to express the various flow parameters at an arbitrary cross section in terms of a number among them. This number designates the number of the independent variables of the problem and, at the same time, equals the number of the available differential equations. For the present case this number equals to two. Details concerning the semi-empirical background for work done before 1981 can be found in reference [3.23]. Here, we shall briefly outline how this semi-empirical frame is constituted and give the necessary background for understanding the present lecture. In addition, information will be given concerning developments realized after the work of reference [3.23] was reported.

It might seem strange that one wants to establish a semi-empirical frame for laminar layers, for which mathematically the problem is well defined and doesn't need additional information. For our case, however, information was lost when integration along a normal was performed (in order to obtain the integral equations) and this lost information must be reconstituted in order to solve the problem.

After this remark, we may state that the basis for constituting the semi-empirical background of both laminar and turbulent shear layers is the fact that the profiles of the various shear layer properties at each station can be described by profiles corresponding to a station of an equilibrium shear layer. Consequently, it is necessary to obtain the properties of all equilibrium shear layers, in order to establish our semi-empirical frame.

For laminar incompressible shear layers Falkner and Skan's^(4.1) similar solutions are used. For these solutions, when the shear stress at the wall τ_{sw} and the shear layer thickness δ are given, then the velocity profile can be specified, for each station. Then, the various thicknesses, form factors, as well as the shear stress profile and corresponding dissipation factor can be obtained.

For these laminar equilibrium shear layers, it is easy to prove that, at the same time, the parameter

$$\Pi = \frac{\delta_1}{|\tau_{sw}|} \frac{dp_w}{ds} \quad (4.1)$$

conserves its value for each individual layer. Note that the way the expression for Π

is written, it accounts for both attached and separated shear layers. This value is known, together with the velocity profile of the corresponding similar solution.

For turbulent incompressible shear layers it was proved experimentally (Clauser^[4.2], Bradshaw^[4.3], among others) that the external part of the velocity profile, as well as the mixing length profile are unique under a certain similarity law for each equilibrium shear layer. The inner and outer parts of the turbulent shear layers obeying different laws (see Coles^{[4.4], [4.5]}), makes it impossible to demand complete similarity for turbulent shear layers. However, for reasonably high Reynolds numbers, the error involved is relatively small.

In the present case, Kuhn and Nielsen's^[4.6] velocity profile family was used, which defines the velocity profile when a free parameter n_1 and the shear layer thickness δ are given. At the same time, the velocity profile expression provides the wall shear stress τ_{sw} . The unique mixing length profile for all equilibrium shear layers, or, alternatively, the method presented in reference [4.7], gives the possibility to obtain the dissipation factor C_p . The two procedures give quite comparable results (Papailiou^[4.7]).

The above applies to both attached and separated shear layers (see Papailiou^[3.13] for detailed information). The relation between \bar{H} (defined by equation (4.1)) and n_1 in this case is established experimentally. In the present work the relation deduced by Papailiou^[4.8] is used, which coincides with that given by Nash^[4.9].

For compressible flow the generalized velocity of van Driest^[4.10] is used. Mathews, Childs and Paynter^[4.11] and Alber^[4.12] have established that, by using it, the semi-empirical incompressible expressions are verified. This fact is in agreement with Morkovin's^[4.13] hypothesis, according to which the turbulence properties are not influenced by compressibility, as long as the Mach number based on the velocity fluctuations remains small. This hypothesis has been confirmed repeatedly and has been used for practically all methods of calculation of turbulent compressible shear layers. It gives the possibility to use turbulence properties established in incompressible flow for calculations up to a Mach number of approximately 3. The turbomachinery range of application is, thus, largely covered. This same hypothesis has been used in order to enable us to state that there exists a class of turbulent equilibrium shear layers for incompressible as well as for compressible flow (see, also, Alber^[4.14]), unseparated or separated, which are completely defined at each station of their development, once two properties along with the external Mach number have been specified.

It is important to consider more particularly the relation between H_{12k}

and H_{32k} . For laminar incompressible shear layers there exists a unique relationship $H_{32k}(H_{12k})$ for unseparated as well as for separated flow. It is presented in figure (4.1). As said above, for turbulent incompressible shear layers, the experimentally established relation $H_{32k}(H_{12k})$ depends slightly upon the Reynolds number. The maximum deviation of the curves for, say, a range of Reynolds numbers based on boundary layer thickness from 5000 to 500000 is of the order of 3%. This relation is presented in figure (4.2). Different calibrations using different representations of the velocity profile have resulted to the same curve. For compressible turbulent shear layers the curves $H_{32k}(H_{12k})$ depend strongly upon the Mach number. If one considers, however, the curves $H_{32k}(H_{12k})$, then one comes very close to the established curve $H_{32k}(H_{12k})$ of figure (4.2).

We can remark that both curves $H_{32k}(H_{12k})$ for laminar and turbulent shear layers present a minimum. This minimum is found very close, for both laminar and turbulent flow, to the point for which the wall shear stress is zero ($\tau_{sw}=0$). For us this is the condition for flow separation. For turbulent flow, in particular, this minimum coincides with the disappearance of the semi-logarithmic region of the semi-empirical velocity profile we are using.

Coming back to the definition of our new form factor L_k (equation (3.16)), we can remark that in order to complete it we need the constant of integration. We take L_k to be zero at the point of the (H_{12k}) -curve, where H_{32k} is minimum. Consequently, for practical purposes, separation is reached when $L_k=0$ for both laminar and turbulent compressible shear layers.

Thus, one can derive the $L_k(H_{12k})$ curves for laminar and turbulent flow. These are presented correspondingly in figures (4.3) and (4.4). Accuracy may be improved for turbulent flow by obtaining each time an $L_k(H_{12k})$ curve for Re_3 constant and using, during the calculation, not a single $L_k(H_{12k})$ curve but all curves in the form of a grid. This has been done and found particularly important near separation.

In deriving the basic equations, we have conserved the normal fluctuation terms. These become very important near separation and in the separated flow region. Details can be found in Papailiou^[3.23] and Huot^[3.8], who have described in this respect, Le Foll's work. Experimental results have been used to calculate the value of the coefficient K , defined in the previous chapter as

$$K = \frac{H_{12k}-1}{H_{32k}-1} \quad (4.2)$$

and of the ratio H_{32k}/H_{12k} . These results plotted in figure (4.5), which were taken for unseparated turbulent shear layers, demonstrate that H_{32k}/H_{12k} can be taken equal to unity and that the

value of K can be taken equal to 0.85.

Accounting of the normal fluctuation terms gave the possibility to predict separation accurately and march correctly within the separated flow region (see references [3.13] and [3.8]).

For extended separated flow regions, however, it was found that K was not constant and that H_{32k}/H_{32k} could not be taken equal to unity. Reference [3.27] establishes the semi-empirical relations needed for the calculation of the fluctuation terms appearing in equations (3.1) and (3.2) for unseparated and separated compressible (including shock/turbulent shear layer interaction) flow. At the same time, similarity laws are established for the normal fluctuation profiles. Figures (4.6), (4.7), (4.8) and (4.9), which present this new information, were taken from reference [3.27]. The possibility to find similarity laws for the normal fluctuation terms, allow us to avoid using the turbulent kinetic energy equation, as it is pointed out in the same reference. On the other hand, one may remark that local similarity is obtained in particularly extreme conditions, as it is the case for the shock/turbulent shear layer interaction.

From the information presented above, it can be deduced that, for laminar flow, the coefficients $\beta_1(L_k)$ and $C_1(L_k)$ appearing in equations (3.26) and (3.27) and defined by equations (3.28) and (3.29) can be established once for all for laminar incompressible flow. The corresponding compressible flow values are not needed in view of the fact that Stewartson's transformation is utilized. Figure (4.10) presents the curves $C_1(L_k)$ and $M_1(L_k)$, from which $\beta_1(L_k)$ can be computed according to (3.28).

For turbulent flow the values of $C_{dt}(L_k, X)$ and $M_t(L_k, X)$ are established once and for all. $M_t(L_k, X)$ is computed from equation (3.44) for compressible flow, or from (3.21) for incompressible flow. For $C_{dt}(L_k, X)$ the following expression is utilized

$$\frac{C_{dt}(1+r(\gamma-1)/2 \cdot M_e^2)}{H_{32k} \rho_{\infty} / \rho_w C_f / 2} = \frac{\beta_1 (H_{12}-1)-r(\gamma-1)M_e^2}{\beta_{1k} H_{12}} F_2 \Pi + 1 \quad (4.3)$$

Details for its development can be found in ref. [3.23]. The corresponding incompressible flow expression reads

$$\frac{C_{dt}}{H_{32k} C_f / 2} = 1 + \frac{H_{12k}-1}{H_{12k}} \Pi \quad (4.3a)$$

The corresponding curves for turbulent attached and separated incompressible shear layers are presented in figure (4.11). For each point of these curves it is necessary to know any two shear layer properties of

the considered section. For establishing the corresponding curves for compressible flow, the external flow Mach number must be known, additionally. Once these curves are established, it is easy to calculate the coefficients appearing in equations (3.36) to (3.46), when the external flow Mach number is specified.

5. The Direct Shear Layer Calculation and its Prediction Capability

The calculation of the development of laminar or turbulent shear layers can be performed utilizing the canonical equations established in Chapter 3 and the semi-empirical frame described in Chapter 4. For such a calculation the initial conditions of the shear layer must be known as well as the external flow velocity (or Mach number) distribution at the solid wall. In addition, the total conditions of the external flow must be specified and the angular velocity, if a rotating system of reference is considered. The wall geometry and its orientation in respect to the rotating axis must, also, be given, in order to evaluate the necessary second order terms and the influence of Coriolis force and streamline curvature. This last influence will be examined later.

The canonical equations have been set up in a form convenient for the solution of the inverse problem. The way the present formulation has been set up, it is possible to pass the separation point (and the singularity existing there) in a direct mode. However, looking at equations (3.34) and (3.35) it can be seen that in the inverse mode their integration reduces to a simple quadrature. Furthermore, everywhere (separated and unseparated flow), it has been found out that the inverse mode solution behaves better than the direct one. It has been decided, then, when dealing with the direct problem, to solve the equation in the inverse mode.

In order to assess the capability of the present method the following remarks are made.

1. Although some transport terms have been retained in the equations, the method reposes upon the hypothesis of local similarity for turbulent flows. In reference [3.23] information is presented which suggests that this hypothesis, within the present context, gives good results for engineering applications. In addition the comparisons that are presented there between theoretical predictions and experimental results including mildly separated flow, give evidence of its good predictive capabilities. Concerning the prediction of non-equilibrium flows with equilibrium data, it is important to note the remark of Albert[3.1], who suggests that, for doing this, it is necessary to "unhook" the pressure gradient dp/dx appearing in Π from the rest of the shear layer properties. The minimum number of integral equations required for this is two. The same

conclusions can be reached following the work of Tani^[5.2] and Lees and Reeves^[5.3] for laminar layers. Opposing the present method, there are some others (for instance Felsch^[5.1] and Nash^[5.11]) that, in order to compute correctly non equilibrium flows (and take into account correctly the history effects), need a third equation, usually called the "lag equation". These utilize as well local equilibrium (similarity) data for their prediction. The main objection that one may raise, is that this "lag equation" is empirical and not derived from the basic flow equations. Otherwise, such methods perform very well^[5.11]. No conclusion can be made at this stage as to which one of the two classes of methods is preferable.

2. From simple numerical calculations one may see that the shear layer development calculation is influenced much more by the value of the derivative dW_{se}/ds than from the value of the velocity itself. This influence becomes critical when separation is approached, as well as inside the separated flow region. Small changes in this derivative may induce failure of the calculation itself. Besides, at the singularity point at separation, this aspect is still valid and this has resulted in published work of considerable volume, around the theme of "viscous/inviscid interaction". To account for this problem, the present direct method employs a simple but efficient approximate viscous/inviscid interaction procedure, which is described below, in brief.

The two (pressure and suction sides) shear layers are computed simultaneously. In addition, an equation is written for global mass conservation across the whole channel passage. This equation requires that the flow passes through the reduced (by the two shear layers blockage) channel width. The approximation lies in the fact that the inviscid external flow velocity-density profile is allowed to be displaced, freezing its first derivative. In this way, the external velocity applied to each of the two (pressure and suction sides) shear layers is modified according to the total blockage.

This procedure implies that five equations are solved simultaneously, two (momentum and energy integral equations) for each shear layer and the global continuity equation, which is satisfied at each station. It protects in a very efficient manner each shear layer computation near separation and in the separated flow region. Of course it cannot substitute the external inviscid computational procedure, but results in reducing the number of iterations required between the inviscid and the viscous flow calculations. Finally, as the procedure is incorporated within the viscous flow calculation method, the corresponding viscous computations can be performed by themselves, independently of the external inviscid ones. The complete algorithm reads as follows:

STEP 1 Calculate the pressure

distribution around the blade, using the external inviscid flow calculation. This computation is initially performed with zero shear layer blockage.

STEP 2 Use the result of the previous inviscid flow calculation and perform the calculation of the two shear layers (suction and pressure sides). The approximate viscous/inviscid interaction procedure is used in this calculation.

STEP 3 Use the results of the previous shear layer calculation in order to specify the boundary conditions (normal velocity at the solid wall and difference in suction and pressure sides pressures at the trailing edge) of the next inviscid flow calculation. The information outlined in Chapter 2 is utilized for this purpose.

STEP 4 Calculate the pressure distribution around the blade, using the external inviscid flow calculation. This computation utilizes the results of STEP 3.

STEP 5 If convergence is achieved, then the calculation procedure is completed. If not, steps 2 to 5 are repeated. The final pressure distribution around the blade must be issued utilizing the corrections presented in Chapter 2.

The approximate viscous/inviscid interaction procedure outlined above was utilized for the calculation of secondary flows cascades by Comte^[5.4] and Papaliiou^[5.9]. Subsequently, it was utilized by Douvika^{[5.5], [5.6]} and Kalantzis^{[5.7], [5.8]} for the calculation of secondary flows in radial and axial flow compressors. For the case of shear layer computation, it was first utilized by T. Lin^{[5.20], [5.21]}. Finally, a detailed description not only for internal flow cases but for external flow ones, as well, is presented by Bouras^[5.32].

3. The information outlined in Chapter 2 must be used when predicting measured shear layers. If pneumatic probes have been used, one has to note that the total velocity value is given at the edge of the shear layer, while the component parallel to the wall of the inviscid external flow is required. The same happens when a laser velocimeter is used. However, in this last case some pressure measurements may be missing and the reconstitution of the complete external flow field may be more difficult.

It is better anyway, to perform the calculation inside the complete domain, when possible, using an external flow calculation method and letting it interact with the one dealing with viscous shear layer.

4. Evidence of the predictive capabilities of the method is given in references [3.3], [3.5], [3.8], [3.28] and [3.12] and summarized in ref.[3.23]. Here, we shall reproduce, in figure (5.1), the transitional flow predictions of Barrio^[3.14], which are base on the

work of Narashima. In order to give evidence of the capabilities of the method to predict separation and reduced separated flow regions, we present some results (figure (5.2)) for shock/turbulent shear layer interaction with flow separation and reattachment produced by Kallast^[3.30],^[3.31] and comparisons of theoretical and experimental results for flow with mild separation, produced by Assasa^[3.13] and Bouras^[3.32] (figures (5.3) and (5.4)). The capability of the method to reproduce the loss versus incidence curve is demonstrated in figures (5.5) and (5.6). The viscous flow calculations were realized by Bouras^[3.32] and Katramatos^[3.33]. The extend of the separated flow region, which has been indicated by the calculation procedure is presented in figure (5.7). Stamatidis^[3.29] has developed the method for laminar separation bubble prediction and some results are presented in figure (5.8). We mention, as well, that Bouras^[3.33] and Katramatos^[3.35] has proved that the method can be successfully extended to calculate unsteady shear layers and that Lytras^[3.34] has extended the method for predicting the development of an asymmetric wake.

6. The Inverse Shear Layer Problem and the General Properties of the Image Plane

Le Foll's Idea

According to what has been said above, all quantities characterizing the state of a shear layer at a cross section can be specified, once two of them are known. Assuming that these, as already said, are L_k and X , one may consider the canonical equations, derived in Chapter 3, in the form

$$\begin{aligned} F_1(W_{ew}, s, L_k, X) &= 0 \\ F_2(W_{ew}, s, L_k, X) &= 0 \end{aligned} \quad (6.1)$$

The usual way of utilizing these equations is to specify the velocity distribution $W_{ew}(s)$ and compute the properties of the shear layer developing under it in the form $L_k(s)$, $X(s)$ (direct problem). It is, of course, possible to compute the solution in the following intrinscic form

$$L_k = L_k(X) \quad (6.2)$$

It is also possible, however, to start by specifying $L_k(X)$ and, using the same equations, compute the distribution $W_{ew}(s)$. In other words it is possible, given the same equations, to select the desired shear layer and, then, calculate the velocity distribution, which is necessary to produce it. Either the computed or the selected $L_k(X)$ curve can be traced on the (L_k, X) -plane. It is then quite evident that, if on the same plane general shear layer properties are available, one can select a curve $L_k(X)$ with desired properties and produce, using equations (6.1), the velocity distribution ensuring that such a shear

layer will develop. Depending upon the device we consider (here, a cascade), it is possible to compute the corresponding solid boundaries, by use of an appropriate inviscid inverse calculation method. These solid boundaries will ensure that the velocity field will have the necessary boundary values, which will ensure that the desired shear layer will develop along the walls. This way of looking at things is specified as inverse (or design) problem.

From what was said above, it is essential to establish on the (L_k, X) -plane (called image plane) as many general shear layer properties as possible. Le Foll^[3.11] developed the idea described above and the properties of the image plane for incompressible attached layers, along with his boundary layer calculation method. This idea of Le Foll is not new. The representation of general properties on a plane along with the individual processes has been done before in several domains. Mollier's diagram is one example. Schlichting^[6.1] has, as well, used a plane, the coordinates of which were the Pohlhausen form factor Λ and R_{e1} . On this plane he traced the neutral stability curve $\Lambda_n = \Lambda_n(R_{e1})$, dividing the plane into a stable and an unstable part. In this way, tracing on the same plane individual shear layers in the form of $\Lambda(R_{e1})$ -image curves, he could identify the point from where each individual layer became unstable. This point was, of course, the intersection between the neutral stability and the individual shear layer image curve.

We shall consider, in the following, separately the laminar and turbulent image planes (L_k, X) in the incompressible attached or detached case and discuss their properties. Then, we shall discuss the compressible case and consider a unique image plane for laminar and turbulent flow. At that point we will develop a way to produce optimized individual shear layer image curves.

The Laminar Image Plane

The laminar image plane is presented in figure (6.1). On it we have traced the $M_1 = \text{const}$ and the $C_D = \text{const}$ curves. The $M_1 = \text{const}$ curves (as M_1 depends only on the value of L_k and $L_k = \text{const}$ defines a laminar equilibrium shear layer) are, as well, image curves of laminar equilibrium shear layers. The particular equilibrium shear layer $L_k = 0$ is by definition one, which is constantly on the verge of separation, so that the image plane is divided into two. The upper part ($L_k > 0$) which contains all unseparated laminar shear layers and the lower part ($L_k < 0$), which contains the separated ones.

Then, the following reasoning can be done. For all equilibrium shear layers (at successive stations), the velocity profiles are similar in the laminar case. As the corresponding skin friction coefficient is constant, the

form factors H_{12k}, H_{32k} and L_k are constant, when the various Reynolds numbers Re_1, Re_2 and Re_3 are increasing. Consequently, for all equilibrium shear layers X is an increasing quantity with distance and dX is a positive quantity. As dE/E is a positive quantity, as explained in Chapter 3, then, from equation (3.25) it can be seen that $(1+2M_1)$ is a positive quantity for all laminar equilibrium shear layers. Considering all the stations of all the equilibrium shear layers, we have considered, according to our basic hypothesis of local equilibrium, all possible stations of any laminar shear layer. Consequently for the general case

$$(1+2M_1) > 0 \quad \text{or} \quad M_1 > -0.5 \quad (6.2)$$

Inversely, now, if equation (6.2) is true and dE/E is a positive quantity for the general case, then dX must be always positive. Consequently, X is an increasing function with distance, which allows a monotonic representation of an individual shear layer on the image plane. This reasoning justifies our choosing X as one of the independent variables of our problem. On the other hand the same reasoning can be applied for turbulent flows, if the quantity $(1+2KM_t)$ is considered positive. The limit $M_t = -0.5$ under which all shear layers exist has been placed on the image plane, figure (6.1). For the laminar separated shear layers, the limit is posed by the laminar equilibrium shear layer, for which $dp/dx=0$. This can be found in Schlichting^[6.1], who reports that two similar solutions exist for each value of R in the interval between the flat plate laminar shear layer ($M_1=0$) and the one corresponding to separation ($M_1=0.327$). He states that this is the sole domain of similar solutions, for which a double solution exists. One branch of these covers the unseparated cases, which are well known, and the other the separated ones. It follows, consequently, that the other side of separation (for $L_k < 0$), we can reach as a limiting case the flat plate equilibrium laminar shear layer, which constitutes at the same time the lower limit of the laminar image plane. It can be added that, as it happens, the separated flat plate ($M_1=0$) shear layer itself is not included in the set of existing solutions. Consequently, it constitutes a case, which cannot be reached.

Lastly, it is possible to transfer Schlichting's^[6.1] neutral stability curve on the image plane. It is known that disturbances of any frequency are damped for a Reynolds number smaller than the critical one. It is presented in figure (6.1) as $L_n(X)$ -curve. Below this curve the laminar shear layer is unstable in the Tollmien-Schlichting mode. Note that this curve cuts the limit $M_1=-0.5$ at $X=10.2$. Consequently, for higher X , stable laminar layers do not exist. The corresponding $q(\theta)$ -curve for the laminar stability curve $L_n(X)$ has been given in ref.[3.23]. We can report here that for low enough Reynolds numbers, the laminar stability curve is compatible with decelerating flow. We can also see, from figure (6.1), that it

cuts the laminar separation line, $L_k=0$, at $X=3.2$.

The Turbulent Image Plane

The turbulent image plane is presented in figures (6.2a) and (6.2b). On figure (6.2a) we have traced the $M_t=\text{const}$ curves and on figure (6.2b) the $C_{pt}=\text{const}$ curves. Here, as well, the locus $L_k=0$ defines turbulent shear layer separation and is the dividing line between unseparated and separated flow. The same remarks concerning the sign of L_k in the separated flow region as for the laminar case are valid here, as well. On this plane, the upper limit for turbulent shear layers ($KM_t=-0.5$) has been placed, as well. The turbulent equilibrium shear layers are presented separately in figure (6.3) for attached and detached flow. The limiting case of the separated constant external flow pressure appears in this figure and has been presented, also, in figure (6.2a), as it designates the limit of the separated turbulent shear layers. The same reasoning as in the laminar case has been used here.

Consider, now, equation (3.22), with K constant and equal to 0.85. This equation tells us that, if we desire to decelerate the flow (dq/dx), this may be done either by requiring dL_k to be negative or by requiring dE to be positive. The part of the deceleration, which is done by increasing dE is the one which is realized by consuming kinetic energy. The part which is done by decreasing dL_k is one, which is realized without losses. During this L_k decrease, the velocity profile is deformed and the outer layers transfer kinetic energy to the inner ones, which need it in order to overcome the pressure gradient. For this reason L_k was named by Le Foll deformation potential.

Whether or not one may be able to decelerate without consuming kinetic energy (that is, without losses), must be examined in connection to the limit negative value of the derivative dL_k/dX . Anyway, even if we could decelerate without losses, equation (3.22) would tell us that this is possible according to the relation

$$KdL_k = dq$$

If we consider such a deceleration up to separation and integrate we get (if "1" indicates initial conditions)

$$\begin{aligned} W_{set} &= e^{-KL_k} \\ \frac{W_{set}}{W_{se2}} &= e^{-L_k} \quad \text{for turbulent flow} \\ W_{se2} &= e^{-L_k} \\ \frac{W_{se2}}{W_{se1}} &= e^{-L_k} \quad \text{for laminar flow} \end{aligned} \quad (6.3)$$

The domain of definition of L_k indicates that this part of the deceleration (considering that separation is to be avoided), although not negligible, is rather small compared with the demands of the current applications. Consequently, one is obliged to spend kinetic energy in order

to decelerate. Then, it is better to consume it in the most efficient way. Looking again at equation (3.22), we can see that for a certain increase in losses, we have the maximum deceleration realized when the coefficient M is maximum, as K is constant. Consequently, the locus of maximum M is at the same time the locus of the optimum deceleration. For unseparated laminar shear layers, such a locus doesn't exist, because $M_1(L_k)$ (as can be seen from figure (4.10)) is a monotonic function, increasing continuously up to separation. For turbulent unseparated shear layers, however, such a locus exists, as can be seen from figure (4.11), in the attached region. On the contrary, a minimum exists in the separated flow region (see figure (4.11)), which indicates that along the corresponding locus, a deceleration is realized with the maximum of kinetic energy loss.

The locus of optimum deceleration $L_k(X)$ is presented on the image plane of figure (6.2) for turbulent shear layers, along with the curves of constant M_1 and constant C_{nt} .

We shall come now to discuss the maximum possible deceleration. In terms of the intrinsic properties of the boundary layer, to demand the maximum possible deceleration, starting from some initial conditions, is equivalent to ask for the maximum negative value that the slope dL_k/dX may assume. Le Foll answered this question empirically. Consider, as he did, the velocity profiles corresponding to various stations of a vertical image curve $X=\text{const}$. This image curve decelerates the boundary layer without losses, by deforming the velocity profile. In order to examine what happens in this extreme case, Le Foll considered such a deceleration along the image curve $X=10.4$, starting from the value of $L_k=0.28$, which corresponds to $d\phi/dx=0$ conditions. Instead of plotting the velocity profiles in the usual form, he plotted them in terms of energy deficit ($W_{\infty}^2 - W_{\infty}^2$) against the stream function ψ , where

$$\psi = \int_y^{y_\infty} W_{\infty} dy \quad (6.4)$$

Non dimensional representations based on initial conditions of energy profiles against the stream function value are given in figure (6.4). In this representation the pressure increase was taken into account in order to render it meaningful. Two important facts are revealed in this manner. The first one is that the energy deficit curves intersect at two points, showing that the kinetic energy in the middle part of the profile decreases, while the corresponding kinetic energy in the two extreme parts increases. This means that kinetic energy from the middle part is directed towards the inner layers, where it is needed in order to help these layers overcome the adverse pressure gradient. Kinetic energy, however,

leaves the middle layers and it is directed towards the outer layers. At the same time, as it can be seen from the limit of each profile (and this is the second important fact), the mass flow inside the boundary layer decreases. This means that the kinetic energy going outwards is given finally to the free stream flow.

Up to now, our knowledge concerning the behaviour of shear layers tends to rule out the possibility of negative entrainment, although this question is still open. Accepting as limit the possibility of zero entrainment (the mass flow inside the shear layer remains constant), then, the shear layer represented by the image curve $X=\text{const}$ is unrealistic. It is instructive to look at an experimental case, which comes close to the one we are discussing now. We have presented in figure (6.5) Stratford's [6.2] two experiments. We can see that before attaining equilibrium, there is a part of the shear layer development to which corresponds a very steep $L_k(X)$ image curve. In figure (6.5) we have presented the corresponding mass flow rate inside the boundary layer, as it changes with distance. It can be seen that it is almost constant, although still slightly increasing. This experimental evidence confirms the physical possibility of suddenly deforming shear layers. At the same time it confirms the existence of equilibrium shear layers near separation. Incidentally, in ref.(6.3) experimental evidence of turbulent equilibrium separated shear layers is presented.

We shall avoid talking here about the positive limit of the derivative dL_k/dX (limit acceleration). This has not yet been fully investigated, along with the phenomenon of relaminarization, which is associated to it. Le Foll, however, on the basis of a trial and error investigation established as limit rate of deformation the value

$$\frac{dL_k}{dX} \Big|_{\max} = -0.5 \quad (6.5)$$

As he points out and as Stratford's experiment shows, higher rates are possible. However, from an engineering point of view, the practical consequences of using higher values are very limited and we shall content ourselves with the value -0.5.

Before closing this discussion, we may make a final remark for the incompressible case, which will help us understanding the behaviour of separated shear layers. For this, assume that we are found at some point of the image plane in the unseparated region near separation and we apply flat plate conditions to our shear layer ($d\phi/dx=0$). Then, from equation (3.22), we can see that the sign of dL_k will be the same as the one taken by KM , in view of the fact that dE is positive. From figure (6.2a) we can see that M is positive, so that L_k will be moving away from separation towards the flat plate case. Assume, now, that we are found at some point of

the image plane in the separated flow region, near separation, and we apply the same external conditions, as previously. Following the same reasoning, it can be seen that L_k will move again towards the (unseparated) flat plate case.

This behaviour may be explained in the following way: if a line of constant L_k is followed, then the corresponding velocity distribution comes out to be a decelerating one. If one relaxes the corresponding negative velocity derivative value, then the image curve starts to move towards separation. If one increases the negative velocity derivative value, then the image curve moves towards the separated flat plate layer. The more, however, one approaches the separated flat plate layer, the smaller the negative derivative value needed to move the image curve towards more negative values of L_k . When the flat plate shear layer is reached, if this is possible, then the corresponding derivative reaches the value zero.

The Compressibility Effects

An investigation was made, concerning compressibility effects on the image plane, when the compressible counterpart of the method was established, as described in Chapters 3 and 4. Results concerning the turbulent shear layers indicate that the equilibrium shear layers and the locus of maximum M_1 conserve approximately their position, provided that instead of X , the quantity X_k , defined as

$$X_k = \ln R e_{3k} + 2L_k \quad (6.6)$$

is used as abscissa for the compressible image plane.

Some of these results are presented in figure (6.6), where we can see that the initial image plane remains practically unchanged for practical applications for Mach numbers up to 2.5.

On the other hand, the equation corresponding to (3.22) for compressible rotating flow reads

$$\frac{dE}{E} = \frac{1}{2} \frac{\omega^2 R^2}{W_s} - \frac{F_1}{F_2} d\left(\frac{L_k}{L_{k1}}\right) \quad (6.7)$$

We can see that the reasoning that was advanced above concerning the optimum deceleration, utilizing equation (3.22) is valid here as well, in spite of the presence of the functions F_1 and F_2 . The term $M_2(1/W_s)d(\omega^2 R^2/2)$ acts as a moderator.

The assumption is made that the transformed (through Stewartson's transformation) laminar image plane conserves its properties for compressible flow and, especially, the laminar stability curve. An investigation is in progress, in order to establish in the transformed plane the laminar stability curves for various Mach numbers. Thus, the image plane will be more accurately specified, without, however, changing its use. Of course, by definition the

line indicating separation remains unchanged.

Before considering the construction of an optimum image curve, some more comments shall be made concerning the part of the deceleration realized by the deformation potential. In practice, situations of rapid deceleration are found in the presence of forward facing steps or when a shock interacts with a turbulent boundary layer. It might be interesting to examine whether the notions established in this lecture may help to understand better their physical aspects.

For both cases referred to above, the turbulent shear layer not having time to absorb kinetic energy from the free stream, uses its proper kinetic energy transferring it from the outer layers to the inner layers which are in need in order to overcome the adverse pressure gradient. The velocity profile is thus deforming itself accordingly, until separation and beyond.

We shall examine this situation using equation (6.7). When the pressure increase takes place in a small distance, the dissipative term can be neglected so that, for a stationary case, equation (6.7) reads

$$\frac{W_{s1}}{W_{s2}} = e^{-\frac{F_1}{F_2} \frac{dL_k}{L_{k1}}} \quad (6.8)$$

where 1 and 2 are the initial and final stations of the rapid deceleration.

The theoretical predictions of this simplified equation and experimental results for incompressible and compressible flow, for the cases mentioned above, are presented in figure (6.7). These results show scatter and uncertainty. They are, however, sufficiently precise for the present analysis purpose, which is to examine whether equation (6.8) can roughly describe such situations.

Through this analysis it is demonstrated that the pressure increase up to separation depends upon the initial value of the form factor L_k (or H_{12k}) and the initial value of the Mach number M_{11} , before the interaction. The existing experimental results, performed under controlled conditions (see references [6.4] and [6.5], where the present investigation is reported in more detail) concerned essentially flat plate cases. For this the velocity free parameter n_1 is constant and the value of H_{12k} depends upon the Reynolds number. Thus, there exists a slight dependence of the experimental results on Reynolds number. For our data, consequently, the pressure rise up to separation must be characterized by the upstream Mach number only, as H_{12k} is almost constant. This is demonstrated in figure (6.7). Note that this theory applies to the incompressible case, as well, of Bradshaw and

Galea^[6.6]. Note, also, that the capacity of the shear layer to sustain a rapid deceleration decreases as the Mach number increases. In terms of pressure rise, however, the deceleration at high Mach numbers is advantageous as the density variation comes into play. Lastly, note that such a deceleration is performed with negligible losses, resulting in a situation, where in the outer "inviscid" flow a drop in the total pressure takes place (across the shock), while in the viscous flow this total pressure drop is much less (see the measurements of Seddon^[6.7]).

7. Individual Shear Layers and the Optimum Image Curve

In Chapter 5 we have given evidence that Le Foll's method compared with experimental results can handle a considerable number of cases with adequate accuracy for engineering applications. We may say, then, that this method can be used for the analysis of situations (existing or at the design stage) in order to inform us about the behaviour of shear layers developing under imposed external velocity distributions.

In the previous Chapter we have examined Le Foll's idea and the general properties of the image plane. In this Chapter we shall examine how it is possible to select an optimum image curve for the most critical shear layer of the blading, that is the suction side for the axial flow machines and the pressure side for the radial flow ones. We shall consider axial machines, first, and comment on radial machines later.

The Conception of an Optimum Suction Side Velocity Distribution

The theory outlined so far, helps us to deal with the problem of designing an optimum velocity distribution in the following manner. We have constructed a plane, called the image plane, on which all possible shear layers can be represented by curves, increasing monotonically with its abscissa. On this plane appear the general properties of the shear layers which can be summarized briefly as follows:

- $L_s(X_k)$ - Schlichting's curve for neutral stability of the laminar shear layers. The region above this curve is stable.
- $L_t(X_k)$ - The locus of maximum M . Along this line the optimum deceleration is obtained.
- $L_k=0$
 - The line corresponding to separation in laminar and turbulent flows.
 - The established upper and lower limits of the attached and separated laminar and turbulent shear layers.

It is possible to select an image curve for the shear layer ensuring

favorable conditions before any calculation has been carried out. For instance, staying above the line $L_k=0$, we ensure that no separation occurs. Staying above Schlichting's curve, laminar instability is avoided and following the line $L_t(X_k)$ an optimum deceleration is ensured.

Once we have selected our image curve, equations (3.26), (3.27) and (3.34), (3.35) may be used in order to arrive at the corresponding velocity distribution.

In the following we shall give a detailed description of how an optimum suction side image curve can be established. The optimization will be based on the following principle. The dissipation factor is an order of magnitude higher for turbulent than for laminar layers. Whereas, the rate of dissipation, which is represented by $!/M$, has a minimum about three times smaller for turbulent layers, which has been established far from separation. The turbulent flow should, therefore, be restricted to the decelerated flow region, and the deceleration adjusted to be the optimum one, or at least these condition should be approximated as closely as possible.

The rest of the flow, starting from the leading edge must be laminar. Near the leading edge, as $w_4 \rightarrow 0$, w_{se} becomes proportional to the arc length, since this is the form of the potential flow close to a cylinder stagnation point. This is achieved with $L_k=0.0436$ for $X \rightarrow -$. For the laminar boundary layer Schlichting's curve presents an optimum image curve, because, as already has been pointed out, M takes its maximum value at separation and, so, on that curve M takes its maximum possible value as long as laminar instability has to be avoided.

Before considering the complete laminar optimum image curve, it will be proved useful to find out what happens to a segment of Schlichting's laminar stability curve, when we change the Reynolds number based on the final arc length (Re_{sf})₁ and keep unchanged the non dimensional form of the velocity distribution $w_{se}/w_{ref} = f(s/s_{ref})$.

Considering an incompressible flow, we can see immediately that a direct consequence of this change of the physical plane, is that the position Reynolds number Φ increases proportionally to the ratio that forms the new Reynolds number (Re_{sf})₂ with the initial Reynolds number (Re_{sf})₁. We have then

$$\frac{\Phi_1}{\Phi_2} = \frac{(Re_{sf})_1}{(Re_{sf})_2} \quad (7.1)$$

We shall come now to the image plane and consider a small segment of the image curve dX , dL_k and the corresponding segment of the (q, Φ) -curve, dq , $d\Phi$.

The situation we are examining is presented schematically for convenience

in figure (7.1).

The following equations establish the correspondence of the image and the physical planes for incompressible flow

$$dq = dL_k + \beta_1(L_k)dx \quad (7.2)$$

$$d\phi = \frac{d(\Psi_k^2)}{2C_1(L_k)} = \frac{e^{2x}dx}{C_1(L_k)} \quad (7.3)$$

Consider now that every $d\phi$ is increased by a factor $a = \Phi_{f2}/\Phi_{f1}$. As dq must be the same for all points of the (q, θ) -curve, in view of equation (7.2), L_k , dx and dL_k must remain constant during the inverse transformation from the (q, θ) -plane to the image plane. During the direct transformation we had

$$(d\phi)_1 = \frac{e^{2x}dx}{C_1(L_k)}$$

and during the inverse transformation we shall have

$$(d\phi)_2 = \frac{e^{2x}dx}{C_1(L_k)}$$

or

$$\frac{(d\phi)_2}{(d\phi)_1} = \frac{\Phi_{f2}}{\Phi_{f1}} = e^{2(x_2 - x_1)}$$

and finally

$$x_2 - x_1 = -\ln \frac{1}{2} \frac{\Phi_{f2}}{\Phi_{f1}} \quad (7.4)$$

Consequently, a change in Reynolds number, keeping the same velocity distribution, results to a displacement of the image curve, expressed by equation (7.4). An increase in Reynolds number displaces the image curve to the right, while a decrease displaces the image curve to the left. When a suction side boundary layer is chosen, it is interesting for us to be able to keep our layer laminar for a chosen interval, not only for one Reynolds number but for the whole Reynolds number range of operation. In order to do this, it is convenient to realize the design for the minimum Reynolds number of operation, which is the most critical for the turbulent layers. We know now that an increase in Reynolds number displaces the image curve of a laminar layer by $0.5 \ln(\Phi_{f2}/\Phi_{f1})$. We can, thus, take into account the maximum possible shift, $0.5 \ln(\Phi_{fmax}/\Phi_{fmin})$, of the image curve to the right, by considering as laminar stability curve for our design, Schlichting's stability curve $L_a(X)$ displaced by $0.5 \ln(\Phi_{fmax}/\Phi_{fmin})$ to the left. For such a situation, if we increase the overall Reynolds number, the image curve we have selected will move to the right but will never exceed the actual Schlichting's curve, as the actual displacement of it will never exceed the value $0.5 \ln(\Phi_{fmax}/\Phi_{fmin})$, which already has been taken into account.

After this remark we may come back to the construction of the laminar part of our optimum image curve. We have presented it as OABC1 in figure (7.2). After the initial stagnation point region, a part with $\beta_1=0$ (flat plate) is being used, if necessary, in order to avoid the deceleration part of Schlichting's curve (see ref.[3.23]), and the corresponding velocity pick.

The segment (BC) that follows corresponds to a displaced Schlichting's neutral stability curve by a distance depending on the range of Reynolds number of operation, as discussed above. "I" represents the point where instability (in the Tollmien-Schlichting 2D mode) is first introduced for the larger Reynolds number of operation. The distance between the point of instability and the region, where the actual transition takes place, depends, at least, on the turbulence level of the external flow as well as on the pressure gradient. A crude criterion which depends only on the level of the external turbulence utilizes by the value taken by the integral

$$I = \int_{X_1}^{X_f} [L_a(X) - L_k(X)] dx \quad (7.5)$$

This criterion, proposed by T.S. Wilkinson, agrees well enough with the available data to predict the order of magnitude of $X_f - X_1$.

This criterion is applied to the situation where the transition region is reduced to a point (as it is described in reference [6.1]). Transition, then, takes place (see figure (7.3)) which presents schematically the corresponding part of the image curve), when the integral I takes a certain value, which depends upon the external turbulence level.

This criterion has been described in more detail in references [3.2], [3.3], [3.7] and [3.10]. The values of I have been deduced from Granville's [7.1] experimental results. Direct proof of the validity of this criterion has been given in ref.(7.2).

The work of Bario[3.14], some results of which have been presented in figure (5.1), opens the possibility to replace the present transition criterion with a transitional calculation. This matter is actually under investigation by Leoutsakos[7.3]. The problem there, in view of the results of Bario, is to model the distance between the instability point and the appearance of turbulence spots. Of course, in turbomachines (see Schlichting[6.1]), other modes of instability are present (Goertler vortices creating 3D disturbances, for instance) and the point of instability is, anyway, influenced by Mach number (see Arnal[7.4]). On the other hand, inverse transition (relaminarization) starts to be tractable now (see Simandirakis[7.5]) with the present calculation method, so

that the old criterion of transition of Wilkinson will be replaced in the near future by other more reliable methods. However, at the present moment, the designer, having no alternative, may resolve this problem by inducing transition in an as short distance as possible, avoiding laminar separation. This can be done by increasing the value of the integral I , following a path parallel to the separation line $L_k=0$ before admitting transition.

Assuming, now, that transition has taken place at T , we shall examine the turbulent part of the image curve. This part must realize an optimum deceleration and starts with a segment of a straight line with a slope which ensures the continuity of the derivative $d\eta/d\theta$ at transition. Then, according to the principles established above for the optimum turbulent deceleration, the locus $L_t(X)$ is followed. In the last part of the image curve, the limit deceleration is employed until the locus $L_k=0$ is reached, if separation is to be avoided. We can profit thus as much as possible from the part of the deceleration which can be realized without losses. Of course, this part can continue in the separated flow region, if incidence considerations permit it. We shall come, in fact, back to this point later.

We have said that the delay $X_f - X_i$ between instability and transition depends on the level of turbulence, which is only roughly estimated in most practical cases. Therefore, to a fixed velocity distribution and a fixed value of Φ_f , corresponds, in fact, a one-parameter family of turbulent boundary layers, and therefore of image curves, depending on the actual position of transition. In general, these curves have completely different shapes, and the differences increase with the interval of X_t , so that, at first sight, it is necessary that the delay in transition corresponding to the lowest possible turbulence levels should be reduced as much as possible, and therefore, for $X > X_i$, $L_k(X)$ should decrease very quickly to a small positive value, so as to increase the value of the integral I as quickly as possible.

It has been found that, in the case of a laminar variation of $L_k(X)$ for $X > X_i$, it is possible to select its slope in order to obtain a family of turbulent boundary layers which end with nearly the same value of L_k although their shapes are different. In addition, the least stable of all is that corresponding to the latest transition. Thus, although the position of transition is not so closely fixed in this case, and the turbulent boundary layers which result from variations of it are different, their final properties are the same, and this is of course all what is required.

The corresponding slope of the image curve in the unstable laminar flow region is about -0.20 for usual design conditions and $X_f - X_i$ is then smaller than 0.15.

Among the general properties that Le Foll had initially established for turbulent boundary layers was the locus of s-wise stability. This locus coincides with the optimum deceleration curve $L_t(X)$. Boundary layers that are found over this curve have the ability to damp with distance disturbances, which were created accidentally at some position upstream.

Le Foll established this property on the basis of an infinitesimal perturbation theory, (see references (3.1) and (3.2)), which lacks generality. It was thought at the beginning that it represented what happens in reality as Clauser^(4.2) had reported having observed such a phenomenon experimentally.

Ever since, various investigators have worked experimentally in the region found between this locus and separation (among others Stratford^(6.2)) and not one reported having observed any instability effects.

This is the reason why the present author has not mentioned this properly. Various workers (among others Le Foll himself) have used a safety margin between the supposed s-wise stability locus and the chosen optimum image curve to account for manufacturing inaccuracies. When this is done we shall report it, having in mind the comments we have made just now.

Before establishing some more features of the image curves, it will be useful to give an example for the incompressible case and thus summarize our results. We shall suppose that the ratio of the maximum to minimum Reynolds number $\Phi_{f,\max}/\Phi_{f,\min}$, at which the profile is to be operated is 2.71. The design of the image curve will start from the displacement of Schlichting's curve by $1/2 \ln 2.71 = 1/2$ to the left. The whole design is represented in figure (7.2). The next parameter to be considered is the abscissa X_i of the point I where the laminar image curve leaves the curve $L_k=L_n(X)$ and the value selected here is $X_i=7.7$. This point I corresponds to incipient transition, i.e. when the laminar boundary layer first becomes unstable.

The first design image curve, shown by the dashed curve of figure (7.2), consists of segments of straight lines, which are selected as follows:

- OA corresponds to the flow in the neighborhood of the leading edge for which $W_{\infty} = s$, which is given by $\beta_1=1$ and $L_k=0.0436$.
- AB a straight line joining OA to segment BC
- BC a curve corresponding to $\beta_1=0$ to avoid the region of decelerated flow which is associated with Schlichting's curve ($X_b=5.2$, $X_c=5.8$).
- CS the curve $L_k = L_n(X+0.5)$

- IS a line defined by the slope $dL/dX=-.2$ which is such that for levels of free stream turbulence greater than 1 1/2 %, transition will occur between I and S.
- SD a segment whose slope is defined by the condition that the derivative $dq/d\theta$ of the velocity distribution should be continuous at the transition point.
- DE the curve $L_k=L(X)+.03$, where .03 represents a safety margin above the turbulent instability curve $X_g=8.3$
- EF a final drop to close the separation with the maximum deceleration not taking into account stability, i.e. $dL/dX=-.5$.

The velocity distribution corresponding to this initial image curve, obtained by integration of equations (3.26), (3.27) and (3.30), (3.31) from F with $q_F=-0.16$ and $\theta_F=0$ (i.e. $X_F=\infty$) is shown by the dashed curve in fig.(7.4) with the corresponding points marked with the same letters.

A smoother velocity curve can be obtained by rounding off the corners of the first image curve, and is plotted as a full curve on fig.(7.4). This smooth curve will be used as the basic image curve from now on. Fig.(7.5) represents the velocity distribution W_{se}/W_{ref} against the fractional arc length. The most striking features of this curve are the steep final deceleration and also the very short length of segment IS in which transition has been located.

Now, transition certainly takes place before S and after I, so that it is necessary to check that turbulent separation is avoided for any position of transition T on the segment IS. To demonstrate this, the shape of the image curves for the given velocity distribution have been drawn as curves 1, 2, 3 and 4 of fig.(7.2) for transition at T_1 , T_2 , T_3 and T_4 . The last point T_4 is outside the possible range, but it is included to show that by advancing the laminar transition point further, turbulent separation really does occur. It can be seen that T_3 is just critical in that it brings the final image point to incipient turbulent separation. The energy dissipation is, also, presented on fig.(7.4) and has a final value of 3.7%. The final position Reynolds number, $\theta_F=1.07 \times 10^6$, corresponds, since the chord of the profile is shorter than s_F , to a chord Reynolds number based on the reference velocity, which is less than $1.07/1.22 \times 10^6$. The value 1.22 comes from the fact that the mean velocity $W_{se,mean}$ equals $1.22 W_{se,2}$.

Now, if θ_F is increased for the same velocity distribution against s/s_F , the laminar part of the image curve is shifted to the right and when this shift exceeds 0.5, transition is no longer controlled. But up to this limit, the velocity distribution against arc length represented on fig.(7.4), gives a

turbulent boundary layer which is increasingly stable and even beyond this limit, it can separate only in the case of a very early transition. If, on the contrary, θ_F is only slightly smaller than 1.07×10^6 , the turbulent boundary layer will separate.

Summarizing, we may say that we have established the form of an optimum image curve to be used for suction side boundary layers of blade sections (compressor or turbine) for the incompressible case. From what has been said in Chapter 6, it can be easily deduced that the same principles apply for the compressible case.

This general optimum image curve form takes into account the desired overall Reynolds number range of operation (although it will be optimum for only one value of the overall Reynolds number), as well as the uncertainty of the external flow level of turbulence on the transition point position.

Looking at this optimum image curve we may see that once the abscissas X_T and X_F have been defined (transition and final points), the whole optimum image curve has very closely been defined completely. This last property may help us to solve the next problem, which is how the choice of one particular image curve may be done, once the general requirements of a particular design have been imposed. These requirements are usually imposed in the physical plane, hence the necessity to relate the general properties of the two planes. This will be done in what follows.

The most interesting properties of a velocity distribution destined for a suction side are:

- The overall Reynolds number of operation, which is imposed.
- The maximum velocity appearing on the suction side. Mach number or noise considerations may demand it to be as low as possible.
- The mean velocity appearing on the suction side. Its value expresses the contribution of the suction side to the blade circulation.
- The losses or some other property of the shear layer.

Supposing that we consider the losses, these are the absolute losses of the suction side. To these, the pressure side losses have to be added and then the sum of the two has to be compared with the circulation per blade before an estimate of the mass averaged loss can be made. We shall consider the first three properties and we shall try to relate them to the two "independent" variables X_T and X_F , which define the optimum image curve.

An interesting property of any (L_k, X) -curve, which will help us to do this, is the following. For any such curve, there exists (see equations (3.26), (3.27) and (3.30), (3.31)) a

unique velocity distribution curve in the form $W_{\infty}/W_{\infty,2} = f(s/s_{ref})$. In this way, all velocity distributions start with the value 0 at the leading edge and end with the value 1 at the trailing edge.

This property gives us the possibility to construct universal curves for all optimum shear layers in order to use them for blade or airfoil design. Let us consider first equations (3.27) and (3.31) for the velocity potential ϕ , which are the following

$$\frac{dRe_4^2}{d\phi} = \frac{C_1(L_k)}{C_1(L_k)}$$

$$\frac{dRe_4}{d\phi} = \frac{C_t(L_k)}{C_t(L_k)}$$

We can see that the potential ϕ increases as the square of $Re_4(\infty X)$ for laminar layers, while it increases as Re_4 for turbulent layers. As the coefficients C_1 and C_t for the range considered are of the same order of magnitude (see ref.[3.23]), we can deduce that the Reynolds number of the resulting velocity distribution will depend principally on the interval in X occupied by the laminar part, that is by the position of the transition point X_T . A plotting of the logarithm of the Reynolds number Re_{eff} based on the final value of the arc length and the exit velocity $W_{\infty,2}$ against X_T is given in fig.(7.6). We can see that in fact X_T plays a secondary role.

Considering now the maximum velocity appearing on the suction side, we can make the following remark. The maximum velocity in respect to the final velocity $W_{\infty,2}$ will depend essentially on the extension of the turbulent part, as this is the part used to realize the required deceleration. A plotting of $W_{\infty,max}/W_{\infty,2}$ against $X_T - X_f$ is given in figure (7.6). It can be seen that we obtain a quasi-unique curve. An explanation for this behaviour can be found in reference (3.6).

Returning now to the third property $W_{\infty,mean}/W_{\infty,2}$ we have decided to plot it against $X_T - X_f$ and the results are presented in fig.(7.6). We can see that there exists an envelope imposing an upper limit. Additionally for $X_f = \text{const.}$, the curve passes from a maximum. This can be understood from the following remark. By fixing the X_f , we practically fix the level of the losses. Now, for small X_T all the loss is given to obtain a turbulent deceleration and consequently high $W_{\infty,max}/W_{\infty,2}$. In moving the transition point to the right we allow the development of a laminar part which creates a plateau on the velocity distribution and, so, at the beginning, the $W_{\infty,mean}/W_{\infty,2}$ is increased in spite of the decrease in $W_{\infty,max}/W_{\infty,2}$. If we move X_T further to the right, there comes a moment when the laminar boundary layer is "too tired" to accept high decelerations and the turbulent deceleration which fixes the level of the plateau becomes so small that the ratio $W_{\infty,mean}/W_{\infty,2}$ starts

decreasing. It is in our interest to choose $X_T - X_f$ values in the region of a maximum $W_{\infty,mean}/W_{\infty,2}$.

Once the three essential design factors have been correlated to boundary layer parameters, some remarks are in order, before we proceed in giving a way of using them.

- a) The given diagram concern unseparated shear layers. That is to say that, in the measure of the approximation of Le Foll's theory, the velocity distributions, which will result, will correspond to unseparated shear layers.
- b) The given diagrams are independent of inlet and outlet velocities, inlet and outlet air angles and generally cascade properties, when the cascade blade case is considered.
- c) Once, a particular problem is considered (the design, for instance, of a cascade) further restrictions are imposed by the potential flow calculation which are independent of the diagrams established. For example, once $W_{\infty,1}/W_{\infty,2}$ has been accepted, the ratio $W_{\infty,max}/W_{\infty,2}$ must necessarily be larger than $W_{\infty,1}/W_{\infty,2}$. The minimum level of $W_{\infty,max}/W_{\infty,2}$ will be fixed then by the thickness of the blade and the amount of turning and these are problems that can be solved only considering inverse potential methods for the calculation of the profile shape.
- d) The choice of an optimum boundary layer for the suction side does not necessarily give the optimum profile. The combination of the deduced velocity distribution from the point of view of closure conditions, will finally define the circulation, which combined with the absolute losses, will give the performance. However, from the experience acquired up to now, we can say that the obtained profiles are good.
- e) The range of operation of the blade, incidence-wise, is not taken into account in the choice. It is possible, however, to design for the maximum incidence, accepting boundary layer separation only for the limit of operation and knowing from experience that in the range between positive and negative stall the profile behaves, normally, without separation.
- f) The curves presented in figure (7.6) concern the specific application. If the optimum image curve changes (for instance, if diffusers are considered), then the curves will change. On the other hand the same happens, if, generally, the image curve form changes for any of a number of reasons. Some of these may be compressibility effects, admission of a separated region on the

suction side or curvature and Coriolis force effects, about which we shall talk later.

Remarks on these will be made in Chapter 10.

We can now proceed with an example of design, giving at the same time a demonstration of the use of the established curves. Assume that we want to design a blade which operates at a Reynolds number of 3×10^5 . We can see immediately that for a given X_f , the value of X_p is fixed and vice versa, although we can also see the impossibility to find solutions for an X_p higher than a certain value. We obtain thus the points A,B,C,D (see figure (7.6)), which are transferred to the mean and maximum velocity curves. We can see now that optimum solutions are obtained around A, but at the same time the maximum velocity risks to be too high and the losses may increase considerably. The final choice will be given by the particular problem we consider (inlet and outlet air angles) and a trading between maximum velocity, mean velocity and losses. In this respect two or three distributions have to be calculated and used as input to the inverse potential calculation before a final choice can be made.

8. The Inverse Inviscid Calculation Method

The present inverse inviscid flow calculation method is addressing the rotating cascade case lying on an arbitrary axisymmetric surface with varying streamtube width. It makes use of Schmidt's equations (refs [8.1], [8.2], [8.3], [8.4]) but it diverges, as will be seen, in the formulation of the solution, the numerical techniques used, as well as the closure conditions. Although not addressed directly in the present lecture, the isolated airfoil case can be treated as well. Again, because of space limitations, only the essential features of the method will be presented.

Position of the Problem and Development of the Equations

It is assumed that the axially symmetric stream surface on which the calculation will be performed is specified (see figure(8.1)). The streamtube width variation with meridional distance, the approximate number of blades N , the inlet stagnation conditions (P_{11}, T_{11}) and velocity vector W_1 , the meridional position of the inlet stagnation point m_1 , the rotational speed and the outlet flow angle are specified as well. Finally, assumed given are the pressure and suction side velocity distributions versus arc length, with the condition that the pressure side velocity distribution will change during the computational procedure as little as possible.

The flow is considered steady, inviscid, compressible subsonic at the inlet and irrotational in the absolute

frame of reference.

An axially symmetric coordinate system (m, θ) is used in respect to which the equations to solve are the following

$$\frac{\partial}{\partial m} (\rho \Delta_n W_m) + \frac{\partial}{\partial \theta} (\rho \Delta_n W_\theta) = 0 \quad (8.1)$$

$$\frac{1}{R} \frac{\partial (RW_\theta + \omega R^2)}{\partial m} - \frac{\partial W_m}{\partial \theta} = 0 \quad (8.2)$$

We consider the coordinate transformation $m=m(\phi, \psi)$ and $\theta=\theta(\phi, \psi)$, where ϕ and ψ are the potential and stream functions, defined as

$$V_s \phi = (W + \omega r) \hat{r} \quad (8.3)$$

$$\hat{n} \times V_s \psi = \rho (\Delta_n) \hat{W} \quad (8.4)$$

n is the unit vector normal to the axisymmetric surface and $V_s(\cdot)$ is the surface gradient operator. In this way, we have transferred our problem from the physical to the (ϕ, ψ) -plane (see figure (8.2)). Writing, also, the velocity components in terms of the velocity magnitude W and the flow angle β as

$$W_m = W \cos \beta ; \quad W_\theta = W \sin \beta \quad (8.5)$$

so that it is possible to write equations (8.1) and (8.2) in the following form

$$\begin{aligned} & A1 (\ln W)_{\phi\phi} + A2 (\ln W)_{\phi\theta} + A3 (\ln W)_{\theta\theta} + A4 (\ln W)_{\theta\phi} + \\ & + A5 (\ln W)_{\phi\phi}^2 + A6 (\ln W)_{\phi\theta} + A7 (\ln W)_{\theta\theta} + \\ & + A8 (\ln W)_{\phi} (\ln W)_{\theta} + A9 = 0 \end{aligned} \quad (8.6)$$

$$\frac{\beta}{\phi} = -(\ln W)_\theta \frac{\rho \Delta_n W}{W + U \sin \beta} - \frac{U \cos \beta}{W + U \sin \beta} -$$

$$-\frac{\partial \ln R}{\partial m} \frac{W \sin \beta + U}{W(W + U \sin \beta)} \quad (8.7)$$

$$\begin{aligned} \frac{\partial \beta}{\partial \psi} &= (\ln W)_\phi \frac{1}{\rho \Delta_n W} \left[\frac{W^2 + U^2 + 2UW \sin \beta}{W + U \sin \beta} - \right. \\ &\left. - \frac{2W^2 (W + U \sin \beta)}{(Y-1)(2c_p T_{IR} - W^2 + U^2)} \right] - (\ln W)_\theta \frac{U \cos \beta}{W + U \sin \beta} + \\ &+ \frac{\partial \ln R}{\partial m} \frac{1}{W(W + U \sin \beta)} \left[\frac{\cos \beta (W^2 - 2U^2)}{(Y-1)(2c_p T_{IR} - W^2 + U^2)} + \frac{2U^2 \cos \beta}{(Y-1)(2c_p T_{IR} - W^2 + U^2)} \right] \\ &+ \frac{\partial \ln \Delta_n}{\partial m} \frac{\cos \beta}{\rho \Delta_n W} \end{aligned} \quad (8.8)$$

The expressions of coefficients A_1 to A_9 are given in ref.(8.5). In the above form ϕ and ψ have been introduced as independent variables, while the velocity modulus and the flow angle are the dependent ones. During the calculation procedure only one of equations (8.7) and (8.8) may be utilized, as they are completely equivalent.

The Boundary Conditions on the (Φ, Ψ) -Plane

Having performed a first transformation from the physical to the (Φ, Ψ) -plane (see figure (8.2)), we shall examine in this plane the corresponding boundary, as well as, some additional relations. We consider:

- (a) The integral mass flux conservation equation, which reads

$$\frac{2\pi R_1}{N} \rho_1 W_1 \cos \beta_1 \Delta_{n1} = \frac{2\pi R_2}{N} \rho_2 W_2 \cos \beta_2 \Delta_{n2} \quad (8.9)$$

so that

$$\rho_2 W_2 = \rho_1 W_1 \frac{R_1}{R_2} \frac{\cos \beta_1}{\cos \beta_2} \frac{\Delta_{n1}}{\Delta_{n2}} \quad (8.9a)$$

- (b) The integral momentum equation in the following form

$$\Gamma = \oint_{\text{blade}} V \cdot ds = \oint_{\text{blade}} W ds + \oint_{\text{blade}} w R^2 d\theta = \frac{2\pi}{N} (R_1 V_{u1} - R_2 V_{u2}) \quad (8.10)$$

where

$$\Gamma_1 = \oint_{\text{blade}} w R^2 d\theta \quad (8.10a)$$

- (c) The isentropic flow relations, along with the energy conservation equation (conservation of the total relative enthalpy) along a meridional streamline

$$T_t = T_t \text{ or } T_1 + \frac{W_1^2 - U_1^2}{2 \cdot c_p} = T_2 + \frac{W_2^2 - U_2^2}{2 \cdot c_p} \quad (8.11)$$

from which we get the following expression

$$\frac{\rho_2}{\rho_1} = \left(1 + \frac{W_1^2 - U_1^2}{2 \cdot c_p T_1} - \frac{W_2^2 - U_2^2}{2 \cdot c_p T_1} \right)^{1/2-1} \quad (8.11a)$$

From the above written equations, it is possible to calculate the conditions at the exit (ρ_2, W_2) , utilizing the data of the problem, which were specified in the previous paragraph. It is not possible, using the same data and equation (8.10), to specify the value of the circulation, if a rotating cascade is considered. For this, the integral Γ_1 must be known, which, in our case, will be computed once the cascade geometry is known. This fact introduces one of the difficulties of the inverse method applied to arbitrary rotating cascades. During the computational procedure the integral Γ_1 will be given an initial plausible value and corrected accordingly, each time a blade shape is computed. In any case, the value of Γ must be compatible with the imposed value of the outlet flow angle β_2 , so that, if the suction side velocity distribution must be maintained, being

the most sensitive, the pressure side velocity distribution must be chosen to satisfy this value of Γ .

Considering, again, figure (8.2), periodic conditions are imposed along the (AB) , (EZ) and $(\Gamma\Gamma)$, (HH) pairs of boundaries. $W(\Phi)$ is specified along the suction and pressure side solid boundaries and the corresponding value of Φ is calculated from the following relation

$$d\Phi = W ds + \omega R^2 d\theta \quad (8.12)$$

Consequently, differences in potential from a station v to a station μ may be calculated as

$$\Delta\Phi \Big|_{v}^{\mu} = \int_v^{\mu} W ds + \int_v^{\mu} \omega R^2 d\theta \quad (8.13)$$

The way the (Φ, Ψ) -plane has been built, we have

$$\Delta\Phi \Big|_{A}^B = \Delta\Phi \Big|_{E}^Z; \Delta\Phi \Big|_{B}^G + \Delta\Phi \Big|_{H}^Z = \Gamma; \Delta\Phi \Big|_{G}^H = \Delta\Phi \Big|_{H}^{\Theta} \quad (8.13a)$$

The magnitudes of $\Delta\Phi|_A$ and $\Delta\Phi|_H$ are specified in our formulation. Their value must, however, be such, so that upstream and downstream uniform conditions must be reached with sufficient accuracy. In this way, the upstream and downstream positions in the physical plane are not specified.

From equation (8.4) we may get

$$d\Psi = \rho(\Delta n) W \cos \beta R d\theta$$

so that the corresponding stream function differences are described by the following relation at the inlet and the outlet stations

$$\Delta\Psi \Big|_{v}^{\mu} = \int_v^{\mu} \rho(\Delta n) W \cos \beta R d\theta \quad (8.14)$$

Along the inlet and outlet stations the flow is uniform with velocities and flow angles, correspondingly, W_1 , W_2 and β_1 , β_2 . Consequently, if $\Psi_g = \Psi_z = \Psi_h = \Psi_0 = 0$ is the stream function value characterizing the lower boundary, then the one characterizing the upper boundary is, according to equation (8.14)

$$\begin{aligned} \Delta\Psi \Big|_{E}^A &= \rho_1 W_1 \cos \beta_1 \frac{2\pi R_1}{N} (\Delta n)_1 = \\ &= \rho_2 W_2 \cos \beta_2 \frac{2\pi R_2}{N} (\Delta n)_2 = \Delta\Psi \Big|_{\Theta}^{\Delta} \end{aligned} \quad (8.14a)$$

Then, the upper boundary being a streamline, $\Psi_A = \Psi_g = \Psi_r = \Psi_0$.

The Numerical Integration of the Equations

In order to solve equations (8.6) and (8.7) or (8.8), a new transformation is performed from the (Φ, Ψ) -plane to an orthogonal (ξ, n) -plane with square cells (see figure (8.2)). This transformed plane is constructed following a body-

fitted coordinate transformation, which maps the (ϕ, ψ) -plane to the (ξ, n) -plane.

Then, the elliptic type equation (8.6) on W is discretized by use of second order accurate finite-difference schemes and the resulting quasi-linear system of algebraic equations is solved iteratively for using the MSIP [8.6], [8.7] approximate factorization procedure, which has been developed for non-symmetric 9-diagonal banded matrices.

Once the velocity field is computed, the flow angle field is obtained by the numerical integration of the ordinary differential equation (8.7) or (8.8) along the iso- n (iso- ψ) or the iso- ξ lines, respectively. A second order Runge-Kutta method is used during that step. In fact, equation (8.7) is first integrated along the cascade mean-streamline and the computed β -mean-streamline values are used as boundary conditions for the integration of equation (8.8) along the iso- ξ lines. This procedure provides the whole $\beta(\phi, \psi)$ field in the most accurate way.

The Computational Algorithm

A computational algorithm was constructed, which possesses the following steps (without considering conditions for the profile closure, which will be examined later).

STEP 1 : The exit plane flow quantities are calculated through equations (8.9a) and (8.11a). A value of the integral Γ_1 is assumed and a velocity distribution for the pressure side compatible with the value of the circulation Γ issued from equation (8.10) is established.

STEP 2 : A first approximation of the (ϕ, ψ) -plane is constructed and the boundary conditions for the velocity (through equations (8.13a) and (8.14a)) are specified, utilizing plausible angle distributions. The interior (ϕ, ψ) -nodes are determined after a linear procedure. In the upstream (ABZE) and downstream ($\Gamma\Delta\Theta H$) regions, the points on the boundary are chosen and the grid constructed, so that periodic conditions can be checked without interpolation. The complete velocity and flow angle fields are initialized making use of the values at the boundaries. An initial estimate for the values of (Δn) and R for each node is made, as well.

STEP 3 : The coefficients A_i ($i=1, 9$) appearing in equation (8.6) are calculated through the derived in ref. [8.5] expressions.

STEP 4 : Equation (8.6) is solved for $W(\phi, \psi)$ using the numerical procedure and technique described in the previous section. At this point, an iterative procedure is performed involving the previous step, that is updating the values of the coefficients A_i . This updating is performed, utilizing the values of the velocity field of the previous iteration.

At the end of the computational

procedure involved in this step, the values of W at the periodic boundaries have been modified along with the complete velocity field.

STEP 5 : The flow angle field $\beta(\phi, \psi)$ is computed after numerical integration of equations (8.7) and (8.8) in the manner described in the previous section. New angle values are computed at the boundaries, as well.

STEP 6 : The blade section shape $\theta = \theta(m)$ is computed using the following geometrical relations

$$m = \int \cos \beta ds = m(s) \quad (8.15)$$

$$\theta = \int \frac{\sin \beta}{R} ds = \theta(s) \quad (8.16)$$

Utilizing the above relations, the values of m and θ are computed along streamlines for the whole flow field. An interpolation procedure is used in order to estimate the new set of values $R(m(s))$ and $\Delta n(m(s))$, which will be used, along with the updated values of the angles.

The exit conditions are calculated at station (2), using the same procedure as in STEP1. The integral Γ_1 is computed and its new value is used to update Γ . The pressure side velocity distribution is modified in order to satisfy the new value of the circulation. The boundaries and associate conditions can be established for a new (ϕ, ψ) -plane. A new grid is established in the (ϕ, ψ) -plane, moving along ψ -lines and computing each time the value of ϕ corresponding to the previously updated values of the velocity field.

STEP 7 : STEPS 3 to 6 are repeated until convergence is achieved.

As observed before, the blade section shape issued from the above described computational procedure is not necessarily closed.

Results and Discussion

Even before starting discussing various aspects of the method it will be useful to show some calculation results. It is easier to perform this demonstration for a plane two-dimensional cascade. Figure (8.3) presents the physical plane and the corresponding velocity distributions along the lower and upper boundaries. In figure (8.4), the generated grid is shown along with the fields of $W(\phi, \psi)$ and $\beta(\phi, \psi)$. In figure (8.5) the calculation results are presented in the (ξ, n) -plane. One may remark the zero velocity value at the inlet stagnation point, as well as the reacceleration of the flow behind the rear stagnation point.

Several stationary cascade and isolated airfoil test cases were used in order to validate the accuracy and capabilities of the present inverse

calculation method. The considered cases were selected in order to cover as many geometrical configurations as possible and the complete Mach number range of application of the method. Exact cases were used where possible, while a direct method of calculation was used when the velocity distribution was not known, given a blade shape. Of course, slight inaccuracies in the results of the direct calculation method resulted in slight inaccuracies of the computed blade shape by the inverse method. All test cases are reported by Bonatuk [8.5]. Here, in order to demonstrate the capability of the method, some cases were chosen and presented in figure (8.6). These contain the Hobson [8.8] exact case (high Mach number, high turning, low pitch to chord ratio), a radial inflow turbine case [8.9] (strong variation of $R(m)$, rotational, variation of $\alpha(m)$) and a hub wind turbine case [8.10] (high pitch to chord ratio, high stagger). Good results are obtained for all cases demonstrating that the present inverse calculation procedure is numerically sound. However, for the tip section of the wind turbine case which was tested but not presented here (for which the value of the pitch to chord ratio was ≈ 3) difficulties were encountered, as important numerical errors were introduced during the integration. The problem was finally solved as a single airfoil case and gave satisfactory results [8.11].

It was already pointed out that, if this procedure was applied using two arbitrary suction and pressure side velocity distributions, it would not necessarily produce a closed blade section. This question is discussed immediately below.

The conditions for blade section closure have been expressed in various ways up to now. Generally speaking, three integral or global conditions must be satisfied in order to obtain a closed shape (see, among others ref.[3.2]). One of these conditions, ensuring that the correct mass flow rate is passing through the cascade, is automatically satisfied in the present case, where the stream function limit values have been correctly imposed. Following an extensive investigation, it was decided for the present work to employ appropriate overall parameters in order to control closure, rather than utilizing the usual integral conditions. The chosen parameters are the ratio of the pressure to suction side arc length and the pitch to chord ratio. This last parameter can be controlled by either modifying the number of blades or the blade chord. For initializing the first parameter a good first guess can be made using an existing blade section shape, which has the desired maximum thickness and, for the same inlet, produced the desired outlet flow angle. On the other hand, when changing the number of blades, it is necessary to bear in mind that the corresponding modification cannot be continuous.

We shall end here the discussion on

the inverse method and take it up again in the following Chapter.

9. The Effects of "Centrifugal" Forces

As "Centrifugal" forces will be denoted non-conservative forces and more particularly their components normal to the mean flow direction. As will be seen, their effects are particularly large for turbomachinery applications and for this reason, a separate Chapter has been dedicated to them.

Dimensional analysis shows that for flows with velocity gradients, non-conservative body forces have marked effects, when acting normal to the flow direction, even in the case where these forces are small compared to the inertia forces. Such non-conservative forces are the Coriolis forces, the forces created by the presence of a curved wall and the buoyancy forces created by a stratified density field.

Before going any further some examples will be given to demonstrate these effects:

1. for $\delta/R_c = 1/300$ a change of 10% in mixing length results [9.1] (R_c is the radius of the wall curvature).
2. For a radius of curvature R_c corresponding to a turning of 35° , a 10% change in distance to separation occurs (Bradshaw [9.2]).
3. The calculation results for the boundary layer developing along the suction side of an optimized compressor blade presented in the next Chapter are given in fig.(9.1). It can be seen that the presence of curvature causes boundary layer separation (detected also experimentally), for a case which would be considered rather far away, if curvature was absent. When this blade was designed, curvature effects were not very well known. Thus, they were not taken into account in the design process. The design having been realized slightly on the conservative side, separation appeared finally at the trailing edge.
4. Reversed transition is taking place (observed experimentally) in the presence of strong Coriolis forces (Johnston [9.3]).

In order to understand the stabilizing effects of such forces consider the case of the Coriolis force acting on a radial flow with a velocity gradient in the circumferential direction (fig.(9.2)). Let us consider also for simplicity the Navier-Stokes equations written for incompressible inviscid flow in a rotating frame of reference, which read

$$\vec{W} \cdot \nabla \vec{W} + 2\omega \times \vec{W} = - \nabla \left(\frac{p^*}{p} \right) \quad (9.1)$$

where p^*/p is the reduced static pressure.

We can see that an additional static pressure gradient is present to balance the Coriolis acceleration. If, now, for some reason, particles of a layer (1-1) with lower velocity w_{r1} arrive at an adjacent layer (2-2) where higher velocity w_{r2} prevails, they will be faced with an increased pressure gradient (due to the increased Coriolis force caused by the higher velocity w_{r2}). Consequently, they will tend to be pushed back to their original position. In this crude sense the situation described in fig.(9.2) is said to be stable and the effects of the Coriolis force are said to be stabilizing. Such a pressure gradient is caused also by the presence of wall curvature and buoyancy forces with the same results. The term "stabilizing" characterizes, thus, situations for which the turbulent intensities tend to reduce. The same goes for the other turbulent stresses. The shear layer, consequently, becomes more "laminar" and tends to support less adverse pressure gradients without separating. The opposite situation is termed "destabilizing", where the shear layer becomes more "turbulent".

Considering the situation in the radial part of the impeller (fig.(9.2)) in this way, we can see that the Coriolis force induces a pressure gradient that intensifies the one created by aerodynamic forces (that is, it is positive from suction to pressure side). It stabilizes the suction side shear layers, while it destabilizes the pressure side ones. Considering, now, the direction of the centripetal acceleration, we can see that the effect of longitudinal (in the main flow direction) surface curvature is stabilizing for convex surfaces and destabilizing for concave ones.

In order to account for these "centrifugal" effects, Bradshaw^(9.4) considered the ratio of "centrifugal" to inertia forces, that is the corresponding Richardson number and, finally (see for more details ref.(3.23) or the original references), established the following correction formula for the mixing length l

$$\frac{l_0}{l} = (1-\beta R_i)^{-1} \text{ for the stable side}$$

$$= 1-\beta R_i \quad \text{for the unstable side}$$

with $\beta=7$ for $R_i>0$ and $\beta=4$ for $R_i<0$.

Johnston^(9.5), working on Coriolis force effects and the corresponding ratio of Coriolis to inertia forces (called Rotation number Ro), came to the same conclusion.

Analysis of experimental results demonstrated that the value of β doesn't remain constant across the shear layer, but that a constant value, as indicated above, may produce good results. On the other hand, this "constant" value is influenced by the value of the overall Curvature Cu and Rotation Ro numbers, which are defined as

$$Ro_6 = - \frac{2\Omega b}{w_{se}} \quad (9.3)$$

$$Cu_6 = 2 \frac{\delta}{R_c}$$

Values for β in terms of Ro_6 and Cu_6 have been deduced from experiment by Papailiou^[3.22] and van den Brabandche^[9.6]. The relation of β (Ro_6 or Cu_6) of Papailiou is presented in figure (9.3). Experimental values from both Curvature and Rotation have been used and it seems that a unique curve can describe both effects. The value $\beta=7$ of Bradshaw corresponds to values of Cu_6 or Ro_6 of the order of 1/100. On the other hand Patel's^[9.7] experiment suggest a value of β as low as 2.5 for Cu_6 or Ro_6 of the order of 0.05. Note that for radial machines the value of Ro_6 exceeds 0.1.

Using the above introduced dimensionless parameters, we shall try and describe the effects of "Centrifugal" forces.

Although the laminar separation is not influenced by the effects of rotation [9.8] or surface curvature [9.9], "centrifugal" effects influence the laminar stability limit (see review on the subject in references [9.5] and [6.1]). Along curved surfaces or where Coriolis forces exist, instability introduced by three-dimensional disturbances leading to the Taylor-Görtler cellular vortices may become predominant (concave surface for surface curvature or leading surface for rotation) over the Tollmien-Schlichting one. The effect of surface curvature on stability for a concave wall is shown in fig.(9.4). One may note that the calculations show an amplification of the disturbance amplitude for all wave lengths for

$$\frac{w_{se}\delta}{v} \sqrt{\frac{\delta}{R_c}} > 16 \quad (9.5)$$

or, in view of equation (9.4), for

$$Ro_6 \sqrt{\frac{Cu_6}{2}} > 16 \quad (9.6)$$

Similar calculations by Conrad for a flat plate show that, for rotation, the stability limit is established by the relation

$$Ro_6 \sqrt{Ro_6} > 8.8 \quad (9.7)$$

From the above discussion one may conclude that on a leading or concave surface, instability will be provoked earlier when strong "centrifugal" forces are present. The opposite effect will be observed on a convex or suction surface, where the Tollmien-Schlichting mode of instability may be predominant. Once instability is introduced, then, the whole region of transition is influenced by the stabilizing or destabilizing effects. No reliable method exists today for reproducing the effects of

"centrifugal" forces to transition. Again, may we observe that the only existing alternative for the designer is to provoke transition as quickly as possible.

Papailiou, Nurzia and Satta (refs.[3.6],[3.17],[3.18], [3.20],[3.22], or the summary presented in ref.[3.23]), have developed, using Bradshaw's formulation, the appropriate correction for curvature effects adapted to an integral method of turbulent shear layer calculation.

The formulation developed by Papailiou, Nurzia and Satta for the correction due to longitudinal wall curvature is applicable to integral methods using the energy equation. The development of the correction was done in relation to the present calculation method. The correction is applicable to the value of the dissipation factor C_D (for details see the cited references) in the form

$$C_D = C_{D0} + (C_{Dcorr})_c + (C_{Dcorr})_R \quad (9.8)$$

where C_{D0} is the uncorrected value and $(C_{Dcorr})_c$, $(C_{Dcorr})_R$ are the corresponding corrections for curvature and Coriolis force effects.

The expressions for $(C_{Dcorr})_c$ and $(C_{Dcorr})_R$ are given below (for details see ref.[3.23])

$$(C_{Dcorr})_c = -\beta A_C (H_{12k}) + \frac{\delta}{R_C} + \beta^2 \left(\frac{\delta}{R_C} \right)^2 B_C (H_{12k}) \quad (9.9)$$

$$(C_{Dcorr})_R = -\beta A_R (H_{12k}) + \frac{\delta \Omega}{W_{ee}} + \beta^2 \left(\frac{\delta \Omega}{W_{ee}} \right)^2 B_R (H_{12k}) \quad (9.10)$$

The values of A_C , B_C , A_R , B_R are presented in figure (9.5). Note that, in addition to what was presented in ref.[3.23], here the values of the coefficients are given, as well, for separated turbulent shear layers. The study has been performed by Leoutsacos[9.10], and has resulted in slightly modified values for the coefficients A_C , B_C , A_R and B_R .

The present formulation has been completed by Huo[3.8] for the effects of Mach number. Huo based his correction on Rotta's[9.11] formula for the Mach number effects given below

$$\frac{1}{l_0} = 1 + \beta R_1 \left(1 + \frac{V-1}{2} M_e \right)^2 \quad (9.11)$$

Utilizing this formula, it results that the coefficients A_C , A_R are practically independent of Mach number, while the coefficients B_C , B_R depend on it in the following way

$$B = 0.467 M_e B_k \quad (9.12)$$

In order to evaluate the effects of the Coriolis forces it is necessary to know Ω . It is given (see also Johnston[9.12]) as follows

$$\Omega = |\omega| \cdot |\sin \gamma| \cos \psi \quad (9.13)$$

where the angles γ and ψ are presented in fig.(86). In other words, in order to know Ω , one must know the projection of the Coriolis force onto the normal to the blade surface. Johnston[9.12] gives the following expression for the angle γ

$$|\sin \gamma| = |\sin \lambda| \cos^2 \beta + \frac{\sin^2 \beta}{\cos^2 \lambda} \quad (9.14)$$

Details for developing the expression for $\cos \psi$ can be found in ref.[3.23]. The resulting formula is

$$\cos \psi = \pm \frac{1}{\sin \lambda} (\sin \lambda \cos \delta - \sin \lambda \sin^2 \beta \sin \delta) \quad (9.15)$$

When $\gamma=0$, we have also $\beta=0$ and so

$$(\cos \psi)_0 = \pm \sin \lambda \quad (9.16)$$

Finally, introducing expression (9.14) and (9.15) to (9.13) we get

$$\Omega = \pm \omega |\sin \lambda \cos \delta - \sin^2 \beta \sin \delta \cos \lambda| \quad (9.17)$$

For a purely axial blade, $\lambda=0$ and so

$$\Omega = \pm \omega \sin^2 \beta \sin \delta \quad (9.18)$$

It is seen, thus, that the blade twist ($\delta=0$) implies the existence of a Coriolis force component normal to the blade, even for a purely axial flow machine (cylindrical stream surfaces). For purely radial blades

$$\lambda = 90^\circ \text{ and so} \quad (9.19)$$

$$\Omega = \pm \omega \cos \delta$$

If additionally the inclination δ of the blade is zero, then $\Omega=\pm \omega$. The sign of the relation (9.15) depends on the blade surface considered. If the projection of the vector normal to this surface on the peripheral direction coincides in direction with the peripheral speed, then the sign (+) is applied.

It is, finally, interesting to demonstrate how the present theory compares with experiment. Besides the comparisons presented here, several comparisons can be found in references [3.3],[3.6],[3.7],[3.8],[3.9],[3.10], [3.12],[3.15],[3.16],[3.17],[3.18], [3.20],[3.22],[3.23].

Figures (9.7), (9.8) and (9.9) present three comparisons of theoretical predictions with experiment for cases, where wall curvature was present. Figure (9.7) concerns the case of an aerofoil (experiments performed in ONERA). Only the turbulent suction and pressure side parts have been plotted. Figure (9.8) concerns again the case of an airfoil suction side (experiments performed in

the Ecole Central of Lyon), where, this time, separation is present. The influence of curvature effects is quite large. In figure (9.9) theoretical predictions of the experiment of So and Mellor are presented. Finally, in figure (9.10) a comparison between theory and experiment is presented for the Coriolis force effects. Moore's experimental results have been used.

10. Results and Discussion

We have been discussing above various aspects of the design of arbitrary blade sections for turbomachinery applications. For this, various aspects of an inverse approach were described and we shall make, now, an attempt to demonstrate how these may be used. One has to state from the very beginning that each application has its own peculiarities and constraints so that no unique way may be traced for the design procedure. It is important, consequently, that the designer is acquainted, performing an investigation, about the order of magnitude of the various design parameters and the shape and level of the various distributions of the input quantities. The inverse methodology offers a considerable flexibility, giving to the geometric shape no constraints at all, but, on the other hand, it cannot take into account in a direct manner all the important parameters and constraints of the problem. In this respect, it may be stated from the very beginning that the inverse tool alone doesn't provide the best solution. It is the combination of an inverse and a good direct methodology that may provide the best possible results.

The above being quite general, we shall try below to explain in more detail what we mean.

In figures (10.1), (10.2) and (10.3) the computational results are presented from a numerical study on the geometry of a straight cascade. Although a particular geometry is addressed, the conclusions that will be drawn are quite general. Firstly, the trailing edge shape influence upon the velocity distribution is studied in figure (10.1). Only a small part of the blade near the trailing edge is deformed. The specified deformation is, however, quite important resulting to a blade angle at the trailing edge ranging from 0° to 45°. Our first observation is that, besides the trailing edge part of the velocity distribution, the rest of it has remained totally unchanged, in spite of the importance of the perturbation induced to the blade shape.

Our second observation is that the larger the wedge angle near the trailing edge, the lower the velocity value induced at the trailing edge and the higher the reacceleration of the flow from the trailing edge to infinity downstream.

We can conclude that the velocity field in the vicinity of the trailing edge is locally dependent upon the blade

shape there (and vice versa), while the wedge angle at the trailing edge (as the theory tells us) depends upon the admitted local value of the velocity at the trailing edge. This information may be used in the design of blade shapes with the inverse method.

Secondly, the leading edge shape influence upon the velocity distribution is studied in figure (10.2). Only a small part of the blade near the leading edge is deformed, in order to adjust it to various radii of curvature around the inlet stagnation point. The suction and pressure side velocity distributions for the four cases studied are presented in the figure. The same general observation can be made as to the local effects of the shape change upon the velocity distribution. On the other hand, although it cannot be clearly seen from the figure, the linearity of the velocity profile near the inlet stagnation point, when the radius of curvature is constant there, is assessed. One may, recognizing the well known fact that the shape of the leading edge influences the off design behaviour of the blading in subsonic flow, proceed in investigating for the blade leading edge shape that will give him satisfaction for this particular problem (or why the NACA combined thickness and camber distribution gives better off design performance than the C-4 circular arc distributions). Such studies result in giving the designer the necessary information, which will permit him to obtain the desired leading edge shape during the inverse (design) phase. Concerning the leading edge problem, we may state, additionally, that the corresponding changes near the leading edge do not appreciably change the shear layer behaviour. They can also be transferred on the image plane, so that they can be included in the choice of the appropriate image curve.

Thirdly, the blade thickness influence is studied in figure (10.3). For this, the mean camber line of the blade and the non-dimensional thickness distribution has been kept unchanged. Only the maximum thickness value has been changed.

The general observation that can be made here is that for an increase in blade thickness both levels of the pressure and suction side velocity distributions increase. The approximate increase may be estimated taking into account the increase of the relative blockage effect in the passage. This estimation can be done for compressible flow, as well. On the same figure one may identify the previously two studied effects, as, simultaneously with the thickness, the inlet radius and the outlet wedge angle were modified.

The above described study may, as one can see, give us information as to how we may deal with the choice of the leading and trailing edge velocity distributions, as well as, how to deal with certain aspects of the mechanical constraints imposed upon the blade design. As one example we present in figure (10.4) a turbine blade which we

used as starting point and the thicker blade that we obtained by increasing the level of the suction and pressure side velocity distributions keeping, at the same time, the same inlet and outlet conditions. This particular design is quite revealing, because changes in the velocity distribution were introduced in such a way, so that the maximum velocity was not increased. On the other hand the linear part of the inlet velocity was kept intact, so that the radius of curvature at the inlet was conserved.

Up to now, we have talked about closed profiles and we have given the parameters, which may help us to obtain closure. No theoretical background may be found as to how one can play with them, in order to obtain closure. We have found out empirically how, and we can state that it is possible to obtain closure with around five iterations. During these iterations the suction side velocity distribution may be kept unchanged or, if the absolute necessity to change it partly or on the whole arises, then an optimum one can be chosen again. During the computational procedure aiming for closure, the parts of the velocity distributions near the leading and trailing edges can remain unchanged, in order to ensure the desired blade section shape locally.

When the Lock and Firmin model is applied, the inviscid flow calculation (direct or inverse) considers the effective blade section surface, which includes the displacement thickness. Consequently, during the complete inverse design procedure, including viscous effects, it will be necessary to subtract from the obtained blade section shape the displacement thickness both from the pressure and the suction sides. The target will be then to obtain a closed blade after the suction and pressure side displacement thicknesses have been subtracted. Obtaining an open profile with a definite distance between the trailing edge suction and pressure sides doesn't constitute a problem for the inverse method. On the other hand, in Chapter 2, the condition concerning the static pressure difference of the inviscid flow at the trailing edge has been specified (equivalent Kutta condition). It is possible to express it in a velocity difference and utilize it during the inverse procedure.

Before going any further, let us apply the design procedure to a specific case, in order to make a demonstration. An old design [3,21] of a compressor blading will be considered. The compressor blading was imposed to have a 45 degrees inlet air angle and an axial discharge. The desired blade chord Reynolds number was approximately 3×10^5 and no additional constraint was imposed, other than that the blade ought to be manufacturable. It was taken that the velocity ratio $V_1/V_2=0.707$ and, considering that $V_{max}/V_1=1.3$ was a reasonable value, we came to the conclusion that V_{max}/V_1 should be of the order of 1.84. Considering figure (7.6), it is possible to see that combining the Reynolds number requirements, the

maximum velocity requirements (for a more or less thick blade) and the requirement to get the V_{mean}/V_1 as high as possible, a good first compromise could be achieved with $X_f = 8.2$ and $X_f - X_t = 2.2$.

It can be seen from figure (7.6) that the choice of the $(X_f - X_t)$ -value doesn't correspond to the maximum of the $(W_{so,mean}/W_{so,2})$ -curve for $X_f=8.2$. One has to remark, however, that, as long as we keep ourselves near the maximum, which is the case here, the corresponding loss in circulation is not important. Figure (10.5) presents different aspects of this case. Once the overall intrinsic values of the image curve were specified, the optimum image curve for the blade suction side was constructed and is presented in figure (10.5(a)). The corresponding suction side velocity distribution was then calculated and is presented in figure (10.5(b)). A pressure side velocity distribution was matched to it and, using the conformal mapping inverse method of A. Goldstein, a blade shape was issued. It is presented in figure (10.5(c)). The image curve corresponding to the pressure side velocity distribution is traced on the image plane, figure (10.5(a)). It was tried to obtain an as extended as possible laminar shear layer.

One may find quite a few deficiencies in this first design, the most important one being that the influence of curvature effects on turbulence was not included. When the blade was tested in the VKI cascade wind tunnel, it was found that, due to the high loading, lateral flow convergence was important and, although it was assessed that transition was located where it was introduced theoretically, the velocity distribution was diverging from the theoretical one and so were the losses. This situation is described in figure (10.5(b)). Subsequent tests conducted in Pratt and Whitney in 2-D conditions, however, demonstrated that the experimental velocity distribution was very close to the theoretical one and so were the losses. Experimental results presented in figure (10.5) obtained in Pratt and Whitney, demonstrate that the level of losses of the optimized blade is quite below that of the NACA series and that its off designed behaviour is quite remarkable.

When the curvature effects on turbulence were incorporated in the method, calculations were performed for the suction side velocity distribution and were reported here in figure (9.1). It can be seen, there, that, without curvature effects, the suction side shear layer is far from separation (a conservative design was adopted). When curvature effects are taken into account, separation is reached near the trailing edge. This separation was observed, also, experimentally.

The case of a wind turbine blading is examined in figure (10.6). This was actually a redesign of the hub blade section, which is presented in figure (8.6.3). The redesign was undertaken,

because it was found that considerable separation was present for the existing case. The same overall target was maintained (as far as number of blades and circulation per blade were concerned). The aim was to get as low losses as possible. It was also decided to avoid turbulent separation for the design point. In figure (10.6) the optimum velocity distribution is given and the corresponding blade shape. Already, one can see that the shape is not conventional and cannot be easily represented by a mean camberline and a thickness distribution. On the other hand, the theoretical calculation tells us that the losses were reduced by a factor of four in respect to the existing blading. More details for this case can be found in references [3.25] and [3.26].

In order to demonstrate the capabilities of the method, a redesign of the blade presented in figure (10.5) was done. This time, however, all effects were included in the computation, while in addition the inlet Mach number was taken to be $M_{in}=0.7$ and a thicker blade was targeted. The calculation results are presented in figure (10.7). It can be seen that the blade is thicker, the local Mach number is over unity and the circulation is higher than in the previous case resulting to a higher pitch to chord ratio. The calculated level of losses, thus obtained, remains still quite low and comparable to the previous case.

The inclusion of curvature and Coriolis force effects in the design procedure must be discussed somewhat further. One has to observe that these effects have as a consequence to displace the optimum deceleration curve (which is the locus of the maximum M_t -values). In figure (10.8) calculation results are presented that demonstrate that the locus of maximum M_t -values for turbulent flow is displaced when these effects are present. On the other hand some calculation results concerning the Coriolis force effects are presented in figure (10.9). A velocity distribution is considered with very high deceleration. Using this velocity distribution, image curves are calculated for various values of the rotation number. The velocity distribution and the sign of the rotation number are assumed to correspond to the radial part of the pressure side of the blading of a centrifugal compressor. It can be seen from figure (10.9) that the initial deceleration is quite high and that early flow separation appears. The Coriolis force effects, however, tend to delay separation, or even suppress it altogether. The results of similar calculations performed for the suction side of the blade radial part of a centrifugal compressor demonstrate that, in the presence of strong Coriolis forces, the deceleration that this part of the blade can sustain is very limited.

It can be seen, from the evidence given above, that the design of radial machines is influenced considerably by these effects. In fact, the design of a

new version of a radial compressor [10.1], [10.2] was done utilizing the present calculation method. The aim of the design was to reduce the axial length of the compressor for the obvious advantages of a multistage arrangement. The compressor pressure ratio was $n=2$ and its mass flow rate $m_a=8\text{kg/s}$. Some results of the calculations are presented in figure [10.10]. They concern the blade suction and pressure side velocity distributions along the mean stream surface. The variation of the streamtube width and radius was taken into account along with the effects of compressibility and those due to the wall curvature and Coriolis force. The shear layer calculation penetrated inside the reverse flow region.

It can be seen from figure (10.10) that the chosen velocity distributions are such that the deceleration is rather mild on the suction side and severe on the pressure side. The "centrifugal" force influence finally provokes separation near the suction side trailing edge, while it suppresses it all together on the pressure side.

Details on the radial compressor and the test results that were performed in ECL can be found in reference [10.2]. It can be seen there that the overall efficiency of the compressor (including the scroll) at the design point was 0.84, a figure which can be considered rather satisfactory. The impeller efficiency at design point was found to be 0.90 and equal to the computed one. This figure, however, alone cannot explain the good overall efficiency. We believe that it was the limited separation admitted for the impeller that provided the diffuser with good initial flow conditions that gave this interesting result. We can also remark the hub shape, which was found to be necessary during the design, in order to obtain the pressure side deceleration, where the Coriolis force effects were effective.

11. Conclusions

The present course tried to propose theoretical tools that may help the designer in his work. In fact, a complete (viscous and inviscid) inverse procedure was proposed, but, it was pointed out, that in order to obtain results, it has to be combined with a sound direct (analysis) one. Various examples were chosen in order to demonstrate the use of the proposed tools. Of course, these examples do not cover all cases, but rather converge to the conclusion that the proposed tools may prove to be quite useful, while, each design must be considered as a separate case.

<u>APPENDIX A1</u>		Re_1	Reynolds number based on displacement thickness
<u>Nomenclature</u>		Re_2	Reynolds number based on momentum thickness
(x, y) or mainstream and normal (m, n, δ) directions		Re_3	Reynolds number based on energy thickness
$\vec{V} (u, v)$ absolute velocity vector having components u, v in the x and y directions		Re_4	Reynolds number defined by equation (1.91)
$\vec{w}(W_m, W_n)$ relative velocity vector having components in the m and n directions		Re_x	Reynolds number based on distance
$M(L_k, X)$ semi empirical functions for laminar and turbulent flows		Re_{∞}	Reynolds Number defined as (see eq. 3.6) $\frac{W_{\infty} \cdot (\delta_2 - \delta_1^*)}{v_w}$
$\beta_1(L_k)$			
$\beta_{11}(L_k, X)$			
$\beta_{12}(L_k, X)$			
$\beta_{13}(L_k, X)$			
$C_1(L_k)$			
$C_{11}(L_k, X)$			
$C_{12}(L_k, X)$			
$C_{13}(L_k, X)$			
$C_{t1}(L_k, X)$			
$C_{t2}(L_k, X)$			
$C_{t3}(L_k, X)$			
c_p specific heat coefficient for constant pressure or pressure recovery coefficient		Ri	local Richardson number
A, B semi-empirical coefficients used for the calculation of the curvature and Coriolis effects		R	radius
c_D dissipation factor		R_c	longitudinal surface curvature
c_f skin friction coefficient		Ro_6	overall rotation number
C_{u6} overall Curvature number		r	recovery factor
E kinetic energy dissipation		S	stability parameter of Prandtl
G Clauser's or Rotta's form factor		T	temperature
$H_{12} = \delta_1 / \delta_2$ momentum thickness from factor		u_t	friction velocity
$H_{32} = \delta_3 / \delta_2$ energy form factor		u^*	reduced velocity used in compressible flow theory
$H_{\rho_2} = \delta_\rho / \delta_2$ density form factor		U, V, W	velocity
I integral used for the calculation of the transition point (equation (7.5))		X	abscissa of Le Foll's plane
K - factor introduced in order to take into account the normal fluctuation terms - curvature		α	angle
k, c constants of law of the wall		β	- "constant" used in the calculation of curvature and Coriolis effects - angle
l mixing length		γ	ratio of specific heats
L length		$w(y/\delta)$	Coles' wake function
L_k ordinate of Le Foll's plane		δ	boundary layer thickness
m power characterizing the equilibrium boundary layer velocity distribution		δ_1	displacement thickness defined as $\frac{\rho_{\infty} \cdot W_{\infty} \cdot R_w \cdot \delta_1}{\delta} = \int R(\rho_e W_{\infty} - \rho W_s) dn$
M_∞ free stream Mach number		δ_2 or θ	momentum thickness defined as $\frac{\rho_{\infty} \cdot W_{\infty} \cdot R_w \cdot \delta_2}{\delta} = \int R_w \rho (W_{\infty} - W_s) dn$
p static pressure			
p^* reduced pressure			
q external velocity logarithm			
Re Reynolds number			

δ_3	energy thickness defined as $\frac{\rho_{\infty} \cdot w_{\infty} \cdot R_w \cdot \delta_3}{\delta} = \int_{R_w}^{\infty} R_w \rho (w_{\infty} - w) dn$	w	wall
	o	o	reference
	corr	corr	correction
	e	e	external flow
δ_{ik} or δ_k	kinetic displacement thickness defined as $\frac{\rho_{\infty} \cdot R_w w_{\infty} \cdot \delta_{ik}}{\delta} = \int_{R_w}^{\infty} R \cdot \rho_e (w_{\infty} - w) dn$	ref,r	reference
	s	s	- separation - tangent to the wall direction
	o	k	kinematic
δ_p	density thickness defined as $\frac{\rho_{\infty} \cdot R_w \cdot \delta_p}{\delta} = \int_{R_w}^{\infty} R (\rho_e - \rho) dn$	t	- total - turbulent
	o	max	maximum
		min	minimum
		f or F	final
δ_h	enthalpy thickness	I	instability
λ	Le Foll's velocity profile family free parameter	T	transition
μ	coefficient of viscosity	n	normal to the wall direction
ν	kinematic viscosity	l	- lower - laminar
ν_t	turbulent kinematic viscosity	u	upper
π_1	Cole's velocity profile family free parameter	in	initial
Γ	circulation	Φ, Ψ	partial derivatives
Π, Π_1	boundary layer equilibrium parameters		$\frac{\partial}{\partial \theta}$ and $\frac{\partial}{\partial \Psi}$
ρ	density		<u>REFERENCES</u>
σ	convergence/divergence or rotation parameter	1.1	LOCK R.C. "A Review of Methods for Predicting Viscous Effects on Aerofoils and Wings at Transonic Speeds" AGARD CP-291, Paper 2.
τ	shearing stress	1.2	LOCK R.C., FIRMIN M.C.P. "Survey of Techniques for Estimating Viscous Effects in External Aerodynamics" IMA Conference, London, 1981.
ϕ	angle	1.3	EAST L.F. "A Representation of Second-Order Boundary Layer Effects in the Momentum Integral Equation and in Viscous-Inviscid Interactions" RAE Technical Report 81002.
Φ	velocity potential Reynolds number	3.1	LE FOLL J. "A Theory of Representation of the Properties of boundary Layers on a Plane" Proc. Seminar on Advanced Problems in Turbomachinery, VKI March 29-30, 1965.
ψ	stream function	3.2	PAPAILIOU K.D. "Blade Optimization Based on Boundary Layer Concepts" Von Karman Institute CN60, 1967.
η	normal to the profile component of the rotating speed vector		
ω	rotational speed		
ω	constant in Sutherland's equation		
<u>Superscripts</u>			
($\bar{}$)	mean value		
($\bar{}$)*	value which takes into account the fluctuating quantities		
.	turbulent fluctuations		
<u>Subscripts</u>			
c	curvature		
R	rotation		

- 3.3 PAPAILIOU K.D.
"Optimization d'Aubage de Compresseur à Forte Charge sur la Base des Théories de Couches Limites"
These de Doctorat en Sciences Appliquées, Université de Liège, 1969.
- 3.4 PAPAILIOU K.D.
"Boundary Layer Optimization for the Design of High Turbine Axial Flow Compressor Blades"
ASME Transactions, Journal of Engineering for Power, 1971, pp 147-155.
- 3.5 PAPAILIOU K.D.
"An Investigation on Le Foll's Method Used for Blade Optimization Based on Boundary Layer Concept"
Proc. Congress of the International Astronautical Federation, Argentina, 1967.
- 3.6 PAPAILIOU K.D., SATTA A., NURZIA F.
"On the Two-Dimensional Boundary Layers as they Appear on Turbomachine Blades"
AGARD AG 164, 1973.
- 3.7 HUO S.
"Blade Optimization Based on Boundary Layer Concept"
AGARD AG 164, 1973.
- 3.8 HUO S.
"Optimization Based on the Boundary Layer Concept for Compressible Decelerating Flows"
These de Doctorat, Université de Bruxelles, 1973.
- 3.9 HUO S.
"Optimization Based on the Boundary Layer Concept for Compressible Decelerating Flows"
ASME Paper 74-GT-86.
- 3.10 PAPAILIOU K.D.
"Calcul d'une Couche Limite Laminaire et Turbulente Bidimensionnelle (Convergente-Divergente et Axisymétrique) Compressible, qui se Développe sur une Plaine ou Courbe" (Problème Direct et Inverse).
Rapport SNECMA. Compte-Rendu YKB No 23/74, 1974.
- 3.11 ASSASSA G.M., PAPAILIOU K.D.
"Calcul des Couches Limites Décollées"
Rapport Final.
Rapport METRAFLU-ECL pour le compte de la SNECMA, 1975.
- 3.12 ASSASSA G.M.
"Calcul par des Méthodes Intégrales de Couches Limites Laminaires ou Turbulentes Incompressibles ou Compressibles Incluant des Zones Faiblement Décollées"
These de Docteur ès Sciences Physiques, Université Claude Bernard, Lyon, 1976.
- 3.13 ASSASSA G.M., PAPAILIOU K.D.
"An Integral Method for the Calculation of the Separated Turbulent Boundary Layer"
Transactions of the ASME, Journal of Fluid Engineering, March 1979, pp 110-116.
- 3.14 BARIO F.
"Contribution à l'Etude de Développement des Couches Limites sur les Aubages de Turbomachines"
These de Doctorat 3ème cycle, Université Claude Bernard, Lyon 1978.
- 3.15 PAPAILIOU K.D.
"Viscous Flows in Centrifugal Compressors"
VKI Lecture Series 95, Short Course on Industrial Centrifugal Compressors, 1977.
- 3.16 PAPAILIOU K.D.
"Optimization des Dispositifs Decelérateurs à Forte Charge, Fondée sur une Théorie Intégrale de la Couche Limite"
These d'Etat. Université Claude Bernard, Lyon 1974.
- 3.17 PAPAILIOU K.D., NURZIA F., SATTA A.
"The Inclusion of Surface Curvature Effects in the Calculation of the Turbulent Boundary Layer With Integral Methods"
Internal Note 37, VKI, 1970.
- 3.18 NURZIA F., SATTA A., PAPAILIOU K.D.
"The Inclusion of Surface Curvature Effects in the Calculation of the Turbulent Boundary Layer With Integral Methods"
Part II, Internal Note 44, VKI, 1973.
- 3.19 PAPAILIOU K.D.
"Boundary Layers in Radial Compressors"
Part I.
La Thermotechnica no 6, June 1973
- 3.20 PAPAILIOU K.D.
"The Coriolis Force Influence when we Calculate Turbulent Boundary Layers in Centrifugal Compressors"
Israel Joint Gas-Turbine Congress, Jul. 1979.
- 3.21 PAPAILIOU K.D.
"Boundary Layer Optimisation for the Design of High Turning Axial Flow Compressor Blades", ASME paper 70-GT-88, 1970. ASME Trans., Journal of Engg. for Power, Vol. 93, pp 147-155, 1971.
- 3.22 PAPAILIOU K.D.
"Viscous Flows in Centrifugal Compressors", Short Course on "Industrial Centrifugal Compressors" VKI Lecture Series 95, 1977

- 3.23 PAPAILIOU K.D.
"Le Foil's Method and the Calculation of Attached and Separated Two-Dimensional Boundary Layers"
Von Karman Institute, Lecture Series on "Separated Flows in Turbomachinery Components"
VKI LS 1981-1, 1981
- 3.24 PAPAILIOU K.D.
"Some Results on Flow Calculations Involving Drag Predictions"
AGARD CP-437, Lisbon Portugal, May 1988.
- 3.25 BOLETIS E., CHAVIAROPOULOS P., BOURAS B., BONATAKI E., PAPAILIOU K.D.
"A complete inverse calculation procedure for the optimization of horizontal-axis wind turbine airfoils"
Proceedings of the European Community Wind Energy Conference, Herning, Denmark, June 6-10, 1988.
- 3.26 PAPAILIOU K.D., CHAVIAROPOULOS P., BONATAKI E., BOURAS B., KAKOYROS G.
"Aerodynamic Investigation of Horizontal Axis Wind Energy Machine Rotors"
Proceedings of the European Community Wind Energy Conference, Herning, Denmark, June 6-10, 1988.
- 3.27 GEROLYMONS G., KALLAS Y., PAPAILIOU K.D.
"The Behaviour of the Normal Fluctuation Terms in the Case of Attached or Detached Turbulent Boundary Layers"
ASME Paper 84-GT-179, 1984
- 3.28 KALLAS J., PAPAILIOU K.D.
"A Method for the Calculation of the Interaction of a Turbulent Boundary Layer with a Shock Wave"
ISABE 87-7074. Proceedings of the 8th Intern. Society of Air Breathing Engines (ISABE), Cincinnati, Ohio, U.S.A., 1987
- 3.29 STAMATIS A., KTENIDIS P., PAPAILIOU K.D.
"Viscous Inviscid Interaction in the Case of a Laminar Separation Bubble"
Proceedings of the 38th Congresso Nazionale ATI, Bari, La Termotecnica, September 28-30, 1983
- 3.30 KALLAS J.
"Shock/Boundary Layer Interaction"
Ph.D. Thesis, NTUA, Greece, 1987
- 3.31 MALAMATENIOS CH., GIANNAKOGLOU K., PAPAILIOU K.D.
"A Calculation Method for Gas-Droplet Flows in Turbomachinery Components Including Viscous Effects"
Paper presented at the International Symposium on Engineering Turbulence and Measurements, Dubrovnik, Yugoslavia, 24-28 September 1990.
- 3.32 BOURAS V.
"Integral Method for the Calculation and Optimization of Laminar and Turbulent Shear Layers in the Presence of Flow Separation"
Ph.D. Thesis, under preparation, NTUA, GREECE.
- 3.33 BOURAS V.
"An Integral Method for the Calculation of Unsteady Turbulent Boundary Layers"
Student Thesis, NTUA, GREECE, 1986.
- 3.34 LYTRAS D.
"An Integral Method for the Calculation of the Turbulent Wake"
Student Thesis, NTUA, GREECE, 1989.
- 3.35 KATRIMATOS D.
"Calculation of Fully Separated Two-Dimensional Shear Layers in Integral Aerodynamic Cases, with Emphasis on Loss Calculation (in Greek)".
Student Thesis, Thermal Turbomachinery Lab., National Technical Univ. of Athens, 1987.
- 3.36 STEWARTSON K.
"Correlated Incompressible and Compressible Boundary Layer"
Proc. Roy. Soc. London, A 200, 1949, pp. 84-100.
- 4.1 FALKNER V.H., SKAN S.W.
"Some Approximate Solutions of the Boundary Layer Equations"
Phil. Mag. 12, 865, 1931. ARC R and M 1314, 1930.
- 4.2 CLAUSER F.H.
"Turbulent Boundary Layers in Adverse Pressure Gradients"
Journal of Aeronautical Sciences, 21, pp 91-108, 1954.
- 4.3 BRADSHAW P.
"The Turbulence Structure of Equilibrium Boundary Layers"
NPL Aero. Rep. 1184, 1966.
- 4.4 COLES D.
"The Law of the Wall in Turbulent Shear Flow"
50 Jahre Grenzschicht Forschung, Verlag Fr. Vieweg, Braunschweig, 1956.
- 4.5 COLES D.
"The Law of the Wake in the Turbulent Boundary Layer"
Guggenheim Aero. Lab., Caltech, 1955.
- 4.6 KUHN J.D., NIELSEN J.N.
"Prediction of Turbulent Separated Boundary Layers"
AIAA Paper No 73-663, July 1973.
- 4.7 PAPAILIOU K.D.
"Calibration of the Dissipation Factor"
VKI IN 25, 1967.
- 4.8 PAPAILIOU K.D.
"The Calculation of an Equilibrium Turbulent Boundary Layer"
VKI IN 23, 1967.

- 4.9 NASH J.F.
Turbulent Boundary Layer Behaviour
and the Auxiliary Equation"
GARDograph 97, Part 1, May 1965,
pp 245-279.
- 4.10 VAN DRIEST E.R.
"Turbulent Boundary Layers in
Compressible Fluids"
Journal of Aero Sciences, Vol.18,
1951.
- 4.11 MATHEWS D.G., CHILDS M.E.,
PAYNTER G.C.
"Use of Coles Universal Wake
Function for Compressible
Turbulent Boundary Layers"
Journal of Aircraft, Vol. 7, No 2,
March-April, pp 137-140, 1970.
- 4.12 ALBER I.E.
"Analytical Investigations of
Equilibrium and Non Equilibrium
Compressible Turbulent Boundary
Layers"
Project Squid Tech. Re DYN-I-PY,
1969.
- 4.13 MORKOVIN M.V.
"Effects of Compressibility on
Turbulent Flows"
Mécanique de la Turbulence,
Colloques Internationaux du Centre
National de la Recherche
Scientifique, Marseille 1961,
Editions du CNRS, Paris 1962.
- 4.14 ALBER I.E.
"Similar Solutions for a Family of
Separated Turbulent Boundary
Layers"
AIAA Paper 71-203, 1971.
- 5.1 KLINE S.J., SOVRAN G., MORKOVIN
M.V., COCKRELL D.J. (Editors)
"Proceedings, Computation of
Turbulent Boundary Layers-1968"
AFOSR-IFP-Stanford Conference,
Volumes I and II, 1968.
- 5.2 TANI I.
"On the Approximate Solution of the
Laminar Boundary Layer Equations"
Journal of Aero. Sci., 21, pp 487-
504, 1954.
- 5.3 LEES L., REEVES B.
"Supersonic Separated and
Reattaching Laminar Flows"
AIAA Journal, Vol. 2, Nov. 11, pp.
1907-1920, 1964.
- 5.4 COMTE A., OHAYON G., PAPAILIOU
K.D.
"A Method for the Calculation
of the Wall Layers Inside the
Passage of a Compressor
Cascade with and without Tip
Clearance", ASME paper 81-GT-
168, ASME Trans., Journal of
Engg. for Power, Vol. 103/3,
1981.
- 5.5 DOUVIKAS D.
"Secondary Losses Calculation
in an Axial Compressor"
PhD Thesis, NTUA, Athens,
Greece, October 1988
- 5.6 DOUVIKAS D., KALDELIS J.,
PAPAILIOU K.D.
"A Secondary Flow Calculation
Method for one Stage
Centrifugal Compressor"
Paper presented in the 9th
International Symposium on
Air Breathing Engines (ISABE),
Athens, Greece, September
1989.
- 5.7 KALDELIS J.
"Calculation of Secondary
Losses in an Axial Transonic
Compressor, with the Presence
of Shock Waves in the Free
Stream Flow Region"
RhD Thesis, NTUA, Athens,
Greece, October 1988.
- 5.8 KALDELIS J., DOUVIKAS D.,
FALCHETTI F., PAPAILIOU K.D.
"A Secondary Flow Calculation
Method for One Stage Axial
Transonic Flow Compressors,
including Shock-Secondary Flow
Interaction"
Paper presented at the 1989
ASME IGTI Intern. Gas
Turbine Aeroengine Congress
and Exposition, Toronto,
Canada. Accepted for public.
in the ASME Trans.
- 5.9 PAPAILIOU K.D.
"A Contribution to the Calculation
of Secondary Flows in an Axial
Compressor"
Proceedings of the 6th
International Symposium of Air
Breathing Engines (ISABE), Paris,
June, 1983.
- 6.1 SCHLICHTING H.
"Boundary Layer Theory"
4th ed., McGraw Hill, 1962.
- 6.2 STRATFORD B.S.
"An Experimental Flow With 2aero
Skin Friction Throughout Its Region
of Pressure Rise"
J. of Fl. Mech., Vol. 5, No 1,
1959, pp. 17-35.
- 6.3 HASTINGS R.C., MORETON K.G.
"An Investigation of a Separated
Equilibrium Turbulent Boundary-
Layer"
Int. Symp. of Appl. L.D.A. to Fl.
Mech., p. 11.1.
- 6.4 PAPAILIOU K.D.
"Boundary Layers in Radial
Compressors"
Parts II and III.
La Thermotechnica no 7, July 1973
no 8, Aug. 1973
- 6.5 PAPAILIOU K.D.
"Correlations concerning the
Process of Flow Deceleration"
Jr. of Engg. for Power, April 1975,
pp. 295-300.
- 6.6 BRADSHAW P., GALEA
"Step-Induced Separation of a
Turbulent Boundary Layer in
Incompressible Flow"
Journal of Fluid Mechanics, Vol.27,
Part I, pp. 111-130, Jan. 1967.

- 6.7 SEDDON J.
"The Flow Produced by Interaction of Turbulent Boundary Layer with a Normal Shock Strength Sufficient to Cause Separation"
RAE Tech. Memo Aero. 667, March 1960.
- 7.1 GRANVILLE P.S.
"The Calculation of Viscous Drag of Bodies of Revolution"
Navy department. The David Taylor Model Basin; Report No 849, 1953.
- 7.2 REAY D.A.
"Tests on a Le Foll Symmetrical Profile at Liverpool Univ."
IRD Report CAP 68-5, 1968.
- 7.3 LEOUTSAKOS G.
"Private Communication"
NTUA, 1990.
- 7.4 ARNAL D.
"Stabilité et transition des Couches Limites Laminaires Bidimensionnelles en Ecoulement Compressible, sur Paroi Athermane"
La Recherche Aérospatiale, No 4, 1988, pp. 15-32.
- 7.5 SIMANDIRAKIS G.
"Accelerated Boundary Layers"
Student Thesis, NTUA, 1987.
- 8.1 SCHMIDT E.
"Computation of Supercritical Compressor and Turbine Cascades With a Design Method for Transonic Flows"
Trans. of ASME, Jr. of Engg. for Power, Vol. 102, pp. 68-74, Jan. 1980.
- 8.2 SCHMIDT E., BERGER P.
"Inverse Design of Supercritical Nozzles and Cascades"
Int. J. Num. Meth. Eng., Vol. 22, Feb. 1986, pp. 417-432.
- 8.3 SCHMIDT E.
"Inverse Methods for Blade Design, Controlled Diffusion Blading for Supercritical Compressor Flow"
VKI-LS 1988-03 Transonic Compressors
- 8.4 SCHMIDT E., KLIMETZEK F.
"Inverse Computation of Transonic Internal Flows With Application for Multi-Point-Design of Supercritical Compressor Blades"
Presented at the Specialists Meeting on Computational Methods for Aerodynamic Design (Inverse) and Optimization, Loen, Norway, May 1989.
- 8.5 BONATAKI E.
"Inviscid Subsonic Inverse Method for the Design of Blade Sections along Arbitrary Axisymmetric Stream Surfaces with Varying Stream Tube Width"
Ph.D. Thesis, in preparation, NTUA, Greece.
- 8.6 ZEDAN M. SCHNEIDER G.E.
"A Three-Dimensional Modified Strongly Implicit Procedure for Heat Conduction"
AIAA Journal, Vol. 21, 1983.
- 8.7 CHAVIAROPOULOS P., GIANNAKOGLOU K., PAPAILOU K.D.
"Numerical Computation of Three-Dimensional Rotational Inviscid Subsonic Flows, Using the Decomposition of the Flow Field into a Potential and a Rotational Part"
ASME paper 86-GT-169.
- 8.8 JONES D.J.
"Test Cases for Inviscid Flow Field Methods, Reference Test Cases and Contributors"
AGARD AR-211.
- 8.9 KATSANIS T.
"Fortran Program for Calculating Transonic Velocities on a Blade-to-Blade Stream Surface of a Turbomachine"
NASA TN D-5427, 1969.
- 8.10 BOLETIS E., CHAVIAROPOULOS P., BONATAKI E., BOURAS B., PAPAILOU K.D.
"A Complete Inverse Calculation Procedure for the Optimization of Horizontal-Axis Wind Turbine Airfoils"
European Community Wind Energy Conference, 6-10 June 1988, Herning, Denmark.
- 8.11 BONATAKI E., BOURAS B., KAKOUROS G., CHAVIAROPOULOS P., PAPAILOU K.D.
"Aerodynamic Investigation of Horizontal Axis Wind Energy Machine Rotors"
Contract final report, EN3W-0035-GR.
- 9.1 BRADSHAW P.
"Advances in Turbulent Shear Flow"
Von Karman Institute Short Course, March 19-23, 1973.
- 9.2 BRADSHAW P.
"Prediction of Turbulent Shear Layers in Turbomachines"
International Symposium on the Fluid Mechanics and Design of Turbomachinery, Penn. State Univ., Sept. 1970.
- 9.3 JOHNSTON J.P.
"The Separation of Shear Layer Turbulence in Rotating Systems"
AGARD CP-93, 1971.
- 9.4 BRADSHAW P.
"The Analogy Between Streamline Curvature and Buoyancy in Turbulent Shear Flow"
N.P.L. Aero Re.1231, ARC 29048, May 1967.
- 9.5 JOHNSTON J.P.
"The Effects of Rotation on Boundary Layers in Turbomachine Rotors"
Report MD 24, Thermoscientific Div., Stanford Univ., May 1970.
- 9.6 VAN DEN BRAEMBUSSCHE R., ZUNINO P.
"Correction for Streamline Curvature and Coriolis Force in a Boundary Layer Integral Method"
ASME paper 81-GT-97, 1981.

- 9.7 PATEL V.C.
 "The Effects of Curvature on the
 Turbulent Boundary Layer"
 ARC R AND M No 3599, Cambridge Un.
 1968.
- 9.8 HALLEEN R.M., JOHNSTON J.P.,
 REYNOLDS W.C.
 "The Laminar Boundary Layer on a
 Rotating Arc Blade"
 ASME Paper No 65 WA/FE 15, 1965.
- 9.9 BLASEY B.S., CLAYTON B.R.
 "Laminar Boundary Layers and Their
 Separation From Curved Surfaces"
 ASME Trans., Jr. of Basic Eng.,
 1965.
 See discussion by J.C. Rotta.
- 9.10 LEOUTSAKOS G., PAPAILIOU K.D.
 "Curvature and Coriolis Correction
 on the Dissipation Factor C_D for
 Turbulent Boundary Layers
 (unseparated and Separated)"
 Thermal Turbomachines Lab.
- 9.11 ROTTA J.C.
 "Effect of Streamwise Curvature on
 Compressible Turbulent Boundary
 Layers"
 Boundary layers and turbulence. The
 Physics of Fluids Supplement, 1967.
- 9.12 JOHNSTON-EIDE J.P.
 "Turbulent Boundary Layers on
 Centrifugal Compressor Blades:
 Prediction of the Effects of
 Surface Curvature and Rotation"
 ASME 76 Fe-10.
- 10.1 CYFFERS J., CRINQUETTE J.M.,
 PAPAILIOU K.D., BOIS G., HONG.A.
 "Etude d'un Etage Centrifuge a
 Grand Rapport de Moyeu, Destiné a
 la Réalisation de Compresseurs
 Multiétages en Ligne pour Gas
 Contenant Eventuellement des
 Particules en Suspension"
 Contrats DGRST, 75-7-1279, 75-7-
 1280 rapport final 1979.
- 10.2 BOIS G., PAPAILIOU K.D.
 "A Contribution to the Study of the
 Design of an Industrial
 Centrifugal Compressor"
 ASME Paper 84-GT-60, 1984.

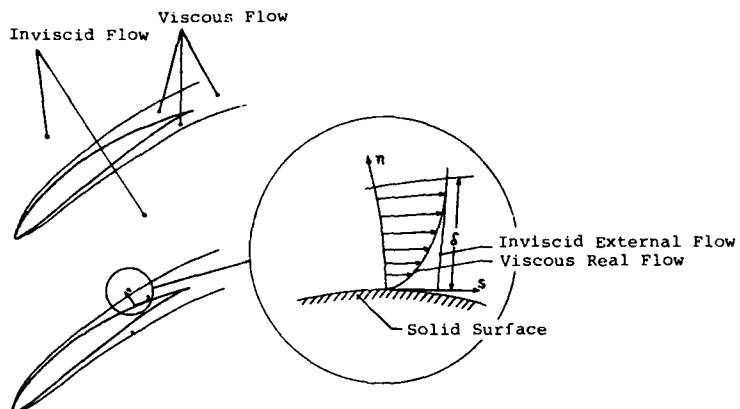


FIG.1 Schematic Representation of the Two-Zone Model for a Two-Dimensional Cascade.

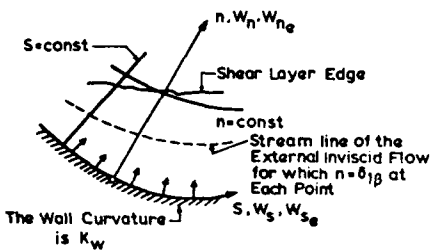


FIG.2.1a The Two-Zone Model in the Lock and Firmin Approximation

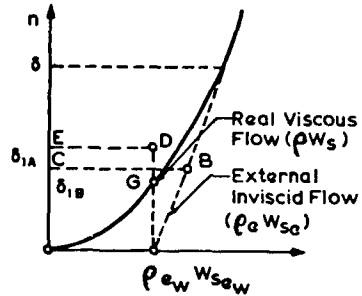


FIG.2.1b Schematic Representation of the Inviscid External and the Viscous Real Flow velocity-density distributions, according to the model.

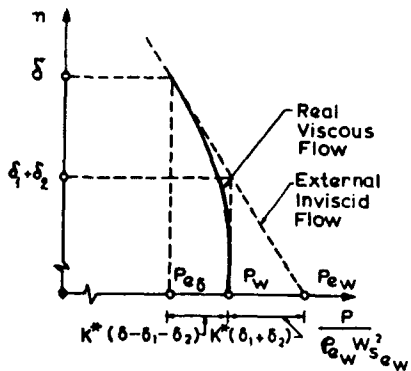


FIG.2.1c Schematic Representation of the Inviscid External and the viscous real flow static pressure distributions, according to the model.

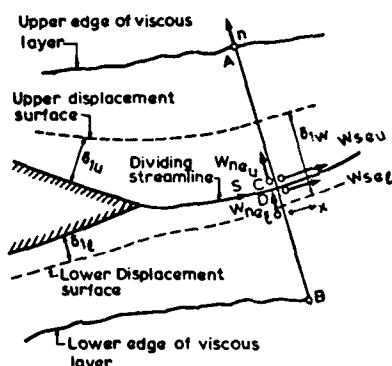


FIG.2.1d Schematic Representation of the flow in the trailing edge region, according to the model.

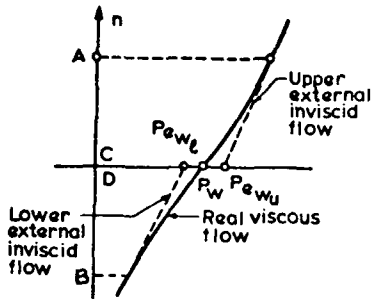


FIG.2.1e Schematic Representation of the Static Pressure distribution across the wake, according to the model.

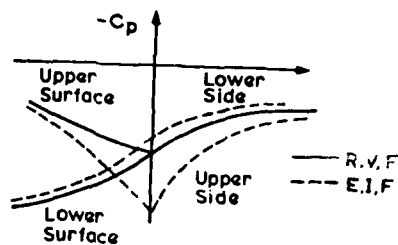


FIG.2.1f Schematic Representation of the pressure distribution in the trailing edge region, according to the model.

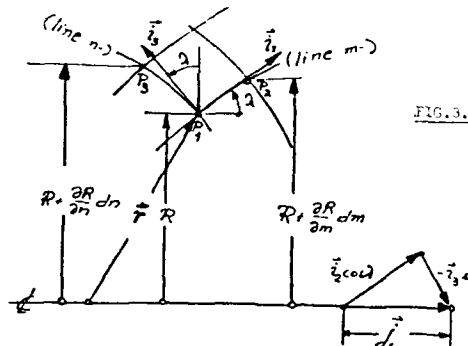
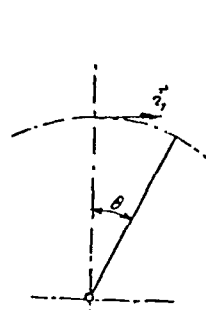


FIG.3.1 Curvilinear orthogonal axially symmetric coordinate system.

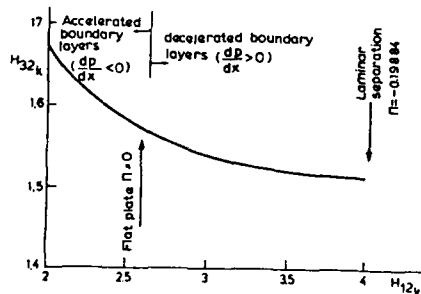


FIG.4.1 The relation $H_{32k}(H_{12k})$ for laminar layers.

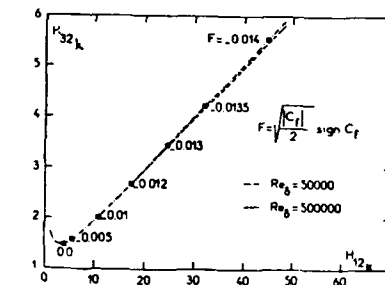


FIG.4.2 The relation $H_{32k}(H_{12k})$ for turbulent (attached and separated) incompressible layers. It is taken to be valid also for compressible flow.

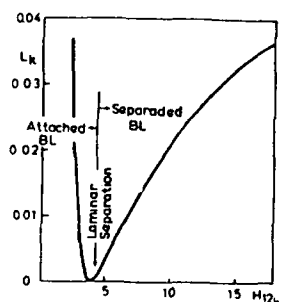


FIG.4.3 The relation $L_k(H_{12k})$ for laminar (attached and separated) incompressible layers.

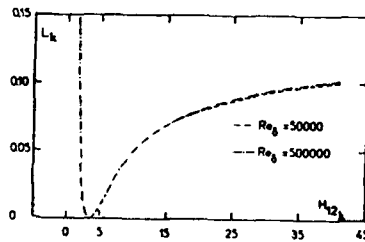


FIG.4.4 The relation $L_k(H_{12k})$ for turbulent (attached and separated) incompressible layers. The same relation is valid for compressible flow.

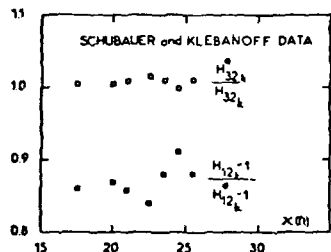


FIG.4.5 Evaluation of the influence of normal fluctuation terms from experiment results coming from un-separated flow.

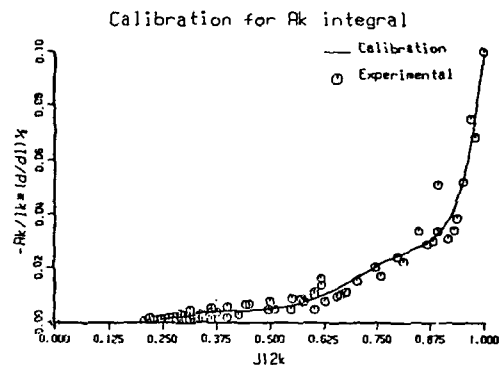


FIG.4.6 The influence of normal fluctuation terms in the momentum integral equation estimated from experimental data taken from incompressible and compressible (including shock/shear layer interaction), unseparated and separated flow.

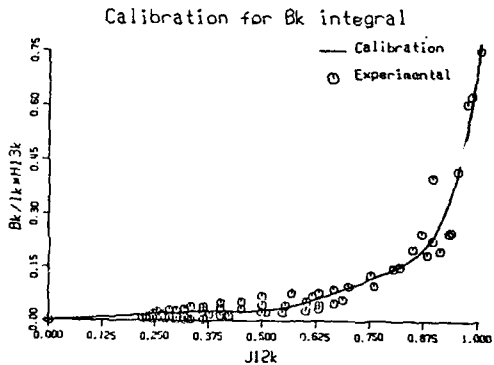


FIG.4.7 The influence of normal fluctuation terms in the energy integral equation, estimated from experimental data taken from incompressible and compressible (including shock/shear layer interaction), unseparated and separated flow.

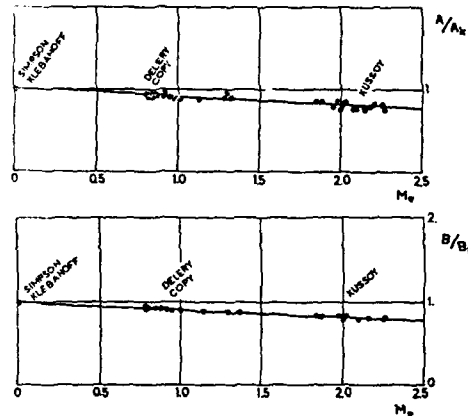


FIG.4.8 The Mach number influence upon the normal fluctuation terms.

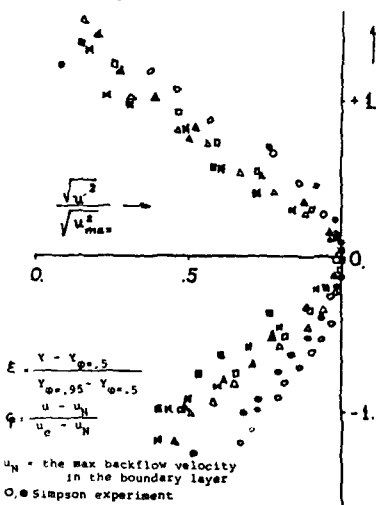


FIG.4.9 Normal fluctuations profile.

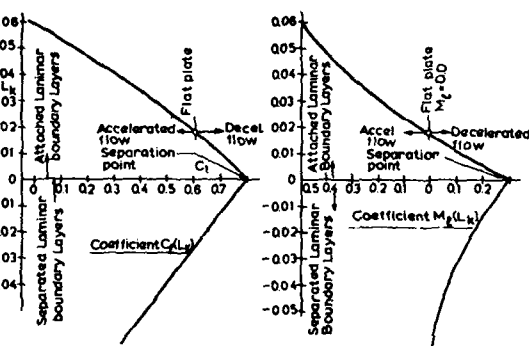


FIG.4.10 The functions C_1 and M_1 for laminar unseparated and separated layers.

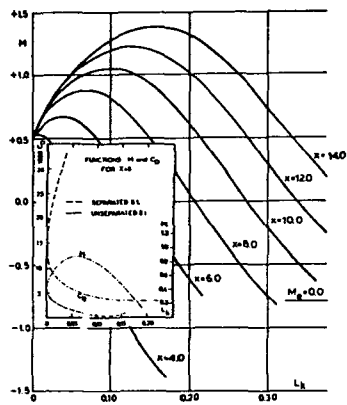


FIG.4.11 The function M_t and C_D for turbulent attached and separated incompressible layers.

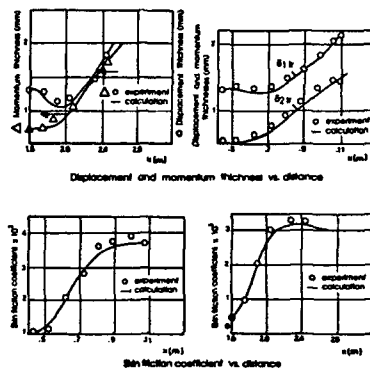


FIG.5.1 Comparison between calculation and experiment. Transitional flow. Experimental results of Schubauer and Klebanoff, Dhawan and Narasimha.

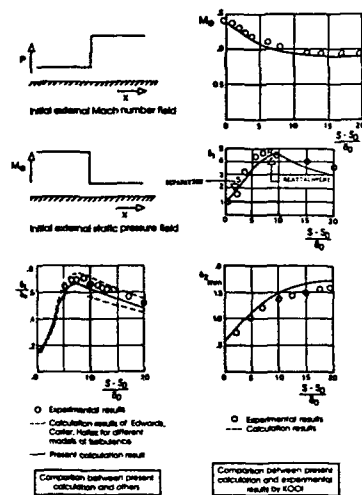


FIG.5.2 Comparison between calculation and experiment. Chor turbulent shear layer interaction with separation and reattachment.

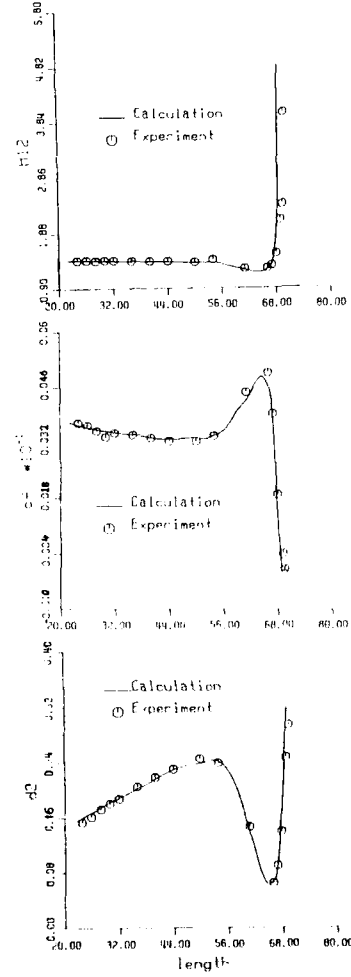


FIG.5.3 Comparison between calculation and experiment. Turbulent separation at mild separated flow. Experimental results of CII (Series I).

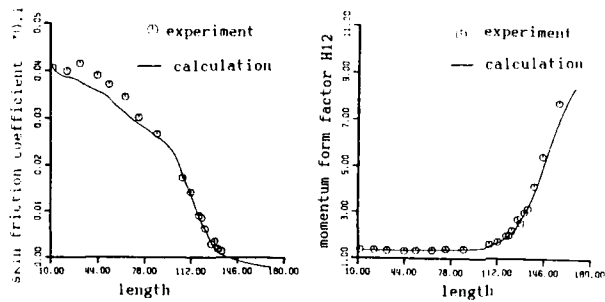
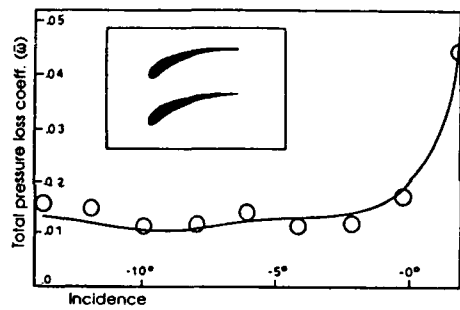
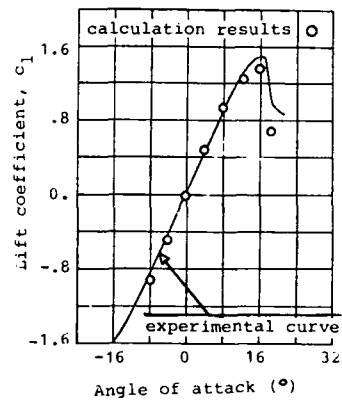


FIG.5.4 Comparison between calculation and experiment. Turbulent separation and mild separated flow. Experimental results of SIMPSON.



Comparison between theory and experiment.
Cascade flow.

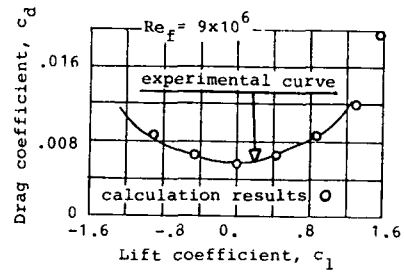


FIG.5.5 Comparison between calculation and experiment. Losses versus incidence for an isolated airfoil NACA 12.

FIG.5.6 Comparison between calculation and experiment. Losses versus incidence for a cascade NACA 65-(12)10

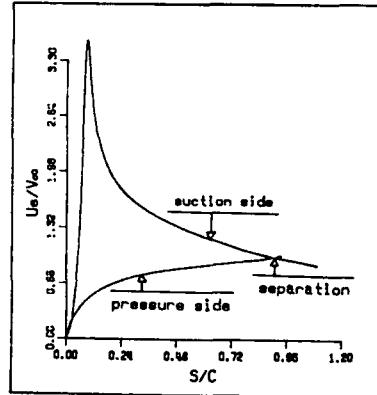
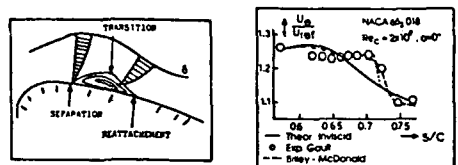
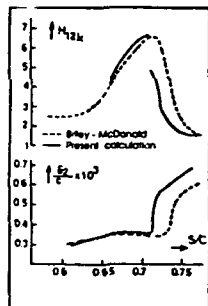


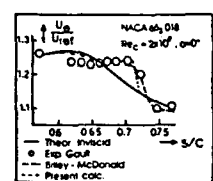
FIG.5.7 Presentation of the separated flow extend as predicted for the measurements at incidence 18° , presented in Fig. 5.5.



Schematic description of the flow region of a laminar separation bubble.



Comparison between theoretical calculations for the various boundary layer quantities. Gault's experimental data.



Comparison between theoretical calculation and experimental results. Gault's experimental data.

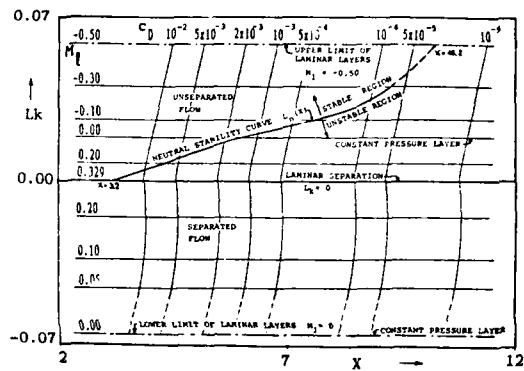


FIG.6.1 The Laminar Image Plane

FIG.5.8 Comparison between calculation and experiment. Laminar separation bubble.

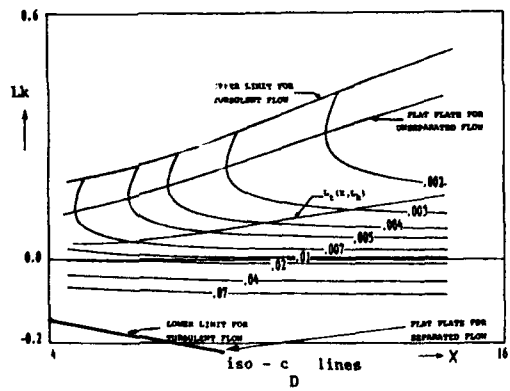
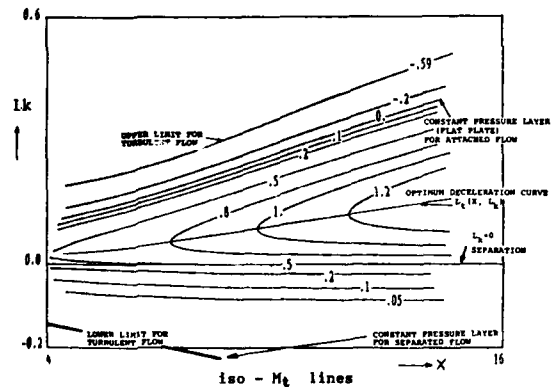


FIG.6.2 The Turbulent Image Plane

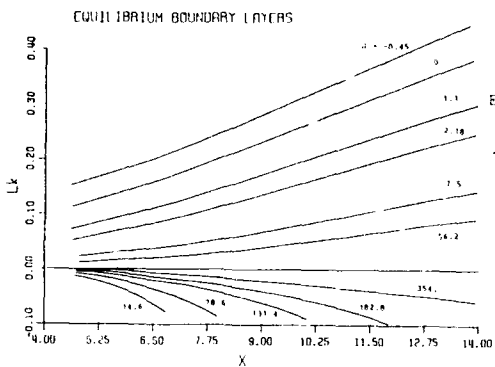


FIG.6.3 Turbulent equilibrium shear layers.

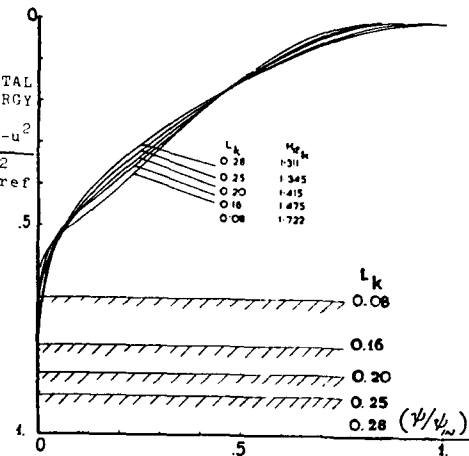
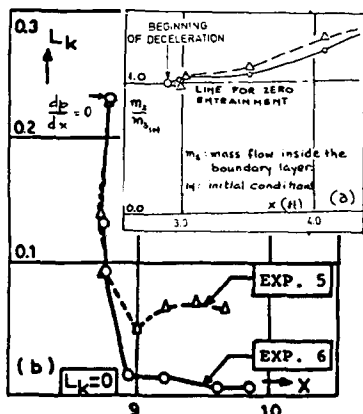
FIG.6.4 Kinetic energy profiles against the stream function for the image curve $X = 10.4$.

FIG.6.5 Experimental evidence of maximum deceleration, Stratford's experiments.

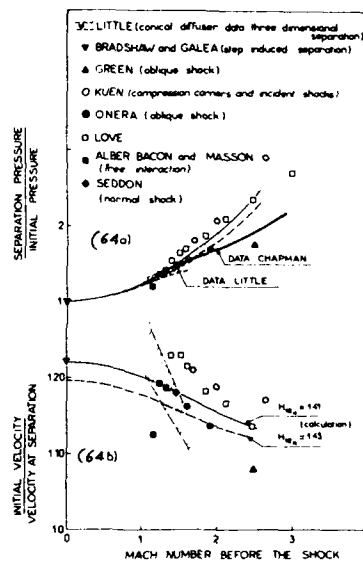


FIG.6.6 Analysis of experimental cases of rapid deceleration, including that of a shock interacting with a shear layer. Velocity and pressure rise up to separation are considered.

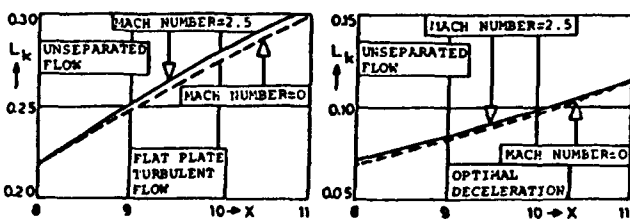


FIG.6.7 Effects of compressibility on some characteristic image curves for turbulent flow.

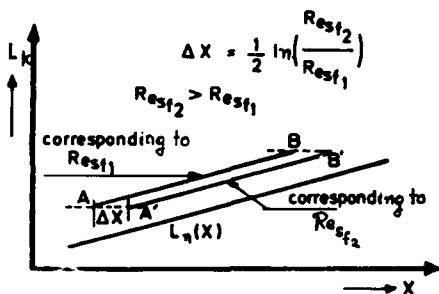


FIG. 7.1 Schematic representation of the displacement of an image curve, when the overall Reynolds number is modified.

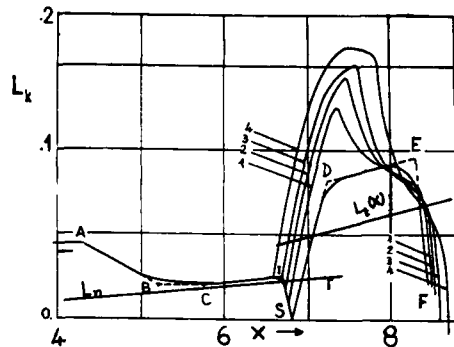


FIG. 7.2 Optimum image curve for the suction side of a blade section.

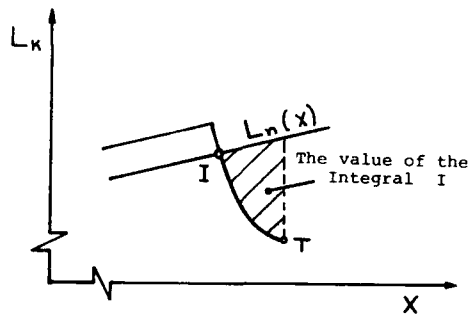


FIG. 7.3 Schematic representation of the transition criterion of T.S. Wilkinson.

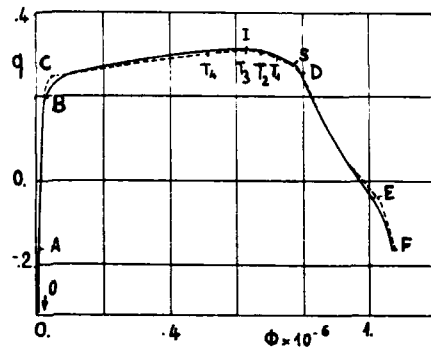


FIG. 7.4 The $\Phi(q)$ -distribution corresponding to the optimum image curve of Fig. (7.2)

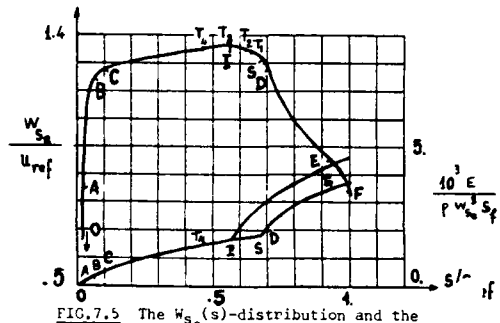


FIG. 7.5 The $W_{se}(s)$ -distribution and the kinetic energy loss distribution corresponding to the optimum image curve of Fig. (7.2)

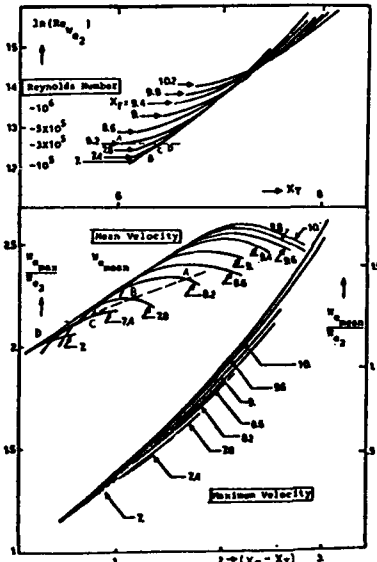
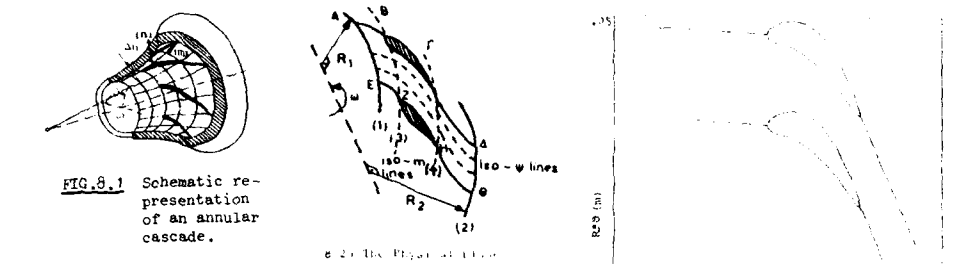


FIG. 7.6 Calculation results, which connect the overall properties of the velocity distribution (mean velocity and Reynolds number based on total arc length) with the overall intrinsic properties of an optimum image curve (x_T and x_F)



8.2a The Physical Plane

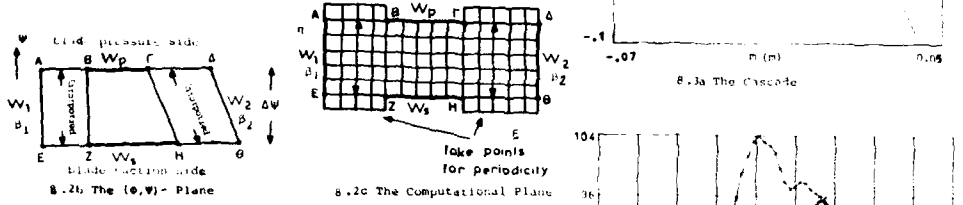


FIG. 8.2 The schematic representation of an annular cascade.

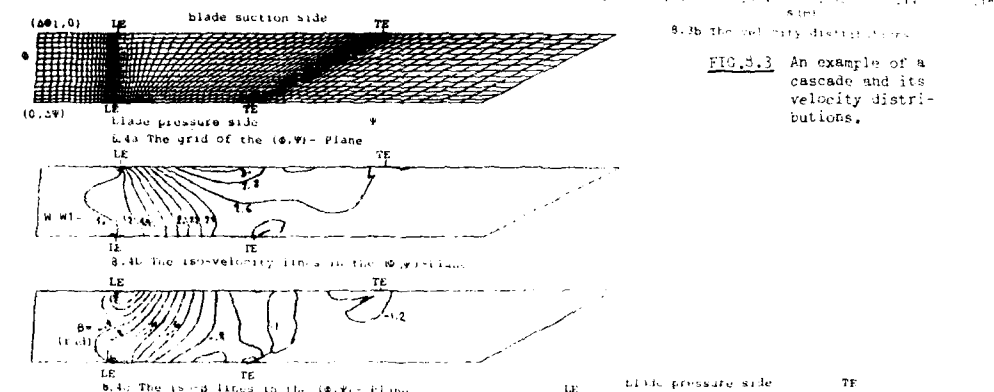
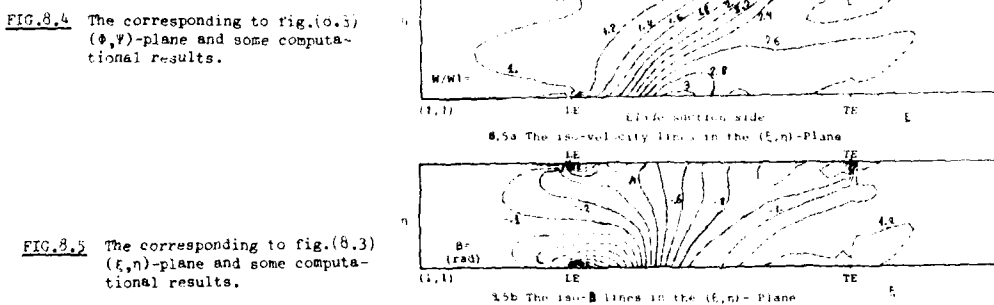
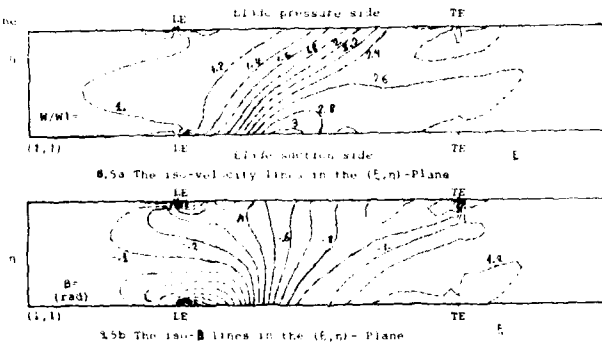


FIG. 8.3 An example of a cascade and its velocity distributions.

FIG. 8.4 The corresponding to fig.(8.3) (θ, ψ) -plane and some computational results.FIG. 8.5 The corresponding to fig.(8.3) (θ, n) -plane and some computational results.

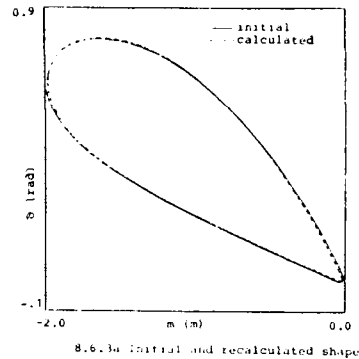
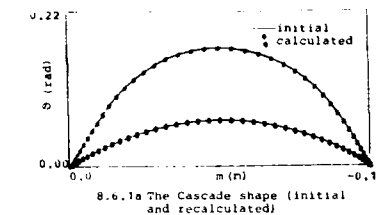


FIG.8.6.1 Test case for the inverse method.
The Hobson cascade.

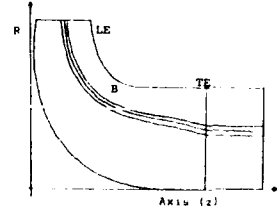
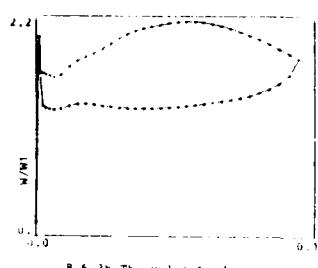
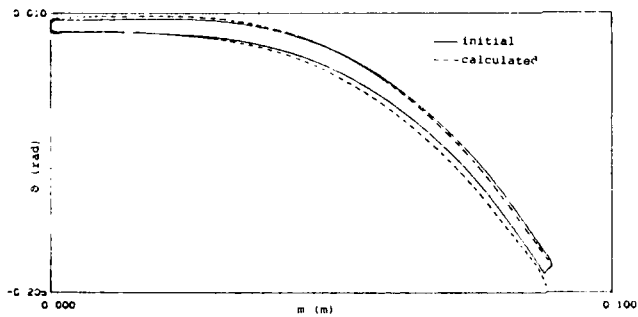
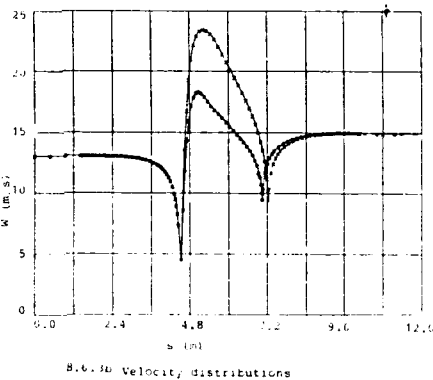


FIG.8.6.2 Test case for the inverse method. A radial inflow turbine.

FIG.8.6.3 Test case for the inverse method. A wind turbine hub blading.

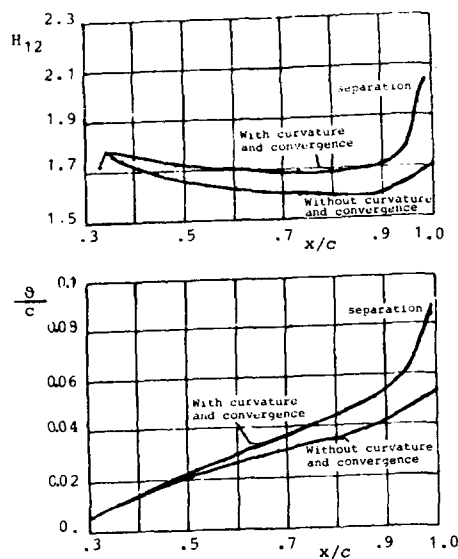


FIG.9.1 Turbulent calculations of a designed compressor blade section demonstrating the effects of surface curvature on the suction side shear layer development.

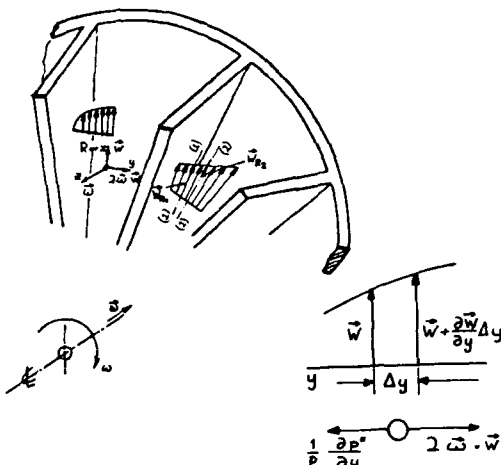


FIG.9.2 The effects of Coriolis forces.

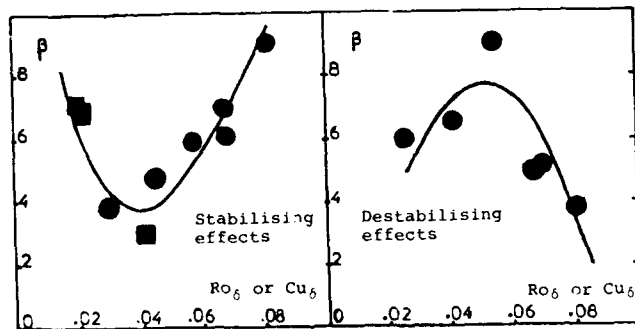


FIG.9.3 Variation of the mean β -value with the overall rotation number Ro_δ and Curvature number Cu_δ .

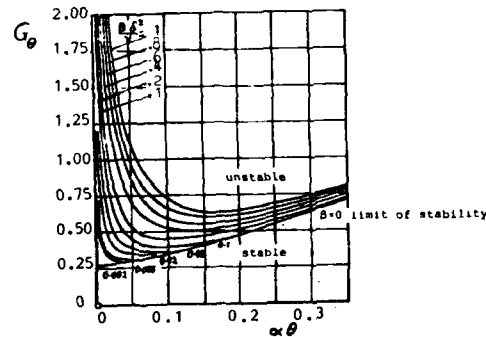


FIG.9.4 Calculations of stability for three-dimensional disturbances as calculated by GOERTLER and HAEMMERLIN (taken from ref.(6.1))

θ momentum thickness
 δ boundary layer thickness
 β amplification factor
 R_c radius of curvature of the wall
 λ wave length of the disturbance
 $\alpha = 2\pi/\lambda$
 $G_\theta = (\text{Goertler number}) = \frac{4\pi\theta}{\lambda} \sqrt{\frac{\theta}{R_c}}$

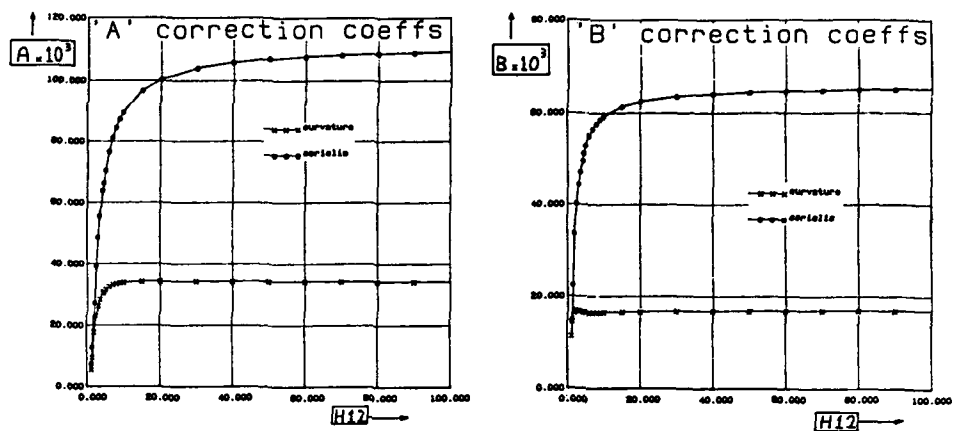


FIG.9.5 The functions $A(H_{12k})$ and $B(H_{12k})$ for curvature and Coriolis effects.

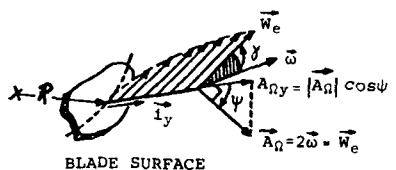


FIG.9.6 Schematic representation of the blade surface along with the different unity vectors associated with it.

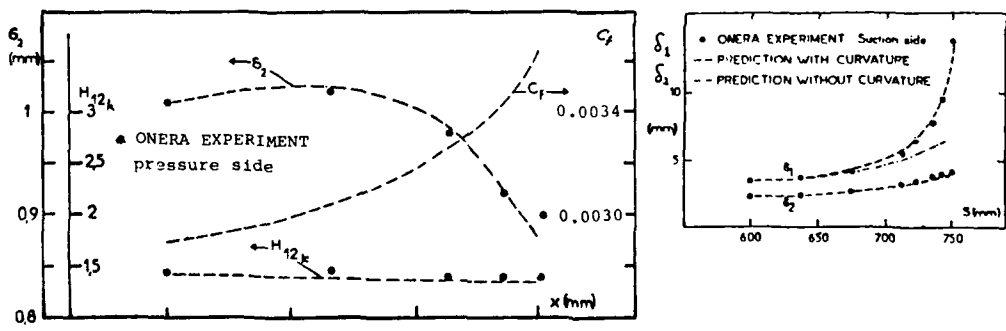
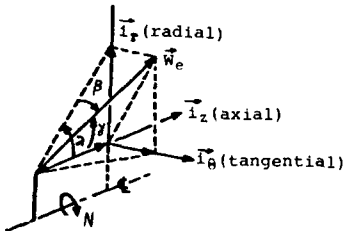
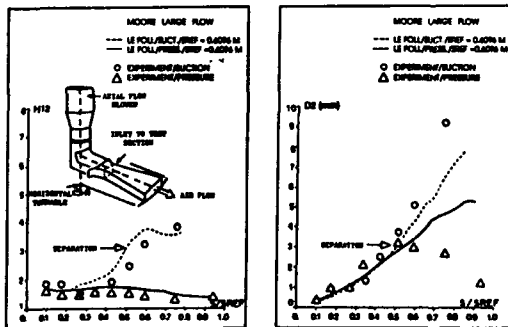
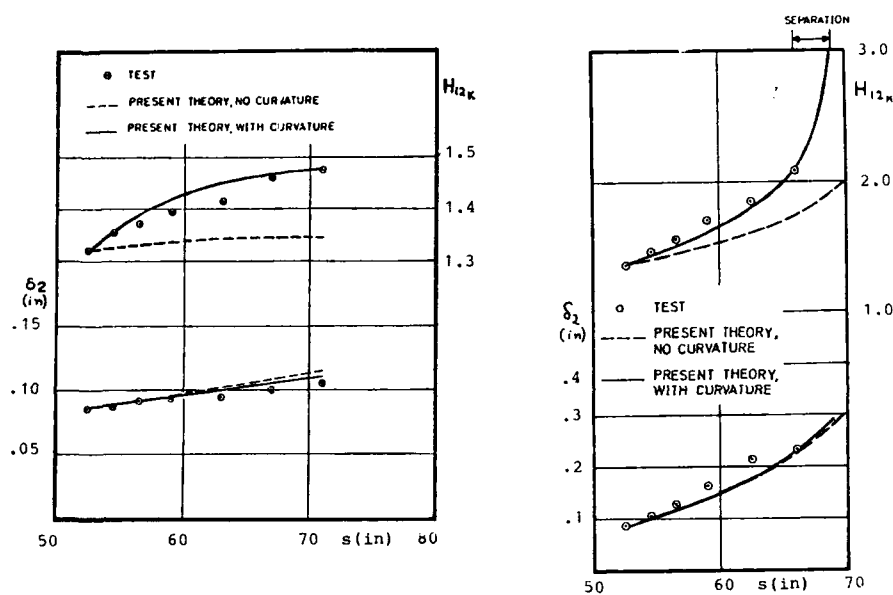
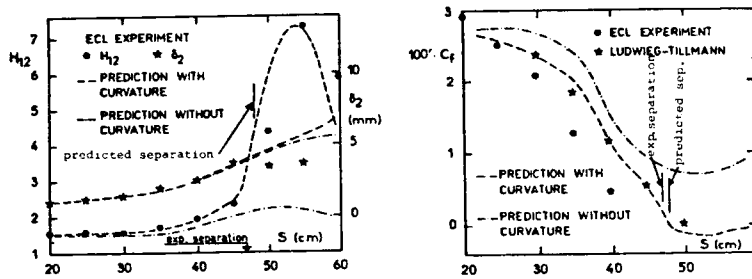


FIG.9.7 Comparison between theory and experiment with surface curvature influence on turbulence. ONERA's experiment.



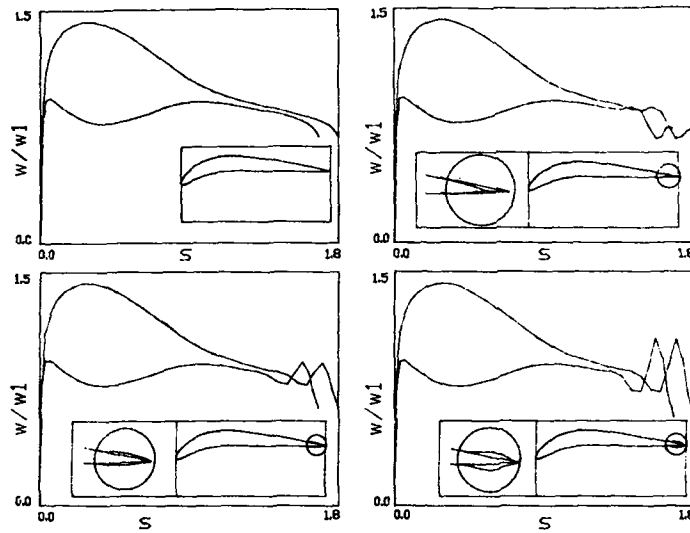


Fig.10.1 Study of the variation of the velocity distribution produced by a local change of the blade shape near the trailing edge.

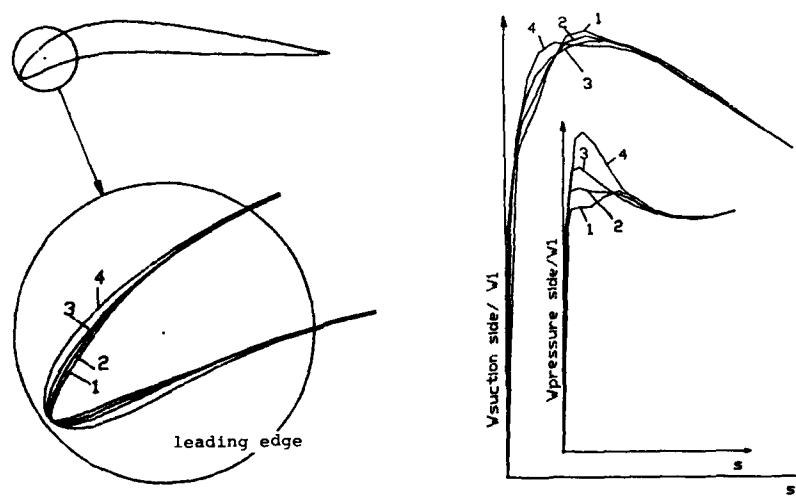


Fig.10.2 Study of the variation of the velocity distribution produced by a local change of the blade shape near the leading edge.

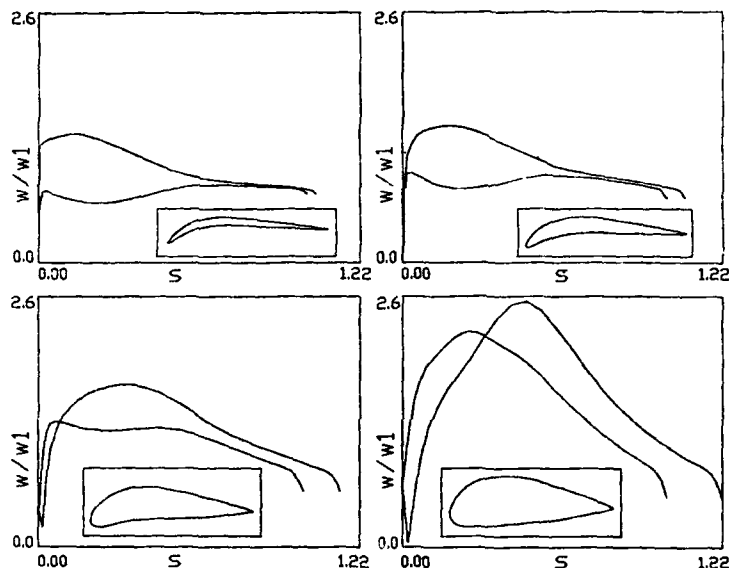


Fig.10.3 Study of the dependence of the velocity distribution produced by a uniform change of the blade thickness.

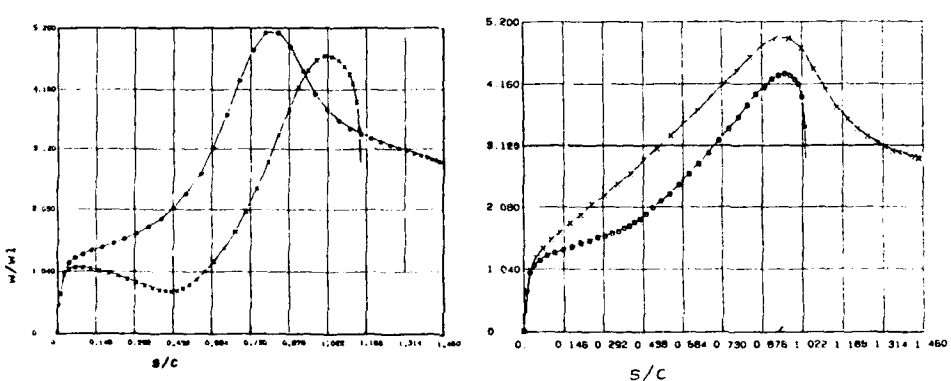
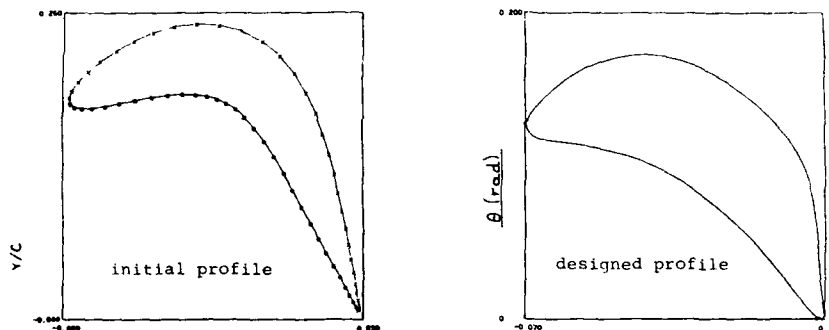
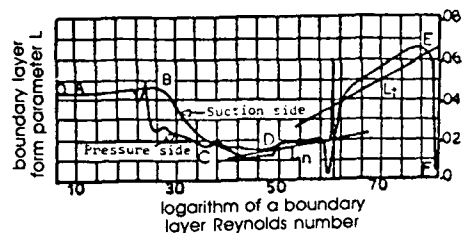
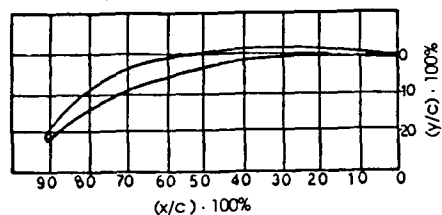


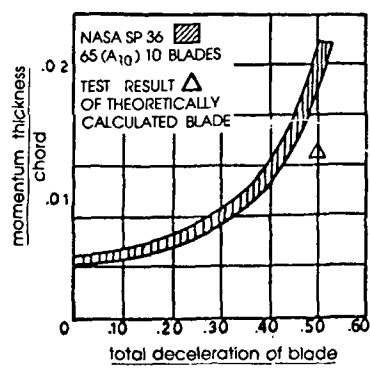
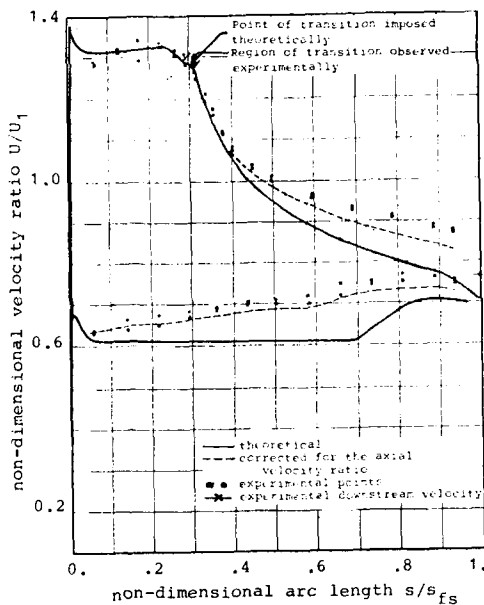
Fig.10.4 Design of a thicker profile using the inverse inviscid flow method.



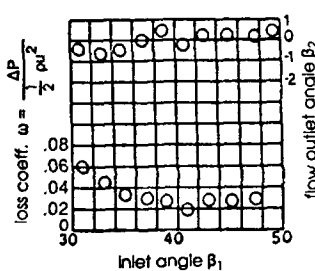
The image curve corresponding to the velocity distributions of the calculated blade



The calculated blade



Test results for the blade designed



The experimental results of the test carried out at Pratt and Whitney Co

FIG.10.5 Various aspects of the design and testing of an optimized highly loaded compressor blading.

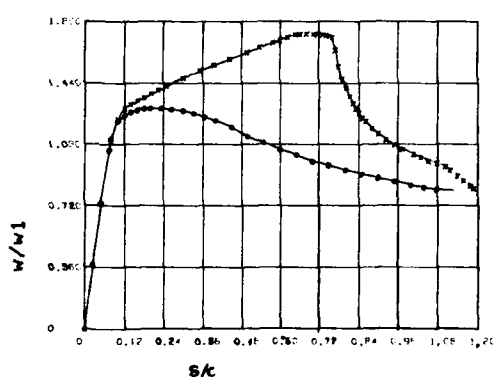
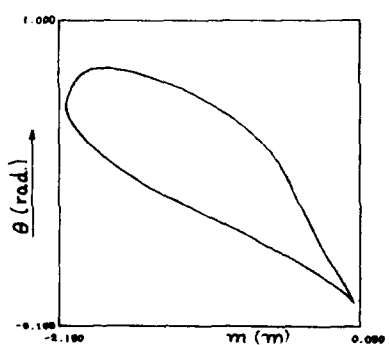


FIG.10.6 Optimized hub profile for a wind energy turbine. Redesign of the one presented in Fig.(8.63).

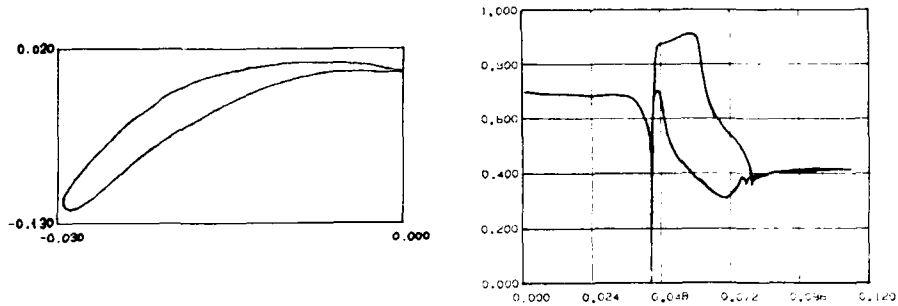


FIG.1. Optimized high subsonic flow, high loaded compressor profile
Redesign of the profile presented in Fig.10.1.

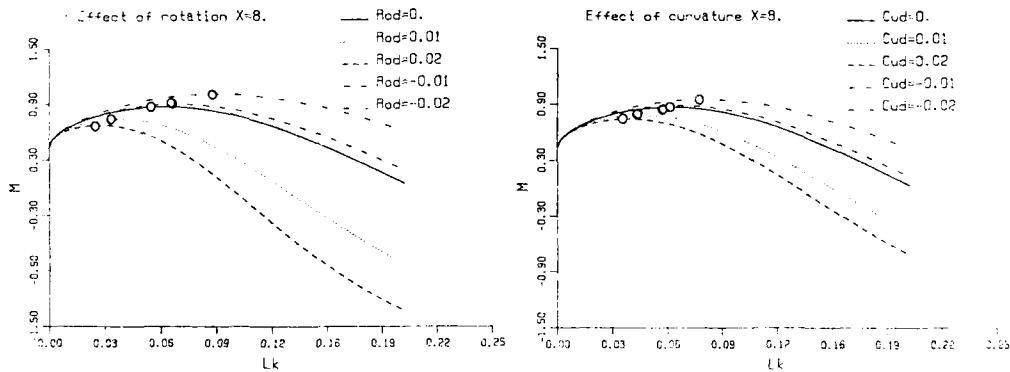


FIG.2. Influence of wall curvature effects on the locus of maximum M_t -values (Optimum Deceleration Curve)

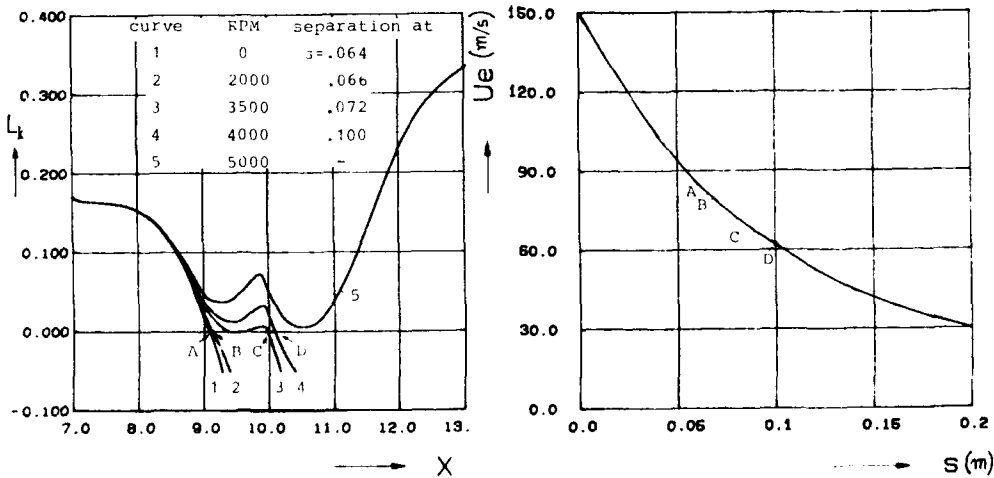


FIG.3. Variation of the circulation coefficient of the profile along the radius in the radial part of the blade in a particular section

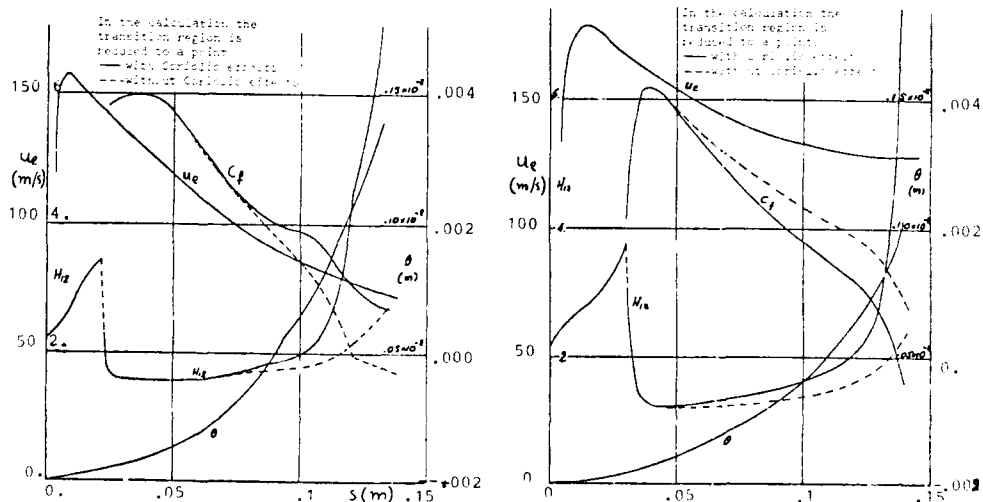
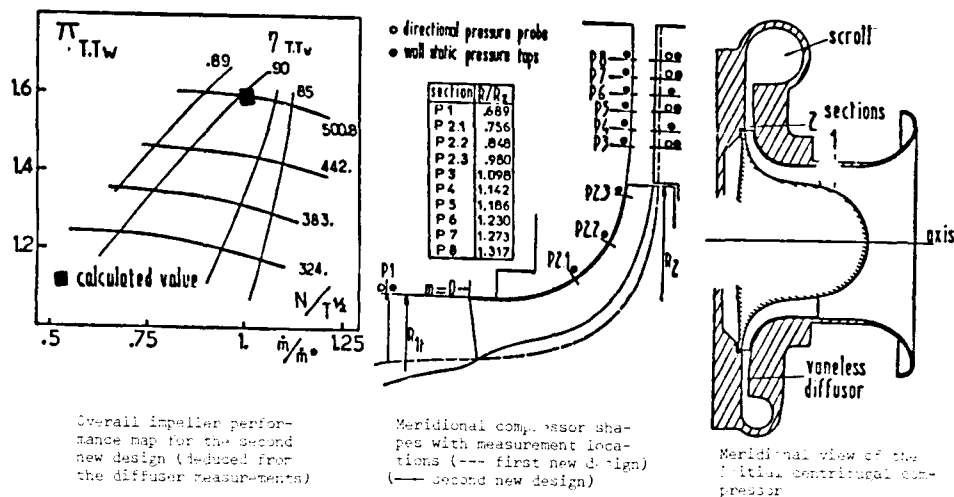


Fig. 10.13 Case study of a radial compressor. Effect of swirl loss on the friction and pressure loss characteristics.

OPTIMIZATION OF TARGET PRESSURE DISTRIBUTIONS

by

R.F. van den Dam, J.A. van Egmond and J.W. Slooff
 National Aerospace Laboratory NLR
 P.O. Box 90502
 1006 BM AMSTERDAM, THE NETHERLANDS

Summary

An overview is presented of the possibilities and problems associated with the use of numerical optimization techniques in aerodynamic design.

First, an inventory is made of the alternative aerodynamic design methods, the numerical optimization approach being one of them. The development of optimizing design methods is outlined and a short exposition of the state-of-the-art in numerical optimization is given. This is followed by a discussion on the practical use of numerical optimization techniques in aerodynamic design, in particular the inverse numerical optimization approach. An important step in this approach is the optimization of target pressure distributions, which are used by inverse methods to find the corresponding geometry. The procedure for finding target pressure distributions is explained, illustrated by some examples.

1. Introduction

Traditionally, aerodynamic theory distinguishes between two different formulations of the problem of computing the flow past a body. In the analysis problem, one seeks to find the flow and aerodynamic characteristics of a body of give shape at give free-stream conditions. In the design problem, the objective is to find the shape and angle-of-attack of a body that has to satisfy given aerodynamic characteristics.

In the aerodynamic design problem the designer wants to have, most of all, control over the aerodynamic quantities such as lift, pitching moment or pressure distributions. In fact, he usually has to deal with aerodynamic requirements at multiple design points (cruise flight, high lift conditions, etc.). However, the designer wants to have explicit control over the geometry as well, at least to a certain extent. He wants to be sure, for instance, that the aerodynamic shape is also acceptable from the point of view of the structural engineer. Another aspect where the aerodynamic designer is confronted with is the question whether the design problem as formulated really has a solution (existence requirement) and whether there is one solution only (uniqueness). The design-problem can also be an ill-posed one in the mathematical sense. And last but not least, the computational effort of the procedure to solve the design problem, which generally is a number of times of that of an analysis method, must be acceptable in order to work with it on a routine basis.

In literature, various computational procedures for aerodynamic design can be found, each having its own abilities and/or inadequacies with respect to meeting the requirements just described. Five different classes of computational procedures for aerodynamic design may be distinguished (Ref. 1):

1. Indirect methods : Indirect methods are characterized by the fact that, in principle, the designer has direct control over neither aerodynamic quantities nor over the geometry. Rather than specifying such quantities directly, the designer has to manipulate a number of (generally non-physical) parameters and sees what comes out of it. The hodograph method (e.g. Ref. 2) and the fictitious gas method (e.g. Ref. 3) are in this category.
2. Inverse methods. This category contains methods for solving the classical inverse problem of aerodynamics, i.e. that of determining the detailed shape of a body that will produce a given pressure distribution (and hence given lift, pitching moment, etc.). The most serious limitation of pure inverse methods is that no direct control can be exercised on the geometry (may lead to unrealistic geometries). In residual correction type of inverse methods (e.g. Ref. 4) it may be possible to impose constraints on the geometry. The specification of the target pressure distribution, however, puts a heavy burden on the aerodynamicist. As an example, for transport aircraft, the target pressure distribution must be chosen such that, at least at the design condition, boundary layer separation is avoided and that drag is minimized while obtaining an acceptable geometry. At the same time the choice should lead to acceptable off-design characteristics.
3. Optimal control methods (Ref. 5). Such a design method may be created by integrating a control function into an analysis method, and inserting a variation procedure based on control theory to reach a minimum of a certain cost function. The control is the shape of the aerodynamic surface, and the cost function may be, for instance, the deviation from a desired surface pressure distribution, but could also represent other measures of performance such as lift or drag. So, the method allows control over the aerodynamics, while the computational effort is still within reasonable bounds (approximately slightly more than pure inverse methods). The numerical implementation of these rather new design methods, however, remains still to be explored.
4. Direct numerical optimization methods. This category is characterized by the use of automated design procedures in which a numerical optimization algorithm and a fluid dynamics solver are linked together to, directly, minimize a given aerodynamic object function (such as drag) by iterating on the geometry. These methods essentially have the same advantages as optimal control methods (control over aerodynamics, multi-point design capabilities, some control on the geometry). The direct numerical optimization procedure, however, becomes extremely expensive as the number of geometry parameters is increased.
5. Inverse numerical optimization methods. In the inverse numerical optimization approach the design variables are parameters describing the pressure distribution rather than the geometry. The optimization algorithm is used to minimize the drag and subject to constraints on lift and pitching moment. With the target pressure distribution established a corresponding geometry can be determined by means of an inverse code. The process is repeated until a geometry is obtained having acceptable off-design performances and satisfying the geometry constraints. This procedure avoids most if not all of the limitations of the pure inverse method, while requiring considerably less computational effort than the direct numerical optimization method.

The paper will especially be focussed on design techniques based on numerical optimization. After explaining the principles of numerical optimization, a brief review of its applications in the past and present will be given. Subsequently, the application of numerical optimization techniques in the inverse numerical optimization procedure will be worked out, and illustrated by some examples.

2. Optimizing design methods

The growth in speed and capacity of digital computers has opened the way to the application of theoretical methods to aerodynamic design problems to an extent which was almost unimaginable thirty years ago. At that time, the basic tools at the disposal of the aerodynamic designer were analytical tools and physical experiments. Analytical methods forced him to make very restrictive and idealized assumptions, and allowed him to consider simple configurations only. These limitations were largely removed by windtunnel tests. Through physical experiments with scaled of actual (parts of) design configurations, the characteristic behaviour can be determined. Windtunnel-experiments, however, are costly and can take up a lot of time, especially if a substantial number of design parameters is involved. Besides, the experimental potentialities are often restricted by the limitations in test conditions and test equipment, and results can be affected by the test environment itself (for example, by wall interference).

With the developments in the field of digital computer technology and numerical methods, it became feasible to use numerical simulation methods in aerodynamic design processes. Using well-developed simulation methods, it is possible to treat complicated designs with, in principle, less restrictive simulation conditions than is the case with windtunnel experiments. Besides mathematical simulation methods are inherently more flexible with respect to changes in the design parameters, and are usually more cost-effective to work with. At first, the computer was almost exclusively used for the theoretical analysis of a proposed design. In fact, any designer wants to achieve the design that is best according some properties. Very probably, his first attempt will lack some essential characteristics or violate some of the imposed design constraints. The designer then modifies the aerodynamic design by changing some of the design parameters. Analysis of the effects of these changes on design characteristics must yield the information he needs in order to decide how to change the parameters to achieve an improvement.

A logical extension of this classical way of designing using computers, is one in which the computer drives the design parameters towards a satisfactory ultimate design (Ref. 6). The simulation methods are then interfaced with an iterative control system (the optimizer), which interprets the analysis results in the light of previous iterations and subsequently decides how to vary the design parameters in order to better meet the design objectives and constraints. Also in this automated procedure, the simulation method is of vital importance.

In fact, the iterative process control system does not function differently from the human optimizer. Both start with an estimate of the design in view and then subsequently iterate to a final solution. When a suitable mathematical optimization technique is used, however, this way of designing will generally be more efficient. Besides, mathematical optimization is applicable to a higher dimensional space than a designer can manipulate. Of course, the restrictions of a particular optimization algorithm must also be realized. Moreover, the use of optimization algorithms and their coupling to simulation methods ask for more programming effort. For example, design criteria and constraints have to be formulated in an explicit way, which is not necessarily needed in inverse methods or indirect methods.

3. Numerical optimization

The application of numerical optimization has been made possible by the development of numerical techniques for obtaining maxima and minima. Though the history of numerical optimization is relatively short, a variety of useful optimization techniques is already available nowadays (see e.g. Ref. 7). Most of these techniques, such as linear and dynamic programming methods, have been developed to deal with specific classes of optimization problems. For most technical applications, however, methods for solving constrained nonlinear optimization problems are more relevant. In recent years, research in this particular field has resulted in a number of efficient and reliable computer codes. Comparative studies (see e.g. Ref. 8) can support the designer in choosing the most appropriate one for solving his particular problem.

The constrained nonlinear program (NLP) problem concerns the determination of design parameters that minimize an objective function, while satisfying a finite number of constraints. In standard notation:

$$\min_{\underline{x}} F(\underline{x}) \mid b_j^L \leq F_j(\underline{x}) \leq b_j^U, j = 1, m$$

Here, b_j^L and b_j^U , respectively, are the lower and upper bounds on the constraint functions $F_j(\underline{x})$. In a NLP problem, one or more of the functions appearing in the notation are nonlinear in \underline{x} .

In general, methods for solving these kind of optimization problems can be subdivided into:
- methods in which the necessary conditions for an optimum are derived and subsequently solved;
- methods based on an iterative search strategy.
The first category of methods is restricted to well-behaved functions only, and even then the algebraic problems that arise from it may be rather complicated and difficult or impossible to solve, even with the numerical methods and computers of the present day.

Optimization methods based on an iterative search strategy operate on the objective function directly and there is no formal intermediate step of specifying necessary conditions for an optimum. In the last decennia, a large number of iterative optimization methods has been developed. Usually, these methods consist of two separated subprocedures, one for the determination of the search direction, and the other to move in this direction in order to find an optimum that is satisfying the constraints. In order to illustrate this process, an example is given in Figure 1. The process is initiated at a starting design \underline{x}^0 . Then an optimum is approached in a sequence of successive steps. In the figure, the choices of the directions are chosen somewhat arbitrarily, however, such that the value of the object function F decreases in each iteration step while not violating the constraints. In general, search methods stop at the first local optimum that is reached.

Two different types of search methods can be distinguished: gradient methods (using gradient information one way or the other) and pattern- and random methods (not using any gradient information). In the latter, the search pattern is determined a priori, or is determined on the ground of experience from previous iterated points and perhaps coincidence. In case of highly nonlinear optimization problems, these methods may be more robust than gradient methods, the rate of convergence to a solution, however, usually is lower than that of gradient methods.

From a mathematical point of view, gradient methods are more sophisticated and, as gradient methods use first (and possibly second) derivatives, this search strategy may be expected to be more efficient. The literature is mainly concerned with this particular class of optimization methods. The following categories of gradient methods may be distinguished:

- o First order methods using first derivatives only (e.g. the steepest-descent method);
- o First order methods using first derivatives, but having second order characteristics (e.g. conjugated gradient methods);
- o Second order methods using approximated second derivatives, the so-called Quasi-Newton methods (variable-metric methods);
- o Second order methods using exact second derivatives, the so-called Newton methods.

There are various ways of handling constraints in the optimization procedure; for instance by:

- o moving along a constraint boundary when that constraint threatens to be violated during the iteration process (the so-called boundary-following methods such as Zoutendijk's method of feasible directions);
- o adding the constraints to the objective function using penalty terms, thus performing a conversion to an unconstrained optimization problem (the so-called penalty-function methods such as SUMT).

In the last decade, developments in the field of constrained nonlinear optimization have especially been focussed on improvements of existing methods. These developments concern, among others, the determination of efficient search steps (e.g. the dogleg-step method, Ref. 9), procedures for specifying a starting solution (often difficult to find by hand), and convergence improvement in the initial phase of the search process (e.g. the trust method, Ref. 10, 11).

The difficulty faced by the practitioner is in choosing which optimization method is the most appropriate one for solving the problem on hand. Several criteria (see Figure 2) may be relevant here:

- Applicability. It is important to realize for which type of problem a particular method has been developed (unconstrained problems, linearly constrained problems, etc.);
- Efficiency. A logical criterium to measure optimization efficiency is the total number of analyses typically required to obtain a near-optimum design. If gradient information is calculated by finite differences, the number of analyses required at each iteration point equals at least the number of design variables plus one, which may lead to unacceptable computer time;
- Convergence characteristics. For instance, rate of convergence and degree of convergence;
- Robustness. Does the method, under various circumstances, always lead to a reliable answer?
- Simplicity of use. The amount of effort necessary to use the method or computer code;
- General applicability. The possibility to apply, without much extra effort, the method to other problems;
- Flexibility. The possibility to use the code in different ways for the problem on hand;
- Requirements from the size of the problem (number of design parameters, constraints, etc.);
- Capacity. How much computer core storage does it use?
- Time and effort that is required to learn to use the method or program code.

It is clear that, in order to make a justified choice, it is necessary to know the possibilities and the limitations at each optimization method or code. In fact, the selection of an optimization algorithm can itself be a major optimization task.

4. Aerodynamic design using numerical optimization

The past decade has seen repeated efforts, some (partly) successful, other less so, to directly address the problem of aerodynamic design by combining computer codes for aerodynamic (drag) analyses (flow solvers) with numerical optimization algorithms (see e.g. Ref. 12). The optimization algorithm then controls variations of a number of independent variables, such as parameters defining the geometry, with the purpose of finding the particular combination of parameters that, subject to given constraints, leads to an optimum value of the object function (e.g. minimum drag). In this process, the flow solver is used to provide values of the object function for each combination of values of the independent variables that is considered to be feasible and "interesting" by the algorithm.

Generally speaking aerodynamic design using numerical optimization requires:

- a choice of object function (drag, lift, etc.)
- a flow solver (aerodynamic analysis code)
- a choice of independent variables
- a choice of constraint functions defining that part of the solution space that is considered to be feasible from the engineering or another (e.g. numerical) point of view
- an optimization algorithm.

With respect to the choice of independent variables one may distinguish two different approaches. One, and indeed the most common choice is to use parameters defining the geometry as the independent variables. This requires a direct or analysis type of flow solver only. The approach is generally referred to as direct numerical optimization.

The approach, pioneered by Hicks et al (Ref. 13) owes its existence entirely to the availability of large and fast computer systems. Because of the excessively large computational requirements, at least in 3D, the approach is sometimes referred to as "design by brute force". Nevertheless it holds great potential for the future. A reappraisal of the technique has been given by Hicks (Ref. 14).

A generalized flow diagram of the numerical optimization technique is presented in figure 3. The process is initiated by the choice of an aerodynamic object function F that is to be minimized (for example, the drag) a number of quantities to be constrained G_i , and a set of design variables. The constraints can be of aerodynamic or geometric nature; e.g. C_L and/or t/c greater than a specified value. The design variables are generally taken to be the coefficients A_i of a number of shape functions

$$Z = Z_0 + \sum_{i=1}^n A_i \cdot f_i$$

describing (modifications to) the (starting) geometry.

The process begins by perturbing, in sequence, each of the shape function coefficients A_i . The resulting n shapes are analyzed by means of the aerodynamic program (determination of F and G_i 's) and the derivatives $\frac{\partial F}{\partial A_i}$, $\frac{\partial G_i}{\partial A_i}$, or rather the difference quotients $\frac{\Delta F}{\Delta A_i}$, $\frac{\Delta G_i}{\Delta A_i}$ are determined. The next step is the formation,

by the optimization program, of the gradient ∇F and the determination of the direction of steepest descent of F , in the n -dimensional space formed by the basis vectors A_i , while satisfying the constraints. The optimization program then executes a number (typically 3) of steps in this direction, with another aerodynamic analysis performed at each step, until either a constraint is met or F attains a minimum. In the first case, or when the minimum of F is lower than the previous minimum, the process is repeated; new gradients are determined, etc. When the latest minimum of F is equal to or higher than the previous one the process is terminated.

The optimization process described above requires typically 10 complete cycles or, in other words, 10 ($n+3$) analysis calculations (Ref. 15). This immediately illustrates the weakest point of the numerical optimization approach. In order to keep the computational effort required within reasonable bounds one has to put severe limitations on the number n of design variables, in particular in 3D flow. The problem is enhanced by the fact that for acceptable convergence of the optimization process it is necessary to avoid "numerical noise" in the partial derivatives of the object function (Refs. 16, 17). This requires that the relaxation process in each analysis calculation must be continued until the residual has reached a level beyond that which is often customary in "normal" analysis calculations. It also appears to exclude the use of analysis codes with simple boundary layer corrections (Ref. 14). The reason for the latter is that the airfoil aerodynamic quantities do not vary consistently enough when boundary layer and potential flow are coupled in the weak interaction sense.

One way to reduce the number of analysis calculations in 3D applications is to evolve the design variables in a series of steps (Ref. 18). For example by first designing the upper surface, section by section, going from root to tip and then the lower surface. Clearly it is also important to select a starting geometry having aerodynamic characteristics which are already close to the target. This asks for an information system/data base approach. With previous experience stored in the data base, the latter can be searched for the most suitable starting solution. As described in Ref. 15 the data base approach can also be used to speed-up the convergence of numerical optimization by at least a factor two. With the results of all preceding geometry perturbations stored it is possible to construct higher partial derivatives of the object function and utilize higher order gradient methods.

With the severe limitations on n , the choice of the shape function is of utmost importance. The choice should be directed towards describing a sufficiently wide class of practical solutions. While simple polynomial expressions were used in early applications (Ref. 13, 19) of the numerical optimization concept, a more sophisticated class of shape functions describing more local geometry modifications was used in later applications (Refs. 16, 17, 19). However, as discussed in Ref. 18 there is a need for still better shape functions with even more localized curvature variations. In fact it can be argued that while curvature based shape functions are suitable for areas with subcritical flow, slope based shape functions might be more appropriate in areas with locally supersonic flow.

An interesting choice for the shape functions is discussed by Aidala et al. (Ref. 20). They consider shape functions generated by means of feeding certain pressure distribution modifications into an inverse program. The result is a set of design shapes that are (almost) orthogonal in an aerodynamic sense, that is, affect only one specific pressure distribution characteristic and no other ones. Another choice for shape functions can be found in Ref. 21.

While the choice of the design variables is of great practical significance, the precise choice of the object function, in conjunction with the choice of the aerodynamic and geometric constraints, is of both more fundamental and practical interest. In two-dimensional transonic applications (Refs. 13, 15, 16, 19) it has been custom to minimize the wave drag subject to constraints on, e.g., airfoil thickness or volume, lift and/or pitching moment. Although it is clear that constraints are necessary in a meaningful drag minimization problem it is by no means clear how exactly the problem should be formulated in order to guarantee a unique solution. The problem is illustrated by figure 4, taken from Ref. 15. Shown are the results of two drag minimization runs with identical free stream conditions and identical constraints on lift and airfoil volume. Only the starting solutions differ. As illustrated by the figure the two resulting airfoils are totally different in shape. Clearly the problem, as formulated, has more than one, local minimum and neither of the two necessarily represents the absolute minimum. An interesting discussion on criteria for suitable aerodynamic object functions can be found in Ref. 20.

Figure 4, the second airfoil in particular, also illustrates another potential problem of direct (inviscid) wave drag minimization. In the absence of (direct) control over the pressure distribution the solution may acquire unrealistically high pressure gradients, such as near the upper surface trailing edge.

A strong point of the numerical optimization approach is the possibility of selecting object functions and constraints suitable for multipoint designs. An example of a two-point design problem directed towards the design of airfoils with low drag creep can be found in Ref. 16. Low speed airfoil design applications are considered in Refs. 22, 23. It is also entirely possible to consider, e.g. transonic drag minimization and low-speed stall requirements simultaneously.

Although a number of different numerical optimization algorithms have been applied in aerodynamic design (see e.g. Refs. 24, 25, 26), the feasible directions/gradient optimization algorithm CONMIN/COPIES, developed by Vanderplaats (Ref. 27), seems to be used almost exclusively in the direct numerical optimization approach, in particular in combination with transonic flow codes.

While the direct minimization of drag is feasible in two dimensions, it is hardly so, at present, in the case of three-dimensional wings. Several unsuccessful attempts in this direction can be found in the literature, (Refs. 17, 18, 28). The main reason for this failure is the lack of accuracy in the determination of the drag with the currently available 3D codes and the limited number of mesh points. Another problem would seem to be that the problem of uniqueness in three dimensions is even more severe than in two dimensions. The accuracy problem may be overcome when more efficient algorithms and/or more computer power (vector/parallel machines) allows the number of mesh points to be increased. The uniqueness problem would probably require the introduction of more constraints or more sophisticated object functions.

Summarizing the discussion on direct numerical optimization, it may be said that the potential possibilities of the approach are enormous with, at present, unique capabilities such as multi-point and constrained design. However, the approach is also unique in terms of required computer resources. Substantial improvements in both flow optimization code algorithms and/or computer efficiency, relative to current general standards, are required before numerical optimization in 3D wing design can be used on a routine basis.

An alternative possibility for computational drag minimization is to use aerodynamic (load and pressure distribution) rather than geometric shape functions as independent variables. In this approach the first step is creating a starting point for the specification of "target" pressure distributions. This starting point could be obtained using a method for constrained spanload optimization (see e.g. Ref. 29). Subsequently, an optimization algorithm is used to optimize the pressure distribution, hereby using a boundary layer code and a wave drag routine. The objective may be the minimization of drag, hereby providing the prescribed spanloads. With the target C_L-distribution established the new geometry can be determined by means of an inverse code. Subsequently the off-design characteristics can be determined using an analysis code. The process is repeated when the new geometry differs significantly from the previous one or when a geometry or off-design constraint is met. In the latter cases (new) constraints will have to be imposed on the values of the parameters describing the pressure distribution. A flow chart of the procedure, which is called inverse numerical optimization (Ref. 30), is given by figure 5.

The first step in the inverse numerical optimization approach, i.e. the determination of optimal spanloads is described in Ref. 29. The second step, i.e. the optimization of target pressure distribution, will be described in the following section.

5. Optimization of target pressure distribution

The approach of using aerodynamic (pressure distributions) rather than geometric shape functions as independent variables in the optimization procedure offers the following advantages:

- It matches the "inverse numerical optimization" design philosophy as described in the preceding section.
 - Only boundary layer calculations are needed during the iterative optimization procedure. So, a large number of iterations is less a problem, allowing a larger number of design variables.
- Of course there are some disadvantages too e.g.
- Care is needed to stay within feasible pressure distributions.
 - Curvature effects in the boundary layer development are taken into account for the starting geometry only and might be different for the new design.
- Nevertheless, from a practical point of view, optimization of the (target) pressure distribution is promising and could be very useful as part of the inverse numerical optimization approach.

In order to make the definition of 2D target pressure distributions accessible for numerical optimization techniques, the pressure distribution has to be described by a limited number of characteristic parameters. The problem faced is: define a large class of possible pressure distribution shapes by means of as few as possible design parameters. Once the pressure distribution defined, only boundary layer calculations are needed to judge the quality of it (drag, transition location, etc.).

Roughly speaking, the velocity distribution on the airfoil upper- and lower surface can be characterized by three specific regions (see Ref. 31):

- (I) Stagnation point, immediately followed by a rapid acceleration.
- (II) A region with slightly accelerating, slightly decelerating or constant velocity, for transonic conditions often ended by a shock wave.
- (III) The pressure recovery region where the velocities decrease to the trailing edge value. For the lower surface of rear loaded airfoils completed by a small region with accelerated flow.

Figure 6 presents a characteristic pressure distribution defined by eight points and linear interpolation between these points. Without shock, points 2 and 2' coincide. With shock, the jump between 2 and 2' is determined by the local mach number at 2. For a given free stream mach number the points 4 (stagnation pressure) and 1 and 8 (trailing edge pressures) are considered to be known and fixed. This leaves level and position of the points 2, 3, 5, and 7 (ten design variables) free to represent a large class of (simplified) pressure distributions. Refinement of this model would be possible by increasing the number of "characteristic" points. Soon, however, large number of points will be needed to represent more realistic shapes, resulting in a prohibitive large number of design variables. Other ways for refinement are, e.g. non-linear interpolation between the points; adding wave functions with amplitudes as design variables to a starting pressure distribution etc. Several of these options have been investigated at NLR and so far, best results have been obtained by a set of "interpolation rules", taking into account the characteristic behavior of the specific part of the pressure distribution to be represented. Each of these so-called aerodynamic shape functions has been derived from well known aerodynamic theory. It is beyond the scope of the present paper to describe the derivation of these functions in detail. It has to be sufficient to present the relations and to note that for certain combinations of the design variables (coefficients and exponents), approximations are possible of the typical classical flow characteristics. The following functions have been defined, with reference to figure 6.

A. Stagnation flow region (3-4-5)

Rather than suggested in figure 6, the stagnation point (4) will usually not occur exactly at the airfoil nose but somewhat downstream on the lower surface. In order to maintain physically realistic pressure distributions in this region, a stagnation flow shape function has been defined, approximating the potential flow velocity

distribution for elliptic cylinders (for small x/c and small incidence):

$$\frac{u}{u_\infty} = \frac{(1+K_{a1}) \sqrt{K_{a3} \cdot \frac{x}{c}} \pm (K_{a2} + K_{a3} \cdot K_{a4} \cdot \frac{x}{c}) \sqrt{1-K_{a3} \cdot \frac{x}{c}}}{\sqrt{K_{a3} \frac{x}{c} + \frac{1}{4} K_{a1}^2}}$$

(N.B. + sign for upper surface; - sign for lower surface)

Here K_{a1}, \dots, K_{a4} represent the design variables to be adjusted by the optimization procedure. Referring to the elliptic cylinder nose radius and (local) incidence at the nose may be estimated from:

$$\left(\frac{x}{c}\right)_\text{nose} = \frac{0.5}{K_{a3}} \cdot K_{a1}^2 \cdot (1-M_\infty^2) \quad \theta = K_{a2} \sqrt{1-M_\infty^2} \text{ (Radians)}$$

B. "High velocity" regions (from 3 to 2 and from 5 to 6, fig. 6)

These regions often exhibit small pressure gradients at design conditions. So, a relatively simple representation can be chosen. In order to be able to represent also laminar flow condition the following function has been chosen:

$$\frac{u}{u_\infty} = K_{b1} + K_{b2} \left\{ \frac{x}{c} - \left(\frac{x}{c}\right)_{b0} \right\}^{1+K_{b3}},$$

which, for $(K_{b1}$ and $\left(\frac{x}{c}\right)_{b0}$ approaching zero, approximates the well known Falkner-Skan solution for similar laminar boundary layers (Index $b0$ refers to the start of the region). K_{b1} to K_{b3} are the design variables to be adjusted by the optimization procedure.

C. Turbulent pressure recovery region (from 2 (2') to 1 and from 6 to 7)

The family of functions for this region should resemble concave and convex shapes, including the Stratford solution for turbulent zero skin friction pressure recovery (Ref. 32). The Stratford solution exhibits two branches. The main branch, transformed from Stratford's canonical pressure coefficient to the ordinary C_p definition, can be generalized as follows:

$$C_p = C_{p_{c0}} + K_{c1} \left[\left\{ 1 + \frac{\frac{x}{c} - \left(\frac{x}{c}\right)_{c0}}{K_{c2}} \right\}^{1/5} - 1 \right]^{K_{c3}}$$

Index $c0$ indicates the start of the recovery region and K_{c1} to K_{c3} are the design variables. This function represents a wide class of shapes, including an approximation of Stratford's pressure recovery solution.

D. Rear loading region (from 7 to 8)

For so called rear loaded airfoils, the lower surface velocity usually accelerates from the end of the pressure recovery region to the trailing edge. For this region, a simple polynomial was defined reading:

$$C_p = K_{d1} \left(\frac{x}{c} - \left(\frac{x}{c}\right)_{d0} \right)^2 + K_{d2} \left(\frac{x}{c} - \left(\frac{x}{c}\right)_{d0} \right) + C_{p_{d0}}$$

Again index $d0$ indicates conditions at the start of the region and K_{d1} and K_{d2} are design variables.

E. Shock relations (possibly at points 2 and/or 6)

Good transonic design conditions usually incorporate weak shocks at upper and/or lower surface. So, a proper shock description is needed. In viscous airfoil flow, the pressure jump measured at the foot of the shock is less than the Rankine-Hugoniot pressure jump. Besides, the shock will be "smeared out" in the boundary layer. So, in order to describe shocks directly in the pressure distribution some empirical relations are needed. From a compilation of experimental data (see fig. 7, taken from Ref. 33) it is seen that the following modification of the Rankine-Hugoniot relation is a reasonable approximation for weak two-dimensional shocks ($M_1 < 1.3$):

$$\frac{p_{ds}}{p_{us}} = 0.7 \left[\frac{7 M_1^2 - 1}{6} \right] + 0.3 \quad C_{p_{ds}} = C_{p_{us}} + 0.7 \left\{ C_{p_{us}} + \frac{1}{0.7 M_\infty^2} \right\} \left(\frac{7(M_1^2 - 1)}{6} \right)$$

(us and ds for upstream and downstream of shock).

An empirical rule for the shock thickness is presented by Delery (Ref. 34) for weak 2 dimensional shocks:

$$\frac{\Delta x}{\delta_{us}^*} \approx 70 (H_{us} - 1) \quad \text{with} \quad M_{1,us} \leq 1.3$$

Here δ_{us}^* and H_{us} represent displacement thickness and kinematic boundary layer shape parameter, respectively, just in front of the shock. The shock representation becomes active only if $M_{1,\text{local}}$ exceeds 1.1 at point 2 and/or point 6.

Characteristic points and functions presented above represent a rather large class of airfoil design pressure distributions. Note that not all of the design variables indicated above are independent. Some of them are directly determined by the requirement of a continuous pressure distribution. With properly selected basic airfoil geometry and design requirements, a boundary layer calculation method and an optimizer as driver for defining the pressure distribution almost all ingredients are available for a system for designing airfoil target pressure distributions. However for transonic conditions with shock wave boundary layer calculations

only do not account for the momentum loss through the shock. So, the evaluation of the pressure distribution has to be completed with an evaluation of the wave drag. A convenient relation to estimate the magnitude of the wave drag has been proposed by Lock (Ref. 35):

$$C_{d_w} = 0.243 \frac{R_s}{c} \left[\frac{1+0.2 M_\infty^2}{M_\infty} \right] \left[\frac{(2-M_1)(M_1-1)^4}{M_1(1+0.2 M_1^2)} \right]$$

Where R_s is the radius of curvature of the airfoil geometry at the shock position. Lock found an accuracy between -10% and +30% of the wave drag for weak shocks ($1.1 < M_1 < 1.5$), which seems sufficient for the present application.

- Finally some remarks concerning the parametrization described above:
- It becomes obvious that the aerodynamic design problem is strongly non linear and it is likely that non-continuous derivatives will occur as well as for object function(s) as for constraint functions.
 - Sometimes a step by step approach is possible by splitting the design problem in several optimization problems of reduced size, e.g. deal with upper- and lower surface separately.

6. Examples

In the following examples the drag and boundary layer characteristics have been computed with an integral method, comprising:

- Laminar boundary layer according to Thwaites
- Prediction of transition location according to Granville
- A fast integral method (lag entrainment) for the turbulent boundary layer
- Drag calculation according to Squire & Young formula

Low speed high lift condition

The design of single element, high lift airfoils by R.H. Liebeck is well known (see e.g. Refs 36, 37). A.M.O. Smith (Ref. 37) published some of Liebeck's results for the so-called turbulent roof-top. The airfoils meet the additional constraints for the flow to remain attached (and subsonic) everywhere on the airfoil. Then the following design problem is formulated:

free stream condition: $M_\infty = 0.10$, $Re_c = 5 \cdot 10^6$
 transition : upper surface $x/c \geq 1\%$
 (lower surface: $x/c \geq 0.51$)
 maximize : C_l
 subject to : no separation

This problem has been solved by changing only the upper surface pressure distribution for a fixed, arbitrarily chosen, lower surface distribution. Two solutions have been generated, both depicted in fig. 8.

- a. With a fixed, approximated Stratford type pressure recovery the flat rooftop solution is found (full line). This compares reasonably well with Liebeck's optimal solution presented in Ref. 37, indicating max. lift for $C_l = 2.6$ and pressure recovery point at $x/c = 0.30$.
- b. With the upper surface entirely free, the broken line is found, representing a slightly better solution than the roof top solution.

Airfoil geometries, inversely calculated, for these two solutions have also been given in fig. 9. The geometries have been computed with the method described in Ref. 38. Note: keeping in mind the approximations made for the present representation (for example, only one branch of the Stratford solution is considered), the above results are not considered to proof that Liebeck's flat roof top solution can be improved. However, it may be concluded that, from a practical point of view, both solutions exhibit comparable high lift capabilities, while solution b has the advantage of a somewhat less "exotic" geometry.

From this example it is concluded that the aerodynamic shape functions are applicable for low speed high lift design.

Transonic low drag solution

A typical transonic pressure distribution is shown in fig. 9 (full line). In order to find out to what extent this pressure distribution can be represented by the aerodynamic shape functions, the optimization procedure was used. With ΔC_p being the difference between the real and the shape function distribution, the functional $\int \Delta C_p dx$ was minimized. The result, designated best fit, is shown in fig. 9 as a broken line.

Apparently, the shape functions lack refinement around the shock and in the nose region. To find out how serious a problem this is, for the practical design situation. A design study has been performed to improve the drag coefficient at the design lift coefficient. With the best fit as starting point the following optimization problem was defined:

free stream condition : $M_\infty = 0.77$, $Re_c = 10 \cdot 10^6$
 transition fixed at : $(x/c)_{us} = 0.05$, $(x/c)_{ls} = 0.10$
 minimize : C_d
 subject to : $C_l \geq 0.60$
 $C_m \geq -0.125$
 thickness ($= -0.5 \bar{C}_p \sqrt{1-M_\infty^2}$) ≤ 0.10 , being the same value as for the best fit (actual starting airfoil $t/c = 0.11$)

The optimized pressure distribution is shown in fig. 10, together with the start ("best fit") indicating a drag improvement of 5 counts.

- Then two possible ways are open to continue the design study.
1. Define a new target pressure distribution by adding the differences between best fit and optimized distribution to the actual airfoil pressure distribution.
 2. Define the optimized pressure distribution directly as the target for a new geometry design. Here, the latter approach was followed in order to find out whether a less refined target will result in an acceptable airfoil design. Using the inverse airfoil design system INTRAFS (Ref. 39), a new geometry has been generated. The new geometry differs only slightly from the original one. Analyses of both airfoils with the VKK program (ref. 40) indeed shows an improved drag coefficient for the new airfoil (see fig. 11). The drag reduction is less than expected from the calculations depicted in fig. 10; three counts versus 5 counts, this maybe due to the relative poor representation of the original pressure distribution. Nevertheless this example illustrates the ability of the present approach to improve transonic airfoil design.

7. Concluding remarks

An overview has been presented of the possibilities and problems associated with the use of numerical optimization in aerodynamic design. It may be stated that aerodynamic design by using direct numerical optimization techniques is hardly feasible in current engineering environments, at least for three dimensional problems, because of the lack of accuracy in the available 3D flow analysis codes in combination with the limited computer power available. The alternative to use numerical optimization for designing "target" pressure distributions and to use inverse methods to find the corresponding geometry, seems to be a good alternative. However, despite the fact that a large number of iterations is not a serious drawback for the present approach, the procedure is still far from "stand alone" applications on routine basis. It is worth to consider improvements such as the implementation of smoothing options (to prevent problems with numerical irregularities), the application of more efficient algorithms, and the scaling of the independent variables. In this way, numerical optimization may have good prospects for being a useful tool in aerodynamic design.

8. References

1. Slooff, J.W. Round table discussion. AGARD Specialists meeting on Computational Methods For Aerodynamic Design (Inverse) and Optimization, Loen, Norway, 22-23 May, 1989.
2. Boerstoel, J.W. Review of the application of hodograph theory to transonic aerofoil design and theoretical and experimental analysis of shock-free aerofoils, Proceeding IUTAM Symposium Transonicum II Springer Verlag 1976.
3. Yu, N.J. Efficient transonic shock-free wing redesign procedure using a fictitious gas method, AIAA Paper No.79-0075, 1979.
4. Fray, J.M.J. Slooff, J.W. Inverse method with geometric constraints for transonic airfoil design, ICIDES, Austin, Texas, October 1984.
5. Kassies, A. Jameson, A. Aerodynamic design via control theory. 12th IMACS World Congress on Scientific Computations, Paris, July 1988.
6. v.d. Dam, R.F. Optimization in design processes: an information point of view. ICIDES, Austin, Texas. Boerstoel, J.W. Daniels, H.A.M. October 1984.
7. Gill, P.E. et al. Practical optimization. Academic Press, London, (1981).
8. Schittkowski, K. Nonlinear programming codes: information, test, performance. Lecture notes in economics and mathematical systems, Vol. 183, Springer-Verlag, Berlin, (1981).
9. Duff, I.S. Nocedal, J. Reid, J.K. The use of non-linear programming for the selection of sparse sets of non-linear equations. SIAM J. Sci.Stat. Comp., Vol. 8, No. 2, March 1987.
10. Schultz, C.A. Schnabel, R.B. Bvrk, N.H. A family of thrust-region-based algorithms for unconstrained minimization with strong-global convergence properties, SIAM J.Sci.Stat.Comp., Vol. 22, No. 1, Feb. 1985.
11. Saad, Y. Krylov subspace methods on supercomputers. SIAM.J.Sci.Stat.Comp. Vol. 10, No. 6, Nov. 1989.
12. Slooff, J.W. Computational method for subsonic and transonic aerodynamic design. AGARD-FDP-VKC Special Course, May 1983.
13. Hicks, R.M. Murman, F.M. Vanderplaats,G.N. An assessment of airfoil design by numerical optimization NASA TM X-30092, 1974.
14. Hicks, R.M. Transonic wing design using potential flow codes - Successes and failures SAE Paper 810565, 1981.
15. Vanderplaats,G.N. An efficient algorithm for numerical airfoil optimization. AIAA-79-0079, 1979.
16. Hicks, R.M. Application of numerical optimization to the design of supercritical airfoils without Vanderplaats,G.N. drag-creep, SAE Paper 770440, 1977.
17. Hicks, R.M. Henne, P.A. Design by numerical optimization AIAA Paper No. 77-1247, 1977
18. Lores, M.E. Smith, P.E. Numerical optimization: an assessment of its role in transport aircraft aerodynamic design through a case study, ICAS-80-1.2, 1980.
19. Large, R.A. Hicks, R.M. et al. Airfoil section drag reduction at transonic speeds by numerical optimization SAE Paper 760477, 1976
20. Aidala, P.V. Davis, W.H. Mason, W.H. Smart aerodynamic optimization. AIAA-83-1836, 1983.
21. Barger, R.L. Moitra, A. On minimizing the number of calculations in Design-by-Analysis codes. NASA TR 2706, 1987.
22. Hicks, R.M. Vanderplaats,G.N. Design of low-speed airfoils by numerical optimization. SAE Paper 750524, 1975.
23. Misegades, K.P. Airfoil optimization, AIAA-84-0053, January 1984.

24. --- ICIDES-II: Second International Conference on Inverse Design Concepts and Optimization in Engineering Sciences, Pennsylvania, USA, Oct. 26-28, 1987.
25. --- AGARD Specialists' meeting on "Computational Methods for Aerodynamic Design (Inverse) and Optimization, Loen, Norway, May, 1989.
26. Gregg, R.D. Transonic Wing Optimization using Evaluation theory.
Misegades, K.P. AIAA Paper 87-0520, 1987.
27. Vanderplaats, G.N. CONMIN- FORTAN Program for Constrained Function Minimization. NASA TMX-62.282. (1973).
28. Haney, H.P. Computational optimization and wind-tunnel test of transonic wing designs AIAA Paper Johnson, R.R. No. 79-0080, 1979.
- Hicks, R.M.
29. Van den Dam, R.F. Constrained spanload optimization for minimum drag of multi-lifting surface configurations. AGARD Specialists' meeting, Loen, Norway, May 1989.
30. Slooff, J.W. Computational methods for subsonic and transonic aerodynamic design. In: Special Course on Subsonic/Transonic Aerodynamic Interference for Aircraft AGARD Rept. No. 712, 1983.
31. v. Egmond, J.A. Numerical Optimization of target pressure distributions for subsonic and transonic airfoil design. AGARD Specialists' Meeting, Loen, Norway, May 1989.
32. Stratford, B.S. The Prediction of Separation of the Turbulent Boundary Layer J. Fluid Mech. Vol. 5, 1959.
33. Tijdeman, H. Investigations of the transonic flow around oscillating airfoils. Dissertation Technical University Delft, the Netherlands, 1977.
34. Delerv, J. L'interaction onde de choc-couche limite turbulente et son controle, AGARD-CP-365 Paper 21, 1984
35. Lock, R.C. Prediction of the drag of wings at subsonic speeds by viscous/inviscid interaction techniques, AGARD-R-723, 1985.
36. Liebeck, R.H. On the design of subsonic airfoils for high lift. AIAA Paper No. 76-406, 1976.
37. Smith, A.M.O. High lift Aerodynamics, AIAA Paper No. 74-939, 1974.
38. Labrujère, T.E. MAD, a system for computer aided analysis and design of multi-element airfoils, NLR TR 83136 L, 1983.
39. Fray, J.M.J. Design of transonic airfoils with given pressure, subject to geometric constraints, NLR Slooff, J.W. TR 849064 U, 1984.
40. Kassies, A. The prediction of viscous effects on aerofoils in transonic flow. RAE TM Aero 1780, Lock, R.C. 1978.

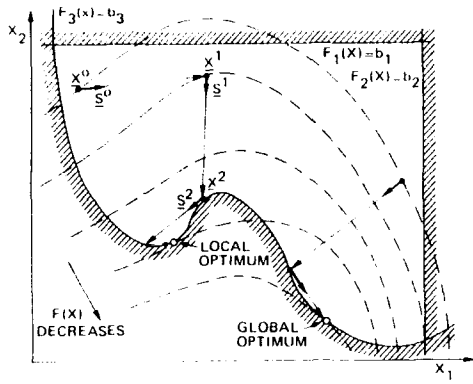


Figure 1. Example of an iterative search procedure

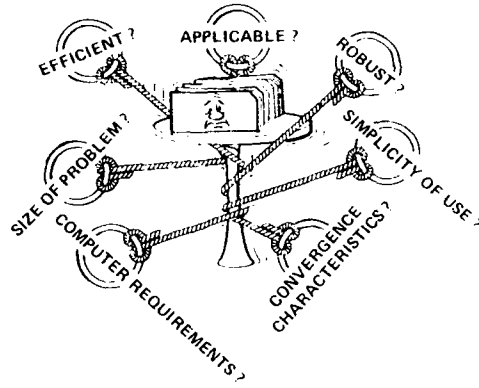


Figure 2. Criteria for selection of optimization algorithms

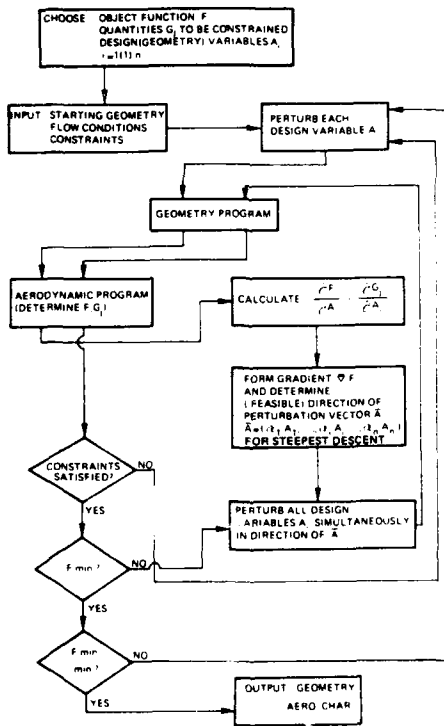


Figure 3. Flow chart of direct numerical optimization

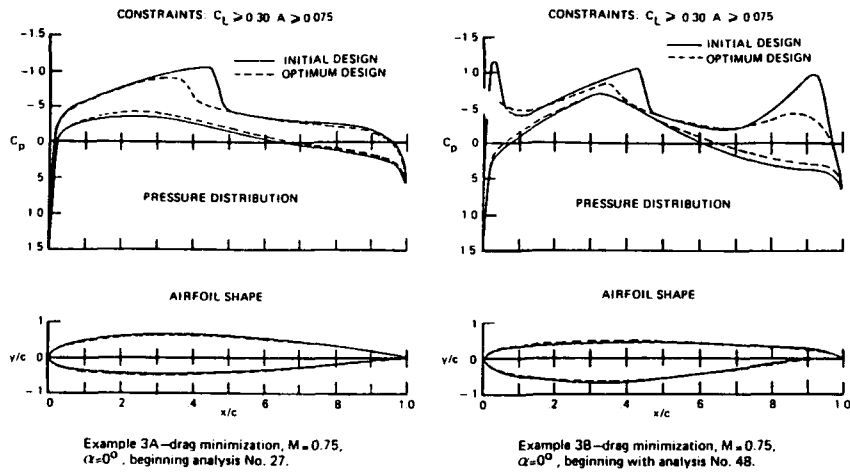


Figure 4. Example of non-uniqueness of wave drag minimization problem

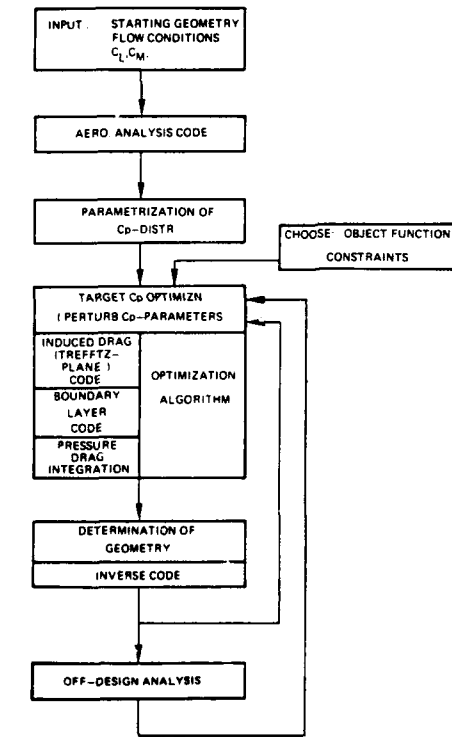


Figure 5. Scheme for inverse numerical optimization

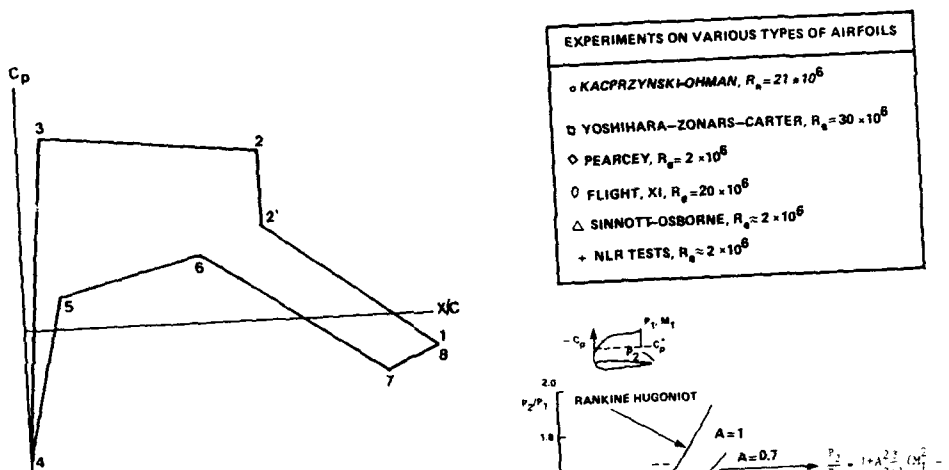


Figure 6. Schematic representation of pressure distributions

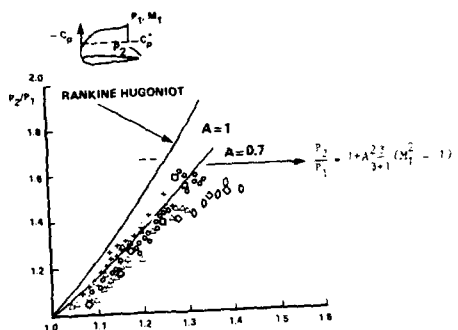


Figure 7. Compilation of experimental shock data

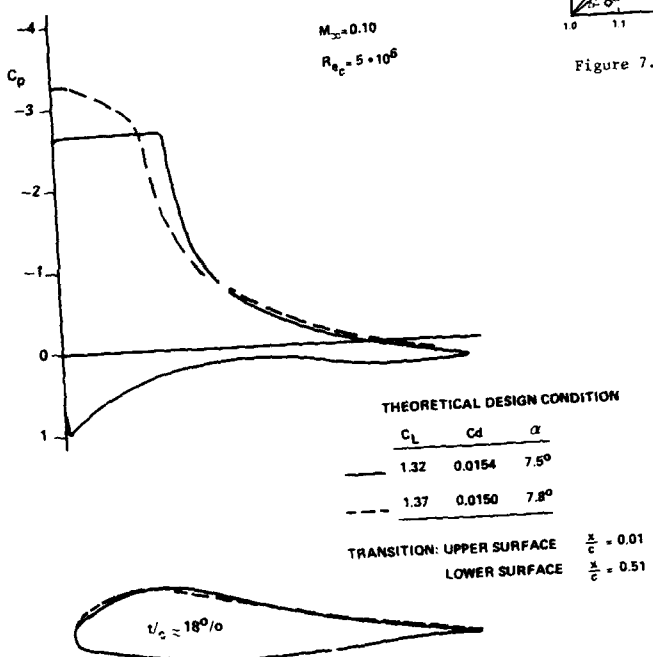


Figure 8. High lift solutions

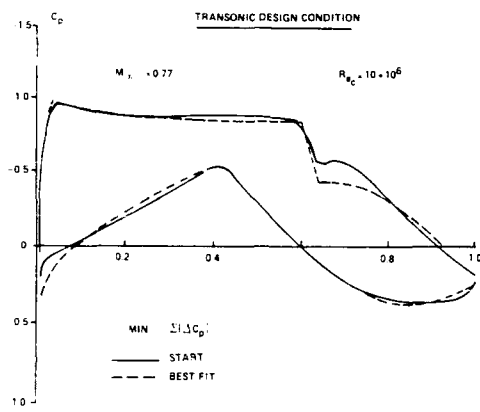


Figure 9. Start conditions

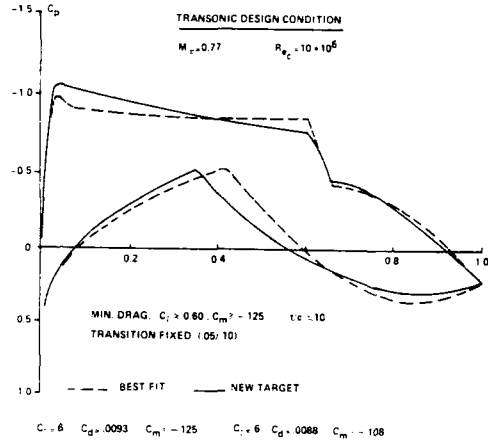


Figure 10. Optimized target compared with start (aerodynamic shape functions)

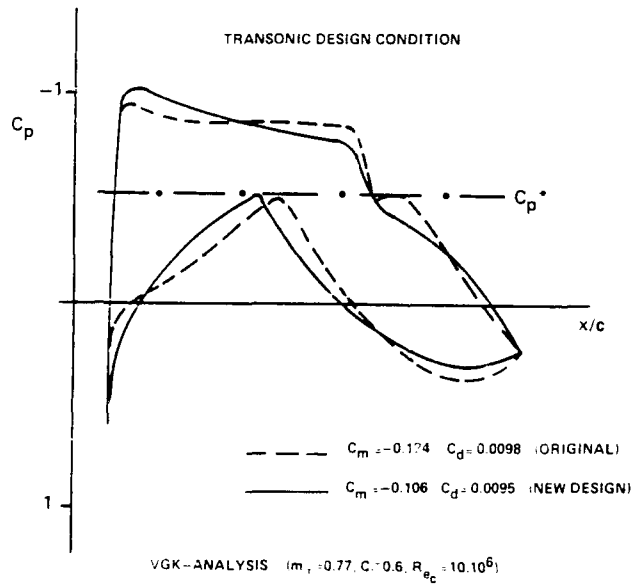


Figure 11. VGK analysis

GEOMETRIC AND SURFACE PRESSURE RESTRICTIONS IN AIRFOIL DESIGN

G. Volpe
Senior Staff Scientist
Grumman Corporate Research Center
Mail Stop A08-35
Bethpage, New York 11714
U.S.A.

SUMMARY

In order to design a physically-acceptable airfoil that corresponds to a prescribed surface pressure or speed distribution, various restrictions have to be met by the imposed target and by the contour. It is shown that the need to meet geometric prerequisites and a specified free-stream value imposes constraints on the prescribed surface values which, unless satisfied, inhibit the existence of a solution. In this classical problem of airfoil design, the prescribed surface distribution must contain enough degrees of freedom in order that it may be modified sufficiently to satisfy the constraints. The nature of the constraints is discussed, and they are expressed in forms which are amenable to numerical solution procedures in transonic as well as incompressible flows. The discussion is accompanied by a description of the general characteristics of airfoil geometries and surface flows.

1. INTRODUCTION

The problem of designing airfoil profiles is older than aviation itself. The Wright Brothers built a wind tunnel to test new airfoil profiles that would give them greater lift. It was obvious that by changing the profile the characteristics of the flow could be altered. Quite early the idea took hold that the airfoils could, or should, be designed to produce specific pressure distributions on them. This was the rationale behind the design of the NACA 1-series wing sections.¹ The development of this series of airfoils, which represents the first family of NACA low drag high-critical-speed wing sections, was also one of the first recorded attempts to design sections having a desired type of pressure distribution. The goal of this early design project was to produce airfoils with extensive laminar boundary layers. It was felt that the laminar flow run could be controlled by having a small, continuously-favorable pressure gradient all the way to the point of minimum pressure, whose location identifies and characterizes the several members of this airfoil family. Lack of adequate theoretical tools made this pre-1939 design exercise extremely difficult, and the design goals were achieved only over a very limited range of lift coefficients. Few sections in this family ever proved useful.

Better theoretical tools (at least for incompressible flow) were being developed during the time during which the NACA 1 and its immediate successor-families (NACA 2-to 5-series) were designed. The NACA 6- and 7-series were designed using new and improved approximate methods² which were derived from the Theodorsen-Garrick³ method of analyzing the potential flow about arbitrary airfoil sections. To obtain these sections, a symmetrical section was designed first, and this was then cambered using linear theory. The first true airfoil design method had been reported in the meantime by Mangler⁴, and a similar approach was later independently developed by Lighthill.⁵ A sound theoretical basis for the design of airfoil profiles corresponding to a specified pressure (or, equivalently, velocity) distribution was finally available.

The usefulness of the Mangler and Lighthill methods obtaining practical designs was debatable, and understandable given the computational resources of the time, but their presentation of this "inverse" problem of airfoil theory was sound and laid the groundwork for many practical methods that followed.⁶⁻¹³

The work of Mangler and Lighthill assumed incompressible flow and could thus use potential theory to describe it. In the inverse problem, the connection between the desired pressure distribution and the ordinates of the corresponding airfoil profile could be expressed in closed form, just as in the "direct" problem, where one seeks the pressure distribution corresponding to a given airfoil profile. The actual computation of a profile was not always feasible, leading to problems of practicality, but the existence of closed form expressions describing the "connection" revealed the existence of certain constraints that had to be satisfied by the desired pressure distribution for a corresponding airfoil to exist. In particular, it was shown that the average speed of the desired surface distribution should be equal to the free-stream speed. In addition, it was shown that the thickness of the trailing edge is itself a function of the prescribed speed. Since trailing edge thickness has to be within some obvious physical and geometrically-realistic limits, additional constraints are imposed on the prescribed surface pressure. Thus, for an arbitrarily prescribed distribution, an airfoil profile with a specific trailing edge thickness exists only if the distribution satisfies these constraints. Fortunately, within the context of potential theory, the above-mentioned constraints can be expressed in integral form. As a result, by allowing some freedom in the imposed distribution (e.g., through adjustable parameters whose values are chosen to satisfy the integral expressions), an airfoil profile can always be obtained. This approach forms the basis of the methods described in Refs. 6-13.

Woods⁷ extended the theory of inverse airfoil design to subcritical compressible flow. Assuming a Karman-Tsien type gas, he derived expressions similar to those of Mangler and Lighthill for incompressible flows. The formulation of an inverse method at supercritical speeds has been problematic because of the impossibility of expressing the constraints in closed form. The existence of constraints for the transonic design problem was intuitively true because the incompressible problem was a subset of the more general compressible problem. The main obstacle concerned the constraint reflecting the connection between free-stream and surface speed. Volpe and Melnik¹⁴ finally offered a formulation of the problem which was valid through the compressible regime. In their formulation, the constraints are satisfied through an iterative procedure in the absence of closed-form expressions.

It is the purpose of this paper to describe these constraints in more detail, as well as the means by which they might be satisfied to produce a practical inverse airfoil design method. The discussion will include the restrictions on the prescribed pressure

distributions which are due to physical requirements and to the achievement of certain flow characteristics, as well as the restrictions imposed by the requirement that the airfoil geometry have specific characteristics. In addition to the above-mentioned restriction on the thickness of the trailing edge, an airfoil should have other obviously desirable features, such as a rounded leading edge and non-crossing upper and lower surfaces. The discussion will cover both the incompressible and compressible regimes, and the connection between imposed pressure distributions and geometry will be illustrated by several examples. As in the preceding discussion, in what follows the assumption is made that the airfoil is to be designed in an inviscid flow. Viscosity will be called on in discussing the prescription of the imposed pressure distribution. To a first approximation, the pressure distribution can be assumed to be the one impressed on the boundary layer and the corresponding airfoil to be the contour from which a "displacement thickness" should be subtracted to achieve a profile operating in a real viscous environment.

2. GEOMETRICAL CHARACTERISTICS

All physically realistic airfoils share certain obvious characteristics. Most obvious are the constraints that the contour be closed and non-reentrant. A closed contour is described by a continuous line whose end points coincide. Taking the end points of this line to be the points corresponding to the lower and upper trailing edge points and the line to run from the former to the latter in a clockwise direction, airfoil "closure" means that the two trailing edge points coincide. Thus the airfoil in Fig. 1a is closed and the one in Fig. 1b is not. In practice some trailing edge thickness, usually on the order of one percent of the chord, is desirable for structural integrity. In such a case the definition of closure is expanded to include the case in which the trailing edge points are separated by some small distance.

A non-reentrant airfoil is one for which the line describing the contour never crosses over itself. An airfoil may be closed but not necessarily non-reentrant. Thus, the airfoil depicted in Fig. 1c is closed but reentrant; the one in Fig. 1d is open and reentrant.

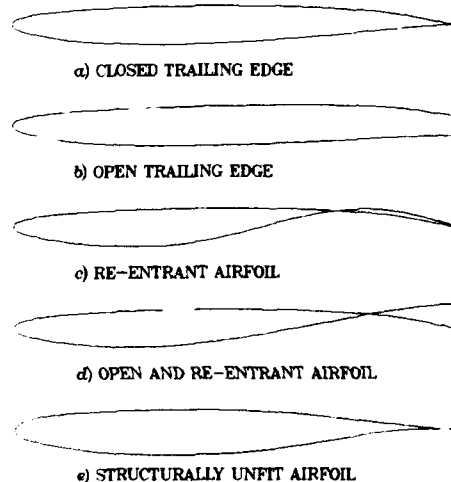


Fig. 1 Airfoil types

Reentrant airfoils are clearly non-physical. Obviously a non-reentrant airfoil exhibits a positive thickness from leading edge to trailing edge. Structural requirements impose some limitations on the minimum acceptable thickness, though. As such, the airfoil that is shown in Fig. 1e is likely undesirable from a practical viewpoint, since its thickness just upstream of the trailing edge is very small, even though positive. In short, structural as well as operational requirements (e.g., need for fuel volume) will place restrictions on the acceptable thickness distribution on the airfoil.

Certain features of the leading edge and trailing edge regions of an airfoil and their relation to the velocity distribution should be mentioned. Most airfoils have rounded leading edges. A rounded leading edge allows operation over a wide range of angle of attack. A sharp leading edge would cause the flow to separate at the corner outside a severely, more limited range of flow incidence. The exception would be offered by airfoils designed for supersonic applications, in which case it is desirable to keep the shock waves attached to the leading edge via a sharp nose. The rest of this paper will be concerned only with subsonic/transonic free-stream Mach numbers, however. Since both the upper and lower surfaces of the airfoil must be streamlines of the flow, a stagnation point must be present on the surface in the leading edge region (see Fig. 2). That stagnation point is also a branch point, since the flow splits into two downstream of it. When designing for an airfoil, the speed distribution that is prescribed must include a stagnation point in the leading edge region.

In the case of an inviscid stream, two possibilities arise for the flow at the trailing edge. If the included angle of the trailing edge is zero (a cusp), it is sufficient that the pressure at the upper and lower surfaces have the same magnitude at that point. For an isentropic flow, the velocities on the two sides are also identical. In such a case, the velocity has a non-zero value, usually slightly less than the free-stream value. If the included angle is not zero, the only way for the pressure and the total velocity at the upper and lower trailing edge points to match is for the velocity to be zero. In this case, the trailing edge point is a stagnation point. These two possibilities are illustrated in Fig. 3a and 3b, which, along with the trailing edge geometry, depict the typical speed distribution of the flow from either side of the airfoil and downstream of the trailing edge. It should be noted that the gradients of the speed distribution in the vicinity of the trailing edge are dependent on the magnitude of the trailing edge angle (see Fig. 3a and 3c). In a viscous flow, the presence of a boundary layer blurs the two distinct possibilities (see Fig. 3d). If one were to design for a speed distribution to be achieved outside the boundary layer (by whatever method), one has to demand only that the velocities on opposite sides of the trailing edge (and outside the boundary layer) match; they do not vanish even for a non-zero included angle. As a consequence, the shape of the trailing edge region is highly dependent on the local distribution of speed in the region.

If one is seeking to generate a contour with specific leading and trailing edge characteristics, these requirements will impose specific restrictions on the prescribed speed restrictions which have to be taken into account in the calculation procedure.

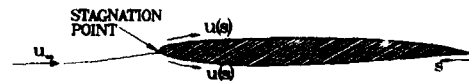


Fig. 2 General features of flow near airfoil

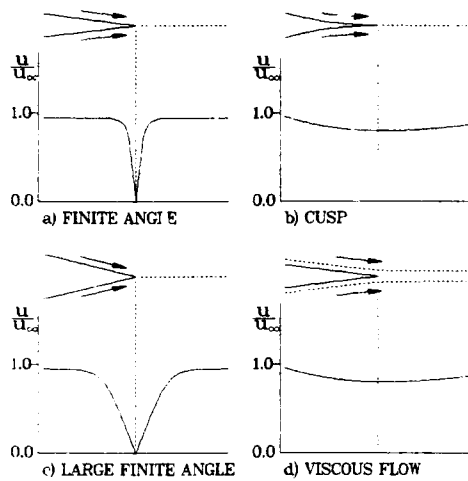


Fig. 3 Possible flow conditions near trailing edge

3. FLOW CHARACTERISTICS

Certain characteristics of the pressure distribution on an airfoil, such as the presence of a stagnation point at the leading edge and possibly another at the trailing edge were mentioned in the previous section. Other features are dependent on the particular design exercise. In all cases, the objective is to obtain a certain lift coefficient at as low a level of drag as possible. In the context of an inverse airfoil design procedure, these goals can be achieved by tailoring the surface pressure, or speed, distribution to the application.

The lift coefficient of an airfoil is known to a good degree of accuracy once the surface speed is prescribed even though the shape is not known yet. Figure 4 depicts the general form of an airfoil surface speed distribution, u , expressed as a function of the arc length along the airfoil surface, s . The origin of s is

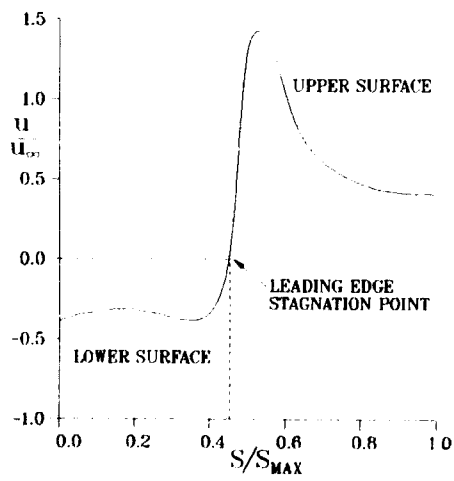


Fig. 4 General form of airfoil speed distribution

assumed to be located at the lower surface trailing edge point, and s is assumed to run clockwise around the contour (see Fig. 2). Without loss of generality, the perimeter of the airfoil can be normalized to one. The lift coefficient, C_L , of an airfoil is given by

$$C_L = \frac{L}{\frac{1}{2} \rho_\infty u_\infty^2 c} \quad (1)$$

where L is the lift, c is the airfoil chord and ρ_∞ and u_∞ are the free-stream values of the density and the velocity, respectively. In potential flows, the lift can be expressed as a function of the circulation, Γ , around the airfoil

$$L = \rho_\infty \Gamma u_\infty, \quad (2)$$

and Γ in turn is obtained by integrating around the contour

$$\Gamma = \int u(s) ds. \quad (3)$$

Hence, the lift coefficient is given by

$$C_L = 2 \int \frac{1}{c} \frac{u(s)}{u_\infty} ds. \quad (4)$$

The value of the chord c is not known until the shape of the contour is determined. However, for most aeronautical profiles, it will have a value not much different from 0.5. As a result, for all practical purposes, C_L is known once $u(s)/u_\infty$ is specified.

In incompressible flow, the pressure drag will be zero for all possible surface speed distributions. At supercritical speeds, wave drag will be present if a shock wave is present in the flow field. Unfortunately, its value is not known until the contour is computed. The goal, as always, is to minimize this value, but the absence of a discontinuity in the pressure distribution (which translates into the absence of a shock wave on the airfoil surface) is no guarantee that there is not a shock wave in the flow. An example is offered in Fig. 5, which shows an airfoil profile and, above it, the

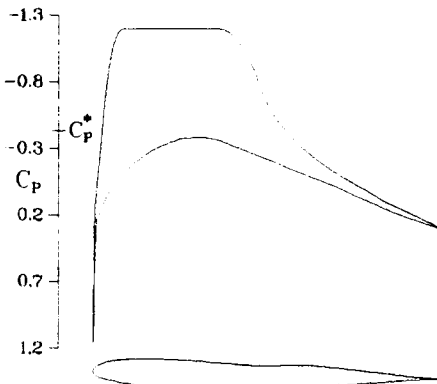


Fig. 5 "Shockless" target pressure distribution and corresponding airfoil

corresponding pressure distribution. In Fig. 6, the Mach number contours of the flow around the airfoil are depicted. In this picture, the existence of a shock wave is borne out by the clustering of contours above the airfoil. Compression lines generated on the concave mid-region of the airfoil converge off the surface into a shock. This figure points out a geometrical feature of airfoils that should be avoided at transonic speed, namely, a region on the upper surface of the airfoil with a curvature concave to the flow.

In the absence of shock waves, drag is due to viscous effects, and some amount of control over these can be retained by proper design of the imposed surface pressure distribution, even within the context of an inviscid airfoil design procedure. By tailoring the pressure distribution, one can control the growth of the boundary layer, delay transition to turbulence and, hopefully, avoid flow separation. All of these effects tend to lower drag levels.

Flow separation is clearly a disastrously deleterious flow feature. In airfoil-type flows, it can be brought about by high adverse pressure gradients as they might occur on the upper surface as the flow is recompressed to stagnation or near-free-stream values at the trailing edge -- for sharp or cusped geometries, respectively. Separation can be avoided by imposing pressure distributions with gentle gradients (see Fig. 7).

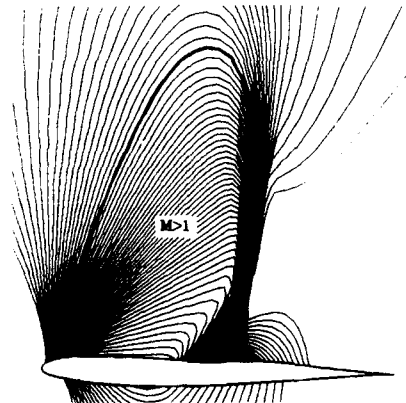


Fig. 6 Isomach contours computed on airfoil designed to "shockless" pressure distribution

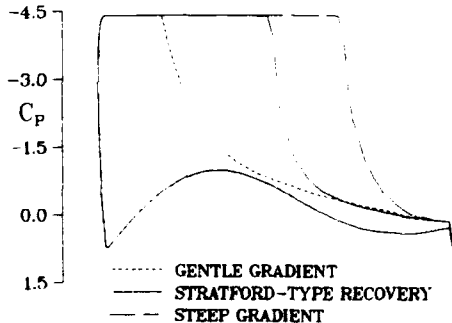


Fig. 7 Types of pressure distributions with various recovery patterns following "rooftop" region

This solution, however, is at odds with the other goal of trying to maximize lift. The latter objective can be achieved by having the flow undergo the required recompression to trailing edge values in the shortest distance possible. The optimum solution is to achieve the shortest possible distance while still avoiding separation. Liebeck⁹ addressed this problem, and the solution was found in the use of pressure distributions, proposed by Stratford,¹⁵ which avoid separation by a constant specified margin (solid line in Fig. 7). Stratford developed an analytical form for such a pressure distribution. In principle, a flow described by a Stratford-type pressure distribution achieves a given recompression in the shortest possible distance or, alternatively, the maximum possible pressure recovery in a given distance. This type of pressure recovery distribution was checked experimentally by Stratford¹⁶ and was found to exhibit a "good margin of stability."

The pressure distributions in Fig. 7 have been drawn with a "rooftop" region preceding the Stratford recovery region. The level and extent of the rooftop region are clearly designed to maximize lift. Liebeck⁹ studied this class of pressure distributions at incompressible speeds and showed through a variational analysis that the level and extent of such a rooftop can be combined with the Stratford canonical distribution to maximize the lift on an airfoil. It is to be remembered that maximizing lift can be at odds with the structural requirements of an airfoil. The airfoil shown in Fig. 8 may exhibit very high lift characteristics but is hardly practical. Regarding such rooftop pressure distributions, it is worth recalling that at compressible speeds, there is a lower limit on the minimum pressure that one can specify in the flow field. The limit is obviously zero, and all practical airfoils will have a pressure minimum well above this limiting value. In a similar vein, lift can be increased by increasing the prescribed pressure levels on the lower surface of the airfoil or by equivalently decreasing the speed distribution there. Clearly, the maximum amount of lift is obtained if the speed is identically zero everywhere on the lower surface. Obviously, such a flow is impossible, and all practical airfoils will have values of the speed on the lower surface well above the stagnation value.

The drag of an airfoil can be significantly lowered by delaying the transition of the flow from laminar to turbulent. Considerable effort has gone into the design of such natural laminar flow airfoils over the past half-

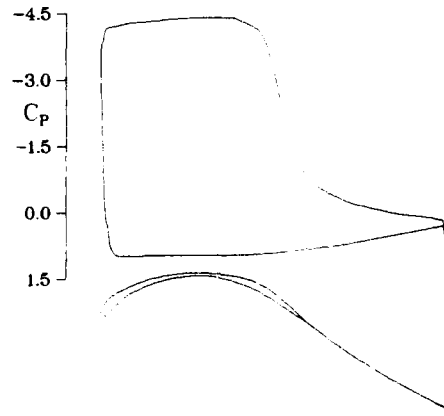


Fig. 8 Maximum lift pressure distribution and corresponding contour

century. The above-mentioned designs of the NACA 1- to 7-series airfoil sections, which constituted some of the earliest efforts of generating contours corresponding to prescribed pressure distributions, all had as a goal the achievement of extensive runs of laminar flow on both the upper and lower surfaces. The criterion of lowering drag by inducing long laminar flow runs through appropriate surface pressure distributions was followed by Liebeck. In these studies, transition was delayed by prescribing a continuously favorable pressure gradient from the leading edge stagnation point to the position of minimum pressure. This acceleration region modifies the ideal rooftop which tends to maximize lift (see Fig. 9). Similarly, Pfenninger^{17,18} used careful tailoring of the surface pressure distribution to control the growth of instabilities that bring about transition of the flow to design a number of natural laminar flow airfoils for transonic applications. An example of such an airfoil is given in Fig. 10.

The shape of a pressure distribution to which an airfoil contour is to be designed depends on the particular application. In this section, some general characteristics of the distribution and certain possible features to design for have been described. In the previous section, the characteristics of physically acceptable -- and practical -- airfoils were indicated, and certain connections between the geometry and the pressure distribution were mentioned. The question of the existence of an airfoil for an arbitrarily prescribed surface pressure distribution (containing some or all of the above-discussed features), whether physically acceptable or not, has to be addressed now. This will be taken up in the following sections, along with the relationship between prescribed pressures and the airfoil geometry.

4. FORMULATION OF THE INVERSE DESIGN PROBLEM

The problem that will be addressed now is the construction of the airfoil profile, which has a surface speed distribution, q_o , equal to some desired function, F , everywhere along its arc length, s . As mentioned earlier, this is to be measured clockwise around the airfoil contour, starting at the lower surface trailing edge

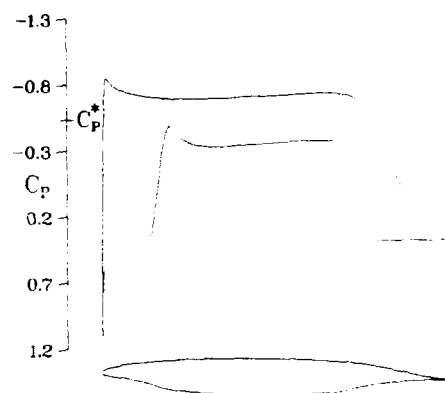


Fig. 10 Designed contour and pressure distribution; case LFC1 $M_\infty = 0.766$, $\alpha = 0^\circ$, $C_L = 0.5166$, $C_D = 0.0001$

point. The airfoil's coordinates, x, y , can be parameterized as functions of s . In Section 2 it was mentioned that a feature of practical airfoil contours is that the trailing edge be either closed or have a very small gap. Thus, a requirement on the to-be-determined airfoil is that the upper and lower surface trailing edge points be separated by prescribed distances Δx and Δy . The horizontal gap, Δx , is usually set to zero, while the vertical gap, Δy , is set to zero or to a small positive number. The free stream is also defined by prescribing values for the free-stream velocity q_∞ , temperature, and pressure (or density). These in turn determine the free-stream Mach number, M_∞ . In incompressible flow, of course, it is necessary only to specify the velocity in order to identify the free stream uniquely. Our formulation applies in its entirety if we specify a surface-pressure distribution instead of a surface speed since the two are uniquely related. Formally, then, the problem is to determine the airfoil profile of a specified trailing edge thickness corresponding to the speed distribution

$$\frac{q_o}{q_\infty} = F(s/s_{\max}) \quad (5)$$

Again, without loss of generality, s_{\max} can be set equal to one; q_o is taken as positive in the clockwise direction around the airfoil. As shown by Theodorsen,³ any airfoil contour can be mapped into the unit circle by the unique conformal transformation

$$\frac{dz}{d\zeta} = \left[i - \frac{1}{\zeta} \right]^{(1-\epsilon)} e^{(P+iQ)} \quad (6)$$

where $z = x + iy$ and $\zeta = re^{i\omega}$ are the coordinates in the physical and mapped planes, respectively, and ϵx is the included trailing edge angle. This transformation leaves the far field, $\zeta \rightarrow \infty$, unchanged, except for a possible rotation (see Fig. 11). Equation 6 can be

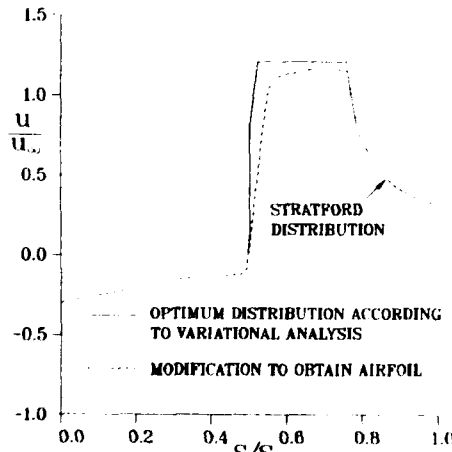


Fig. 9 Optimum speed distribution and modification needed to obtain airfoil contour

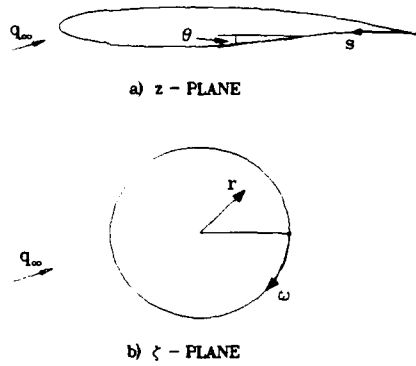


Fig. 11 Mapping of airfoil to circle

separated into its real and imaginary parts. Thus, on $r = 1$,

$$\frac{ds}{d\omega} = \left[2 \sin \frac{\omega}{2} \right]^{(1-\epsilon)} e^P \quad (7)$$

$$\theta = \frac{1}{2} (1 + \epsilon) (\pi - \omega) - \frac{\pi}{2} + Q \quad (8)$$

where θ is the local slope of the airfoil. Q is the Fourier series

$$Q = \sum_{n=0}^N (A_n \sin n\omega - B_n \cos n\omega) \quad (9)$$

and P is its conjugate series. Because θ is known as a function of s , the coefficients of the series can be found by standard Fourier analysis as described in Ref. 10.

With this mapping procedure, the leading terms of the series are related to the trailing edge gap ($\Delta x, \Delta y$) by

$$A_1 = -\left(\frac{\Delta x}{2\pi}\right) \sin B_o - \left(\frac{\Delta y}{2\pi}\right) \cos B_o + (1 - \epsilon) \quad (10)$$

$$B_1 = -\left(\frac{\Delta x}{2\pi}\right) \cos B_o - \left(\frac{\Delta y}{2\pi}\right) \sin B_o.$$

The transformation the airfoil profile into a circle simplifies the problem of constructing a solution for the flow about the airfoil. Generating a solution for the flow about a circle is a relatively straightforward process. In fact, for incompressible flow, it can be expressed analytically. For transonic flows, it can be computed numerically by a number of methods (see, for example, Ref. 19). The velocity components at any point on the airfoil or in the flow field can be obtained by dividing the respective components of the flow at the corresponding point in the circle plane by the metric of the

transformation, $\left| \frac{dz}{d\zeta} \right|$, evaluated at the point in question.

Obviously, the total speed in the two planes are similarly related.

In the case of incompressible flow, the complex potential, w , for the incompressible flow past the circle is given by

$$w = q_\infty \left(\zeta e^{-i\alpha} + \frac{e^{i\alpha}}{\zeta} \right) + i\Gamma \log \zeta \quad (11)$$

where α is the angle of attack of the free stream and Γ is the circulation around the circle. Since the far field is not altered by the transformation, q_∞ is also the value of the free stream in the physical plane. The conjugate of

the velocity is given by $\frac{dw}{d\bar{\zeta}}$, and the value of Γ is

obtained by requiring that this $\frac{dw}{d\bar{\zeta}}$ be zero at the point on the circle corresponding to the airfoil's trailing edge. The velocity in the physical plane (around the airfoil) is then given by

$$\frac{dw}{dz} = \frac{dw}{d\zeta} \left(\frac{dz}{d\zeta} \right)^{-1}. \quad (12)$$

Thus, the calculation of the flow about any airfoil can be reduced to the computation of the two factors on the right hand side of Eq. (12), which can be computed from Eq. (6) and (11), respectively. Moreover, Eq. (12) can be used to generate an airfoil profile by re-arranging it in the form

$$\frac{ds}{d\omega} = \left| \frac{dz}{d\zeta} \right| = \left| \frac{dw}{d\zeta} \right| \left| \frac{dw}{dz} \right|^{-1}. \quad (13)$$

If one now assumes $\left| \frac{dw}{dz} \right|$ to be the q_o , the speed distribution that the airfoil profile is prescribed to have, the expression can be used to obtain the arc length and the slope of the airfoil as a function of ω , and hence the ordinates of the airfoil. Assuming q_o is prescribed as a function of the ω , then the right hand side of Eq. (13) is completely known as a function of ω . Using Eq. (7) and (9), the coefficients of the series of the transformation

can be evaluated. Once $\left| \frac{dz}{d\zeta} \right|$ has been expressed as a trigonometric series in ω , the airfoil coordinates, z , are found by integration.

If q_o is prescribed as a function of arc length, s , some iteration would be required since $\left| \frac{dw}{dz} \right|$, which is needed in Eq. (13), will not be known as a function of ω until after $s(\omega)$ is found. However, the design of the airfoil is still a straightforward process.

For compressible flow of a perfect gas, the flow past the circle cannot be expressed in closed form. It can be computed numerically, though, and a similar iterative procedure can be formulated for compressible flow.

Specifically, the procedure could be as follows. An initial airfoil contour is mapped into the unit circle, and the flow around the circle is solved subject to the conditions on the circle boundary that the tangential speed be the required total speed. The passage from $q_0(s)$ to $q_0(\omega)$ is done using the current $s(\omega)$. In this flow, the circle boundary is not necessarily a streamline, and the departure of the boundary from a streamline can be used to find a correction to the airfoil contour. Using the new metric, the process can then be repeated.

5. CONSTRAINTS IN INCOMPRESSIBLE FLOW

The question that must be asked at this point is whether an airfoil solution exists for an arbitrarily prescribed speed distribution. For incompressible flow, Mangler and Lighthill showed that, in fact, a solution exists only if certain integral constraints are satisfied by q_0 , and this can be demonstrated as follows.

Since a lifting flow over a circle can be reduced to the nonlifting, symmetric flow as shown in Ref. 5 and 20, it is sufficient to consider the nonlifting case in order to simplify the discussion. The mapping between the z and ζ planes must have the form

$$z = \zeta + \sum_{n=0}^{\infty} a_n \zeta^{-n}$$

If the flow in the far field is to remain unscaled. Here, the a_n 's are complex constants. Therefore,

$$\frac{dz}{d\zeta} = 1 - \sum_{n=1}^{\infty} n a_n \zeta^{-(n+1)}.$$

Differentiating Eq. (11) gives

$$\frac{dw}{d\zeta} = q_\infty \left(1 - \frac{1}{\zeta^2} \right).$$

Hence, by combining the last two equations, one obtains

$$\frac{dw}{dz} = q_\infty \left(1 + \sum_{n=2}^{\infty} b_n \zeta^{-n} \right). \quad (14)$$

Since $(dw/dz) = q_0 e^{-i\theta}$, it follows that

$$\log \left| \frac{q_0}{q_\infty} \right| = \sum_{n=2}^{\infty} b'_n \zeta^{-n}. \quad (15)$$

As pointed out by Lighthill and Thwaites, $\log |q_0/q_\infty|$ is an analytic function in the domain outside the circle. (It fails to be analytic at stagnation points on the circle where $q_0 = 0$.) Therefore, it can be expanded in a Fourier series on the circle itself. However, from Eq. (15) it can be seen that the series cannot have terms of zero or first order. In fact, q_0 must be such that

$$\int_0^{2\pi} \log \left| \frac{q_0}{q_\infty} \right| \left\{ \begin{array}{l} \cos \omega \\ \sin \omega \end{array} \right\} d\omega = 0. \quad (16)$$

These are the three integral constraints that the prescribed speed distribution must satisfy for an airfoil solution to exist. These three constraints have arisen from the requirements that the airfoil be closed and from the imposition of a value on the free stream. It can be safely assumed that similar constraints exist also at supercritical speeds. The above discussion indicates that the prescribed speed distribution should contain, in general, three adjustable parameters to guarantee that the constraints may be satisfied. Thus, the surface speed distribution should be prescribed in the form

$$\frac{q_0}{q_\infty} = F(s/s_{\max}; p_1, p_2, p_3) \quad (17)$$

where p_1, p_2 , and p_3 are the three parameters that are found as part of the solution.

The above discussion has not dealt with the possibility of the contour being reentrant. The constraint that the thickness of the airfoil be always positive, or even always greater than some minimum value cannot be expressed in a simple relation, as Eq. (16). It could be accounted for, and satisfied, through a numerical procedure by the introduction of additional parameters in Eq. (17). Such parameters could be adjusted to guarantee that the thickness at selected chord locations have values above specified values. The particular functional forms chosen to introduce the parameters in Eq. (17) will, of course, affect the class of airfoil solutions that can be obtained.

6. AN ALTERNATIVE LOOK AT THE CONSTRAINTS

For compressible flow ($M_\infty \neq 0$), Eq. (16) is no longer valid. In order to formulate a well-posed inverse design procedure which would be valid at compressible speeds, the nature of the constraints must be re-examined, and they must be expressed in a form useful for a design procedure. It is logical to do this in the context of the computational method that has been outlined. The two constraints that arose because of the required trailing edge gap are of a geometrical nature. Hence, one can set up a procedure in which, by monitoring the trailing edge gap size, the target speed can be modified in order to drive the gap's dimensions to its specified values. The first constraint creates a problem because there is no single, physical quantity that reflects the constraint. This first condition is a statement of "compatibility" between the prescribed surface speed and the free-stream speed. If the latter is also being prescribed, as is usually the case, the surface speed prescription has to be modified for the constraint to be satisfied. If the free-stream speed is not specified, in the case of incompressible flow its value can be found from Eq. (16). In the absence of a closed-form expression, which would be valid at compressible speeds, the problem is to define a procedure whereby either the surface speed or the free-stream speed might be changed to bring about "compatibility."

Consider the incompressible flow over a circle again. As mentioned earlier, it will be sufficient to consider the nonlifting symmetric flow. The general solution for the flow on the outside of a circle of unit radius can be represented in the form

$$G = a_0 + a_1 r \cos \omega + \sum_{n=1}^N \frac{b_n}{r^n} \cos n\omega,$$

N being a sufficiently large number. Here G represents the potential function of the flow.

This is the most general solution to Laplace's equation that yields a uniform free-stream flow in the far field ($r \rightarrow \infty$). Hence

$$\frac{\partial G}{\partial r} = \left(a_1 - \frac{b_1}{r^2} \right) \cos \omega - \sum_{n=2}^N \frac{n b_n}{r^{n+1}} \cos n\omega \quad (18)$$

and

$$\frac{1}{r} \frac{\partial G}{\partial \omega} = - \left(a_1 - \frac{b_1}{r^2} \right) \sin \omega - \sum_{n=2}^N \frac{n b_n}{r^{n+1}} \sin n\omega. \quad (19)$$

It follows that the total velocity

$$q = \left(G_r - \frac{i}{r} G_\omega \right) e^{-i\omega}$$

must be of the form

$$q = a_1 - \sum_{n=2}^N b'_n \zeta^{-n} \quad (20)$$

In the far field, as $\zeta \rightarrow \infty$, $q = q_\infty$. Hence, and $a_1 = q_\infty$ and

$$q = q_\infty - \sum_{n=2}^N b'_n \zeta^{-n} \quad (21)$$

which reflects the result expressed in Eq. (15). Thus, if the flow over the circle is determined with the condition that $q = q_0(\omega)$ on the boundary $r = 1$, it can be seen that if $q_0(\omega)$ is expanded in a series

$$q_0(\omega) = c_0 + \sum_{n=1}^N c_n e^{-in\omega} \quad (22)$$

restrictions on q_0 immediately arise, echoing the constraints described by Lighthill and Mangler. In particular, one sees that $c_0 = q_\infty$, the first constraint. Also, c_1 must vanish, implying two additional restrictions on the speed, since c_1 is a complex constant.

It is interesting to note that Eq. (21) can be factored into the form

$$q = q_\infty \left(1 - \frac{1}{\zeta^2} \right) \left[1 - \sum_{n=2}^N b'_n \zeta^{-n} \right]. \quad (23)$$

Since the first part on the right-hand side of this expression represents the solution for the flow over the unit circle, the expression in brackets formally gives the mapping $|\zeta|/dz|$, which generates the airfoil corresponding to $q = q_0(\omega)$ (assuming q_0 satisfies the constraints).

It is also obvious that an integration of Eq. (22) around the perimeter of the circle yields

$$\int_0^{2\pi} q_0(\omega) d\omega = 2\pi q_\infty. \quad (24)$$

This means that the average speed on the surface of the circle must be equal to the free-stream speed, a conclusion that could have been made from Eq. (16) also. This interpretation of the first constraint was used by McFadden²¹ in the formulation of his airfoil design procedure.

At this point the reader should be reminded from the discussion in Section 2 that a proper speed distribution for an airfoil should contain at least one zero corresponding to the leading edge stagnation point, and two zeroes if the trailing edge is not cusped. A result of Eq. (23) is that a design procedure utilizing the circle plane must ensure that the zeroes of q match the zeroes of the flow over the circle if the metric is to be free of singularities, with the possible exception of the trailing edge.

The stagnation, or branch, points of the prescribed flow must necessarily be at specific locations on the circle. It can be shown that requiring that the branch points be on the circle forces the first constraint to be satisfied. In fact, as with q in Eq. (21), Eq. (22) can be factored into

$$q_0(\omega) = c_0 \left(1 - \frac{1}{\zeta^2} \right) \left[1 - \sum_{n=1}^N c'_n e^{-in\omega} \right].$$

For simplicity, the expression in brackets will be called h . As before, this represents a mapping of the flow. The other factors,

$$c_1 = c_0 \left(1 - \frac{1}{\zeta^2} \right)$$

can be interpreted as the flow over a circle imbedded in a stationary fluid and moving in the negative x direction with a speed equal to c_0 . Adding to this a free stream moving in the positive x direction with a speed equal to $(q_\infty - c_0)$ gives the velocity field

$$q_2 = q_\infty - \frac{c_0}{\zeta^2}. \quad (25)$$

This represents the flow over a unit circle moving with a speed equal to c_0 in the negative x direction within a stream moving at a speed equal to q_∞ in the opposite direction. The speed of this flow in the far field is q_∞ , naturally. On the unit circle it is

$$q_s = \left[\frac{1}{h} q_o(\omega) + (q_\infty - c_o) \right]. \quad (26)$$

If $q_\infty = c_o$, the speed on the circle is exactly the prescribed speed. Moreover, the stagnation points of the flow are exactly on the circle, since setting $q_2 = 0$ in Eq. (25) gives

$$\zeta^2 = \frac{c_o}{q_\infty} = 1. \quad (27)$$

Analogously, requiring that the stagnation points be on the circle ($\zeta=1$) means that $c_o = q_\infty$, and, again, the speed on the circle is the prescribed speed. The requirement that the branch points of the flow must be on the circle boundary is equivalent to the requirement that the first constraint expressed in Eq. (16) be satisfied. Either condition can be used in a design procedure to find the value of the appropriate free parameter in Eq. (17) reflecting this requirement.

The equivalency of the two conditions was proved numerically by Volpe and Melnik.¹⁴ They described a procedure to generate an airfoil corresponding to a given speed distribution by successive modifications of an initial airfoil profile. In the procedure, which is valid at compressible speeds, the initial profile is mapped into a circle, and the flow around the circle is solved subject to the boundary conditions that the tangential speed on the circle be the required value. Since this is a Dirichlet problem, the normal speed on the circle boundary is not necessarily zero. It would be if the airfoil contour were exactly the required airfoil. The normal velocity component is used to modify the initial contour and the process is repeated. The procedure converges rapidly in the sense that the computed normal velocity component goes to zero quite fast, and the modifications to the airfoil contour become progressively smaller. In their test, Volpe and Melnik took the speed distribution, $f(s)$, computed on a Korn airfoil at $M_\infty = 0.100$ and an angle of attack of 1.7° (see Fig. 12 for the corresponding pressure distribution) and multiplied it by an arbitrary factor, p . They then

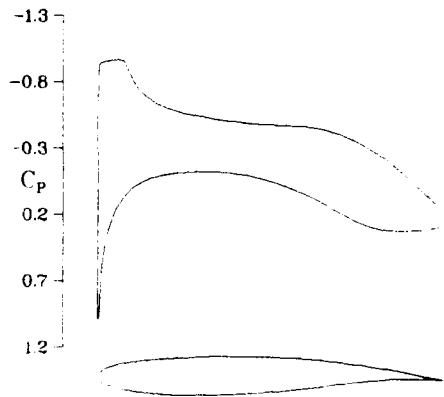


Fig. 12 Pressure distribution on Korn airfoil;
 $M_\infty = 0.100, \alpha = 1.7^\circ, C_L = 0.5262,$
 $C_D = 0.0001$

requested the numerical procedure to generate the airfoil corresponding to this scaled distribution. A one degree of freedom was introduced in the form of a scaling factor, p_1 . Thus, Eq. (17) was given the specific form

$$\frac{q_2}{q_\infty} = p_1 [p f(s)]. \quad (28)$$

Since $f(s)$ was computed for a closed airfoil, the distribution in Eq. (28) satisfies the other two constraints automatically and, as a result, p_2 and p_3 can be set to zero. An application of the integral relation expressed in Eq. (16) quickly reveals that an airfoil solution can exist only if $p_1 p = 1$. Of course, the resulting airfoil is in each case the Korn airfoil. The scheme used by Volpe and Melnik found a value for p_1 using the condition that the normal velocity component vanish at the leading edge point where the tangential velocity is prescribed to be zero. In other words, the stagnation points of the flow are forced to be on the circle boundary. (The introduction of a mass flow term is used in the procedure to force the trailing edge stagnation point to be on the circle.) In the numerical scheme, regardless of the initial value of p , the resulting value found for p_1 was such that their product was unity, as required by the integral relation. This is shown in Fig. 13. The total scaling of the speed distribution ($p_1 p$) is driven toward one very quickly. Here, flow field sweeps mean the number of iterations required by the procedure to compute the flow field over the initial airfoil contour, and design cycles indicate the number of airfoil updates.

The advantage of using the stagnation point condition over the integral relation to enforce the first constraint lies in the fact that the former can in principle

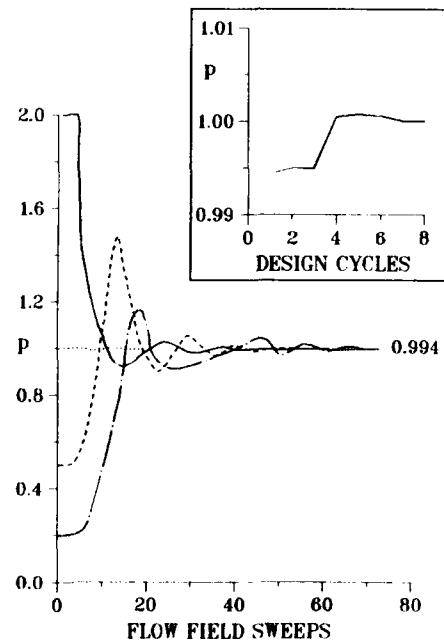


Fig. 13 Convergence history of scale factor for Korn airfoil design; $M_\infty = 0.100$

be used at transonic speeds, as it was, in fact, done in Ref. 22. It is worth mentioning again that this constraint arises from the imposition of a value for the free stream. If this were to be left free, the constraint apparently disappears. In reality, it does not. The removal of the need for a p_1 in Eq. (17) is obtained at the cost of making q_∞ a free parameter; p_1 has now really become q_∞ . In incompressible flow, the value of q_∞ is found by an application of the integral constraint, and it can be found, for compressible flows, by applying the stagnation point condition. Letting q_∞ float is equivalent to introducing the parameters p_1 in the form of a scaling factor as in Eq. (28). In this expression, whether q_∞ is fixed and p_1 is free to float, or vice versa, the ratio (q_0/q_∞), which is the quantity of interest, is the same. As a final point, it must be noted that if a speed distribution does not satisfy the first constraint, the incompatibility between the surface speed and the free stream renders the flow mathematically impossible, and no airfoil solution, no matter how unrealistic a shape it may have, is possible. Failure to satisfy the trailing edge constraints, however, does not preclude a solution, but the resulting shape may be unrealistic or unacceptable.

7. SENSITIVITIES OF GEOMETRIC CHARACTERISTICS TO PRESCRIBED SURFACE DISTRIBUTIONS

Families of airfoils have been designed by various authors by varying some parameters that characterize an otherwise similar surface speed distribution to examine the effect on the parameter on the resulting geometrical contour. In some cases, the pressure distributions were chosen and the airfoils were designed with the purpose of achieving certain lift and drag characteristics. These results can be used to perform sensitivity studies.

Nonweiler⁸ designed a series of low drag airfoils using Lighthill's procedure. The prescribed pressure distributions were systematically altered, and the differences in the resulting shapes can be observed. In Fig. 14, two airfoils designed to distributions that differ basically in the trailing edge region are shown. As a result of the differences in the imposed pressures, the trailing edge angle of the resulting airfoils increases with increased local loading. Slight differences in the distributions in the leading edge region generate airfoils of dramatically different leading edge radii and thickness, as can be seen in Fig. 15. The effect of

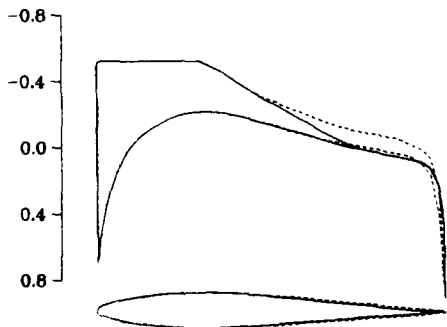


Fig. 14 Effect of pressure distribution near trailing edge on airfoil shape; incompressible flow; $C_L = 0.24$

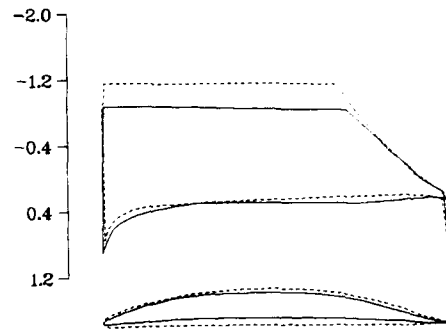


Fig. 15 Effect of pressure distribution near leading edge on airfoil shape; incompressible flow; solid line: $C_L = 1.07$; dashed line: $C_L = 1.05$

extending the region of favorable pressure gradients on the upper surface is depicted in Fig. 16. It should be noted that enforcement of the constraints alters the ideally prescribed distributions. As a result, the modified imposed pressure distributions for which the airfoils are found differ by more than the changes that would be expected by the single parametric change. This is true for all such studies regardless of the particular procedure to generate the contours. The additional differences in the pressure distributions depend on the particular functional form chosen for Eq. (17).

Liebeck⁹ also performed studies which examined the relationships between airfoil shapes and imposed pressure distributions. As mentioned earlier, Liebeck concentrated on formulating the optimal shape for a velocity distribution with which boundary layer could be controlled (e.g., transition location could be delayed, flow separation avoided) in addition to maximizing the lift. The general appearance of the Liebeck velocity distribution is depicted in Fig. 9. The extent of the rooftop region and, as a result, that of the Stratford recovery region depend on the level of the rooftop. In Fig. 17, various airfoils corresponding to different levels (e.g., maximum velocity) are depicted. The contours were computed using a numerical procedure due to

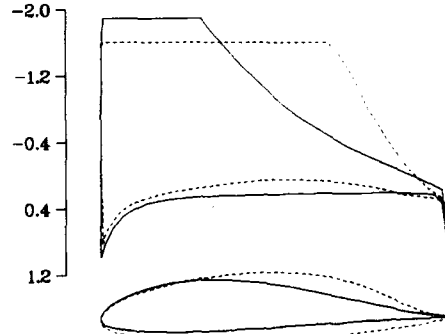


Fig. 16 Effect of extent of favorable upper surface pressure gradient on airfoil shape; solid line: $C_L = 1.28$; dashed line: $C_L = 1.22$; incompressible flow

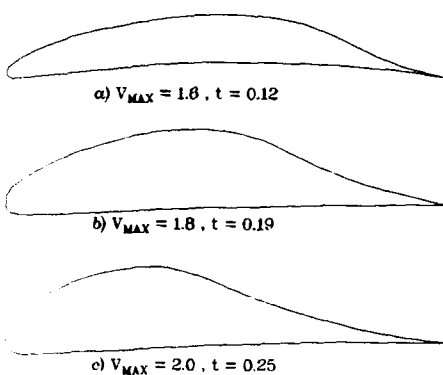


Fig. 17 Effect of maximum rooftop velocity on airfoil shape; incompressible flow

James.²³ The effect of increasing design lift on airfoil thickness is demonstrated in Fig. 18. In this example, laminar flow over the entire rooftop region was assumed in the prescription of the pressure distribution.

8. EFFECTS OF PRESCRIBED DISTRIBUTIONS ON CONSTRAINTS AT TRANSONIC SPEEDS

A study which indicates how Eq. (17) could be formulated at transonic velocities was performed by Volpe.²⁴ The study was done by designing airfoils to pressure distributions which were systematically changed. The numerical procedure was that described in Ref. 14. In the study, trailing edge closure was not enforced. As a result, the airfoils were generally open. Therefore, the designed airfoils present a view of the sensitivity of the trailing edge closure to particular characteristics in the pressure distribution and, also, give an indication of the changes in the latter needed to bring about closure. In the study, the parameter p_1 is identified with a floating value of q_{∞} , as discussed earlier. Thus, the effect of the pressure variations on q_{∞} can also be examined.

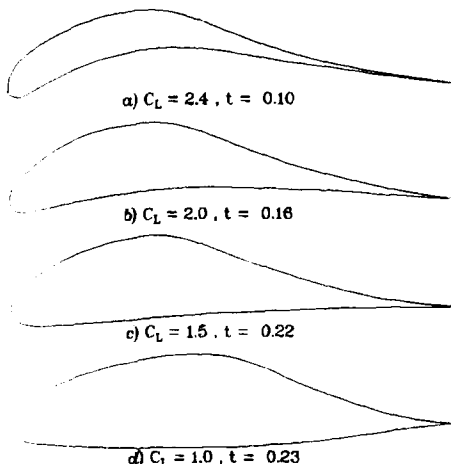


Fig. 18 Effect of design lift on airfoil shape; incompressible flow

The first example examines the sensitivity of the solution to changes in the target pressures in the forward portion of the lower surface, as shown in Fig. 19. In this figure, the pressures are plotted as a function of arc length, around a flat plate with a chord length equal to 0.5. The two pressure distributions are different only between 23% and 47% of the arc length. Otherwise they are identical, even in the stagnation point region. As in all the other examples that will be shown in this section, the angle of attack is chosen to be zero and the free stream Mach number is 0.800. The flow is thus supercritical on both the upper and lower

surfaces, as can be seen in Fig. 19 (C_p^* denotes the value of the critical pressure coefficient). The resulting airfoils corresponding to these two target distributions are shown in Fig. 20, along with the pressure distributions that are computed by a direct analysis of the contours. It should be pointed out that in each case, the result of the analysis is identical to the target for the inverse problem. The target distribution is scaled from the originally defined distribution because usually q_{∞} turns out to be some value other than one, as in this case. The abscissas of the results of the two cases are lined up in such a way that the lower surface trailing edge points coincide. The differences in pressure distributions are due to the very different scaling factors (q_{∞}) resulting for the two cases. The shapes of the original targets are both retained. The vertical gap size (Δy) is also dramatically different for the two examples, while only a slight difference in the horizontal gap is present. Note also the different chord lengths of the two airfoils.

The effect of changing the pressure distribution in the aft section of the lower surface can be seen for the cases shown in Fig. 21, whose results are shown in Fig. 22. Lowering the pressure coefficient in this area again increases q_{∞} substantially, causing the different levels in computed pressure. Δy is now greatly increased

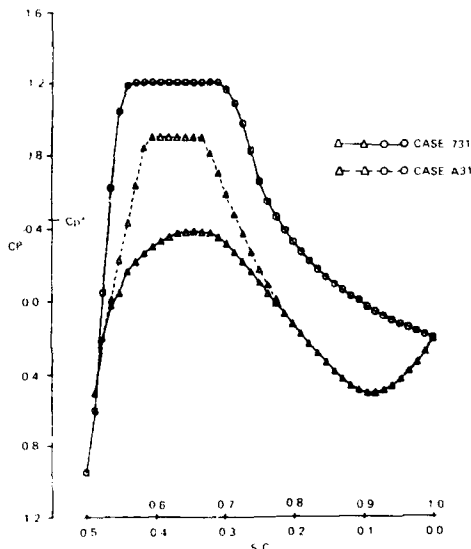


Fig. 19 Target pressure distributions to study effect of forward loading on design; cases 731, A31; $M_{\infty} = 0.800$

while the change in Δx is small. Figure 23 shows two velocity distributions near the stagnation point. Except for the difference shown in this region, they are otherwise identical and, in fact, correspond to the pressure distribution given as a dashed line in Fig. 19. The location of the stagnation point itself is unchanged. The solutions for these two cases are shown in Fig. 24.

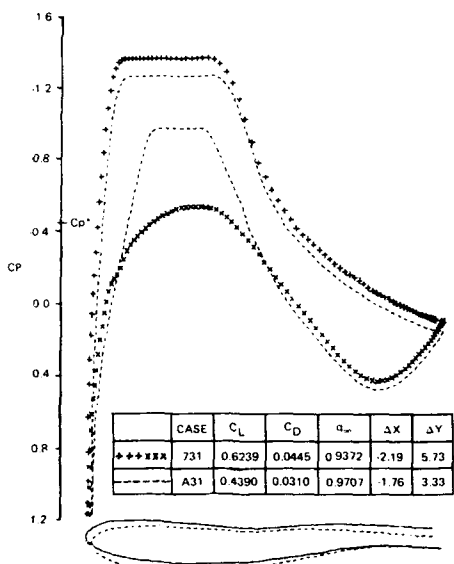


Fig. 20 Effect of forward loading:
designed airfoil contours and direct
solutions; cases 731, A31; $M_{\infty} = 0.800$

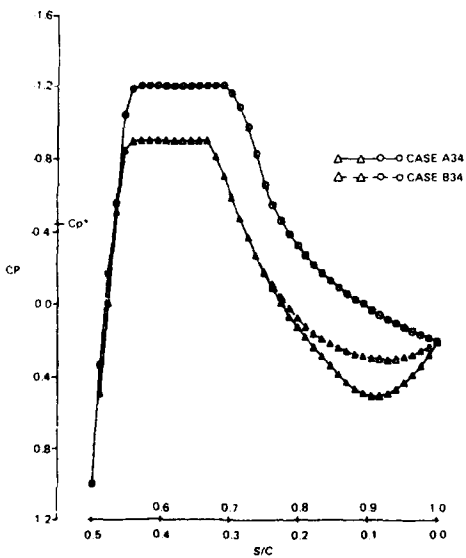


Fig. 21 Target pressure distribution to study
effect of aft loading on design; cases
A34, B34; $M_{\infty} = 0.800$

Finally, the effect of the location of the stagnation point on the solution is examined. The two speed distributions in Fig. 25 are identical except in a region extending approximately 5% on either side of the stagnation point. In fact the dashed line is only a lateral movement of the curve locally. As can be seen in Fig. 26, their corresponding solutions differ only minutely in q_{∞} and Δy , but substantially in Δx . In the pressure plot, the dashed pressure distribution represents the solution for the dashed airfoil which is drawn by making the lower surface trailing edge points line up with the corresponding points on the other airfoil. This accounts for the differences in the pressures seen on the upper surface. If the upper surface trailing edge points are made to coincide, such differences are reduced. The different chord lengths of the airfoils, which are the abscissas, account for the remaining differences.

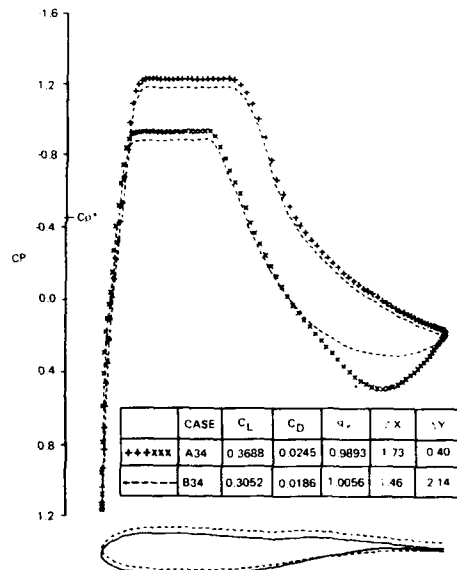


Fig. 22 Effect of aft loading:
designed airfoil contours and direct
solutions; cases A34, B34; $M_{\infty} = 0.800$

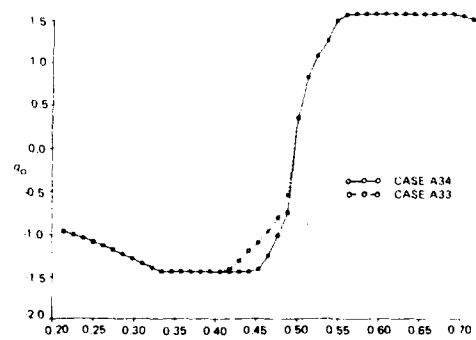


Fig. 23 Target speed distribution to study effect
of stagnation point region on design;
cases A34, A33; $M_{\infty} = 0.800$

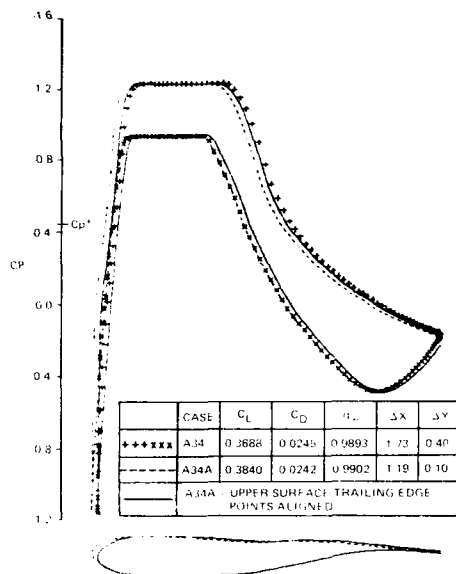


Fig. 24 Effect of stagnation point location:
designed airfoil contours and direct
solutions; cases A34, A34A; $M_{\infty} = 0.800$

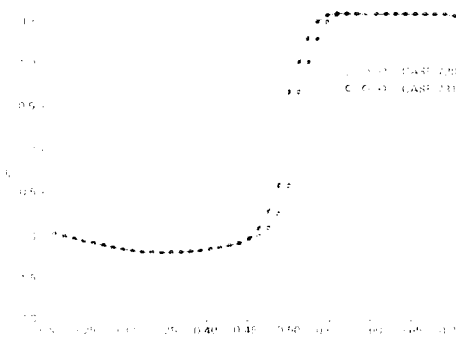


Fig. 25 Target speed distribution to study effect
of stagnation point location on design;
cases 728, 731; $M_{\infty} = 0.800$

In designing airfoils to prescribed pressure distributions, the contour generated is highly dependent on the particular form assumed for Eq. (17) if the ideal distribution (the one for which p_1 , p_2 and p_3 in Eq. (17) vanish). The results of studies such as this, as well as those of Liebeck, Nonweiler and others, can be used as a guide to select proper ways of altering the ideal distribution in order to satisfy the constraints.

9. CONCLUDING REMARKS

In three dimensions, the problems associated with designing a physically acceptable structure are magnified. The earlier discussion associated with the 2-D airfoil is pertinent to the cross section of the wing at any station along its span. In addition, the several cross

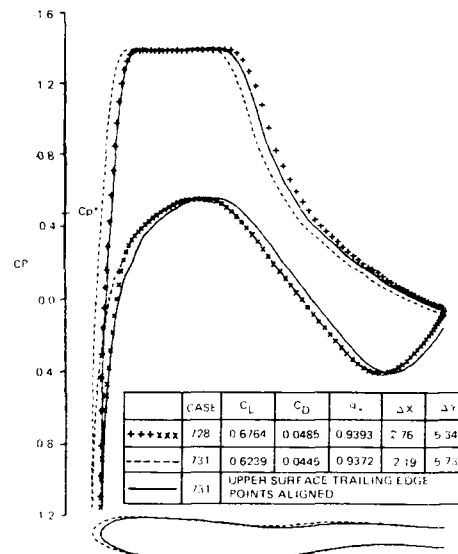


Fig. 26 Effect of stagnation point location:
designed airfoil contours and direct
solutions; cases 728, 731; $M_{\infty} = 0.800$

sections must "blend" into each other. Therefore, the sections' chord lines have to adhere to a specific distribution, which is at least piecewise continuous. The spanwise thickness distribution and the location of the point of maximum thickness are also required to vary continuously and -- in most cases -- monotonically. The wing should also close at the tip, of course. These physical requirements translate into restrictions on the pressure distribution to be specified on the wing.

It is safe to assume that a constraint expressing a compatibility condition between some average of the surface speed and the free stream exists. It should be possible to express such a constraint in closed form for incompressible flows. It is yet to be determined if any analytical relationships between imposed pressures and wing geometry exist in three dimensions. It is not clear if even a general description of such relationships is possible. Because of this difficulty, 3-D wing design at present is limited to the re-design of certain portions of it. This particular re-design usually involves the use of 2-D surface modification techniques applied in each of the cross sections in question. The imposed target speed distributions are perturbations of the flow computed over the wing to be modified using an appropriate 3-D analysis program. A designer must interact with the design procedure in order to guarantee an acceptable shape.

The existence of the various restrictions on geometry and the associated constraints on the imposed pressure distributions have made airfoil design an interesting and fertile field of research. Because of the practical implications, the field of 3-D wing design is just as rewarding. Because of the inherent difficulties of the problem, it is unlikely that the above-mentioned user-interactive procedure for design will ever be supplanted. Probably, it is not even desirable. Progress in understanding the relationships between 3-D wing flow characteristics and geometric features will contribute substantially to the development of numerical tools to be used in the design procedure.

10. REFERENCES

1. Jacobs, Eastman N., "Preliminary Report on Laminar Flow Airfoils and New Methods Adopted for Airfoil and Boundary-layer Investigations," NACA ACR, June 1939 (Wartime Rept. No. L-345).
2. Abbot, Ira H., von Doenhoff, Albert E., and Stivers, Louis S., "Summary of Airfoil Data" NACA Rept. No. 824, 1945.
3. Theodorsen, Theodore, and Garrick, I.E., "General Potential Theory of Arbitrary Wing Sections," NACA Rept. No. 452, 1933.
4. Mangler, W., "Die Berechnung eines Tragflügelprofiles mit Vorgeschrriebener Druckverteilung," Jahrbuch der Deutschen Luftfahrtforschung, Vol. 1, 1938, pp. 46-53.
5. Lighthill, M.J., "A New Method of Two-Dimensional Aerodynamic Design," R&M 2112, Aeronautical Research Council, London, England, 1945.
7. Woods, L.C., "Aerofoil Design in Two-Dimensional Subsonic Compressible Flow," R&M 2845, Aeronautical Research Council, London, England, March 1952.
8. Nonweiler, T., "A New Series of Low Drag Aerofoils," Rept. 6801, University of Glasgow, Dept. of Aeronautics and Fluid Mechanics, March 1968.
9. Liebeck, R.H., "On the Design of Subsonic Airfoils for High Lift," AIAA Paper 76-406, July 1976.
10. Van Ingen, J.L., "A Program for Airfoil Section Design Utilizing Computer Graphics," Agard Short Course Notes, 1969.
11. Arlinger, B., "An Exact Method of Two-Dimensional Airfoil Design," TN67, Saab, Sweden, 1970.
12. Strand, T., "Exact Method of Designing Airfoils with Given Velocity Distribution in Incompressible Flow," *J. Aircraft*, Vol. 10, 1973, pp. 651-659.
13. Polito, L., "Un Metodo Esatto per il Progetto di Profili Alari in Corrente Incompressibile Aventi un Prestabilito Andamento della Velocita sul Contorno," Universita degli Studi di Pisa, Italy, Rept. 42, 1974.
14. Volpe, G. and Melnik, R.E., "The Role of Constraints in the Inverse Design Problem for Transonic Airfoils," AIAA Paper 81-1233, 1981.
15. Stratford, B.S., "The Prediction of Separation of the Turbulent Boundary Layer," *J. Fluid Mech.*, Vol. 5, 1959.
16. Stratford, B.S., "An Experimental Flow with Zero Skin Friction Throughout Its Region of Pressure Rise," *J. Fluid Mech.*, Vol. 5, 1959.
17. Pfenninger, W., Viken, J.K., Vemuru, C.S., and Volpe, G., "All Laminar SC LFC Airfoils with Natural Laminar Flow in the Region of the Main Wing Structure," AIAA Paper 86-2625, 1986.
18. Pfenninger, W. and Vemuru, C.S., "Design of Low Reynolds Number Airfoils-1," AIAA Paper No. 88-2572, June 1988.
19. Jameson, A., "Acceleration of Transonic Potential Flow Calculations on Arbitrary Meshes by the Multiple Grid Method," AIAA Paper 79-1458, 1979.
20. Thwaites, B., Incompressible Aerodynamics, Oxford University Press, 1960.
21. McFadden, G.N., "An Artificial Viscosity Method for the Design of Supercritical Airfoils," Research and Development Report C00-3077-158, Courant Inst. Math. Sci., New York University, July 1979.
22. Volpe, G. and Melnik, R.E., "Method for Designing Closed Airfoils for Arbitrary Supercritical Speed Distributions," *J. Aircraft*, pp. 775-782, Oct. 1986.
23. James, R.M., "A New Look at Two-Dimensional Incompressible Airfoil Theory," Rept. No. MDC J0918/01, Douglas Aircraft Co., Long Beach, CA, 1971.
24. Volpe, G., "The Inverse Design of Closed Airfoils in Transonic Flow," AIAA Paper 83-504, 1983.

TRANSonic SHOCK FREE WING DESIGN

G. Volpe
Senior Staff Scientist
Grumman Corporate Research Center
Mail Stop A08-35
Bethpage, New York 11714
U.S.A.

SUMMARY

The problem of constructing wing profiles that yield specified pressure distributions and/or performance characteristics is discussed. A practical solution to the problem, which consists of a physically acceptable profile, exist only if certain constraints are satisfied by the prescribed characteristics and by the profile itself. These constraints are addressed in various manners by the several methodologies that have been proposed. The various approaches are discussed along with the relative advantages and disadvantages of each. The inverse approach is considered in detail to provide a link to the classical incompressible design problem and to establish a raison d'être for the other methodologies.

1. INTRODUCTION

The design of wings and wing sections is a problem of considerable interest not only to the aerodynamic configuration engineer but also to the developer of methods for achieving such designs. The reasons are obvious. The aerodynamic and economic efficiencies of an aircraft are highly dependent on the layout of the wing and the shape of its profile. The best possible aircraft (whether commercial or military) is the one that meets its design goals in an optimal manner (assuming one has established a definition for optimality). The degree to which a design team will come to obtaining the best possible configuration for a given set of design parameters (e.g., range, speed, volume) is, of course, a function of the skills of its members and the theoretical tools they have available. The time constraint plays a major role in the design cycle, also. Missing the best gives rise to inferior performance which can be translated into lower cruise speeds, decreased range, insufficient carrying capacity, etc. The penalties involved in missing the best design have always been well known facts. As aircraft started operating routinely in the transonic range the penalties became larger because of the deleterious effects of the shock waves on the flow field around the aircraft. As a consequence, the avoidance of these penalties has a bigger payoff for supercritical designs. It is a small wonder, then, that a lot of effort has gone, and is still being put, into the development of techniques for designing shockless wings.

The design of a wing begins with the selection of its section profile (or profiles). Some deformation of the two-dimensional section may occur in the course of performing the three dimensional design, but this first step is currently indispensable. Tailoring of the airfoil profile to the specific requirements of the wing as opposed to selecting one from a stockpile may be highly desirable. This paper will be mainly concerned with airfoil design, since theoretical tools are most highly developed for such a problem. In addition at present, such tools are the most easily portable, because three-dimensional methods, in large, reflect the design philosophy of the developer.

The various algorithms available for the design of airfoil sections can be placed in one of several classes of methodologies. Whereas in the case of subcritical flows all methods developed for that purpose could be categorized as inverse methods, a number of "alternate" methods have been developed for transonic flows because of the difficulty of extending the incompressible flow approach to the supercritical regime. Some of these alternate methodologies demonstrated certain advantages over the original inverse technique. In practice, defining a section for a particular application entails the use of various methods. In an inverse-type method of airfoil design, the speed -- or, equivalently, pressure -- distribution (throughout the paper both terms will be used and they will be interchangeable) one desires on the surface of the profile is specified along with the magnitude and direction of the free stream. Mangler¹ and Lighthill² discussed this "inverse" problem of airfoil theory for the case of incompressible flow and proposed various analytical solutions. Their methodology was refined and adapted for application on large and small computers by successive researchers.³⁻⁷ However, the difficulty in extending the methodology developed for incompressible flow to the transonic regime eventually gave rise to a number of alternate methods. In a pure inverse-type method of airfoil design -- such as those of Mangler and Lighthill -- the speed (or pressure) distributions desired on the surface of the profile are specified along with the magnitude and direction of the free stream. In contrast to the direct problem in which the shape of the airfoil profile is specified and the surface speed is computed through a solution of a Neumann-type problem, the inverse problem does not necessarily have a solution. A solution to the inverse problem exists only if a certain constraint between the free-stream speed and the surface speed is satisfied. In incompressible flow, which can be described by Laplace's equation, this can easily be shown and the constraint can be expressed in closed form. If, in addition, it is required that the airfoil profile be closed (or have a particular trailing edge thickness), two additional constraints appear. They can also be expressed in closed form for incompressible flow. The existence of these constraints has been known since the work of Mangler and Lighthill, and Woods has extended the analysis to subcritical compressible flows of a Karman-Tsien-type gas. The work of these authors indicated that a specified surface speed distribution had to be altered in such a manner as to satisfy the three constraints in order to guarantee a solution. In their methods, as in the refinements that followed,⁴⁻⁷ the approach was to prescribe the surface speed distributions with three free parameters whose values were to be adjusted to satisfy the three constraints.

The formulation of an inverse method at supercritical speeds has been problematic because of the lack of closed-form expressions for the three constraints. The existence of constraints for the transonic design problem was intuitively true because the incompressible design problem was a subset of the

more general compressible problem. The lack of a clear understanding of the nature of the first constraint was the main source of the difficulties. A formulation of the inverse problem for transonic speeds was finally given by Volpe and Melnik,^{8,9} who devised a numerical procedure to guarantee satisfaction of the three constraints. The procedure is based on the discovery that the first constraint would be satisfied if the branch points of the flow were enforced to be on the airfoil.

An obvious advantage of inverse methods is the control the designer has over the force characteristics of the airfoil profile and over the boundary layer development on its surface, a control gained through the pressure (speed) distribution that is specified. This control can still be retained when making the changes that might be necessary to satisfy the constraints. The introduction of the three free parameters can be arranged such that an "ideal" speed distribution is modified only over selected segments of the airfoil surface. Desired characteristics of a speed distribution (e.g., "rooftops," Stratford-type pressure recovery, rear or front loading) can be retained with little or no modifications. Indeed, the satisfaction of three constraints does not necessarily guarantee a realistic airfoil. Re-entrant shapes, where the upper and lower surfaces cross before the trailing edge, are not ruled out by this formulation. However, additional parameters could be introduced in an inverse design procedure to prevent this from occurring.

The problems created by the constraints can be avoided by the use of so-called indirect methods of design, such as those of Hicks et al.,¹⁰ Davis,¹¹ McFadden¹² and others. In these methods the solutions (pressure and/or force characteristics) for the flow over some arbitrary initial airfoil contour are compared with a desired set of values for the pressure distribution or forces. The differences between the "target" and "current" characteristics are used in some rational way to modify the airfoil profile in the hope of reducing these differences. The process obviously has to be iterated. One advantage of such methods is that a realistic airfoil profile is always obtained at every step of the iteration. The biggest disadvantage, however, is the lack of a guarantee that the iteration will converge with the differences between computed and target values reduced to arbitrarily small levels. The question of the existence of an airfoil solution for a particular "target" pressure distribution is skirted in these methods and, in fact, they will not converge for arbitrarily prescribed pressure distributions that do not satisfy the three constraints. This approach to airfoil design is best suited to applications where the target pressure distribution is a "small" modification of the one computed over the initial profile.

Another approach pioneered by Sobieczky¹³ is built around the concept of the fictitious gas in regions of supercritical flow. This approach is ideally suited to the redesign of an existing contour in a way that the new contour will have shock-free flow. This technique is much easier to implement than hodograph methods for the design of shock-free airfoils such as those of Garabedian and Korn (see Ref. 14) and Boerstoel,¹⁵ whose mathematical elegance is unfortunately offset by the need of a highly-skilled user. In neither of these classes of methods does the user have control of the pressure distribution. Such control can be exercised only with an inverse method.

The implementation of an inverse, or even an indirect, method of design involves the all-important task of defining the pressure distribution. This is not impossible (see Ref. 16 and 17, for example). In

addition, in many applications one can use the distribution over a known profile as a baseline on which desired characteristics are injected. This "modification" approach to the definition of surface characteristics is one of the major reasons for the practical success of indirect methods. The definition of a surface speed distribution can be avoided entirely if the differences in some other parameters -- such as lift, drag, maximum thickness and combinations thereof -- are used as drivers of the design process. In fact, by assigning appropriate weighting factors to the various parameters being taken into account some optimal configuration could be attained. This is the idea underlying the method described by Hicks et al.,¹⁸ in which optimization techniques are the vehicles for performing the design. In a similar vein Jameson¹⁹ has used control theory as the vehicle for the design.

Optimization techniques can be used to generate designs that satisfy multiple design points. A shortcoming of inverse and many indirect methods is the fact that the resulting shapes are "point" designs, whose off-design performance may be unsatisfactory. At times, this shortcoming is of little consequence. For example, a transport aircraft which spends most of its time at a prescribed speed and altitude is essentially a point design. If better off-design performance is desired, however, it could be attained (at the expense of trading away some of the best at the design point) by defining additional design points with associated weighting factors in the optimization process. It should be realized, however, that such a design exercise becomes progressively longer and more difficult as the number of design parameters grows. Such an approach, while possible in principle, may be unrealistic in practice. The use of an optimization technique used to refine a design obtained by an inverse technique might offer the most efficient solution in such a case.

The paper will discuss at some length an inverse approach to transonic airfoil design because of its roots in the classical incompressible problem, and because it is the technique by which desired flow characteristics can be attained most closely. It will be followed by some discussion of indirect methods and optimization techniques.

2. THE INVERSE DESIGN PROBLEM FORMULATION

The problem that will be addressed now is the construction of the airfoil profile, which has a surface speed distribution, q_s , equal to some desired function, F , everywhere along its arc length, s . This is to be measured clockwise around the airfoil contour starting at the lower surface trailing edge point. The airfoil's coordinates, x, y , can be parameterized as functions of s . A feature of practical airfoil contours is that the trailing edge be either closed or have a very small gap. Thus, a requirement on the to-be-determined airfoil is that the upper and lower surface trailing edge points be separated by prescribed distances Δx and Δy . The horizontal gap, Δx , is usually set to zero, while the vertical gap, Δy , is set to zero (a closed airfoil) or to a small positive number. The free stream is also defined by prescribing values for the free-stream velocity q_∞ , temperature, and pressure (or density). These, in turn, determine the free-stream Mach number, M_∞ . In incompressible flow, of course, it is only necessary to specify the velocity in order to identify the free stream uniquely. It is to be reminded that speed and pressure distributions will be used interchangeably. Formally,

then, the problem is to determine the airfoil profile of a specified trailing edge thickness corresponding to the speed distribution

$$\frac{q_0}{q_\infty} = F(s/s_{\max}) \quad (1)$$

Without loss of generality, s_{\max} can be set equal to one; q_0 is taken as positive in the clockwise direction around the airfoil.

As shown by Mangler¹ and Lighthill² for incompressible flow and by Volpe and Melnik³ for supercritical flows the problem, as stated, does not have a solution unless the function $F(s/s_{\max})$ satisfies three constraints. Volpe²⁰ discusses these constraints in some detail. The constraints are due to requirements that, at the trailing edge, Δx and Δy have specified values and, that the specified surface flow be compatible with the flow in the far field where it approaches a uniform free stream plus a circulatory component, as discussed by Ludford.²¹ In incompressible flow, these three constraints can be expressed in closed form. Unfortunately, this is not possible at transonic speeds.

As a consequence of the constraints, an airfoil solution will be found only if F contains three free parameters. The most general speed distribution that can be specified is, therefore,

$$\frac{q_0}{q_\infty} = F(s; p_1, p_2, p_3),$$

where p_1, p_2, p_3 are the three adjustable parameters whose values are to be found together with the airfoil contour. In this paper it will be assumed that the target speed is of the form

$$\frac{q_0}{q_\infty} = f_1(s; p_1) [f_0(s) + f_2(s; p_2) + f_3(s; p_3)] \quad (2)$$

where $f_0(s)$ represents the ideal target speed distribution that, in practice, is usually a tabulated function. The functions f_1, f_2 , and f_3 are introduced to modify the ideal target in order to satisfy the three constraints. In general, it is desirable to localize the effect of f_1, f_2 , and f_3 so that the resulting surface speed will be close to the ideal speed distribution, $f_0(s)$, over most of the airfoil surface. Since in transonic flow it is not possible to relate p_1, p_2 , and p_3 to the three constraints in closed form, a numerical search for the parameters must be made. The search is greatly facilitated by choosing f_1, f_2 , and f_3 in such a way that each significantly affects only one of the constraints. We would then have three one-dimensional searches for p_1, p_2 , and p_3 . In Ref. 22 the sensitivity of a designed airfoil contour to various changes in the speed distribution is reported. This and other studies (see Ref. 16 and 23, for example) can be used to define the forms for f_1, f_2 , and f_3 in Eq. 2. Three separate schemes will be described here.

Satisfaction of the first constraint is guaranteed by adjustment of p_1 . By definition, f_1 causes a scaling of surface speed (q_0/q_∞). In scheme 1, f_1 is set equal to p_1 . This results in a scaling that is uniform along the airfoil. In this case one could consider p_1 as a scaling on either q_0 or q_∞ . In the latter case, q_∞ is essentially floating, and it would be determined as part of the solution. As mentioned above, the value of p_1 is chosen to guarantee that the specified leading edge stagnation point will truly be a branch point of the flow.

Control over Δy , the vertical separation between the upper and lower surface trailing edge points, can be exercised by defining

$$f_2 = p_2 \sin\left(\frac{8}{3}\omega\right), \omega \leq \frac{3}{4}\pi \quad (3)$$

Outside this range f_2 is zero. Here, the ordinate is substituted for the ordinate ω in the computational plane for the arc length s . All airfoil flows can be mapped into flows about the unit circle. The ordinate ω (running from 0 to 2π), then identifies the length along the airfoil surface from the trailing edge point along the lower surface to the corresponding point on the upper surface. It is more convenient to use ω rather than s , and the formulation of the problem is not affected by this substitution. The function f_3 is the hardest to define. The horizontal separation between the two trailing edge points, Δx , is affected primarily by the location of the leading edge stagnation point. As shown in Ref. 22, a small shift in this stagnation point along the surface of the airfoil, on the order of 2% of the chord length, can alter the horizontal gap by 5-6%. It should be pointed out that a 2% shift in the stagnation point along the surface is hardly noticeable when viewed as a shift along the chord. In order to maintain loose coupling among p_1, p_2 , and p_3 , the shift must be accomplished without altering the local velocity gradients. This can be accomplished by shifting the functional dependence of q_0 on s locally, near the leading edge. Thus, one can define

$$f_3(s) = f_0(s') - f_0(s)$$

with

$$s' = s - p_3 h(s)$$

where

$$\begin{aligned} h(s) &= \frac{1}{2} \left[1 - \cos\left(\frac{\pi}{\Delta s}(s - s_T + 2\Delta s)\right) \right], s_T - 2\Delta s \leq s \leq s_T - \Delta s \\ &= 1, s_T - \Delta s \leq s \leq s_T + \Delta s \\ &= \frac{1}{2} \left[1 + \cos\left(\frac{\pi}{\Delta s}(s - s_T - \Delta s)\right) \right], s_T + \Delta s \leq s \leq s_T + 2\Delta s \end{aligned}$$

Elsewhere, $h(s)$ is zero. The point s_T denotes the location where $f_0(s)$ is zero in the leading edge region and Δs is some appropriate distance, typically 2.5% of

the total arc length. This form for f_3 shifts the leading edge stagnation point smoothly without introducing any "wiggles" in the target speed distribution and, in addition, has hardly any effect on the values of p_1 and p_2 . This form for f_3 is common to all the three schemes described here.

A second scheme for modifying the target distribution uses a different definition for f_2 in Eq. (2). The expression given in Eq. (3) alters the target speed distribution only on the lower surface of the airfoil. It would, therefore, be unsatisfactory if one were trying to design a symmetric airfoil. An alternative form for f_2 is

$$\begin{aligned} f_2 &= p_2 \left[1 - \frac{\omega}{\omega_1} \right] \quad , \quad \omega \leq \omega_1 \\ &= p_2 \left[\frac{2\pi - \omega}{\omega_1} - 1 \right] \quad , \quad \omega \geq 2\pi - \omega_1 \end{aligned} \quad (4)$$

This function alters the magnitude of the speed in the neighborhood of the trailing edge symmetrically. In this computational scheme, the speed takes on opposite signs on the upper and lower surfaces, accounting for the sign difference between the two parts of Eq. (4); ω_1 is typically taken as $\pi/3$. A third scheme can be formulated by substituting for $f_1 = p_1$ in scheme 1 the function

$$f_1 = \sqrt{1 + p_1 \sin^2 \left(\frac{\omega}{2} \right)}$$

which concentrates the scaling in the front half of the airfoil.

As discussed by Volpe,²⁰ the first constraint of the inverse airfoil design problem is a statement of compatibility between the prescribed surface speed and the prescribed free-stream speed. The constraint can be satisfied if the surface speed is prescribed with an adjustable parameter (p_1 in this case) or if q_∞ is allowed to float. If p_1 is introduced as a scaling parameter, as in schemes 1 and 2, one could interpret p_1 as being q_∞ and use the latter as the free parameter. q_∞ can at any time be scaled to any desired value without altering the formulation of the problem by simply scaling q_0 by an equal amount. This operation would leave the pertinent ratio, q_0/q_∞ , unchanged.

2.1 Airfoil Design Scheme

The shape of the airfoil which gives rise to the speed distribution represented by Eq. 2 can be obtained by iteratively modifying some initial contour, as shown by Volpe and Melnik.⁹ This initial contour need not be close to the sought-after profile for the iteration to converge. As described in Ref. 9, this initial contour is mapped into the unit circle by the unique conformal transformation

$$\frac{dz}{d\zeta} = \left[1 - \frac{1}{\zeta} \right]^{(1-\varepsilon)} e^{(P+iQ)} \quad (5)$$

where $z = x + iy$ and $\zeta = re^{i\omega}$ are the coordinates in the physical and mapped planes, respectively, and $\varepsilon\pi$ is the included trailing edge angle. This equation can be separated into its real and imaginary parts. Thus, on $r = 1$,

$$\frac{ds}{d\omega} = \left[2 \sin \frac{\omega}{2} \right]^{(1-\varepsilon)} e^P \quad (6)$$

$$\theta = \frac{1}{2} (1+\varepsilon) (\pi - \omega) - \frac{\pi}{2} + Q \quad (7)$$

where θ is the local slope of the airfoil. Q is the Fourier series

$$Q = \sum_{n=0}^N (A_n \sin n\omega - B_n \cos n\omega) \quad (8)$$

and P is its conjugate series. Because θ is known as a function of s , the coefficients of the series can be found by standard Fourier analysis as described in Ref. 4. With this mapping procedure, the leading terms of the series are related to the trailing edge gap ($\Delta x, \Delta y$) by

$$\begin{aligned} A_1 &= -\left(\frac{\Delta x}{2\pi}\right) \sin B_o - \left(\frac{\Delta y}{2\pi}\right) \cos B_o + (1-\varepsilon) \\ B_1 &= -\left(\frac{\Delta x}{2\pi}\right) \cos B_o - \left(\frac{\Delta y}{2\pi}\right) \sin B_o \end{aligned} \quad (9)$$

For convenience the infinite flow field around a unit circle can, in turn, be transformed into the finite region inside the circle. The modulus of the transformation of the physical plane, z , to the inside of the circle is then written as

$$H = \frac{1}{r^2} \left| \frac{dz}{d\zeta} \right|$$

In the inverse design problem $dz/d\zeta$ is, of course, the quantity to be found since it describes the transformation of the unknown airfoil profile into the circle. It should be recalled that the transformation is conformal everywhere except at the airfoil's trailing edge where the metric $h=|dz/d\zeta|$ vanishes.

The mapping of the airfoil into a circle simplifies the computation of the flow field around the contour. In an analysis problem, where the shape of the contour is given, q_∞ is usually set to unity and the flow is computed subject to the boundary conditions that the velocity component normal to the surface, v , be zero. For incompressible flow, which can be described by Laplace's equation, this solution can actually be expressed in closed form. For transonic flow, the solution must be determined numerically. Whether one assumes the potential equation or the Euler equations to be descriptive of the flow, the flow field can be computed by a number of numerical schemes. The schemes described by Jameson,^{24,25} for example, are widely used for these classes of computations.

Flow fields with no shocks, or only weak ones, (and inviscid, of course) can be described adequately

by the potential equation. In such a case the flow in the circle plane is described by the continuity equation

$$\frac{\partial}{\partial \omega} (\rho U) + r \frac{\partial}{\partial r} (\rho V) = 0 \quad (10)$$

U and V are the transformed circle plane velocity components in the r and ω directions, respectively. For irrotational flow they can be expressed as gradients of a potential function ϕ ; thus

$$U = \phi_{\omega}, \quad V = r \phi_r, \quad (11)$$

Using the energy equation the density ρ is evaluated from u and v , the velocity components in the physical plane. These are related to the components in the circle plane by

$$u = \frac{rU}{h}, \quad v = \frac{rV}{h} \quad (12)$$

Clearly the flow within the circle cannot be computed if h is not known; the assumed initial shape for the airfoil provides the initial estimate for h . In the limit of M_{∞} going to zero, Eq. (10) reduces to Laplace's equation.

The mapping introduces singularities at infinity, but they can be removed by subtracting from the potential its behavior in the far field. As discussed by Ludford,²¹ the solution in the far field is made up of a uniform stream plus a circulatory component. The potential functions describing these terms are known. Thus, one can define a reduced potential function.

$$G = \phi - q_{\infty} \left(r + \frac{1}{r} \right) \cos(\omega + \alpha) - E \tan^{-1} \left[\sqrt{(1 - M_{\infty})^2} \tan(\omega + \alpha) \right]$$

where α is the flow incidence and E is a circulation constant. This reduced potential is continuous and single valued everywhere.

At infinity ($r = 0$) $G = G_{\infty}$, a constant that can be set at zero in direct (Neumann) problems, but which must be determined as part of the solution in inverse (Dirichlet) problems by extrapolating from the interior of the flow field.

For the direct (analysis) problem, q_{∞} is usually set to unity and the boundary conditions demand that $v=0$ at the surface. The solution for the flow field is computed numerically by discretizing the flow field in conservation form along a polar coordinate mesh. The set of difference equations that approximates Eq. (10) is solved for the discrete values of the reduced potential, G , at the nodes of the computational mesh by an approximate factorization multigrid scheme similar to the one described by Jameson.²⁴ The value of the circulation constant, E , is determined from the Kutta condition, which requires that u be finite at the trailing edge. Since $h=0$ at the trailing edge, U must be made to vanish at this point. In this direct problem the surface speed $q_0(s)=u(s)$ is computed from the potential function G .

For the inverse design problem the boundary conditions at $r=1$ are imposed on u rather than v . Using the known functional relation between s and ω for the current contour, the target speed distribution q_0 can then be expressed as a function of ω . Then, at the boundary in the circle plane one can set $u_0=u(\omega)$ equal to $q_0(s(\omega))$. Of course, this would be true if h were the true mapping metric; in general, it is not. Hence, the boundary is not necessarily a streamline of the flow. In other words, v is not necessarily zero at the boundary. The flow field is computed subject to the boundary condition $u_0=q_0(s(\omega))$ at $r=1$ by a numerical scheme identical to the one used for the direct problem. The Dirichlet boundary conditions are implemented by integrating q_0 around the airfoil to find the reduced potential G at the boundary points. A constant of integration G_0 can be prescribed arbitrarily. The numerical problem that has boundaries at both $r=0$ and $r=1$ is well posed since the value at the inner boundary, G_{∞} , is determined as part of the solution. The circulation constant is determined by integrating u_0 around the full boundary. In general, in the Dirichlet problem there is a net mass flow emitted from the boundary. To allow for this, a source term $\sigma \log r$ is subtracted from the potential leading to a new reduced potential, \bar{G} defined by

$$G = \bar{G} - \sigma \log r$$

The far-field boundary condition will then have the additional term

$$\frac{\sigma}{2} \log [1 - M_{\infty}^2 \sin^2(\omega + \alpha)]$$

In this Dirichlet problem the normal velocity component, V , computed on the circle boundary will not be zero, in general. There is also no guarantee, at this point, that an airfoil-like shape corresponding to $q_0(\omega)$ exists. The above mentioned constraints on $F(s)$ have not been satisfied. The constraints are satisfied by adjusting p_1 , p_2 , and p_3 in Eq. 2. Two of the parameters, p_2 and p_3 , can be reset by monitoring the trailing edge gap values, Δx and Δy . p_1 is reset by monitoring the value of q_{∞} . As shown in Ref. 8 and 20 the first constraint can be satisfied if the branch points of the flow are forced to be on the circle itself. This can be accomplished if V can be made to vanish at points where U vanishes. U is zero at the leading edge stagnation point where q_0 is zero, and at the trailing edge where the metric, h , and possibly, q_0 , are zero. V can be set to zero at these two points by adjusting two parameters. One parameter is the source flow term, σ , which has a role similar to that of the circulation term from the Neumann problem. The other parameter is q_{∞} , the free-stream speed. As discussed earlier this can be allowed to float to satisfy the first constraint. It can be returned to its original value by subsequently adjusting p_1 .

Because of the definition of the reduced potential V is directly proportional to σ and to $-q_{\infty} \cos(\omega + \alpha)$. New values of σ and q_{∞} can then be found by solving simultaneously two equations of the type

$$\Delta q_{\infty} \cos(\omega_i + \alpha) - \Delta \sigma = V_i$$

where ω_i are the two branch points where $U=0$ and V_i are the computed values of the normal velocity components. The corrections $\Delta q_{\infty} = q_{\infty,new} - q_{\infty,old}$ and $\Delta \sigma = \sigma_{new} - \sigma_{old}$ are the values that are required to drive $V_{1,2}$ to zero.

2.2 Contour Modification

The solution to the Dirichlet problem, in general, will give a non-zero normal velocity at the circle boundary except at the enforced branch points.

A non-zero normal velocity V implies that the actual streamline is (to first order) rotated from the boundary by an angle of magnitude

$$\delta\theta = \tan^{-1}\left(\frac{V}{U}\right) \quad (13)$$

This equation is used to modify the initial slope distribution expressed by Eq. 7. New Fourier series for

Q and P can then be computed, as well as a new $\frac{ds}{d\omega}$, from Eq. 6, and finally

$$\frac{dx}{d\omega} = -\frac{ds}{d\omega} \cos \theta, \quad \frac{dy}{d\omega} = -\frac{ds}{d\omega} \sin \theta$$

The actual ordinates of the new airfoil contour are then obtained by integration. This new airfoil provides a new approximation for the metric h and a new relation $s(\omega)$, which are needed to set up a new Dirichlet problem in the circle plane. This process can be repeated until a desired tolerance in the maximum value of V/U is reached. It should be noted that the ratio expressed in Eq. 13 is finite at all times since $V=0$ where $U=0$.

2.3 Iteration Procedure

The procedure for iteratively modifying some initial airfoil into the shape that generates the surface speed distribution expressed by Eq. 2 can be made to converge regardless of the assumed initial shape by under-relaxing the changes suggested by Eq. 13. The values of p_1 , p_2 , and p_3 are found as part of the solution. A convergent iteration process is described as follows. A Dirichlet problem for the flow inside the circle is set up using the metric of the initial assumed contour, and, as boundary condition the requirement that the tangential velocity u be equal to the total speed distribution, q_{∞} . (This is actually true only at convergence.) The Dirichlet problem is solved numerically through sequential sweeps of the flow field computational mesh, as in the technique described in Ref. 24.

At the end of every sweep of the flow field, q_{∞} and σ are determined by forcing v to be zero both at the leading edge point where u is zero and at the trailing edge. The factor p_1 is then adjusted to scale q_{∞} back to its specified value, and the flow field is swept again.

The value of the normal component of velocity at the leading edge stagnation point, v , goes to zero quite fast (due to the continuous resetting of p_1). When v is below a given tolerance (typically 10^{-5} - 10^{-6}), estimates are made of the values that A_1 and B_1 , the first-order terms of the series in Eq. (8), would have if the airfoil were modified at that stage. These values are compared with the values they should have for the airfoil to have the desired trailing edge gap dimensions, as given by Eq. (9). The differences between the current and desired values, δA_1 and δB_1 , are then used to change p_2 and p_3 , respectively. The change in p_2 is made proportional to δA_1 , and the change in p_3 is proportional to $(-\delta B_1)$. Since p_1 is introduced as a multiplier, a change in the surface boundary conditions due to a new p_1 can be transmitted through the entire flow field by scaling the entire potential field. Using this procedure p_1 can be updated after each multigrid sweep of the flow field without seriously affecting the convergence rate of the numerical scheme. This procedure is not possible with p_2 and p_3 ; therefore, they are updated infrequently. However, the method of false position can be used to accelerate convergence of p_2 and p_3 . The flow field is assumed to be converged when all the residuals at all the flow field node points are below a specified tolerance, and v at the leading edge stagnation point together with δA_1 and δB_1 are below their respective tolerances. At this point the airfoil contour is modified and another Dirichlet problem is set up. There is no need to analyze the new airfoil contour with this procedure. A direct analysis can be made at the very end of the calculation just to check the results.

To ensure convergence of the design process only a fraction of the changes suggested by Eq. (13) is actually taken in the early design cycles. After several contour modifications the factor can be increased. The tangential velocity $u(\omega)$ at the boundary, which is interpolated from the desired $q_{\infty} = F(s)$, is also under-relaxed when a new design cycle is started.

At convergence, the mass flow term σ goes to zero, as it should, since there cannot be any sources in the flow field. As a final note, the angle of incidence, α , of the free stream is free to be specified. The final airfoil shape is independent of α , however; only its orientation will vary according to the value of α . As a result, the incidence can simply be set at zero.

3. EXAMPLES OF INVERSE DESIGN

In this section airfoil design using the procedure described above is illustrated. All the examples that will be presented have been computed on a mesh containing 192 points in the circumferential direction and 32 points in the radial direction.

At supercritical speeds, "shockless" airfoils are usually the goal. A reasonable target speed distribution might be the distribution depicted by the symbols in Fig. 1. This distribution represents the function $f_0(s)$ in Eq. 2. The free-stream Mach number is 0.800. In order to satisfy the three constraints, the target distribution must be modified into the distribution depicted by the solid line. This modification was achieved automatically using the above-mentioned scheme 1.

The shift in the location of the stagnation point should be noticed in this figure. The shift is achieved

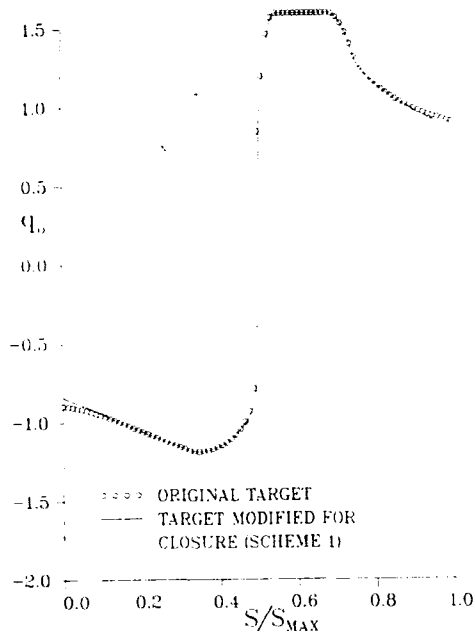


Fig. 1 Original and modified target speed distributions; "shockless" case, $M_{\infty} = 0.800$, $\alpha = 0^\circ$

smoothly and makes it possible to close the x -gap in the airfoil. The designed airfoil is depicted in Fig. 2 along with the computed pressure distribution. This pressure distribution is the result of a direct solution of the flow field over the designed airfoil contour, and it agrees to three decimal places with the pressure distribution that corresponds to the target speed distribution (the solid line in Fig. 1). This airfoil solution is obtained regardless of the airfoil contour initially prescribed to start the iteration procedure. In Fig. 3 the designed airfoil contour is compared with four different starting shapes: the Korn airfoil, the NACA 0012, the NACA 0002, and, finally, a "needle" -- two straight lines joined at the trailing edge and at the leading edge tangent to a semicircle of radius equal to 0.25% of the chord.

It is satisfying to note that the values of p_1 , p_2 , and p_3 are identical regardless of the starting shape (i.e., the modified target speed distribution is the same in all cases). Apparently, by decoupling the three parameters, it can be ensured that only a single set of values exists that satisfies the three constraints. It is possible that, if the three parameters had been coupled, more than one set of values might exist that would satisfy the constraints. Even though there is no formal proof of this, decoupling appears to guarantee a unique solution as well as making the search simpler and faster. The convergence rate of the method for the various "starter" profiles is given in Fig. 4, which depicts the maximum value of $|v/u|$ as a function of design cycles. Again, after 10-12 cycles it is difficult to distinguish any changes in the airfoil shape. Typically, the code is run to a level where the maximum $|v/u|$ is 0.001 or smaller. A converged solution generally requires 4-5 min. on a Cray-1M computer and about 20 min. on the IBM 3081 machine.

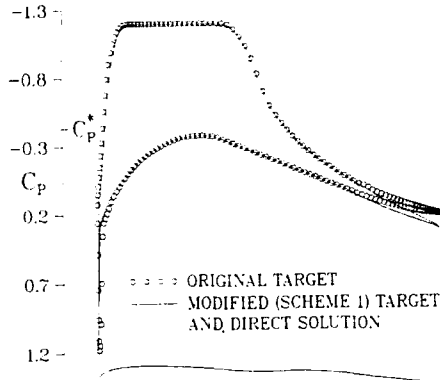


Fig. 2 Designed contour, original target and computed pressure distribution; "shockless" case, $M_{\infty} = 0.800$, $\alpha = 0^\circ$, $C_L = 0.4801$, $C_D = 0.0232$

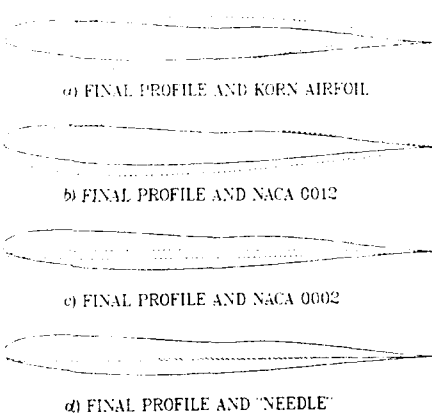


Fig. 3 Final airfoil profile (solid line) compared with starting profiles (dashed line)

The pressure distribution depicted in Fig. 2 appears to have very desirable features; in particular, the "plateau" region on the upper surface suggests the absence of a shock. However, a very large drag ($C_D = 0.0232$) is present even at the design point. A look at the Mach number contours in Fig. 5, reveals that, while there is no shock at the airfoil surface itself, a very strong shock is present off the surface. The contours represent increments of 0.01 in Mach number, and only contours for values greater than the free stream are shown. At off-design conditions, the shock reaches the surface. Several authors have observed this feature. A smooth recompression along the surface does not necessarily mean that the flow field is shockless. Thus, the airfoil shown in Fig. 2 is impractical because of its high drag.

A truly shockless closed airfoil is depicted in Fig. 6, along with the computed pressure distribution (i.e., modified target) and the original, unmodified target. Note the low computed drag ($C_D = 0.0005$) of this airfoil.

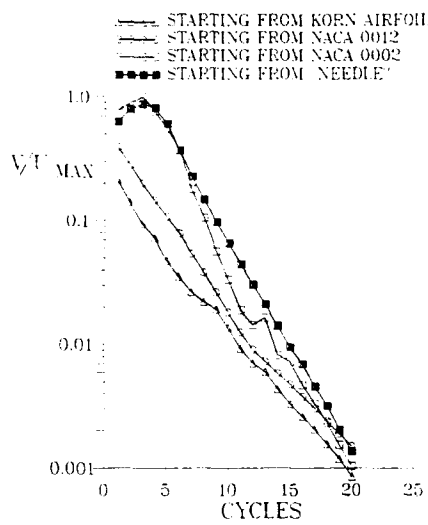


Fig. 4 Convergence history of maximum surface velocity ratio for various starter profiles; "shockless" case, $M_{\infty} = 0.800$, $\alpha = 0^\circ$

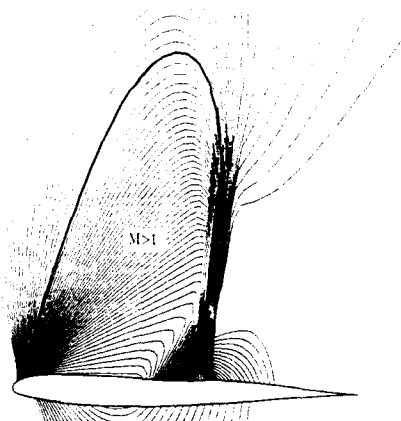


Fig. 5 Design point isomachs; "shockless" case, $M_{\infty} = 0.800$, $\alpha = 0^\circ$; contours shown at 0.01 intervals beginning with $M = 0.810$

The computed isomach pattern in Fig. 7 shows that the flow over this airfoil is truly shock free, and at off-design points only a weak shock develops. This case was computed using scheme 2 described above. It should also be noted that in this case the modifications made to the ideal target pressure distribution are considerably larger than those that resulted in the previous case. The changes on the lower surface reflect mostly the effect of f_2 , as given by Eq. (4). An example of an airfoil designed using scheme 3 is shown in Fig. 8. Note, in this case again, the very low value for the drag and the considerable lift coefficient. The modifications to the ideal target that should be noticed apart from the scaling are concentrated near the trailing edge.

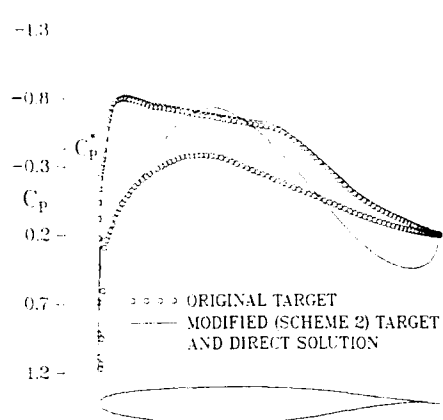


Fig. 6 Designed contour, original target and computed pressure distribution; case 2, $M_{\infty} = 0.800$, $\alpha = 0^\circ$, $C_L = 0.2673$, $C_D = 0.0005$

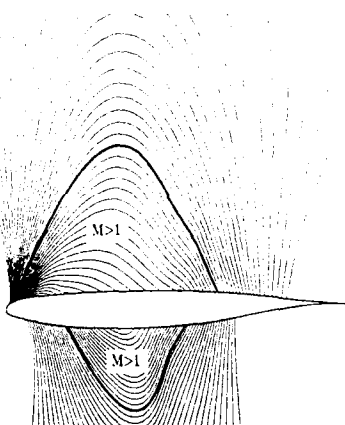


Fig. 7 Design point isomachs; case 2, $M_{\infty} = 0.800$, $\alpha = 0^\circ$; contours shown at 0.01 intervals beginning with $\Psi = 0.810$

A very interesting profile designed to an unusual pressure distribution is depicted in Fig. 9. The airfoil was designed for laminar flow (remember that this method is purely inviscid) to a distribution devised by Pfenninger¹⁷ for $M_{\infty} = 0.766$. It is only one of a series of airfoils designed for such purposes. The scheme used was scheme 1. Since the ideal pressure distribution was based on the considerable personal experience of its designer, minor modifications were needed to generate the airfoil solution. The computed Mach number contours are depicted in Fig. 10. Notice the shallowness of the supersonic region as compared to its length. This airfoil exhibits very low drag for a considerable range of flow conditions around its design point. As mentioned earlier, the method will generate airfoil contours of arbitrary trailing edge thickness. The contour shown in Fig. 11 has a trailing edge thickness equal to 2% of its chord. Like the previous example, this

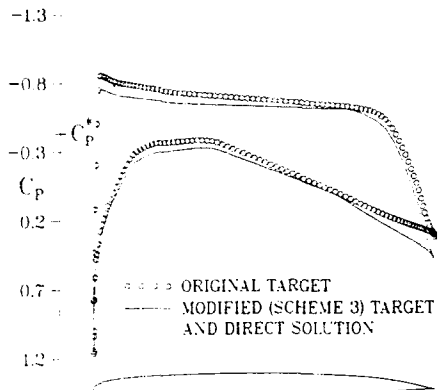


Fig. 8 Designed contour, original target and computed pressure distribution; case 3, $M_{\infty} = 0.800$, $\alpha = 0^\circ$, $C_L = 0.4972$, $C_D = 0.0002$

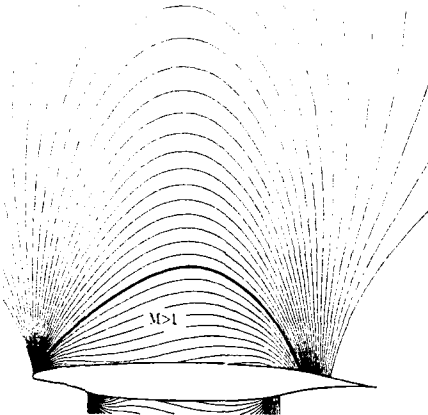


Fig. 10 Design point isomachs; case LFC1, $M_{\infty} = 0.766$, $\alpha = 0^\circ$; contours shown at 0.01 intervals beginning with $M = 0.770$

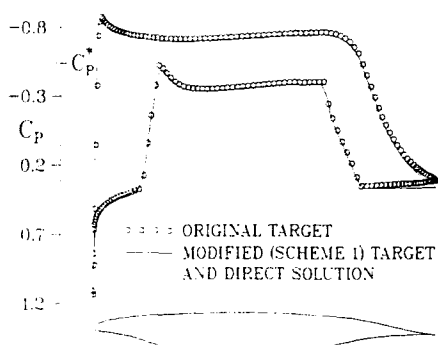


Fig. 9 Designed contour, original target and computed pressure distribution; case LFC1, $M_{\infty} = 0.766$, $\alpha = 0^\circ$, $C_L = 0.5166$, $C_D = 0.0001$

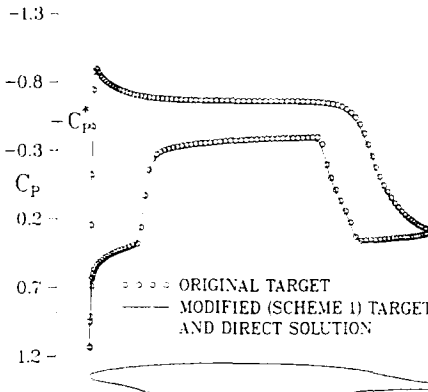


Fig. 11 Designed contour, original target, and computed pressure distribution; case LFC2, 2% trailing edge thickness; $M_{\infty} = 0.775$, $\alpha = 0^\circ$, $C_L = 0.4805$, $C_D = 0.0001$

represents an interesting design that, in addition to front loading, has a long and shallow supersonic flow region.

4. INDIRECT METHODS

The design of wing sections can be accomplished by a procedure in which the changes to some initial contour are driven by the difference between the pressure distribution computed over the given profile and the target pressure distribution. The shape changes are made according to some specified set of rules and the procedure is iterated in order to drive the differences between computed and target distributions toward zero. Such methods are often referred to as direct methods since they involve repeated calculations of the flow field over a known contour -- a direct, or Neumann problem, as opposed to the inverse, or Dirichlet problem. It should be

mentioned that in such an approach to design, the procedure for computing the flow field is completely divorced from the shape modification step.

In this class of methods the issue of constraints is avoided. The set of rules controlling the shape changes can always be defined in such a way as to yield a realistic airfoil. It is also true, however, that by such a technique the differences between computed and target distributions will not necessarily be driven to an arbitrarily low value, and, in fact, the obtainable minimum value may be quite high. Nonetheless, methods in this class are quite useful, especially when "small" design changes are involved. It is not uncommon in practice to specify the target pressure distribution to be a modification of the distribution computed over a known airfoil profile. In such a case (in)direct methods work quite well. A pair of techniques illustrating this type of approach will be described briefly.

4.1 Wavy-Wall Method

Within the context of small disturbance theory (see Ref. 26) the value of the pressure coefficient (C_p) over a wavy-wall is given by an expression of the type

$$C_p = g_1 (M_\infty) \frac{dy}{dx} \quad (14)$$

if M_∞ is greater than 1, and by

$$C_p = g_2 (M_\infty) \frac{d^2y}{dx^2} \quad (15)$$

If M_∞ is less than one, Davis¹¹ suggested that expressions of this type could be used to guide the shape changes needed to achieve a target pressure distribution. This could be done by interpreting Eq. 14 and 15 as being expressive of the sensitivity of the "local" pressure coefficient to the "local" surface shape, and vice versa. Based on the work of Spreiter and Alksne,²⁷ who used local linearizations of the transonic equation to develop separate expressions for the supersonic and subsonic regions of flow over an airfoil, Davis proposed variations of Eq. 14 and 15 above, which are more accurate and are compatible with a potential assumption for the flow field. While the forms of the expressions are changed, their basic nature is not, however. Thus, at supersonic points the local pressure coefficient is still related to the local slope of the surface by an expression of the type

$$C_p = g_3 \left(M, \left(\frac{dy}{dx} \right)^{2/3} \right), \quad (16)$$

where M is the local Mach number.

At subsonic points it is related to the local curvature of the surface by

$$C_p = g_4 \left(M^*, \left(\frac{d^2y}{dx^2} \right)^{2/3} \right) \quad (17)$$

where M^* is a reference value that ensures smooth switching between subsonic and supersonic regions.

In the "wavy-wall" method of design the flow over some initial airfoil is first computed (by the method proposed in Ref. 24, for example). At points on the airfoil where the flow is locally supersonic a new slope is proposed. This new slope is computed by

$$\left(\frac{dy}{dx} \right)_{new} = \left(\frac{dy}{dx} \right)_{old} + \frac{d}{dC_p} \left(\frac{dy}{dx} \right)_{old} (C_p^T - C_p) \quad (18)$$

Here C_p is the pressure distribution computed over the airfoil and C_p^T is the target distribution. The gradient of the slope with respect to the pressure coefficient is computed from Eq. 16, which is interpreted as being

descriptive of the relationship between the two quantities. Similarly at subsonic points a new curvature is proposed by

$$\left(\frac{d^2y}{dx^2} \right)_{new} = \left(\frac{d^2y}{dx^2} \right)_{old} + \frac{d}{dC_p} \left(\frac{d^2y}{dx^2} \right)_{old} (C_p^T - C_p) \quad (19)$$

The gradient of the curvature with respect to C_p is to be computed from Eq. 17. With these new distributions of slope and curvature a new airfoil contour can be constructed by integration and the procedure can be repeated. It should be noted that the changes suggested by Eq. 18 and 19 are under-relaxed since Eq. 16 and 17 are only approximations.

This technique can be used to re-design only part of an airfoil contour. This is actually the preferred mode of operation. The accuracy of the technique in the leading edge region is low since the integration for the new shape is performed in the physical plane where the curvature is very high. An example of an airfoil design using this method is given in Fig. 12. Here an airfoil contour is iteratively modified on the upper surface starting from a location 0.6% of the chord away from the leading edge. The lower surface was kept fixed. The target pressure distribution represented by the symbols in Fig. 12 was a modification of the distribution computed on the initial contour (the dashed line). The latter distribution featured a shock which was to be weakened by the prescribed target. The final modified section, which is pictured in Fig. 12, differed only slightly from the initial contour, but the target pressure distribution was in large part achieved, as can be seen. Slight differences between the target and the final achieved result can be noticed, especially in the trailing edge region. It is to be recalled that this technique does not necessarily drive these differences to zero.

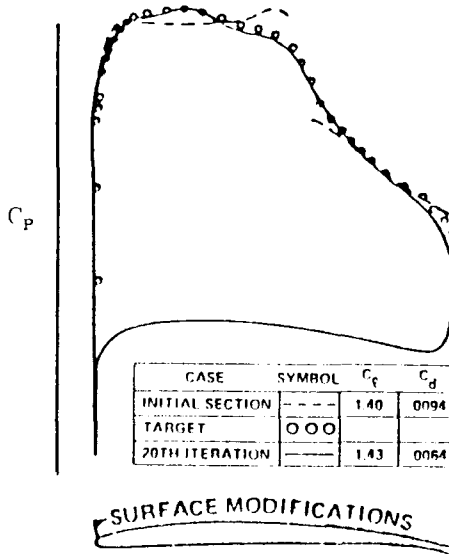


Fig. 12 Airfoil re-design with wavy-wall technique;
 $M_\infty = 0.680$

An approach similar to the one described above has been developed by Fray et al.²⁸ who combined the wavy-wall concept in supersonic zones with the subsonic thin wing inverse code of Fray and Sloot.²⁹ In the formulation of Ref. 29 the design of entire airfoil can be tackled in a practical manner, since better control over the design of the leading edge region -- which can be safely assumed to be subsonic -- is obtained through the use of an inverse approach there. Through the inverse approach trailing edge closure is also addressed by Fray et al., a goal that can be achieved only through a trial-and-error process of modification of the target distribution in the Davis technique.

4.2 Modified Mapping Technique

It was mentioned earlier that the flow over any airfoil and the flow over the unit circle are related by the transformation, h , that maps the airfoil into the circle. Specifically one can write

$$h = \frac{ds}{d\omega} = \left| \frac{dz}{d\zeta} \right| \approx \left| \frac{dw}{d\zeta} \right| \left| \frac{dw}{dz} \right|^{-1} \quad (20)$$

and, in the physical plane, $\left| \frac{dw}{dz} \right| = q_o$, the speed on the airfoil surface. For incompressible flow the solution for the flow over the circle can be expressed analytically as a function of ζ . In this case the metric, and thus the airfoil, can be constructed immediately. In fact, this is the basis of all inverse methods for incompressible design. For compressible flows, where the solution in the circle plane is not known a priori and can be computed numerically only if some value of the metric (i.e., an initial contour) is provided, this is not possible. Equation 20 can be used to provide the means by which an airfoil profile can be iteratively altered to achieve a desired speed distribution, q_c . This was the approach proposed by McFadden.¹² In this method Eq. 20 on the unit circle is written as

$$\frac{ds}{d\omega} = \frac{1}{q_o(s(\omega))} \Phi_\omega. \quad (21)$$

Here, q_o is the prescribed speed distribution expressed as a function of ω . The mapping of the starting airfoil contour into the circle is used to provide a functional relationship between s and ω as was done above in the case of the inverse method. Φ_ω is the speed on the circle computed numerically using, again, this same mapping function. The solution for the flow is obtained subject to the boundary condition that the velocity normal to the circle is zero (the Neumann problem), so that Φ_ω is the total speed. Equation 21 is basically a re-writing of the first of Eq. 12. The new twist is to interpret the left-hand side of Eq. 21 as the new metric. Then, as shown in Section 2, the ordinates of the airfoil, x and y , can be generated by integration. In practice the metric changes are under-relaxed. As in the Davis approach the procedure for computing the flow over the circle can be used as a "black box," and the design process involves the sequential analyses of airfoil profiles iteratively modified by the rule provided by Eq. 21.

An approach similar to McFadden's was developed by Jameson³⁰ and has been used by

Taverna³¹ in designing propellers for general aviation applications. Jameson also interprets the left-hand side of Eq. 21 as the new metric. Φ_ω on the right-hand side is the product of the speed computed over the starting airfoil, q_o , and the old metric. Thus, one can write

$$h_{new} = \frac{q_c}{q_o} h_{old}$$

and finally

$$\log(h_{new}) = \log(h_{old}) + \log\left(\frac{q_c}{q_o}\right) \quad (22)$$

The second term on the right-hand side in Eq. 22 provides the sought-after airfoil modification. In practice it is multiplied by an under-relaxation factor.

In this type of technique special care has to be taken to ensure that the zeroes (i.e., stagnation points) in the computed speed distribution (Φ_ω or q_c) and the target distribution match in order to avoid unwanted singularities in the new metric. McFadden and Jameson apply modifications to the target distribution to bring this about. In addition, at any step in the iteration process q_o may develop shock waves even though q_c may be shockless. Some smoothing of the gradients near these shocks must be provided to prevent the airfoil from developing corners. The issue of constraints (which is ignored in the Davis method) is addressed indirectly in these methods. Specifically, the issue of compatibility between free stream and surface speed (the first constraint) is resolved by letting q_∞ float. The value of q_∞ is obtained by first calculating the average value of q_c/q_∞ over the airfoil (or circle to which it is mapped). For incompressible flow this value is zero, as shown by Mangler,¹ Lighthill,² and Volpe.¹⁴ For the target distribution, q_0/q_∞ , the average should be zero if a solution is to exist. McFadden chooses for q_∞ a value that minimizes a functional expressing the difference (in a mean-square sense) between these two average values. In the Jameson method q_∞ is chosen to equalize the averages. In either case the rationale is based on the fact that since the direct solution over the starting airfoil necessarily satisfies the first constraint, keeping the average value of the target speed "close" to the initial average will modify the target distribution in such a way that it always satisfies the constraint. The re-setting of q_∞ results in a scaling of q_0/q_∞ which is analogous to the scaling introduced in schemes 1 and 2 of Volpe's method discussed earlier.

In the McFadden and Jameson methods trailing edge closure is not addressed explicitly. As in the wavy-wall method, if an airfoil has an undesirable trailing edge, a new design problem can be set up with a modified distribution. Trailing edge closure can also be brought about by an a-posteriori resetting of the Fourier coefficients of the new metric. Choosing the first order terms, A_1 and B_1 , according to Eq. 9 instead of assigning to them the values suggested by Eq. 21 or 22, will result in a contour which always has the correct trailing edge gap, Δx and Δy . The speed computed over this airfoil is no longer the target speed, however, and the differences from the target are not necessarily small.

5. OPTIMIZATION METHODS

In another class of design techniques, which has been proposed, successive modifications to some initially prescribed contour are performed in such a way as to minimize the value of some chosen object function, or of a combination of several such functions. The object function might be the difference between the pressure distribution over the initial profile and a prescribed target distribution. It could also be the value of the total drag. Multi-point design can be addressed by such methods by defining several functions encompassing different flow conditions. As in the case of indirect methods, this class of techniques uses a series of direct analyses of the current airfoil shape to determine the necessary modifications. Most methods use classical optimization techniques (see Ref. 32, for example) to determine the changes, and the procedure for analyzing the airfoil is truly a "black box." A more recent approach, proposed by Jameson,¹⁹ borrows ideas from control theory to formulate an adjoint equation, which embodies the object function, and whose structure reflects the nature of the direct solver.

5.1 Design via Numerical Optimization

The technique described by Hicks and Vanderplaats¹⁸ is typical of an optimization approach and will be described briefly since it contains the concepts common to all such techniques. In this technique the ordinates, z , of the airfoil are expressed parametrically in the form

$$z = z_0 + \sum_{i=1}^N a_i f_i \quad (23)$$

where z_0 denotes the shape of the initial contour, f_i some specified shape functions (typically polynomials in x , the abscissa), and a_i are coefficients to be found, whose values will determine the new airfoil contour. The design problem consists of defining an object function, I , whose value is to be minimized (or, in certain cases, maximized) subject -- possibly -- to a number of constraints, G_j , on desired quantities. The object function, I , might be the drag of the airfoil, or the lift, or the pitching moment. The design problem may try to achieve a specified speed distribution, q_T , in which case the object function could be described by

$$I = \int_s (q - q_T)^2 ds \quad (24)$$

where q is the speed over the initial contour and the integral is performed over this contour. Regardless of how it is defined, I is assumed to be a function of the design variables, a_i .

The constraints may be of a geometric or an aerodynamic nature and they are assumed to be functions of the design variables, also. A constraint might be the requirement that the enclosed volume of the airfoil, V , be greater than or equal to a specified value V_{Min} , in which case, the constraint could be expressed as

$$G(a_i) = 1 - \frac{V}{V_{Min}} \leq 0$$

It should be mentioned that trailing edge closure could be satisfied at all times by appropriate choices of the polynomials f_i in Eq. 23, independently of the value of the a_i 's. Other constraints to be imposed might include minimum values of thickness and curvature at various stations along the airfoil, maximum pressure coefficient, off-design drag rise limits and minimum (or maximum) values of force and moment coefficient at various flow conditions.

The design process begins by perturbing separately each of the N design variables, a_i , in Eq. 23, and analyzing the corresponding N different contours. The flow solutions will yield N separate values for the object function, I_N , and for each of the constraints, G_{jN} . These values together with the values for the object and the constraint functions pertinent to the original configuration ($a_i=0$) are used to estimate values of the derivatives of the functions with respect to the

design variables $\left(\frac{\partial I}{\partial a_i}\right), \left(\frac{\partial G_j}{\partial a_i}\right)$. The critical step, which follows and is to be performed by the selected optimization procedure, is to determine, now, the direction of steepest descent of I in the N -dimensional space. In other words, the optimization procedure is to assign new values to the a_i 's such that the resulting contour will have an object function closer to the sought-after minimum. In the N -dimensional space each of the constraints is represented by a surface and the space on one side of this surface denotes the region where the particular constraint is satisfied and the other side the region where it is not. When all constraints are considered there will be -- hopefully -- a region where all the constraints are satisfied. Such a region is termed the feasible region. Care has to be taken to begin the design process in the feasible region and to remain there. CONMIN, the optimization program developed by Vanderplaats³³ is used in the design procedure of Ref. 18 and in others.

Having found the direction of steepest descent

from the estimates of the $\left(\frac{\partial I}{\partial a_i}\right)$ (usually through one-sided differences) all the a_i 's are modified along that direction in an amount proportional to some given factor, λ . Then, the flow at various points, typically three, along this direction, corresponding to various values of λ , is computed and the object and constraint functions are obtained at each point. Movement (i.e., variation of the a_i 's) along that direction is continued until the object function starts to increase or until one or more of the constraints should be violated. The former case might occur because of non-linearities in the design space. In either case the procedure for determining a direction for minimizing I is repeated, by sequentially and separately varying the a_i 's to obtain

new derivatives, $\left(\frac{\partial I}{\partial a_i}\right)$. In the case where a constraint surface is crossed, a "feasible" direction, which keeps the design variables within the feasible region, is

determined using the gradients $\frac{\partial G_j}{\partial a_i}$. If no constraint surfaces are crossed the direction of steepest descent is again used. The design process is terminated when movement along the gradient (or the feasible) direction leads to an increase in the object function.

By appropriate choice of the shape functions in Eq. 23 the procedure can be used to re-design only a portion of an airfoil, as it is done in the example shown in Fig. 13. Here, the upper surface of a 13 percent thick NACA 6-series airfoil - the initial contour - is to be reshaped to weaken the shock it exhibits at $M_\infty = 0.7$, $\alpha = 0^\circ$. The object function is defined by a minimum of the (drag/as computed by an inviscid potential flow program) which in this case is entirely due to shock losses. The design was performed subject to a lower limit on the value of the cross-sectional area (or volume) of the airfoil (a constraint). The design objective was attained in this case. It is not certain, however, that this might be the best possible design, even if subject to the given constraint. An optimization procedure will drive the design toward a local minimum of the object function with no assurance that the local minimum will be an absolute one. It is even possible that a different local minimum is obtained when the design process is started from different initial conditions.

Design by optimization is a costly process. Typically, 10 to 15 cycles involving new estimates of the gradient directions are needed to attain the minimum. Each cycle in turn requires N analyses of the flow field corresponding to the N separate variations of the a_i 's, plus -- usually -- three analyses of the flow along the newly-estimated direction. Thus, the total number of flow analyses grows linearly with the number of design variables. One would have to keep the number of design variables low to keep program running times within desirable limits. However, the number of attainable designs will be limited by the number of design variables. This number should be as large as possible, regardless of the choice of shape functions, in order to make available a wide design space. The need to express the airfoil in terms of parameters (design variables) appears to be the most serious limitation of this technique.

5.2 Design via Control Theory

An interesting technique recently proposed by Jameson¹⁹ obviates the need for a parametric representation of the shape of the airfoil, and cuts down substantially the number of flow solutions needed to estimate the direction of the changes to the contour needed to drive the object function toward the minimum. The technique regards the design problem as a control problem in which the airfoil profile is the control.

The process, again, begins with a definition of an object, or cost function, I . This might be given as in Eq. 24, for example. In the procedure, the variation in the cost function, δI , is expressed as a product of the variation in the shape, δz , and some appropriately chosen function, g . The choice of g is dependent on the particular equations assumed to govern the physics and geometry of the flow. In the illustration of the method given in Ref. 19, the two-dimensional flow about the airfoil is analyzed in the circle plane and is described by the potential equation, as in Section 2. The metric h is descriptive of the airfoil shape in this case and δh can be substituted for δz . A variation in the metric results in a variation in the potential, the speed on the surface, etc. In turn, it will cause a variation in the cost function, which, when defined as in Eq. 24, can be expressed as

$$\delta I = \int_0^{2\pi} (q - q_T) \delta q \, d\omega$$

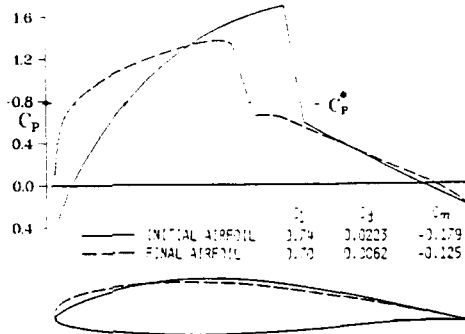


Fig. 13 Inviscid drag minimization; $M = 0.70$, $\alpha = 0^\circ$

Here, the integral over the circle boundary is substituted for the integral over the airfoil surface. Jameson¹⁹ shows that this integral can be put in the form

$$\delta I = \int_0^{2\pi} g \delta f \, d\omega \quad (25)$$

where $\delta f = \delta h / h$ and g is a gradient function

$$g = \frac{\partial P}{\partial r} - (q - q_T) q \quad (26)$$

P is obtained by solving a Poisson equation whose forcing term is the product of the gradient of the potential and the gradient of an auxiliary function ψ .

$$\Delta P = \rho M^2 \nabla \phi \cdot \nabla \psi \quad (27)$$

The function ψ is calculated by solving an adjoint equation

$$L\psi = 0 \quad (28)$$

whose operator L is the same operator which would be obtained for the potential if Eq. 10 were to be expanded for ϕ and terms containing derivatives of the mapping functions were to be dropped.

The key element in this design procedure is to make modifications to the airfoil through changes in the mapping function. These changes are given by

$$\delta f = \frac{\delta h}{h} = -\lambda g \quad (29)$$

where λ is a small positive number. If this expression is substituted in Eq. 25 one notes that the change in the cost function resulting from the selected modifications to the airfoil is necessarily negative. This means that the new airfoil has a cost function which is smaller than that corresponding to the previous contour. The airfoil

modification process converges in a direction which tends to minimize the cost, as desired.

The design cycle begins by first solving for the flow field. This yields the potential, φ , the velocity components and the density. The adjoint Eq. 28 is then solved for ψ , and P is subsequently obtained by solving Eq. 27. The function g is computed from Eq. 25, and the mapping function is corrected according to Eq. 29.

The constraints, which concern compatibility of surface speed and the free stream and trailing edge closure, and which were discussed earlier, can be accommodated in this procedure by using on the right-hand side of Eq. 29 a modified function \bar{g} which is obtained by subtracting from g terms that force the constraints to be satisfied. As in the case of methods using the modified mapping modulus approach, the appearance of shock waves might cause numerical problems, since in such a case $(q-q_T)$ would not be differentiable and, consequently, $\delta\psi$ might develop "spikes." This can be avoided by a more sophisticated choice of the cost function, a choice which in effect entails using a smoothed distribution of $(q-q_T)$. The cost function could be defined in a way that could account for additional design constraints. These constraints could call for specific lift values at several flow conditions, and a minimization of the drag. This could be done by taking as the cost function the sum of the cost functions separately defined for each design goal. It should be noted that the second part of the gradient function g in Eq. 26 reflects the variation of the cost function and thus changes with the definition of the latter.

The example in Fig. 14 illustrates the method in the drag minimization mode. In this case the target speed is taken to be the speed actually computed over the RAE 2822 airfoil at $M_\infty = 0.730$, $\alpha = 2^\circ$. A target

speed distribution has to be imposed in addition to the zero drag requirement to prevent the procedure from generating a flat plate at zero angle of attack. The imposed distribution forces the lift of the designed profile to be close to the prescribed one. After six cycles the design is essentially frozen. The final airfoil has a drag coefficient of 0.0016, as compared to a value of 0.0170 for the initial profile. In the drag minimization mode the technique converges faster than it does in the "design to pressure" mode, in which case it requires 15 to 25 cycles, typically.

The procedure can be formulated in a similar fashion for the case where the flow is to be described by a different set of governing equations. A set of adjoint and auxiliary equations can be found by a similar analysis. The basic idea, as before, is to express the variation in the cost function as a product of a gradient function, g , and the variation of the shape, $\delta\psi$, as in Eq. 25.

This technique avoids the need for, and the restrictions accompanying, a parametric representation of the shape. In addition it offers considerable savings in computing costs over the classical constrained optimization approach. Each iteration cycle basically involves the solution of the equivalent of two flow fields, one for φ and one for ψ , since the adjoint equation is "close" to the potential equation. The solution of the auxiliary equations, and in particular Eq. 27, is relatively fast. As a result, the cost per cycle is slightly more than two flow field solutions as opposed to the approximately $(N+3)$ solutions required for the optimization methods. The technique does suffer from some of the same problems as the latter method, however. In particular, if more than one local minimum exist in the solution space, the method will not necessarily converge to the absolute minimum, and might, in fact, reach different minima from different initial conditions. Also, as in the optimization methods, the

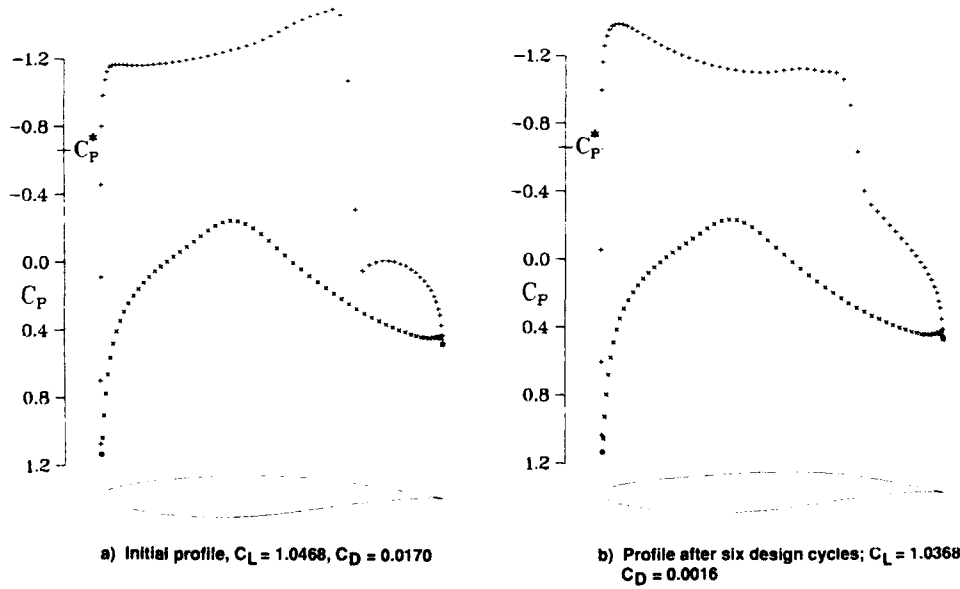


Fig. 14 Re-design of RAE 2822 airfoil to reduce drag; $M_\infty = 0.730$

success of the technique is dependant on the accuracy of the numerical procedures. If the gradients which determine the direction in which the shape is to be changed are not computed accurately enough, convergence might be impaired or prevented.

6. CONCLUDING REMARKS

The preceding discussion of various methodologies available for wing design has been restricted to inviscid, two-dimensional flows for several reasons. The most obvious is that the presentation of a method is most easily done under these conditions. Another reason comes from the fact that design methods - just as analysis methods - are more fully developed for such flow conditions. Viscous effects could be incorporated in the above-mentioned approaches in a straight-forward manner. For example, indirect methods and optimization procedures, which use direct solvers as "black boxes" could use Navier-Stokes codes instead of potential or Euler codes. A purely inverse code, such as the one described in Section 2, could similarly be formulated using the Navier-Stokes equations instead of the potential flow equation. A simpler approach in that inverse method would be to compute a boundary layer on the contour using the prescribed pressure distributions as a boundary condition. As shown by Lighthill³⁴ the displacement thickness of the boundary layer can be represented by a transpiration velocity normal to the surface. This could be added to the normal velocity computed by the solution to the Dirichlet problem to give a total normal velocity which is to be used to make the contour modifications.

Extension of the various methodologies to three dimensions has been difficult and has met with varying degrees of success due to the obvious difficulties introduced by the third dimension. All 3-D methods have concentrated on re-designing portions of a wing. Basically they used the 2-D approaches to modify cross-sections at one or more stations along the span of a large aspect ratio wing. Henne³⁵ formulated a method which can be categorized as an indirect approach rather than an inverse one because it does not design strictly to a pressure distribution containing the various parameters needed to satisfy constraints, but to a distribution that is periodically re-adjusted by the user to yield a satisfactory surface. Henne and Hicks³⁶ used an optimization procedure in 3-D analogous to that formulated by Hicks for 2-D. A procedure that incorporates ideas from the inverse approach as well as the wavy-wall method has been proposed by Brandsma and Fray.³⁷

As discussed above each of the various approaches to wing design has its merits and entails particular disadvantages. In practice, it is not likely that a single method (i.e., computer program) can be formulated to satisfy the design needs of even a particular organization. A pure inverse code with enough constraints to yield a structurally-satisfactory shape can be set up, but the result is a point design. This may not be always satisfactory. A successful wing design will most likely rely on a procedure, that utilizes several techniques, rather than a single approach. The procedure will be iterative and will contain a man in the loop. The user will interact with and will be an essential element of the procedure. He will decide at any one step of the iteration if the design exercise is headed toward a satisfactory result or if the design targets need to be altered. The procedure provides the steps to be followed in order to achieve the prescribed targets and guidelines for changing these targets. It will also reflect

the design philosophy of the designer(s). The various design techniques described above provide the tools with which the procedure will perform its task.

7. REFERENCES

1. Mangler, W., "Die Berechnung eines Tragflügelprofiles mit Vorgeschriebener Druckverteilung," *Jahrbuch der Deutschen Luftfahrtforschung*, Vol. 1, pp. 46-53, 1938.
2. Lighthill, M.J., "A New Method of Two-Dimensional Aerodynamic Design," R&M 2112, Aeronautical Research Council, London, England, 1945.
3. Woods, L.C., "Aerofoil Design in Two-Dimensional Subsonic Compressible Flow," R&M 2845, Aeronautical Research Council, London, England, March 1952.
4. Van Ingen, J.L., "A Program for Airfoil Section Design Utilizing Computer Graphics," Agard Short Course Notes, 1969.
5. Arlinger, B., "An Exact Method of Two-Dimensional Airfoil Design," TN67, Saab, Sweden, 1970.
6. Strand, T., "Exact Method of Designing Airfoils with Given Velocity Distribution in Incompressible Flow," *J. Aircraft*, Vol. 10, 1973, pp. 651-659.
7. Polito, L., "Un Metodo Esatto per il Progetto di Profili Alari in Corrente Incompressibile Aventi un Prestabilito Andamento della Velocita sul Contorno," Universita degli Studi di Pisa, Pisa, Italy, Rept. 42, 1974.
8. Volpe, G. and Melnik, R.E., "The Role of Constraints in the Inverse Design Problem for Transonic Airfoils," AIAA Paper 81-1233, 1981, also *AIAA J.*, Vol. 22, pp. 1770-1778.
9. Volpe, G. and Melnik, R.E., "Method for Designing Closed Airfoils for Arbitrary Supercritical Speed Distributions," *J. Aircraft*, Vol. 23, pp. 775-782, Oct. 1986.
10. Hicks, R.M., Vanderplaats, G.N., Murman, E.M. and King, R.R., "Airfoil Section Drag Reduction at Transonic Speeds by Numerical Optimization," NASA TMX-73097, Feb. 1976.
11. Davis, W.M., "Technique for Developing Design Tools from the Analysis Methods of Computational Aerodynamics," AIAA Paper 79-1529, 1979.
12. McFadden, G.N., "An Artificial Viscosity Method for the Design of Supercritical Airfoils," Research and Development Report C00-3077-158, Courant Inst Math Sci, New York University, July 1979.
13. Sobieczky, M., Fung, K.Y. and Seebass, A.R., "A New Method for Designing Shock-free Transonic Configurations," AIAA Paper 78-1114, 1978.
14. Bauer, F., Garabedian, P. and Korn, D., "Supercritical Wing Sections," Springer Verlag, 1972.

15. Boerstoel, J.W., and Muizing, G.H., "Transonic Shock-Free Airfoil Design by an Analytic Hodograph Method," AIAA Paper 74-439, 1974.
16. Liebeck, R.H., "On the Design of Subsonic Airfoils for High Lift," AIAA Paper 76-406, July 1976.
17. Pfenninger, W., Viken, J.K., Vemuru, C.S. and Volpe, G., "All Laminar SC LFC Airfoils with Natural Laminar Flow in the Region of the Main Wing Structure," AIAA Paper 86-2625, 1986.
18. Hicks, R.M. and Vanderplaats, G.N., "Design of Low Speed Airfoils by Numerical Optimization," SAE Paper 75-0524, 1975.
19. Jameson, A., "Aerodynamic Design via Control Theory," *J. Scientific Computing*, Vol. 3, pp. 233-260, 1988.
20. Volpe, G., "Geometric and Surface Pressure Restrictions in Airfoil Design," Agard Short Course Notes, 1990.
21. Ludford, G.S., "The Behavior at Infinity of the Potential Function of a Two-Dimensional Subsonic Compressible Flow," *J. of Mathematical Physics*, Vol. 30, 1951, pp. 117-130.
22. Volpe, G., "The Inverse Design of Closed Airfoils in Transonic Flow," AIAA Paper 83-504, 1983.
23. Nonweiler, T., "A New Series of Low Drag Aerofoils," Rept. 6801, University of Glasgow, Dept. of Aeronautics and Fluid Mechanics, 1968.
24. Jameson, A., "Acceleration of Transonic Potential Flow Calculations on Arbitrary Meshes by the Multiple Grid Method," AIAA Paper 79-1458, 1979.
25. Jameson, A., "Solution of the Euler Equations by a Multigrid Method," *Applied Math and Computation*, Vol. 13, pp. 327-356, 1983.
26. Liepmann, H.W. and Roshko, A., "Elements of Gas Dynamics," John Wiley and Sons, New York, 1957.
27. Spreiter, J.R. and Alksne, A.Y., "Thin Airfoil Theory Based on Approximate Solution of the Transonic Flow Equation," NACA Rept. 1359, 1958.
28. Fray, J.M.J., Slooff, J.W., Boerstoel, J.W. and Kassies, A., "Design of Transonic Airfoils with Given Pressure Distribution, Subject to Geometric Constraints," NLR TR 84064 U, 1984..
29. Fray, J.M.J. and Slooff, J.W., "A Constrained Inverse Method for the Aerodynamic Design of Thick Wings with Given Pressure Distribution in Subsonic Flow," AGARD CP-285, Paper 16, 1980.
30. Jameson, A., Private Communication.
31. Taverna, F., "Advanced Airfoil Design for General Aviation Propellers," AIAA Paper 83-1791, 1983.
32. Vanderplaats, G.N. and Moses, F., "Structural Optimization by Methods of Feasible Directions," *Computers Structures*, Vol. 3, pp. 739-755, July 1973.
33. Vanderplaats, G.N., "CONMIN - A Fortran Program for Constrained Function Minimization," NASA TM X-62,282, 1973.
34. Lighthill, M.J., "On Displacement Thickness," *J. Fluid Mech.*, Vol. 4, 1958.
35. Henne, P.A., "An Inverse Transonic Wing Design Method," AIAA Paper 80-0330, 1980.
36. Hicks, R.M. and Henne, P.A., "Wing Design by Numerical Optimization," AIAA Paper 77-1247, 1977.
37. Brandsma, F.J. and Fray, J.M.J., "A System for Transonic Wing Design with Geometric Constraints Based on an Inverse Method," AGARD CP-463, Paper 7, 1990.

**A STREAM-FUNCTION-COORDINATE (SFC) CONCEPT
IN AERODYNAMIC SHAPE DESIGN**

George S. Dulikravich
Penn State University
Department of Aerospace Engineering
University Park, PA 16802, USA

1. SUMMARY

A new approach to the inverse design of two-dimensional aerodynamic shapes has been developed. This formulation is based on a Stream-Function-Coordinate (SFC) concept for steady, irrotational, compressible, inviscid, planar flows. It differs from the classical stream function formulation in that it treats the y-coordinate of each point on a streamline as a function of the x-coordinate and the stream function ψ , that is, $Y = Y(x, \psi)$. This new formulation is especially suitable for the computation of stream line shapes, and therefore, for determination of aerodynamic shapes subject to specified surface pressure distributions. An additional advantage of this new formulation is that it requires the generation of only a one-dimensional grid in the x-direction. The grid in the y-direction is computed as a part of the solution since y-coordinates of the streamlines are treated as the unknowns in the SFC formulation. In addition, the SFC method is equally suitable for the analysis of the flowfields around given shapes. A computer code has been developed on the basis of SFC formulation. It is capable of performing flowfield analysis and inverse design of airfoil cascade shapes by changing a single input parameter.

2. INTRODUCTION

In a recently published article, Huang and Dulikravich [1] gave detailed derivations of the new Stream Function Coordinate (SFC) concept for inviscid, steady, two-dimensional and three-dimensional compressible flows. The SFC concept reflects the main objective of the inverse design where the ultimate goal is to determine the shape, that is, the coordinates of a surface contour which is compatible with the desired surface pressure distribution. Thus, it is logical to solve for the coordinates directly. Recently, Chen and Zhang [2] have published a paper on inverse design of multiple cascade shapes. They used a special form of the SFC formulation suitable for axisymmetric surfaces of turbomachinery and they have successfully computed shapes of simple cascades as well as shapes of multiple cascades with splitter blades inside the flow passages. Owen and Pearson [3] have developed a complete threedimensional formulation based on a general concept by solving directly for the coordinates. They have applied their formulation to different duct flows and to free jet flows [4].

3. ANALYSIS

Instead of using the standard formulation where the stream function ψ is a function of the x and y coordinates

$$(1 - K^2 \psi_y^2) \psi_{xx} + 2 K^2 \psi_x \psi_y \psi_{xy} + (1 - K^2 \psi_x^2) \psi_{yy} = 0 \quad (1)$$

Huang and Dulikravich [1] performed a transformation

$$\psi = \psi(x, y) \leftrightarrow Y = Y(x, \psi) \quad (2)$$

which transforms (1) into the SFC equation

$$(Y_y^2 - K^2) Y_{xx} - 2 Y_x Y_y Y_{xy} + (1 + Y_x^2) Y_{yy} = 0 \quad (3)$$

where the Y-coordinate of each streamline is treated as an unknown and x and ψ are known. Here, the compressibility coefficient K^2 is defined as

$$K^2 = \frac{1}{\left(\frac{\rho}{\rho_*}\right)^2 \left(\frac{a}{a_*}\right)^2} \quad (4)$$

where ρ is the local density and a is the local speed of sound. Details of the derivation and evaluation of K^2 are given in Appendix A. The SFC formulation has significant advantages over the classical stream function formulation where $\psi = \psi(x, y)$. For two-dimensional problems SFC requires only a one-dimensional grid in the x-direction. The other family of grid lines is determined as a part of the solution where Y are the unknown coordinates of the streamlines $\psi = \text{constant}$. Because of the SFC formulation, true upwind differencing could be achieved without the complexity of determining the direction of the local velocity vectors since one family of the grid lines corresponds to the streamlines. This simplifies the extension of the code to transonic flows [2]. Huang and Dulikravich [1] clearly pointed out that the SFC formulation where $Y = Y(x, \psi)$ is singular at all locations where the x-component of the velocity vector becomes zero. These singularities are nonphysical since they are created by the transformation and cannot be eliminated simply by using grid clustering within the regions of singular points [1].

Thus, strictly speaking, the SFC formulation is suitable for the flow field analysis and shape inverse design of objects having cusped leading and trailing edge points where there are no stagnation points. In practice, leading and trailing edges are often [5] modified when using the SFC formulation by adding artificial cusps to them.

When the SFC method is used in the forward (analysis) mode, solid portions of the upper and lower airfoil boundary from the leading to the trailing edge remain fixed since they represent the given airfoil surface. Since these Y coordinates are prescribed, the SFC equation is not solved on the solid boundaries in the analysis mode. In the inverse (design) mode, the input geometry of the airfoil surface is used only as an initial guess. The evolution of the upper and lower boundary shape is driven by the specified surface Mach number, critical Mach number, or coefficient of pressure distribution which uniquely determines the local value of the compressibility coefficient K on the surface (Appendix A). Second order central difference expressions with variable grid size were used throughout the domain (Appendix B). Rather than transforming the SFC equation to a uniform grid, all computations were performed in the actual physical (x, y) plane. The resulting algebraic finite difference equations were solved using artificially time-dependent SLOR in

conjunction with the Generalized Non-Linear Minimal Residual Method (GNLMR) [6] which significantly accelerates the convergence rate. Details of the GNLMR methodology as applied to SFC equation are provided in the Appendix C and Appendix D.

In both analysis and the inverse design case, the periodic boundaries are free to move vertically since they represent stagnation streamlines and their shape is not known in advance. They are subject only to the periodicity constraint that the gap between the upper and the lower stagnation streamline remains constant (Appendix E). In the design mode, the leading edge point of the airfoil must remain fixed in order to keep the entire cascade from moving within the domain. Due to the similarity of the boundary conditions for the two modes of operation, switching between the analysis mode and the design mode is accomplished by means of a single input parameter.

4 RESULTS

Based on the formulations presented in this paper, a computer code was developed on VAX 3550 computer. The code was exercised in both forward (analysis) and inverse mode on periodic channel flows. Each domain was discretized with a fixed clustered grid having 20 grid cells on the bottom and on the top surface, 20 cells upstream, and 20 cells downstream of the object, with 20 streamtubes across the channel. First objective was to evaluate the error resulting from the SFC transformation singularity at stagnation points. Steady, incompressible, irrotational, inviscid flow through a cascade of dipoles has a known analytic solution [7] and was chosen to be the first test geometry. When using the SFC code in an analysis mode the initial streamlines (Fig. 1) converged within 50 iterations to their correct shapes (Fig. 2). The resulting pressure field (Fig. 3) compares well with the analytical solution (Fig. 4). The computed surface C_p distribution indicates very narrow regions of locally high error (Fig. 5) due to the singularity arising from the SFC transformation. Since this is an extreme example of a blunt leading edge, it can be concluded that the singularities generate only very local errors. Consequently, by using grid clustering, no need is perceived for the use of artificial extensions (cusps) at the leading and trailing edges. When the SFC code was exercised in its inverse design mode, free stream coefficient of pressure distribution was specified along the top and bottom surface of the circle. Evolution history of the entire lower boundary is depicted in Fig. 6. The corresponding convergence history (Fig. 7) indicates that only 200 iterations were needed to achieve the correct shape (Fig. 8) of the channel. When running a high subsonic test case ($M_\infty = 0.62$) with a non-staggered cascade of 12% biconvex airfoils having sharp edges (Fig. 9), practically no error at the stagnation points could be detected (Fig. 10 and Fig. 11). By specifying the wall C_p -distribution to be the same as that of the freestream, a straight channel was obtained (Fig. 12) very rapidly (Fig. 13). The iterative process can be further enhanced by using our GNLMR method (Fig. 14) explained in the Appendix C.

5 CONCLUSIONS

The SFC formulation is straightforward to perform analytically and simple to implement computationally. It is very fast and could be formulated for multidimensional and multiply connected domains. It is equally applicable to the analysis of the flow around the existing configurations and to the inverse shape design.

6 ACKNOWLEDGMENTS

The author would like to thank Ms. Amy Myers for her superb typing. Special thanks are due to Apple Computer and SUN Microsystems, Inc. for their computer equipment that was donated to our Interdisciplinary Computational Fluid Dynamics Laboratory at Penn State University where this work was performed.

7 REFERENCES

- Huang, C. Y. and Dulikravich, G. S., "Stream Function and Stream-Function-Coordinate (SFC) Formulation for Inviscid Flow Field Calculations," Computer Methods in Appl. Mechanics and Eng., Vol. 59, 1986, pp. 155-177.
- Chen, N.-X. and Zhang, F.-X., "A Generalized Numerical Method for Solving Direct, Inverse and Hybrid Problems of Blade Cascade Flow by Using Streamline-Coordinate Equation," ASME Paper No. 87-GT-29, Anaheim, CA, 1987.
- Owen, D. R. and Pearson, C. E., "Numerical Solution of a Class of Steady-State Euler Equations by a Modified Streamline Method," AIAA paper 88-0625, Reno, NV, Jan. 1988.
- Pearson, C. E., "Extension of a Numerical Streamline Method," Communications in Appl. Num. Meth., Vol. 1, 1985, pp. 177.
- Singhal, A. K., "Flow in Axial Turbomachinery Cascades," Ph.D. Dissertation, Dept. of Mech. Engr., University of London, UK, May 1977.
- Huang, C. Y. and Dulikravich, G. S., "Fast Iterative Algorithms Based on Optimal Explicit Time-Stepping," Computer Meth. in Appl. Mech. and Eng., Vol. 63, 1987, pp. 15-36.
- Milne-Thompson, L. M., "Theoretical Hydrodynamics," 4th Edition, MacMillan & Co., 1962, pp. 229.
- Ives, D., "Approximate Inversion of the Stream-Tube-Area Relations," Grumman Research Dept. Memo., RM-452, July 1969.

APPENDIX A: Derivation of the Compressibility Coefficient K

Notice that

$$\frac{T}{T_0} = \left(\frac{2}{Y+1} \right)^{\frac{T}{T_*}} \quad (A.1)$$

where T is the absolute temperature, T_0 is stagnation temperature and T_* is the critical temperature. In terms of local Mach numbers this becomes

$$\frac{1}{\left[1 + \frac{Y-1}{2} M^2 \right]} = \left(\frac{2}{Y+1} \right) \left[\frac{Y+1}{2} - \frac{Y-1}{2} M_*^2 \right] \quad (A.2)$$

This can be rewritten as

$$\frac{Y+1}{2} \left(\frac{1}{\left[\frac{Y+1}{2} - \frac{Y-1}{2} M_*^2 \right]} \right)^{\frac{Y-1}{Y+1}} =$$

$$\left[1 + \frac{Y-1}{2} M^2 \right] \quad (A.3)$$

Nevertheless

$$M^2 = \frac{M_*^2}{a_*^2/a_*^2} = \frac{M_*^2}{[\frac{Y+1}{2} - \frac{Y-1}{2} M_*^2]} \quad (A.4)$$

Hence, A.3 can be rewritten as

$$\begin{aligned} \frac{Y+1}{2} \left(\frac{M^2}{M_*^2} - \frac{1}{\frac{Y-1}{2} - \frac{Y-1}{2} M_*^2} \right) &= \frac{Y-1}{Y+1} \\ - \frac{Y-1}{2} M^2 - 1 &= 0 \end{aligned} \quad (A.5)$$

Since

$$\frac{P_-}{P_*} = [\frac{Y+1}{2} - \frac{Y-1}{2} M_*^2] \frac{1}{Y-1} \quad (A.6)$$

it follows that A.5 becomes

$$\frac{Y+1}{2} \left(\frac{M^2}{\frac{P_-}{P_*} M_*^2} \right)^{\frac{Y-1}{Y+1}} - \frac{Y-1}{2} M^2 - 1 = 0 \quad (A.7)$$

Notice now that

$$M^2 = \left(\frac{P_-}{P_*} \right)^2 M_*^2 \left(\frac{1}{\frac{P_-}{P_*} \frac{a_*^2}{a_*^2}} \right) = \left(\frac{P_-}{P_*} \right)^2 M_*^2 K^2 \quad (A.8)$$

Since the compressibility coefficient K is defined as

$$K^2 = \frac{1}{a_*^2/a_*^2} = \left[\frac{Y+1}{2} - \frac{Y-1}{2} M_*^2 \right]^{-\frac{1}{Y-1}} \quad (A.9)$$

it follows that A.7 divided with $(Y-1)$ becomes

$$\begin{aligned} \frac{Y+1}{Y-1} (K^2)^{\frac{Y-1}{Y+1}} - \left[\frac{Y+1}{2} - \frac{Y-1}{2} M_*^2 \right]^2 M_*^2 K^2 \\ - \frac{2}{Y-1} = 0 \end{aligned} \quad (A.10)$$

At the same time notice that

$$\begin{aligned} \left(\frac{P_-}{P_*} \right)^2 M_*^2 &= \left(\frac{P_- u}{P_* a_*} \right)^2 + \left(\frac{P_- v}{P_* a_*} \right)^2 = (u_y)^2 + (v_x)^2 \\ &= \frac{1}{Y_\psi^2} + (v_x)^2 = \frac{1 + v_x^2}{Y_\psi^2} \end{aligned} \quad (A.11)$$

Finally, A.10 becomes

$$\frac{Y+1}{Y-1} (K^2)^{\frac{Y-1}{Y+1}} - \left(\frac{1 + v_x^2}{Y_\psi^2} \right) K^2 - \frac{2}{Y-1} = 0 \quad (A.12)$$

Since Y_x and Y_ψ will be changing during the iterative process, this means that

$$F = \frac{Y+1}{Y-1} (K^2)^{\frac{Y-1}{Y+1}} - \left(\frac{1 + v_x^2}{Y_\psi^2} \right) K^2 - \frac{2}{Y-1} \neq 0 \quad (A.13)$$

Thus, at every point in the flow field for the given instantaneous values of Y_x and Y_ψ we can iteratively determine the corresponding instantaneous local values of the compressibility coefficient K . Second order (modified) Newton's iteration yields

$$\frac{dF}{dK} = 2 \left[K^{\frac{Y-3}{Y+1}} - \left(\frac{1 + v_x^2}{Y_\psi^2} \right) K \right] \quad (A.14)$$

$$\frac{d^2 F}{dK^2} = 2 \left[\frac{Y-3}{Y+1} K^{\frac{-4}{Y+1}} - \left(\frac{1 + v_x^2}{Y_\psi^2} \right) \right] \quad (A.15)$$

so that

$$K^{(n+1)} = K^{(n)} - F \frac{dF}{dK} / \left[\left(\frac{dF}{dK} \right)^2 - F \frac{d^2 F}{dK^2} \right] \quad (A.16)$$

where the superscript n is the iteration counter.

An approximate relation between the mass flow rate and the local Mach number is given by Ives [8] and can be used instead of the iterative procedure.

APPENDIX B: Finite Difference Formulas

Second order accurate central differencing for x derivatives was used throughout the domain.

The central differences for the derivatives in ψ direction have an entirely analogous form. The difference expressions were substituted into the SFC equation (3).

APPENDIX C: GNLMR Method Applied to the Iterative Solution of the SFC Equation

Let the non-linear operator governing SFC formulation be designated as N , that is,

$$N = (Y_\psi^2 - K^2) Y_{xx} - 2Y_x Y_\psi Y_{x\psi} + (1 + v_x^2) Y_{\psi\psi} = 0 \quad (C.1)$$

A one step iterative algorithm for solving (C.1) can be defined by calculating the new value of the Y coordinate of a streamline from a simple relaxation algorithm

$$Y^{(t+1)} = Y^{(t)} + \omega \delta^{(t)} \quad (C.2)$$

where superscript t designates the iteration level, ω is the relaxation factor and $\delta^{(t)}$ is the correction at the t -th iteration level based on some basic iteration method.

An M -step method can be defined for advancing the iterative algorithm from iteration level t to iteration level $t+1$ with M steps combined. That is,

$$Y^{(t+1)} = Y^{(t)} + \sum_{m=1}^M \omega^{(m)} \delta^{(m)}$$

where $\delta^{(m)}$ are the corrections evaluated at intermediate steps. They are obtained by successively applying M simple relaxation ($\omega = 1$) iterations to the solution of C.1.

The optimal values of $\omega^{(m)}$ can be found [6] by solving a matrix problem

$$\sum_{m=1}^M \sum_{n=1}^N a^{(m)} a^{(n)} u^{(n)} = - \sum_{m=1}^M r^{(t)} a^{(m)} \quad (C.4)$$

where the residual at iteration level t is

$$r^{(t)} = N(Y_x, Y_\psi, Y_{xx}, Y_{x\psi}, Y_{\psi\psi}) \quad (C.5)$$

and

$$\begin{aligned} a^{(m)} &= \frac{\partial N}{\partial Y_x} \delta_x^{(m)} + \frac{\partial N}{\partial Y_\psi} \delta_\psi^{(m)} + \frac{\partial N}{\partial Y_{xx}} \delta_{xx}^{(m)} \\ &\quad + \frac{\partial N}{\partial Y_{x\psi}} \delta_{x\psi}^{(m)} + \frac{\partial N}{\partial Y_{\psi\psi}} \delta_{\psi\psi}^{(m)} \end{aligned} \quad (C.6)$$

Thus, for example,

$$\begin{aligned} a^{(1)} &= \{2(-Y_\psi Y_{x\psi} + Y_x Y_{\psi\psi}) - \frac{\partial(K^2)}{\partial Y_x} Y_{xx}\} \delta_x^{(1)} \\ &\quad + \{2(-Y_\psi Y_{xx} + Y_x Y_{x\psi}) - \frac{\partial(K^2)}{\partial Y_\psi} Y_{x\psi}\} \delta_\psi^{(1)} \\ &\quad + \{Y_\psi^2 - K^2\} \delta_{xx}^{(1)} + \{-2Y_x Y_\psi\} \delta_{x\psi}^{(1)} + \{1 + Y_x^2\} \delta_{\psi\psi}^{(1)} \end{aligned} \quad (C.7)$$

where the values for $\partial(K^2)/\partial Y_x$ and $\partial(K^2)/\partial Y_\psi$ are given in Appendix D.

APPENDIX D: Derivatives of the Compressibility Coefficient K

When evaluating derivatives $\partial N/\partial Y_x$ and $\partial N/\partial Y_\psi$ it is important to notice that the compressibility coefficient K is a function of Y_x and Y_ψ . This can be shown by combining A.13, A.11 and A.7. The result is that

$$\frac{1 + Y_x^2}{Y_\psi^2} = \frac{(Y+1)(K^2) \frac{Y-1}{Y+1}}{(Y-1) K^2} = 2 \quad (D.1)$$

Taking a partial derivative of both sides of D.1 with respect to Y_x gives

$$\frac{\partial(K^2)}{\partial Y_x} = \frac{(Y+1) Y_x (K^2)^2}{Y_\psi [1 - (K^2) \frac{Y-1}{Y+1}]} \quad (D.2)$$

Similarly, partial derivative of D.1 with respect to Y_ψ gives (after making an additional use of D.1) the following

$$\frac{\partial(K^2)}{\partial Y_\psi} = \frac{2(K^2) - (Y+1)(K^2) \frac{Y-1}{Y+1}}{Y_\psi [1 - (K^2) \frac{Y-1}{Y+1}]} \quad (D.3)$$

APPENDIX E: Boundary Conditions

The periodic boundary conditions were enforced upstream and downstream of the airfoil as follows

$$Y(i,jmax+1) = Y(i,jmin+1) + GAP \quad (E.1)$$

$$Y(i,jmin-1) = Y(i,jmax-1) - GAP \quad (E.2)$$

$$YMID = (Y(i,jmin) + (Y(i,jmax))/2) \quad (E.3)$$

$$Y(i,jmin) = YMID + GAP/2 \quad (E.4)$$

$$Y(i,jmax) = YMID - GAP/2 \quad (E.5)$$

where GAP is the y -distance between the leading edges of two airfoils.

The values of ψ at the overlapping layers of points $(jmin-1)$ and $(jmax+1)$ were set according to the similar expressions

$$PSI(i,jmin-1) = PSI(i,jmax-1) - PSITOT \quad (E.6)$$

$$PSI(i,jmax+1) = PSI(i,jmin+1) + PSITOT \quad (E.7)$$

where

$$\begin{aligned} PSITOT &= PSI(i,jmax) - PSI(i,jmin) \\ &= (\frac{\rho}{\rho_{\infty} M_{\infty}^2}) \text{GAP/CHORD} \end{aligned} \quad (E.8)$$

Here, M_{∞} is the x -component of the critical Mach number and CHORD is the chord length of the airfoil.

Inlet and exit boundary conditions were enforced by specifying the vertical variation of ψ between the lower and the upper stagnation streamline and enforcing the inlet flow angle α_1 and the exit flow angle α_2 in design mode. In the analysis mode, the Kutta-Zhukovskii condition was enforced at the trailing edge instead of the angle α_2 at the exit. Solid wall tangency boundary conditions were enforced by evaluating Y at the wall points via one-sided second order differencing and then deducing the appropriate values at the imaginary points $(jmin-1)$ and $(jmax+1)$ from the second order central difference formula for Y at the wall.

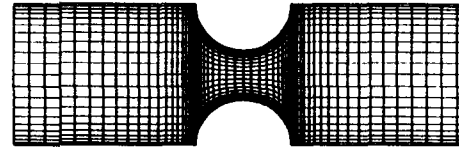


Fig. 1 Initial Y - x grid consisting of $(20+20+20) \times 20$ cells for the flow through a cascade of dipoles

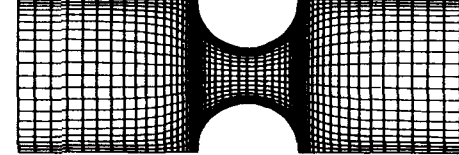


Fig. 2 Final streamline shapes for the flow through a cascade of dipoles

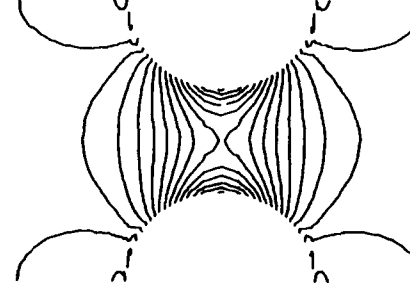


Fig. 3 Computed isobars for the $M_\infty = 0.05$ flow through a cascade of dipoles

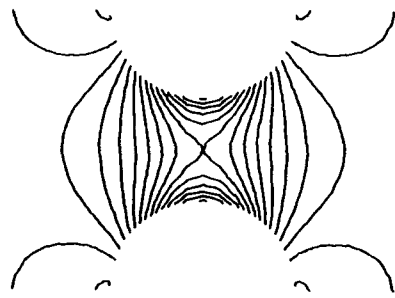


Fig. 4 Analytic values for isobars for an incompressible flow through a cascade of dipoles

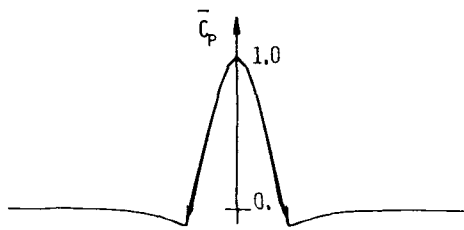


Fig. 5 Superimposed analytic and computed surface C_p values for the $M_\infty = 0.0$ and $M_\infty = 0.05$ flow through a cascade of dipoles



Fig. 6 Intermediate shapes of the bottom wall during the inverse design from a cascade of dipoles to a straight channel

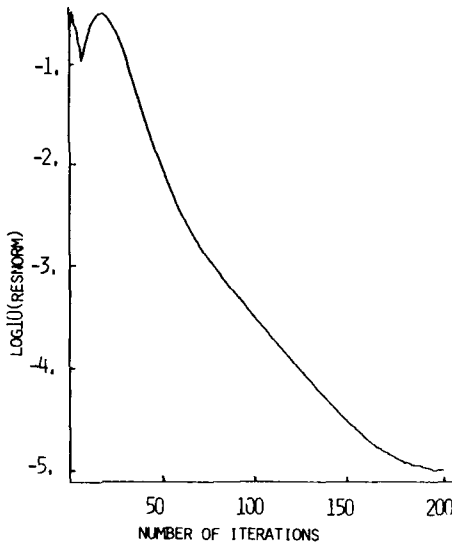


Fig. 7 Convergence history for the inverse design from a cascade of dipoles to a straight channel

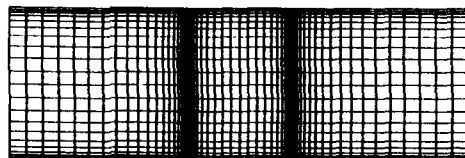


Fig. 8 Streamlines for the inversely designed straight channel when starting from a cascade of dipoles



Fig. 9 Streamlines for the converged analysis of the cascade of 12% thick biconvex airfoils at $M_\infty = 0.62$.

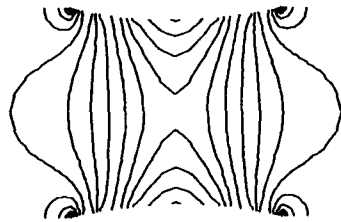


Fig. 10 Computed isobars for the analysis of a flow through the cascade of 12% thick biconvex airfoils at $M_{\infty} = 0.62$.

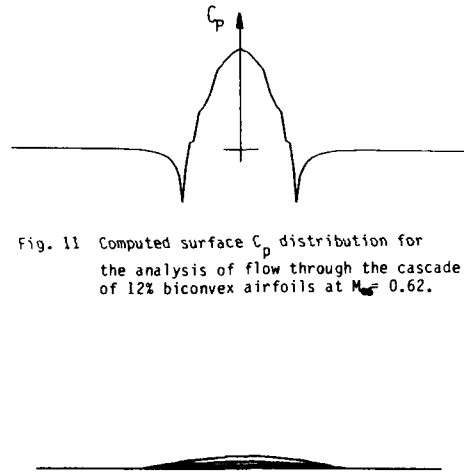


Fig. 11 Computed surface C_p distribution for the analysis of flow through the cascade of 12% biconvex airfoils at $M_{\infty} = 0.62$.

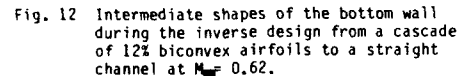


Fig. 12 Intermediate shapes of the bottom wall during the inverse design from a cascade of 12% biconvex airfoils to a straight channel at $M_{\infty} = 0.62$.

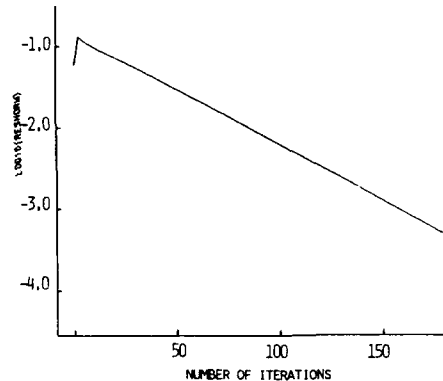


Fig. 13 Convergence history for the inverse design from a cascade of 12% biconvex airfoils to a straight channel at $M_{\infty} = 0.62$.

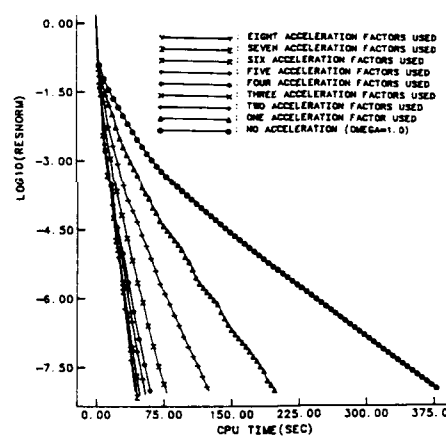


Fig. 14 Typical convergence histories for SFC compressible flow with SLDR and DMR method

SUBSONIC AND TRANSONIC CASCADE DESIGN

Olivier LEONARD

von Karman Institute
for Fluid Dynamics
72, chaussée de Waterloo
1640 Rhode-Saint-Genèse
Belgium

ABSTRACT

Two iterative methods for blade design, using direct flow solvers and a blade geometry modification algorithm, are presented. Both procedures start with the analysis of a given cascade geometry using an existing flow solver. The difference between the calculated velocity distribution and the required one is used to calculate a flow distortion. In the first method, this flow distortion is produced by singularities while in the second method the distortion is derived by imposing the required velocity distribution as a boundary condition. This flow distortion is used by the modification algorithm and results in a new blade shape for which the calculated velocity is closer to the desired one.

Examples for both subsonic and transonic flows are presented and show a rapid convergence to the geometry required for the desired velocity distribution. The main advantage of the proposed method is that existing analysis codes can be used, for the design and for the off-design analysis.

Some restrictions which have to be imposed on the required velocity distribution are also discussed.

LIST OF SYMBOLS

a	speed of sound
c	chord length
H	coupling factor
l	left eigenvector
M	isentropic Mach number
n	normal coordinate
n_x, n_y	normal vector components
N	number of vortices
p^0	total pressure
p	static pressure
s	curvilinear coordinate
t	time coordinate
T^0	total temperature
U	vector of unknowns
u, v	velocity components
V	velocity
x, y	geometry coordinates

greek symbols

β	slope of the blade contour
β_1	inlet flow angle (with resp. \bar{w})
β_2	outlet flow angle (with resp. \bar{w})
γ	vortex strength
Γ	circulation
λ	eigenvalue
ρ	density
σ	cascade solidity
ξ, η	vortex coordinates

subscripts

n	normal component
t	tangential component
ti	tangential component, inside
to	tangential component, outside
1	cascade inlet
2	cascade outlet

superscript

α	equation number
new	value at the time $n+1$
old	value at the time n
req	required value
*	intermediate value

1. A CLASSIFICATION OF INVERSE METHODS.

In a **Direct Method**, the computing task consists in determining the aerodynamic performances of a given blade section shape. A designer specifies an arbitrary cascade geometry which is then analysed with a computer code to define its performances. Based on the results, the designer modifies the blade shape in accordance with his experience. This is essentially equivalent to the wind tunnel design method of "trial and error", but with a computer instead of the wind tunnel.

An alternative way to achieve an aerodynamic design is the **Inverse Method**, where the geometry of the blade results from the calculation and is supposed to give the required performances. *Inverse methods* can be categorized according to various criteria, for example the flow regime (subsonic, transonic or supersonic) for which the methods are valid, the way the problem is solved (analytical or numerical), the modification method, the assumptions made.

Two main families of inverse methods can be distinguished: the methods in which the problem can be solved analytically, resulting directly in the geometry of the blade, and those for which a numerical procedure is necessary.

Methods of the first class have been widely developed before computer facilities were available, in order to find a solution to the inverse problem that could be calculated manually. They therefore need severe assumptions to formulate the equations in a simple enough form to allow an analytical solution. Although they are very restrictive, they permit to develop a complete theory for the inverse problem, including the constraints that the required velocity distribution has to verify in order to obtain a physical solution (Lighthill, 1945, Woods, 1955).

Analytical methods make use of the conformal mapping of the cascade plane into a circle (or a row of circles) and solve the incompressible potential flow equations (Lighthill, 1945, Schwering, 1970, Murugesan and Raily, 1969, Ubaldi, 1984). With the need of higher performances, resulting in transonic flow regimes, their limits have been exceeded and other less restrictive methods have been sought, resulting in the second family.

The second class of methods has been developed in parallel with the classical direct solvers which calculate the flow for a given geometry. A numerical scheme is used to solve the non linear equations. Some of these methods make use of a transformation to uncouple the calculation domain from the initially unknown blade geometry. No first guess of the blade geometry is necessary if the potential equation is solved; the potential stream function plane may be used for the calculation (Stanitz, 1953, Schmidt, 1980). Another possibility is to solve the potential equation in the hodograph plane which also allows to linearize the equations (Bauer, Garabedian and Korn, 1972, 1975 and 1977, Sanz, 1983, 1984, 1988).

If non potential flow fields are considered, the Euler equations must be integrated. Since the flow is computed in the physical plane, a first guess of the geometry is necessary to start the calculation. This initial geometry may be modified during the flow calculation, adapting it step by step to achieve the imposed pressure or velocity distribution (Meauze, 1980 and 1982, Giles and Drela, 1985 and 1987, Zannetti, 1984 and 1988) and at the same time verifying the slip condition on the blade wall.

At the other hand, the initial geometry can be modified after convergence of the flow calculation which has been performed by the solver. The blade is then modified to satisfy the boundary condition which has not been respected during the flow calculation. This procedure results in the so-called **Iterative Inverse Methods**.

The blade modification can be performed using a physical model which relates the displacement of each point of the geometry to the difference between the current pressure distribution and the required one, or by means of a mathematical algorithm minimizing an object function defined by the user, and subject to some constraints. Although these latter methods should lead to a solution, even if the required pressure or velocity distribution does not correspond to a physical geometry, they still have the disadvantage to be very expensive in terms of CPU time (Vanderplaats, 1979 and 1984, Hicks, 1981).

This paper deals with iterative inverse methods using a physical algorithm to modify the blades. The main feature of these iterative inverse methods is the modification of the blade geometry based on a velocity field which verifies the prescribed velocity or pressure distribution but does not respect any more the slip condition on the blade wall. By resetting the blade wall parallel to the flow or by using the concept of transpiration, the blade is modified and a new direct calculation is performed by the flow solver. This procedure is repeated until the difference between required and calculated velocity is small enough (see the flow chart on figure 1).

These methods may differ by the way the velocity field around the blades is derived from the prescribed distribution, and two different approaches will be discussed here.

Since the main advantage of these methods is that they make use of direct solvers, whose accuracy and reliability

have been proven many times, the first idea is therefore to use these solvers just as a black box. The boundary conditions implemented in these direct solvers provide a velocity field tangent to the blade wall. A supplementary algorithm is required to provide a correction of the velocity field from the difference between the imposed and the calculated velocity distributions.

Another idea is to modify the boundary conditions inside the solver in order to impose directly the prescribed pressure distribution. The converged velocity field resulting from the iterative calculation will therefore include the distortion with respect to the tangential situation, and the blade geometry can be directly modified.

2. MODIFICATION OF THE GEOMETRY.

As said previously, the choice has been made to implement the concept of iterative inverse methods, starting from classical direct solvers. Any modification of the pressure distribution on the blade wall will induce a distortion of the complete flow field and therefore a displacement of the streamlines.

The geometry modification algorithm that is used is therefore based on the calculation of the new streamlines position, starting from the initial blade wall which is not a streamline any more. This calculation makes use of the velocity component normal to the initial blade, produced from the difference between the initial and the required pressure distributions. The calculation of the normal velocity component will be discussed in details in the next chapter.

As the new streamlines can intersect with the old blade shape, wherein the flow quantities are not defined, the position of the new streamlines must be calculated from the old ones, namely from the old blade wall.

In the **transpiration model**, the old blade wall is considered as porous with a normal velocity going through it. The mass balance is applied in the cell defined by the points $(i)^{old}$, $(i-1)^{old}$, $(i)^{new}$ and $(i-1)^{new}$ as shown in fig. 2.

This results in:

$$d(\rho V_t \Delta n) = \rho V_n ds \quad (1)$$

or in discretized form:

$$\Delta n \rho \dot{V}_t|_{i-1} + \Delta s \frac{\rho V_n|_i + \rho V_n|_{i-1}}{2} = \Delta n \rho \dot{V}_t|_i \quad (2)$$

The ingoing velocity $\dot{V}_t|_{i-1}$ is taken as the mean value of the tangential velocity along the normal direction at the point $i-1$, namely

$$\dot{V}_t|_{i-1} = \frac{V_t|_{i-1} + V_t^{req}|_{i-1}}{2} \quad (3)$$

The outgoing velocity $\dot{V}_t|_i$ is calculated in the same way.

Expression (2) allows the calculation of the shift Δn_i if Δn_{i-1} is known. The modification starts at the stagnation point, where the value Δn_i is set to zero. The modification of the pressure side and the suction side are calculated separately and it is hoped that both contours do not cross, which would result in an unphysical blade shape. This depends on the accuracy of the numerical integration procedure and on the accuracy of the normal velocities calculation.

The streamline model calculates the position of the new blade wall by setting this wall parallel to the local velocity $\bar{V} = \bar{V}_t + \bar{V}_n$ as illustrated in fig. 3.

This results in:

$$\Delta n(s) = \int_0^s \frac{dn}{ds} ds = \int_0^s \frac{V_n}{V_t} ds \quad (4)$$

The discretized form of (4) is:

$$\begin{aligned} x_i^{new} - x_{i-1}^{new} &= x_i^{old} - x_{i-1}^{old} + \frac{\Delta s}{2} \left\{ \frac{dn}{ds}_{i-1} + \frac{dn}{ds}_i \right\} n_x \\ y_i^{new} - y_{i-1}^{new} &= y_i^{old} - y_{i-1}^{old} + \frac{\Delta s}{2} \left\{ \frac{dn}{ds}_{i-1} + \frac{dn}{ds}_i \right\} n_y \end{aligned} \quad (5)$$

The closer the new blade contour follows a real streamline, the smaller are the chances that pressure and suction sides cross each other.

Both models have given good results; they reduce to the same expression for incompressible flow fields. After the modification, a new discretization of the flow field must be done for the new blade geometry, and another flow calculation is performed.

The modification algorithms that are proposed imply that the velocity at the blade wall has a component normal to the blade wall due to the fact that the required pressure or velocity does not correspond to the current geometry. However, any direct solver (potential or Euler) provides a velocity field which is tangent to the actual blade wall, due to the slip condition that is imposed as the boundary condition on the blade wall, and which does not necessarily satisfy the required pressure distribution.

Moreover, the well-posed problem theory prohibits that both boundary conditions (slip condition and required pressure) could be imposed together on the blade wall. Two possibilities are then offered:

- either the direct solver is kept with the classical slip condition, and a supplementary algorithm is implemented in order to calculate the distortion of the flow field due to the required pressure; the method presented here makes use of vortices to modify the flow field;
- or the boundary condition imposed at the blade wall is modified inside the flow solver (that cannot be called *direct solver* any more!) and the resulting flow field will respect the required pressure but not the slip condition; the walls are supposed to be permeable.

The first option has the advantage that existing direct solvers can be used as black boxes, but the second option may be theoretically more correct, as will be shown later. Both ideas have been developed and will be discussed in the next chapters.

3. NORMAL VELOCITIES CALCULATED BY VORTICES.

The velocity field resulting from the direct solver respects the slip condition but does not agree with the required velocity. The basic idea is to distribute singularities, such

as vortices, on the blade contour, in order to increase or to decrease locally the velocity on the blade and to set it equal to the required value (Murugesan and Railly, 1969, Van den Braembussche et al., 1989).

The first effect of a vortex distribution is to create a difference between the tangential velocity at the outer and the inner part of the contour:

$$\gamma = V_{to} - V_{ti} \quad (6)$$

this difference being equal to the local vortex strength. Moreover, the flow field induced by the vortices must be defined in such a way that zero tangential velocity inside the contour is obtained as a kinematic condition. Therefore we have:

$$\gamma = V_{to} \quad (7)$$

If we want to increase or decrease locally an already existing velocity at the outer side of the blade, a vortex can be placed on the blade contour with its strength defined as:

$$\gamma = \Delta V_t \quad (8)$$

or

$$\gamma = V_t - V_t^{eq} \quad (9)$$

A second effect of this vortex distribution is the creation of a velocity normal to the blade contour, which for a cascade of blades at a pitch t is given by:

$$V_n = \frac{1}{2t} \oint \frac{\sinh X \cos \beta + \sin Y \sin \beta}{\cosh X - \cos Y} \gamma ds \quad (10)$$

with:

$$\begin{aligned} X &= \frac{2\pi}{t}(x - \xi) \\ Y &= \frac{2\pi}{t}(y - \eta) \end{aligned} \quad (11)$$

where ξ, η are the vortex coordinates and x, y is the location where the value of V_n is calculated.

The discretization of (10) for N intervals results in:

$$V_n(i) = \frac{1}{2t} \sum_{j=1}^N H(i, j) \gamma(j) \Delta s(j) \quad (12)$$

with

$$H(i, j) = \frac{\sinh X \cos \beta + \sin Y \sin \beta}{\cosh X - \cos Y} \quad (13)$$

Calculation of the normal velocities V_n at the N positions where the vortices are located results in the following linear system of N equations:

$$\begin{pmatrix} V_n(1) \\ V_n(2) \\ \vdots \\ V_n(N) \end{pmatrix} = \begin{pmatrix} 0 & \dots & H(1, N) \\ H(2, 1) & \ddots & H(2, N) \\ \vdots & \vdots & \vdots \\ H(N, 1) & \dots & 0 \end{pmatrix} \begin{pmatrix} \gamma'(1) \\ \gamma'(2) \\ \vdots \\ \gamma'(N) \end{pmatrix} \quad (14)$$

with

$$\gamma'(j) = \gamma(j) \Delta s(j) \quad (15)$$

Unfortunately the matrix H has a zero diagonal since a vortex has no contribution to the local normal velocity. This system of equations is ill-conditioned and can give rise to a wavy velocity distribution since two adjacent vortices $\gamma(i-1)$ and $\gamma(i+1)$ of the same sign and equal strength induce zero normal velocity at the point i .

Since a vortex cannot create flow, the total mass flux induced by each vortex across the closed profile must be equal to zero. Therefore we have:

$$\oint V_n ds = 0 \quad \text{for each vortex} \quad (16)$$

or

$$\sum_{i=1}^N H(i,j) \gamma(j) \Delta s(i) = 0 \quad j=1,..,N \quad (17)$$

In order to correct the numerical error introduced by the discretization, a normal velocity is calculated by (17) for each vortex and added, at the point where the vortex is located, to the one calculated using (12). This correction reduces the chances that the new suction and pressure sides intersect or diverge from each other.

As this method is based on the superposition principle, it is therefore correct only for incompressible potential flows; however, also for a compressible flow, it gives a blade correction which is in the right direction, and which anyway vanishes as the velocity distribution converges to the required one. Another weakness of the method is that the correction calculated using the vortices is incorrect if a supersonic pocket is present in the flow field, since a vortex from this zone induces a normal velocity upstream, which is not in agreement with the hyperbolic character of the flow. However, experience has shown that it can also be efficiently used for transonic flows.

The method has the great advantage of simplicity, allowing the use of accurate and efficient direct solvers which have been developed in the past and are well documented in the literature. Another advantage of the use of a direct solver is that, once the blade geometry has been determined, the off-design analysis can be carried out using the same flow solver and input file.

This method has been used together with two different direct solvers, an incompressible potential code (Van den Braembussche, 1984) and a Time Marching procedure solving the Euler equations (Arts, 1982). Two examples will illustrate each code.

The first example demonstrates the procedure in the design of a compressor blade for incompressible flow with the required velocity distribution shown in figure 4a. The calculations use as a first guess a NACA-65(18A₁₀)10 blade at zero stagger (fig. 4b). The ratio of local velocity over inlet velocity obtained from a first analysis at $\beta_1 = 30$ deg. and a pitch-chord ratio of 0.9, is shown in figure 4c.

For the same inlet air angle and pitch-chord ratio a new blade shape, shown in figure 4d, is obtained after 40 modifications. With a blade definition of 40 points, the CPU time on a VAX 780 for this example is 55 sec.. This new geometry is very different from the first guess (fig. 4b). The stagger angle has increased from 0 to 4.6 deg. and the new blade is much thicker. This large trailing edge thickness results from the required velocity distribution and accounts for both the geometrical blade thickness and the boundary layer displacement thickness on the pressure and suction side.

The potential flow calculation method does not account for wakes and the blade contour is therefore closed by rounding-off at the trailing edge. The blade velocity distribution agrees very well with the required one as shown in figure 4e. Discrepancies are observed only at the last two points on the pressure and suction side, at the trailing edge round-off. The local overshoot of the velocity is due to

the flow acceleration around the thick circular trailing edge and cannot be avoided with potential flow calculations.

The second example demonstrates the procedure in the redesign of a turbine rotor hub section. The velocity distribution on the initial blade is compared to the desired one in figure 5a. The last one has a considerably larger loading than the initial blade and the pitch-chord ratio has been increased proportionally to obtain the same outlet flow conditions.

The new blade shape, obtained after only 10 modifications, is compared to the initial shape on figure 5b. Also shown are the initial and new cascade parameters. Figure 5c shows the comparison between the required velocity distribution and that corresponding to the final blade shape. Discrepancies are observed at the leading edge pressure side where the calculated velocity is higher than the required one, because the mean value of the required pressure and suction side velocity at the leading edge is lower than the inlet velocity. This would imply a negative blade thickness (negative blockage). The discrepancy does not disappear when the number of modifications is increased.

A code solving the Euler equations has been developed in order to serve as a basis of the different steps of the development of the inverse method. The code is based on a Time Marching procedure, a finite volume approach, and on a scheme investigated by Arts (1982).

The numerical domain is represented on fig. 6. It is made up of several pseudo streamlines and pitchwise lines. The control surfaces used in the finite volume approach are bi-trapezoidal.

The time derivative is discretized by means of a corrected viscosity scheme:

$$\begin{aligned} U_{i,k}^{\text{new}} &= \frac{\Delta t}{A} (\text{transport terms}) \\ &+ \frac{1}{4} [U_{i-1,j}^{\text{new}} + U_{i,j+1}^{\text{old}} + U_{i+1,j}^{\text{old}} + U_{i,j-1}^{\text{old}}] \\ &- \frac{\alpha}{4} [U_{i-1,j}^* + U_{i,j+1}^* + U_{i+1,j}^* + U_{i,j-1}^*] \end{aligned} \quad (18)$$

The terms superscripted by an asterisk are updated every 20 iterations; α is a numerical viscosity coefficient which is function of the density gradient:

$$\alpha = VC \left[1 - \frac{\rho_{i-1,j}^* + \rho_{i,j-1}^* + \rho_{i+1,j}^* + \rho_{i,j+1}^* - 4\rho_{i,j}^*}{4} \right] \quad (19)$$

where VC is an empirical coefficient (typically 0.98).

Using this flow solver, the iterative method was first demonstrated with a required velocity distribution calculated from a classical NACA-65 (12A₂I₆₀)10 blade. The first guess was a NACA-65 (12A₁₀)10 blade. The geometries of both blades are compared in figure 7a. The velocity distribution on the initial blade and the required velocity distribution are shown on fig. 7b.

The flow conditions are: $p_1^0 = 1.33$ bar, $T_1^0 = 341.5$ K, $\beta_1 = 45$ deg, $p_2 = 1.173$ bar. The cascade geometry is defined by a stagger angle of 31 deg and a solidity of 1 for both blades.

Figures 7c and 7d show the convergence of the calculated velocity. Good agreement with the prescribed velocity distribution is evident in fig. 7d, except for the leading edge

and the trailing edge regions. This can be due to the fact that the discretization with a H-type grid is not suited to describe accurately the flow field in these regions. The comparison between the final blade geometry and the NACA-65 (12A₁A₂)10 is shown in figure 7e. The calculations are made with 71 stations in the streamwise direction and 21 points in the pitchwise direction. The CPU time on a VAX 780 was about 5 hours for 12 modifications.

The fourth example demonstrates the procedure in the design of a turbine blade. The starting geometry is that of the workshop VKI-LS 82-05 (Arts, 1982). The flow conditions are: $p_1^0 = 1$ bar, $T_1^0 = 278$ K, $\beta_1 = 0$ deg, $M_1 = 1.2$. The cascade geometry is defined by a stagger angle of -60 deg and a solidity of 1.25.

Problems have been encountered modifying the suction and pressure surfaces at the same time, since there is a strong interaction between both surfaces in the throat region. The expansion waves starting from the pressure side trailing edge interact with the suction side.

To work around this problem, only the pressure side velocity was imposed during the first modifications. This reduces the expansion in the trailing edge region. Figures 8a shows the starting velocity distribution and the required velocity distribution, while figure 8b shows the velocity distribution after 2 modifications.

Once the required velocity distribution has been obtained on the pressure side, a similar procedure has been applied on the suction side, in which we impose simultaneously the suction and pressure side velocity distributions. Six modifications were needed to obtain the required suction side velocity distribution. Figure 8c shows the final velocity distribution while the comparison between the initial and the final blade geometry can be seen in figure 8d.

Using the same Time Marching solver, an off-design analysis has been made for this final blade. Results are shown on figures 9a for $M_2 = 1$ and 9b for $M_2 = 0.8$. One can see that a blade which has been optimized for one outlet Mach number does not necessarily give a good velocity distribution at other outlet Mach numbers.

4. PERMEABLE WALL.

The problems encountered using the vortices for transonic blade design have led to the idea of developing a theoretically more correct modification method, which would account for compressibility and respect the hyperbolic character of the unsteady Euler equations. This can be achieved by imposing directly the required pressure distribution on the blade wall, inside the Time Marching calculation.

Imposing simultaneously the pressure and the slip condition on a wall leads to a ill-posed problem in a mathematical point of view since the problem is over-determined; this means that the inverse problem has no solution in general. If the required performances correspond to a physical geometry, one of the two boundary conditions drops out and the design is possible.

Since it was chosen to impose the required pressure as the boundary condition on the wall, the velocity is allowed to have a component normal to the blade wall which therefore has to be considered as permeable. This normal velocity component will be used for the geometry modification after convergence of the Time Marching calculation.

4.1. Characteristic Surfaces and Wave-like Solutions.

Boundary conditions connect the calculation domain with the surrounding flow field and should express correctly the propagation of the information which is described by the equations. Especially the boundary conditions and the calculation of the unknowns at the blade wall have to be discussed in more detail, since the information propagating along the streamlines doesn't propagate any more along the blade wall. The way the information is propagated is discussed here for first order systems of equations.

A system of two first-order equations can be written in the form:

$$\begin{aligned} a \frac{\partial u}{\partial x} + 2b \frac{\partial u}{\partial y} + c \frac{\partial v}{\partial y} &= 0 \\ \frac{\partial v}{\partial x} - \frac{\partial u}{\partial y} &= 0 \end{aligned} \quad (20)$$

or in the matrix form:

$$A_1 \frac{\partial U}{\partial x} + A_2 \frac{\partial U}{\partial y} = 0 \quad (21)$$

with

$$U = \begin{bmatrix} u \\ v \end{bmatrix} \quad A_1 = \begin{bmatrix} a & 0 \\ 0 & 1 \end{bmatrix} \quad A_2 = \begin{bmatrix} 2b & c \\ -1 & 0 \end{bmatrix} \quad (22)$$

Since these equations describe a convection process, information may propagate like waves under some conditions. If a simple wave solution is sought, propagating in the direction \bar{n} , it has the form:

$$U = \hat{U} e^{i(n_x z + n_y y)} \quad (23)$$

This solution for U can be substituted in equation (21), and the condition to obtain such solutions is that the determinant of the matrix $(A_1 n_x + A_2 n_y)$ vanishes:

$$\begin{vmatrix} an_x + 2bn_y & cn_y \\ -n_y & n_x \end{vmatrix} = 0 \quad (24)$$

Hence from the roots of

$$a \left(\frac{n_x}{n_y} \right)^2 + 2b \left(\frac{n_x}{n_y} \right) + c = 0 \quad (25)$$

the conditions defining the type of the quasi-linear differential system of equations are obtained. If $(b^2 - 4ac) > 0$ there are two wave-like solutions and the system is hyperbolic, while for $(b^2 - 4ac) < 0$ the two solutions are complex conjugate and the equation is elliptic. When $(b^2 - 4ac) = 0$ the two solutions are reduced to one single direction of propagation and the equation is parabolic.

A wave front surface may be defined, which separates the points already influenced by the propagating disturbance from the points not yet reached by the information. If $S(x, y) = S_o$ (where S_o is a constant) is such a surface, the propagation direction \bar{n} is normal to the surface S :

$$\bar{n} = \nabla S \quad (26)$$

The surfaces $S(x, y)$ which satisfy equation (25) for real values of n_x and n_y are called characteristic surfaces, which transport certain properties of the flow.

The general definition for a system of n partial differential equations, containing n unknowns u^j in the m -dimensional space x^k , written in the quasi-linear form, is:

$$A_{ij}^k \frac{\partial u^j}{\partial x^k} = 0 \quad i, j = 1, \dots, n \quad k = 1, \dots, m \quad (27)$$

or in the matrix form:

$$A^k \frac{\partial U}{\partial x^k} = 0 \quad k = 1, \dots, m \quad (28)$$

The $(n \times n)$ matrices A^k can depend on x^k and U but not of the derivatives of U . A plane wave solution will exist if the system

$$[A^k n_k] \hat{U} = 0 \quad (29)$$

has non-trivial solutions. This will be the case if the determinant of the system vanishes, that is, if

$$|A^k n_k| = 0 \quad (30)$$

There are, at most, n solutions and therefore, at most, n characteristic surfaces. The system is said to be hyperbolic if all the n normals are real and if the solutions of the n associated systems of equations are linearly independent. If all the characteristics are complex, the system is said to be elliptic and if some are real and some are complex, the system is considered as hybrid. If the matrix $[A^k n_k]$ is not of rank n , then the system is said to be parabolic.

If one space variable, say x^m , is singled out and the corresponding Jacobian matrix A^m is the unit matrix, this variable is called a time-like variable. The system (28) is written as

$$\frac{\partial U}{\partial t} + A^k \frac{\partial U}{\partial x^k} = 0 \quad (31)$$

The characteristic condition, equation (30), becomes

$$|n_k I + A^k n_k| = 0 \quad k = 1, \dots, m-1 \quad (32)$$

Equation (32) is therefore an eigenvalue problem where the characteristic normals are obtained as the eigenvalues of the matrix

$$K_{ij} = A_{ij}^k n_k \quad k = 1, \dots, m-1 \quad (33)$$

If the n eigenvalues are real there are n characteristic surfaces which transport information in the \bar{n} direction.

If the unsteady two-dimensional Euler equations are considered, their quasi-linear form can be written as:

$$\frac{\partial U}{\partial t} + A \frac{\partial U}{\partial x} + B \frac{\partial U}{\partial y} = 0 \quad (34)$$

If the primitive variables ρ , V and p are used, we have

$$U = \begin{bmatrix} \rho \\ u \\ v \\ p \end{bmatrix} \quad A = \begin{bmatrix} u & \rho & 0 & 0 \\ 0 & u & 0 & 1/\rho \\ 0 & 0 & u & 0 \\ 0 & \rho a^2 & 0 & u \end{bmatrix}$$

$$B = \begin{bmatrix} v & 0 & \rho & 0 \\ 0 & v & 0 & 0 \\ 0 & 0 & v & 1/\rho \\ 0 & 0 & \rho a^2 & v \end{bmatrix}$$

Since the system is hyperbolic, a matrix $C_{\bar{n}}$ may be defined as

$$C_{\bar{n}} = An_{\bar{n}} + Bn_{\bar{n}} \quad \forall \bar{n} \quad (35)$$

This matrix has real eigenvalues and a complete set of eigenvectors.

Eigenvalues of $C_{\bar{n}}$ are: $\bar{V}\bar{n}$, $\bar{V}\bar{n}$, $\bar{V}\bar{n} + a$ and $\bar{V}\bar{n} - a$

4.2. Boundary Conditions.

The information necessary for the initial and boundary conditions to be imposed with a given system of differential equations, in order to have a well-posed problem, can be gained from the preceding considerations. A solution of the system of first-order partial differential equations can be written as a superposition of wave-like solutions corresponding to the n eigenvalues of the matrix K . For an hyperbolic problem, all the eigenvalues are real and expression (23) shows that no amplified mode are generated (an amplified mode is not physically acceptable). Therefore n boundary conditions have to be given to determine completely the solution. These boundary conditions have to be distributed along the boundaries at all values of t , according to the direction of propagation of the corresponding waves.

If the information propagated by one wave front is impinging a boundary point, coming from the inside of the calculation domain (positive eigenvalue if \bar{n} is the outgoing normal vector), the value of the corresponding unknown must be calculated from this information and not from a boundary condition. At the other hand, if the information comes from the outside of the calculation domain (negative eigenvalue), the value of the unknown at this boundary point must be imposed by a boundary condition. These considerations have to be applied in the different boundary problems of a blade-to-blade calculation.

For the inlet boundary (and if a subsonic axial velocity is considered), only $\bar{V}\bar{n} + a$ is positive and three boundary conditions must be imposed, usually the total conditions (p^* and T^*) and the inlet flow angle.

If the slip condition is imposed on the blade wall, only the eigenvalue $\bar{V}\bar{n} - a$ is negative and therefore only one boundary condition must be imposed, i.e. the velocity direction at that point.

At the other hand, if the static pressure p is imposed on the blade wall, a component of velocity normal to the blade will appear and depending upon its sign, 2 or 0 additional conditions must be imposed. Three problems have to be solved:

- how to calculate the sign of the normal velocity component ?
- which boundary conditions to apply in addition to the static pressure ?
- how to calculate the value of the unknowns that are not imposed by the boundary conditions ?

These problems can be solved by introducing the compatibility relations.

4.3. Compatibility Relations.

An alternative definition of characteristic surfaces and hyperbolicity can be obtained from the fact that wave front surfaces carry certain properties and that a complete de-

scription of the physical system is obtained when all these properties are known. This implies that the original system of equations, if hyperbolic, can be reformulated as differential relations written along the wave fronts (characteristic surfaces) only. The original system of equations can be transformed, through a linear combination, into an equivalent system of equations containing only derivatives along the characteristic surfaces S . For any equation of the system (31) we have:

$$l \left[\frac{\partial U}{\partial t} + A^k \frac{\partial U}{\partial x^k} \right] = 0 \quad (36)$$

or

$$\sum_{i=1}^n l_i \left[\frac{\partial u^i}{\partial t} + \sum_{j=1}^n A_{ij}^k \frac{\partial u^j}{\partial x^k} \right] = 0 \quad (37)$$

or

$$\sum_{j=1}^n \left[\sum_{i=1}^n \delta_{ij} l_i \frac{\partial}{\partial t} + \sum_{i=1}^n l_i A_{ij}^k \frac{\partial}{\partial x^k} \right] u_j = 0 \quad (38)$$

where the l_i are n arbitrary coefficients.

For a two-dimensional system ($k=1,2$), we can define a set of n vectors \bar{Z}_j , such as

$$\bar{Z}_j = l_j \bar{t}_t + \sum_{i=1}^n l_i (A_{ij} \bar{t}_x + B_{ij} \bar{t}_y) \quad (39)$$

and the linear combination (36) can be written as

$$\sum_{j=1}^n \bar{Z}_j \bar{\nabla} u_j = 0 \quad (40)$$

This expression can be interpreted as a sum of derivatives along curves which are tangential to vectors \bar{Z}_j . The coefficients l_i are chosen such that equation (36) contains only derivatives in a two-dimensional subspace of the (x, y, t) space, namely the characteristic surface S whose normal is \bar{n} . The condition for that is given by

$$\bar{Z}_j \bar{n} = 0 \quad \forall j \quad (41)$$

or

$$l_j n_t + \sum_{i=1}^n l_i (A_{ij} n_x + B_{ij} n_y) = 0 \quad \forall j \quad (42)$$

The relation can be written using the definition of the matrix $C_{\bar{n}}$ (35):

$$l_j n_t + \sum_{i=1}^n l_i [C_{\bar{n}}]_{ij} = 0 \quad \forall j \quad (43)$$

which expresses that l is an eigenvector of the matrix $C_{\bar{n}}$, with $-n_t = \lambda$ the corresponding eigenvalue.

If the unsteady two-dimensional Euler equations are considered, the discretized form of the compatibility relations (36) is, for the equation (36) is,

$$(I_1^{\alpha})^{old} \left(\frac{\rho^{new} - \rho^{old}}{\Delta t} + \mathcal{F}_1^{old} \right) + \dots \\ (I_4^{\alpha})^{old} \left(\frac{\rho^{new} - \rho^{old}}{\Delta t} + \mathcal{F}_4^{old} \right) = 0 \quad (44)$$

The terms \mathcal{F}^{old} denote numerical approximations of the divergence terms; they can be estimated from the Euler equations. For the density we have:

$$\frac{\rho^* - \rho^{old}}{\Delta t} + \mathcal{F}_1^{old} = 0 \quad (45)$$

The compatibility relations become:

$$(I_1^*)^{old} (\rho^{new} - \rho^*) + (I_2^*)^{old} (V_t^{new} - V^*) \\ + (I_4^*)^{old} (p^{new} - p^*) = 0 \quad (46)$$

where the superscript asterisk means the this variable is estimated from the discretization of the Euler equations; then the new value of the unknown is computed using the compatibility relation, if the corresponding eigenvalue is positive. The four compatibility relations and the corresponding eigenvalues are:

eigenvalue	compatibility relation
V_n	$-a^2(\rho^{new} - \rho^*) + (p^{new} - p^*) = 0$
V_n	$V_t^{new} - V_t^* = 0$
$V_n - a$	$-\rho a(V_t^{new} - V_t^*) + (p^{new} - p^*) = 0$
$V_n + a$	$\rho a(V_t^{new} - V_t^*) + (p^{new} - p^*) = 0$

where the values of the density ρ and the speed of sound a are taken at the old time level.

The first problem evoked in the section 4.2. can be solved by the fact that the eigenvalue $V_n + a$ is always positive, if the assumption is made of a subsonic normal component. This means that the corresponding compatibility relation may be used to calculate the value and the sign of V_n , since the information propagating with this wave comes from the interior of the calculation domain. The pressure p^{new} in the relation is obviously the required pressure.

If the normal velocity is positive, one boundary condition (the required static pressure) must be imposed, since only one eigenvalue $V_n - a$ is negative. If the normal velocity is negative, two additional boundary conditions must be imposed, since V_n is negative as well. It has been found that the best solution is to impose the total pressure and total temperatures at that point.

A summary of the different cases at the blade wall is proposed now. In the following examples, CR means that the compatibility relation is used, and BC that a boundary condition is imposed. The compatibility relation corresponding with $V_n - a$ is never used since this eigenvalue is always negative.

example: impermeable wall

$$\begin{aligned} 1 \text{ BC: } V_t^{new} &= 0 \\ 3 \text{ CR: } V_t^{new} &= V_t^* + (p^{new} - p^*) / (\rho a) \\ \rho^{new} &= \rho^* + (p^{new} - p^*) / a^2 \\ V_t^{new} &= V_t^* \end{aligned}$$

example: subsonic inlet

$$\begin{aligned} 1 \text{ CR: } V_t^{new} &= V_t^* + (p^{new} - p^*) / (\rho a) \\ 3 \text{ BC: } p^{new} &= p^{req} \\ \rho^{new} &= F(T_0, p_0, p^{new}) \\ V_t^{new} &= F(T_0, p_0, p^{new}) \end{aligned}$$

example: subsonic outlet

$$\begin{aligned} 3 \text{ CR: } V_t^{new} &= V_t^* + (p^{new} - p^*) / (\rho a) \\ \rho^{new} &= \rho^* + (p^{new} - p^*) / a^2 \\ V_t^{new} &= V_t^* \\ 1 \text{ BC: } p^{new} &= p^{req} \end{aligned}$$

From the four variables ρ^{new} , p^{new} , V_t^{new} and V_t^{new} the new value of the primitive variables or of the conservative variables can be calculated.

4.4. The Euler Flow Solver.

A code solving the Euler equations has been developed in order to serve as a basis of the different steps of the development of the inverse method. The code is based on a Time Marching procedure, a finite volume approach, and on a scheme investigated by Jameson (1981).

For the space discretization, non-intersecting finite volumes are used together with a cell-vertex approach. The physical domain is shown in figure 10. C-grids are used for a better leading edge modelisation.

For the time discretization, both second order and fourth order Jameson viscosities are used. In order to preserve the conservation form of the scheme, the artificial dissipative terms are introduced by adding dissipative fluxes. For the cell i, j the equilibrium is written:

$$A_{i,j} \left(\frac{\partial}{\partial t} U_{i,j} \right) + \sum_{k=1}^4 \overline{F}_{i,j}^k s_{i,j}^k = D_{i,j} \quad (47)$$

The dissipative operator is defined by:

$$D_{i,j} = d_{i+\frac{1}{2},j} - d_{i-\frac{1}{2},j} + d_{i,j+\frac{1}{2}} - d_{i,j-\frac{1}{2}} \quad (48)$$

where the dissipative flux $d_{i+\frac{1}{2},j}$ is given as

$$\begin{aligned} d_{i+\frac{1}{2},j} &= \alpha_{i+\frac{1}{2},j} \epsilon_{i+\frac{1}{2},j}^2 (U_{i+1,j} - U_{i,j}) \\ &- \alpha_{i+\frac{1}{2},j} \epsilon_{i+\frac{1}{2},j}^4 (U_{i+2,j} - 3U_{i+1,j} + 3U_{i,j} - U_{i-1,j}) \end{aligned} \quad (49)$$

Here $\epsilon_{i+\frac{1}{2},j}^2$ and $\epsilon_{i+\frac{1}{2},j}^4$ are adaptative coefficients designed to switch on enough dissipation where it is needed:

$$\epsilon_{i+\frac{1}{2},j}^2 = k^2 \max(\nu_{i+2,j}, \nu_{i+1,j}, \nu_{i,j}, \nu_{i-1,j}) \quad (50)$$

$$\epsilon_{i+\frac{1}{2},j}^4 = \max(0, k^4 - \epsilon_{i+\frac{1}{2},j}^2) \quad (51)$$

where $\nu_{i,j}$ is defined as

$$\nu_{i,j} = \frac{|p_{i+1,j} - 2p_{i,j} + p_{i-1,j}|}{|p_{i+1,j} + 2p_{i,j} + p_{i-1,j}|} \quad (52)$$

and k^2, k^4 are constants (typically 0.5 and 0.015).

The coefficient ϵ^2 is proportional to the second derivative of the pressure and therefore in smooth regions of the flow proportional to the square of the mesh size, while ϵ^4 is of the order one. The dissipative fluxes in the smooth regions are then of third order in comparison to the convective fluxes. However, in the regions where the pressure changes rapidly, the sensor $\nu_{i,j}$ is of order one and with the help of formula (51) the third order difference operator is switched off. The dissipation is then of second order and the finite volume scheme behaves like a first order accurate scheme.

The coefficient $\alpha_{i+\frac{1}{2},j}$ is chosen to give the dissipative term the proper weight:

$$\alpha_{i+\frac{1}{2},j} = \frac{1}{2} \left(\frac{A_{i,j}}{\Delta t_{i,j}^*} + \frac{A_{i+1,j}}{\Delta t_{i+1,j}^*} \right) \quad (53)$$

where $\Delta t_{i,j}^*$ is an estimate of the time step for a unit CFL number.

A fourth order Runge-Kutta scheme is used for the time-stepping, requiring a minimum of computer storage:

$$\begin{aligned} U^0 &= U^{\text{old}} \\ U^1 &= U^{\text{old}} - \Delta t \text{ RHS}^0 / 4 \\ U^2 &= U^{\text{old}} - \Delta t \text{ RHS}^1 / 3 \\ U^3 &= U^{\text{old}} - \Delta t \text{ RHS}^2 / 2 \\ U^4 &= U^{\text{old}} - \Delta t \text{ RHS}^3 \\ U^{\text{new}} &= U^4 \end{aligned} \quad (54)$$

This four-stage scheme is second order accurate for nonlinear problems and allows a maximum CFL number of $2\sqrt{2}$.

4.5. Results.

The method has first been tried starting from the NACA-65 (12A₁₀)10 blade geometry in a cascade defined by a stagger angle of 31 deg and a solidity of 1. A new blade geometry is calculated by imposing a Mach number distribution slightly different from the result of the direct calculation having a lower value of the maximum Mach number on the suction side. The Mach number distribution on the initial blade and the required Mach number distribution are shown on fig. 11a. The flow conditions are: $p_1^0 = 1.33$ bar, $T_1^0 = 341.5$ K, $\beta_1 = 45$ deg, $p_2 = 1.173$ bar.

Figures 11b and 11c show the convergence of the calculated velocity. A good agreement with the required velocity is obtained after 2 geometry modifications only.

The advantages of the method have been demonstrated by solving the same example used previously for vortices, namely the Mach number distribution of an existing geometry (the NACA-65 (12A₁₀)10 blade) has been imposed as the required Mach number distribution, starting from the NACA-65 (12A₁₀)10 blade geometry. The flow conditions and the cascade geometry are the same as for the previous example.

The figure 12a shows the original and the required Mach number distributions. Because of the big difference between both distributions, an under-relaxation factor of 0.5 has been introduced into the first geometry modification, results of which are shown in fig. 12b. The final results (fig. 12c) show a good agreement between the calculated and the prescribed Mach number distribution, except for the trailing edge, because the discretization does not allow to impose a Mach number value at that point.

The third example concerns the redesign of a transonic compressor blade. The NACA-65 (12A₁₀)10 is the original geometry, for which a shock is present on the suction side (fig. 13a and 13b). The flow conditions are: $p_1^0 = 1.33$ bar, $T_1^0 = 341.5$ K, $\beta_1 = 45$ deg, $p_2 = 1.136$ bar. The cascade geometry is defined by a stagger angle of 31 deg and a solidity of 1.25.

The shockless transonic Mach number distribution shown in fig. 13c has been imposed. Figures 13d and 13e show the convergence of the calculated Mach number distribution to the required one. The original and final geometries are compared in fig. 13f.

The fourth example demonstrates the procedure in the design of a turbine blade. The starting geometry is that of the workshop VKI-LS 82-05 (Arts, 1982). The flow conditions are: $p_1^0 = 1$ bar, $T_1^0 = 278$ K, $\beta_1 = 0$ deg, $M_1 = 1.0$. The cascade geometry is defined by a stagger angle of 60 deg and a solidity of 1.25.

A shockless transonic Mach number distribution has been imposed on the suction side (fig. 14a). The calculated mach number distribution converges as close as possible to the required one (fig. 14b and 14c) but not completely, probably because this required distribution does not correspond to a physical geometry. This problem of existence of a solution will be discussed in details in the next chapter.

5. RESTRICTIONS ON THE REQUIRED VELOCITY DISTRIBUTION.

Blade designs in which the required velocity is obtained from the analysis of an existing cascade do not show any particular problem. Under-relaxation is sometimes needed if the required velocity distribution is far from the initial one, but the method rapidly converges to the correct blade shape.

However, solutions for blade designs to be derived from arbitrary suction and pressure side velocity distributions do not always converge. This is related to the problem of the existence of a solution. The required velocity distribution must be compatible with the free stream conditions upstream and downstream of the cascade and must result in a realistic blade profile (closed with a positive thickness). These constraints generate restrictions on the required velocity distribution, analytical expressions for which are available only for incompressible potential flows over isolated airfoils and cascades (Lighthill, 1945, Woods, 1955). Expressions for the constraints cannot be derived for the compressible flow of a perfect gas, but their existence can be inferred from the fact that the incompressible flow case is a subcase of the more general compressible flow problem.

A solution can be obtained by introducing some freedom into the prescribed velocity distribution, expressed by some parameters relating the velocity distribution to the free stream flow conditions. These parameters are then modified until the prescribed velocity distribution corresponds to a physical solution (Volpe and Melnik, 1984).

Another way to obtain a solution is to modify some geometrical parameters of the blades and the cascade such as pitch, stagger and trailing edge thickness.

The modification method presented here should theoretically not suffer from problems with contour intersection because the blade is defined by streamlines. However contour intersections can occur for different reasons:

- the flow distortion is not correctly calculated, due to the incompressible approximation when vortices are used;
- the numerical errors introduced when integrating the streamlines.

One may like to impose some limitations to the cascade such as:

- a minimum trailing edge thickness in order to avoid unrealistic blade geometries,
- a fixed pitch resulting from a given number of blades on the circumference of a stage.

The stagger angle is free and results from the calculation.

Taking into account these limitations there may be no geometry that corresponds to the required velocity distribution. If vortices are used, the calculated velocity will not converge to the required one from one modification to the next. If the required pressure distribution is directly imposed during the normal velocities calculation, the Time Marching procedure will not converge to the required precision since this would imply crossing or diverging streamlines, and it may not be possible to define a geometry where the normal velocity component vanishes. However these methods have the advantage to converge as close as possible to the required pressure distribution.

Experience has shown that some simple restrictions on the desired velocity distribution can be defined. The blockage created by the non zero blade thickness requires the average prescribed velocity at the leading and the trailing edge to be higher than the free stream velocity upstream and downstream of the cascade. Violation of this condition will prevent the method from converging. Increasing or decreasing the average of the required velocity at leading and trailing edges allows the local blade thickness to be increased or decreased. Similar restrictions also apply to the velocity distribution between leading and trailing edges. These are more difficult to formulate because they depend on the local flow direction which is not a priori known.

If an inviscid solver is used, the trailing edge thickness will also include the boundary layer displacement thickness. This boundary layer displacement thickness can be calculated in advance since the required velocity distribution is known. A Navier-Stokes solver can be used together with vortices, for incompressible and non separated flow calculations. Since the velocity at the wall is zero, the vortices should be defined as to correct the free stream velocity, and therefore located outside the boundary layer. In the case of viscous calculations, no displacement thickness has to be removed from the resulting geometry.

Other problems arise from the fact that Time Marching Euler solvers require as downstream boundary condition the static pressure, velocity or Mach number. These outlet conditions can be calculated from the required velocity distribution and the continuity equation before starting the inverse calculations.

The circulation around the blades is calculated from

$$\Gamma = \oint V_t^{\text{req}} ds \quad (55)$$

and is related to the inlet and outlet tangential velocities by

$$\Gamma = (V_2 \sin \beta_2 - V_1 \sin \beta_1)t \quad (56)$$

The downstream axial velocity component is derived from the continuity equation :

$$\rho_1 V_1 \cos \beta_1 = \rho_2 V_2 \cos \beta_2 \quad (57)$$

The density at the outlet is a function of the outlet static pressure and therefore is a function of the unknown outlet velocity V_2 . For this reason, an iterative procedure is used to solve equations (55) to (57). The procedure just described is valid only for irrotational flows and is therefore not exact if shocks are present.

6. CONCLUSION.

Two iterative inverse methods, based on existing direct solvers and on a separated geometry modification algorithm, have been presented. The first one makes use of vortices to calculate the flow distortion which is necessary to respect the required velocity distribution. This method is strictly correct for incompressible flow calculations only, but experience has shown that it can be used successfully for compressible subsonic and even transonic designs. This method, when coupled with an incompressible direct flow solver, is very fast and allowed the accumulation of experience about the problems related to the existence of a solution. A fast convergence to the required velocity distribution is observed and the method has proven to be robust. The method has also been successfully tested, coupled with an Euler direct solver, since the correction is in the right direction and vanishes when the calculated velocity distribution has converged to the required one.

The second method has been developed for subsonic and transonic blade design. The required Mach number distribution is imposed, in terms of static pressure, directly on a permeable blade wall during the flow calculation. This method is much faster than the previous one since the correction is calculated in an more accurate way. Subsonic and transonic designs have been performed and shock free blades have been designed starting from geometries for which a shock was present in the Mach number distribution.

REFERENCES

- ARTS, T., 1982, "Numerical methods for flow in turbomachine bladings", Workshop on 2D and 3D flow calculations in turbine bladings, VKI LS 1982-05.
- BAUER, F., GARABEDIAN, P. and KORN, D., 1972, "Supercritical Wing Sections", Vols. I, Springer-Verlag, New York.
- BAUER, F., GARABEDIAN, P. and KORN, D., 1975, "Supercritical Wing Sections", Vols. II, Springer-Verlag, New York.
- BAUER, F., GARABEDIAN, P. and KORN, D., 1977, "Supercritical Wing Sections", Vols. III, Springer-Verlag, New York.
- GILES, M.B., DRELA, M. and THOMPKINS Jr., W. T., 1985, "Newton Solution of Direct and Inverse Transonic Euler Equations", AIAA paper 85-1530.
- GILES, M.B. and DRELA, M., 1987, "Two-Dimensional Transonic Aerodynamic Design Method", AIAA Journal, Vol. 25, No. 9, pp 1199-1206.
- HICKS, R.M., 1981, "Transonic Wing Design Using Potential Flow Codes - Successes and Failures", SAE Paper 810565.
- JAMESON, A., SCHMIDT, W. and TURKEL, E., 1981, "Numerical Solutions of the Euler Equations by Finite Volume Methods Using Runge Kutta Time Stepping Schemes", AIAA Paper 81-1259.
- LIGHTHILL, J.M., 1945, "A New Method of Two-Dimensional Aerodynamic Design", ARC R&M 2112.
- MEAUZE, G., 1980, "Méthode de calcul aérodynamique inverse pseudo-instantanée", La Recherche Aérospatiale, No. 1, pp 23-30.
- MEAUZE, G., 1982, "An Inverse Time Marching Method for the Definition of Cascade Geometry", Journal of Engineering for Power, Vol. 104, pp 650-656.
- MURUGESAN, K. and RAILLY, J.W., 1969, "Pure Design Method for Airfoils in Cascade", Journal Mechanical Engineering Science, Vol. 11, No. 5, pp 454-465.
- SANZ, J.M., 1983, "Design of Supercritical Cascades with High Solidity", AIAA Journal, vol. 21, No. 9, pp 1289-1293.
- SANZ, J.M., 1984, "Improved Design of Subcritical and Supercritical Cascades Using Complex Characteristics and Boundary Layer Correction", AIAA Journal, vol. 22, No. 7, pp 950-956.
- SANZ, J.M., 1988, "Automated Design of Controlled Diffusion Blades", ASME paper 88-GT-139.
- SCHMIDT, E., 1980, "Computation of Supercritical Compressor and Turbine Cascades with a Design Method for Transonic Flows", Journal of Engineering and Power, Vol. 102, pp 68-74.
- SCHWERING, W., 1970, "Design of Cascades for Incompressible Plane Potential Flows with Prescribed Velocity Distribution", ASME paper 70-GT-57.
- STANITZ, J.D., 1953, "Design of Two-Dimensional Channels with Prescribed Velocity Distributions along the Channel Walls", NACA rep. No. 1115.
- UBALDI, M., 1984, "Un metodo di progetto per profili in schiera basato sulla teoria delle equazioni integrali", AIMETA, VII Congr. Nazionale, Trieste.
- VAN DEN BRAEMBUSSCHE, R., 1984, "The application of the singularity method to blade-to-blade calculations", in "Thermodynamics and Fluid Mechanics of Turbomachinery", NATO Advanced Sciences Institutes Series, series E, Applied Sciences, No 97A, eds A.S. Ucer, P.Stow and Ch. Hirsch, pp. 167-191.
- VAN DEN BRAEMBUSSCHE, R., LEONARD, O. and NEKMOUCHE, L., 1989, "Subsonic and Transonic Blade Design By Means of Analysis Codes", AGARD-CP-463.
- VANDERPLAATS, G.N., 1979, "Approximation Concepts for Numerical Airfoils Optimization", NASA TP-1370.
- VANDERPLAATS, G.N., 1984, "Numerical Optimization Techniques for Engineering Design", Mc. Graw-Hill Book Company.
- VOLPE, G and MELNIK, R E, 1984, "Role of Constraints in Inverse Design for Transonic Airfoils", AIAA Journal, Vol. 22, No 12, pp. 1770-1778.
- ZANNETTI, L. and PANDOLFI, M., 1984, "Inverse Design Technique for Cascades", NASA CR 3836.
- ZANNETTI, L., LAROCCA, F. and MARSILIO, R., 1988, "Euler Solver for 3D Inverse Problems", AIMETTA Congr. Nazionale, Bari.

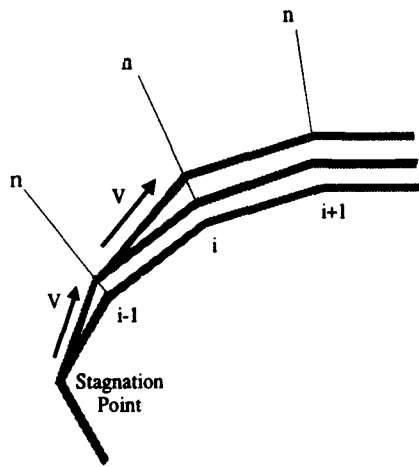
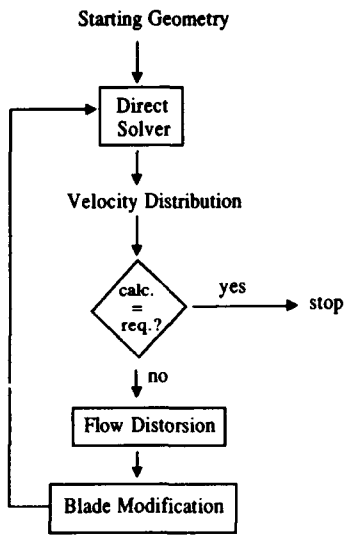


Fig. 3 Blade modification

Fig. 1 Flow chart

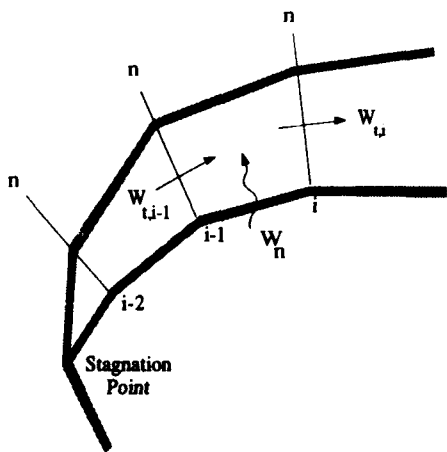


Fig. 2 Blade modification

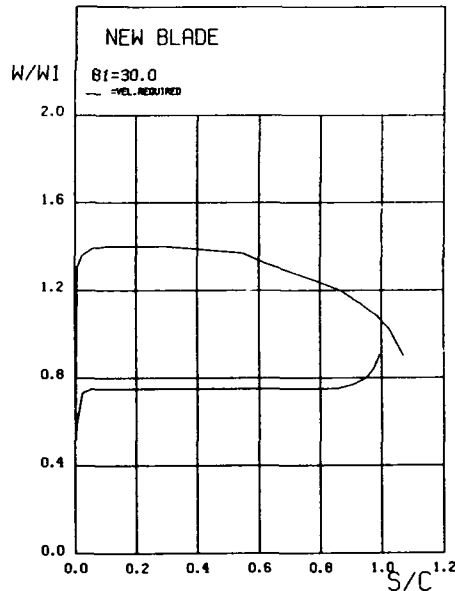


Fig. 4a Required velocity distribution

7-12



NACA65(18A10)10
T/C=0.900 EL=0.0

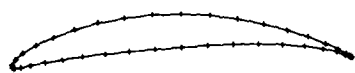


Fig. 4b Initial geometry

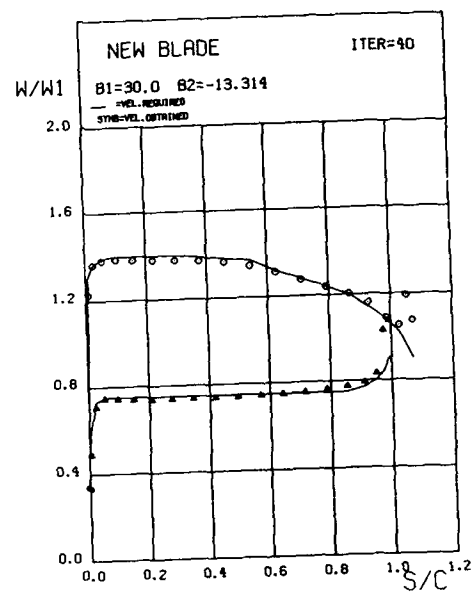


Fig. 4e Final velocity distribution

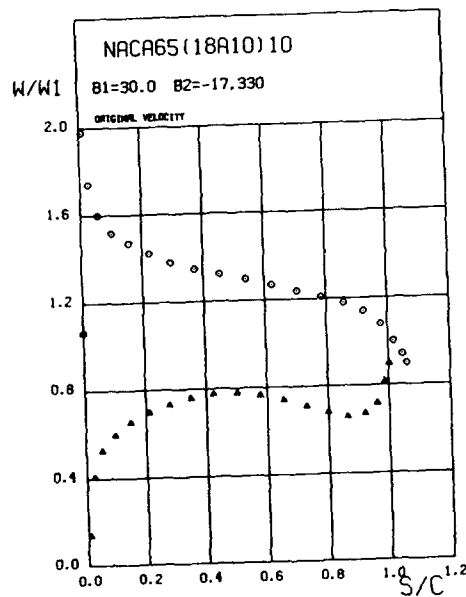


Fig. 4c Initial velocity distribution

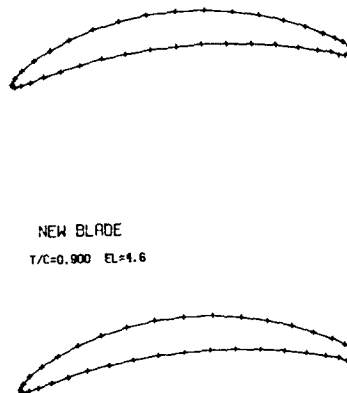


Fig. 4d Final blade geometry

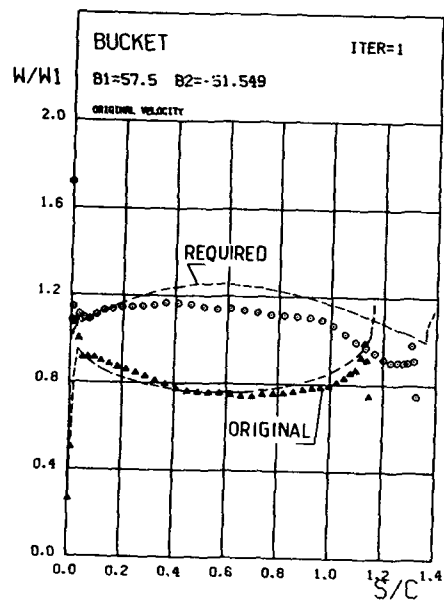


Fig. 5a Initial and required velocity distributions

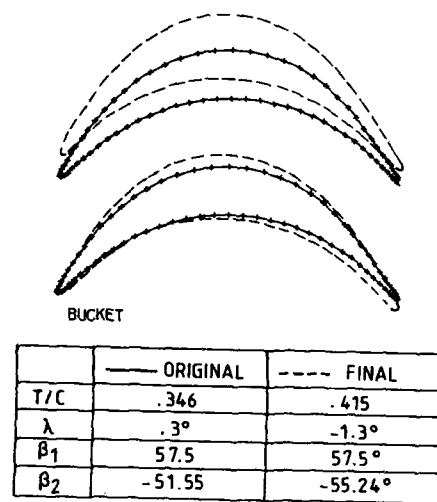


Fig. 5b Initial and final blade geometries

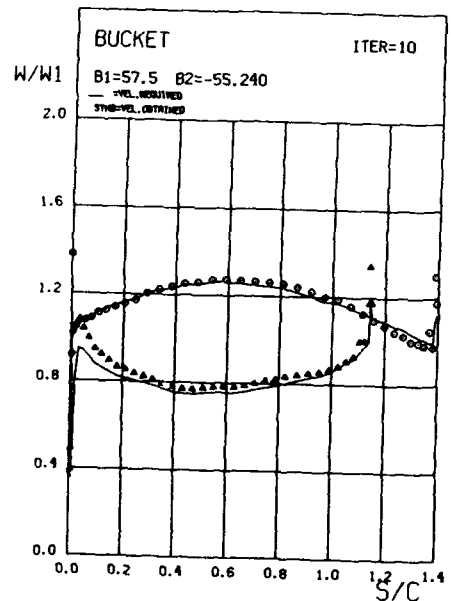


Fig. 5c Final velocity distribution

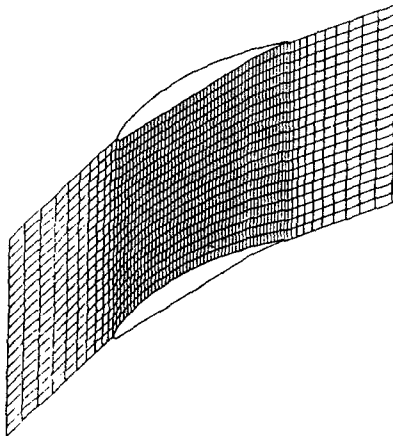


Fig. 6 H-grid discretization

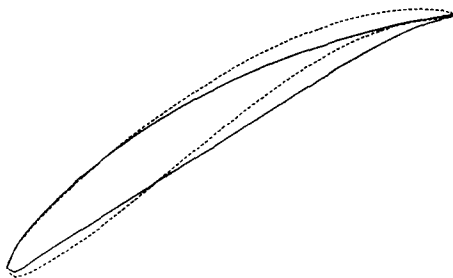


Fig. 7a NACA-65 (12A_{10b})10 (--) and
NACA-65 (12A₁₀)10 (—)

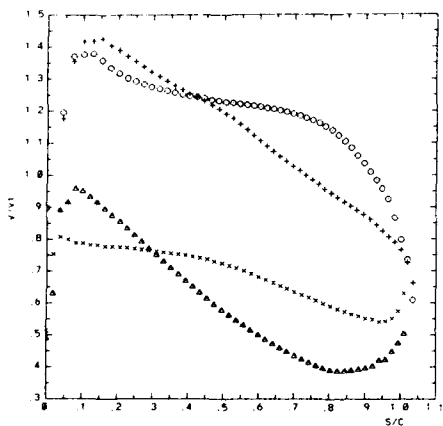


Fig. 7b Initial (+, x) and required (○, △)
velocity distributions

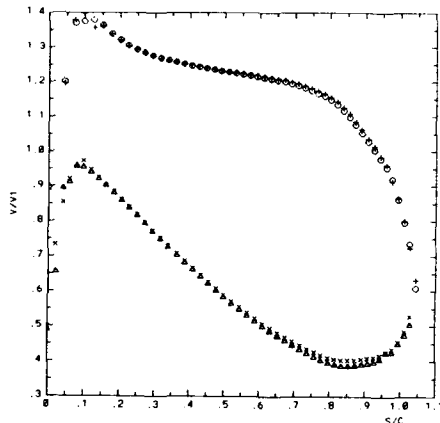


Fig. 7d required velocity (○, △) versus
distribution obtained after 12 modifications (+, x)

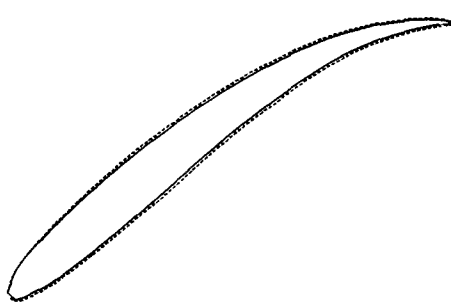


Fig. 7e Final blade shape (---) versus
NACA-65 (12A_{10b})10 (—)

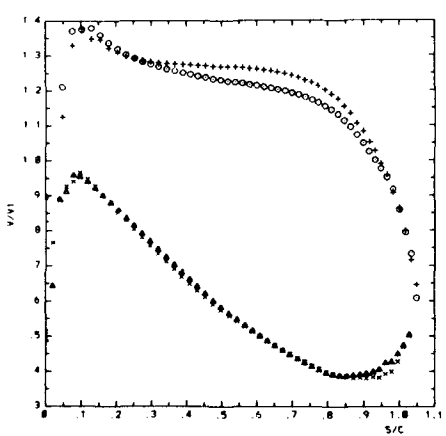


Fig. 7c required velocity (○, △) versus
distribution obtained after 5 modifications (+, x)

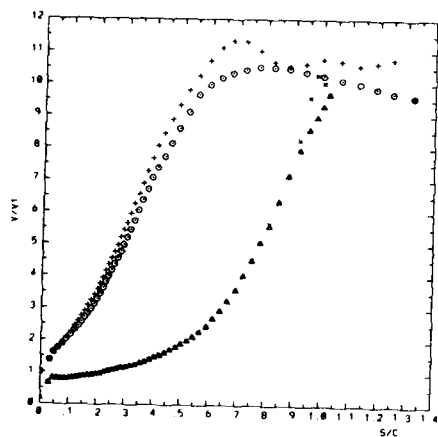


Fig. 8a Initial (+, x) and required (O, Δ) velocity distributions

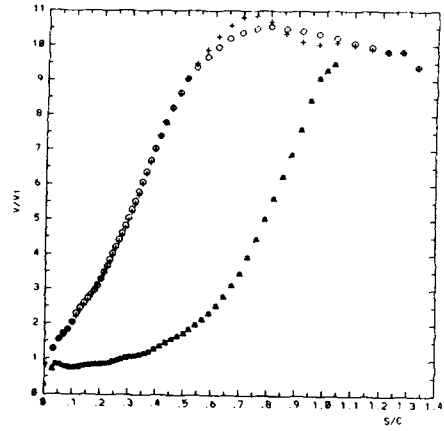


Fig. 8b Velocity distribution after 2 modifications of the pressure side

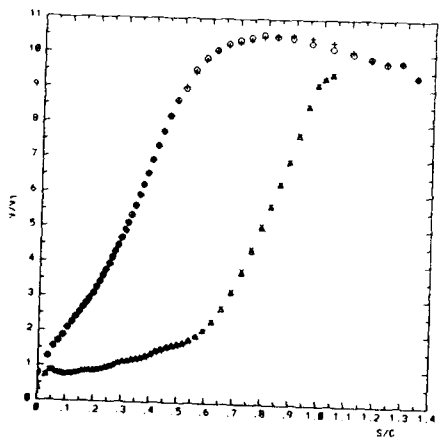


Fig. 8c required velocity (O, Δ) versus velocity distribution obtained after 8 modifications (+, x)

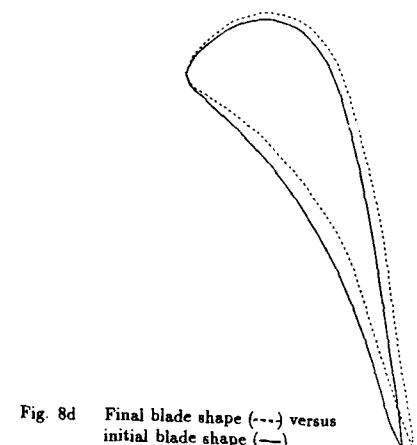


Fig. 8d Final blade shape (---) versus initial blade shape (—)

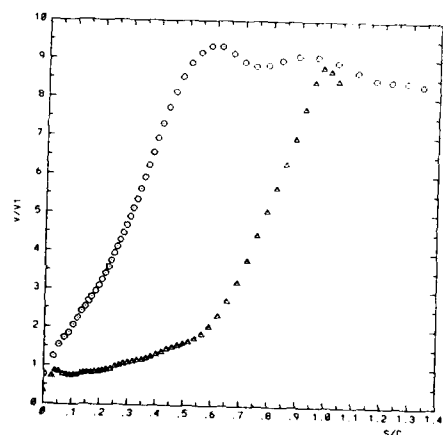


Fig. 9a Off-design velocity distribution ($M_2 = 1$)

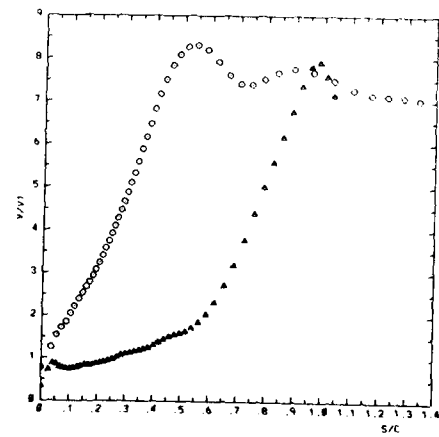


Fig. 9b Off-design velocity distribution ($M_2 = 0.8$)

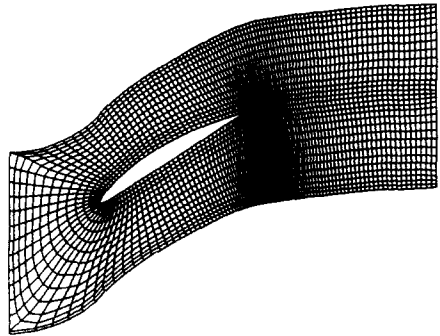


Fig. 10 C-grid discretization

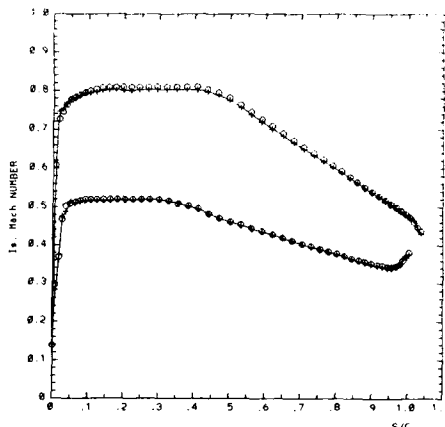


Fig. 11c Calculated (+) and required (○) Mach number distributions after 2 modifications

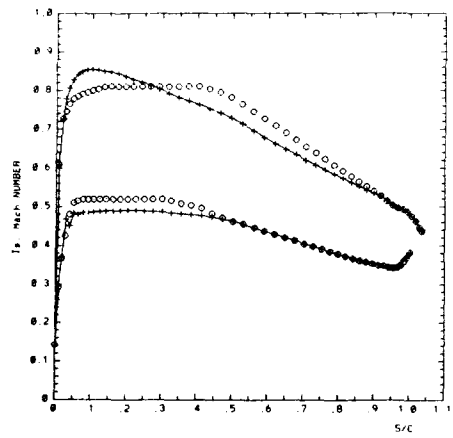


Fig. 11a Initial (+) and required (○) Mach number distributions

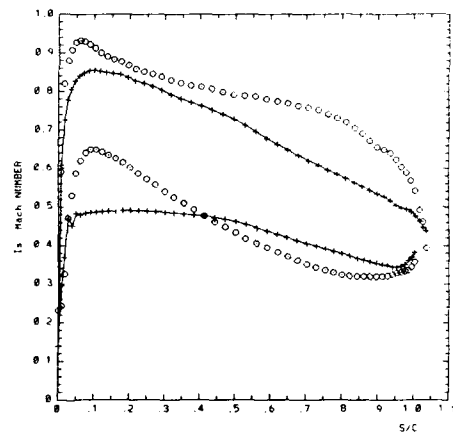


Fig. 12a Initial (+) and required (○) Mach number distributions

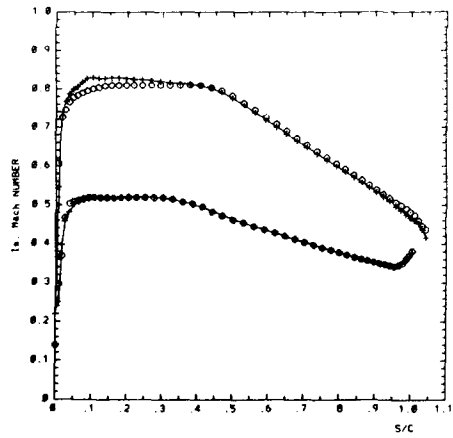


Fig. 11b Calculated (+) and required (○) Mach number distributions after 1 modification

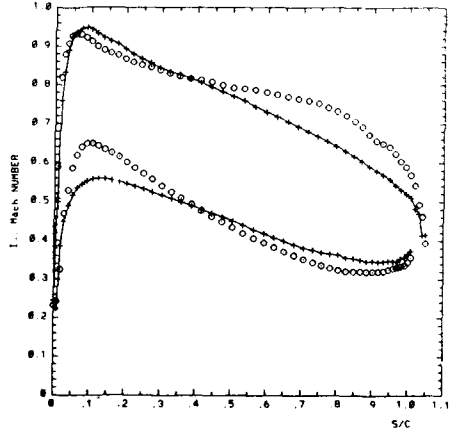


Fig. 12b Calculated (+) and required (○) Mach number distributions after 1 modification

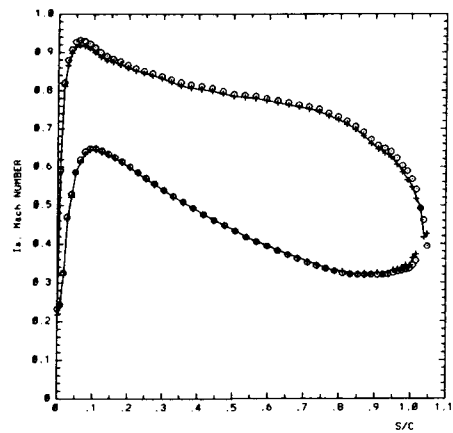


Fig. 12c Calculated (+) and required (○) Mach number distributions after 4 modifications

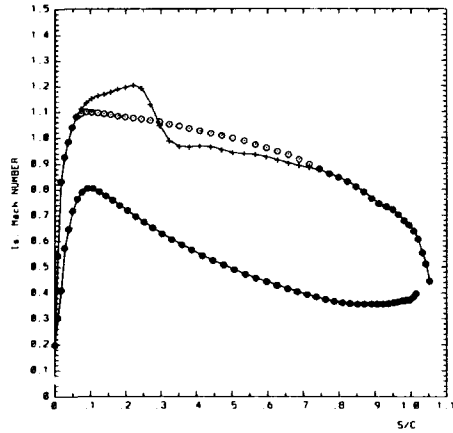


Fig. 13c Initial (+) and required (○) Mach number distributions

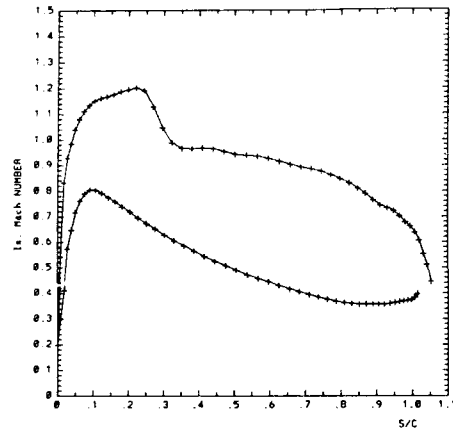


Fig. 13a Original Mach number distribution

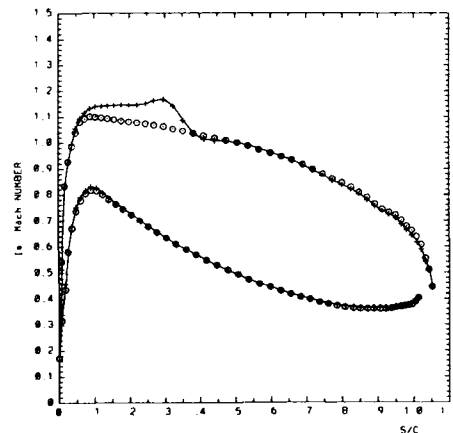


Fig. 13d Calculated (+) and required (○) Mach number distributions after 2 modifications

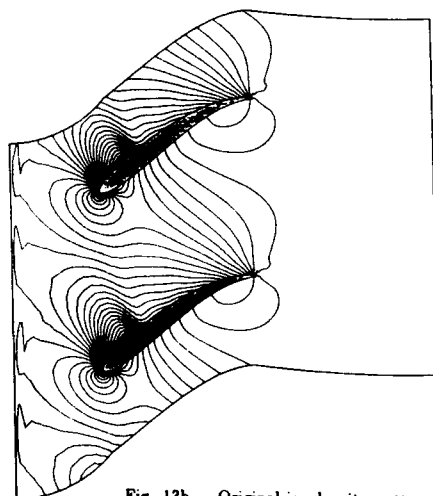


Fig. 13b Original iso-density pattern

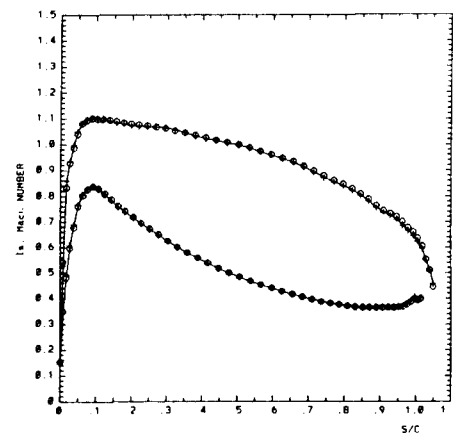


Fig. 13e Calculated (+) and required (○) Mach number distributions after 3 modifications

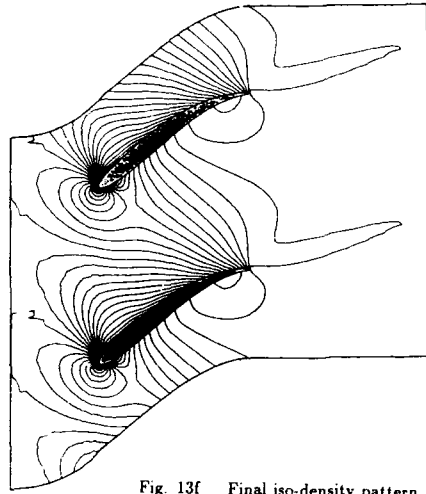


Fig. 13f Final iso-density pattern

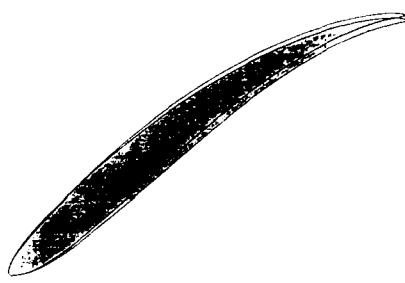


Fig. 13g Original and final geometries

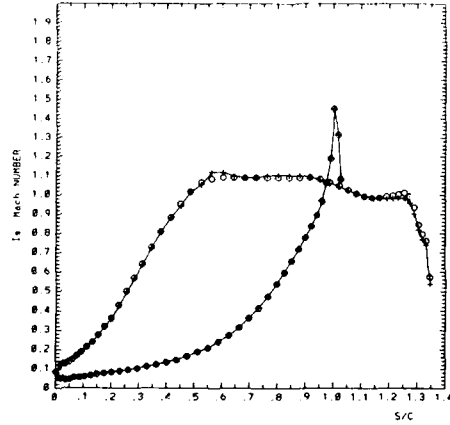


Fig. 14b Calculated (+) and required (○) Mach number distributions after 1 modification

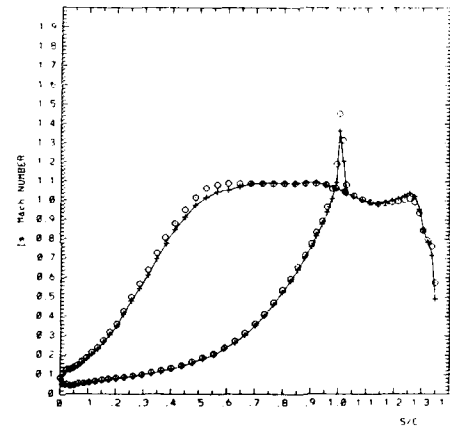


Fig. 14c Calculated (+) and required (○) Mach number distributions after 2 modifications

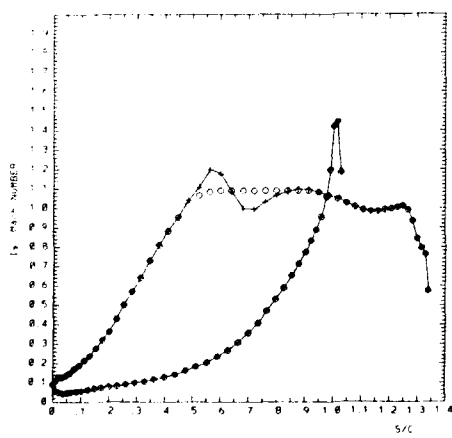


Fig. 14a Initial (+) and required (○) Mach number distributions

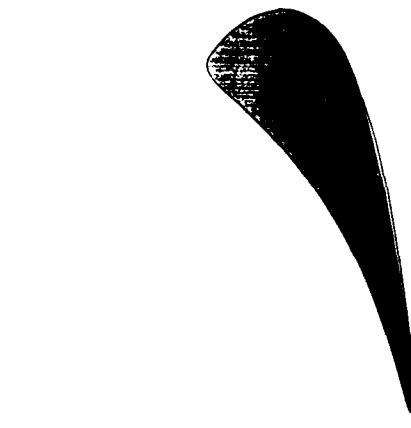


Fig. 14d Original and final geometries

Inverse Methods for 3D Internal Flows

Luca Zannetti
 Politecnico di Torino, Corso Duca degli Abruzzi 24, 10129, Turin, Italy
 Francesco Larocca
 FIAT AVIO, Corso Ferrucci 112, 10129, Turin Italy

Abstract

The objective of this paper is a numerical method for designing three-dimensional ducts and blade rows. The method applies to inviscid compressible rotational flow, and it is based on the time-dependent technique. The walls where the design pressure is prescribed are considered as flexible and impermeable. Starting from some initial guessed configuration, the computation follows the transient which occurs while the flexible walls move and finally reach a steady shape.

1 Introduction

This report describes a methodology to solve inverse design problems for channels and blade rows, assuming the flow to be multidimensional and the fluid inviscid, compressible and ideal. The methodology is based on the procedures described in [1] for the solution of inverse problems in 2D channels, in [2] for 2D inverse cascade problems, in [4] for 3D inverse blade rows problems. An updated version of the methodology is described in [5] for both 2D and 3D inverse problems in channels and blade rows.

The basic idea is described in [1]. Briefly, a time-dependent computation is performed in a duct, where a distribution of pressure is prescribed on a wall, the geometry of which is unknown and has to be determined. Such a wall is a boundary of the flow field and it is assumed as a flexible and impermeable surface. Some initial configuration is guessed for the shape of the wall and for the internal flowfield. During the following transient the flexible wall move in a wavy fashion and, at the end, it will assume the steady shape required by the prescribed pressure on it and in agreement with the steady internal flow.

A coordinate transformation is used in order to map the physical region, whose shape depends on time, into a computational domain, whose shape is independent of time. The Euler equations are integrated in time by a finite difference method on the time-dependent, body fitted, grid defined by the mapping.

Fig. 1 shows one of the possible problems that can be solved. The domain is bounded by the solid wall AB, the flexible wall CD, the entry permeable surface AC, and the exit permeable surface BD. The flexible wall is constrained at the point C, while the point D can move along the exit surface BD.

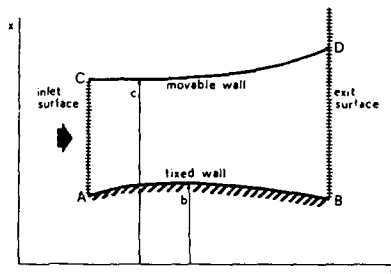


Figure 1: the physical model

Fig. 1 does not represent the only possible configuration, but both impermeable walls may be movable, or be partly movable and partly solid, or be each other constrained by periodicity as in cascade problems. In order to show the way the solution is gained in time, we report here one of the examples of [1]. The Ringleb flow [8] was taken as benchmark case. A set of streamlines $\psi = \text{const}$ of the Ringleb flow are plotted in fig. 2. Once two streamlines are selected, they may be regarded as the solid walls of a channel, and, from the point of view of an inverse problem, the theoretical pressure acting on these may be taken as the design input datum. The chosen channel is in the transonic region, and is confined by the streamlines $\psi = 0.8$, $\psi = 1.0$ and by the radial coordinate lines $\theta = 40^\circ$, $\theta = 90^\circ$.

Fig. 3 shows the shapes of the walls during the transient. Both of them are assumed to be movable. Their shapes at the beginning of the computation ($K = 0$) are taken far from the theoretical ones, while the pressure acting on them is assumed to be the same as the theoretical one and is prescribed as function of the angle θ in the polar frame of reference. At the time step $K = 500$ the walls finally reach the steady location. The solid lines in fig. 3 denote the computed shape of the walls, while the dots are the theoretical locations. The relative error of the computed shape of the walls is plotted in fig. 4, while the relative error of the computed Mach number is shown as isolevel curves in the flowfield, in fig. 5. This example was performed using a 19×47 mesh.

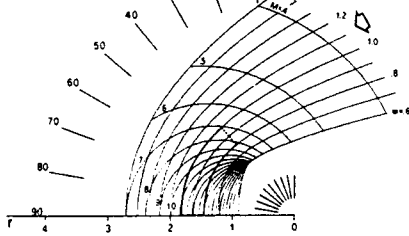


Figure 2: Ringleb flow

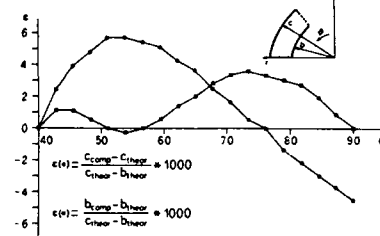


Figure 4: Wall location error

Since [1] was published, several improvements have been done. Upwind numerical schemes have been adopted to attain consistency with the wave propagation phenomena described by the Euler equations, as a consequence the computation at the boundaries has been improved; the extension to 3D problems has been shown feasible; different formulations have been attempted. The path of the evolution we followed runs from [1] to [5].

We describe in section 2 the physical model that we use to solve the inverse problem for 2D cascades of airfoils; we discuss briefly the well posedness of the problem, the boundary conditions, and we show some numerical examples. In section 3 the general numerical procedure to integrate the 3D time-dependent Euler equations is described. In section 4 we show the algorithm that we use to compute the boundaries in the case a 3D duct has to be designed. In section 5 the procedure to design 3D blade rows is presented, and in section 6 numerical examples are shown.

2 The cascade problem

For a 2D cascade of airfoils, the inverse problem consists of finding the geometry of a cascade producing a flow of which some parameters are prescribed. There is a certain freedom in the formulation of the problem. For example, in addition to suitable condition at infinity one may:

- prescribe the distribution of thickness and load along the chord of a profile, and inquire for the geometry of the camber line,
- prescribe the distribution of thickness and pressure on one side of the profile, and again inquire for the geometry of the camber line, or
- prescribe the pressure distribution around the profile and inquire for its geometry.

Novak and Haymann-Haber [13] have given a solution to problem i), based on the Taylor expansion of the equations of the steady motion for a compressible inviscid flow. We solve

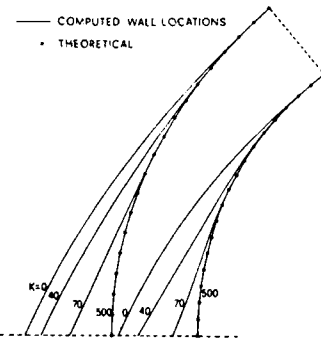


Figure 3: time evolution of the movable walls

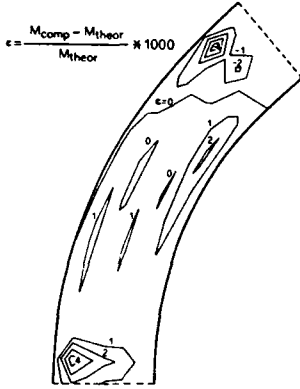


Figure 5: Mach number error

the problems i), ii), iii) by a different technique as briefly outlined in the previous section: time-dependent computation is performed, in which the boundary conditions are imposed according to the formulation of the inverse problem, until a steady state is reached asymptotically. The contours of the blades are considered as impermeable but perfectly deformable. An initial geometry is assumed. Since such a geometry is incompatible with a steady motion, consistent with the prescribed conditions, a transient is generated. During the transient, the walls of the blades change in shape, in order to satisfy the condition of impenetrability as well as the boundary conditions, compatible with problem i), ii), or iii) above. The solution of the inverse problem is given by a geometry obtained asymptotically.

Other approaches to the inverse problem, similar in some aspects to the one described here, have been developed independently in [6] e [7]. However, the formulations of the problem are different from the present one and the methods proposed seem to converge to a solution only if the initial configuration is very close to the solution itself.

A very important point has to be discussed when dealing with inverse problems: the well-posedness of the problem. Problem iii) is discussed in the case of a single airfoil in [14], where it is shown that the design data cannot be prescribed with complete freedom. In fact they must satisfy some constraints which are dictated by the consistency of the data with the flow conditions at infinity and by the requirements that the contour of the airfoil must be closed. The number of constraints depends on the way the inverse problem is formulated. This matter is analytically clear for incompressible potential flow, [15], [16]. Unfortunately, there is not an exhaustive theory capable of prescribing the constraints that lead to a well-posed problem for compressible rotational flow. In [14] a way is provided to circumvent such difficulties, but the suggestion

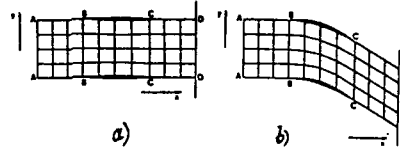


Figure 6:

given there cannot be applied to the present cases, due to the peculiar formulation of the inverse problem.

We address the subject with a different attitude. We use a physical time-dependent technique. If the design data which we impose violate the constraints needed by the steady well-posed problem, we expect the computation never to become steady. Moreover, the well-posedness of a time-dependent formulation also depends on the upstream and downstream boundary conditions, as discussed in [17]. In fact, instabilities can be generated by upstream and/or downstream conditions that, together with conditions prescribed along the blade surfaces, do not allow the flow to get stabilized but, on the contrary, amplify its unsteadiness until the computations blow up. In particular, as discussed in [2], having prescribed a certain downstream pressure, there are two possible solutions to problem i), only one of which is stable from the viewpoint of a time-dependent technique.

Formulation ii) also presents an ambiguous feature which is discussed in [2]. When the pressure distribution is prescribed on one side of the blade, together with its thickness, it cannot be said *a priori* whether that side has to play the role of a suction side or of a pressure side. The computation itself will select the role of the side on which the pressure distribution has been assigned. According to the numerical results shown in [2], the computation selects that side as the pressure side

We confine the discussion in the present report to problems i) for the 2D and 3D cases. The reader may refer to Ref.[2] and Ref.[6] for the discussion of the 2D ii) and iii) problems.

2.1 The physical problem

We proceed now to describe the process, in particular the boundary conditions, that we have chosen to generate the solution, confining ourselves to the physical viewpoint. A more detailed description of our method, based on the theory of hyperbolic systems, is given in the sections 3, 4 and 5, where the 3D problem is discussed.

Figs. 6a) and 6b) show typical initial and final configurations. The flow is assumed to be confined between two consecutive blades, the arcs BC, and two parallel lines issuing from the leading edge and the trailing edge of the blades. The lines in front of the blades are denoted by AB. The lines behind the blades are denoted by CD. Such boundaries are assumed to be impermeable and perfectly deformable; there-

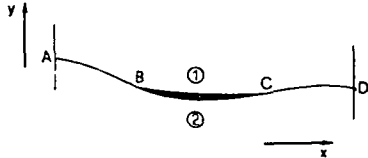


Figure 7:

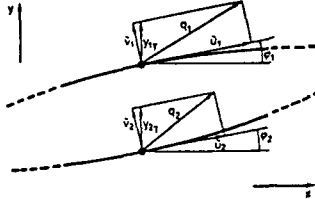


Figure 8:

fore, we can think in terms of a flow within a channel, the geometry of which may change in time, although its width (measured parallel to the y -axis) is independent of time. The channel is confined by the permeable boundaries AA and DD, upstream and downstream, respectively. The inlet boundary AA is considered fixed in time, whereas the exit boundary DD can slide upwards and downwards, maintaining a constant pitch. A time-dependent computational grid, which fits the boundaries, is defined inside the channel.

The design data are prescribed, according to problem i), by giving the distribution of thickness $\tau(z)$ and pressure jump between the two sides of the blades, $\Delta p(z)$. Since the flow is periodic, the upper and lower boundaries of figs. 6 can be reduced to a single boundary for a single blade, as in fig. 7. Note that the upper part of the ABCD line in figs. 6 is the lower boundary in fig. 7, and viceversa.

The arcs, AB and CD are deformable and impermeable interfaces, across which the pressure is continuous but the tangential velocity component may be discontinuous. In formulating the boundary conditions, the whole ABCD arc can be treated homogeneously. The interfaces can be considered as surfaces of blades for which a vanishing thickness and a vanishing pressure jump are prescribed. With this convention in mind, we proceed to describe the technique for any blade surface.

In fig. 8 we show two grid points on two different sides of the blade, at the same abscissa. The velocity vector is decomposed along the tangent and the normal to the blade

at each point. Since the blade is impermeable, the two flow velocities and the blade velocity must have the same normal component. From fig. 8 we see, thus, that:

$$y_{1t} = \frac{\hat{v}_1}{\cos \phi_1}, \quad y_{2t} = \frac{\hat{v}_2}{\cos \phi_2} \quad (1)$$

In addition, the thickness is constant in time; therefore:

$$y_{1t} = y_{2t} \quad (2)$$

The pressure jump, $\Delta p(z)$, is constant in time; consequently:

$$\frac{\partial p_1}{\partial t} = \frac{\partial p_2}{\partial t} \quad (3)$$

Equations (2) and (3) are the boundary condition that allow the geometry and the flow to be updated at each computational step.

At the inlet boundary AA (figs. 6) we prescribe the total pressure, the total temperature and the flow angle, if the flow is subsonic, whereas all the flow quantities are prescribed if the flow is axially supersonic.

At the exit boundary DD no boundary conditions are needed if the flow is axially supersonic, while in the case of subsonic flow, the kind of boundary conditions to be enforced has to be selected carefully, in fact, as it is discussed in the next section, the inverse problem i) has not an uniquely defined solution. The kind of boundary conditions that is used selects one solution among the possible ones.

2.2 Flow deflection and force acting on a blade

With reference to fig. 9, let us consider a subsonic cascade with inlet and outlet boundaries located sufficiently far upstream and downstream, so that the flow at such boundaries does not depend on y .

For the sake of simplicity the flow is considered homentropic, so it is sufficient to prescribe the total temperature, Θ_i^0 , and the flow angle, σ_i , at the inlet boundary. Let us now choose to prescribe the static pressure p_e as downstream boundary condition. In a steady state configuration, the tangential force F acting on one blade is related to the upstream and downstream y -components of the flow velocity:

$$F = \dot{m} (v_e - v_i) \quad (4)$$

On the other hand, F can be determined as a function of the exit flow angle, σ_e , as follows:

a) The exit velocity, q_e , is a known function of Θ_e^0 and p_e :

$$q_e = \sqrt{2c_p(\Theta_e^0 - p_e^{\frac{2-1}{\gamma}})}$$

b) Assume a value of σ_e , the velocity components u_e and v_e are:

$$u_e = q_e \cos \sigma_e \quad v_e = q_e \sin \sigma_e$$

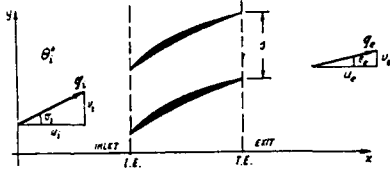


Figure 9:

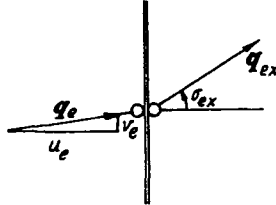


Figure 11:

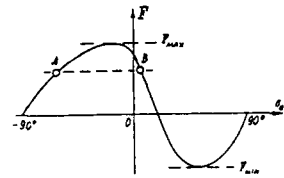


Figure 10:

c) The mass flow can thus be evaluated:

$$\dot{m} = su_e \rho_e \quad \text{with} \quad \rho_e = p_e^{\frac{1}{\gamma}}$$

d) p_e and the inlet velocity components are obtained by solving

$$\dot{m} = s q_i \cos \sigma_i \rho_i$$

where

$$\rho_i = p_i^{\frac{1}{\gamma}}, \quad q_i = \sqrt{2c_p(\Theta_i^0 - p_i^{\frac{\gamma-1}{\gamma}})}$$

and \dot{m} is the same as obtained in c).

e) Now the force F is computed, according to eq. (4)

From a prescribed set of values for Θ_i^0 , σ_i , and p_e , one can compute $F(\sigma_e)$. This relationship is plotted in fig. 10. We see that the F vanishes for three values of σ_e . At $\sigma_e = \pm 90^\circ$, because u_e and, consequently, \dot{m} , vanish. In these two points, the blades are so deflected at the trailing edge, that the flow has no axial velocity component. In addition, F vanishes for $\sigma_e = \sigma_i$, that is, when the blade does not deflect the flow. The force is positive when $\sigma_e < \sigma_i$, and vice versa.

Assume now that the inverse problem has to be solved with a set of boundary conditions (Θ_i^0 , σ_i , and p_e) and a prescribed distribution of load over one blade ($\Delta p(x)$). On the basis of

the previous considerations, two different geometries of the blade may satisfy the problem, or none. The force F results as

$$F = \int \Delta p(x) dx$$

with the integral carried over the x -axis between leading and trailing edge. If $F > F_{max}$ or $F < F_{min}$, no solution exists, but if $F_{min} < F < F_{max}$, two different cascades may be obtained, providing the same force (such as A and B, for example). The same force, thus, may be balanced, according to eq. (4), by a lower mass flow and a larger deflection at point A, or by a higher mass flow and a smaller deflection at B. However, if we prescribe the downstream pressure p_e as exit boundary condition, only the configuration described by point B can be reached.

Let us, indeed, consider a cascade providing an exit angle, σ_e , slightly smaller than $(\sigma_e)_A$, and a steady flow through it, which acts on the blades with a force slightly smaller than F_A . Let us now increase the pressure jump of this initial configuration so that the force reaches the value F_A and, at the same time, let the blade adjust itself to the new condition. Since F_A is larger than the initial force, the curvature of the blade must increase and σ_e decreases instead of increasing towards $(\sigma_e)_A$. Thus, the blade geometry tends to move farther and farther away from A. The opposite motion of the blade occurs if the initial value of σ_e is slightly larger than $(\sigma_e)_A$, and the force, originally greater than F_A , is decreased. In this case, however, the geometry of the blade will eventually reach point B. In conclusion, B represents a stable configuration and it is the only one which can be reached using the numerical procedure and the exit boundary condition, as formulated above.

In order to succeed in obtaining a geometry of the A-type, one should try to make the function $F(\sigma_e)$ single valued. All difficulties, indeed, seem to arise from the fact that different mass flows can provide the same force with different deflections. To achieve our goal, we replace the downstream boundary condition (constant static pressure p_e) by an exit surface modeled in the spirit of Ref. [18]. As shown in fig. 11, a discontinuity is located at the exit boundary, which simulates a guide forcing the flow to be discharged to the right at the prescribed static pressure, p_{ex} , and with the given angle, σ_{ex} .

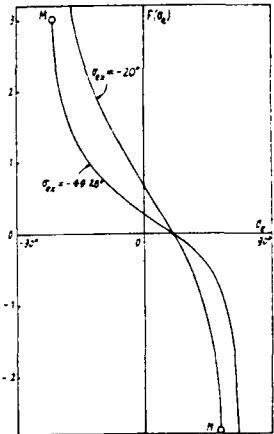


Figure 12:

We assume that the mass flow and total pressure are the same on both sides of the discontinuity:

$$\begin{aligned} \rho_r u_r &= \rho_{rx} q_{rx} \cos \sigma_{rx} \\ \rho_r &= p_r^{\frac{1}{\gamma}}, \quad \rho_{rx} = p_{rx}^{\frac{1}{\gamma}} \\ p_r^{\frac{x-1}{2}} + \frac{1}{2 c_p} (u_r^2 + v_r^2) &= p_{rx}^{\frac{x-1}{2}} + \frac{1}{2 c_p} q_{rx}^2 \end{aligned} \quad (5)$$

Eqs. (5), p_{rx} , σ_{rx} are the downstream boundary conditions that define a unique solution to the inverse problem. In fact, once the steady state is reached, the relationship $F(\sigma_e)$ can be found:

a) from p_{rx} and σ_{rx} , the mass flow is computed:

$$m = \rho_r q_{rx} \cos \sigma_{rx} \quad \text{with} \quad q_{rx} = \sqrt{2 c_p (p_r^{\frac{x-1}{2}} - p_{rx}^{\frac{x-1}{2}})}$$

b) and from the computed values of u_r and v_r , we get:

$$\sigma_r = \arctan \frac{v_r}{u_r}$$

The function $F(\sigma_r)$ is now monotonic, as shown in fig. 12. The curve is limited by two points, M and N. For $\sigma_r < \sigma_r M$ and $\sigma_r > \sigma_r N$ it is no longer possible to maintain the same mass flow required by p_{rx} and σ_{rx} . If a force is prescribed, such that $F_M < F < F_N$, there is only one acceptable geometry which can be shown to be stable, using an argument similar to the one employed above.

A more detailed discussion and several numerical examples on this matter are presented in Ref.[2]. In particular, the

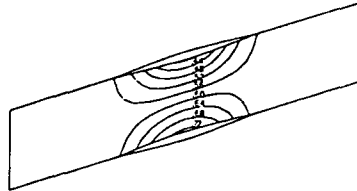


Figure 13:

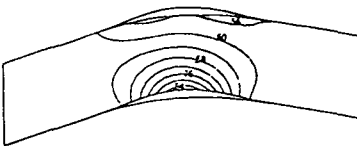


Figure 14:

effectiveness and limitation of the second kind of exit boundary conditions on producing high cambered airfoils is shown. Briefly, we suggest the following recipe: if the design point is located on the stable branch of fig. 10, then it is safe and simple to enforce the downstream pressure, p_r , as exit boundary condition; whereas, if the design point is in the unstable branch, the second kind of exit boundary condition has to be used, but some instability may still be experienced, as shown in [2], especially when dealing with strongly cambered blades.

2.3 2D numerical example

Two numerical examples are here presented according to formulation i) and prescribing the static pressure p_r as exit boundary condition. Further examples are shown in Ref. [2].

Fig. 13 shows the initial configuration and fig. 14 the steady solution to the inverse problem for the case corresponding to

$$r = .025 [1 - \cos(2\pi x)] \quad (0 < x < 1)$$

$$\Delta p = .1 [1 - \cos(2\pi x)] \quad (0 < x < 1)$$

The ratio p_r/p^* between downstream pressure and total pressure is 0.8, the upstream flow angle σ_r is 20° , and the upstream total temperature Θ^* is 1. Both this case and the following one have been computed using 40 intervals in x and 10 in y .

A check on the accuracy of the computation is shown in fig. 15, where the theoretical behavior of the y -momentum is compared with the numerical result. The maximum error is less than 1%.

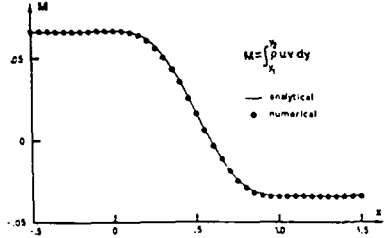


Figure 15:

equations, avoiding the need for spurious additional numerical boundary conditions. This point is crucial for the success of our method, in fact the computation in a domain whose physical shape depends on the solution is very sensitive to the way the boundary condition are enforced and any wrong treatment may produce catastrophic instabilities. Details on this matter can be found in [11].

Moreover, the inverse problems that generally one asks to be solved are shockless and the need for shock-capturing capability is rare; if this capability is requested, the scheme can be easily converted in a conservative Flux Vector Splitting scheme, as described in [12].

Let us take into consideration the more general 3D case, we denote by y^n , ($n = 1, \dots, 4$), the cartesian coordinate in the Euclidean space-time four-dimensional space, E^4 , reserving the apex 4 to denote time. Let us denote by x^n , ($n = 1, \dots, 4$), a curvilinear frame of reference in E^4 , whose transformation from the Cartesian coordinates has the form:

$$\begin{aligned} x^{n'} &= x^n(y^n) \quad (n = 1, \dots, 3) \quad (n = 1, \dots, 4) \\ x^4 &= y^4 \end{aligned} \quad (6)$$

The mapping (6) is sufficiently general to define the curvilinear, time-dependent, body-fitted grid we use to discretize the physical domain in our inverse method. Moreover, we define a vector \mathbf{Q} in E^4 , whose (contravariant) components Q^α ($\alpha = 1, \dots, 3$) coincide with the components of the flow velocity \mathbf{q} and whose time component is constant and equal to one, $Q^4 = 1$. With such assumptions, the Euler equations can be written in a form invariant for transformations with the form (6). According to tensor notations, the 3D time-dependent Euler equations can be written as:

$$\begin{aligned} Q^n a_n + \delta a Q_{,n}^\alpha &= 0 \\ Q^n Q_{,n}^\alpha + a \left(\frac{\alpha p}{\delta} - \kappa s_{,\alpha} \right) g^{n\beta} &= 0 \\ Q_{,n}^\alpha s_{,\alpha} &= 0 \end{aligned} \quad (7)$$

where latin indexes run from 1 to 4, greek indexes run from 1 to 3, " denotes tensor derivative, a is the speed of sound, $\delta = 2/(\gamma - 1)$, $\kappa = a/(2\gamma\delta)$, γ is the specific heats ratio and $g^{n\beta}$ is the metric tensor and all the variables are normalized with respect to suitable reference values.

Following Ref. [11], eqs. (7) can be rearranged in a form suitable for upwind discretization by decomposing the 3D unsteady motion as due to waves fronts parallel to the coordinate surfaces; the resulting set of equations prompts an upwind discretization that preserves the 3D nature of the actual flow and that is particularly convenient from the point of view of the treatment of the boundaries:

$$\begin{aligned} a_4 &= \frac{\delta}{2} [\xi_d + \xi_r + \eta_d + \eta_r + \zeta_d + \zeta_r] + \delta \kappa s_4 \\ Q_{,4}^1 &= \frac{1}{2} \left\{ \sqrt{g^{23}} \left[2\eta_r + \frac{g^{21}}{g^{22}} (\eta_r - \eta_d) \right] + \right. \\ &\quad \left. \sqrt{g^{11}} [\xi_r - \xi_d] + \sqrt{g^{33}} \left[2\zeta_d + \frac{g^{23}}{g^{33}} (\zeta_r - \zeta_d) \right] \right\} \end{aligned}$$

The case of fig. 16 has the same r , σ_1 , and Θ' as in the preceding case, but

$$\Delta p = .15[1 - \cos(2\pi x)] \quad (0 < x < 1)$$

and $p_r/p'' = 0.71$.

The resulting cascade is supercritical but unchoked and shockless. It can be seen from the isoMach lines of fig. 16 that a supersonic bubble appears on the upper side of the blade, but the lower side is entirely subsonic. The pressure cannot be discontinuous on the subsonic side; therefore, it must be continuous on the supersonic side as well, since Δp is prescribed as a continuous function of x .

3 The general numerical procedure

The numerical process we use is a variation of the *lambda*-scheme [9] and, more generally, it can be considered as belonging to the SCM [10] family. It exploits the hyperbolic nature of the Euler equations, which are discretized according to an upwind finite difference scheme. The scheme we use approximates the governing equations written in quasi-linear form, as a consequence it is not conservative and weak solutions are not captured spontaneously, but they need some special treatment. This shortcoming is the price to be paid for the main advantage that our numerical process offers: the capability of computing the boundaries in a way consistent with domain of dependence due to the hyperbolic nature of the governing

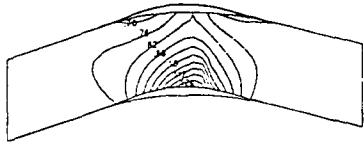


Figure 16:

$$(8) \quad Q_A^2 = \frac{1}{2} \left\{ \sqrt{g^{11}} \left[2\xi_b + \frac{g^{12}}{g^{11}} (\xi_c - \xi_d) \right] + \sqrt{g^{22}} [\eta_c - \eta_d] + \sqrt{g^{33}} \left[2\xi_c + \frac{g^{31}}{g^{33}} (\zeta_r - \zeta_s) \right] \right\}$$

$$Q_A^2 = \frac{1}{2} \left\{ \sqrt{g^{11}} \left[2\xi_r + \frac{g^{12}}{g^{11}} (\xi_c - \xi_d) \right] + \sqrt{g^{22}} \left[2\eta_r + \frac{g^{23}}{g^{22}} (\eta_c - \eta_d) \right] + \sqrt{g^{33}} [\zeta_r - \zeta_d] \right\}$$

$$\xi_a = \xi_a + \eta_a + \zeta_a$$

The terms ξ_a, η_a, ζ_a in eqs. (8) are relative to waves fronts parallel to $x^1 = \text{const.}, x^2 = \text{const.}, x^3 = \text{const.}$ surfaces, propagating with the speeds λ_a, Φ_a, μ_a , respectively:

$$\begin{aligned} \xi_a &\approx -\lambda_a s_1 & \lambda_a &= Q^1 \\ \xi_b &= -\lambda_b \left(\frac{Q_{,1}^2}{\sqrt{g^{11}}} - \frac{g^{12}}{g^{11}} \frac{Q_{,1}^1}{\sqrt{g^{11}}} \right) & \lambda_b &= Q^1 \\ \xi_c &= -\lambda_c \left(\frac{Q_{,1}^2}{\sqrt{g^{11}}} - \frac{g^{12}}{g^{11}} \frac{Q_{,1}^1}{\sqrt{g^{11}}} \right) & \lambda_c &= Q^1 \\ \xi_d &= -\lambda_d \left(\frac{a_1}{\delta} - \kappa s_{,1} + \frac{Q_{,1}^1}{\sqrt{g^{11}}} \right) & \lambda_d &= Q^1 + a\sqrt{g^{11}} \\ \xi_r &= -\lambda_r \left(\frac{a_1}{\delta} - \kappa s_{,1} - \frac{Q_{,1}^1}{\sqrt{g^{11}}} \right) & \lambda_r &= Q^1 - a\sqrt{g^{11}} \\ \eta_a &= -\Phi_a s_{,2} & \Phi_a &= Q^2 \\ \eta_b &= -\Phi_b \left(\frac{Q_{,2}^2}{\sqrt{g^{22}}} - \frac{g^{23}}{g^{22}} \frac{Q_{,2}^3}{\sqrt{g^{22}}} \right) & \Phi_b &= Q^2 \\ \eta_c &= -\Phi_c \left(\frac{Q_{,2}^2}{\sqrt{g^{22}}} - \frac{g^{23}}{g^{22}} \frac{Q_{,2}^3}{\sqrt{g^{22}}} \right) & \Phi_c &= Q^2 \\ \eta_d &= -\Phi_d \left(\frac{a_2}{\delta} - \kappa s_{,2} + \frac{Q_{,2}^3}{\sqrt{g^{22}}} \right) & \Phi_d &= Q^2 + a\sqrt{g^{22}} \\ \eta_r &= -\Phi_r \left(\frac{a_2}{\delta} - \kappa s_{,2} - \frac{Q_{,2}^3}{\sqrt{g^{22}}} \right) & \Phi_r &= Q^2 - a\sqrt{g^{22}} \\ \zeta_a &\approx -\mu_a s_{,3} & \mu_a &= Q^3 \\ \zeta_b &= -\mu_b \left(\frac{Q_{,3}^2}{\sqrt{g^{33}}} - \frac{g^{31}}{g^{33}} \frac{Q_{,3}^1}{\sqrt{g^{33}}} \right) & \mu_b &= Q^3 \\ \zeta_c &= -\mu_c \left(\frac{Q_{,3}^2}{\sqrt{g^{33}}} - \frac{g^{31}}{g^{33}} \frac{Q_{,3}^1}{\sqrt{g^{33}}} \right) & \mu_c &= Q^3 \\ \zeta_d &= -\mu_d \left(\frac{a_3}{\delta} - \kappa s_{,3} + \frac{Q_{,3}^1}{\sqrt{g^{33}}} \right) & \mu_d &= Q^3 + a\sqrt{g^{33}} \\ \zeta_r &= -\mu_r \left(\frac{a_3}{\delta} - \kappa s_{,3} - \frac{Q_{,3}^1}{\sqrt{g^{33}}} \right) & \mu_r &= Q^3 - a\sqrt{g^{33}} \end{aligned} \quad (9)$$

The terms ξ_a, η_a, ζ_a , roughly speaking, express quantities carried by the waves in the unsteady motion, in a numerical process they have to be approximated by an upwind numerical scheme to preserve correctly the domain of dependence of the compute points. A more rigorous analysis about our numerical approximation of hyperbolic equations is attempted in [11].

The numerical scheme we use is explicit, second order accurate in time and space. Let us describe the scheme we use for the case of a scalar advection equation, being obvious the extension to eqs.(8):

$$u_t = \xi \quad \text{with} \quad \xi = -\lambda u_x \quad (10)$$

The scheme is a two step predictor-corrector scheme:
predictor:

$$u_k^{n+1/2} = u_k^n + \xi_k^n \frac{\Delta t}{2} \quad (11)$$

with $\xi_k^n = -\lambda_k^n \frac{(u_j^n - u_{j-1}^n)}{\Delta x}$

corrector:

$$\begin{aligned} u_k^{n+1} &= u_k^{n+1/2} + \xi_k^{n+1/2} \frac{\Delta t}{2} \\ \xi_k^{n+1/2} &= -\lambda_k^{n+1/2} \left[2(u_j^{n+1/2} - u_{j-1}^{n+1/2}) - \frac{\xi_{j-1}^n}{\lambda_{j-1}^n} \right] \frac{\Delta t}{2} \\ \text{with } h &= \frac{\Delta x}{\|\lambda_h\|} \quad j = k + \frac{12-h}{2} \end{aligned}$$

In order to simplify the computation and to improve the accuracy, we prefer to avoid explicit evaluation of Christoffel symbols when computing the tensor derivatives of the vector Q . In fact, a tensor derivative has the general form:

$$Q_{,m}^k = \frac{\partial Q^k}{\partial x^m} + Q^n \Gamma_{nm}^k \quad (12)$$

The balancing in (12) of the partial derivative, approximated by one-sided differences, and the Christoffel symbol Γ_{nm}^k , evaluated on nodes, is quite delicate. We prefer to base our approximation on the formula:

$$Q_{,m}^k = \frac{\partial U^j}{\partial x^m} \frac{\partial x^k}{\partial y^j} \quad (13)$$

where U^j are the Cartesian components of Q and the derivatives $\frac{\partial U^j}{\partial x^m}$ are approximated by finite differences, according to the integration scheme (11).

It is also convenient to integrate in time the Cartesian components of Q , getting their derivatives in time from eqs. (8) and the formula:

$$\frac{\partial U^k}{\partial x^4} = Q_{,4}^j \frac{\partial y^k}{\partial x^j} \quad (14)$$

avoiding again the evaluation of Christoffel symbols.

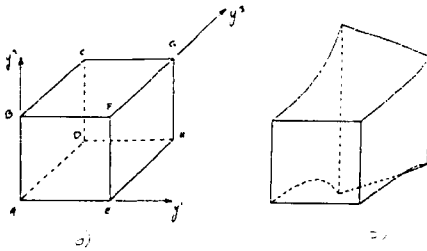


Figure 17:

4 The computation at the boundaries

The numerical process that we follow to solve 3D inverse problems is based on physical models that are straight forward extension of the 2D model of Ref. [1], for the case of ducts, and of Ref. [2], briefly described in section 2, for the case of blade rows. The idea is shown in figs. 17a) and 17b) for the case of a 3D duct: a channel is considered whose side walls are partly (or entirely) flexible and impermeable and partly solid. For instance, the walls ABCD and EFGH of fig. 17a) are solid, the walls BFGC and AEHD are flexible and impermeable, ABFE is a permeable inlet surface and DHGC is a permeable exit surface. The inlet and the exit surfaces are $y^3 = \text{const.}$ plane surfaces, the equations of the solid surfaces are:

$$\begin{aligned} ABCD : \quad y^1 &= b(y^2, y^3) \\ EFGH : \quad y^1 &= c(y^2, y^3) \end{aligned} \quad (15)$$

The equations defining the flexible walls are:

$$\begin{aligned} AEHD : \quad y^2 &= d(y^1, y^3, y^4) \\ BFGC : \quad y^2 &= e(y^1, y^3, y^4) \end{aligned} \quad (16)$$

The coordinate transformation:

$$\begin{aligned} x^1 &= \frac{(y^1 - b)}{(c - b)} \\ x^2 &= \frac{(y^2 - d)}{(e - d)} \\ x^3 &= y^3 \\ x^4 &= y^4 \end{aligned} \quad (17)$$

is used to define a time-dependent grid that fits the walls and adapts itself to the motion of the flexible walls.

The design pressure distributions $p = p'(y^1, y^3)$ are prescribed over the flexible walls; total temperature, entropy and flow direction are prescribed at the inlet surface, static pressure is prescribed at the exit surface in case of subsonic flow, while all the flow properties are prescribed at the inlet surface and nothing is prescribed at the exit surface when the flow is supersonic; the vanishing of the normal component of the flow velocity is imposed on solid walls. With such boundary conditions a time dependent computation is performed over the x^1 grid, according to the numerical scheme described on the previous section. Fig. 17b), for instance, shows the shape that the channel has at the end of the transient, solving the inverse problem for the prescribed pressure distributions over the flexible walls.

As mentioned above, the enforcement of the boundary conditions is the most delicate operation of the numerical process. We use the same general idea of [1]: at each boundary a certain number of ξ , or η , or ζ , expresses the propagation of signals coming inward from the boundary, such terms depend on the boundary conditions and are independent of the internal flow field. In the numerical process, they cannot be computed according to eqs. (11), but they must be computed enforcing some boundary conditions. The number of boundary conditions needed by the finite difference equations (FDE) does not necessarily match the number of boundary conditions needed by the partial differential equations (PDE); if the boundary conditions needed by the FDE outnumber the boundary conditions needed by the PDE some additional numerical boundary conditions must be enforced. It is quite obvious that an algorithm that asks always the same boundary conditions for the FDE as for the PDE is optimal, this is the case of the scheme (11) applied to eqs. (8).

Let us consider, for instance the ABCD surface of Figs. 17a), 17b). At this boundary, the ξ , related to positive speeds of propagation, $\lambda_s > 0$, have to be computed enforcing the boundary conditions. The ABCD surface is a solid wall, the physical boundary condition is the vanishing of the normal component of the flow velocity, that is:

$$Q^1 = 0 \quad (18)$$

There is one positive speed of propagation in x^1 direction: λ_d , as a consequence there is one term, ξ_d , to be evaluated enforcing eq. (18). Let us differentiate in time eq. (18) and then integrate it numerically in time, with the same time step, $\frac{\Delta x^1}{2}$, which is used by the scheme (11) at the predictor and corrector step. With this process in mind, the boundary condition (18) is given by the equation:

$$\left(U^1 + \frac{\partial U^1}{\partial x^4} \frac{\Delta x^4}{2} \right) \frac{\partial x^1}{\partial y^1} = 0 \quad (19)$$

where the contravariant component of the velocity, Q^1 has been expressed by means of the cartesian components U^1 .

By substituting eqs. (14) and (8) in eq. (19) we obtain one algebraic equation in one unknown, ξ_d , which satisfies eq. (18) in both predictor and corrector steps of the integration scheme (11).

Any boundary can be computed following the same idea: differentiate in time the boundary conditions, integrate them

in time, consistently with the scheme (11), substitute them in the governing equations (8), and get as many equations as many are the ξ , η , ζ , unknown at the boundary. In [11] it is shown that this procedure is consistent with the characteristic theory for 1D flow and, more generally, with the wave reflection concept in multidimensional flow.

Let us consider now a moveable wall, for instance the AEHD surfaces of Figs. 17a), 17b). At this boundary the η , with positive Φ , have to be assumed as unknowns to be evaluated by means of the boundary conditions. There is again one unknown, η_d and one boundary condition: the pressure is prescribed as a given function of time, $p = p(x^4)$, (generally it is prescribed to be constant in time). We satisfy the boundary condition by enforcing, in the predictor and corrector steps, that at each boundary point:

$$p(x^4) + \frac{\gamma p}{a} \left(\frac{\partial a}{\partial x^4} \frac{1}{\delta} - \kappa \frac{\partial s}{\partial x^4} \right) \frac{\Delta x^4}{2} = p \left(x^4 + \frac{\Delta x^4}{2} \right) \quad (20)$$

where

$$\frac{\gamma p}{a} \left(\frac{\partial a}{\partial x^4} \frac{1}{\delta} - \kappa \frac{\partial s}{\partial x^4} \right) = \frac{\partial p}{\partial x^4}$$

By substituting eqs. (8) in eq. (20), we get one equation that allows the unknown η_d to be computed.

At each predictor and corrector step we update the geometry of the wall, given in general form by eq. (16), by means of the eq.:

$$d \left(y^1, y^3, y^4 + \frac{\Delta y^4}{2} \right) = d(y^1, y^3, y^4) + \frac{\partial d}{\partial y^4} \frac{\Delta y^4}{2} \quad (21)$$

where the derivative $\frac{\partial d}{\partial y^4}$ is expressed by the condition of impermeability of the wall: at a moving wall, as well as at a fixed wall, the contravariant component normal to the wall of the vector \mathbf{Q} has to be zero, $Q^2 = 0$. In fact, let us consider the wall AEHD, whose geometry is defined by the first of eqs. (16). This wall is the coordinate surface $x^2 = 0$, as it can be deduced from the second of eqs.(17). Because of the impermeability of the wall and because of the continuity of the fluid, a fluid particle which is on the wall, has to move without leaving the wall, that is preserving its coordinate $x^2 = 0$, that is with $Q^2 = 0$. By definition of contravariant component, it is:

$$Q^2 = \mathbf{Q} \cdot \nabla x^2 = U^j \frac{\partial}{\partial y^j} (y^2 - d) \quad (22)$$

Enforcing $Q^2 = 0$ and considering that $U^4 = 1$, from eq. (22) it follows:

$$\frac{\partial d}{\partial y^4} = U^1 - U^n \frac{\partial d}{\partial x^n} \frac{\partial x^n}{\partial y^4} \quad (n = 1, 3) \quad (\alpha = 1, 2, 3) \quad (23)$$

In computing eq. (23), $\partial d / \partial x^n$ are approximated by finite differences.

The other solid or moveable walls are computed in the same way, once the proper unknown terms ξ , or η , are detected.

The corner lines common to solid and moveable walls, as for instance the line AD of Figs. 1a), 1b), are computed by using both the boundary conditions (19) and (20).

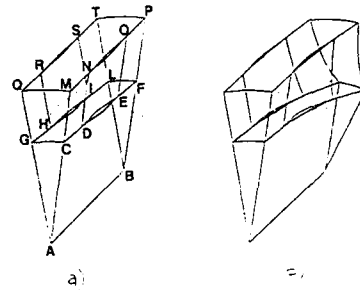


Figure 18:

The inlet and outlet boundaries are computed following the same general idea: the boundary conditions are written in numerical integral forms, as eq. (19) for solid walls or eq. (20) for moveable walls, the resulting set of algebraic equations, obtained by substituting eqs. (8), allows the proper unknown terms ζ , to be determined.

5 Design of 3D blade rows

The method for designing 3D blade to blade channels is similar to the method for designing 3D ducts. We use the same set of equations (8) and we formulate the problem in the same way: as shown in Figs.18a) and 18b), we take into consideration a channel whose walls GLTQ and CFPM are impermeable and deformable, with DEON and HISF representing the suction and pressure sides of the blades, respectively. The surfaces GCFL and QMPT are the annulus solids walls, the surface GCMQ is the inlet surface and LFPT is the outlet surface. Fig. 18a) shows a typical initial configuration and Fig. 18b) the shape of the channel solving a given inverse problem.

There are two differences between the method of solution of inverse problems in ducts and in blade to blade channels, the first one concerning the mathematical model and the second one concerning the formulation of the inverse problem:

- Because of the geometry of blade rows, it is more convenient to use as physical frame of reference a sort of 4D cylindrical coordinates instead of Cartesian coordinates, therefore the equations of section 3 and 4 have now to be read considering y^1 as radius, y^2 as tangential angle, y^3 as axial coordinate, y^4 as time, and U^j as the contravariant components of the vector \mathbf{Q} in this frame of reference. Therefore the relationship (13) is now:

$$Q_{,m}^k = U^j \frac{\partial x^k}{\partial y^j} \frac{\partial y^i}{\partial x^m} = \left(\frac{\partial U^j}{\partial y^i} + U^n \Gamma_{,n}^{j,i} \right) \frac{\partial x^k}{\partial y^j} \frac{\partial y^i}{\partial x^m} \quad (24)$$

where $\Gamma_{,n}^{j,i}$ are the Christoffel symbols in the cylindrical frame of reference.

We base the numerical approximation of (24) on the formula:

$$Q_{\text{ext}}^k = \left(\frac{\partial U^1}{\partial x^m} + U^n \Gamma_m^j \frac{\partial y^j}{\partial x^m} \right) \frac{\partial x^k}{\partial y^l} \quad (25)$$

by replacing the derivatives $\frac{\partial U^1}{\partial x^m}$ by finite differences, according to the integration scheme (11).

2. Inverse problems for blade to blade flows are constrained by the periodicity or by the requirement, identical from the geometrical viewpoint, that the blade profiles must be closed: in fact, the pitch is a geometrical parameter that is known a priori as function of the radius and that must be satisfied by the solution of the inverse problem. As discussed in section 2 for the 2D case, different formulations of the inverse problem are possible: one may a) prescribe pressure distributions on pressure and suction sides and look for the blades shape or b) prescribe the pressure on one side and the thickness of the blades and look for the camber distribution or c) prescribe the loading and the thickness and look for camber distribution. Problem a) reduces to a problem identical to the duct problem, but does not satisfy a priori the closure condition; problem b) shows the same ambiguities of the 2D case, casting doubts on its well posedness; the only problem that seems well posed satisfying the periodicity condition is problem c), within the limits discussed in section 2 and Ref [2]. We choose to formulate the 3D inverse problem for blade to blade flows as a problem c): we prescribe a design pressure jump between pressure and suction sides Δp and design thickness τ :

$$\Delta p = f(y^1, y^3) \quad , \quad \tau = g(y^1, y^3) \quad (26)$$

The whole flexible surfaces CFPM and GLTQ are computed satisfying eqs. (26): in the CDNM, EFPO, GHRQ and ILTS surfaces in front and behind the blades eqs. (26) reduce to:

$$\Delta p = 0, \quad \tau = 0 \quad (27)$$

Eqs. (26) are the boundary conditions that allow the flexible walls to be computed. Following the same general idea expressed in section 4 for the boundary treatment, the first of eqs. (26), is replaced by:

$$\begin{aligned} & \left\{ p(x^4) + \frac{\gamma p}{a} \left(\frac{\partial a}{\partial x^4} \frac{1}{\delta} - \kappa \frac{\partial s}{\partial x^4} \right) \frac{\Delta x^4}{2} \right\}_P = \\ & \left\{ p(x^4) + \frac{\gamma p}{a} \left(\frac{\partial a}{\partial x^4} \frac{1}{\delta} - \kappa \frac{\partial s}{\partial x^4} \right) \frac{\Delta x^4}{2} \right\}_S = \Delta p \quad (28) \end{aligned}$$

with "P" and "S" denoting pressure and suction sides, respectively, and d, e are defined by eqs. (16). The second of eqs. (26) can be written as:

$$d - e = \tau + \text{pitch}$$

that is

$$\frac{\partial d}{\partial y^4} = \frac{\partial e}{\partial y^4} \quad (29)$$

Again according to the general treatment of boundaries, eq. (29) is replaced by:

$$\frac{\partial d}{\partial y^4} + \frac{\partial^2 d}{\partial(y^4)^2} \frac{\Delta y^4}{2} = \frac{\partial e}{\partial y^4} + \frac{\partial^2 e}{\partial(y^4)^2} \frac{\Delta y^4}{2} \quad (30)$$

and substituting eq. (23) into eq. (30) we obtain:

$$\begin{aligned} & \left\{ U^2 - U^n \frac{\partial d}{\partial x^n} \frac{\partial x^n}{\partial y^4} + \left(\frac{\partial U^2}{\partial y^4} - \frac{\partial U^n}{\partial y^4} \frac{\partial d}{\partial x^n} \frac{\partial x^n}{\partial y^n} \right) \frac{\Delta y^4}{2} \right\}_P = \\ & \left\{ U^2 - U^n \frac{\partial e}{\partial x^n} \frac{\partial x^n}{\partial y^4} + \left(\frac{\partial U^2}{\partial y^4} - \frac{\partial U^n}{\partial y^4} \frac{\partial e}{\partial x^n} \frac{\partial x^n}{\partial y^n} \right) \frac{\Delta y^4}{2} \right\}_S \quad (31) \end{aligned}$$

where the cross derivatives are neglected, vanishing at the steady state, and where $\alpha = 1, 2, 3$; $n = 1, 3$, and $\partial d/\partial x^n$, $\partial e/\partial x^n$ are approximated by finite differences.

Eq. (28) and eq. (31), combined with eqs. (8), allow η_d , unknown at the pressure side boundary, and η_s , unknown at the suction side boundary, be evaluated satisfying the boundary conditions (26).

The geometry of the pressure and suction sides are updated as in the duct case, integrating in time the derivatives $\frac{\partial d}{\partial y^4} = \frac{\partial e}{\partial y^4}$, according to eq. (23).

The inlet and exit boundary conditions are the same as those of the inverse problem for a 3D duct, briefly described in section 4.

6 Numerical examples

We present here three numerical results, the first one refers to the design of a 3D rotational, transonic, convergent-divergent nozzle, while the other two refer to the design of turbomachinery bladings.

6.1 Example 1

In order to test the capabilities of the present inverse technique, we choose an example with a distorted geometry, quite far from the guessed initial one. Fig. 19a) shows the 3D view of the initial configuration and Fig. 19b) the final one that solves the inverse problem. The solid walls are planes, whose equations are:

$$y_b^1 = 0; \quad y_r^1 = -1y^3 + k$$

The design pressure distribution on the lower moveable wall is

$$p_d = .8 - .7x^3$$

on the upper wall:

$$p_r = .8 - .35[1 - \cos(\pi x^3)]$$

On the inlet boundary we impose that the total temperature is uniform and constant in time $\Theta^0 = 1$, that the flow

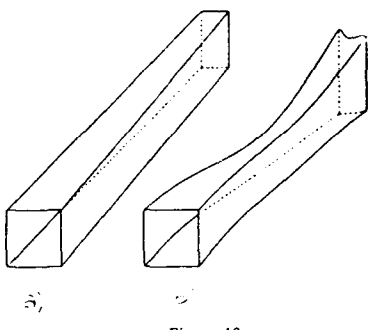


Figure 19:

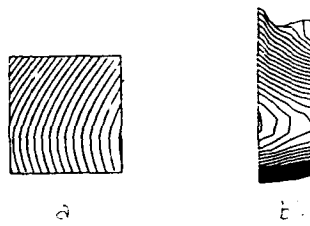


Figure 22:

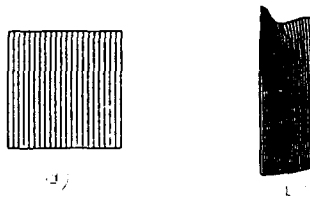


Figure 23:

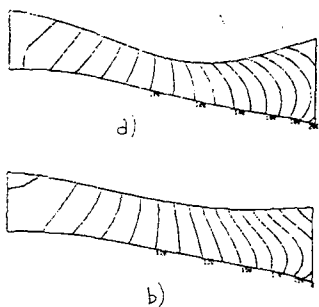


Figure 20:

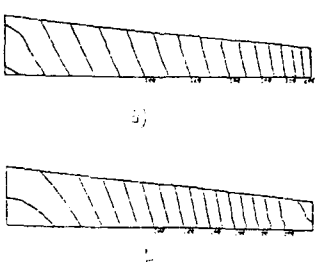


Figure 21:

velocity has the direction of the x^3 coordinate lines and that the total pressure obeys the law:

$$p^0 = 1 - \Delta p^0(y^1 - y_r^1)/(y_b^1 - y_r^1); \quad \Delta p^0 = .1$$

The resulting flow is rotational and non homoentropic.

Figg. 20a), 20b) show the isoMach lines over the left and right solid walls, Figg. 21a), 21b) over the upper and the lower moveable walls and Figg. 22a), 22b) over the inlet and exit surfaces, respectively. Figg. 23a), 23b) show the constant-entropy lines on the inlet and exit surfaces, respectively.

6.2 Example 2

The second example refers to the design of the blades of a stator. Figg. 24a), 24b), show the initial and final 3D view, respectively. The tip and hub solid annulus walls are cylindrical:

$$y_r^1 = r_t \quad ; \quad y_b^1 = r_h$$

with $r_t/r_h = 1.5$.

The design thickness is:

$$\tau = .07 \sin \left[\pi \frac{y^3 - y_l^3}{y_r^3 - y_l^3} \right]$$

with $y_r^3 - y_l^3$ = axial chord.

The design loading is:

$$\Delta p = .08 \sin \left[\pi \frac{y^3 - y_l^3}{y_r^3 - y_l^3} \right]$$

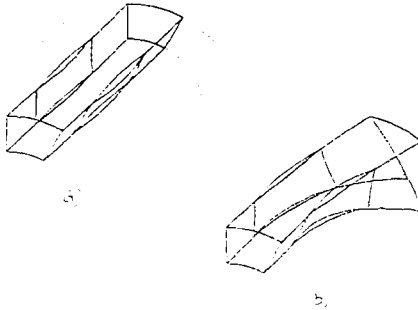


Figure 24:

At the inlet boundary the flow is axial. The total temperature is kept constant $\Theta^0 = 1$, while the total pressure is distorted:

$$p^0 = g\sqrt{y^1} + h$$

with $g = .1/(\sqrt{r_t} - \sqrt{r_h})$, $h = 1 - g\sqrt{r_t}$.

At the exit surface, a distribution of pressure, in agreement with an approximate solution based on the radial equilibrium theory, is given as boundary condition, with $p_h = .7$ at hub radius.

Figs. 25a), 25b) show the isoMach lines on the blade to blade surfaces at the hub and tip radii, Figg. 26a), 26b) on the pressure and suction sides of the blades, respectively. Figg. 27a) and 27b) show the constant entropy lines at the inlet and exit surfaces.

The constant entropy surfaces coincide with stream-surfaces; as it has been pointed out in Ref. [4], looking at Figg. 27a) and 27b) one would expect to see the typical rotation of such surfaces as consequence of the secondary flows generated in 3D rotational flow. Actually, a streamwise component of the vorticity is correctly generated, it does not reveal itself as a rotation of the streamtubes, but rather as a peculiar twisting of the blades: the loading is prescribed as design datum and it cannot be decreased as a consequence of secondary flows, but the lower is the total pressure (and density) the higher the deflection to provide such loading.

Finally, two integral checks have been done on the continuity and angular momentum of the computed flow field: Fig. 28 shows the mass flow computed on cross sections along the blade to blade channel; Fig. 29 compares the angular momentum evaluated on cross sections along the channel with the corresponding theoretical torque due to the design loading.

6.3 Example 3

In the third example the annulus walls form a conical surface at hub radius, and a cylindrical surface at tip radius. The flow at entry is assumed to have axial direction, with constant total temperature and a parabolic distribution of total pressure, the smallest being at hub radius. A certain distribution of thickness and pressure jump as functions of the radial and axial coordinates are assumed, $\tau = g(y^1, y^3)$,

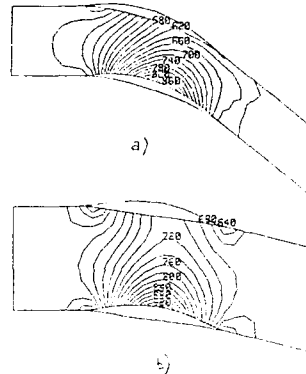


Figure 25:

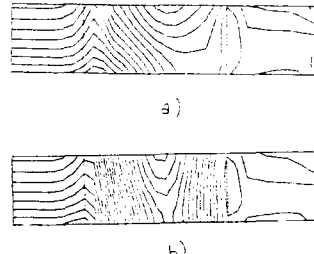


Figure 26:

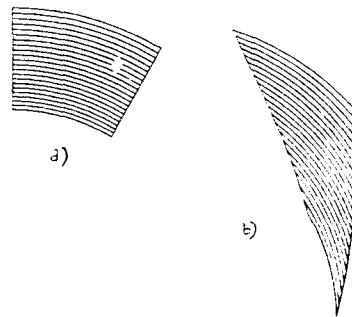


Figure 27:

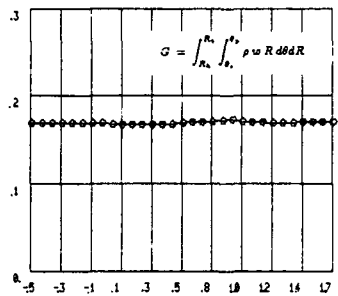


Figure 28:

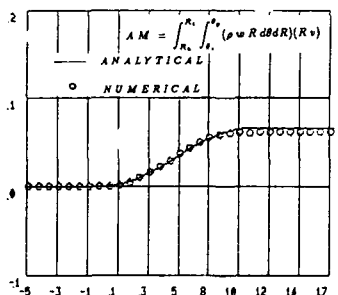


Figure 29:



Figure 30:

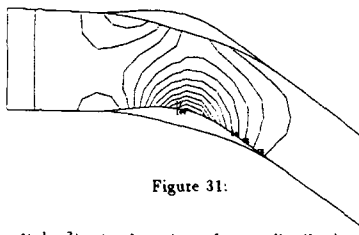


Figure 31:

$\Delta p = f(y^1, y^3)$. At the exit surface, a distribution of pressure, in agreement with an approximate solution based on the radial equilibrium theory, is given as boundary condition, as well as in the previous example.

The initial configuration of the blade row is shown in fig. 18a). The blades are without camber and twist. Fig. 18b) shows the final configuration of the blade row. Figg. 30 and 31 represent the isomach lines of the initial and final configuration of blade to blade section at hub radius, respectively. Figg. 32-37 represent the final configurations of the intermediate and tip blade to blade sections. The threedimensional nature of the flow field and the twisting of blades is shown in these results.

The flow is transonic, in fact a supersonic bubble extends from hub to tip on the section side. Figg. 38 and 39 show the isomach lines on the projection on the meridional plane of the suction and pressure sides of the blades, respectively. Finally, figg. 40a) and 40b) show constant entropy lines on the sections normal to the axis, corresponding to the trailing edges and the exit of the stremtube.

The constant entropy surfaces coincide with stream-surfaces. Figg. 40a) and 40b) show the absence of the typical rotation of such surfaces and the peculiar twisting of the blade to blade channel, as well as in the previous example.

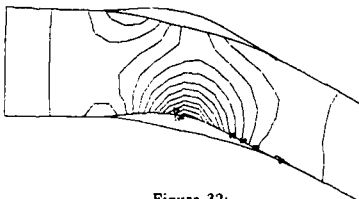


Figure 32:

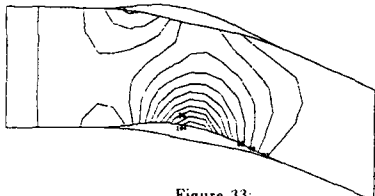


Figure 33:

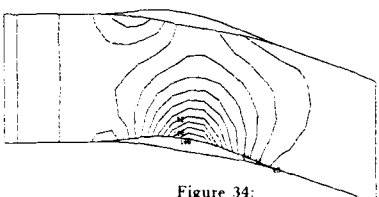


Figure 34:

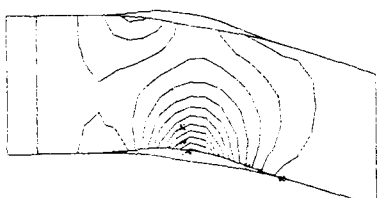


Figure 35:

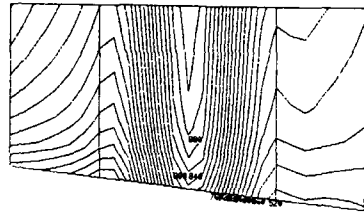


Figure 38:

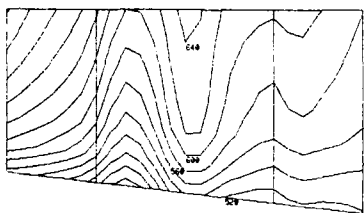


Figure 39:

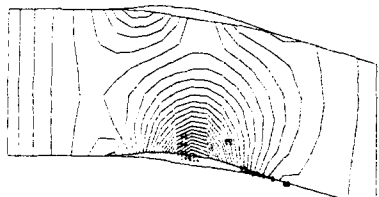


Figure 36:

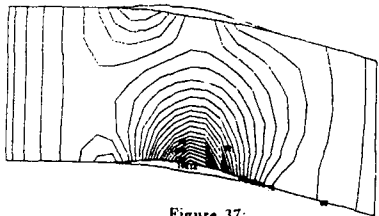


Figure 37:

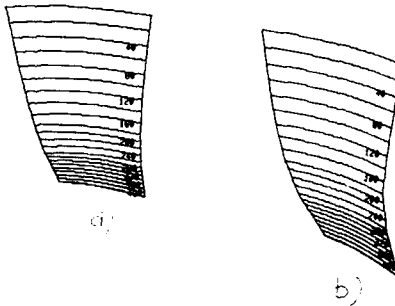


Figure 40:

References

- [1] L. Zannetti, *Time Dependent Method to Solve Inverse Problems for Internal Flows*, AIAA J., 18 July 1980, pp. 754-758.
- [2] L. Zannetti, M. Pandolfi, *Inverse Design Technique for Cascades*, NASA CR 3836, Nov. 1984.
- [3] L. Zannetti, *A Natural Formulation for the Solution of 2D or Axisymmetric Inverse Problems*, Int. J. Num. Meth. in Eng., Vol. 22, Feb. 1986, pp. 451-463.
- [4] L. Zannetti, T. T. Ayele, *Time Dependent computation of the Euler Equations for Designing Fully 3D Turbomachinery Blade Rows, Including the Case of Transonic Shock Free Design*, AIAA 25th Aerospace Sciences Meeting, Reno, Nevada, Jan. 1987, AIAA-87-0007.
- [5] L. Zannetti, F. Larocca, *Time Dependent Solution of Multidimensional Inverse Problems*, 2nd Int. Conf. on Inverse Design Concept Optimization in Engineering Sciences, University Park, Pen. Oct. 1988.
- [6] G. Meauze, *An Inverse Time Marching Method for the Definition of Cascade Geometry*, ASME Paper 81-GT-167.
- [7] W. T. Thompkins, Sia Shing Tong, *Inverse Design Calculation for non Potential Flow in Turbomachinery Blade Passages*, J. Eng. for Power, 104, pp. 281-285.
- [8] F. Ringleb, *Ezakte Losungen der Differentialgleichungen einer adiabatischen Gasstromung*, ZAMM, Vol. 20, N. 4, 1940, pp. 785-798.
- [9] G. Moretti *The lambda-scheme*, Comput. Fluids, 7, 191-205 (1979).
- [10] S. R. Chakravarthy, D. A. Anderson and M. D. Salas, *The split-coefficient matrix method for hyperbolic systems of gasdynamic equations*, AIAA Paper 80-0268.
- [11] L. Zannetti, B. Favini, *About the numerical modelling of multidimensional unsteady compressible flow*, Comput. Fluids, 17 289-299 (1989).
- [12] L. Zannetti, B. Favini, *A difference scheme for weak solution of gasdynamic equations*, AIAA Paper 87-0537.
- [13] R. E. Novak and G. Haymann-Haber, *A mixed flow cascade passage design based on power series expansion*, ASME Rep. 82-GT-121.
- [14] G. Volpe, R. E. Melnick, *The role of constraints in the inverse design problem for transonic airfoils*, AIAA Paper N. 81-123, 1981.
- [15] M. J. Lighthill, *A new method of two-dimensional aerodynamic design*, R&M 2112, April 1945, ARC London.
- [16] M. J. Lighthill, *A mathematical method of cascade design*, R&M 2104, June 1945, ARC London.
- [17] G. Moretti, M. Pandolfi, *Critical study of calculations of subsonic flow in ducts*, AIAA Jou., 19 April 1981, pp. 449-457.
- [18] M. Pandolfi, L. Zannetti, *Some permeable boundaries in multidimensional flows*, 6th Int. Conf. on Num. Meth. in Fluid Dyn., Tbilisi 1978, Lecture Notes in Physics N. 90, Springer-Verlag, pp. 439-446.

Viscous and Inviscid Inverse Schemes Using Newton's Method

Mark Drela

Carl Richard Soderberg Assistant Professor
MIT Department of Aeronautics and Astronautics
Cambridge, Massachusetts 02139 USA

Summary

Recent developments in design/analysis methodology for airfoils and cascades are presented. Shortcomings of standard inverse methods in flows involving shock waves are overcome by a modal geometry perturbation inverse method driven by a least-squares pressure mismatch minimization. The method is incorporated into an existing viscous/inviscid zonal method. Simultaneous solution of the flowfield equations and the pressure mismatch minimization equations is obtained by a full Newton method. This leads to very large computational savings compared to traditional minimization methods. The method is also applicable to viscous flows with or without separation regions present.

The Newton-based solution scheme, which yields sensitivity information as a by-product, also allows very efficient solution of general optimization problems. Perturbation of the geometry and flowfield is specified outside of the Newton solver so as to drive any aerodynamic and/or geometric quantity to its minimum. The availability of free sensitivity information and the rapid reconvergence property of the Newton method after each optimization cycle again gives very large computational savings over traditional optimization techniques. Examples are given for drag minimization of transonic and low Reynolds number airfoils, and loss minimization in a transonic compressor cascade. The applicability of drag optimization methods to airfoil design is assessed.

1 Introduction

Inverse methods developed to date for airfoil and cascade design have employed a wide variety of formulations. For incompressible or linearized compressible flows, Eppler and Somers [1] have employed a complex-mapping method initially treated by Mangler [2] and Lighthill [3]. Transonic inverse problems have been approached by solving the full potential equation with Dirichlet boundary conditions. Volpe and Melnik [4] transform the exterior flow problem into the interior of the unit circle, while Daripa and Sirovich [5] solve the problem in the potential-streamfunction plane. Bauer et al [6] use the alternative approach of solving the compressible potential equation via complex characteristics. Physical-plane inverse methods have also been reported, employing either the full potential equation as in the method of Carlson [7], or the Euler equations as in the method of Giles and Drela [8].

A very useful feature of a compressible inverse method is the ability to accept surface pressure distributions containing shock discontinuities. The difficulty with any such method [4,8] is that such a distribution will in general produce an airfoil surface slope discontinuity at the foot of the shock. Although the discontinuity can be minimized by specifying surface pressures which are consistent with the correct shock pressure jump, such a requirement is a nuisance to the practicing airfoil designer.

For a majority of design problems, treating the flow as inviscid is adequate and entirely appropriate. In certain cases, however, especially those involving transonic and/or low Reynolds number flow, the boundary layer displacement effects can very significantly alter the effective geometry gen-

erated by an inviscid inverse method. A useful feature of an inverse method, therefore, is the ability to account for this viscous displacement effect. In principle, one can subtract from the airfoil contour a displacement thickness calculated separately from the specified pressure distribution. In practice, this may lead to irregularities in the calculated airfoil shape, since the displacement thickness always changes rapidly at the transition or shock location. This irregularity will then be directly transferred to the airfoil contour. Also, this approach cannot be used for low Reynolds number flows ($Re < 10^6$), in which some flow separation is invariably present and a displacement thickness distribution cannot be generated from a specified pressure distribution. The few viscous inverse methods reported to date, such as those of Giles et al [9] and Hirose et al [10], have not addressed these more general inverse problems. The transonic viscous mixed-inverse case presented in reference [9], for example, uses a specified pressure distribution which is shock-free, and the transition point is outside the inverse part of the airfoil. As a result, the resulting modified airfoil geometry is smooth. However, the method cannot be used if even a small amount of separation occurs. The viscous inverse solutions presented in reference [10] also appear to have difficulty in dealing with flow separation, and shocked cases are not presented.

Although it might seem pointless to design for shock waves and flow separation, the fact is that transonic flows involving weak shock waves and low Reynolds number flows involving small separation bubbles frequently represent optimum airfoil design solutions. Also, shock waves are sometimes inevitable, as in the case of flow through a transonic compressor cascade. Hence, an inverse method which can readily handle such flows has substantial engineering interest.

The inverse viscous formulation presented here is aimed at generating airfoil shapes which are guaranteed to be smooth even if flow separation and/or shocked flow occurs, and the displacement thickness distributions have strong irregularities. The technique is to limit the airfoil geometry change generated by an inverse solution to a relatively small number (ten or less) of smooth geometric modes. Such a modal geometry perturbation formulation has been commonly used in optimization-based inverse methods, such as those of Vanderplaats [11], Hicks et al [12], and Cosentino and Holst [13]. The present method is novel in that it uses a Newton solution technique to solve the flowfield equations simultaneously with a set of least-squares surface pressure mismatch constraints which govern the geometric mode amplitudes. Each Newton iteration produces the sensitivities of all the least-squares constraints to each geometric mode amplitude. These sensitivities are then used to update the geometric mode amplitudes within each Newton iteration.

The advantage of the present technique of generating the sensitivities of the surface pressures (or any other flow quantity) from the Newton solver is that it leads to very large savings in computational effort. Standard optimization-based methods normally obtain the sensitivities by sequentially perturbing each mode and recalculating a direct solution by the "black-box" direct solver — a very expensive process

even if only a few modes are used. The no-overhead generation of these sensitivities by the Newton method results in the entire modal inverse solution requiring about the same CPU time as one direct or one full- or mixed-inverse calculation — typically 5 minutes or less on a VaxStation 3200 machine. This is a substantial improvement over the pure optimization-based methods which only deal with the direct solver as a "black-box", and may require tens or even hundreds of direct solutions to perform one inverse solution. Furthermore, the inclusion of viscous effects into the present inverse solver via a simultaneously-coupled integral boundary solution has little effect on the overall calculation time. Again this represents a large cost advantage over previously-reported viscous inverse solvers [10] which are based on the Navier-Stokes equations and require hours of supercomputer time for an inverse solution.

The Newton solution procedure allows economical implementation of general optimization procedures, such as minimization of profile drag at fixed angle of attack or fixed lift. The modal-inverse method is a particular optimization method which incidentally can also be incorporated implicitly into the flowfield Newton solution. More general optimization must be performed outside of the flow solver, but is able to make full use of the "free" sensitivity information available from the Newton method. The result is that any well-posed optimization problem can be solved with a very modest computational effort — comparable to that needed for several direct solutions.

The present modal-inverse and optimization methods have been implemented as additional options to the successful ISES airfoil/cascade code [9,14,8,15]. This code already has two standard inverse mode capabilities — a full-inverse mode where the pressure is prescribed over the entire airfoil surface, and a mixed-inverse mode where the pressure is prescribed over only a part of the airfoil surface and the geometry is prescribed over the remainder. Inverse solution examples have been presented in references [9,8]. The new modal-inverse variant presented in this paper is similar to these two existing inverse formulations, except that the airfoil contour change is restricted to the smooth geometric modes as mentioned above. The smooth geometric modes in the present formulation can represent either the perturbation of one airfoil side or the perturbation of the airfoil camber line. Allowing only one surface to change is most useful in isolated airfoil design, where the two surfaces are typically tailored separately at two different operating conditions. Allowing only the camber line to change (which preserves the airfoil thickness) is most useful in turbomachinery compressor blading design applications, where the airfoil thickness is more or less fixed by draconian structural requirements.

This paper will give a summary of the ISES code formulation into which the present modal-inverse method is incorporated. The Newton solution method unique to the method will be addressed in more detail. An extension of the method to optimisation problems involving drag minimization will also be presented. Design examples for airfoils and turbomachinery blading will be presented to illustrate the usefulness of the modal inverse method. The role of optimisation techniques in airfoil design will also be assessed.

2 Numerical Formulation of ISES Code

The ISES code has been extensively documented in the literature [16,17,8,15,14]. Here, only a brief description of the basic method will be given. The boundary conditions pertinent to the various direct, inverse, and optimisation options are central to the present work, however, and will be presented in more detail.

2.1 Interior flowfield equations

The ability of the ISES code to handle both direct and inverse problems stems from its streamline-based discretization of the steady Euler equations. This discretization is similar to the older streamline curvature methods [18] commonly used in turbomachinery applications. A number of key differences, however, allow the ISES code to handle transonic flows, and to easily accept inverse or direct boundary conditions with or without boundary layer effects included.

Streamline curvature codes typically discretized the non-conservative Euler equations expressed in local intrinsic $s-n$ coordinates. In contrast, ISES discretizes the Euler equations in conservative form. A conservation cell is defined by two streamlines and three "quasi-normals" (they do not need to be normal to the streamlines) as shown in Figure 1. The standard Euler variables of density ρ , pressure p , velocities u, v , are located at the center of the quasi-normal cell face. There is no convection across the streamline faces, so that only the pressure p and the streamline node position x, y are needed as unknowns there. The lack of convection across the streamline faces of each cell also allows the continuity and energy equations to be replaced by simple algebraic statements of constant mass flux and stagnation enthalpy in each streamtube. This reduces the number of equations and the number of unknowns per cell to only two. Only the normal position n of each grid node, and the density ρ on each quasi-normal cell face remain as variables. The streamline grid is thus determined as part of the solution. This permits a very simple extension of the method to inverse problems, where the airfoil is determined by the calculated shape of its two bounding streamlines.

In supersonic regions, ISES adds a speed-upwinding dissipation term to the streamwise component of the momentum equation. This has the appearance of the physical bulk viscosity term, and mainly comes into effect in steep speed gradients, allowing shock waves to be captured. More details are available in references [16,17].

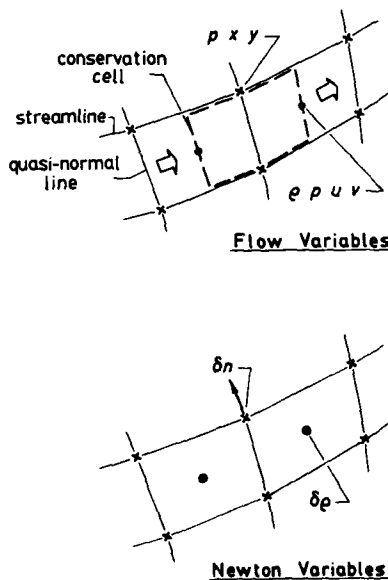


Figure 1: Euler grid node and variable locations.

2.2 Newton solution method

A key feature of ISES is the global Newton solver which is used to solve all the governing equations as a fully-coupled system. This system contains all the interior equations, as well as all the airfoil and farfield boundary conditions (described later). An initial streamline grid corresponding to incompressible flow, and a uniform density equal to its freestream value, are used for the initial guess. The variables determined by each Newton iteration are the streamline node movement δn along a specified direction (typically normal to the streamline), and the density change $\delta \rho$ at each quasi-normal face. The linear system which governs these changes for each Newton iteration has the form

$$\begin{bmatrix} \bar{\mathbf{J}} \\ \delta \mathbf{n} \\ \delta \rho \\ \delta \mathbf{G} \end{bmatrix} = \begin{bmatrix} \delta \mathbf{n} \\ \delta \rho \\ -\mathbf{R} \\ \end{bmatrix} \quad (1)$$

where $\bar{\mathbf{J}}$ is the known Jacobian matrix and \mathbf{R} is the vector of all residuals. Because each variable δn and $\delta \rho$ affects only the nearby residuals, the matrix is tightly banded for the most part. However, the system also typically contains several "global" variable changes δG which affect a large number of residuals. Examples of these are the changes in the inlet and outlet flow angles ϑ which enter the boundary conditions in cascade cases, and the change in the circulation Γ which affects the farfield boundary conditions in isolated airfoil cases (the boundary conditions will be discussed in more detail in the next section). The additional variables are implicitly constrained by equations such as the Kutta condition, which appears as additional residuals in the vector \mathbf{R} . The large, sparse, linear system (1) resulting from each Newton iteration is solved by a custom banded solver. For even the largest two-dimensional problems encountered in actual applications — approximately 10 000 variables — this is faster and much more reliable than iterative solvers.

2.3 Farfield boundary conditions

The two interior variables n and ρ and the two interior momentum equations are unchanged for all the types of flow problems handled by ISES. Cascade and airfoil cases are distinguished only by the farfield boundary conditions, which also depend on whether the flow at the boundary is subsonic or supersonic. Typically, the streamline angle ϑ and the stagnation density ρ_0 are imposed at the domain inflow boundary. The flow angle is either prescribed or corrected for the solution farfield behavior obtained from the Prandtl-Meyer function $\nu(M)$ or an asymptotic compressible potential expansion.

$$\vartheta = \vartheta_{\text{spec}} \quad \text{subsonic cascade} \quad (2)$$

$$\vartheta \pm \nu(M) = \vartheta_{\text{spec}} \quad \text{supersonic cascade} \quad (3)$$

$$\tan \vartheta = \Phi_s / \Phi_z \quad \text{subsonic airfoil} \quad (4)$$

The Prandtl-Meyer boundary condition prevents spurious reflection of waves back into the domain, and automatically returns the unique-incidence condition of supersonic cascades [19]. The airfoil farfield potential $\Phi(z, y; \Gamma)$ depends on the circulation constant Γ , which is implicitly determined by imposing a Kutta condition. It can also optionally include airfoil doublet terms for more accuracy. In addition to giving the inflow angle, this potential also gives the farfield pressure which is imposed on the outermost streamlines in the airfoil case. This high-order boundary condition treatment allows the outer boundary to be placed within a few chords of the airfoil. References [14,8] give more details on the airfoil farfield boundary conditions.

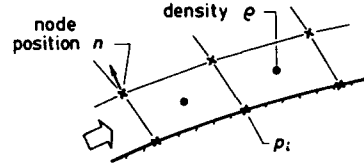


Figure 2: Six streamline nodes and two density variables determining surface pressure p_i .

2.4 Direct and inverse surface boundary conditions

The farfield boundary conditions described above distinguish between cascade and airfoil cases, and between subsonic and supersonic flows. However, whether a particular case is viscous or inviscid, or is of the direct or inverse type, is only determined by the boundary conditions on the airfoil surface. At each streamline node on an airfoil surface, one boundary condition is required to close the entire equation set. In an inviscid direct problem, the position of the streamline adjacent to the airfoil is fixed, and hence the movement δn_i of the node is simply set to zero.

$$\delta n_i = 0 \quad (5)$$

In an inverse problem, the pressure at a surface grid node (explicitly related to the neighboring density and streamline node position variables shown in Figure 2) is set to a specified value. With s_i being the arc length position of surface node i , the pressure is enforced by the following expression.

$$p_i = p_{\text{spec}}(s_i) + A_1 f_1(s_i) + A_2 f_2(s_i) \quad (6)$$

The present streamline Euler formulation allows the surface node pressure p_i to be explicitly related to the neighboring streamline nodes and density values as shown in Figure 2. The linearization of equation (6) which is incorporated into the Newton system () therefore has the form

$$\sum_k \frac{\partial p_i}{\partial n_k} \delta n_k + \sum_k \frac{\partial p_i}{\partial \rho_k} \delta \rho_k = \delta A_1 f_1(s_i) + \delta A_2 f_2(s_i) \\ = p_{\text{spec}}(s_i) + A_1 f_1(s_i) + A_2 f_2(s_i) - p_i \quad (7)$$

where the summations are carried over the local n and ρ variables which influence p_i .

Note that the specified pressure distribution $p_{\text{spec}}(s)$ has added terms which consist of specified modes $f_1(s)$ and $f_2(s)$ weighted by unknown free parameters A_1 and A_2 . These two parameters are additional "global" variables implicitly determined during the Newton solution to satisfy two geometric airfoil closure conditions. In full-inverse problems where the pressure is imposed over the entire airfoil surface, it is appropriate to specify that the leading be closed, and that the trailing edge gap be equal to some specified value h_{re} .

$$\Delta n_{i_{\text{LS}}} = 0 \quad (8)$$

$$\Delta n_{i_{\text{TS}}} = h_{\text{re}} \quad (9)$$

The corresponding linearized equations are then

$$\delta n_{i_{\text{LS}}}^{\text{upper}} - \delta n_{i_{\text{LS}}}^{\text{lower}} = -\Delta n_{i_{\text{LS}}} \quad (10)$$

$$\delta n_{i_{\text{TS}}}^{\text{upper}} - \delta n_{i_{\text{TS}}}^{\text{lower}} = h_{\text{re}} - \Delta n_{i_{\text{TS}}} \quad (11)$$

In mixed-inverse problems, geometric closure must be specified at the left and right blend points i_L and i_R joining the direct and inverse segments of the airfoil (Figure 3).

$$\Delta n_{i_L} = 0 \quad (12)$$

$$\delta n_{i_L} = -\Delta n_{i_L} \quad (13)$$

The actual surface pressure distribution $p(s)$ which results from an inverse solution will differ from the prescribed distribution $p_{\text{spec}}(s)$ by the additional terms in equation (6). This must of course be accepted in any inverse method as originally proved by Lighthill [3] for incompressible cases. Voilé and Melnik [4] have argued that the same must be true for compressible cases. Note that it is possible to obtain the exact specified pressure over a part of the airfoil by setting the mode shapes $f_1(s)$ and $f_2(s)$ to be zero there, and nonzero elsewhere. This is rarely necessary, however, and simple linear mode functions (shown in Figure 3) have proved to be effective in practice.

Woods [20] has treated the incompressible mixed-inverse problem by using a conformal mapping into the complex potential plane. His method required three integral constraints on the specified surface speed, which is inconsistent with the present scheme needing only two constraints. This inconsistency is somewhat puzzling, particularly since the present scheme gives reliable convergence with any specified pressure distribution, and hence is likely to be well posed. It is suspected that the discrepancy between Woods's result and the present method is somehow related to regularity in the pressure gradient distribution. The geometry regularity condition at each blend point (12) still allows a discontinuity in the surface curvature, which in turn produces a \sqrt{s} behavior in the local surface pressure on the prescribed-geometry side of the blend point. Woods's analytic flow-field description precluded such behavior, and hence an additional constraint naturally arose. In the present mixed-inverse method, pressure gradient regularity can be enforced by adding an additional free parameter term to equation (6). Woods's requirement of only one additional constraint suggests that if regularity is obtained at one blend point, the other point will be regular as well. However, this would only be true if no discretization error were involved. To allow perfect control at each blend point, two additional terms $A_3 f_3(s)$ and $A_4 f_4(s)$ can be added to equation (6) as indicated in Figure 3. The additional unknowns A_3 and A_4 are then determined by enforcing the second derivative in pressure at the blend points to be equal to a fixed values stored from the seed airfoil solution. In discrete form, this is expressed as

$$p_{i-1} - 2p_i + p_{i+1} = (p_{i-1} - 2p_i + p_{i+1})_{\text{spec}} \quad (14)$$

where i is the index of a blend point. This equation is linearized in terms of the local Euler variables δn , δp , and added to the Newton system. Instead of constraining the second derivative in the pressure, it is of course possible to directly specify the curvature at the blend points. However, the surface pressure is the relevant aerodynamic quantity, and constraining it instead of the curvature has been found to be more effective. The mode shapes $f_3(s)$ and $f_4(s)$ for these additional constraints are again arbitrary, but the best results are obtained if each mode is restricted to be nonzero only in the vicinity of the corresponding blend point to be constrained. Finally, it must be mentioned that the \sqrt{s} behavior in the surface pressure is often imperceptible, and becomes apparent only if severe changes in the surface pressure distribution are specified. For most cases, only the two leading additional terms added to the specified surface pressure are adequate.

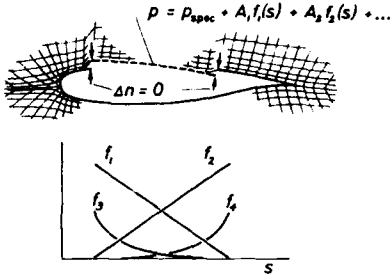


Figure 3: Mixed-inverse problem with two geometry continuity constraints.

The key feature of the ISES code which enables the wide variety of inverse problems to be specified is the global Newton solution method and the associated direct banded matrix solver. The solver sees a boundary condition as simply another equation in the Newton system — the particular form of that equation is immaterial (it only needs to produce a sufficiently well-conditioned linearized system). Thus, any well-posed boundary condition can be easily implemented with no change to the remainder of the overall solution procedure. An iterative solution strategy would strongly depend on the boundary condition equation stencil as well as the magnitudes of the stencil elements. Particularly troublesome would be the determination of the global variables A_1 - A_4 which influence all the surface nodes where the pressure is specified. The influence of these variables on the closure constraints (9,12) cannot be easily obtained, especially for transonic flows. They would therefore be difficult to incorporate into a relaxation scheme.

2.5 Specified thickness and loading

For turbomachine blading calculations, it is often highly advantageous to strongly constrain the structural properties of a thin cascade airfoil during an inverse calculation. The simplest approach is to preserve the thickness and modify the camber line by imposing the loading Δp across the airfoil. Note that this allows only partial control of the pressure distribution on one particular surface, but this concession must be made to avoid an over-specified problem.

In any direct or inverse problem, two boundary conditions are needed at each surface node position — one for each airfoil side. In the thickness/loading inverse problem, these two conditions are

$$t_i = t_{\text{spec}}(s_i) \quad (15)$$

$$\Delta p_i \equiv p_i^{\text{lower}} - p_i^{\text{upper}} = \Delta p_{\text{spec}}(s_i) + A_1 f_1(s_i) + A_2 f_2(s_i) \quad (16)$$

where t_i is the airfoil thickness at node i . Equation (15) in linearized form is

$$\delta n_i^{\text{upper}} - \delta n_i^{\text{lower}} = t_{\text{spec}}(s_i) - t_i \quad (17)$$

while the linearized form of equation (6) has the same form as equation (7). These linearized equations are then included into the Newton system as usual.

The appropriate constraints on the free parameters A_1 and A_2 in equation (16) are the usual geometry continuity constraints at the left and right blend points i_L, i_R joining the direct and inverse airfoil segments.

$$\delta n_{i_L}^{\text{upper}} + \delta n_{i_L}^{\text{lower}} = 0 \quad (18)$$

$$\delta n_{i_R}^{\text{upper}} + \delta n_{i_R}^{\text{lower}} = 0 \quad (19)$$

The one exception to this is the special case where the inverse segment extends all the way to the trailing edge, and the trailing edge is left free to move up and down. In this case, the two extra terms in equation (16) are not used. Correspondingly, two equations must be discarded to retain a closed system, these being the right geometry continuity equation (19) and the trailing edge Kutta condition. The latter is taken care of by equation (16) being applied at the trailing edge. Only the remaining left geometry closure equation (18) is imposed, and this now implicitly constrains the airfoil circulation in airfoil cases, or the exit flow angle or exit pressure in cascade cases.

2.6 Leading edge geometry considerations

The full-inverse formulation in the ISES code has not found to be particularly effective for blunt leading edge geometries. Difficulties arise near the stagnation point, where the surface contour is extremely sensitive to the local imposed pressures. This is to be expected of any inverse method which requires pressures rather than surface speeds to be specified, as the pressure variation near the stagnation point is quadratic while the speed variation is linear. If the prescribed pressure even slightly exceeds the stagnation pressure, the method must fail. The mixed-inverse formulation circumvents this difficulty by allowing the geometry to be imposed near the stagnation point, and hence is a much more effective and robust design tool for airfoils with blunt leading edges.

For airfoils with very small leading edge radii, such as turbomachinery compressor blades, it is often advantageous to not resolve the leading edge, especially in preliminary design stages. This lack of resolution eliminates the stagnation point in the numerical solution, making the full-inverse method practical for these cases.

2.7 Inviscid inverse example: Transonic airfoil

Figure 4 shows a NASA supercritical airfoil from reference [21] operating at $M = 0.75$, $C_L = 0.8$. Ten Newton iterations were required for this direct calculation, which consumed a total of 12 minutes CPU time on a VaxStation 3200 for the typical 132×32 grid. A fairly strong shock wave occurs at this condition on the suction side of the airfoil, producing the unacceptably high wave drag of $C_D = 0.01095$. This shock can be weakened via a mixed-inverse redesign of most of the upper surface. Figure 5 shows the original and new specified C_p distributions. Although the shock wave could be replaced by an isentropic recompression, the resulting airfoil would likely have undesirable off-design performance. Also, a smooth recompression often results in a stand-off shock [22,8] which still carries a significant wave drag penalty. For these reasons, specifying a weak shock at the design point usually produces a better overall airfoil.

Figure 6 shows the final surface C_p and geometry of the new airfoil resulting from the inverse calculation. The angle of attack α was left as a free variable in the overall Newton problem to allow the design $C_L = 0.8$ to be maintained exactly. This also caused a slight change in the lower surface C_p distribution. Four additional Newton iterations (5 minutes CPU on a VaxStation 3200) were needed to converge this case starting from the direct solution. The small and certainly acceptable discrepancy between the specified and final surface C_p distributions is the two additional terms in

equation (6) which were set to obtain geometric closure at the two blend points.

Figure 7 shows the new calculated airfoil shape to have a slope discontinuity at the shock location, and the local geometric angle θ and normalized curvature κc to have oscillations there. These features arise from the specified C_p surface values within the smeared shock being inconsistent with the values which would be obtained on a smooth surface. In particular, no special attention was paid to ensuring that the surface C_p near the shock was consistent with the correct Rankine-Hugoniot jump condition and the post-shock Zierep pressure singularity. This consistency is not easily achieved, as the Zierep pressure singularity depends on the curvature of the final airfoil which is not known a priori, and the numerical structure of the smeared shock is difficult to predict. If there is no shock within the inverse segment, such problems of course do not arise, but here the geometric disturbance at the shock is a continual nuisance when many redesigns are performed. Elimination of this problem is one of the primary motivations behind the modal-inverse method described in the next section.

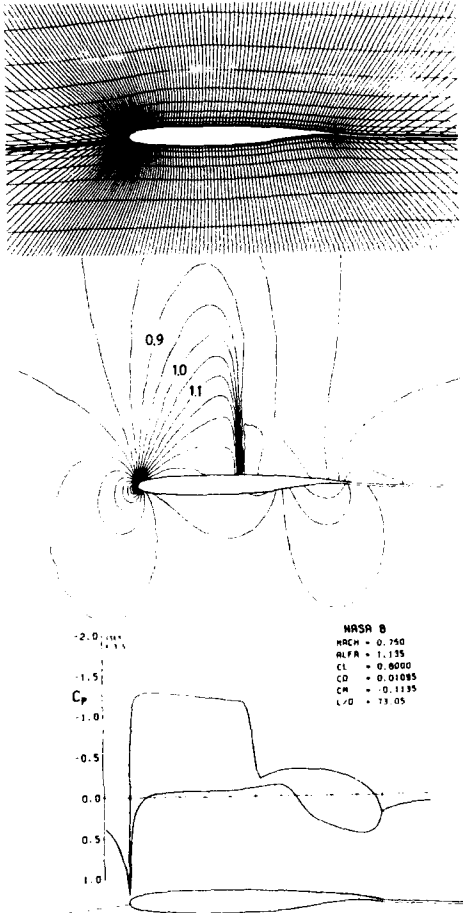


Figure 4: 132×32 grid, Mach contours, and surface C_p distribution for inviscid supercritical airfoil.

3 Modal-Inverse Formulation

The modal inverse formulation implemented in ISES is actually more closely related to a direct than an inverse method. The boundary condition applied at a modal-inverse surface node is

$$\delta n_i = \sum_{\ell=1}^L \delta \tilde{n}_\ell g_\ell(s_i) \quad (20)$$

which is equivalent to perturbing the airfoil contour by the L geometric modes $g_\ell(s)$. The same perturbation condition can also be applied to opposing points on the two airfoil surfaces. This preserves the airfoil thickness distribution, and is equivalent to perturbing the airfoil's camber line. The mode shapes specified in the ISES code are shown in Figure 8. Since the modes are smooth, the perturbed geometry is also guaranteed to be smooth.

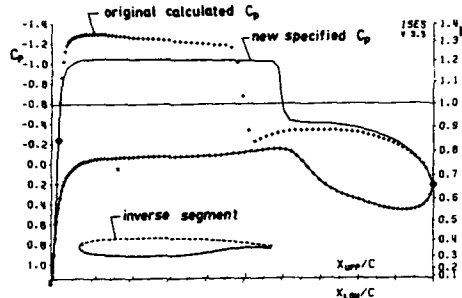


Figure 5: Calculated C_p on original airfoil, and specified C_p for mixed-inverse redesign.

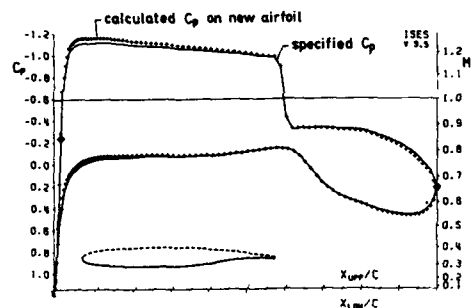


Figure 6: Specified and new calculated C_p distributions on redesigned airfoil.

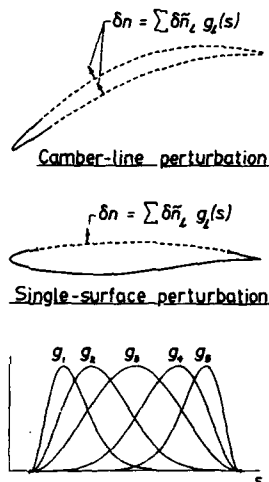


Figure 8: Camber-line and single-surface modal geometry perturbations.

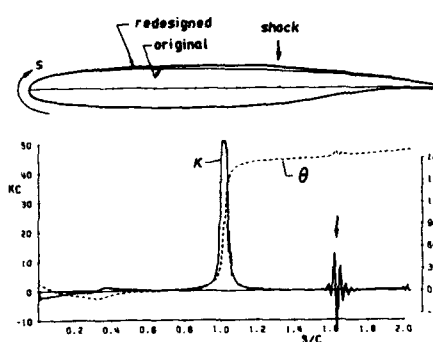


Figure 7: Comparison between original and mixed-inverse redesigned airfoil. Surface angle and curvature distributions on redesigned airfoil.

The mode amplitudes \tilde{n}_ℓ are determined by minimizing the integrated mismatch between the specified and resulting surface pressure distributions. The discrete form of this mismatch integral I is defined as

$$I \equiv \frac{1}{2} \sum_i (p_i - p_{\text{spec}}(s_i))^2 \quad (21)$$

where the summation is taken only over the inverse segment. The L minimization constraints with respect to all the mode amplitudes are obtained by setting the integral variations to zero.

$$\frac{\partial I}{\partial \tilde{n}_\ell} \equiv \sum_i (p_i - p_{\text{spec}}(s_i)) \frac{\partial p_i}{\partial \tilde{n}_\ell} = 0 ; \quad 1 \leq \ell \leq L \quad (22)$$

Linearizing this about the current solution, one obtains L Newton equations for the L mode variable changes $\delta \tilde{n}$.

$$\begin{aligned} \sum_{m=1}^L \delta \tilde{n}_m \sum_i & \left[\frac{\partial p_i}{\partial \tilde{n}_m} \frac{\partial p_i}{\partial \tilde{n}_\ell} + (p_i - p_{\text{spec}}(s_i)) \frac{\partial}{\partial \tilde{n}_m} \left(\frac{\partial p_i}{\partial \tilde{n}_\ell} \right) \right] \\ & = - \sum_i (p_i - p_{\text{spec}}(s_i)) \frac{\partial p_i}{\partial \tilde{n}_\ell} ; \quad 1 \leq \ell \leq L \quad (23) \end{aligned}$$

The quantity in the square brackets is therefore an element

of the Hessian matrix for the pressure-mismatch integral I . It is necessary in practice to neglect the second term inside the brackets, since calculation of the cross-sensitivity of p_i with respect to \tilde{n}_ℓ and \tilde{n}_m is impractical. The Newton equations actually used are therefore the following.

$$\sum_{m=1}^L \delta \tilde{n}_m \sum_i \frac{\partial p_i}{\partial \tilde{n}_m} \frac{\partial p_i}{\partial \tilde{n}_\ell} = - \sum_i (p_i - p_{\text{spec}}(s_i)) \frac{\partial p_i}{\partial \tilde{n}_\ell} ; \quad 1 \leq \ell \leq L \quad (24)$$

Fortunately, the neglected term has a minor impact on the terminal convergence rate of the global Newton procedure, since $p_i - p_{\text{spec}}(s_i)$ becomes small and $\partial p_i / \partial \tilde{n}_\ell$ rapidly tends to a constant as convergence is approached, making the entire term a higher-order quantity.

Even if the second term in equation (24) is discarded, it is still not possible to immediately incorporate the system (24) into the global Newton system in the usual manner, since the sensitivities $\partial p_i / \partial \tilde{n}_\ell$ are normally known only after the global Newton system is solved. This problem is circumvented by the following modified Newton procedure.

The L columns corresponding to the Newton variables $\delta \tilde{n}_\ell$ are placed on the righthand side, to obtain a Newton system of the form

$$\begin{bmatrix} \bar{J} \\ \delta n \\ \delta \rho \\ \delta G \end{bmatrix} \begin{Bmatrix} \delta n \\ \delta \rho \\ \delta G \end{Bmatrix} = \begin{Bmatrix} -R \\ 0 \\ 0 \end{Bmatrix} + \delta \tilde{n}_1 \begin{Bmatrix} g_1 \\ g_1 \\ g_1 \end{Bmatrix} \dots + \delta \tilde{n}_L \begin{Bmatrix} g_L \\ g_L \\ g_L \end{Bmatrix} \quad (25)$$

where the unknown vector on the lefthand side contains all the flowfield Euler unknowns δn , $\delta \rho$, δG , and R is the vector of all the interior flowfield equation, boundary condition, and global constraint residuals. Since \bar{J} is now a square non-singular matrix, the system (25) can be solved by Gaussian elimination to obtain partially-determined solution.

$$\begin{Bmatrix} \delta n \\ \delta \rho \\ \delta G \end{Bmatrix} = \begin{Bmatrix} \delta \bar{n} \\ \delta \bar{\rho} \\ \delta \bar{G} \end{Bmatrix} + \delta \tilde{n}_1 \begin{Bmatrix} \bar{g}_1 \\ \bar{g}_1 \\ \bar{g}_1 \end{Bmatrix} \dots + \delta \tilde{n}_L \begin{Bmatrix} \bar{g}_L \\ \bar{g}_L \\ \bar{g}_L \end{Bmatrix} \quad (26)$$

The vectors $\delta \bar{n}$, $\delta \bar{\rho}$, and \bar{g}_ℓ are now known, and the geometric mode amplitude changes $\delta \tilde{n}_\ell$ are still undetermined. The surface pressure at any node is a known function $p(n, \rho)$ of the neighboring streamline node positions and density variables (see Figure 2), so one can explicitly determine the sensitivity of each surface pressure p_i to each geometric mode amplitude \tilde{n}_ℓ as follows.

$$\frac{\partial p_i}{\partial \tilde{n}_\ell} = \sum_k \frac{\partial p_i}{\partial n_k} \frac{\partial n_k}{\partial \tilde{n}_\ell} + \sum_k \frac{\partial p_i}{\partial \rho_k} \frac{\partial \rho_k}{\partial \tilde{n}_\ell} ; \quad 1 \leq \ell \leq L \quad (27)$$

where the summations are carried over the nodes adjacent to node i , shown in Figure 2. As discussed earlier, $\partial p_i / \partial n_k$ and $\partial p_i / \partial \rho_k$ are explicitly calculated by differentiating $p(n_k, \rho_k)$, and $\partial n_k / \partial \tilde{n}_\ell$ and $\partial \rho_k / \partial \tilde{n}_\ell$ are simply the known elements of the column vector \bar{g}_ℓ in the vector equation (26). With all the sensitivities $\partial p_i / \partial \tilde{n}_\ell$ thus determined, the L equations (24) become an $L \times L$ linear system for $\delta \tilde{n}_1 \dots \delta \tilde{n}_L$ which is easily solved. Substituting the resulting $\delta \tilde{n}$ values into the vector equation (26) then fully determines all the remaining Newton changes δn and $\delta \rho$ at all the flowfield grid nodes. The Newton update can then proceed as usual. The streamline adjacent to the modal inverse segment will move during this update, thus automatically adjusting for the change in the airfoil geometry.

As mentioned earlier, this modified Newton solution procedure does not constitute a "proper" Newton method, as

the modal constraints (24) are not the exact linearized forms of the least-squares constraints (22). The overall convergence rate is therefore no longer quadratic, but degrades to linear. However, the discarded linearization terms are so small that an order of magnitude decrease in the residuals per iteration is typically obtained in practice. Four or five iterations therefore suffice to converge a modal-inverse case.

3.1 Specified thickness and loading with Modal-Inverse

As mentioned in the previous section, turbomachinery blading airfoils lend themselves well to inverse calculations with a specified thickness and loading Δp . This same approach can also be easily incorporated into a modal-inverse method. In this case, the geometry perturbation modes are used to equally change each surface rather than the single surface. This naturally preserves the airfoil thickness and is equivalent to only perturbing the airfoil's camber line. The discrete pressure-mismatch integral now takes the form

$$I \equiv \frac{1}{2} \sum_i (\Delta p_i - \Delta p_{\text{spec}}(s_i))^2 \quad (28)$$

where the summation is performed only over the part of the airfoil where the camber line is being perturbed. The remainder of the solution algorithm is essentially identical to the one-surface modal-inverse method described above.

3.2 Inviscid Modal-inverse example: Transonic airfoil

The transonic airfoil inverse example presented in the previous section is an obvious candidate for a modal-inverse calculation. Using the same specified C_p distribution shown in Figure 5, a modal-inverse calculation is performed using the five geometric perturbation modes shown in Figure 8. Again, α is left as a free variable to allow the design $C_L = 0.8$ to be maintained. Five Newton iterations (7 minutes CPU on the VaxStation 3200) are required for convergence, starting from the converged original airfoil case. The final surface C_p is shown in Figure 9, and the new airfoil geometry is compared with the original geometry in Figure 10. As expected, the new geometry is smooth, and the match between the specified and resulting surface pressures is certainly acceptable. A better match could naturally be obtained by incorporating more geometry perturbation modes. The computational effort increases by only about 3% for each additional mode, so using many modes is very attractive. The low cost per mode is due to each mode only adding a right-hand side to the Newton system. This righthand side is a trivial additional burden for the direct banded matrix solver used in ISES. For iterative solvers, the cost per mode would naturally be higher.

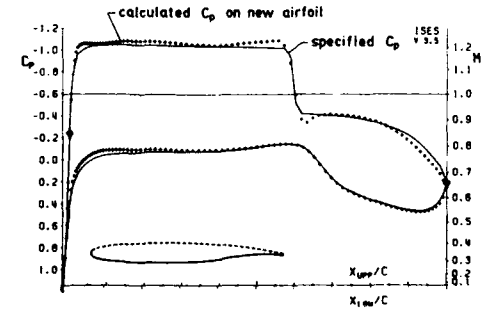


Figure 9 Specified and new calculated C_p distributions on airfoil redesigned using modal-inverse.

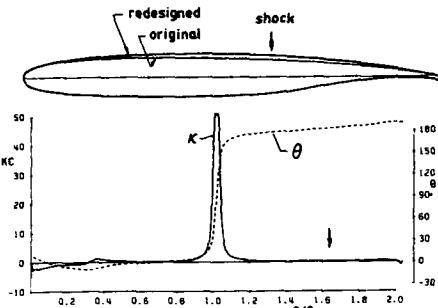


Figure 10: Comparison between original and modal-inverse redesigned airfoil. Surface angle and curvature distributions on redesigned airfoil.

The ISES code is structured so that the specified C_r distributions can be easily edited and the solution reconverged at any time. The relatively quick execution, particularly for subcritical cases which converge in 2-3 iterations, allows the designer to efficiently determine the most effective solution to a particular airfoil design problem.

4 Viscous Inverse Solutions

The ISES code can optionally incorporate viscous effects into any direct or inverse Euler solution by modifying the airfoil (and wake) surface boundary conditions via the displacement surface concept. In the direct and modal-inverse modes, the condition of the surface streamline being fixed to the airfoil is replaced by the requirement that the streamline be displaced from the airfoil surface by a distance equal to the viscous displacement thickness. Referring to Figure 11, the linearized boundary condition which replaces equation (5) in direct viscous problems is

$$\delta n_i - \delta(\delta_i^*) = \delta_i^* - \Delta n_i \quad (29)$$

where δ^* is the displacement thickness, and Δn is the streamline offset distance. On the trailing wake, the gap between the two streamlines bounding the wake is likewise driven to the wake displacement thickness, and also the pressure jump across the wake is specified to be zero. More details are given in references [15,23]. In modal-inverse solutions, the boundary condition which replaces equation (20) is

$$\delta n_i - \delta(\delta_i^*) = \delta_i^* - \Delta n_i + \sum_{\ell=1}^L \delta \tilde{n}_\ell g_\ell(s_i) \quad (30)$$

so that the streamline is still offset from the airfoil by δ^* , but the airfoil surface itself can be displaced by the geometry modes. The wake displacement condition is unaffected.

The boundary conditions modified for the displacement effect have introduced the new variable $\delta(\delta^*)$ at each airfoil surface and wake node into the Newton system. Two additional viscous variables are further added to describe the viscous layer, these being the Newton changes of the momentum thickness $\delta\theta$ and the max shear stress coefficient δC_r . To obtain a closed system, three new equations must therefore be introduced at each node to govern the three new variables. As described in reference [15], ISES employs the standard von Karman integral momentum equation, the kinetic energy shape parameter equation, and a dissipation lag equation. In turbulent flow regions, these equations have the following form.

$$\frac{d\theta}{ds} = f_1(\theta, \delta^*, u_s) \quad (31)$$

$$\frac{d|H^*(\theta, \delta^*, u_s)|}{ds} = f_2(\theta, \delta^*, u_s, C_r) \quad (32)$$

$$\frac{dC_r}{ds} = f_3(\theta, \delta^*, u_s, C_r) \quad (33)$$

Like the surface pressure p_i in Figure 2, the boundary layer edge velocity is a known function $u_s(n_k, \rho_k)$ of the neighboring Euler variables n and ρ , and hence does not constitute an additional unknown. In laminar flow regions, a maximum disturbance amplitude variable \bar{N} replaces C_r , and an amplification equation of the form

$$\frac{d\bar{N}}{ds} = f_4(\theta, \delta^*, u_s) \quad (34)$$

replaces the lag equation (33). The transition point is determined by the variable N exceeding a specified critical value \bar{N}_{crit} . The result is roughly equivalent to the e^0 transition prediction method of Smith and Gamberoni [24] and van Ingen [25].

The boundary layer equations are discretized using two-point central differencing and their linearized forms are added to the global Newton system. The Newton changes $\delta(\delta^*)$, $\delta\theta$, δC_r needed to update the boundary layer solution are thus calculated simultaneously with the Euler solution in both direct and inverse cases. Because the viscous and inviscid solutions are fully coupled in this solution procedure, flows involving separation can be readily computed.

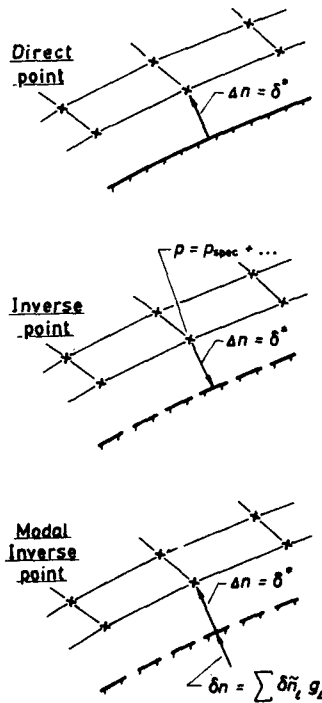


Figure 11: Viscous wall boundary conditions at direct and inverse points.

For full- or mixed-inverse cases with boundary layer coupling included, the specified-pressure boundary condition (6) is unchanged. The boundary layer equations are still solved as part of the global Newton system, but on the specified-pressure portions of the airfoil, δ^* no longer affects the position of the streamline nearest the airfoil surface. Instead, the airfoil contour is simply offset from the inviscid streamline by a distance equal to δ^* as shown in Figure 11. In full-inverse cases, this is essentially equivalent (except for the wake displacement effect) to performing a standard specified- u_* boundary layer calculation and correcting the airfoil shape by δ^* as a post-processing step. In mixed-inverse viscous calculations, the direct boundary condition (29) is used at the fixed-geometry portion of the airfoil, and hence there is a two-way coupling between the boundary layers and the inverse solution flowfield.

As discussed in the Introduction, if transition or a shock wave occurs within the inverse segment, the displacement thickness will change rapidly, and this change will be transferred to the calculated airfoil shape as a geometric irregularity. This is a nuisance in viscous inverse calculations, and is one of the motivations for the modal-inverse method. A far more serious problem in both full- and mixed-inverse problems is that the overall solution will fail outright if the boundary layer separates anywhere the surface pressure is imposed. At such locations the boundary layer is effectively being solved in the conventional specified- u_* mode, which is known to allow unconstrained perturbations in δ^* at separation (the cause of the well-known Goldstein separation singularity). This in turn produces a singular Jacobian matrix in the global Newton system and results in solution failure. The direct and modal-inverse boundary conditions (29,30) sidestep this problem by directly constraining the local δ^* perturbations. The modal-inverse method can thus be safely used with limited separation regions present. One instance where the modal-inverse method is expected to fail, however, is when one or more of the geometry perturbation modes $g_i(s)$ in equation (30) is confined to an entirely-separated region. This geometry mode will then have almost no influence on the surface pressure distribution, since it cannot affect the inviscid streamline pattern and pressure field through the "soft" separated boundary layer. As a consequence, $\partial p_i / \partial n_i$ in equation (24) will nearly vanish, and an ill-conditioned system for all the mode amplitude changes $\delta \hat{n}$ will result. In practice, this problem can be easily avoided by selecting broadly-distributed modes such as those pictured in Figure 8.

4.1 Viscous modal-inverse example: Low-speed compressor cascade

Figure 12 shows the calculated and experimental pressure distributions for a low-speed compressor section tested at UTRC and reported in reference [26]. Transitional separation bubbles are predicted on both surfaces due to the relatively low Reynolds number. In order to increase the flow turning and the stage work of this cascade, a thickness/loading modal-inverse calculation can be performed with an increased specified loading. Figure 13 shows the calculated and new specified surface loading. The airfoil camber line has been allowed to deform everywhere with the leading edge point being fixed. For commonality with the usual single-side inverse mode, the pressure p on each surface rather than the loading Δp is input by the user. For the thickness/loading inverse option, however, the program only makes use of the difference $\Delta p \equiv p^{\text{lower}} - p^{\text{upper}}$.

In order for the cascade to achieve its higher loading, its trailing edge must be set free to move so that the over-

all camber line can increase with the inlet flow angle fixed. Since the geometric perturbation modes pictured in Figure 8 cannot allow the trailing edge to move, an additional mode of the form $g = s - \sin(s)$ has been added to the system. The result of the modal-inverse calculation is shown in Figure 14. The turning angle has been increased by 16°. The specified and resulting loading distributions match closely, although the pressure distribution on an individual surface cannot be controlled independently — an unavoidable feature of the thickness/loading inverse formulation.

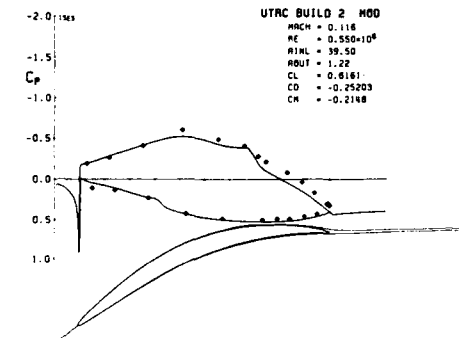


Figure 12: Calculated and experimental C_p distributions on low-speed compressor cascade.

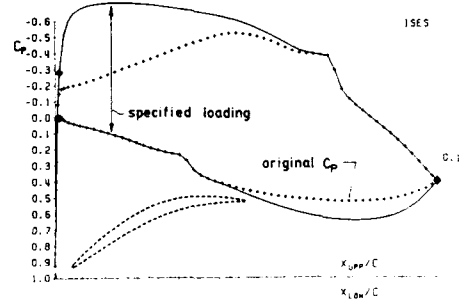


Figure 13: Specified surface loading Δp for modal-inverse redesign.

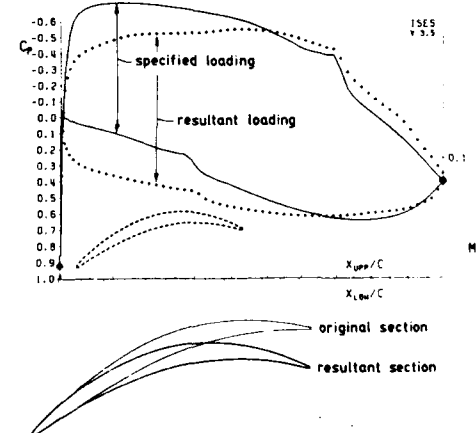


Figure 14: Result of modal-inverse redesign of low-speed compressor section.

5 Optimization Applications

The present solution scheme based on the Newton method lends itself well to embedding in a global optimization scheme. Because gradient information on any aerodynamic quantity is a nearly "free" by-product available after each Newton iteration, that quantity can be readily driven towards a desired optimum. Jameson [27] has recently reported an optimization-type inverse technique which employs an inexpensive perturbation sensitivity calculation employing the same operator as the full-potential equation which governs the flowfield. This is similar to the present method in that the sensitivity vector for each flow variable can be calculated in parallel with the flow solution, and hence repeated perturbation of a direct solution is avoided.

The geometry perturbation modes used in the modal-inverse method can be included in the inviscid or viscous solid wall boundary conditions (20,30) at any time. To recover the standard direct or viscous problem, the trivial Newton system constraints

$$\delta\tilde{n}_\ell = 0 \quad (35)$$

can be used in lieu of the modal-inverse pressure mismatch minimization constraints (22). A more interesting case results, however, if the amplitudes $\delta\tilde{n}_\ell$ are specified so that the airfoil shape and flowfield are altered to obtain desired aerodynamic or geometric properties. The modal-inverse problem described earlier is a specific example of such a method, with the required aerodynamic property being a least-squares fit to the specified surface pressure distribution. In the general case, the required property is that an arbitrary cost function I be minimized. For airfoil design, a typical goal is to minimize drag at a fixed lift, hence

$$I \equiv C_D \quad (36)$$

with the understanding that any variation of I is at a fixed C_L .

In ISES, the airfoil profile drag or cascade profile loss are determined from the viscous momentum thickness θ_∞ at the last wake point, and from the shock wave momentum defect at the domain exit plane, much like in an experimental wake survey.

$$C_D = \frac{2\theta_\infty}{c} + \frac{2}{\rho_\infty q_\infty^2 c} \sum_j (q_\infty - q_j) m_j \quad (37)$$

The summation is taken over all the streamtubes with m_j being the mass flux in streamtube j , and q_j corresponding to the streamtube speed which would result if the flow isentropically reached the freestream pressure (or inlet pressure for cascades). This isobaric speed q_j is readily obtained from the wake total pressure profile $p_{w,t}$, and the known freestream static pressure p_∞ and total enthalpy h_∞ .

$$q_j^2 = 2h_\infty \left[1 - \left(\frac{p_\infty}{p_{w,t}} \right)^{\frac{2}{\gamma-1}} \right] \quad (38)$$

Formally, the equations governing all the L geometry mode amplitudes are obtained by setting the variations of $I \equiv C_D$ to zero.

$$\begin{aligned} \frac{\partial I}{\partial \tilde{n}_\ell} &\equiv \frac{2}{c} \frac{\partial \theta_\infty}{\partial \tilde{n}_\ell} - \frac{2}{\rho_\infty q_\infty^2 c} \sum_j \frac{\partial p_{w,t}}{\partial \tilde{n}_\ell} \frac{\partial q_j}{\partial p_{w,t}} m_j \\ &= 0 ; \quad 1 \leq \ell \leq L \end{aligned} \quad (39)$$

Here $\partial q_j / \partial p_{w,t}$ is obtained directly by differentiating relation (38). The mode amplitude sensitivities $\partial \theta_\infty / \partial \tilde{n}_\ell$ and $\partial p_{w,t} / \partial \tilde{n}_\ell$ are obtained directly from the appropriate elements in vectors \mathbf{g}_ℓ in the partially-determined Newton solution (26). The fundamental difference between the drag minimization constraints (39) and the pressure-mismatch minimization constraints (22) is that the latter can be approximately linearized into the form given in equation (24) and incorporated into the overall Newton system. Equations (39), in contrast, must be solved outside of the Newton system by using classical minimization methods such as steepest-descent or conjugate-gradient. The two different formulations are illustrated in Figures 15,16. In general, any type of cost function in least-squares form can be included implicitly into the Newton solution, while more general cost definitions must be treated explicitly. The simple steepest-descent method, for example, is implemented by explicitly setting

$$\delta\tilde{n}_\ell = -\epsilon \frac{\partial I}{\partial \tilde{n}_\ell} ; \quad 1 \leq \ell \leq L \quad (40)$$

outside of the Newton iteration cycle, with ϵ an empirical constant. These mode amplitude changes are then used to generate the new airfoil geometry, which will decrease the cost I for a sufficiently small ϵ . An important advantage of the present streamline-based method is the flowfield can be updated together with the airfoil geometry, with the streamline grid moving to accommodate the new airfoil shape. Specifically, the flowfield is updated by the changes δn , δG , calculated directly by inserting the mode amplitude changes $\delta\tilde{n}_\ell$ into the inverted Newton system (25) available from the last Newton iteration, as indicated in Figure 16. This update, corresponding to the linearized response of the flow to the geometry perturbation, is effectively one "free" Newton iteration for the next estimate of the flow which minimizes I . A few additional Newton iterations are then performed to converge the flow with the airfoil geometry frozen to ensure that the sensitivities $\partial I / \partial \tilde{n}_\ell$ are sufficiently accurate for the next optimization step.

Although for the drag minimization problem the modal geometry perturbations are incorporated explicitly outside of the global Newton solution, this approach is still very efficient compared to the brute-force optimization technique, since the cost sensitivities $\partial I / \partial \tilde{n}_\ell$ are obtained cheaply as by-products of the Newton solution. The present method also lends itself well to multi-point optimization, since the external geometry perturbation indicated in Figure 16 can in fact receive contributions to the cost function I from any number of parallel solutions, which may correspond to different specified C_L , Reynolds number, and/or Mach number values. The geometry perturbations $\delta\tilde{n}_\ell$ would then be sent to each solution which would then be reconverged independently until the next optimization step.

It is important to note that the solution to any optimization problem is influenced by the global constraints imposed on the flow problem. For example, the sensitivities $\partial \theta_\infty / \partial \tilde{n}_\ell$ will take on different values if the airfoil α is held fixed, or the C_L is held fixed. Each instance will clearly lead to a different optimal airfoil solution. In actual applications, it may also be necessary to add geometric constraints to the cost function I , such as a prescribed maximum thickness or enclosed area. In this case, these geometric terms will add contributions to the sensitivities $\partial I / \partial \tilde{n}_\ell$ which can be obtained in a straightforward manner using the known mode shapes.

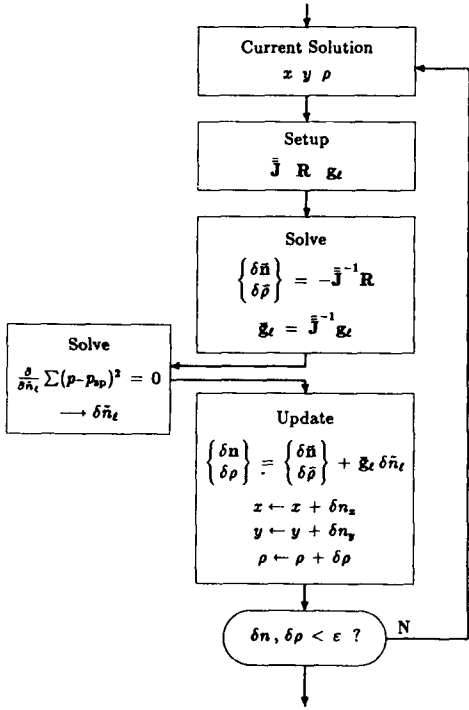


Figure 15: Newton method with embedded optimization (modal-inverse).

5.1 RAE 2822 airfoil optimization example

Figure 17 shows the calculated solution for the RAE 2822 airfoil Case 10 experiment reported in reference [28]. The freestream Mach number of 0.75 and the specified experimental $C_L = 0.743$ produce a shock-induced separation over about 10% of the chord, which was also observed in the experiment. The airfoil is well past the drag-divergence point, as evidenced by the rather high level of computed drag $C_D = 0.0149$. In an attempt to reduce the drag (or equivalently increase the drag-divergence Mach number), a viscous optimization calculation was performed to minimize the simple cost function $I \equiv C_D$. The five geometric perturbation modes pictured in Figure 8 were specified to act on most of the upper surface from 1.5% chord to the trailing edge. For simplicity, no constraints were placed on the enclosed area or maximum thickness, these being unable to change drastically anyway due to the leading edge radius being fixed.

The internal Newton loop illustrated in Figure 16 was executed with the original $C_L = 0.743$ being specified, effectively giving an L/D maximization problem. Five optimization passes were performed, with the geometry mode amplitudes calculated from equation (40) using $\epsilon = 0.002$, with the mode shapes themselves having unit amplitude. A significantly larger step size would result in erratic changes in the cost function from one optimization step to the next. Two or three Newton iterations were used between each optimization step for a total execution time of 15 minutes CPU on the VaxStation 3200 computer — roughly the time needed for two isolated direct solutions. The evolution of the cost function C_D during this process is shown in Fig-

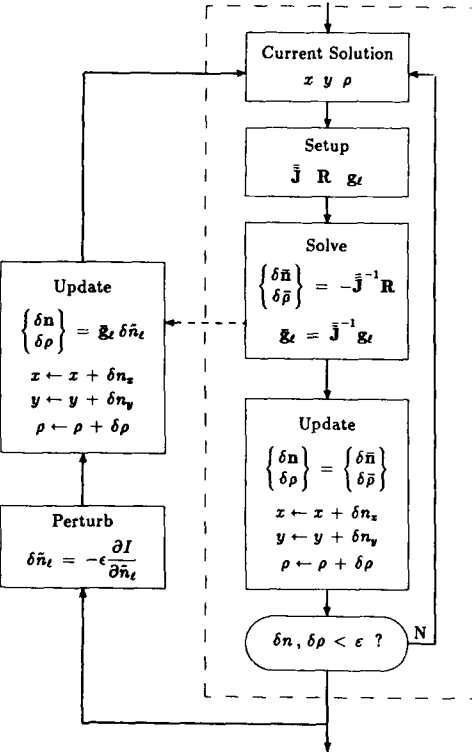


Figure 16: Newton method with external optimization.

ure 18. Figure 19 shows the final calculated surface C_p distribution on the new airfoil and a comparison between the old and new geometries. A rather drastic drag decrease from $C_D = 0.0229$ to $C_D = 0.0129$ has been obtained, with most of this reduction coming from a decrease in wave drag as indicated in Figure 18. While the drag decrease appears very attractive, it is in fact largely illusory. Figure 20 shows Mach-sweep calculations for the two airfoils. Apparently the drag reduction obtained by the optimization procedure at $M = 0.75$ carries a severe drag penalty at lower Mach numbers, which in actual applications would probably be unacceptable. Clearly, the optimization approach must be used with great caution.

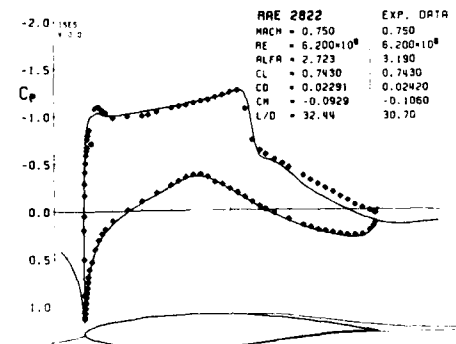


Figure 17: RAE 2822 airfoil calculation and experimental data.

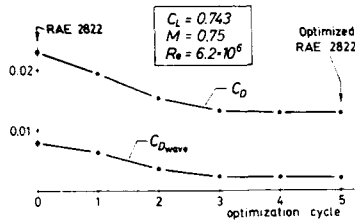


Figure 18: Reduction in total and wave C_D during RAE 2822 airfoil optimization.

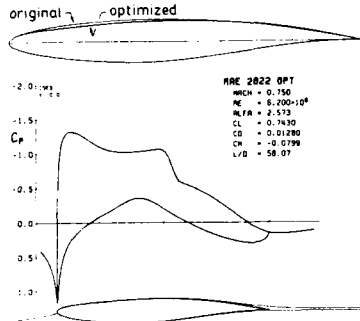


Figure 19: Calculated C_p on optimized RAE 2822 airfoil and geometry comparison.

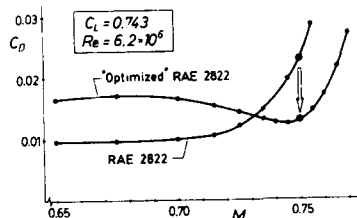


Figure 20: Drag-divergence behavior for original and optimized RAE 2822 airfoils.

5.2 Transonic compressor cascade optimization example

Figure 21 shows a calculated viscous solution for a typical transonic compressor tip section cascade. The inlet Mach number is 1.3, and the stage pressure ratio is 1.95. The fairly fine 132×32 grid used in the calculation is necessary to capture the total pressure loss of the small leading edge bow shock, whose wake is visible in the Mach contours in Figure 21. A massive shock-induced separation region extends over nearly the entire suction surface past the shock, and the total stage losses are correspondingly high. Examination of the flowfield reveals that the cascade has excessive rear camber which aggravates the separation problem. To

find a more effective camber shape, an optimization calculation can be performed to minimize the cascade loss. A suitable definition of this loss is C_D as defined by equations (37,38). With this definition, the first term in equation (37) represents the blade profile loss, while the second term represents the total pressure loss of the bow shock and main passage shock.

To preserve the inlet Mach number, incidence, and mass flow, which are typically imposed by the specifications on the overall turbomachine, it is necessary to preserve the geometry of the front supersonic portion of the blade. This portion, which determines the inlet incidence and Mach number via the upstream-running waves [19], is therefore left fixed during the optimization. Specifically, only the rear 75% of the blade is allowed to be deformed by the geometric modes. Both sides are specified to be perturbed equally, so that the airfoil thickness and hence structural properties are affected as little as possible. As with the low-speed inverse cascade example presented earlier, camber-changing modes were added to those shown in Figure 8 to allow the trailing edge to move.

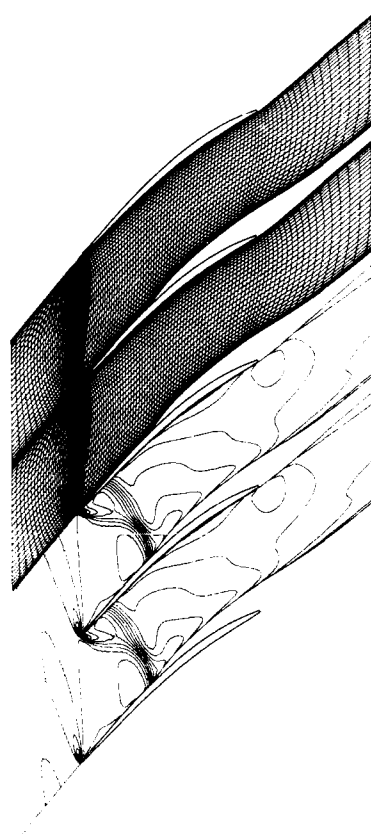


Figure 21: Final 132×32 grid and calculated Mach contours ($\Delta M = 0.05$) for transonic compressor cascade.

Five optimization cycles were performed for this case, using $\epsilon = 0.01$ in equation (40). Figure 22 shows the resulting flowfield and compares the old and new geometries. The evolution of the loss during the optimization process is shown in Figure 23. A very substantial 50% loss reduction has been achieved, this resulting entirely from a reduction in the blade profile loss — the shock loss has not been changed significantly. Although the optimum has clearly not yet been reached, it was necessary to halt the optimization cycle to prevent the passage shock from being expelled from the inlet and "unstarting" the cascade. As Figure 22 shows, the passage shock is now closer to the inlet, indicating that the maximum pressure ratio sustainable by the cascade has in fact decreased. The exit flow angle has also decreased by 4.5° . The loss reduction has therefore been attained at the price of reduced stall margin and reduced stage work. Whether this tradeoff is favorable can probably only be answered by considering the characteristics and specifications of the entire compressor.

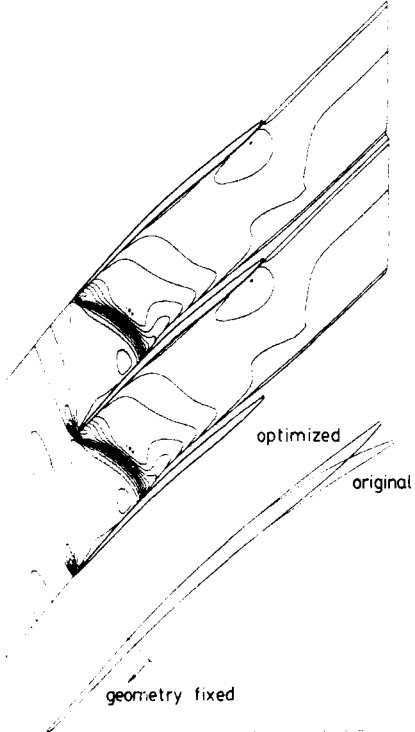


Figure 22: Calculated flow for optimized compressor cascade and geometry comparison.

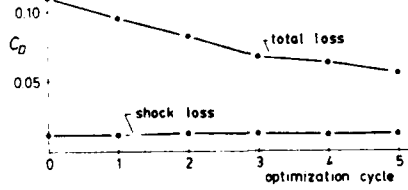


Figure 23: Reduction in total and shock loss during compressor cascade optimization.

5.3 LA203A airfoil optimization example

The LA203A is a low Reynolds number Liebeck airfoil reported in reference [29]. Figure 24 shows the calculated and experimental C_p distributions at a Reynolds number of 250000. The large transitional separation bubbles visible in the calculated and experimental surface pressure distributions are typical for this Reynolds number regime. As in the previous transonic airfoil example, an optimization calculation was carried out allowing the entire upper surface from stagnation point to trailing edge to deform. Eight optimization cycles were needed to minimize drag with the lift coefficient fixed at its original value of 1.08. For this case, it was possible to use the relatively large steepest-descent step size $\epsilon = 0.02$ compared with the transonic airfoil case above.

Figure 25 shows the final calculated C_p distribution on the new airfoil together with the geometry comparison between the new and original airfoils. The optimization has changed the airfoil so that a weak adverse pressure gradient is now imposed over most of the upper surface ahead of the transition location. This causes increased disturbance amplification and forces transition to occur earlier in the bubble. The resulting reduction in the bubble's size has decreased the overall drag coefficient by 18.5% from 0.01485 to 0.01210. A similar optimization has been performed at $C_L = 1.5$, with the results shown in Figure 26. Again, a substantial reduction in drag has been achieved, although the optimized airfoil shape is quite different from the $C_L = 1.08$ case.

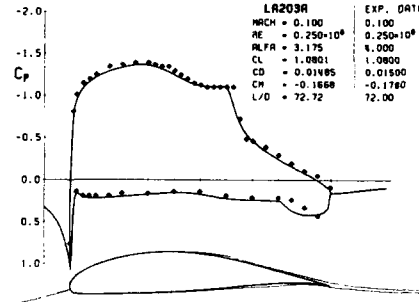


Figure 24: Calculated and experimental surface C_p for LA203A airfoil.

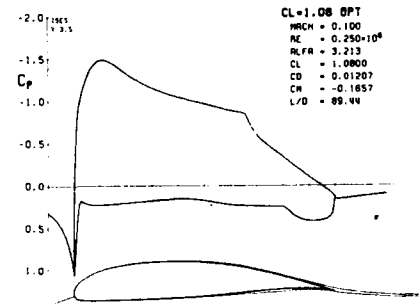


Figure 25: Calculated C_p distribution for airfoil optimized at $C_L = 1.08$.

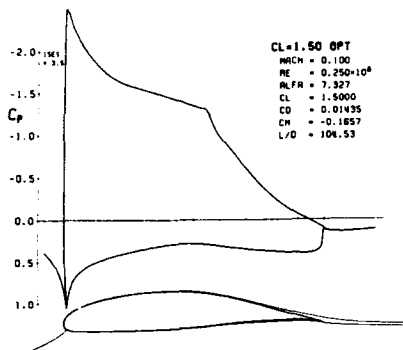


Figure 26: Calculated C_p distribution for airfoil optimized at $C_L = 1.50$.

To investigate the effect of the optimizations on the overall airfoil performance, a polar sweep was calculated over the entire usable α range of each airfoil. The polars are plotted in Figure 27, together with the polar for a two-point optimized airfoil described below. It is clear that the drag advantage gained through a single-point optimization procedure is realized only in the vicinity of the design C_L . In fact, the two single-point "optimized" airfoils can be considered inferior to the original airfoil in an overall sense.

This optimization study serves to illustrate the pitfalls which can befall a simple optimization approach to airfoil design. The two-point optimization, as suggested in reference [30], was intended as a possible solution to this problem. The cost function was defined as a weighted sum of the C_D values at the two C_L operating points used in the single-point optimizations.

$$I \equiv \frac{1}{3} (C_D)_{C_L=1.08} + \frac{2}{3} (C_D)_{C_L=1.50} \quad (41)$$

A larger weight was placed on the $C_L = 1.50$ point since the single-point polars in Figure 27 suggest that the $C_L = 1.08$ point might cause excessive loss in $C_{L\max}$ if allowed to strongly influence the optimization. Over one optimization cycle, the two solutions were independently converged in parallel. The sensitivities from each solution were then used together to determine the mode changes needed to drive the cost function (44) to its minimum. The changes were then sent to each solution and the cycle was repeated. The final optimized C_p distributions at the two "sampled" points are shown in Figure 28. Interestingly, the two-point optimization produced a weaker adverse pressure gradient ahead of the separation bubble than either of the single-point optimizations. The geometry of all three new airfoils is compared with the original LA203A geometry in Figure 29.

Figure 27 shows that the two-point airfoil is fairly satisfactory, with an attractive reduction in minimum C_D gained at the expense of a small but still significant loss in $C_{L\max}$ and a loss in thickness of about 1% of chord. Also, maximum C_L/C_D has not changed significantly, while the endurance parameter $C_L^{1/2}/C_D$ has decreased slightly. Overall, the new airfoil may be slightly better or slightly worse than the original LA203A depending on the application.

It may be possible to further improve the two-point optimization result by a better choice of the C_L values where the cost function is to be evaluated. However, these points are uncertain at the outset, and suitable weights for the C_D values at the different points must be guessed. For the RAE 2822 optimization case, the excessive drag created at lower Mach numbers might be alleviated by a two-point op-

timization that included the drag contribution at some Mach number below the design value. Knowing which other Mach number to use is certainly not clear a priori. In any case, these examples strongly suggest that even with optimization design techniques available, designer-driven iterative approach to airfoil design is still necessary, with each successive design stage being a response to the problems uncovered in the previous design stages. On a more positive note, the single-point optimized airfoils do clearly indicate what qualities are needed in a low Reynolds number airfoil to achieve low drag. The features of the two-point optimized airfoil indicate how the conflicting requirements at different operating points might be reconciled.

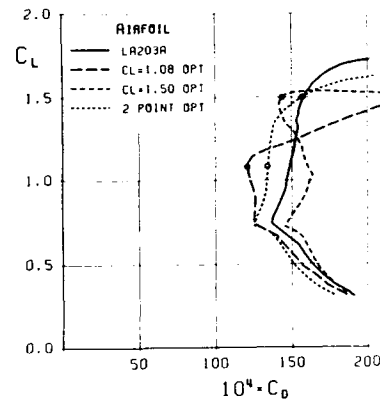


Figure 27: Calculated polars for original LA203A, single-point, and two-point optimized airfoils.

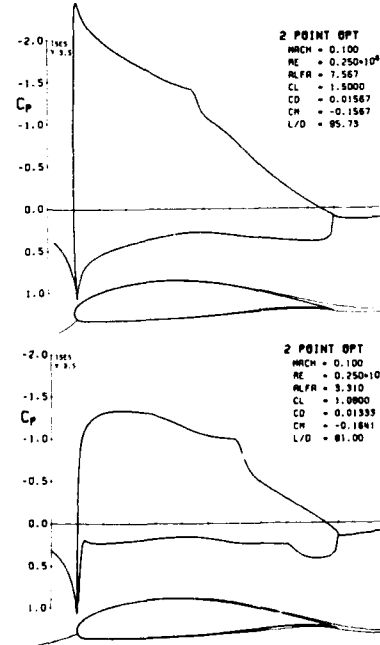


Figure 28: Final C_p distributions at the two sampled C_L values for two-point optimization calculation.

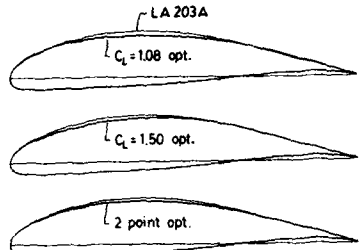


Figure 29: Geometry comparison between optimized airfoils and original LA203A airfoil.

5.4 The role of optimization in airfoil design

It is the opinion of this author that any working airfoil optimization method is unlikely to represent a "solution" to the general airfoil design problem. Most real airfoil design problems are far too complex to be quantifiable as a cost function which is to be minimized. Often, constraints or requirements either cannot be reliably quantified (e.g. manufacturability, roughness sensitivity, etc.), or the best numerical weight to place on a particular cost function term is not known *a priori*. Such factors in the design problem are usually determined or discovered with numerical and/or experimental data as the design evolves. Hence they cannot be used to formulate the mythical all-encompassing cost function at the outset.

The best role for optimization appears to be as another item in the airfoil designer's numerical toolbox. An optimization solution to a necessarily simple and hence imperfect cost function can serve as a guide to the designer by indicating which way the design "wants to go" from a purely aerodynamic viewpoint, say. The designer's role is then to reconcile this naive optimum solution with other constraints which may be either unquantifiable, or too complex to lump into a cost function. For this part of the design cycle, other design tools such as inverse methods are likely to be more appropriate.

6 Conclusions

This paper has presented several recent developments in design/analysis methodology for viscous and inviscid airfoil and cascade flows at transonic speeds. A variety of new inverse and optimization formulations have been incorporated into the existing ISES airfoil/cascade code. The salient features of the overall methodology are:

- A coupled Euler plus integral boundary layer flowfield representation.
- A streamline-based Euler discretization which allows airfoil geometry changes to be obtained during flow-field solution.
- Flexibility in specification of direct or inverse boundary conditions.
- A full Newton solution scheme for all viscous and inviscid variables.
- Sensitivity information for optimisation procedures is obtainable from the Newton solver at negligible extra cost.

The inverse options in the method allow specification of pressure distributions on any portion of the airfoil surface. Alternatively, the loading and airfoil thickness distributions can be specified if strong structural constraints are present. The geometry changes can be arbitrary, or can be restricted to relatively few smooth geometric modes. It is shown that the latter option is more effective, and may even be necessary, if shock waves or separation regions are present in the flow. Inverse calculation examples involving a transonic airfoil and a low-speed cascade illustrate the advantages of the modal geometry representation.

The Newton-based sensitivity calculation technique has been shown to allow extremely inexpensive optimization calculations. The optimisation examples presented consisted of drag minimization of a viscous transonic airfoil with shock-induced separation, and drag minimization of a low Reynolds number airfoil with transitional separation bubbles. Two-point optimization of the low Reynolds number airfoil was shown to be necessary to partially overcome severe problems inherent in single-point optimization.

Acknowledgment

Support for this work was provided by the NSF Presidential Young Investigator program, and the MIT Dean of Engineering Office through the Carl Richard Soderberg Chair.

References

- [1] R. Eppler and D. M. Somers. *A Computer Program for the Design and Analysis of Low-Speed Airfoils*. NASA TM 80210, Aug 1980.
- [2] K. W. Mangler. *Die Berechnung eines Tragflügelprofils mit Vorgeschriebener Druckverteilung*. Jahrbuch Der Deutcher Luftfahrtforschung, 1938.
- [3] M. J. Lighthill. *A New Method of Two-Dimensional Aerodynamic Design*. R & M Report 2112, Aeronautical Research Council, Jun 1945.
- [4] G. Volpe and R. E. Melnik. The design of transonic airfoils by a well-posed inverse method. In *International Conference on Inverse Design Concepts in Engineering Sciences*, Austin, Texas, 1984.
- [5] P. Daripa and L. Sirovich. An inverse method for subcritical flows. *Journal of Computational Physics*, 63:311–328, Apr 1986.
- [6] F. Bauer, P. Garabedian, D. Korn, and A. Jameson. Supercritical wing sections I, II, III. In *Lecture Notes in Economics and Mathematical Systems*, Springer-Verlag, New York, 1972, 1975, 1977.
- [7] L. A. Carlson. Transonic airfoil analysis and design using cartesian coordinates. *Journal of Aircraft*, 13, May 1976.
- [8] M. B. Giles and M. Drela. Two-dimensional transonic aerodynamic design method. *AIAA Journal*, 25(9), Sep 1987.
- [9] M. B. Giles, M. Drela, and W. T. Thompkins. Newton solution of direct and inverse transonic Euler equations. In *AIAA 7th Computational Fluid Dynamics Conference*, Cincinnati, Ohio, Jul 1985. AIAA-85-1530.

- [10] N. Hirose, S. Takanashi, and N. Kawai. Transonic airfoil design procedure utilizing a navier-stokes analysis code. *AIAA Journal*, 25(3):353–359, Mar 1987.
- [11] G. N. Vanderplaats. *An Efficient Algorithm for Numerical Airfoil Optimization*. AIAA-79-0079, 1979.
- [12] R. M. Hicks, E. M. Murman, and G. N. Vanderplaats. *An Assessment of Airfoil Design by Numerical Optimization*. NASA TM X-3092, July 1974.
- [13] G. B. Cosentino and T. L. Holst. Numerical optimization design of advanced transonic wing configurations. *Journal of Aircraft*, 23(3):192–199, 1986.
- [14] M. Drela and M. B. Giles. *ISES: A Two-Dimensional Viscous Aerodynamic Design and Analysis Code*. AIAA-87-0424, Jan 1987.
- [15] M. Drela and M. B. Giles. Viscous-inviscid analysis of transonic and low Reynolds number airfoils. *AIAA Journal*, 25(10), Oct 1987.
- [16] M.B. Giles. *Newton Solution of Steady Two-Dimensional Transonic Flow*. PhD thesis, MIT, Jun 1985. Also, MIT Gas Turbine & Plasma Dynamics Laboratory Report No. 186, Oct 1985.
- [17] M. Drela. *Two-Dimensional Transonic Aerodynamic Design and Analysis Using the Euler Equations*. PhD thesis, MIT, Dec 1985. Also, MIT Gas Turbine & Plasma Dynamics Laboratory Report No. 187, Feb 1986.
- [18] R. A. Novak. Streamline curvature computing procedures for fluid-flow problems. In *Winter Annual Meeting of the American Society of Mechanical Engineers*, Nov 1966. 66-WA/GT-3.
- [19] J. P. Goetelow. *Cascade Aerodynamics*. Pergamon Press, Oxford, 1984.
- [20] L. C. Woods. The design of two-dimensional aerofoils with mixed boundary conditions. *Quarterly Journal of Applied Mathematics*, 13(2):139–146, 1955.
- [21] E. Omar, T. Zierten, and A. Mahal. *Two-Dimensional Wind Tunnel Tests of a NASA Supercritical Airfoil With Various High-Lift Systems*. Contractor Report 2214, NASA, 1977.
- [22] G. Volpe and R. E. Melnik. Method for designing closed airfoils for arbitrary supercritical speed distributions. *Journal of Aircraft*, 23(10), Oct 1986.
- [23] M. Drela. *An Integral Boundary Layer Formulation for Blunt Trailing Edges*. AIAA-89-2200, Aug 1989.
- [24] A. M. O. Smith and N. Gamberoni. *Transition, pressure gradient, and stability theory*. Report ES 26388, Douglas Aircraft Co., 1956.
- [25] J. L. van Ingen. *A suggested semi-empirical method for the calculation of the boundary layer transition region*. Report VTH-74, Delft University of Technology, Dept. of Aerospace Engineering, 1956.
- [26] D. E. Hobbs, J. H. Wagner, J. F. Dannenhoffer, and R.P. Dring. *Wake Experiments and Modeling for Fore-and Aft-Loaded Compressor Cascades*. Report FR-13514, Pratt and Whitney Supercritical Airfoil Technology Program, Sep 1980.
- [27] A. Jameon. Computational aerodynamics for aircraft design. *Science*, 245:361–371, 1989.
- [28] P. H. Cook, M. A. McDonald, and M. C. P. Firmin. Aerofoil RAE 2822 pressure distributions and boundary layer and wake measurements. In *Experimental Data Base for Computer Program Assessment*, AR-198, AGARD, 1979.
- [29] R. H. Liebeck and P. P. Camacho. Airfoil design at low Reynolds number with constrained pitching moment. In *Conference on Low Reynolds Number Airfoil Aerodynamics*, UNDAS-CP-77B129, University of Notre Dame, Jun 1985.
- [30] R. M. Hicks and G. N. Vanderplaats. *Application of Numerical Optimization to the Design of Supercritical Airfoils Without Drag-Creep*. SAE Paper 760477, 1977.

**ONE POINT AND MULTI-POINT DESIGN OPTIMIZATION FOR AIRPLANE
AND HELICOPTER APPLICATION**

J.J. THIBERT, Aerodynamics Department
ONERA - BP 72 - 92322 Chatillon Cedex - FRANCE

SUMMARY

The paper describes numerical optimization techniques and shows how these techniques can be used in aerodynamic design. Emphasis is put on the applications with various optimization cases described in details. One point optimization cases for airfoil and wing designs with different objective functions, constraints and design variables are presented as well as multiple design points cases for helicopter blade airfoil applications.

LIST OF SYMBOLS

A	General augmented Lagrangian - Also matrix of the gradients of the active constraints
a	Displacement in the search direction. Also angle of attack
a, β , c, r	scalars
B	Matrix of the gradients of the equality constraints
c	Chord
C, D	Submatrices of B
C, H	Equality constraints
C _D	Drag coefficient
C _L	Lift coefficient
C _p	Pressure coefficient
F, OBJ	Objective function
G	Inequality constraints
H	Hessian matrix
K	Coefficient in the analytical polar drag
L/D	Lift to drag ratio
λ	Lagrangian multiplier
M	Mach number
P	Penalty function - Also power coefficient and parameter
P _i	Legendre polynomials
ϕ	Function
ψ	Azimuth angle
R	Blade radius
Re	Reynolds number
S	Direction of displacement
s	Curvilinear abscissa
T	Temperature
t/c	Thickness to chord ratio
θ	Momentum thickness of the boundary layer
X	Vector of the design variables
x, y, z	Coordinates

SUBSCRIPTS

i	incompressible
i, j, k	integers
Max	maximum value
Min	minimum value
o	first iteration value or value for C _L = 0
RP	reference plane

SUPERSCRIPTS

q	iteration number
*	optimum value

1. INTRODUCTION

The different design tools which are available can be classified in three categories :
 - indirect methods

- inverse methods
- numerical optimization methods

Each of these methods has its advantages and its shortcomings and so they have to be considered as complementary and not competitive. Each offers a different way of finding efficient aerodynamic shapes without resorting to expensive cut and try wind tunnel testing. However, the challenge of designing practical transport or fighter aircraft or helicopter which also demanding higher performance levels is one of the most difficult tasks facing the aerospace designer. For these aircraft, designs must satisfy somewhat different and conflicting aerodynamic objectives. Other considerations, such as radar cross-sectional area, wing or blade bending moment or wing thickness are becoming increasingly important in the final design. Clearly an automated system which is capable of finding the "best compromise" to the problem of aircraft design would be very useful. In that way numerical optimization techniques appears to be a rational, directed design procedure. They give an ordered approach to design decisions where before aerodynamicist relied heavily on intuition and experience.

A CFD analysis program is coupled with a numerical optimization algorithm in such a way as to create a design tool. Aerodynamic quantities such as lift, drag, pitching moment, pressure distribution are computed by the CFD algorithm for a certain configuration and are used in defining an objective function to be minimized by the optimizer. This objective function must relate changes in geometry to improvements in the aerodynamic quality of the design.

Minimization of this objective function through proper choice of the geometric design variables should then correspond to a configuration that is "optimal" in some sense. While this is true only for a given flight condition, it is possible to find a design which will most nearly satisfy optimal requirements for a range of flight regimes by the use of multiple design points.

In addition to the merits of multiple point designs, numerical optimization also allows a great deal of control over both the aerodynamic qualities and the physical shape of the final configuration design. However, a great deal of user expertise may be necessary to take advantage of this high degree of flexibility.

The design process is not reduced to a few computer runs and the intuition and experience are still very important. The most persistent criticism of numerical optimization procedures is the large amount of computer time required for the optimization algorithm to "sort out" and decide which configuration is best. The computer time being largely due to the CFD algorithm used, current improvements in computer and CFD algorithm speed may soon eliminate this shortcoming.

The purpose of this paper is to give in a first part a rapid but basic knowledge of numerical optimization algorithms, to present in a second part the optimization techniques i.e. how to choice the objective function, the constraints and the design variables, and finally to present in a third part a large variety of design applications.

Since it is not the objective of this paper to describe in details all the possible minimization algorithms, only the most widely used are presented. More details can be found in [1] where various algorithms are presented. It is hoped that the paper will encourage practicing engineer to use this powerful tool in design.

2. NUMERICAL OPTIMIZATION TECHNIQUES

2.1. General problems statement

Assume we wish to find the minimum value of the following algebraic function :

$$(1) \quad F(x) = 10x_1^4 + 20x_1^2x_2 + 10x_2^2 + x_1^2 - 2x_1 + 5$$

$F(x)$ is referred to as the objective function which is to be minimized and we wish to determine the combination of the variables x_1 and x_2 which will achieve this goal. The vector x contains x_1 and x_2 and we call them the design variables. Fig. 1 is a graphical representation of the function where lines of constant value of $F(x)$ are drawn. Fig. 1 is referred to as a two variable design space where the design variables x_1 and x_2 correspond to the coordinate axis. If no limits are imposed on the values of x_1 and x_2 and no additional conditions must be met for the "design", $F(x)$ is said to be unconstrained and the solution is represented on Fig. 1 by the point A.

Now assume that for some reasons the design variables x_1 and x_2 have to meet some requirements for example :

$$(2) \quad x_1 \leq 1, \quad x_2 \leq 2,$$

and assume also that we add the additional condition

$$(3) \quad G(x) = 3x_2 + 5x_1 - 2 \leq 0$$

Now the minimum value of eq. (1) subject to the additional conditions given by eq. (2) and (3) is represented on Fig. 2 by the point B. Eq. (2) and (3) define the constraints on the design problems. The constraints given by eq. (2) are often referred to as side constraints because they directly impose bounds on the values of the design variables;

The portion of the design space of Fig. 2 inside the constraint boundaries defined by the hatched lines is referred to as the feasible design space.

In general a design space will be n dimensional and we can write the nonlinear constrained optimization problem mathematically as follow :

(4) Minimise $F(X)$ objective function
subject to

$$(5) \quad g_j(x) \leq 0 \quad j = 1, m \quad \text{inequality constraints}$$

$$(6) \quad h_k(x) = 0 \quad k = 1, l \quad \text{equality constraints}$$

$$(7) \quad x_i^l \leq x_i \leq x_i^u \quad i = 1, n \quad \text{side constraints}$$

$$\text{where } X = \begin{Bmatrix} X_1 \\ X_2 \\ \vdots \\ X_n \end{Bmatrix} \quad \text{design variables}$$

The above form of stating the optimization problems is not unique and various other statements equivalent to this are presented in the literature.

2.2. The iterative optimization procedure

Most optimization algorithms require that an initial set of design variables, X^0 , must be specified. Beginning from this starting point, the design is updated iteratively. Probably the most common form of this iterative procedure is given by

$$(4) \quad X^q = X^{q-1} + \alpha^q S^q$$

where q is the iteration number and S is a vector search direction in the design space. The scalar quantity α^q defines the distance that we wish to move in direction S .

To see how the iterative relationship given by Eq. (4) is applied to the optimization process, consider the two-variable problem shown in Fig. 3.

Assume we begin at point X^0 and we wish to reduce the objective function. We will begin by searching in the direction S^1 given by

$$(5) \quad S^1 = \begin{Bmatrix} -1.0 \\ -0.5 \end{Bmatrix}$$

The choice of S is somewhat arbitrary as long as a small move in this direction will reduce the objective function without violating any constraints. In this case, the S^1 vector is approximately the negative of the gradient of the objective function, that is, the direction of steepest descent. It is now necessary to find the scalar α^q in Eq. (4) so that the objective is minimized in this direction without violating any constraints.

We now evaluate X and the corresponding objective and constraint functions for several values of α to give

$$\alpha = 0 \quad X = \begin{Bmatrix} 2.0 \\ 1.0 \end{Bmatrix}$$

$$(6a) \quad F(\alpha) = 10.0 \quad g(\alpha) = -1.0$$

$$\alpha = 1.0 \quad X = \begin{Bmatrix} 2.0 \\ 1.0 \end{Bmatrix} + 1.0 \begin{Bmatrix} -1.0 \\ -0.5 \end{Bmatrix} = \begin{Bmatrix} 1.0 \\ 0.5 \end{Bmatrix}$$

$$(6b) \quad F(\alpha) = 8.4 \quad g(\alpha) = -0.2$$

$$\alpha = 1.5 \quad X = \begin{Bmatrix} 2.0 \\ 1.0 \end{Bmatrix} + 1.5 \begin{Bmatrix} -1.0 \\ -0.5 \end{Bmatrix} = \begin{Bmatrix} 0.50 \\ 0.25 \end{Bmatrix}$$

$$(6c) \quad F(\alpha) = 7.6 \quad g(\alpha) = 0.2$$

$$(5) \quad \alpha^* = 1.25 \quad X^* = \begin{Bmatrix} 2.0 \\ 1.0 \end{Bmatrix} + 1.25 \begin{Bmatrix} -1.0 \\ -0.5 \end{Bmatrix} = \begin{Bmatrix} 0.750 \\ 0.375 \end{Bmatrix}$$

$$(6d) \quad F(\alpha^*) = 8 \quad g(\alpha^*) = 0.0$$

where the objective and constraint values are estimated using Fig. 3. In practice, we would evaluate these functions on the computer, and, using several proposed values of α , we would apply a numerical interpolation scheme to estimate α^* . This would provide the minimum $F(X)$ in this search direction which does not violate any constraints. Note that by searching in a specified direction, we have actually converted the problem from one in n variable X to one variable α . Thus, we refer to this as a one-dimensional search. At point X^1 , we must find a new search direction such that we can continue to reduce the objective without violating constraints. In this way, Eq. (4) is used repetitively until no further design improvement can be made.

From this simple example, it is seen that nonlinear optimization algorithms based on Eq. (4) can be separated into two basic parts. The first is determination of a direction of search S , which will improve the objective function subject to constraints. The second is determination of the scalar parameter α^* defining the distance of travel in direction S . Each of these components plays a fundamental role in efficiency and reliability of a given optimization algorithm.

2.3. Optimization algorithms

It is not the objective of the paper to describe in detail all the possible algorithms. However the main features of the more widely used will be described in the following chapters. We will first begin by the techniques available to find the search directions.

2.3.1. Unconstrained function of n variables

Fig. 4 provides a general flowchart for multivariable unconstrained minimization. As seen from the figure, an actual optimization programs consists of three major components :

1. Determine the direction in which to search
2. Perform the actual one-dimensional search
3. Determine when the process has converged to an acceptable solution.

2.3.1.1. Zero-order methods

Optimization techniques which require function values only are called zero-order methods. These methods are considered most useful for problems in which the function evaluation is not computationally expensive. The random search method and the Powell's method [2] are the most popular methods.

Powell's method is based on the concept of conjugate directions, where directions S^i and S^j are conjugate if

$$(7) \quad (S^i)^T H S^j = 0$$

where H is the Hessian matrix (i.e. the matrix of the second partial derivatives of the objective with respect to the design variables).

The basic concept of Powell's method is to first search in n orthogonal directions, S^i , $i = 1, n$ being the coordinate directions, where each search consists of updating the X vector according to Eq. (4). These directions are not usually conjugate but provide a starting point from which conjugate directions are built. Having completed the n unidirectional searches, a new search direction is created by connecting the first and last design point. This becomes the $n + 1$ search direction. The process is shown geometrically in Fig. 5.

The first search is in the X_1 direction, followed by a search in the X_2 direction. Note that the α_i^* in Eq. (4) is negative, assuming the S^i vector is in the positive X_1 direction. In practice, we may first search in the positive X_1 direction and, failing to improve the design, then search in the negative X_1 direction. This allows for writing a one-dimensional search algorithm which only searches in the positive α domain.

At the end of the second iteration the $n + 1$ search direction S^3 is found by connecting the initial design X^0 with the current design X^2 as shown.

The method of Hooke and Jeeves [3] and the somewhat more complicated method of Rosenbrock [4] utilize exploratory searches conceptually similar to Powell's univariant searches, followed by acceleration steps. In each case, the idea is to gain useful information about the shape of the design space which can be used to accelerate convergence.

2.3.1.2. First-order methods

First-order methods, those which utilize gradient information, are usually more efficient than zero-order methods. The price paid for this efficiency is that gradient information must be supplied, either by finite-difference computations or analytically, and that these methods often perform poorly for functions which have discontinuous first derivatives. However, for the majority of problems, first-order methods can be expected to perform better than zero-order methods because the user is providing more information on which to base optimization decisions.

In the following section, two basic first-order approaches are presented, steepest-descent and conjugate-directions.

Steepest descent

The steepest descent method is probably the best known and yet the worst performing of the first-order methods. The principal importance of the method is that it usually forms the starting point for the more sophisticated first-order methods.

In the steepest descent method, the search direction S is taken as the negative of the gradient of the objective function. That is, at iteration q

$$(8) \quad S^q = -\nabla F(X^q)$$

The S vector is used in Eq. (4) to perform the one-dimensional search. The optimization algorithm for the steepest descent method is shown in Fig. 6.

Figure 7 shows the sequence of one-dimensional search. As seen from the figure, the convergence rate of the method is very poor. This is principally due to the fact that the steepest descent method does not utilize information from previous iterations in order to accelerate the convergence. Therefore, the steepest descent algorithm is not recommended for general application, although the steepest descent direction will be used as an initial search direction in the more powerful algorithm of the following section.

The conjugate direction method

The conjugate direction method of Fletcher and Reeves [5] requires only a simple modification of the steepest descent algorithm and yet dramatically improve the convergence rate of the optimization process.

The basic approach is to pick search directions which are conjugate by the definition of Eq. (4). This is accomplished by specifying an initial search vector as the steepest descent direction defined by Eq. (8). On subsequent iterations a conjugate direction is defined as:

$$(9) \quad S^q = -\nabla F(X^q) + \beta_q S^{q-1}$$

when the scalar β_q is defined as:

$$(10) \quad \beta_q = \frac{|\nabla F(X^q)|^2}{|\nabla F(X^{q-1})|^2}$$

Fig. 8 shows the iteration history of the algorithm.

2.3.1.3. Second-order methods : Newton's method

Newton's method, together with various modifications to improve efficiency, is the classical second-order method. This technique begins with a second-order Taylor series expansion given by:

$$(11a) \quad F(x) = F(X^q) + \nabla F(X^q) \cdot \delta X + \frac{1}{2} \delta X \cdot H(X^q) \delta X$$

where

$$(11b) \quad \delta X = X^{q+1} - X^q$$

Solving Eq. (11a) for the stationary conditions gives:

$$(12) \quad \delta X = -[H(X^q)]^{-1} \nabla F(X^q)$$

Rearranging Eq. (11b), we have, using Eq. (12):

$$(13) \quad \begin{aligned} X^{q+1} &= X^q + \delta X \\ &= X^q - [H(X^q)]^{-1} \nabla F(X^q) \end{aligned}$$

Comparing the last term in Eq. (13) to the S vector in Eq. (4) (with $a^* = 1$), we have

$$(14) \quad S^q = -[H(X^q)]^{-1} \nabla F(X^q)$$

Therefore, Eq. (14) provides us with a search direction to use in a general one-dimensional search. We will not actually invert H but will instead solve the set of simultaneous equations $HS = -\nabla F$.

Here we must provide not only function values and gradient information, but the second-derivative matrix H as well. If the function being minimized is a true quadratic in the design variables, the use of this search direction with a move parameter $a^* = 1$ will provide the solution in only one iteration. In practice, because we wish to minimize a general function, we can modify the algorithm to improve efficiency. First, we can actually search in direction S^q , noting that $a = 1$ should be an excellent first estimate for a_{q^*} . A second modification is to only calculate the H matrix every few iterations, but calculate the ∇F vector on each iteration. This assumes that the second derivatives of the function do not change too rapidly and so need not be determined as often as the first-derivative information. If the calculation of the Hessian matrix is expensive, this can markedly improve overall optimization efficiency without significantly affecting the final result.

If we are fortunate enough to be able to calculate the matrix of second derivatives easily, Newton's method is almost always the preferred approach. While most engineering problems do not lend themselves to easy calculation of the second derivatives, it is often possible through the use of approximation techniques to convert the problem to a form ideally suited for solution by this method.

2.3.2. Constrained functions of n variables

2.3.2.1. *Linear programming*

Undoubtedly, the most thoroughly developed and understood optimization problem is the one in which the objective and constraints are linear functions of the design variables X . Such problems are referred to as linear programming (abbreviated LP) problems. Most engineering problems of practical interest are not of this form. Therefore, in the study of numerical optimization techniques, linear programming is often overlooked in favor of proceeding directly to the problem at hand. However, the discussion of linear programming is important because it is often possible to simplify a nonlinear optimization problem by linearization and then to solve it using these techniques.

The most common method for the solution of LP problems is referred to as the *simplex* method. This method is attributable to Dantzig and was developed in the late 1940s [6]. Computer codes based on this method are available on most computer systems. These have usually been extensively tested and are highly reliable.

Standard linear programming form

The standard form of the LP problem is defined by

Minimize :

$$(15) \quad F(X) = \sum_{i=1}^n C_i X_i$$

Subject to :

$$(16) \quad \sum_{i=1}^n a_{ij} X_i = b_j \quad j = 1, m$$

$$(17) \quad X_i \geq 0 \quad i = 1, n$$

This is an equality-constrained problem with nonnegative design variables. Most problems of interest are not of this form. However, all LP problems can be converted to this form.

Equation (17) appears at first glance to be a major restriction to the method. However, this restriction can be conveniently overcome by replacing variable X_i by two positive variables and taking their difference; that is,

$$(18a) \quad X_i = X_i' - X_i''$$

$$(18b) \quad X_i' \geq 0 \quad X_i'' \geq 0 \quad i = 1, n$$

Now for any finite value of X_i , either positive or negative, there must exist two variables X_i' and X_i'' such that their difference will equal X_i . Therefore, by using Eq. (18) in Eqs (15) and (16) and solving with respect to the new variables, the problem can be solved directly. After solution, the values X_i corresponding to the optimum can be determined using Eq. (18a). Note, however, that this transformation has been expensive. We have doubled the number of design variables which must be considered in the optimization problem.

An alternative approach would be to add a constant to each of the design variables X_i so that

$$(19) \quad X_i = X_i' - Q_i$$

where Q_i is a large positive number. Eq. (19) can be substituted into Eq. (15) to (17) without increasing the number of design variables in the problem.

The simplex method proceeds in two phases : Phase I finds an initial basic feasible solution which has only m nonzero variables X_i , and these variables are positive (or zero). Phase II moves from one basic feasible solution to another until the optimum is found.

2.3.2.2. *Sequential unconstrained minimization techniques*

Here we deal with the more general design optimization problem where both the objective function and constraint functions are nonlinear. This general problem statement is defined by Eq. (4) to (7) repeated here :

Minimize :

$$(20) \quad F(X)$$

Subject to :

$$(21) \quad g_j(X) \leq 0 \quad j = 1, m$$

$$(22) \quad h_k(X) = 0 \quad k = 1, l$$

note that the side constraints are included in the inequality-constraint set.

The general approach will be to minimize the objective function as an unconstrained function but to provide some penalty to limit constraint violations. Because the way in which this penalty is imposed often leads to a numerically ill-conditioned problem, a method is devised whereby only a moderate penalty is provided in the initial optimization stages, and this penalty is increased as the optimization progresses. This requires the solution of several unconstrained minimization problems in obtaining the optimum constrained design ; thus the term *sequential unconstrained minimization techniques or SUMT* to identify these methods.

The classical approach to using SUMT is to create a pseudo-objective function of the form

$$(23) \quad \phi(X, r_p) = F(X) + r_p P(X)$$

where $F(X)$ is the original objective function. $P(X)$ is an imposed penalty function, the form of which depends on the SUMT being employed. The scalar r_p is a multiplier which determines the magnitude of the penalty, and r_p is held constant for a complete unconstrained minimization. The subscript p is the unconstrained minimization number.

The first and easiest to incorporate into the design algorithm is referred to as an exterior penalty function method because it penalizes the objective function only when constraints are violated.

The penalty function $P(X)$ is typically given by

$$(24) \quad P(X) = \sum_{j=1}^m [\max(0, g_j(X))]^2 + \sum_{k=1}^l [h_k(X)]^2$$

From Eq. (24), we see that no penalty is imposed if all constraints are satisfied [all $g_j(X) \leq 0$ and all $h_k(X) = 0$], but whenever one or more constraints are violated, the square of this constraint is included in the penalty function.

The second approach, known as the interior penalty function method, penalizes the objective function as the design approaches a constraint, but constraint violations are never allowed. Therefore, a sequence of improving feasible design is produced.

Probably the most common penalty function used in the interior method is

$$(25) \quad P(X) = \sum_{j=1}^m \frac{1}{g_j(X)}$$

However the numerical ill-conditioning often encountered in the two previous techniques can be substantially reduced by using another method known as the augmented Lagrange multiplier method (ALM).

In that method the objective function is replaced by the general augmented Lagrangian.

$$(26) \quad A(X, \lambda, r_p) = F(X) + \sum_{j=1}^m (\lambda_j \psi_j + r_p \psi_j^2) + \sum_{k=1}^l (\lambda_{k+m} h_k(X) + r_p [h_k(X)]^2)$$

where

$$(27) \quad \psi_j = \max \left[g_j(X), \frac{-\lambda_j}{2r_p} \right]$$

The update formulas for the Lagrangian multipliers are now

$$(28) \quad \lambda_j^{p+1} = \lambda_j^p + 2r_p \left\{ \max \left[g_j(X), \frac{-\lambda_j^p}{2r_p} \right] \right\} \quad j = 1, m$$

$$(29) \quad \lambda_{k+m}^{p+1} = \lambda_{k+m}^p + 2r_p h_k(X) \quad k = 1, l$$

The general algorithm is given in Fig. 9. In summary, the method has several attractive features.

1. The method is relatively insensitive to the value of r_p . It is not necessary to increase r_p to ∞ .
2. Precise $g_j(X) = 0$ and $h_k(X) = 0$ is possible.
3. Acceleration is achieved by updating the Lagrange multipliers.
4. The starting point may be either feasible or infeasible.
5. At the optimum, the value of $\lambda_j^* = 0$ will automatically identify the active constraint set.

2.3.2.3. Direct methods

Techniques dealing with the constraints directly in the search for the optimum are numerous. We can list for example :

- the random search technique
- the sequential linear programming
- the method of centers
- the generalized reduced gradient method.
- the feasible direction methods.

Only the last one will be described briefly. The optimization algorithm associated to the method begins with the determination of the search direction, then considers the one-dimensional search and finally address the problem of initially infeasible designs.

The search direction

Assume that at iteration q there are J active constraints. We now wish to find a usable-feasible direction which will reduce the objective function as rapidly as possible. For now we will consider inequality constraints only, dealing with equality constraints later as a special case. Now, instead of finding a direction slightly away from the constraint boundaries, we will find a direction S which will follow the constraints but will allow for the design to leave a constraint boundary if such a direction will reduce the objective most rapidly. In other words, we wish to find a "constrained steepest descent" direction. This is easily done by considering the following problem :

Maximize :

$$(30) \quad -\nabla F(X) \cdot S$$

Subject to :

$$(31) \quad \nabla g_j(X) \cdot S \leq 0 \quad j \in J$$

$$(32) \quad S \cdot S \leq 1$$

Solving this problem gives a search direction which is tangent to the critical constraint boundaries, unless the objective can be reduced more rapidly by moving away from one or more constraints. We can identify the case where the search direction is away from a currently active constraint by taking the scalar product of the gradient of each critical constraint with the S vector. If the result is less than zero within a small tolerance [it will never be greater than zero by virtue of Eq. (31)] we omit this from our set of active constraints. Another possible solution is that S is a null vector (say numerically all $|S_i| < 0.001$, $i = 1, n$).

Assuming an S vector is found for which one or more $\nabla g_j(X) \cdot S = 0$, $j \in J$, we will choose a set of dependent variables as in the generalized reduced gradient method. We then perform a one-dimensional search with respect to the independent variables, updating the dependent variables using Newton's method. For example, in Fig. 10 we may pick X_2 as the independent variable and update X_1 as the dependent variable at each step in the one-dimensional search.

Equality constraints

In that special case the direction finding problem becomes :

Maximize :

$$(33) \quad -\nabla F(X) \cdot S$$

Subject to :

$$(34) \quad AS \leq 0$$

$$(35) \quad BS = 0$$

$$(36) \quad S \cdot S \leq 1$$

where now the rows of A contain only the gradient of the active constraints. The rows of matrix B contain the gradient of the equality constraints

$$(37) \quad B = \begin{bmatrix} \nabla^T h_1(X) \\ \nabla^T h_2(X) \\ \vdots \\ \nabla^T h_l(X) \end{bmatrix}_{l \times n}$$

Now, for each equality constraint, we can choose one of the design variables (and the corresponding component of S) as a dependent variable. Thus, we partition Eq. (35) as

$$(38) \quad BS = [C \ D] \begin{Bmatrix} S_I \\ S_D \end{Bmatrix} = 0$$

where S_I are independent variables, S_D are dependent variables, and C and D are the corresponding submatrices of B . There are I terms in S_D and they need not be the last terms in S . We simply partition the equations this way for clarity. We can now solve for S_D in terms of S_I , substitute this into Eqs. (33), (34), and (36) and solve for the reduced set of components S_I , just as for inequality constraints.

Equation (39) $S_D = -D^{-1}CS_I$ is then used to obtain the components of S corresponding to the dependent variables.

Initially infeasible designs

If an initial design X^0 is specified such that one or more constraints are violated, the first priority is to find a feasible design.

We begin by treating all violated constraints as if they are inequality constraints. Any equality constraints which are satisfied (or nearly satisfied) are used to define dependent variables to give a reduced direction-finding problem similar to the one described in the previous section.

Therefore, we can treat constraint violations in the same manner as in the method of feasible directions to provide a search direction which points toward the feasible region.

Having determined the S vector, we define dependent variables associated with all equality constraints, but not inequality constraints, and then search in the S_I direction. Here we search to overcome the constraint violations associated with inequality constraints but do not necessarily stop at the constraint boundary. During the search we use Newton's method to drive the equality constraints to zero so, ideally, at the end of the one-dimensional search, the equality constraints are satisfied precisely and the inequality constraints are at least satisfied. In practice, this may require several iterations, so that during each search we reduce the infeasibility as much as possible. This is because the problem may be so nonlinear that we cannot overcome the constraint violations in one iteration.

Infrequent gradient calculations

The cost of optimization in practical design is usually directly proportional to the number of function evaluations needed to reach the solution. This is particularly true when finite-difference gradients are calculated because n function evaluations are needed, in addition to the nominal design, to compute the gradient information. Therefore, we should consider the possibility that it may not be necessary to compute gradients at each iteration of the optimization process.

Consider now the first-order Taylor series expansion of a general function $f(X)$:

$$(40) \quad f(X^q) = f(X^{q-1}) + \nabla f(X^{q-1}) \cdot \delta X^q$$

where $f(X)$ may be any objective or constraint function, and

$$(41) \quad \delta X^q = X^q - X^{q-1}$$

Now if we have completed iteration q and we evaluate the true function $f(X^q)$, we can compare this to its approximation $f(X^q)$. If they agree within an acceptable tolerance, we can use $\nabla f(X^{q-1})$ again. We can identify the situation where the gradient is changing rapidly if the approximate and precise objective and constraint function values do not agree within a specified tolerance or if Newton's method for determining the values of dependent variables fails to converge or converges slowly. In either case, or when some new constraint becomes active for which we do not have the gradient, we would calculate new gradient information.

Note that the technique of infrequent gradient calculations is not limited to the method discussed here but may be incorporated into other methods.

To summarize, we again emphasize the importance of making the best use of whatever information is available at each step in the optimization process. The algorithm of the feasible direction method described above is given Fig. 11.

2.3.3. One-dimensional search techniques

In the previous chapters, various techniques for finding the direction in which to search have been described. As said at the beginning of chapter 2.3.1. The second step of the optimization process is to perform the displacement in the search direction which provide the minimum $F(X)$ which does not violate any constraints. The solution of this problem will give a^* in Eq. (4). This problem is called the one-dimensional search since the only variable is a .

Several techniques can be used to treat the problem :

- polynomial interpolation
- golden section method

For each of these methods the objective function F is calculated for several values of a in order to find a^* . Several other techniques can be found in [1] for the cases where the one variable function is subject to constraints.

When using the feasible direction method described in section 2.3.2.3., the following method can be used.

Considering the matrix Q defined by :

$$(42) \quad Q = \begin{bmatrix} \nabla^T g_1(X) \\ \nabla^T g_2(X) \\ \vdots \\ \nabla^T g_J(X) \\ \nabla^T h_1(X) \\ \vdots \\ \nabla^T h_l(X) \end{bmatrix}_{(J+l) \times n}$$

From here, using Gaussian elimination with pivot search, we identify the set of dependent variables. Having done this, we partition the S vector as :

$$(43) \quad S = \left\{ \begin{array}{l} S_I \\ S_D \end{array} \right\}$$

where now the set of dependent variables includes those associated with inequality constraints as well as equality constraints.

We now perform the one-dimensional search with respect to the independent variables as :

$$(44) \quad X_I^q = X_I^{q-1} + a_I^* S_I^q$$

For each proposed a_I , we update the values of the dependent variables using Newton's method, just as in the generalized reduced gradient method. A first estimate for the dependent variables is obtained using Eq. (43) to give :

$$(45) \quad X_D^q = X_D^{q-1} + a_I^* S_D^q$$

where this is precise for linear constraints. For nonlinear constraints, we use Newton's method to ensure precise satisfaction of the constraints.

If we have only calculated the gradient of the J active constraints, our first proposed a in the one-dimensional search is a somewhat arbitrary one. However, if adequate computer storage is available, we can also calculate the gradients of some subset K of nearly active constraints to give $\nabla g_j(X)$, $j \in K$. Now we can obtain a reasonable first estimate for a_I from :

$$(46) \quad a_I = \min_{a > 0} \left| a_j = \frac{-g_j(X)}{\nabla g_j(X) \cdot S} \right| \quad j \in K$$

In Eq. (46) any negative a_j is not used because the search direction is actually away from that constraint.

By calculating the gradients of only a few additional constraints, we can expect to improve the efficiency of the one-dimensional search since this will usually provide a good initial estimate to a_I^* . It is recognized that some other constraint not contained in the set K may actually limit the search or that a_I^* will correspond to an unconstrained minimum with respect to X_I . However, this approach usually provides significant efficiency in the one-dimensional search.

2.3.4. Convergence criteria

Concerning the convergence of the optimization algorithms, the most widely criteria used are :

- the maximum number of iterations.
- some prescribed value for the absolute or the relative change in the objective function.

The summary of the main optimization algorithms is presented Fig. 12. Some of these algorithms are included in the most widely used numerical optimization codes which are :

- CONMIN [7]
- COPES [8]
- QNMDIF [9]
- E04 [10]

2.4. Optimization techniques

The formulation of the optimization problem is of great importance because it will play a major role in the optimization process. This formulation includes the choice of the objective function, the selection of the constraints as well as the selection of the design variables. Concerning the objective function, its choice depends on the aerodynamic code which will be used with the optimization code while the constraints will be selected regarding both the performance of the aerodynamic and of the optimization codes.

Since the solution of the optimization problem will be a combination of the design variable, it is obvious that their selection has to be made carefully.

2.4.1. Selection of the objective function

It is very attractive to choose as objective function the main performance which has to be improved like the drag or the C_L max. However, these two coefficients suffer from the questionable accuracy of their evaluation with current methods. However if their gradients with respect to each design variable and constraint are accurately determined the optimization will give some improvement even if the absolute values of these coefficients are not accurate.

However, taking the drag or L/D as objective function can give no design improvement since they do change with angle of attack and may mislead the optimiser. To avoid this problem, the lift coefficient value for which the drag has to be improved can be put as a side constraint but a more efficient solution is to use for the objective function an analytical representation of the drag polar [11][12]. For example in [12] the drag polar is expressed as :

$$(47) \quad C_D = C_{D\min} + K(C_L - C_{L\min})^2$$

If the optimization drag result is evaluated as a change in drag relative to a baseline drag polar, then a simple lift change in angle of attack will not mathematically appear as a design improvement. The baseline drag polar would be given by equation (47). The parameters $C_{D\min}$, K and $C_{L\min}$ can be determined by three numerical analyses and the baseline drag problem is actually a curve fit to the results. Equation (47) becomes

$$(48) \quad C_{D\text{base}} = C_D^* + K(C_L - C_L^*)^2$$

where the nomenclature is changed to indicate a local curve fit to a baseline polar. A new drag result would be evaluated as

$$(49a) \quad \Delta C_D = C_D - C_{D\text{base}}$$

$$(49b) \quad \Delta C_D = C_D - (C_D^* + K(C_L - C_L^*)^2)$$

within the accuracy of the curve fit, this results in $\Delta C_D = 0$ for an angle of attack change with the baseline geometry. Thus the optimizer does not have a bias towards reducing lift in order to reduce the drag.

Eq. (49) can be manipulated to yield several different objective functions that can be used as part of the optimization criteria. The objective function could be expressed as a change in K :

$$(50) \quad K_{\text{new}} = (C_D - C_D^*)/(C_L - C_L^*)^2$$

where a smaller K_{new} is a better design. Alternatively, the objective function could be expressed as a change in C_L^* .

$$(51) \quad C_{L\text{new}}^* = C_L - (C_D - C_D^*)/K$$

and the optimization seeks to maximize $C_{L\text{new}}^*$.

Finally, the optimizer may be used to minimize C_D^{new} :

$$(52) \quad C_{D\text{new}}^* = C_D - K(C_L - C_L^*)^2$$

As applied to an optimization problem, the following factors will influence the success of the particular objective function used :

- Analysis inaccuracies may change the baseline drag polar or the increments due to geometry changes.
- The lift changes (with the baseline geometry) may exceed the range that is accurately modeled by the curve fit drag polar.
- As the design progresses (i.e. the geometry changes), the original baseline drag polar curve fit will become inappropriate.

However as the design progresses, the curve fit can be revised to more accurately represent the drag polar of the current geometry.

Another objective function which is widely used is a target pressure distribution prescribed by the designer. In that case the optimization problem is formulated in the form of :

$$(53) \quad \text{OBJ} = \frac{1}{N} \left\{ \sum_{i=1}^N (C_{P_i}^T - C_{P_i})^2 \right\}^{1/2}$$

that is, minimization of the "error" between target and analysis pressures. The optimization procedure is then used to obtain essentially the same results as the inverse methods. The success of this type of objective function is due to the fact that the aerodynamicist is comfortable with pressure distributions and the analysis codes are generally easier to use than the inverse methods. However, an advantage of wing optimization procedure in that way is that it is easy to control the geometry of the design through constraints while it is not the case with most of the existing inverse methods. An extension of the previous objective function can be found in [13] where a non-linear least squares minimization is formulated as follows :

let the residuals $r_i (P_1 \dots P_M)$, $i = 1, 2 \dots N$, be functions of M design parameters. To minimize r_i , in the least-squares sense, value for the parameters, P_j , are found which minimizes :

$$(54) \quad F(P_1, P_2, \dots, P_M) = \sum_{i=1}^N [r_i(P_1, P_2, \dots, P_M)]^2$$

where r_i denotes the difference between the N specified reference plane quantities and corresponding N computed quantities associated with the M parameters. The reference plane fluid state variables are the total pressure P_T , the total temperature T_T , the directional Mach number M_x, M_y, M_z .

Eq. (54) can be written in vector form $R(P)^T R(P)$ where $R(P)$ is a vector with components r_i . Variable constants are imposed by addition of barrier functions, added to the objective function..

Thus the expression $R^T R$ becomes :

$$\begin{aligned} R^T R = & \sum_{i=1}^{N_r} [(P_{T_{rp}} - P_{T_i})^2 + (T_{T_{rp}} - T_{T_i})^2 + (M_{x_{rp}} - M_{x_i})^2 + (M_{y_{rp}} - M_{y_i})^2 \\ & + (M_{z_{rp}} - M_{z_i})^2] + \sum_{j=1}^{N_c} \phi_j^2 \end{aligned}$$

where N_r is the number of geometrical distinct reference plane points, ϕ_j represents the barrier functions, and N_c is the number of parameter constraints.

The non linear least square form of Eq. (54) is then minimized using an extension of the Gauss-Newton method.

The examples presented above show that various objective functions, simple ones or complex ones can be used. However complex objective functions in which several aerodynamic coefficients are present can lead to the following problems :

- very long optimization process
- great probability to go to a "relative" optimum during the optimization process
- no guarantee that the value of all terms appearing in the objective function decreases during the optimization procedure.

In most cases it is so recommended to use a simple objective function and to complete the objective function with the constraints.

2.4.2. Selection of the constraints

The constraints can be used to control the design shape or to complete the objective function or to discipline the modification during the optimization process.

- In the first case constraints are put for example on the thickness to chord ratio or on the thickness for several prescribed locations for an airfoil or a wing design. For bodies of revolution or wing design volume constraints are sometimes taken into account.
- In the second case when optimizing the drag, constraints on the lift range for which we want to have a drag reduction can be used.

Another example is the $C_{L\max}$ optimization. Since this coefficient is generally not directly given by most of the codes it cannot be chosen for the objective function so the problem can be formulated as follow :

Objective : C_D at high angle of attack
constraints : $|C_p|$ level limit coming from experimental data on airfoils of the same type.

- In the third case the constraints are used in order to take into account some other aerodynamic performance than the one(s) included in the objective function. For example when optimizing the drag or the $C_{L\max}$, a constraint on the pitching moment coefficient can be used or when several design points are to be considered, the optimization can be performed for one point with constraints put on some aerodynamic coefficients on the second point for example :

$\text{obj} : C_D(M_1, \alpha_1)$ $\text{constraint} : C_D(M_2, \alpha_2)$	first design point second design point
---	---

The gradient of the constraints being computed by the optimization code, generally increasing the number of constraints will increase the computing time. Moreover some optimization codes are not very efficient when constraints are included and some parameters have to be adjusted in order to force the convergence. This is illustrated by the following example which compares the performance of the CONMIN code and of the EO4VAF code (from the NAG library) for the Rosen and Suzuki problem.

The problem is formulated as follow :

- The function to be minimized is :

$$\text{OBJ}(X) = X_1^2 + X_2^2 + 2X_3^2 + X_4^2 - 5X_1 - 5X_2 - 21X_3 + 7X_4$$

- The constraints are :

$$\begin{aligned} & X_1^2 - X_2^2 - X_3^2 - X_4^2 - X_1 + X_2 - X_3 + X_4 + 8 \geq 0 \\ & X_1^2 - 2X_2^2 - X_3^2 - 2X_4^2 + X_1 + X_4 + 10 \geq 0 \\ & -2X_1^2 - X_2^2 - X_3^2 - 2X_1 + X_2 + X_4 + 5 \geq 0 \end{aligned}$$

The initial conditions are $X_i = (0, 0, 0, 0)$.

The CONMIN code uses a feasible direction method from Zoutendijk when the constraint are active while in the EO4VAF code constraints are included in the objective function through the use of a Lagrangian function as follow :

$$\text{OBJ}' = \text{OBJ} + \sum_{i=1}^M (\lambda_i C_i + \rho |C_i|^2)$$

C_i being equality constraints which are formulated from the inequality constraints.

Fig. 13 shows the convergence history of the CONMIN code for two values of the parameters ALPHAX and ABOBJ1 which control the initial displacement for the one-dimensional search. The exact solution ($\text{OBJ} = -44$ for $X(0, 1, 2, -1)$) is obtained after 43 objective function and constraints evaluations.

Fig. 14 shows the convergence history of the EO4VAF code with several values of the ρ parameter which controls the weight of the constraints. For $\rho = 1$ the convergence is fast but in final solution the constraints are violated. For $\rho = 100$ the convergence is very slow.

This example shows the necessity for the designer to know in details the optimization code he wants to use especially if constrained optimizations are to be performed.

Some authors [14] use the constraints to force the optimization process to go rapidly towards the solution. In that case a constraint (initially violated) is put on the same parameter than the one included in the objective function.

2.4.3. Selection of the design variables

The final result of the optimization process being a combination of the design variables their choice is very important.

The design variables must be selected to converge the optimization process quickly and generate a wide variety of geometries. The functional relations well-adapted to this problem can be described mathematically in many ways. Numerical tests are needed to determine the value of the mathematical model proposed. Two types of shape functions exist : analytical functions and shape functions of aerodynamic origin.

2.4.3.1. Analytical shape functions

- Legendre polynomials.

When the Legendre polynomials or other orthogonal expressions are used, the optimization algorithm becomes highly effective and the initial airfoil is modified regularly.

The coordinates of the modified area are expressed as a function of reduced abscissa $X = x/x_0$, where x is the real abscissa and $[0, x_0]$ is the modified area :

$$\begin{aligned} Y = Y_1 + (1 - X)^3 (a_1 \sqrt{X} + a_2 (P_2 + 1) + a_3 (P_3 - 1) \\ + a_4 (P_4 + 1) + a_5 (P_5 - 1) + a_6 (P_6 + 1)) \end{aligned}$$

where P_2, P_3, P_4, P_5 and P_6 designate the Legendre polynomials over $[0, 1]$ and a_1, a_2, a_3, a_4, a_5 and a_6 are the design variables :

$$\begin{aligned}P_2 &= 2X - 1, \\P_3 &= 6X^2 - 6X + 1, \\P_4 &= 20X^3 - 30X^2 + 12X - 1, \\P_5 &= 70X^4 - 140X^3 + 90X^2 - 20X + 1, \\P_6 &= 252X^5 - 630X^4 + 560X^3 - 210X^2 + 30X - 1.\end{aligned}$$

The square root term is introduced to modify the leading edge of the airfoil, and factoring by $(1 - X)^3$ ensure the continuity of the radius of curvature at the point X_0 .

Figure 15 shows the six corresponding shape functions.

This approach is used in modifying the part of the upper or lower airfoil surface upstream of a given abscissa $x_{g/c}$.

- Other polynomial functions.

Some other functions can be selected to address the modification qualitatively. These functions are added linearly to the starting geometry.

Wagner functions may be used (Fig. 16a), which permit a fairly large variation as far as the shape of the airfoil upper and lower surface are concerned. However, they cannot be used at the highest harmonics ($n > 7$) because they can cause waves in the geometry (changes in the sign of the slope over a small part of the chord). These functions are unsuitable to modify the camberline significantly (starting, for instance, from a symmetrical airfoil).

The Hicks-Henne (H.H.) functions (Fig. 16b) and the polynomial functions (Fig. 16c) have a simpler form, which makes them particularly suited for even substantial changes of the camberline ; hence they are mainly used for this purpose. They are characterized by different curvature towards the trailing edge : H.H. functions are concave, polynomial functions are convex. The use of these functions during the optimization permits, in general the attainment of the desired behavior in the upper surface portion just forward of the trailing edge : both concave and convex geometries are thus obtained, according to the requirements. Other functions have been derived from the need to reproduce other geometrical behaviors typical of the transonic design : such as lower surface cusp for rear loading, and deflection of leading edge and trailing edge flaps.

All mentioned functions could be used concurrently in the modification of the airfoil, but this would give rise to some problems. A first advice contrary to such a use comes from the expansion of the computation time. In the design of an airfoil required to operate at high C_L , starting for instance from a symmetrical profile, functions for the refinement of the thickness distribution should be used only when the geometry has already been cambered enough. Moreover, a modification using all variables at the same time, "masks" the impact that each type of function has on the geometry. To have a knowledge of such an impact is on the other hand important because it may suggest the introduction of new, complementary functions. The only shortcoming associated to the sequential use of sets of functions is, this being a non-linear problem, that the sequence in which these functions are used influence the final result. Once again, design experience must give indications on the most adequate sequence.

- Analytical definitions of an airfoil

Instead of using perturbation functions to be added to an initial airfoil, it is very attractive to deal directly with the airfoil coordinates. However it is not easy to define an airfoil contour with only a few parameters. An example is given however by the Boudigues formulation.

S. Boudigues'formulation is particularly well-adapted to representing existing airfoils in analytical form. The point at coordinates $x(t), y(t)$ describes the airfoil starting at the leading edge, as t varies from 0 to $2n$. The expressions are established as a function of the (x_k, y_k) coordinates of $2n$ points on the airfoil. x_k is given by the law :

$$x_k = \frac{c}{2} \left(1 - \cos\left(\frac{kn}{n}\right) \right), \quad k = 0, \dots, 2n$$

Then :

$$\begin{aligned}x(t) &= \frac{c}{2} \left(1 - \cos t \right), \\y(t) &= \sum_{k=0}^{2n-1} \frac{y_k \sin \left| n \left(t - \frac{kn}{n} \right) \right|}{2n \operatorname{tg} \left| \frac{1}{2} \left(t - \frac{kn}{n} \right) \right|}\end{aligned}$$

or :

$$x(t) = \frac{c}{2} (1 - \cos t),$$

$$y(t) = \frac{A_0 + A_n \cos(nt)}{2} + \sum_{q=1}^{n-1} (A_q \cos(qt) + B_q \sin(qt)).$$

where :

$$A_q = \frac{1}{n} \sum_{k=0}^{2n-1} y_k \cos\left(\frac{qk\pi}{n}\right),$$

$$B_q = \frac{1}{n} \sum_{k=0}^{2n-1} y_k \sin\left(\frac{qk\pi}{n}\right).$$

The number $2n$ points to be retained depends on the initial geometry. The parametric expressions are generally obtained with a good precision for $n = 18$. The result can be smoothed by canceling the high-order harmonics, and in this case the definition includes some twenty coefficients.

This parametric formulation, which is also an advantageous smoothing method, considers the A_q , B_q coefficients as so many decision variables.

2.4.3.2. Shape functions of aerodynamic origin

There are two advantages to using shape functions of aerodynamic origin, having a physical meaning. Firstly, the user can choose those best adapted to the problem at hand and, in this case, the small number of design variables reduces the calculation time. Secondly, the airfoil and pressure distributions are more realistic.

These advantages are put to use in the two approaches explained below, one using an airfoil library [8] [11] [15] [16] and the other the concept of aerofunctions [11] [12].

2.4.3.2.1. Airfoil library

The numerical optimization algorithm is associated with an airfoil library. The airfoil is defined by a linear combination of basic airfoils, and the optimization program determines the relative importance of the various shapes in defining the optimum airfoil.

The possibility remains of modifying the upper and lower surface independently and imposing geometric constraints in the airfoil, as long as the basic airfoils stay within the properties demanded of the optimized airfoil.

Using airfoils as a set of shape functions in the optimization process produces realistic solutions at a relatively low cost. This is an easy way of modifying existing airfoil or defining new ones.

2.4.3.2.2. Aerofunctions

It is easier to choose airfoil shape functions for a particular problem if these functions are of aerodynamic origin. Shape functions can then be defined by an inverse program, to change a given pressure distribution as desired. These shape functions are called "aerofunctions".

Ref. [12] presents several aerofunctions shapes which are reproduced Fig. 17.

These modifications were chosen as follows :

- SHAPE1 (Fig. 17a) - control leading edge expansion
- SHAPE2 (Fig. 17b) - smooth upper surface shock
- SHAPE3 (Fig. 17c) - control airfoil thickness with lower surface modifications
- SHAPE4 (Fig. 17d) - control upper surface supersonic plateau
- SHAPE5A (Fig. 17e) - move upper surface shock forward
- SHAPE5B (Fig. 17f) - move upper surface shock aft.

When used in a design optimization, the aerofunction shapes would be added to a baseline geometry by a scaling factor. The scaling factor would be the design variable controlled by the optimizer.

2.4.3.3. Other possible design variables

Van Egmond ref. [17] uses a parametrization of the pressure distribution to optimize a target pressure distribution directly.

The pressure distribution over the airfoil is divided in several regions (Fig. 18). For each region the pressure distribution is described by an analytical function with some parameters which are the design variables.

2.4.4. Multi design points

A great advantage of the optimization methods over the inverse methods is that several design points can be taken into account. Several examples will be presented in the chapter 3.2. which concerns propeller or helicopter blade airfoils design.

In that case the objective function is formulated as follows in the case of the drag minimization.

$$OB^2 = K_1 C_D(M_1, \alpha_1) + K_2 C_D(M_2, \alpha_2)$$

where (M_1, α_1) represents the first design point and (M_2, α_2) the second one. The coefficients K_1 and K_2 can be used as weighted coefficients in order to put more emphasis on one design point.

Since the objective function is more complex, the optimization process is longer than for a one point optimization. However it allows the designer to find a good compromise between several design points which are generally conflicting.

2.5 Advantages and limitations of numerical optimization

Some advantages and limitations of numerical optimization techniques are listed here [1].

2.5.1. Advantages of using numerical optimization

- A major advantage is the reduction in design time -this is especially true when the same computer program can be applied to many design projects.
- Optimization provides a systematized logical design procedure.
- We can deal with a wide variety of design variables and constraints which are difficult to visualize using graphical or tabular methods.
- Optimization virtually always yields some design improvement.
- It is not biased by intuition or experience in engineering. Therefore, the possibility of obtaining improved, nontraditional designs is enhanced.
- Optimization requires a minimal amount of human-machine interaction.

2.5.2 Limitations of numerical optimization

- Computational time increases as the number of design variables increases. If one wishes to consider all possible design variables, the cost of automated design is often prohibitive. Also, as the number of design variables increases, these methods tend to become numerically ill-conditioned.
- Optimization techniques have no stored experience or intuition on which to draw. they are limited to the range of applicability of the analysis program.
- If the analysis program is not theoretically precise, the results of optimization may be misleading, and therefore the results should always be checked very carefully. Optimization will invariably take advantage of analysis errors in order to provide mathematical design improvement.
- Most optimization algorithms have difficulty in dealing with discontinuous functions. Also, highly nonlinear problems may converge slowly or not at all. This requires that we be particularly careful in formulating the automated design problem.
- It can seldom be guaranteed that the optimization algorithm will obtain the global design optimum. Therefore, it may be necessary to restart the optimization process from several different points to provide reasonable assurance of obtaining the global optimum.
- Because many analysis programs were not written with automated design in mind, adaptation of these programs to an optimization code may require significant reprogramming of the analysis routines.

In order to reduce the computing time, two techniques can be used :

- The first one is to use Taylor approximations for the objective function and the constraints [14].

For the initial design variables X the objective function F and the constraint functions G_j are approximated by a second order Taylor series :

$$F(X) = F^0 + \Delta X^T \nabla F^0 + \frac{1}{2} \Delta X^T H^0 \Delta X$$

$$G_j(X) = G_j^0 + \Delta X^T \nabla G_j^0 + \frac{1}{2} \Delta X^T H_j^0 \Delta X$$

Using these Taylor approximations instead of the correct analysis calculation, an improved design is found by the optimization procedures described before. Thereby the step width has to be limited in order not to move too far away from the centre of the Taylor series. Finally now the correct analysis has to be done for this approximately improved design. These exact objective and constraint function values together with the preceding ones are used to determine the Taylor approximation at the new initial design. By this procedure only one exact calculation is necessary per optimization step and the approximation gets better and better. Only the "starting procedure" at the very beginning of the optimization needs more calculations because the complete 2nd order Taylor series requires $1 + n + n(n + 1)/2$ points of support. The COPES code uses a starting procedure which improves the design already during building up the initial Taylor series. The starting procedure can be influenced by prescribing the starting design variable sets. It can be drastically shortened by the input of already known results, e.g. from an interrupted optimization or from similar optimization with different constraints.

- The second one developed by Rizk [18] is based on the idea of updating the flow variable iterative solutions and design parameters iterative solutions simultaneously.

To conclude this chapter, another approach due to Jameson [19] has to be mentioned.

The method determines the configuration (e.g. shape of an airfoil) satisfying the given design objective (e.g. a desirable pressure distribution). Such a design method might be created by integrating a variation function into an analysis method, and inserting an iteration procedure to minimize the design objective function following the steepest descent. A. Jameson [19] illustrates this "design via control theory" by three applications in aerodynamic design.

3. APPLICATIONS OF NUMERICAL OPTIMIZATION

In this chapter are presented some applications of numerical optimization techniques for aerodynamic design. The large variety of design problems which are described will show how powerful can be the numerical optimization technique.

In the first section, airfoil design with various objective functions are described while in the second section some 2 design points optimization are presented. In the third section some 3D designs have been selected and in the last section unsteady optimization process for helicopter blade airfoil design is described.

3.1. Airfoil design

3.1.1. Drag minimization

- The first example is described in [11]. The CONMIN code is used for an optimization of a transport aircraft wing airfoil.

The PV39GEO airfoil used to generate transport aircraft wings was optimized for a Mach number of 0.76 to decrease the drag coefficient C_D with a C_L between 0.5 and 0.6 and to delay the upper surface separation that develops at high C_L . To take structural constraints into account, the PV39GEO airfoil was optimized with the constraint of prescribed values of the airfoil thickness in the area of the spar box, at 15 and 60 % chord.

The polar graph $C_L = f(C_D)$ is approximated by a parabola and the objective function used expresses the improvement of the overall aerodynamic coefficient C_D and C_L .

$$OBJ = \frac{(C_D - 0.0095)}{(C_L - 0.25)^2} \times 10$$

Figure 19 gives the geometry of the PV39GEO airfoil and the pressure distribution at the design point, with Mach number 0.76, $\alpha = 0.2^\circ$ and $Re = 4 \times 10^6$. The boundary layer is calculated with a transition fixed at 7 %.

The numerical optimization algorithm uses the set of airfoils presented in figure 20. The five basic airfoils are supercritical, with a thickness law modified by affinity to stay within the thickness constraints at 15 and 60 % of

the chord. The minimization program determines the relative participation of the various shapes, to define the optimum airfoil.

Four iterations were run, occupying the CRAY 1-S for 1,000 seconds. The convergence history is given in figure 21. The variation of the objective function shows a major improvement in the aerodynamic characteristics starting at the first iteration.

The pressure distributions of the PV39GEO and optimized PV39GEO airfoils are compared at the optimization point in figure 22. The optimized airfoil exhibits a delayed upper surface shock, of lesser intensity, a more regular lower surface pressure distribution and a slightly higher rear loading. The pressure distribution of the optimized airfoil is shown at a lower angle of attack in figure 23.

The aerodynamic characteristics of the airfoils in figure 24 show a decrease in the drag coefficient C_D of the optimized PV39GEO airfoil for C_L values above 0.35. This decrease is approximately 15 % for a C_L of 0.6.

On the other hand, the modification of the PV39GEO airfoil slightly increases the absolute value of the moment coefficient from 0.095. The C_D variation as a function of the Mach is plotted in figure 25 for a C_L of 0.55. It seems that the improved aerodynamic characteristics at high C_L are maintained over a large Mach number domain.

- The second example concerns the optimization of a propeller airfoil [20] with CONMIN.

The specifications for an airfoil located at 70 % of the blade span can be stated as :

- high maximum lift coefficient at moderate Mach number $M = 0.47$ to 0.63 , for high static thrust requirements at take-off conditions ;
- high lift/drag ratio C_L/C_D for Mach numbers ranging from 0.54 to 0.67 and lift coefficients between 0.65 and 1.05 corresponding to climb conditions ;
- high drag divergence mach numbers for C_L between 0.38 and 0.65 , corresponding to cruise conditions ;
- thickness to chord ratio = 7 %.

The numerical optimization method was used to improve the aerodynamic characteristics of the HORØ7 airfoil which previously was designed using a direct method.

The precise purpose of the optimization presented here was to increase performance at high C_L for take-off ($M = 0.55$) and to reduce the drag under cruise conditions ($M = 0.70$).

The corresponding computed results for the HORØ7 airfoil are presented in Fig. 26 and Fig. 27.

Shocks wave are present on the suction side under take-off conditions and on the pressure side under cruise conditions.

The upper and the lower surfaces of the initial airfoil have been successively modified using analytical shape functions.

- The suction side was optimized to reduce C_D at $M = 0.55$ and $C_L = 1.35$, with the constraint on suction side maximum expansion $C_{p\min} > -3$.
- The pressure side was optimized to reduce C_D at $M = 0.70$ and $C_L = 0.38$.

Moreover, a geometric constraint was imposed on the thickness to chord ratio : $6.5 \% \leq t/c \leq 7.5 \%$.

The computed pressure distributions on the optimized HORØ7 show improvements for the two optimization points :

- under the climb conditions at $M = 0.55$, the intensity of the suction side shock is reduced due to an upstream isentropic pressure recovery and the leading edge expansion is decreased by 10 %. The drag coefficient C_D is reduced by 24 % at the take-off optimization point.
- under the cruise conditions at $M = 0.70$, the lower surface shock wave is suppressed and the maximum expansion decreases by 12 %. The C_D is reduced by 9 % at the cruise optimization point.

The 2-D tests on the HORØ7 and optimized HORØ7 airfoils in the S3MA wind tunnel confirmed these predicted aerodynamic characteristics (Figs. 28-29).

For these two first examples the aerodynamic code associated with the optimization code is a direct viscous transonic flow method developed by Bousquet [22].

- The third example from [21] is the optimization of the GAW 1 airfoil with polynomials functions (spline) used for the geometry description. Two coordinates at $x/c = 65 \%$ and 85% constitute the design variables. The drag minimization is performed at $M = 0.25$, $\alpha = 0^\circ$ and $Re = 6.10^6$ and the aerodynamic code is DOFOIL, a viscous, steady, compressible flows computer program developed by Dornier.

Figure 30 shows the results of the optimization, where open symbols denote values of approximations from COPES to C_D . Closed symbols denote the corresponding exact values from DOFOIL. Note that the first two airfoils (A and B) were generated for the purpose of building the Taylor series approximations. The next 10 iterations show little further improvement in C_D , with the actual effort being placed on increasing the value of the constraint C_L to a value greater than 0.52. Figure 31 shows the variation of C_L , C_m and of the two design parameters for the 10 iterations.

Figure 32 shows that the upper surface curvature has somewhat decreased, and the start of recompression has been moved rearward;

One danger of optimizing at a particular flight condition is that off-design performance can become worse. As is seen in figure 33, this is not the case in this example. Indeed, for Mach numbers other than 0.25 and non-zero angles of attack, the improvement in performance is the same if not greater than that at the design point.

- As it has already been mentioned, the accuracy of the aerodynamic code in evaluating the objective function must be good enough to be sure that the optimization will improve the design. For example in [16] using a 3D inviscid code for the drag minimization of a high aspect ratio rectangular wing gives unsatisfactory result when the pressure drag is taken for the objective function while good results are obtained with the wave drag (Fig. 34). This is due to the fact that the wave drag which is computed by the integration of the momentum equation along a surface surrounding the supersonic zone as suggested in [23] is more accurate than the pressure drag obtained by the pressure integration on the wing surface;

The last example of drag minimization is taken from [24]. Aerofunctions like those presented Fig. 17 are used as design variables. The FLO-36 analysis code is the aerodynamic code.

Design conditions for the design were $M = 0.75$, $C_L = 0.5$, $C_m = -0.02$, and $t/c = 0.12$. Viscous analysis of a previously designed airfoil (optimization using polynomial shapes) for these conditions is shown in Fig. 35 and the airfoil in Fig. 36. The airfoil showed unacceptable trailing edge flow separation, 0.83 chord, at the design point, did not meet the C_m requirement, and had leading and trailing edge shapes that were considered unacceptable. The leading edge exhibited a double nose radius and the upper surface of the trailing edge was concave.

A TRO-2D optimization was run using drag as the objective function with inequality constraints on lift, moment, and thickness. Side constraints on leading and trailing edge camber design variables were set so as to preclude any upper surface concavity.

The TRO-2D designed airfoil is compared to the original design in Fig. 37. Note the more conventional nose shape and trailing edge for the TRO-2D design. Analysis of the TRO-2D airfoil at the design Mach and lift coefficient, as shown in Fig. 38, shows that the moment constraint has been met, no flow separation is predicted, and a 30% reduction of drag is predicted compared to the original airfoil. CONMIN required four cycles to reach a final solution in approximately one minute of CPU time on the CRAY-1M computer.

3.1.2 Flow field characteristic as objective function

Ref. [13] described an interesting optimization case with a prescribed velocity field used as the objective function in a reference plane. The problem is formulated as described in section 2.4.1.

A NACA0012 airfoil was used as a simple example to illustrate aerodynamic optimization in the presence of separated flow. This is a common airfoil which has been extensively analyzed and is defined by :

$$y(x) = 5t(0.2969x^{1/2} - 0.126x - 0.3516x^2 + 0.2843x^3 - 0.1015x^4)$$

where the parameter, t , determines the maximum airfoil thickness. For the NACA0012 airfoil, the thickness parameter is specified as 0.12.

The PARC CFD code was used to define the target RP properties by computing the laminar flow field about this airfoil, subject to the indicated boundary conditions indicated in Fig. 39. A Reynolds number, based on chord length, of 10^6 was specified which produced a flow field with an attached boundary layer (Fig. 40). Defining the target profile numerically assured that an absolute global minimum existed within the design space. The RP was located at the airfoil trailing edge and extended to the boundary of the computational domain, although the influence of the body was minimal approximately two chord lengths into the domain. The desired RP properties were then used to form the nonlinear least-squares objective function, which was minimized by application of Broyden's algorithm.

The design parameter (airfoil thickness) was doubled as an initial guess to begin the optimization. This value was selected since the contour subject to the stated boundary conditions produced a flow field which was highly separated (Fig. 41) in contrast to the attached target solution (Fig. 40). As noted, the reference plane was placed at the trailing edge of the airfoil passing through the region of separated flow.

For this example the correct optimum was located, by Broyden's algorithm, within 0.1 percent in six iterations requiring seven function evaluations. Figure 42 compares the target geometric profile with the initial guess profile, the first iteration profile, and the optimal profile as determined by Broyden's algorithm. Figure 43 and 44 show the reduction of the objective function and the convergence history of the design parameter, t , versus iteration number, respectively. As evidenced by these figures, the Broyden's algorithm isolated the global minimum quite efficiently. The optimum was located within 1 percent in four iterations and was isolated within 0.1 percent in six iterations.

3.1.3. Pressure distribution optimization

Van Egmond in [17] presents different cases of pressure distribution optimization. As an example, the case presented here concerns the definition of the max. lift contribution that can be obtained with stable laminar over the first 60 % of an airfoil. Stable with respect to the instability criterium for Tollmien Schlichting waves; instability occurs if $Re_0/Re_{0i} > 1$. With the requirement of just sonic conditions at $s/c = 0.60$ for $M_\infty = 0.65$ and $Re_c = 15.10^6$. Then the problem definition reads : find the Cp-distribution between $s/c = 0$; $M_{loc} = 0$ and $s/c = 0.60$; $M_{loc} = 1$ such that $\int_0^{0.6} Cp \, ds/c$ is maximum while everywhere Re_0/Re_{0i} approaches 1 as close as possible ; or minimize $= \int_0^{0.6} Cp \, ds/c + \int_0^{0.6} \max(0, Re_0/Re_{0i} - 1) \, ds/c$. After a few attempts with different relations for $Cp = f(s/c)$ it was observed that reasonable results could be obtained with the following relation for the pressure gradient :

$$\frac{dCp}{ds/c} = \frac{A}{\frac{s}{c} + \epsilon} + B \left(\frac{s}{c} + \epsilon \right)^N$$

where ϵ is a small value, to prevent the singularity at $s/c = 0$.

Then, by integration :

$$Cp = Cp_{st} + A \ln \left(\frac{\frac{s}{c} + \epsilon}{\epsilon} \right) + B \left[\left(\frac{s}{c} + \epsilon \right)^N - \epsilon^N \right]$$

Where A, B, $\epsilon (> 0)$ and N are design variables and Cp_{st} is pressure coefficient at stagnation point. Three of the design variables are independent, the fourth follows from the requirement of sonic flow at $s/c \approx 0.60$. Fig. 45 shows the results of the above problem. The Cp distribution for stable laminar flow over the whole region is depicted in Fig. 45a, while Fig. 45b shows that indeed Re_0 and Re_{0i} nearly coincide over the largest part of the region. These results were relatively easily obtained.

3.1.4. $C_{L,max}$ optimization

- The first example of $C_{L,max}$ optimization is taken from [8]. It has been done using the approximation concept. The design variables are 4 NACA airfoils and 2 linear functions which are used to impose the closure of the trailing edge. The analysis code [25] is used to perform the computation at $M = 0.1$, $\alpha = 6^\circ$

Figure 46 shows the results of optimization of an airfoil for maximum lift. The design constraints are listed on the figure. This optimization required 19 aerodynamic analyses. Although it may be argued that this airfoil is impractical, it must be remembered that this airfoil mathematically satisfies the design constraints. The lift coefficient obtained here is $C_L = 1.144$.

The quality of the approximation to the lift coefficient may be judged from figure 47. Because there are four independent design variables, the full second-order Taylor series expansion of the functions requires 15 analyses. It is intriguing to note that on the sixteenth analysis and beyond, the approximation for this case is quite precise.

- The second example from [20] concerns an airfoil for an ultra light aircraft; A first design called OAULM01 was defined with a set of airfoils in order to obtain a high C_L with low upper surface maximum expansion and a moment coefficient less than 0.04.

The tests in the S10 wind tunnel of the CEAT in Toulouse showed that the aerodynamic characteristics were of interest for the application considered, except that the stall was too steep.

To remedy this, the airfoil was optimized to reduce the rise in the boundary layer shape parameter between 30 and 50 % chord, to avoid a leading edge type of stall. The OAULM02 airfoil is the result of this second optimization.

Figure 48 shows the calculated boundary layer shape factor along the upper surface of the OAULM01 and OAULM02 airfoils, for a lift coefficient $C_L = 2$.

The geometry of the two airfoils and their pressure distributions for $C_L = 1$ and $C_L = 2$ are presented in Fig. 49. The pressure recovery of the OAULM02 airfoil is smoother up to 35 % of the chord length. The computed transition location is about $x/c = 15\%$.

The experimental lift and moment coefficient of the OAULM01 and OAULM02 airfoils are presented in Fig. 50 for a Mach number $M = 0.12$ and a Reynolds number $Re = 1.4.10^6$.

The stall behaviour of the OAULM02 airfoil is better.

3.1.5. High lift systems optimization

Since the optimization of the relative locations of a multi-element airfoil needs a high number of analysis calculations, an optimization process will save computer time. In [26], such an optimization is performed for a two-element airfoil using COPES coupled with a subsonic multi-element airfoil analysis code PSM developed by K. Jacob.

Figure 51 shows the starting design and the best design of a flap position optimization. The contour geometry of the two-element airfoil DOAS is kept constant. The specifications are :

Design objective : C_L should become a maximum.

Design variables : x, y-coordinates of a flap fixed point in main coordinate system.

Constraint : slot width s/c ≥ 0.01

Constant values : $M = 0.1$, $Re_c = 5.10^6$, $\alpha = 10^\circ$, flap deflection $\eta = -40^\circ$.

As the design objective C_L in this case depends on only two design variables, the optimization procedure can be graphically illustrated. Figure 52 shows the lift coefficient C_L in the area of interest for the flap fixed reference point. It can be seen that the reference point has to move from the starting position (starting design of figure 51) to the constraint line s/c = 0.01 nearer to the main element.

The same situation is shown again in figure 53 but now in form of iso-lift lines. The optimization path found by the COPES code is also indicated. After the first 3 analysis calculations (to find the initial gradient) COPES was free to find its way to the optimum which was reached after totally 30 analysis calculations (plotting the iso-lift lines of course needed much more). The lift coefficient was improved from $C_L = 2.5$ to 3.6 (45 %).

3.2. Examples of multi-design points optimization

3.2.1. Airfoils for helicopter blade

Specifications for the design of an helicopter blade airfoil concern generally the conditions which are encountered by the airfoil during a revolution of the rotor that is to say advancing blade condition and retreating blade condition. To find the best compromise between these two flight conditions it seems particularly interesting to use numerical optimization techniques [11].

- The first example concerns a 7 % thick airfoil called OA207. The CONMIN code is coupled with the analysis code [22]. The problem is formulated in order to reduce the drag :

- under advancing blade conditions :

$$M = 0.85 \text{ and } C_L = 0$$

with the aerodynamic constraint limiting the absolute value of the moment coefficient :

$$-0.01 \leq C_m \leq 0.01.$$

- under retreating blade conditions :

$$M = 0.40 \text{ and } C_L = 0.8,$$

with a limiting constraint on the upper surface expansion :

$$C_p \text{ min} < -3.5$$

Figure 54 shows the two optimization points considered on the aerodynamic polar curves of the OA 207 airfoil.

The objective function is represented by a linear combination of the C_D at the two design points :

$$\text{OBJ} = 0.8 C_{D1} + 0.2 C_{D2}$$

Six shape functions, constructed from the Legendre polynomials were used to modify 50 % of the airfoil upper surface;

Figures 55 and 56 show how the pressure distributions were modified at the two design points. For the configuration corresponding to a Mach number of 0.85, the local Mach number decrease in front of the shock obtained by an isentropic recompression reduces the intensity of the upper surface shock. This same modification decreases leading edge expansion on the upper surface by 10 % at a Mach number of 0.40 and a C_L of 0.83.

For the advancing blade conditions ($C_L = 0$), C_D is reduced by 16 % at the design point. The gain is smaller for Mach numbers less than 0.85, since the reduction of C_D mainly affects the wave drag. For the second design point ($M = 0.40$ and $C_L = 0.83$), the improvement in the aerodynamic characteristics is a 6 % decrease in the drag coefficient C_D .

- The second example concerns a 12 % thick airfoil design for the inner blade sections [20]. The initial airfoil is called OA 213 and was designed previously using an inverse method.

The design conditions are

$$\begin{aligned} M &= 0.75 \quad C_L = 0 \\ M &= 0.4 \quad C_L = 1.5 \end{aligned}$$

The objective function is the sum of the drag for the two design conditions and two constraints were laid down to control the pitching moment for zero lift and the maximum expansion level for $M = 0.4$ and high C_L .

The tests performed on this new airfoil OA312 in the S3MA wind tunnel have demonstrated the efficiency of the design process.

As shown in figure 57, the OA312 airfoil has lower drag under advancing blade conditions due to a large reduction of the leading edge lower surface pressure peak level which also leads to a reduced nose down pitching moment coefficient. The Mach drag divergence is 0.78 for the OA312 airfoil which gives $\Delta M_{dd} = 0.03$.

For $M = 0.4$, the maximum lift coefficient measured in the S3MA wind tunnel was 1.5, whereas it was 1.54 for the OA312 airfoil under the same conditions.

As shown in figure 58, the drag level is better with the new airfoil at high lift levels.

The shapes of the two airfoils and their total performances are compared in figure 59.

- The third example from [20] concerns an airfoil for a shrouded tail rotor.

The purpose was to design an airfoil having a large range of angles of attack with a drag level lower than 0.02 in order to minimize the power required for the shrouded tail rotor. The optimization has been applied for a Mach number of 0.62 and a Reynolds number of 1.1.106.

The range of angles of attack corresponding to the different flight conditions is $-5^\circ \leq \alpha_p \leq 12^\circ$, α_p being referenced to the zero lift angle of attack. Within this range, the drag level of the airfoil should remain lower than 0.02. Moreover, the nominal value for the angle of attack is $\alpha_p = +6^\circ$ (design point) and for this point the drag level should be lower than 0.01. For this Mach number, shock waves are present on the initial airfoil for large positive and negative values of the angle of attack. So a first optimization was carried out in inviscid flow under the following conditions :

Objective function : wave drag 1 + wave drag 2
 wave drag 1 corresponding to $M = 0.62$, $\alpha_p = -6^\circ$
 wave drag 2 corresponding to $M = 0.62$, $\alpha_p = +7.5^\circ$

For the second point, a constraint was laid down in order to control the camber of the airfoil.

This constraint expressed in the form $10.3^\circ < \alpha_p < 10.8^\circ$ was computed using the C_L obtained for the two points.

In this first optimization, a library of airfoils having the same thickness to chord ratio ($t/c = 10.2\%$) was used.

Having minimized the wave drag for a large range of angles of attack, a second optimization was performed in viscous flow in order to obtain a sufficient range of angles of attack beyond the design point with a drag level lower than 0.02.

The corresponding objective function is :

$$-\alpha_p = -\frac{(\alpha_2 - \alpha_1)C_{L_2}}{C_{L_2} - C_{L_1}}$$

with $\alpha_1 = -4^\circ$
 $\alpha_2 = 5.4^\circ$.

The Mach number being 0.62 and the Reynolds number 1.1.106. These values of angle of attack have been kept lower than those for the first optimization in order to stay within the limits of the viscous transonic aerodynamic code. For the second point, the constraint $C_D < 0.02$ has been given. Eight design variables acting on the camber line of the airfoil were used and two cycles were performed.

The optimized airfoil OAF102 has been tested in the S3MA wind tunnel. The tests were carried out for three values of the stagnation pressure. The corresponding Reynolds numbers are 1, 2 and 3.106 for $M = 0.62$. The $C_{L,\max}$ values plotted in figure 60 show that the highest performances were obtained for the design Mach number $M = 0.62$.

The curves also show an important Reynolds number effect up to high Mach number values. The performances of the airfoil are plotted in figure 61 for $M = 0.62$ and $Re = 1.106$.

It can be shown from Fig. 60 that the best results have been obtained for the Mach number used for the optimization which demonstrate the efficiency of the process.

3.2.2. Helicopter blade design

To conclude this section devoted to examples of multi-design points, an example of a spanwise blade section distribution optimization taken from [27] is presented. The problem is to find the spanwise distribution of two airfoils which will minimize the power of the rotor under different flight conditions. Two flight conditions are considered :

Point 1 $M = 8t$ $z = 0$ $v = 250 \text{ km/h}$
 Point 1 $M = 8t$ $z = 3000 \text{ m}$ $v = 360 \text{ km/h}$

The objective function is :

$$\text{OBJ} = (1 - n) P_1 + n P_2$$

P_1 and P_2 being the power needed respectively for the flight conditions and n being a coefficient which is used in order to privilege one flight condition.

The design variables are the span locations of two airfoils sections (OA312 and OA309) noted R_1/R and R_2/R . Fig. 62 shows the power reduction obtained for the two flight conditions versus the n coefficient. In Fig. 63 are plotted the optimized airfoils locations versus the n coefficient. For the best compromise corresponding to $n = 4$ the rotor performance are compared to the ones of the initial rotor ($R_1/R = 0.8$, $R_2/R = 0.9$).

3.3. Examples of 3D optimization

3.3.1. Wing drag optimization

The first example from [28] concerns the various wing drag components minimizations. The CONMIN code is coupled to the 3D inviscid flow analysis code [29]. The DLR F4 wing is used for the optimization (Fig. 65). Four spanwise sections are used to define the wing. The twist distribution is linear between the sections. The flow conditions taken for the optimization are $M = 0.75$ - $C_L = 0.67$. Four objective functions were successively used for the optimization of the twist distribution with a constraint on the lift coefficient $C_L \geq 0.67$.

The objective functions chosen were :

- 1) lift-induced drag
- 2) wave drag
- 3) lift-induced drag + wave drag
- 4) pressure drag.

A additional unconstrained calculation was also done aiming at an elliptical load distribution. The drag was computed using "farfield" techniques as described in [30] and [31].

Fig. 66 summarizes the results. Minimizing the lift-induced drag loads the wing in the outer part (Fig. 67) while minimizing the C_{Dw} term loads the inner part. Minimizing $C_{Dl} + C_w$ drag or C_{Dp} drag gives results which are very close (Fig. 68). In that case the twist distribution is somewhat different of the one of the real F4 wing. However Fig. 69 shows that changing the conditions from $M = 0.75$ to $M = 0.785$ gives a twist distribution closer to the F4 one.

16000 grid points are used for these computations which might be considered not sufficient for accurate drag prediction. However this number of grid points has been selected after a parametric study of the accuracy of the far field computed drag versus the number of grid points. This mesh realizes the best compromise between the computer time and the drag accuracy. However it is clear that different values of the various drag components will be obtained with a finer grid but the results will exhibit the same tendencies which means that the conclusions will be the same. Each optimization requires between 1 H and 2.30 H computing time on a CRAY X-MP computer.

The second example of wing drag minimization has been done by Cosentino and al. [32]. It concerns the CESSNA model 650 wing used on the new citation III aircraft. The design was made at $M = 0.81$ and $C_L = 0.57$. The objective function is the wing L/D which is computed by the TWING code which is coupled to the quasi-Newton QNMDIF code.

The geometry, as shown in Fig. 70, has a fairly high leading-edge sweep of 37° before the break, and 27° after. The aspect ratio is 9.0, and no wing dihedral is present. This wing is defined by different airfoil sections at the root, break, and tip stations, and the twist distribution is incorporated in the airfoil coordinates. These three airfoils, along with the locations of the fixed and the three movable spline support points are shown in Fig. 71. As can be seen, three movable points were chosen at each defining station for this case.

The results of this design case are presented in Fig. 72 at three span stations. Again, reasonably smooth pressure distributions and airfoil shapes are observed, with reduced shock strengths at every station (the 48.5 % span station is nearly shock-free). The slight pressure peak at the root station at about 6 % of chord might be

eliminated by redistributing spline support points and reinterpolating. The remaining stations are quite well behaved. Note that actually very little modification to the shape of thickness of any section was required to achieve the desired result. This is an indication that the wing was very well designed and highly efficient before any optimization redesign. Some data summarizing this design are presented in Fig. 73.

This design required only six optimization iterations and was completed in just under 1 hr of CRAY X-MP CPU time (about 90 % of the improvement required about 20 min of CPU time). The inviscid drag-to-lift ratio of this wing has been increased by over 85 % at the expense of just over 10 % of the lift, yielding a reasonable and efficient design at nominal computational expense. Figure 73 displays the drag-rise characteristics of the original and optimized wings at fixed lift coefficient. The coefficient of drag (scaled by a factor of 100) is plotted at several Mach numbers for both wings. As can be seen, the optimized wing displays superior drag-rise characteristics as the mach number is increased, yet does not suffer any undesirable off-design behavior at the lower Mach numbers. Note that the drag divergence mach number has been increased by approximately 0.03.

Other examples of wing optimizations can be found in the literature [33] [34].

3.3.2. Complete configuration optimization

At the present time there is no examples of complete configuration optimization using 3D potential or Euler codes due to the large computer time associated with these methods and the poor reliability of the aerodynamic coefficients which are computed with the coarse grids generally used.

An interesting approach of this complex problem is given by Van den Dam in [35]. The aircraft is projected onto a plane normal to the flight direction and is approximated by a number of straight line segments representing the various elements of the configuration. The contributions of the various elements to the lift and the lift induced drag are computed in the Trefftz-plane while the viscous drag is computed using DATCOM's formulae.

An induced drag minimization case including propeller slipstream is presented here as an example.

In order to examine the effects of the propeller slipstream on the aircraft induced drag, the axial and tangential velocities in the propeller slipstream have to be given. For a particular example design condition, the distribution of propeller induced velocities of figure 74 has been used (advance ratio of $J = 0.13$ and a thrust coefficient of $C_T = 0.12$).

For a wing configuration with two "up-inboard" rotating propellers, located at 25 % of the semispan with a diameter-to-span ratio of 13 %, the optimal spanwise bound circulation distribution is shown in figure 75. This distribution greatly differs from the optimal "clean wing" distribution that is also shown in figure 75. With this distribution, the wing is capable of restoring much of the loss associated with slipstream swirl.

In figure 76, the effects of the horizontal propeller position for different rotating concepts of the propellers on the minimum induced drag coefficient have been plotted. As can be seen clearly from this figure, two up-inboard rotating propellers lead to a most favourable configuration with respect to the minimum induced drag. If the location of the propeller-centre is moved outboard, induced drag will decrease for two up-inboard rotating propellers and will be a minimum when the propellers are located at the wing tips.

3.3.3. Wing-engine interference reduction

Optimization of a wing + engine configuration should aim at reducing the drag increment created by the interference. However reliable estimation of this drag increment is still beyond the reach of analysis methods, let alone such inexpensive methods as might be incorporated into an optimization procedure. The example presented here from [28] uses the following simplified methodology. The engine effect on the wing is balanced by an opposite perturbation obtained through wing shape modifications (Fig. 77). So the modified wing with the engine will exhibit the same pressure distribution than the original clean wing.

Fig. 78 shows the perturbation of the wing pressure distribution due to the engines. Four successive optimizations for each side of the pylons have been successively performed. The objective functions are defined by target pressure distributions in the wing sections where the perturbations are maximum. The CONMIN code was coupled with the analysis code [29] of Bredif. Eight aerofunctions for the lower side and three for the upper side were designed with inverse 2D computations in order to modify the pressure distribution at the prescribed spanwise locations (Fig. 79).

Fig. 80 shows the results of the optimizations in term of ΔC_D between the modified motorized wing and the initial clean wing. Comparing to Fig. 78 it is clear that the perturbations have been greatly reduced which demonstrates the efficiency of the process.

3.3.4. Inviscid 3D nozzle design

The last 3D example is the design of a 3D rectangular nozzle [13] presented Fig. 31. The nozzle geometry and interior grid were defined by a 3D Bezier polynomial.

Four control points were specified at each of five axial planes such that each axial cross section was rectangular. The design parameters were two coefficients, P_1 and P_2 , which implicitly determined the distance between the control points in the 'y' and 'z' directions at the mid-plane (Fig. 81). The target geometry corresponded to values of unity for each parameter which produced a nozzle with a nominal exit to throat area ratio of 2.5. Total conditions were specified at the nozzle inlet and a static pressure below second critical was selected at the nozzle exit which provided supersonic flow development in the divergent portion of the nozzle. This geometry and these boundary conditions produced a flow with a nominal exit Mach number of 2.5 when analyzed by application of the Euler version of the PARC code.

For an initial guess, the design parameter P_1 and P_2 were set equal to 2.0 and 2.5, respectively, which produced a high area ratio nozzle with a nominal exit Mach number of 5.8. Unlike the target nozzle, which was square at each axial cross section, the initial guess geometry had a square cross section at the inflow plane, which transitioned to a rectangular cross section at the mid-plane, and then transitioned again to a square at the exit plane. The large difference in exit flow conditions for the initial guess was imposed to illustrate that the initial guess flow field does not necessarily need to closely resemble the desired optimum to obtain acceptable results. The difference in the flow fields for the target and initial guess nozzles is illustrated by comparing the centerline Mach number profiles for the two designs (Fig. 82).

A sensitivity analysis on the geometric design parameters indicated that the objective function partial derivatives were very sensitive to parameter step size because of nonlinear effects and numerical error inherent in the objective function evaluations. Although the most stable step size determined was applied, Broyden's algorithm did not converge to the global minimum. However, the Gauss-Newton algorithm was successfully applied and the optimum was reached in six iterations requiring eighteen function evaluations. Figure 89 illustrates the RP convergence by comparing RP Mach number profiles along the y-axis for various iterations. The achieved reduction in objective function and the design parameter convergence is depicted in Figs. 84 and 85, respectively.

3.4. Unsteady optimization

In order to design new helicopter blade airfoils, an optimization technique has been developed at ONERA by H. Bezard.

The method results from the association of :

- an unsteady full potential code [36]
- a 3D unsteady boundary layer code from R. Houdeville and J. Cousteix of the ONERA-CERT/DERAT department
- the CONMIN optimization code.

The design variables are 4 airfoils with a thickness to chord ratio of 0.12 presented Fig. 86, the first one the NACA0012 airfoil being used as the initial design.

- The first optimization case has been done under the following conditions :

• Mach number

$$M = 0.67 + 0.18 \sin \psi$$

• Angle of attack

$$\alpha^\circ = \alpha_m^\circ - 3^\circ 25 \sin \psi$$

ψ being the azimuth angle ($0 \leq \psi \leq 360^\circ$ and α_m the 5e design variable).

• Objective function

$$OBJ = \overline{C_D} \text{ wave} + \overline{C_D} \text{ viscous}$$

$\overline{C_D}$ are the mean values of the drag components given by :

$$\overline{C_D} = \frac{1}{360} \times \frac{1}{(0.67)^3} \int_0^{360} C_D \times M^3 d\psi$$

C_D , and M being the drag and the Mach number at each time (azimuth) step. C_D wave is obtained through the integration of the unsteady momentum equation over a contour surrounding the shock at each time step while C_D viscous is obtained by applying the Squire and Young formulae.

• One constraint on the mean value of the C_L

$$\overline{C_L} \geq 0.3$$

The optimization history is presented Fig. 87. After 8 optimization cycles the objective function has decreased by 24 % and the constraint is not active. 55 unsteady aerodynamic computations have been performed. On the figure are also drawn the evolutions of the design variables during the optimization process. The overall computing time is 1 H 37 mn on a CRAY-2 computer.

- The second optimization case is the same than the previous one with a second constraint applied on the maximum unsteady pressure coefficient value :

$$|C_p \text{ min}| \leq 2$$

The objective function has been modified in order to obtain some penalty when a separation appears on the airfoil.

$$\text{OBJ} = (\bar{C_D \text{ wave}} + \bar{C_D \text{ viscous}}) / X_s$$

X_s being the maximum location of the separation (from the trailing edge) computed during one cycle.

For that case, the optimization history presented Fig. 88 is less smooth than for the first case due to boundary layer separation appearing during the optimization. After 8 optimization cycles, the constraint n° 1 ($\bar{C_L}$) is non active while constraint n° 2 ($|C_p|$) is just active.

On Fig. 89 are plotted the design variables. The additional constraint influences greatly the final solution as it can be shown by comparing Fig. 89 and Fig. 87.

The airfoils contour obtained with these two optimizations are plotted on Fig. 90. The airfoil from case n° 2 exhibits more camber which is confirmed by the pressure distribution computed for two azimuth angles plotted Fig. 91.

Fig. 92 compares the unsteady aerodynamic coefficients of the two airfoils versus the azimuth angle.

The viscous and the wave drag mean values of airfoil n° 2 are higher than those of airfoil n° 1 which has been optimized without the constraint on the $|C_p \text{ min}|$; however, a separation occurs on the airfoil upper and lower surfaces for a large range of azimuth angles which is not the case for airfoil n° 2.

This design method which is presently under development will certainly in the near future become a powerful and valuable design tool for unsteady designs.

4. CONCLUSION

Through the various examples presented in the paper it has been shown that numerical optimizations may be used for solving a lot of design problems. Even if the computing time is somewhat higher than the one of other design techniques, numerical optimization provides generally a reduction in total design time. The major advantage of numerical optimization is the possibility to deal with a wide variety of design variables and constraints and yield improved, efficient and economical designs.

However it is important to understand the limitations of optimization techniques and use these methods as only one of many tools which are available. It can seldom be guaranteed that the optimization algorithm will obtain the global design optimum. Therefore it may be necessary to restart the optimization process from several different points or with different design variables to provide reasonable assurance of obtaining the global optimum.

As it is said in [1], expectations of achieving the absolute "best" design will invariably lead to "maximum" disappointment.

Acknowledgements

The author wishes to thank Mr D. Destarac and Mr J. Reneaux for their help in preparing this paper.

- [1] Vanderplaats G.N. Numerical Optimization Techniques for Engineering Design with Applications. Mac Graw-Hill series in Mechanical Engineering, 1984.
- [2] Powell M.J.D. An Efficient Method for Finding the Minimum of a Function of Several Variables without Calculating Derivatives. Computer Journal, Vol. 7 n° 4, 1964.
- [3] Hooke R. and T.A. Jeeves. Direct Search Solution of Numerical and Statistical Problems. J. Assoc. Computer Math., Vol. 8, 1961.
- [4] Rosenbrock H.H. An Automated Method for Finding the Greatest or Least value of a Function. Computer Journal, Vol. 3, 1960.
- [5] Fletcher R. and C.M. Reeves. Function Minimization by Conjugate Gradients. Br. Computer Journal, Vol. 7, 1964.
- [6] Dantzig G.B. Programming in a Linear Structure, Comptroller, USAF, Washington DC, February 1948.

- [7] Vanderplaats G.N. CONMIN - a Fortran program for Constrained Function Minimization. NASA TMX 62 282, 1973.
- [8] Vanderplaats G.N. Approximation Concepts for Numerical Airfoil Optimization; NASA TP-1370, 1979.
- [9] Gill P.E., Murray W. Quasi-Newton Methods for Unconstrained Optimization. Journal Institute Mathematics Applications, Vol. 9, 1972.
- [10] Gill P.E., Murray W. and Wright M.H. Practical Optimization Academic Press London, 1981.
- [11] Reneaux J. Numerical Optimization Method for Airfoil Design. Recherche Aérospatiale n° 1984-5.
- [12] Aidala P.V., Davis W.H. Jr and Mason W.H. Smart Aerodynamic Optimization. AIAA 83-1863.
- [13] Huddleston D.H. and Mastin C.W. Optimization of Aerodynamic Designs Using Computational Fluid Dynamics. AGARD CP n° 463, Paper n° 23.
- [14] Ghielmi L., Marazzi R. and Baron A. A Tool for Automatic Design of Airfoils in Different Operating Conditions. AGARD CP n° 463, Paper n° 18.
- [15] Vanderplaats G.N. and Hicks R. Numerical Airfoil Optimization Using a Reduced Number of Design Coordinates. NASA TMX 73 151, (1976).
- [16] Destarac D, Reneaux J and Gisquet D. Optimisation Numérique de Voilures en Régime Transsonique. AGARD CP n° 463, paper n° 21.
- [17] Van Egmond J.A. Numerical Optimization of Target Pressure Distributions for Subsonic and Transonic Airfoil Design. AGARD CP n° 463, Paper n° 17.
- [18] Rizk M.H. Aerodynamic Optimization by Simultaneously Updating Flow Variables and Design parameters. AGARD CP n° 463, Paper n° 15.
- [19] Jameson A. Airfoil design via Control Theory. AGARD CP n° 463, Paper n° 22.
- [20] Reneaux J., Thibert J.J. The Use of Numerical Optimization for Airfoil Design. ONERA TP 1985-135. AIAA Paper 85-5026.
- [21] Misegades K.P. Airfoil Optimization. AIAA Paper 84-0053.
- [22] Bousquet J. Calculs Bidimensionnels Transsoniques avec Couche Limite. AAAF 11^e Colloque Aérodynamique Appliquée, 1977.
- [23] Thibert J.J. Prévision de la trainée à partir des méthodes de calcul. ONERA TP 1988-74. AGARD AR256.
- [24] Davis W. TRO-2D. A Code for Rational Transonic Aero Optimization. AIAA-85-0425.
- [25] Jameson A. Transonic Flow Calculations for Airfoils and Bodies of Revolution. Gruman Aerodynamics Report 390-71, 1971.
- [26] Bock K.W. Aerodynamic Design by Optimization. AGARD CP n° 463, Paper n° 20.
- [27] Reneaux J., Allongue M. Définitions de profils et de pales d'hélicoptère par optimisation numérique. AGARD CP n° 463, Paper n° 19.
- [28] Destarac D., Reneaux J. Transport Aircraft Aerodynamic Improvement by Numerical Optimization. 17th Congress ICAS, 1990 - Paper n° 6-7-4.
- [29] Brédif M. Finite Element Calculation of Potential Flow around Wings. Lecture notes in Physics, Vol. 218, Springer Verlag, 1985.
- [30] Slooff J.W. Technical Status Review on Drag Prediction and Analysis from CFD. AGARD AR n° 256.
- [31] Lock R.C. Comment on "Numerical Optimization Design of Advanced Transonic Wing Configurations". Journal of Aircraft, Vol. 24, N° 8, August 1987.
- [32] Cosentino G.B., Boulder C.O. and Holst T.L. Numerical Optimization Design of Advanced Transonic Wing Configurations. AIAA 85-0424.
- [33] Hicks R. Wing Design by Numerical Optimization. AIAA Paper n° 77-1247.

- [34] Haney H.P. and Johnson R.R. Computational Optimization and Wind Tunnel Test of Transonic Wing Designs. AIAA Paper n° 79-0080.
- [35] Van den Dam R.F. Constrained Spanload Optimization for Minimum Drag of Multi-Lifting Surface Configurations. AGARD CP n° 463, Paper n° 16.
- [36] Bezard H., Costes M. An Improved Method for the Computation of Unsteady Transonic Potential Flow. Application for Airfoil and Blade Performance Prediction. 15th European Rotorcraft Forum. Amsterdam, 1989. ONERA TP n° 1989-154.

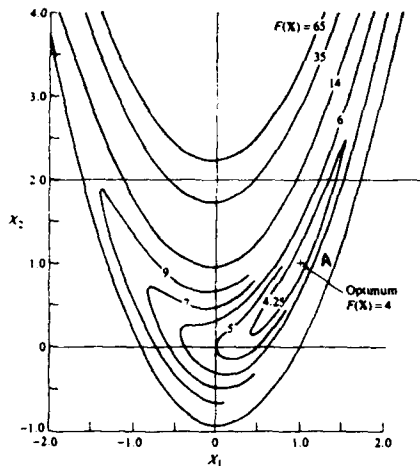


Fig. 1 - Two-variable function space. No constraint.

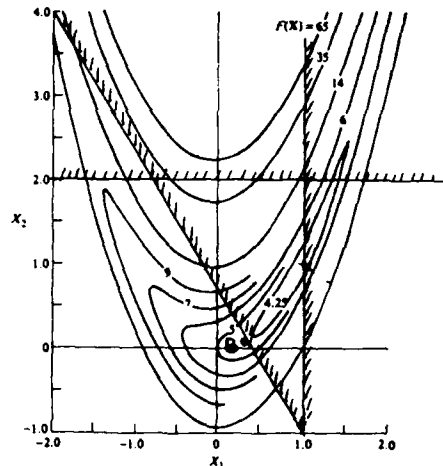


Fig. 2 - Two-variable function space. With constraints.

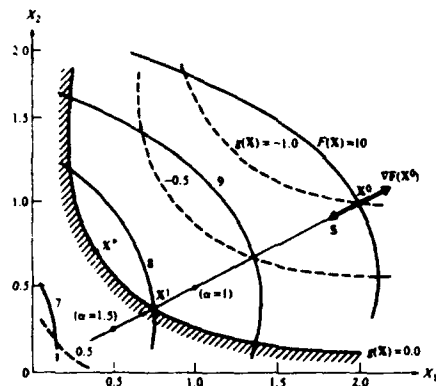


Fig. 3 - Search in direction S.

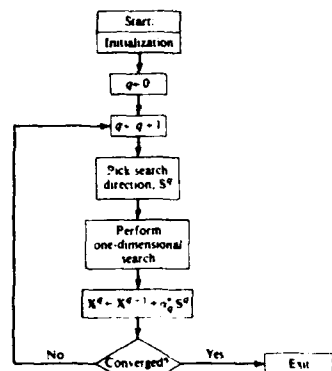


Fig. 4 - General unconstrained minimization strategy.

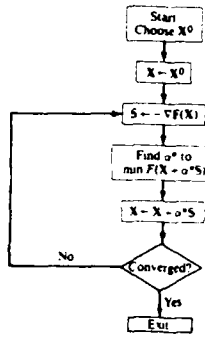
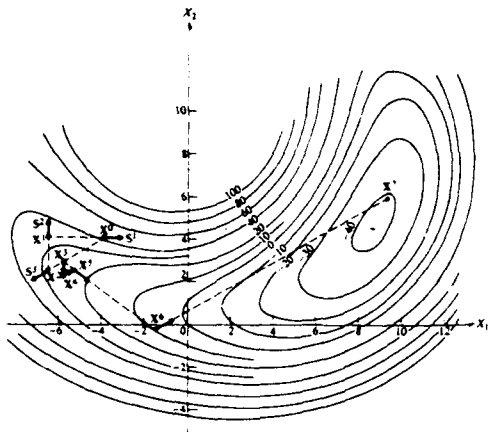


Fig. 6 - Algorithm for the steepest descent method.

Fig. 5 - Geometric interpretation of Powell's method.

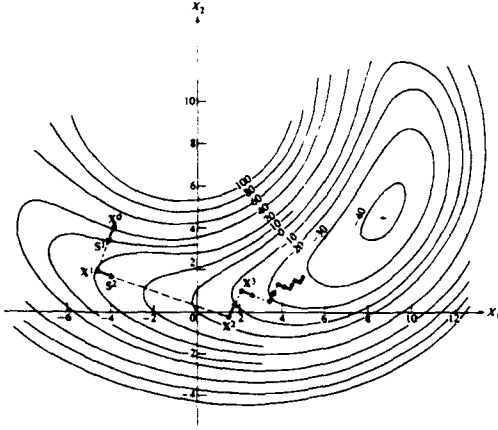


Fig. 7 - Geometric interpretation of the steepest descent method.

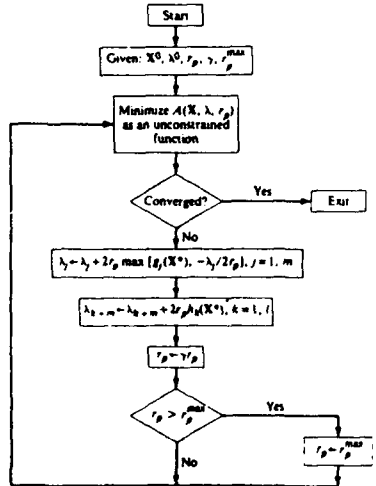


Fig. 9 - Algorithm for the ALM method: general case.

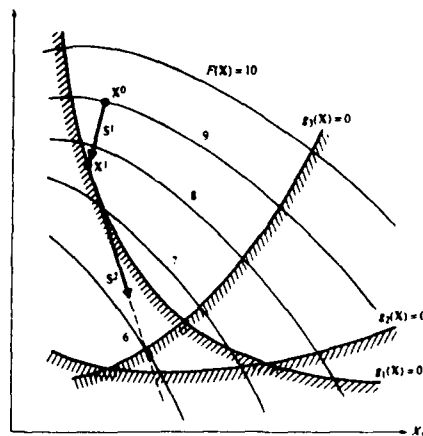


Fig. 10 - The search direction.

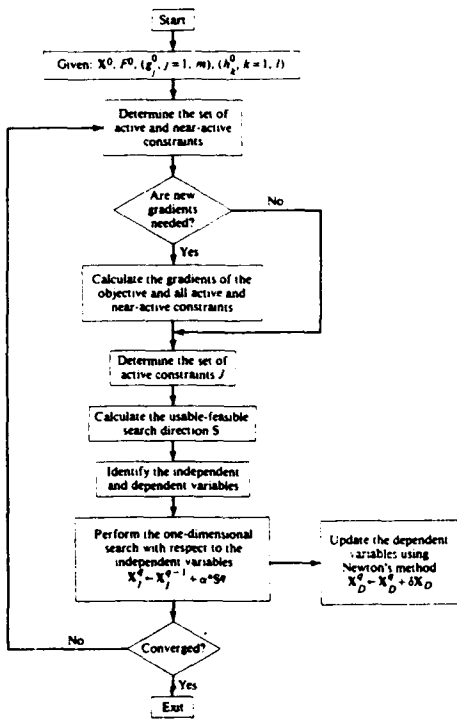


Fig. 11 - Algorithm for the robust feasible directions method.

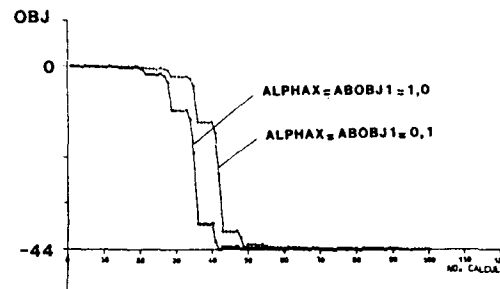


Fig. 13 - Rosen and Suzuki problem. CONMIN convergence history.

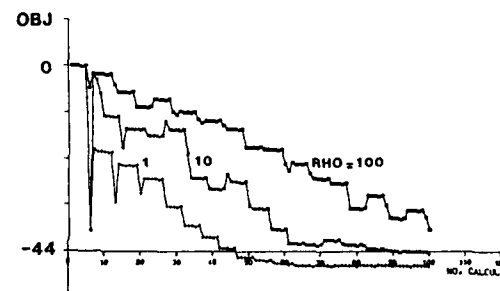


Fig. 14 - Rosen and Suzuki problem. EO4VAF convergence history.

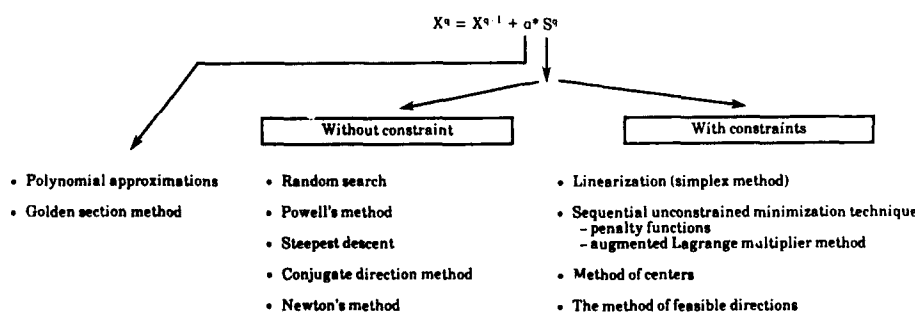


Fig. 12 - Summary of the main optimization algorithms.

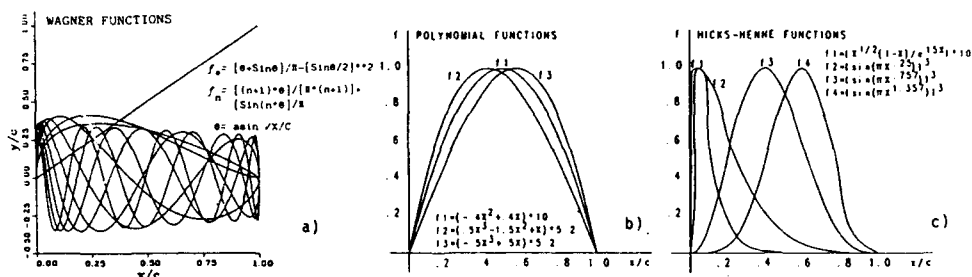
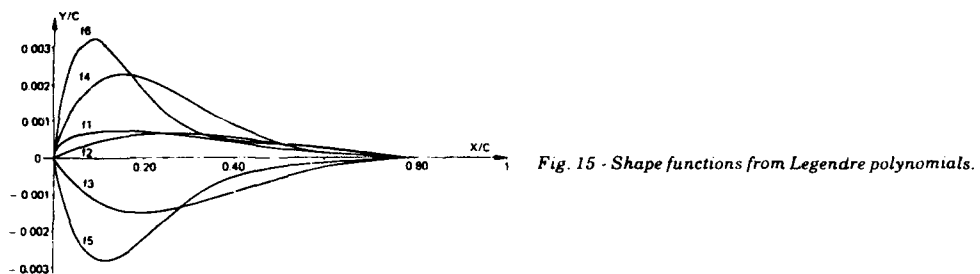
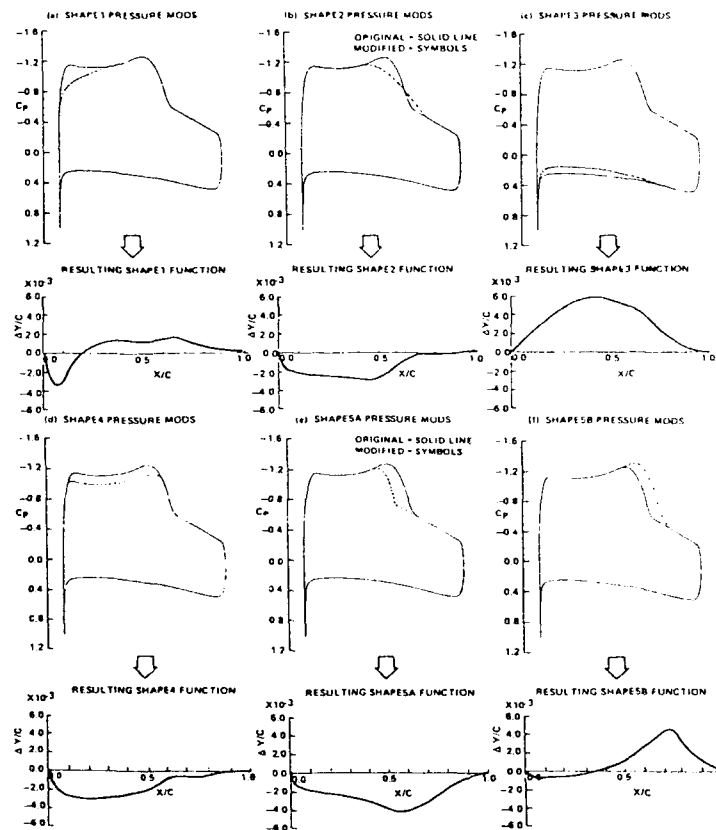


Fig. 16 - Examples of shape functions for airfoil design.

Fig. 17 - EMOD2 pressure distribution ($M = 0.683$, $C_L = 1.2$). Pressure mods (above) and resulting shape functions (below).

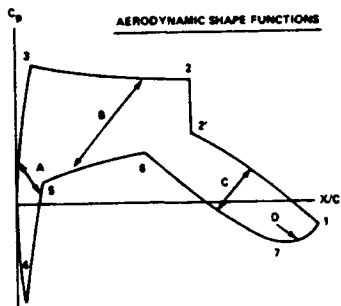


Fig. 18 - Analytical representation of the pressure distribution.

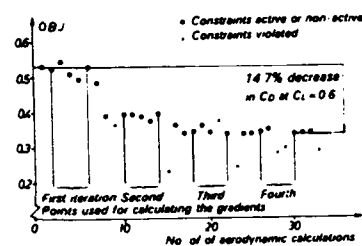


Fig. 21 - Convergence history of the PV39GEO airfoil.
Variation of the objective function.

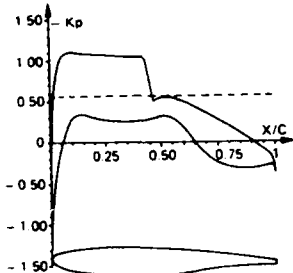


Fig. 19 - PV39GEO airfoil (transport aircraft airfoil).

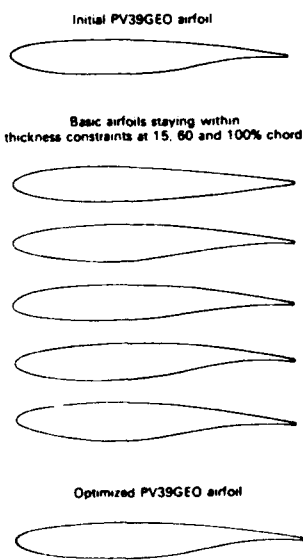


Fig. 20 - Set of airfoils.

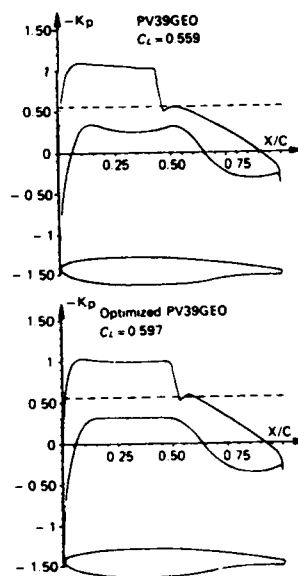


Fig. 22 - Pressure distribution compared at $Mach = 0.76$,
 $\alpha = 0.2^\circ$ and $Re = 4 \times 10^6$.

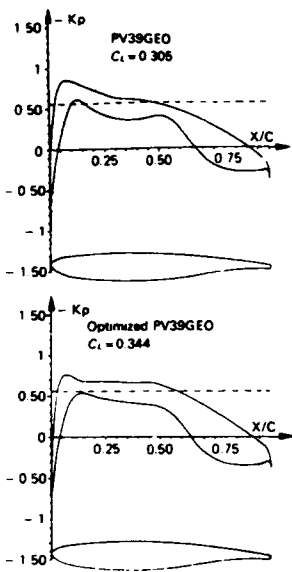


Fig. 23 - Pressure distribution compared at Mach = 0.76.
 $\alpha = -1^\circ$ and $Re = 4 \times 10^6$.

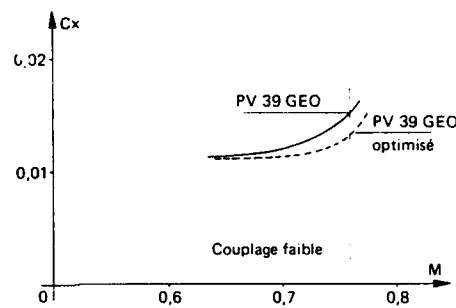


Fig. 25 - Variation of C_d as a function of the Mach number, at $C_L = 0.55$, for the PV39GEO and optimized PV39GEO airfoils, at $Re = 4.10^6$.

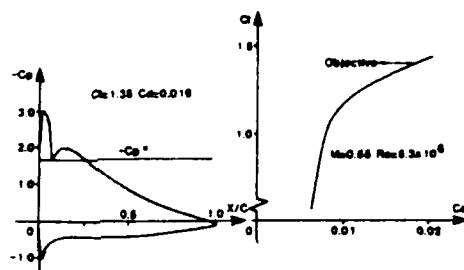


Fig. 26 - HOR07 airfoil computed performances in take-off conditions.

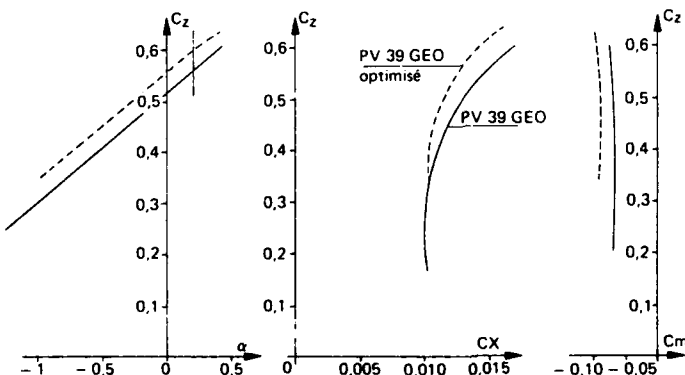


Fig. 24 - Comparative aerodynamic characteristics of the PV39GEO and optimized PV39GEO airfoils, for Mach 0.76 and $Re = 4.10^6$.

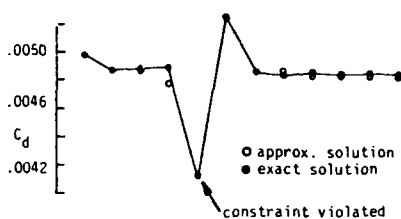
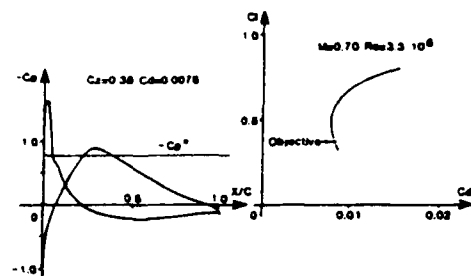


Fig. 27 - HORØ7 airfoil computed performances in cruise conditions.

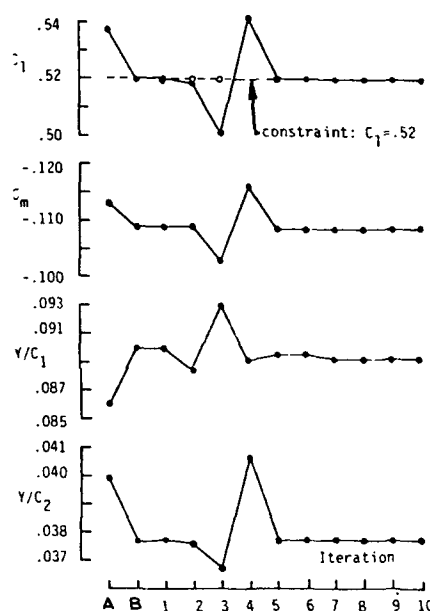
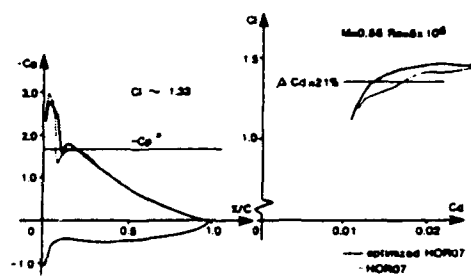
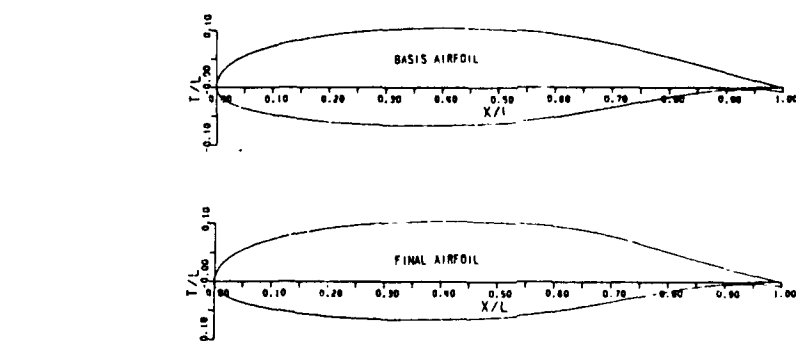
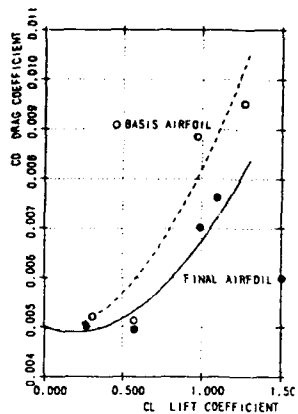
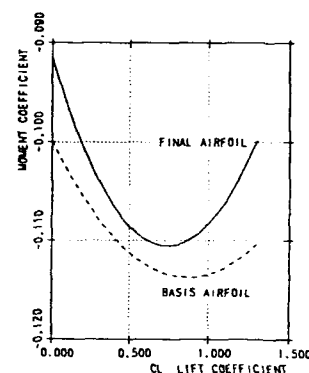
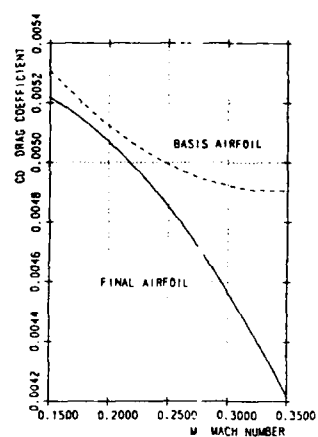
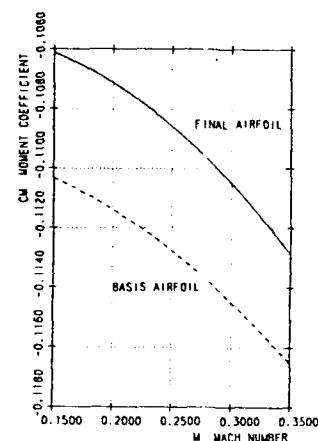
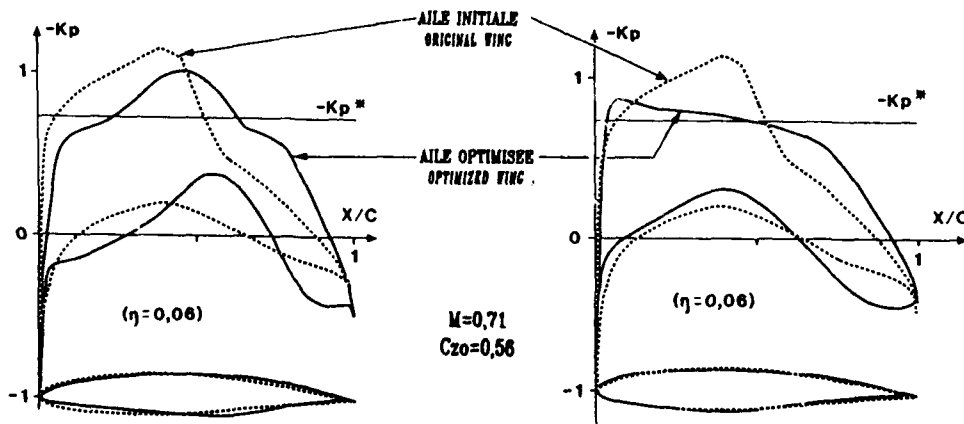


Fig. 29 - HORØ7 and optimized HORØ7 airfoils : experimental performances in cruise conditions.



Fig. 33a - Off-design performance C_D - vs - C_L ($M = 0.25$).Fig. 33b - Off-design performance C_m - vs - C_L ($M = 0.25$).Fig. 33c - Off-design performance C_D - vs - M ($\alpha = 0$).Fig. 33d - Off-design performance C_m - vs - M ($\alpha = 0$).Fig. 34 - Optimization of a rectangular wing. Drag minimization. Constraint : $C_L \geq C_{L0}$.

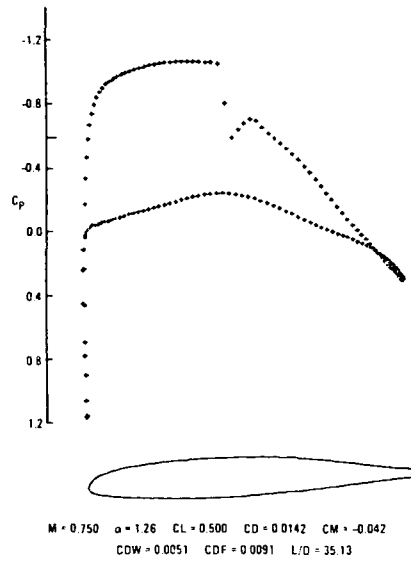


Fig. 35 - Case 2. Viscous analysis of original airfoil with KGBJ.

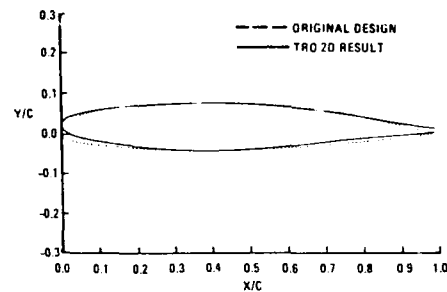


Fig. 37 - Case 2. Comparison of TRO-2D drag optimized airfoil to previous design.

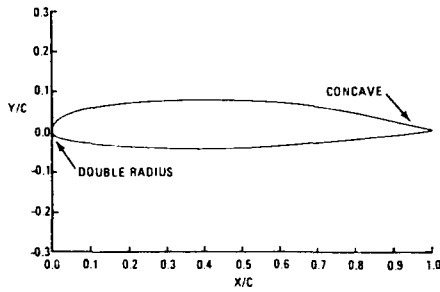


Fig. 36 - Case 2. Geometry previously designed airfoil: geometrically and aerodynamically unacceptable.

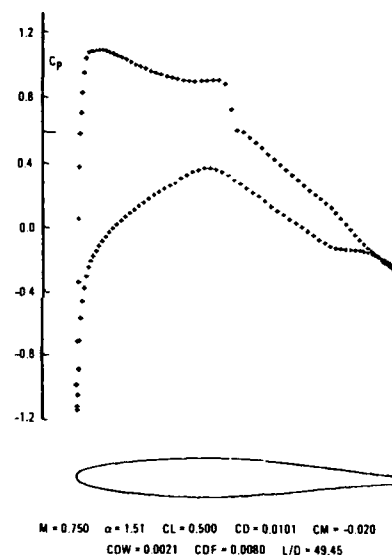


Fig. 38 - Case 2. Viscous analysis of TRO-2D design using KGBJ.

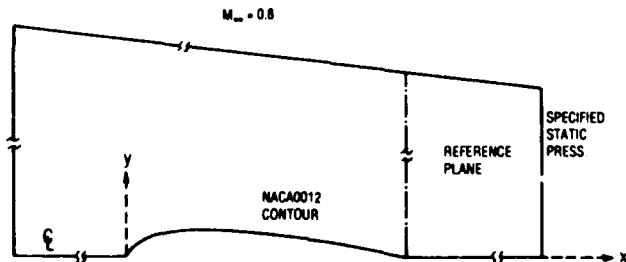


Fig. 39 - Viscous airfoil test case.

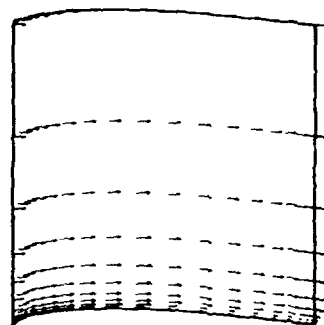


Fig. 40 - Viscous airfoil target velocity field.

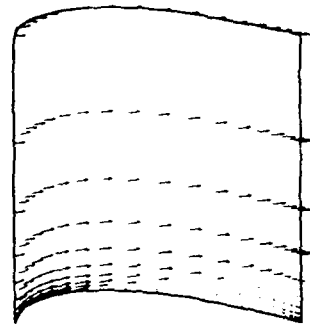


Fig. 41 - Viscous airfoil initial guess velocity field.

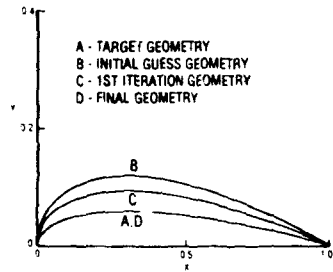


Fig. 42 - Viscous airfoil contour variation.

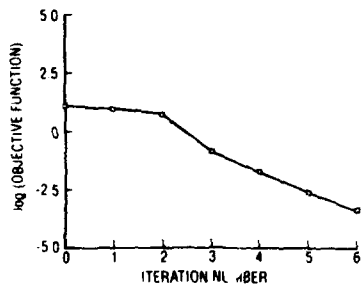


Fig. 43 - Viscous airfoil objective function reduction.

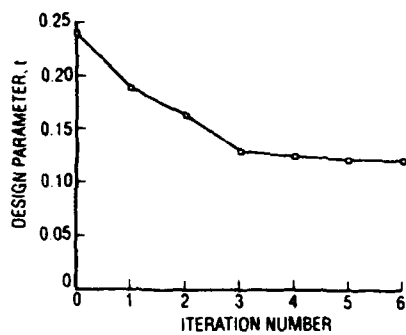
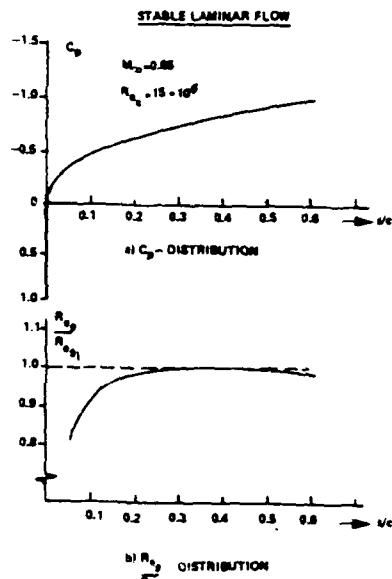
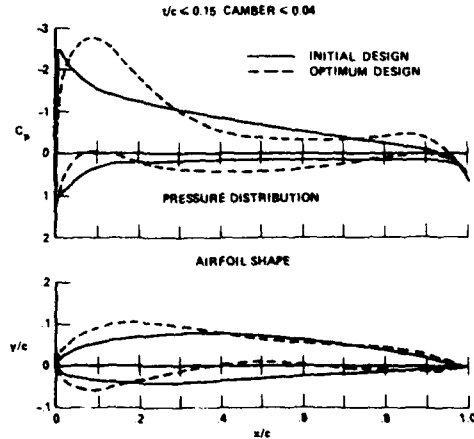


Fig. 44 - Viscous airfoil design parameter convergence.

Fig. 45.
CONSTRAINTS: $|C_{p_{\text{inf}}}(x/c = 0.01)| \leq 2.0$ $|C_{p_{\text{inf}}}| \leq 0.075$ $A \geq 0.075$
 $x/c \leq 0.15$ CAMBER ≤ 0.04 Fig. 46 - Lift maximization, $M = 0.1$, $\alpha = 6^\circ$.

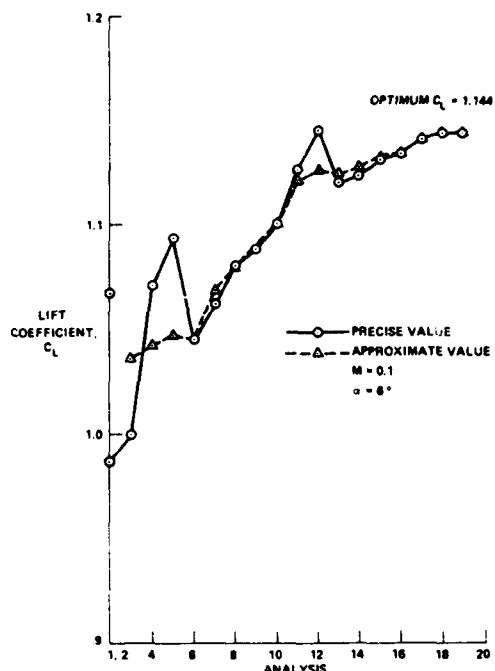


Fig. 47 - Optimization history.

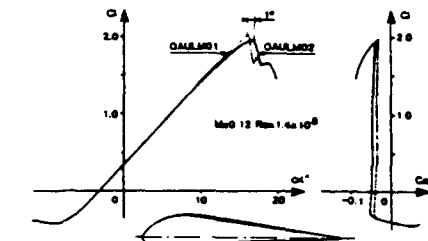


Fig. 50 - OAULM01 and OAULM02 airfoils. Lift and pitching moment. Experimental data.

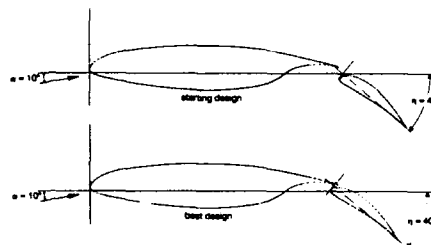


Fig. 51 - Starting and best design of flap position optimization.

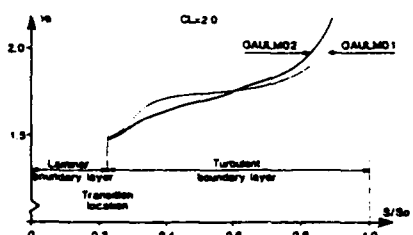


Fig. 48 - OAULM01 and OAULM02 airfoils. Computed suction side shape factor.

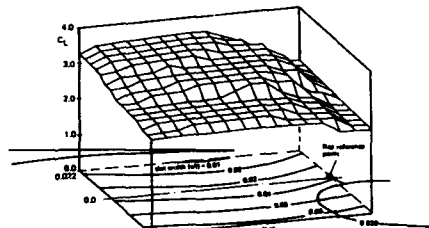


Fig. 52 - Lift and slot width depending on flap position.

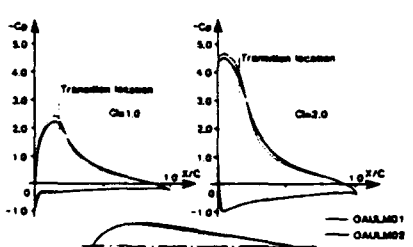
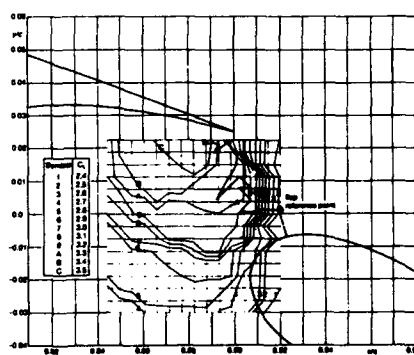
Fig. 49 - OAULM01 and OAULM02 airfoils. Pressure distributions. $M = 0.12, Re = 1.4 \cdot 10^6$.

Fig. 53 - Optimization progress of flap position optimization.

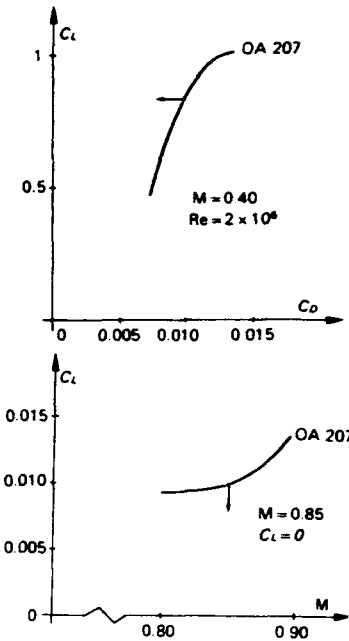


Fig. 54 - Two design point optimization of the OA207 airfoil.

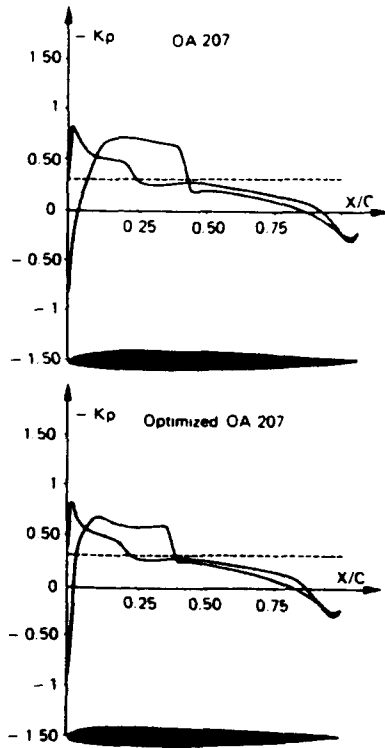


Fig. 55 - Comparison of pressure distributions at $M = 0.85, \alpha = 0.5^\circ, Re = 3.7 \cdot 10^6$

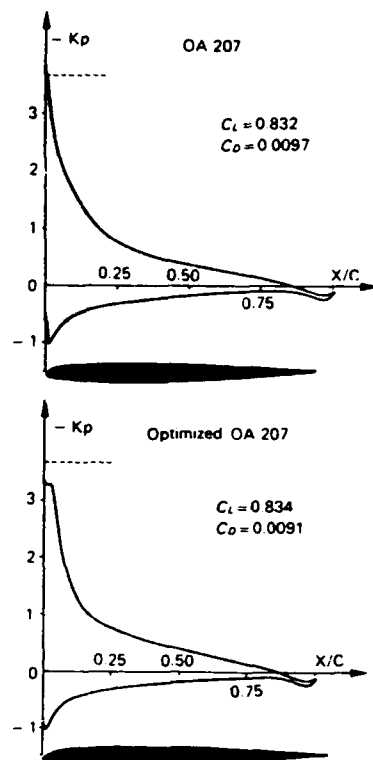
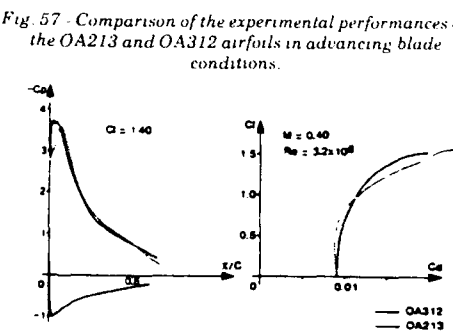
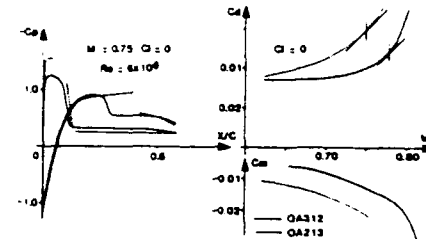


Fig. 56 - Comparison of pressure distributions at $M = 0.4, \alpha = 7.5^\circ, Re = 2.1 \cdot 10^6$



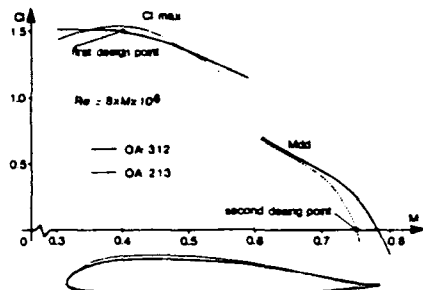


Fig. 59 - Performances of OA213 and OA312 airfoils.
Experimental data.

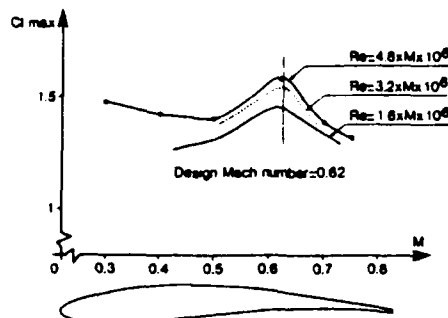


Fig. 60 - OAF102 airfoil evolution of the $C_{L\max}$ with
Mach number and Reynolds number.

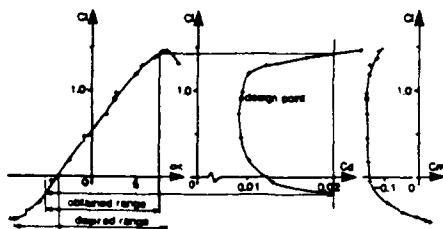


Fig. 61 - OAF102 airfoil. Experimental data $M = 0.62$,
 $Re = 1.106$.

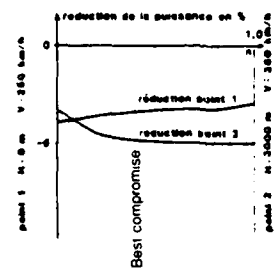


Fig. 62 - Power reduction versus n .

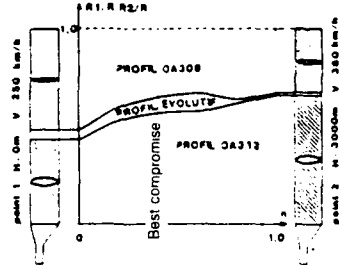


Fig. 63 - Airfoil distribution along the span vs. the n
coefficient.

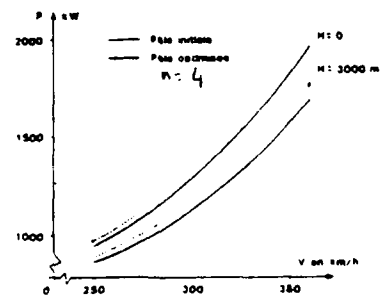


Fig. 64 - Performance gain with the optimized blade.

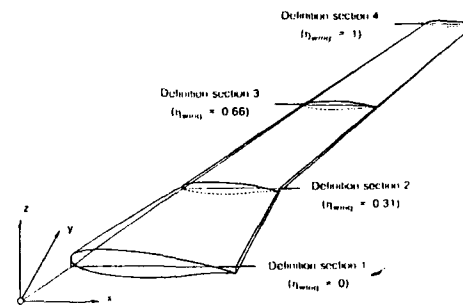


Fig. 65 - DLR F4 wing.

		$C_{D_l} (\times 10^4)$	$C_{D_w} (\times 10^4)$	$C_{D_l} + C_{D_w} (\times 10^4)$	$C_{D_s} (\times 10^4)$
F4 wing		199.1	21.3	220.4	255.2
Initial untwisted wing		203.9	33.3	237.2	267.3
Calculation	Objective	$C_{D_l} (\times 10^4)$	$C_{D_w} (\times 10^4)$	$C_{D_l} + C_{D_w} (\times 10^4)$	$C_{D_s} (\times 10^4)$
1	C_{D_l}	197.6	24.1	221.7	256.3
2	C_{D_w}	204.5	21.1	225.6	258.7
3	$C_{D_l} + C_{D_w}$	197.9	22.7	220.6	255.0
4	C_{D_s}	198.4	22.4	220.8	254.9
5	Elliptical load	197.5	23.8	221.3	255.8

Fig. 66 - Drag minimization by wing-twist optimization.

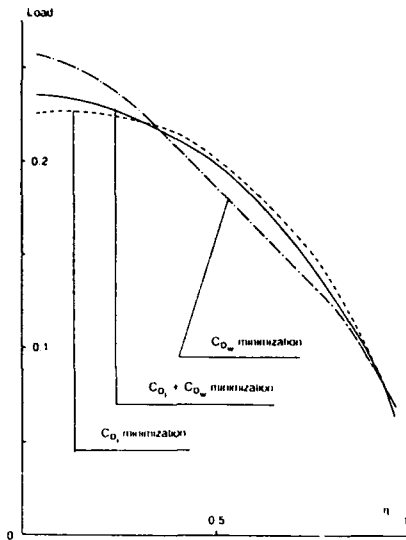


Fig. 67 - Wing twist optimization for drag minimization ($M = 0.75, C_L = 0.67$). Spanwise load distributions.

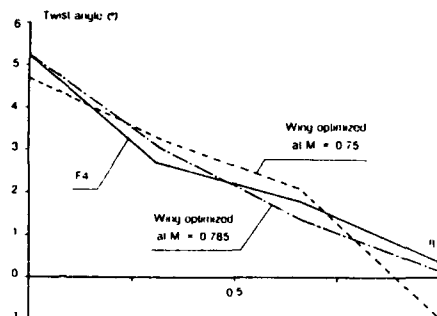


Fig. 69 - Wave + induced drag minimization at two operating points. Optimized twist distributions.

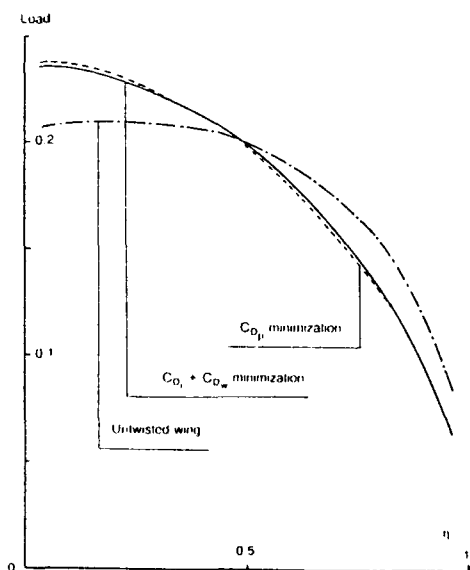


Fig. 68 - Wing twist optimization for total inviscid drag minimization ($M = 0.75, C_L = 0.67$). Spanwise load distributions.

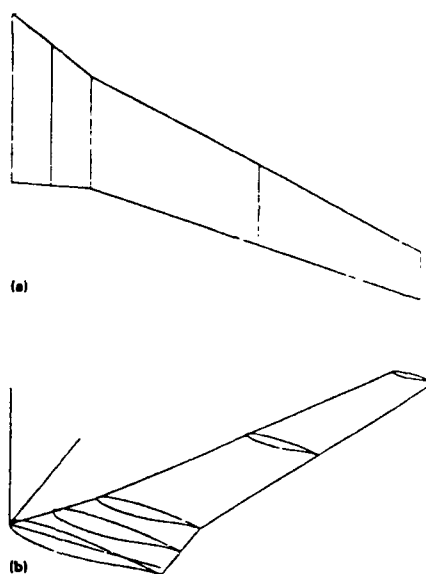


Fig. 70 - Two views of the Cessna citation III model 650 wing geometry with aspect ratio 9.0 and leading edge sweep of 27.2° . a) Planform view; b) isometric view.

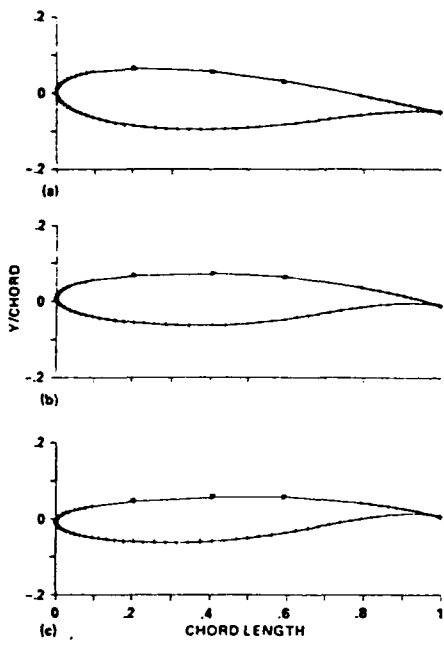


Fig. 71 - Location of the fixed (+) and movable (•) spline support points on the three Cessna airfoils. a) Root station; b) break station ; c) tip station.

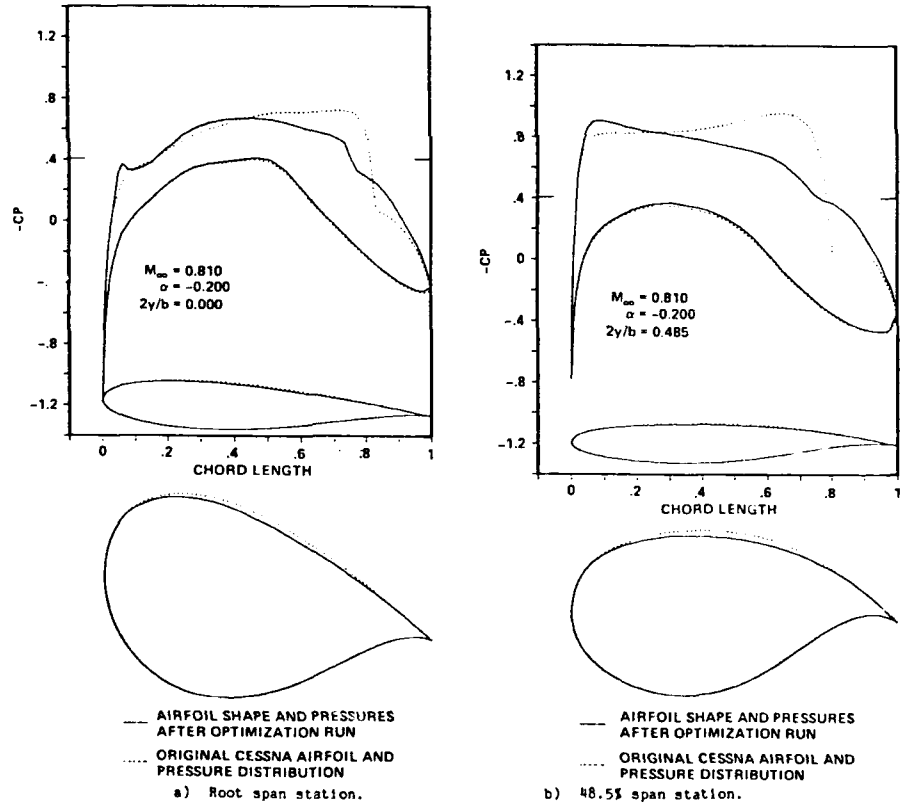


Fig. 72 - TWING/QNM drag-to-lift ratio minimization result - Cessna model 650 wing design.

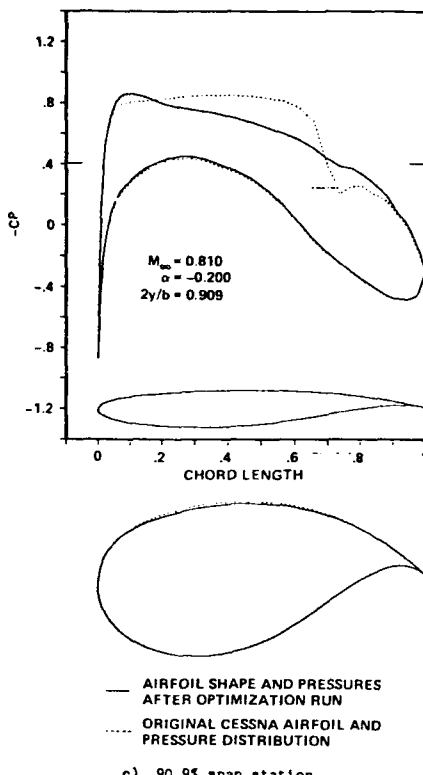


Fig. 72 - Concluded

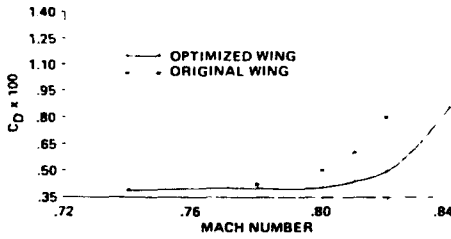
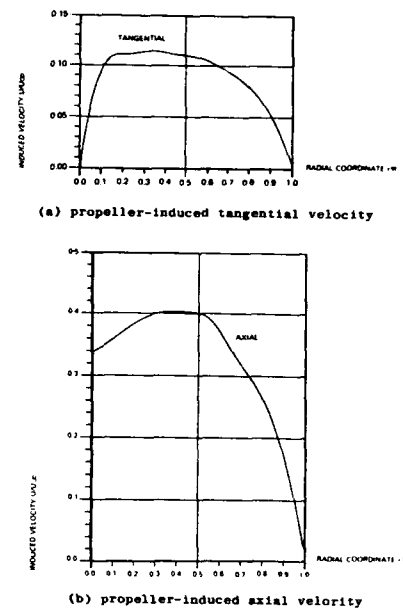
Fig. 73 - Coefficient of drag ($\times 100$) versus Mach number for the original and optimized wing - Cessna 650 case, $C_L \approx 0.506$.

Fig. 74 - Propeller-induced velocities.

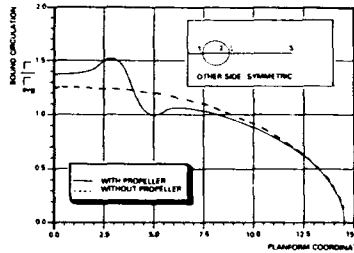
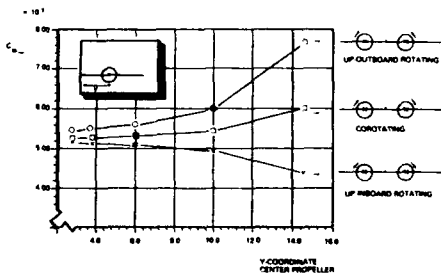
Fig. 75 - Optimal bound circulation distribution r for a wing with two up-inboard rotating propellers.

Fig. 76 - Effects of the horizontal propeller location on the minimum induced drag.

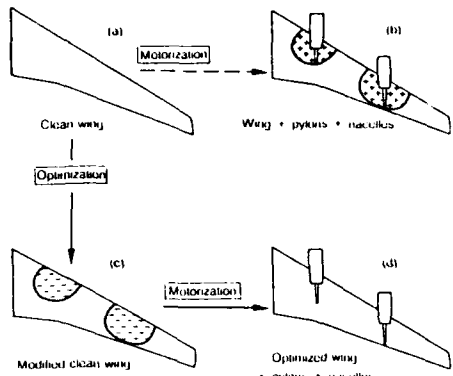


Fig. 77 - Optimization of a four-engined jet aircraft wing taking into account the effects of the propulsive system.

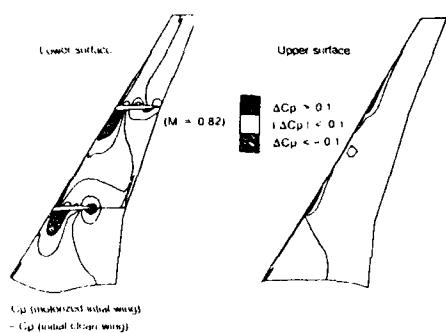


Fig. 78 - Wing C_p disturbance due to the engines.

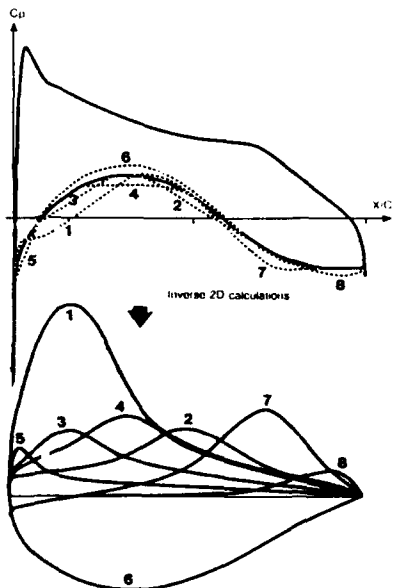


Fig. 79 - Examples of geometrical modification functions for the optimization.

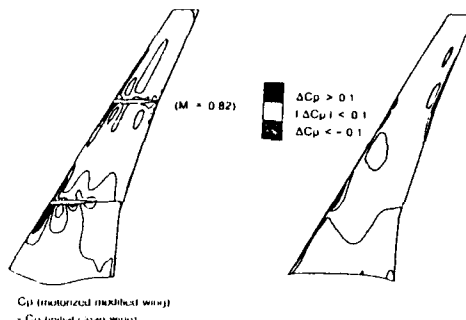


Fig. 80 - Optimized wing.

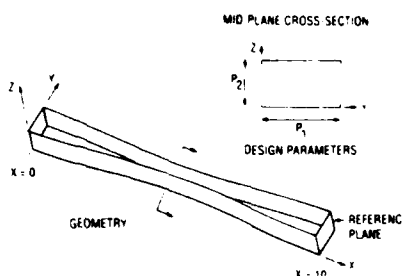


Fig. 81 - 3-D nozzle test case.

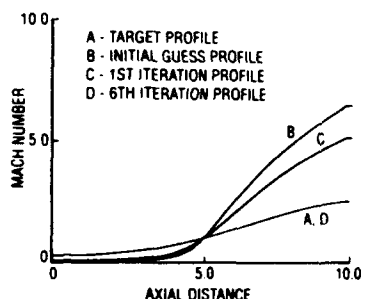


Fig. 82 - 3-D nozzle centerline Mach number contours.

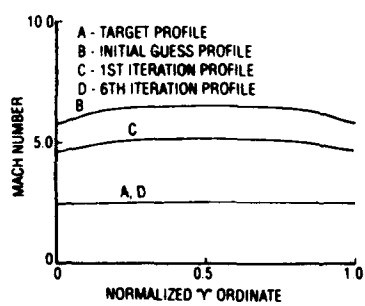


Fig. 83 - 3-D nozzle RP Mach number variation.

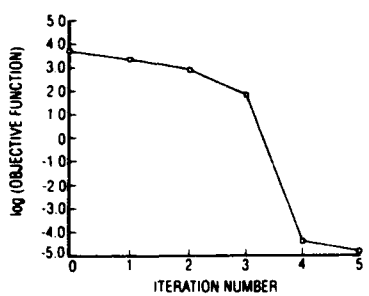


Fig. 84 - 3-D nozzle objective function reduction.

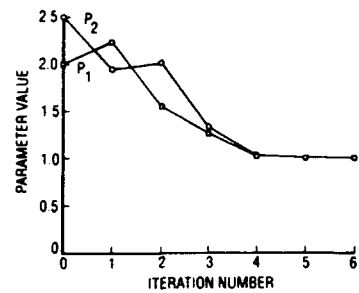


Fig. 85 - 3-D nozzle parameter convergence.

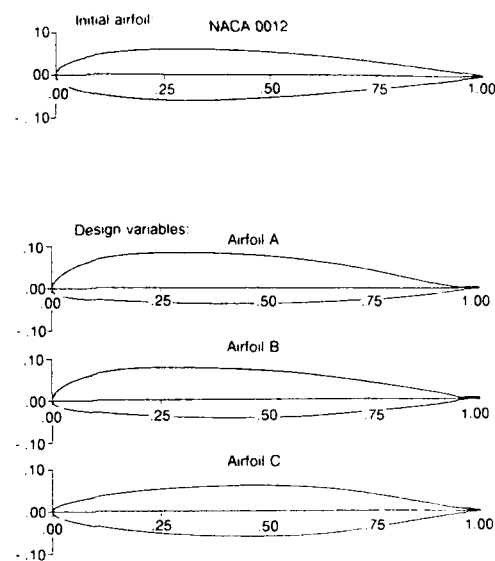


Fig. 86 - Airfoil library for unsteady optimization.

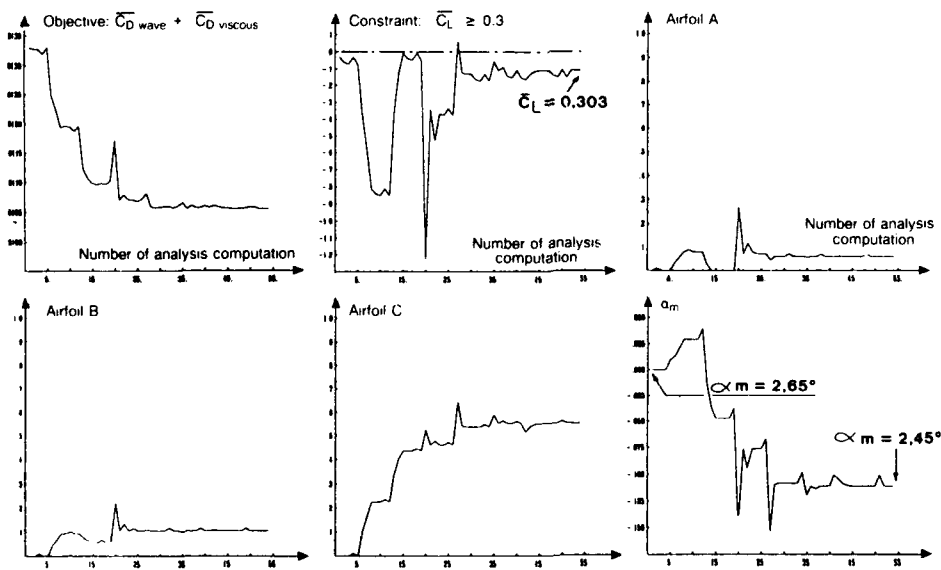


Fig. 87 - Case n°1. Convergence history.

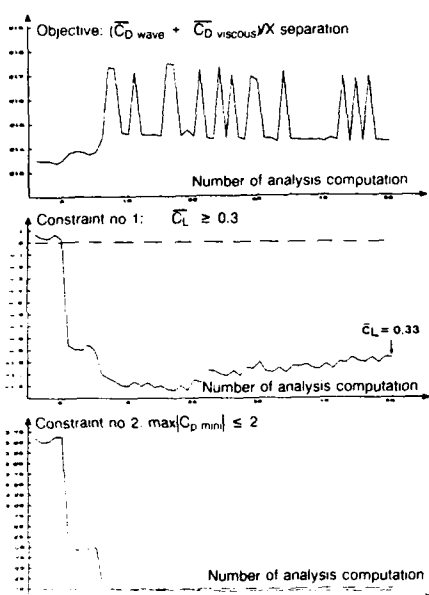


Fig. 88 - Case n°2. Convergence history.

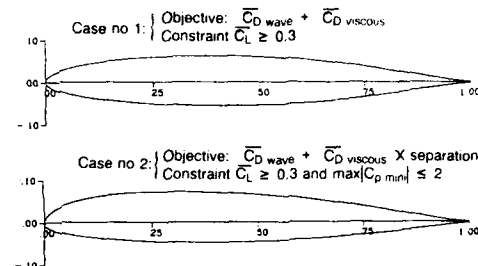


Fig. 90 - Unsteady optimized airfoils.

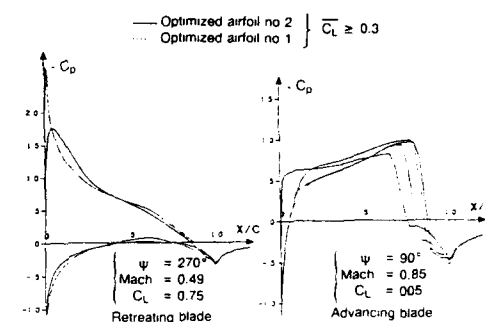


Fig. 91 - Unsteady pressure distribution, optimized airfoils.

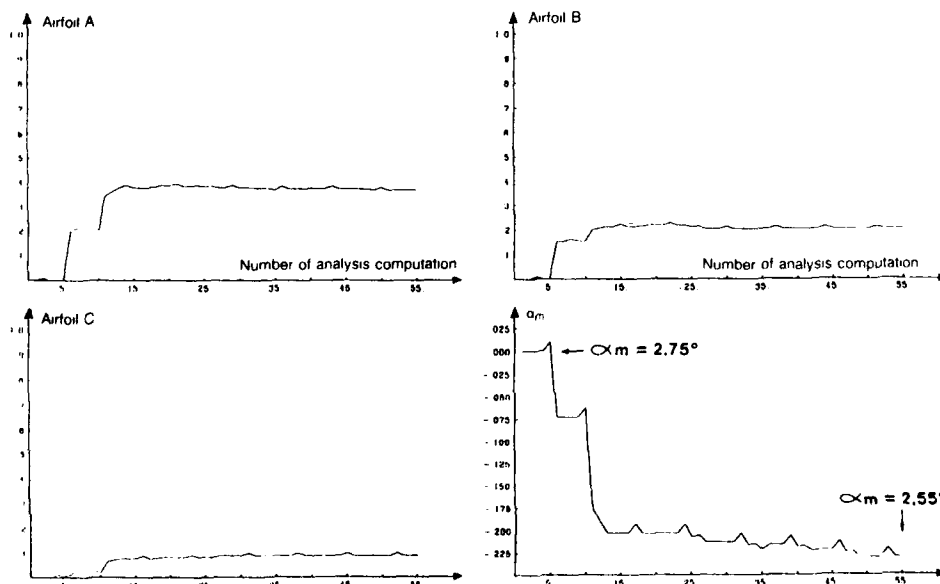


Fig. 89 - Case n°2. Design variables evolution.

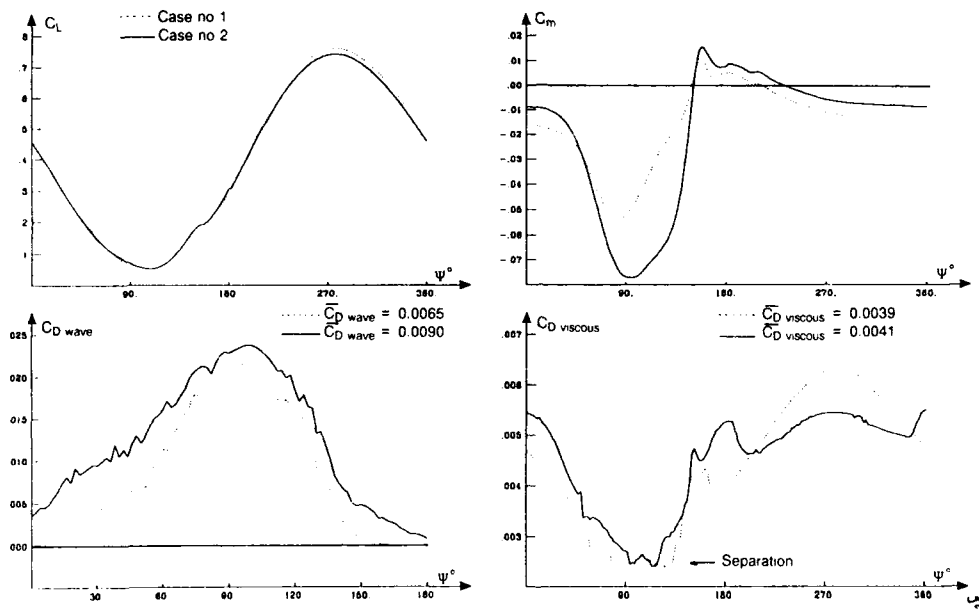


Fig. 92 - Unsteady aerodynamic performance for the optimized airfoils $C_L = 0.3$.

CONSTRANED SPANLOAD OPTIMIZATION
FOR MINIMUM DRAG OF MULTI-LIFTING-SURFACE CONFIGURATIONS

R.F. van den Dam
National Aerospace Laboratory NLR
P.O. Box 90502 Amsterdam The Netherlands

SUMMARY

This paper presents a practical method for the determination of optimal spanloads for multi-lifting-surface configurations. It comprises algorithms for choosing the spanwise distributions of lift, pitching moment, chord and thickness-to-chord ratio of lifting elements. The choices are optimal in that they minimize induced plus viscous drag while satisfying constraints of aerodynamic, flight-mechanical and structural nature. The configuration that can be dealt with, may consist of a number of segments representing, for instance, wings or parts of wings, horizontal tails or canards, winglets, flaprail-fairings, etc. Also the interaction between propellers and lifting elements may be included in the procedure.

The induced drag is computed using the Trefftz-plane integral (farfield-analysis), while the viscous drag follows from form factor methods. Novel mathematical formulations of the constrained optimization problem are used, that are based on the calculus of variations. The method can be used as a first step in the inverse numerical optimization approach to provide a starting point for the specification of target pressure distributions. These target pressure distributions are then used by an inverse code to determine the corresponding geometry. This paper presents the theoretical models and methods underlying the analysis and optimization capability, comparisons with other theories, and some examples of application.

1 INTRODUCTION

The success of an aircraft design depends largely upon finding an optimal balance between the contributions of the disciplines involved. Moreover, many of the benefits from emerging technologies can only be fully exploited through their interactions with other disciplines. Good examples of these are the technologies of active control and composites which make it possible to design aircraft with forward swept wings and relaxed static stability. In order to find an optimal balance between the contributions of the disciplines and to take maximum advantage of technology advances, the interactions should be identified and quantified before the main decisions concerning the overall configuration design are made. This implies the necessity of developing the analysis and design capability to a suitable breadth and depth for earlier application in the design process. Increased breadth means the inclusion of the appropriate spectrum of disciplines and new technologies early in the design. Increased depth in the early design stage is required to assure that the interactions are correctly quantified before the main decisions are made. An example of developing methods of this nature is the method for drag minimization studies described in the paper.

Minimization of (aerodynamic) drag is an important goal in aircraft configuration design studies as it helps to improve upon fuel efficiency. In these studies, it has been common practise to decompose the aircraft drag in components that are to a large extent independent. Computational Fluid Dynamics have created possibilities for drag breakdown that is based on physical principles (Sect. 2.3 of Ref. 1). In such a breakdown it is convenient to distinguish between viscous (boundary layer) drag, induced (or vortex) drag and wave drag.

With respect to the choice of independent variables in drag minimization problems one may distinguish different approaches. One is to use parameters defining the geometry as the independent variables (direct numerical optimization). While this approach is feasible in two dimensions (see e.g. Ref. 2) it is hardly so, at present, in the case of three-dimensional configurations because of the lack of accuracy in the available three-dimensional codes in combination with the limited computer power available (Ref. 3).

Yet an alternative approach may be adopted, namely the use of aerodynamic (load and pressure distributions) rather than geometric shape functions as independent variables (Ref. 4). This approach, called inverse numerical optimization (see Fig. 1), involves the successive determination of optimal target spanloads (using methods as described in the paper), target pressure distributions (optimal with respect to the specified drag characteristics and providing the prescribed spanloads), and corresponding lifting-surface geometries (using an inverse code). This process is repeated until a geometry is obtained having acceptable performances for all flight conditions.

This paper concerns the first step in the inverse numerical optimization approach: the determination of optimal spanloads. In literature, various theoretical methods can be found for determining spanloads for minimum drag. Almost all of them consider induced drag only in determining optimal spanloads (see e.g. Ref. 5, 6, 7). Inclusion of other drag components in the optimization procedure can produce substantially different minimum drag spanloads compared with induced-drag-only results.

Methods that extend the induced drag minimization theory to include other components as well, and can be used in preliminary aircraft design, are the subcritical design code of Kuhlman (Ref. 8) and the transonic optimization scheme of Mason (Ref. 9).

The method described in this paper provides capabilities for choosing the spanwise distributions of lift, pitching moment, chord and thickness-to-chord ratio of lifting elements of an aircraft configuration. The choices are optimal in the sense that they minimize induced plus viscous drag, or induced drag only, while satisfying constraints on, for example, pitching moment and section lift coefficients. Determining minimum drag spanloads, also the interaction between propellers and lifting elements may be included in the procedure. With an optimal spanload, the wing can restore much of the (rotational) energy loss associated with propeller swirl (Ref. 10, 11). The method may provide direct input for more detailed aerodynamic design (e.g. the inverse numerical optimization procedure), but may also be used for parametric airplane configuration design studies. In these parametric design studies, the method is used to quickly assess the consequences of changes in the configuration of (complex) aircraft.

In the following sections, an outline of the analysis and minimization technique developed is presented. Comparisons with other theories are given and the capabilities of the method will be illustrated by some examples of application.

2 FORMULATION OF THE PROBLEM

It is assumed that the projection of the aircraft configuration onto a plane perpendicular to the flight direction can be approximated by a number of straight line segments, representing the various elements of the configuration. An example is shown in figure 2(a). The geometry description can include wings (or parts of wings), tailsurfaces, pylons, winglets, etc. The planform geometries of the configuration lifting elements can be described by the spanwise distributions of chord-length, together with the coordinates of the 1/4-chord point locations, defining the planform sweeps (see Fig. 2(b)). The vortex sheets aft of the configuration are assumed to remain undistorted. The latter can be argued to be a reasonable approximation in the case of planar optimal spanloads. It is assumed that this also holds for optimal spanloads of non-planar configurations. The airplane lift and drag are thought of as being composed of wing, tail and/or canard, fuselage and nacelle contributions, as illustrated in figure 2(c). The lift of the fuselage is modelled using the principle of lift carry-over from the wing, resulting in a constant distribution of bound circulation of the fuselage width.

If the interaction between propellers and lifting elements has to be considered as well, each propeller is assumed to shed a helical vortex sheet that is not influenced by the presence of the wing (Ref. 12), and that is confined inside a cylindrical "stream" tube parallel to the flight direction. The velocity distribution inside the slipstream has to be known for a specified propeller and required thrust.

The following problems are to be addressed:

- determination of optimal spanwise lift-distributions plus, if applicable, spanwise pitching moment distributions that result in either minimum induced drag or minimum induced plus viscous drag. In this procedure, constraints may be imposed on total pitching moment (trimmed aircraft), section liftcoefficients (feasible airfoils), rolling moment and, if applicable, bending moment. A part of the total spanwise lift-distribution may be specified in advance. In that case, the induced (plus viscous) drag is to be minimized by adjusting the remaining part of the lift-distribution.
- computation of the induced (plus viscous) drag for given (non-optimal) spanwise lift distributions. For instance, to quickly quantify the penalties that arise from the use of non-optimal loadings, to determine the performance under off-design conditions, or to estimate the induced drag associated with flap deflection.

3 DETERMINATION OF DRAG AND LIFT

The aircraft is assumed to fly with a constant velocity in a uniform, inviscid and irrotational medium. An expression for the induced drag in the Trefftz-plane can be derived by applying the momentum theorem to a control surface enveloping the aircraft (Ref. 4, 13). Consider a control surface S of the type as indicated in figure 3. Several subsurfaces of S can be distinguished: the Trefftz plane (S_u), a similar plane far upstream (S_T), the top and bottom plane (S_m), the body surface (S_B), the shockwave surface (S_s), the vortex sheet surface (S_v), the propeller surface (S_p) and the slip-stream surface (S_{sl}). Application of the conservation laws of momentum leads to the integral expression:

$$\oint_S [pn_x + \rho u q_n] dS = 0, \quad (1)$$

where $S = S_u + S_T + S_m + S_B + S_p + S_v + S_{sl} + S_s$.

p is the (local) static pressure, \vec{q} is the total velocity vector, ρ is the density, \vec{n} is the unit outward normal to the control surface, and u is the component in the free-stream (x -)direction of \vec{q} .

Splitting-off the body pressure integral and realizing that $q_n = 0$ on S_B leads to the following expression for the total pressure drag of the aircraft:

$$D = \oint_{S_B} p n_x dS = - \int_{S-S_B} (pn_x + \rho u q_n) dS. \quad (2)$$

Working out this expression and splitting-off the wave drag integral the following Trefftz-plane integral for the induced drag can be derived (see Ref. 14):

$$D_I = \int_{S_T} \left\{ (p-p_\infty) + \rho(u-u_\infty)u - \rho \frac{(H-H_\infty)u}{u_\infty} \right\} dS - \sum_{i=1}^{n_p} \frac{1}{J_i} \langle \frac{Q}{D} \rangle_i, \quad (3)$$

H represents the stagnation enthalpy, D is the slipstream diameter, J is the propeller advance ratio ($= u_\infty/\omega D$, where ω is the propeller angular velocity), Q is the propeller torque and n_p is the number of propellers.

Assuming small perturbations in the Trefftz-plane, the flow being isentropic, and using the law of Biot-Savart, equation (3) may be worked out further to obtain (see again Ref. 14):

$$D_I/D_\infty = \frac{1}{2} \int_{S_V \cap S_T} \Gamma(n) v_n(n) dn + \int_{S_V \cap (S_{T_{II}} + S_{T_{III}})} \Gamma(n) (\vec{V}_p \cdot \vec{n}) dn + \frac{1}{2} C^* S_{ref} u_\infty^2 \quad (4)$$

where

$$C^* = \frac{2}{S_{ref} u_\infty^2} \left\{ \frac{1}{2} \int_{S_T} \vec{V}_p \cdot \vec{V}_p ds - \sum_{i=1}^{n_p} \frac{1}{J_i} \langle \frac{Q}{D} \rangle_i \right\}.$$

Γ is the bound circulation, v_n is the velocity induced in the Trefftz-plane normal to the vortex sheet segment, and $\vec{V}_p = (u_p, v_p, w_p)$ is the (fixed) perturbation velocity in the slipstream of an isolated propeller, n denotes the distance (spanwise parameter) along $S_v \cap S_T$. The last term in equation (4) represents the magnitude of the "swirl loss" of the propeller. In the first right-hand term of equation (4) the integration is performed over all lifting elements, in the second term the integration is performed over the lifting elements in the slipstream only. The local trailing vortex sheet strength is equal to the derivative of the bound circulation at that spanwise position; so, using the law of Biot-Savart, the following expression for v_n can be derived:

$$v_n(n) = \frac{1}{2\pi} \int \frac{d\Gamma(\tau)}{d\tau} \cdot \frac{\vec{n}(n) \cdot (\vec{r}(\tau, n) \times \vec{e}_x)}{|\vec{r}(\tau, n)|^2} d\tau \quad (5)$$

Again, the line integral is taken over the projections of all lifting configuration elements onto the Trefftz-plane. $\vec{n}(n)$ is the unit vector normal to the position n , and \vec{e}_x is the (downstream directed) unit vector along the x -axis. The vector $\vec{r}(\tau, n)$ denotes the vector from the spanwise position τ to the spanwise position n . Integrating by part with respect to τ , equation (5) can be rewritten into:

$$v_n(n) = S_{ref} u_\infty^2 \int f(\tau, n) \Gamma(\tau) d\tau \quad (6)$$

where

$$f(\tau, n) = - \frac{1}{2\pi S_{ref} u_\infty^2} \frac{d}{d\tau} \left(\frac{\vec{n}(n) \cdot (\vec{r}(\tau, n) \times \vec{e}_x)}{|\vec{r}(\tau, n)|^2} \right) \quad (7)$$

The other term at the right side of (6) has disappeared since $\Gamma = 0$ at the free end of a lifting element. Substitution of (6) in (4) yields:

$$C_{D_I} = \iint f(\tau, n) \Gamma(\tau) \Gamma(n) d\tau dn + \frac{2}{S_{ref} u_\infty^2} \int \Gamma(n) (\vec{V}_p(n) \cdot \vec{n}(n)) dn + C^* \quad (8)$$

Thus, the optimal circulation distribution may be computed with the propeller and wing located both far upstream, eliminating the 3D-computation of velocities induced by the wing on the propeller and by the propeller bound vorticity on the wing. In fact, this expression underlines the correctness of the postulation of reference 10 concerning the generalisation of the stagger theorem of Munk. The generalized version of the stagger theorem allows the farfield computation as it states that also for propeller-wing combinations the "net force in the streamwise direction is independent of the streamwise position of lifting surfaces with a given circulation distribution".

Viscous drag

The viscous drag is derived for given airfoil characteristics. These airfoil characteristics define the viscous drag at each spanwise station as a function of the local section lift coefficient. An expression for the viscous drag can be derived using the (2D, incompressible) DATCOM/Hoerner formulae:

$$C_{d_{visc}} = C_F \left\{ 1 + k(t/c) + 100 (t/c)^4 \right\} \cdot \frac{S_{wet}}{S_{ref}} \quad (9)$$

C_F denotes the flat plate friction coefficient (depends on location of transition point and local Reynolds number, see Ref. 14) and t/c is the thickness location factor (depends on location of maximum thickness). t/c represents the thickness-to-chord ratio. For common airfoils, the wetted surface S_{wet} is about twice the reference surface S_{ref} .

Applying thin airfoil theory and considering the velocity distribution and the drag contribution of both the upper surface and lower surface individually (hereby assuming the same class of pressure distributions, see Fig. 4), expression (9) can be written in the form:

$$\begin{aligned} C_{d_{visc}} = & C_{F_{up}} \left\{ 1 + k_{up} (\bar{u}_t + \bar{u}_l) + 100 (\bar{u}_t + \bar{u}_l)^4 \right\} + \\ & + C_{F_{lo}} \left\{ 1 + k_{lo} (\bar{u}_t - \bar{u}_l) + 100 (\bar{u}_t - \bar{u}_l)^4 \right\} \end{aligned} \quad (10)$$

\bar{u}_t and \bar{u}_l represent average perturbation velocities as a result of airfoil thickness and lift, respectively:

$$\bar{u}_l = \frac{1}{4} C_L \quad \text{and} \quad \bar{u}_t \approx \frac{(t/c) \cos \Lambda}{B_n} \quad (11)$$

$$\text{where } B_n = \sqrt{1 - M_\infty^2 \cos^2 \Lambda} \quad (12)$$

Λ denotes the sweepback and M_∞ denotes the (3D) undisturbed Mach number. C_L denotes the (3D-) lift coefficient that is linked, according to the Kutta-Joukowski theorem, to the bound circulation (see eq. 15). Substitution of (11) in (10) leads to an expression for the viscous drag as function of C_L and t/c . It is plausible to assume, on the basis of DATCOM's formulae, that k varies continuously with the position of the pressure recovery starting point x_R (see Fig. 4):

$$k = 2 \frac{x_R/c}{0.3} \sim 8.26 \left(\frac{x_R}{c} - 0.3 \right) \approx 2.5 - 1.6 \frac{x_R}{c}$$

Using this formula, $k = 2$ for $x_R/c = 0.3$ and $k = 1.2$ for $x_R/c = 0.8$, which corresponds with DATCOM's formulae.

In the C_L -range of interest, the viscous drag function (10) is approximated by a polar of the form

$$C_{d_{visc}} (C_L(\Gamma(n))) = C_{visc}^* + K^* (C_L - C_L^*)^2, \quad (13)$$

where the factors C_{visc}^* , K^* and C_L^* follow from a least square fit to the function. Integration results in the total viscous profile drag:

$$C_{D_{visc}} = \int \frac{C_{d_{visc}}(\Gamma(n), n) c(n)}{S_{ref}} dn. \quad (14)$$

Expressions for lift and moments

An expression for the local lift follows from the Kutta-Joukowski theorem applied in the lift direction:

$$C_L(n) = g_1^*(n) \Gamma(n) \quad \text{where} \quad g_1^*(n) = \frac{2 \cos(\psi(n))}{u(n)c(n)} \quad (15)$$

$u(n)$ is the local upstream velocity for a lifting element at the position n . If (a part of) the lifting element is situated in the slipstream, $u(n)$ differs from the undisturbed velocity. $\psi(n)$ denotes the dihedral angle. The total lift of the configuration follows from integration:

$$C_L = \int g_1(n) \Gamma(n) dn \quad \text{where} \quad g_1(n) = \frac{2 \cos(\psi(n)) u(n)}{S_{ref} u_\infty^2} \quad (16)$$

If the section pitching moment distribution is not given, it can be deduced from the pressure recovery point locations. For the class of pressure distributions given in figure 4, the next expression for the section pitching moment C_m w.r.t. the quarter chord point $x_{1/4}$ can be derived:

$$C_m(C_L) = C_m^* - A^* C_L \quad (17a)$$

where

$$C_m^* = m_1 \left(\frac{4(t/c) \cos \Lambda}{\sqrt{1 - M_\infty^2 \cos^2 \Lambda}} + .4 \right) \left(\frac{a_1 a_4 - a_2 a_3}{a_1 + a_2} \right) \quad (17b)$$

$$A^* = m_2 \left(\frac{a_3 + a_4}{a_1 + a_2} \right) \quad (17c)$$

and

$$a_1 = \frac{1}{2} + \frac{1}{2} x_{R_u}, \quad a_3 = \frac{1}{24} + \frac{1}{24} x_{R_u} + \frac{1}{6} x_{R_u}^2,$$

$$a_2 = \frac{1}{2} + \frac{1}{2} x_{R_L}, \quad a_4 = \frac{1}{24} + \frac{1}{24} x_{R_L} + \frac{1}{6} x_{R_L}^2.$$

C_L follows from (15). m_1 and m_2 are known constants. With the section pitching moment defined with respect to the quarter-chord point, the total contribution of the lifting elements to the aircraft pitching moment w.r.t. the centre of gravity then follows from:

$$C_M = \int g_2(\eta) \Gamma(\eta) d\eta + \frac{1}{S_{ref} c_{ref} u_\infty^2} \int C_m^*(\eta) c^2(\eta) u^2(\eta) d\eta \quad (18a)$$

where

$$g_2(\eta) = \frac{2 u(\eta)}{S_{ref} c_{ref} u_\infty^2} (x_{c.g.} - x_{1/4}(\eta) - A^*(\eta) c(\eta)) \cos(\varphi(\eta)) \quad (18b)$$

c_{ref} denotes the length of the reference chord, and $x_{c.g.}$ is the longitudinal coordinate of the configuration centre-of-gravity.

If the aircraft configuration is asymmetrical, (e.g. a configuration with propellers all rotating in the same direction), a rolling moment constraint C_R w.r.t. the point $\eta = 0$ (in the plane of symmetry) may be imposed:

$$C_R = \int g_3(\eta) \Gamma(\eta) d\eta \quad (19a)$$

where

$$g_3(\eta) = \frac{2 u(\eta)}{S_{ref} b_{ref} u_\infty^2} [(y(\eta) - y(0)) \cos(\varphi(\eta)) + (z(\eta) - z(0)) \sin(\varphi(\eta))] \quad (19b)$$

b_{ref} is the reference span. Note that the rolling moment coefficient C_R equals 0 if the aircraft configuration is symmetrical.

Limitation in design c_L , t/c , c_m and M

In order to ensure that the computer program works with feasible airfoil characteristics, a relation defining feasible combinations of (design) lift coefficient, (design) Mach number, wing thickness-to-chord ratio and pitching moment coefficient may be formulated. For supercritical airfoils, a graphical representation of such a relation between t/c , c_L and M is given in figure 5 for $c_m = -.110$. Data for other c_m -levels follow from the relation $\delta(t/c)/\delta c_m = -0.6$. The relation can be considered to represent a "condensed" section characteristics data base for a feasible class of supercritical airfoils. This class is described by a relation between allowable combinations of design c_L , M , t/c , c_m . The data base holds for 2D-airfoils. If a sweep angle Λ is applied, the 3D-values have to be calculated from the 2D-values using the relations:

$$C_L(3D) = c_L(2D) \cos \Lambda, \quad C_m(3D) = c_m(2D) \cos^2 \Lambda, \\ \frac{t}{c}(3D) = \frac{t}{c}(2D) \cos \Lambda, \quad M(3D) = M(2D) / \cos \Lambda.$$

The data base is used when imposing (local) lift coefficient constraints in drag minimization procedures. In the case that the user provides pitching moment coefficient distributions, the combination of t/c , M and c_m directly leads to the upper limit of the allowed range for the (design) lift coefficient. If the pitching moment coefficients are not directly specified, the combination of t/c and M only results in a feasible c_L - c_m area. In that case, the pitching moment coefficient

distribution may be defined by relation (17), which further restricts the possible combinations of c_m and c_l in this feasible area. Both c_m and c_l are then found as part of the solution.

It is emphasized that the "data base" of feasible characteristics is representative for a certain class of airfoils. The user should check whether this data base is compatible with his own experience. If required, the relation may be modified to his own experience.

4 DRAG MINIMIZATION

General

The numerical optimization of drag is based on an approach, in which the evaluation of double integrals (see eq. 8) is avoided. This is realized by first deriving analytically the necessary optimality equations before doing any discretization. Discretization of the bound-circulation distribution in the (single) integrals is performed starting from these analytical necessary optimality equations.

Analytical necessary optimality equations

The drag minimization problem can be stated as follows: determine the function $\Gamma(n)$ that minimizes the functional $C_{D_1} + C_{D_{visc}}$ subject to constraints imposed on C_L , C_M and, if required, on C_R :

$$\begin{aligned} G_1 &= C_L - C_{L_{des}} = 0 \\ G_2 &= C_M - C_{M_{des}} = 0 \\ G_3 &= C_R - C_Q = 0 \end{aligned} \quad (20)$$

Also $C_l(n)$ may be constrained:

$$G_4(n) = C_l(n) - C_{l_{des}}(n) \leq 0, \quad \forall n. \quad (21)$$

$C_{L_{des}}$, $C_{M_{des}}$ and the (dimensionalized) propeller torque C_Q are prescribed values for C_L (eq. 16), C_M (eq. 18) and C_R (eq. 19). $C_{l_{des}}(n)$ follows from the relation between c_l , t/c , c_m and M as described in the preceding section. Expression (8) and (14) specify the induced drag C_{D_1} and viscous drag $C_{D_{visc}}$, respectively.

The problem may be solved through the introduction of Lagrange multipliers. That is, the augmented integral

$$I = C_{D_1} + C_{D_{visc}} + \sum_{i=1}^3 \lambda_i G_i + \int u(n) G_4(n) dn$$

is formed, where the Lagrange multipliers λ_i ($i = 1, 2, 3$) and $u(n)$ are to be determined. The next step towards the solution of the optimization problem is to write $\Gamma(n) = \Gamma(n) + \delta\Gamma(n)$, and to form the first variation δI of I with respect to variations of $\Gamma(n)$,

$$\begin{aligned} \delta I = & \int_n \left[2 \int f(\tau, n) \dot{\Gamma}(\tau) d\tau + \frac{2}{S_{ref} U_\infty^2} (\vec{v}_p(n) \cdot \vec{n}(n)) + \right. \\ & \left. + 2 K^*(n) g_1^{*2}(n) \dot{\Gamma}(n) - 2 K^*(n) g_1^*(n) C_l^*(n) + \sum_{i=1}^3 \lambda_i g_i(n) + u(n) g_4^*(n) \right] \delta \Gamma(n) dn \end{aligned} \quad (22)$$

In this variation, the parameters v_p , K^* and C_l^* , and all geometry-related parameters, have fixed values.

The necessary condition for the minimization of I is that the first variation vanishes. This condition holds for any arbitrary function $\delta\Gamma(n)$, hence the term between brackets in (22) must vanish at all spanwise positions. In fact, this necessary condition for the minimization of I is nothing else but the Euler-Lagrange equations of variational calculus. Upon substitution of the expression (6) for $f(\tau, n)$, the condition can also be written in the form:

$$\frac{2}{S_{ref} U_\infty^2} \left(\vec{v}_n(n) + \vec{v}_p(n) \cdot \vec{n}(n) \right) + 2 K^*(n) g_1^{*2}(n) \Gamma(n) - 2 K^*(n) g_1^*(n) C_l^*(n) + \sum_{i=1}^3 \lambda_i g_i(n) + u(n) g_4^*(n) = 0 \quad (23)$$

that must hold for all n . In combination with the constraint relations (20) for C_L , C_M and C_R , and the constraint for $C_l(n)$ written in the form

$$\left. \begin{aligned} u(n)(C_L(n) - C_{L_{des}}(n)) &= 0 \\ u(n) &\geq 0 \end{aligned} \right\} \quad \forall n \quad (24)$$

the optimal bound circulation is determined.

It may be noted that, if only the induced drag is minimized ($K = 0$) in a flow without propeller slipstreams ($V_p = 0$) and imposing the total lift constraint only, the necessary condition reduces to Munk's criterium for minimum induced drag (Ref.15).

$$\frac{2}{S_{ref} u_\infty} v_n(n) + \lambda_1(C_L - C_{L_{des}}) = 0, \quad \forall n$$

In words, "the induced drag will be a minimum when the component of the induced velocity normal to the lifting element at each point is proportional to the cosine of the dihedral angle of the lifting element at that point ($v_n = w_0 \cos \psi$)".

Numerical approach

The necessary optimality conditions (23) for the drag minimization includes an integral expression for v_n . Direct integration can be done analytically only for the most simple bound circulation distributions. Thus, to solve the integral equation (23) by approximation, it is necessary to assume a priori a convenient shape of the bound-circulation distribution function $\Gamma(n)$. The discretization model adopted here is the same as that utilized by Kuhlman (Ref.7) viz. a piecewise quadratically varying bound circulation:

$$\frac{d\Gamma_i(\rho)}{d\rho} = Y_{i-1} + \frac{\rho + h_i}{2h_i} (Y_i - Y_{i-1}), \quad -h_i \leq \rho \leq h_i \quad (25)$$

where h_i is the half-width of the panel i . ρ is the panel coordinate: $\rho = 0$ coincides with the panel midpoint, while ρ is positive if located outboard of this point. Y_i and Y_{i-1} denote the trailing vortex sheet strength at the panel ends. Using this discretization model and a suitable panel-spacing technique, sufficiently accurate solutions can be obtained with a relatively small number of panels.

The integral expression (5) for the normal velocity v_n can be written as a summation of panel integrals. Upon substitution of the discretization model, the following expression for v_n induced at panel j and at a distance τ from its midpoint can be derived from (5) and (25):

$$v_{n_j}(\tau) = \frac{1}{2\pi} \sum_{i=1}^{2k} \left\{ \frac{Y_{i-1} + Y_i}{2} \int_{-h_i}^{+h_i} A(\rho, \tau) d\rho + \frac{Y_i - Y_{i-1}}{2h_i} \int_{-h_i}^{+h_i} \rho A(\rho, \tau) d\rho \right\} \quad (26)$$

where

$$A(\rho, \tau) = \frac{\hat{n}(\tau) \cdot (\hat{r}(\rho, \tau) \times \hat{e}_x)}{|\hat{r}(\rho, \tau)|^2} \quad \text{and} \quad \tau = [-h_j, h_j]$$

The summation is performed over all $(2k)$ panels at both sides of the (xz) plane of symmetry. The integrals in equation (26) over each individual panel are evaluated analytically.

From equation (25) follows

$$\Gamma(\tau) = \Gamma(h_i) - \frac{Y_{i-1} + 3Y_i}{4} h_i + \frac{Y_i + Y_{i-1}}{2} \tau + \frac{Y_i - Y_{i-1}}{4h_i} \tau^2 \quad (-h_i \leq \tau \leq h_i) \quad (27)$$

where

$$\Gamma(h_i) = - \sum_m (Y_{m-1} + Y_m) h_m.$$

The summation is performed over all panels located outboard panel i . Application of the necessary condition (23) at all panel midpoints, using expressions (26) and (27) for v_n and Γ respectively, then results in $2k$ relations for the unknown trailing vortex sheet strength values Y_i and Lagrange multipliers λ_i and μ_j :

$$\sum_{i=1}^{2k} B_{ij} Y_i + \sum_{i=1}^3 g_{ij} \lambda_i + u_j g_{ij}^* = b_j, \quad j = 1, 2k \quad (28)$$

where the index j indicates the panel at the midpoint of which the necessary condition is imposed.

Substituting the discrete bound-circulation model (25) in the equations (16), (18), (19) and (15) for C_c , C_M , C_B and $C_{\ell}(n)$, respectively, these equations can be integrated analytically and can be expressed in terms of the trailing vortex-sheet strength values γ_1 . Together with the 2k-relations (28) and the constraints (20) and (24) they form a system of linear equations for the unknown trailing vortex-sheet strengths and Lagrange multipliers. This system determines the optimal spanwise bound-circulation distribution that results in minimum drag.

The method developed automatically takes care of satisfying Helmholtz' theorem at configuration element intersections, which is manifested by jumps in the bound circulation distribution. If a symmetrical aircraft configuration is considered (no propellers, or a counterrotating pair of propellers) this results in k unknown vortex sheet strengths γ_1 and the range of j in equation (28) reduces to $j = 1, k$. In addition, the rolling moment constraint may be deleted.

In order to avoid rather complicated and computationally expensive integrals the drag components are calculated using a numerical integration rule, instead of integrating analytically. Using a panel arrangement method with properly increased panel density in regions with comparatively large v -variations, use of the midpoint rule already results in a sufficiently accurate approximation with a relatively small number of panels. An alternative might be the Simpson rule.

Knowing the spanwise bound-circulations also other quantities of interest can be determined. Examples are trimdrag, bending moment distribution, and the overall forces acting on the aircraft components.

5 EXAMPLES OF APPLICATIONS

In this section, a number of typical examples is presented that demonstrate some of the capabilities of the method developed. The examples do not represent actual design studies.

Induced drag only

Obviously, the accuracy of numerical induced drag methods is affected by the discretization model of the bound circulation distribution. It has been shown for a planar wing (Ref. 7), that methods using piecewise quadratically varying bound circulations, are approximately four to five times as accurate in computing the induced drag as a vortex-lattice method with the same equal-sized panel arrangements. In figure 6, the present method is compared, for a planar wing, with the method of Kuhlman (Ref. 7), in which also quadratically varying bound circulations are used. Although the present method is less time-consuming than Kuhlman's method, it can be seen that the differences in accuracy and convergence are very small; both methods approach the exact value of the induced drag rapidly as the number of panels increases. Using 10 wake panels per semi-span, the minimum induced drag of the planar wing is computed with an accuracy of about 0.2 percent.

For a non-planar configuration, the present method is compared with a result obtained by Lundv using a conformal-mapping technique (Ref. 16). In figure 7, the optimal bound circulations are compared for a wing configuration with vertical endplates (or winglets). In figure 8, the induced drag values are compared. As can be seen, the results of both methods agree well.

In figure 9, some of the system capabilities with respect to trimmed induced drag minimization are demonstrated for a transport-aircraft type configuration, a sketch of which is given. The minimum induced drag as function of the centre-of-gravity location for three different vertical positions of the horizontal tail is shown in figure 9a. The spanwise C_c -distribution was specified ($C_c(n) = -0.106 | 0 \leq n \leq b/2$) and for the body pitching moment coefficient, $C_{M,B} = +0.007$ was adopted. This figure shows that for (conventional) cases of negative tail loads, the minimum induced drag increases with increasing height of the horizontal tail. Note that the lowest values of minimum induced drag are obtained for high-tail configurations with positive tail loads. This suggests that, from the point of view of induced drag, there might be a preference for high-tail positions for configurations combining relaxed static stability with active control technology.

In figure 9b, the influence of the tail-to-wing span ratio and the vertical position of the horizontal tail on the minimum induced drag is displayed for two different positions of the centre-of-gravity. It can be seen that, for a fixed height of the horizontal tail, the minimum induced drag increases with decreasing tail-to-wing span ratio.

The inclusion of $C_c(n)$ -constraints in the optimization procedure is realized using a relation between $c_{\ell}(\text{des})$, $c_c(\text{des})$, M and t/c (see section 4). As an example, the same configuration of figure 9 is considered for $M = .735$. The limitations in design c_{ℓ} , t/c , c_c and M of figure 5 (supercritical airfoils) are used. Instead of giving a specified spanwise C_c -distribution, now the pressure recovery point locations have been given ($x_{R_{\text{des}}}(n) = .5 | 0 \leq n \leq b/2$). With this, a relation between C_c and C_{ℓ} is specified (see eq.(17), $(\gamma/\gamma_{\infty}) = 15.5 z | 0 \leq n \leq b/2$). In figure 10, the optimal C_c -distribution is compared with those of the "no wing-thickness constraint" option ($x_{R_{\text{des}}} = 30 z$ MAC). The figure shows that, in this particular example, the C_c -distribution has changed $\frac{1}{4}$ constant C_c over a portion of the wing. The inclusion of wing-thickness constraints results in an induced-drag increase of about 2 %.

Induced drag minimization including propeller slipstreams

In order to examine the effects of the propeller slipstream on the aircraft induced drag, the axial and tangential velocities in the propeller slipstream have to be given. For a particular example design condition, the distribution of propeller induced velocities of figure 11 has been used (advance ratio of $J = 0.13$ and a thrust coefficient of $C_T = 0.12$).

For a wing configuration with two "up-inboard" rotating propellers, located at 25% of the semispan with a diameter-to-span ratio of 13%, the optimal spanwise bound circulation distribution is shown in figure 12. This distribution greatly differs from the optimal "clean wing" distribution that is also shown in figure 12. With this distribution, the wing is capable of restoring much of the loss associated with slipstream swirl.

In figure 13, the effects of the horizontal propeller position for different rotating concepts of the propellers on the minimum induced drag coefficient have been plotted. As can be seen clearly from this figure, two up-inboard rotating propellers lead to a most favourable configuration with respect to the minimum induced drag. If the location of the propeller-centre is moved outboard, induced drag will decrease for two up-inboard rotating propellers and will be a minimum when the propellers are located at the wing tips (see also Ref. 11).

It is apparent from the results above that favourable lifting-element/propeller interference resulting in lower induced drag or, equivalently, induced thrust, may be produced by appropriate wing design. The required C_L -distribution may be realized by, for instance, adjusting twist, thickness, camber and chord distributions. The results obtained agree with those of Kroo (Ref. 10), who showed that in some cases all of the swirl loss can be recovered.

Also proper design of the engine nacelle/pylon may possibly contribute to swirl loss recovery. Figure 14 presents the optimum span loads for two configurations (with up-inboard rotating propellers) one utilizing passive (streamline) shaping of the pylon and the other having an active loading on the pylon. In this particular example, a 9 % reduction of the minimum induced drag is realized. Of course, this is not an actual design case and the benefit can be realized only at the cost of a more complicated detailed design, but it may be interesting to investigate the possibilities of a more active role of the nacelle/pylon.

Induced + viscous drag minimization

The importance of including the viscous drag component in the minimization procedure is illustrated by the next example. This example concerns a wing-canard configuration. In this example, the pressure recovery point locations have been given $(x/c)_{R,u} = .5$; $(x/c)_{R,i} = .4$, while for the thickness-to-chord ratio (t/c) a constant value of 12 % has been adopted.

In figure 15, the drag as function of the centre-of-gravity location is displayed. The upper set of drag curves represent the sum of induced + viscous drag (only the viscous drag of wing and canard is considered), while the lower curves are for the induced drag alone. By optimizing the sum of the induced and viscous drag, the total drag is less than it would have been if only the induced drag was minimized and the viscous drag added afterwards. Of course, the induced drag alone is greater when the sum of the drags is minimized than when induced drag alone is optimized. In addition, the total drag minimum is located about 10% b/2 ahead of the minimum induced drag alone position, stressing the importance to include (estimation of) viscous drag in configuration design studies.

In figure 16, the section C_d 's for both minimum induced-drag and minimum induced plus viscous drag are given for the minimum (induced + viscous) drag c.g.-position. As can be seen, the inclusion of profile drag results in a reduction of peak section C_d and an inboard shift of the spanloading for the main wing.

The results agree with those of Mason (Ref. 9), who showed that a drag reduction of about 5% could be achieved by including the profile drag in the optimization procedure.

Configuration design studies

The method developed can also be used for parametric preliminary design studies, for instance, to assess the effect of changes in size, location, dihedral and sweepback of wing, tail or canard, winglets, etc. The configuration may be of the conventional type (tail-aft) or nonconventional type (canard, three-surface configuration, forward swept wing, etc.).

A typical example of a nonconventional aircraft configuration is the three-surface aircraft (canard, wing and aft tail) given in figure 17. For the canard-wing and wing-tail configuration, the specification of the centre-of-gravity position (static margin) and the trim condition are most decisive to fix the balance of lift between the wing and control surface, but for the canard-wing-tail configuration the lift distribution among the surfaces can be chosen to reduce the total induced drag while retaining trimmed conditions at a specified static margin. The three-surface circulation distributions of figure 17 are only presented to illustrate the capabilities of the system and are not meant to represent an actual configuration design study.

In the past couple of years, there has also been a renewed interest in aircraft configurations with forward swept wings (FSW). According to reference 17, the application of forward swept wings may result in, among others, lower induced drag and higher maximum lift coefficient as compared with an aft swept wing (ASW). The problem of aero-elastic problems for forward swept wings may nowadays be solved by using an aero-elastically tailored wing using composite materials. Figure 18 shows that in the case of forward swept wings, the tendency of spanwise loading for minimum trimmed induced drag is to move inboard.

Configuration design studies may concern the composition of the total aircraft lay-out as well as local alterations of the aircraft configuration as is the case, for instance, when the effectiveness of winglets is investigated.

6 CONCLUSIONS

An induced (plus viscous) drag analysis and minimization method has been developed that provides a low cost and useful tool, that can be used both for preliminary aircraft design purposes, and for providing direct input to detailed aerodynamic design procedures. In the latter function, the method provides bound-circulation distributions that may be used in specifying target pressure distributions for inverse aerodynamic design codes.

Complementary to the determination of optimal spanloads, the method can also be used to support selection of spanwise distributions of pitching moment, chord and thickness-to-chord ratio. In the procedure, the interaction between propellers and lifting elements may be included. Compared to other methods in this spirit, the present method is less time-consuming than near field methods and more accurate than vortex-lattice methods. Comparisons with known solutions of other theoretical methods have proven excellent agreement.

The examples shown in this paper illustrate the importance of considering, early in the design, all aspects that may influence the drag characteristics. The inclusion of, for instance, viscous drag and/or propeller slipstreams may lead to other choices for the spanwise distributions of lift, pitching moment, chord, and thickness-to-chord ratio than when only the induced drag without propeller-slipstream is considered.

The method is fast and easy to use, and therefore very suitable for interactive design purposes in which rapid configuration trade-offs have to be made. It has a wide field of application and may be especially useful to support the assessment of unconventional design concepts in which lack of experience precludes good design decisions. Examples of unconventional concepts are three-surface configurations, relaxed static stability, "active" nacelles/pylons, forward swept wings, etc. The capabilities of the method are exploited more efficiently when used in a multidisciplinary design environment.

7 REFERENCES

1. Holst, T.L., Slooff, J.W., Yoshihara, H., Ballhaus, W.F., Applied computational transonic aerodynamics. AGARD-AG-266, 1982.
2. Vanderplaats, G.N., Approximation concepts for numerical airfoil optimization. NASA TP-1370, 1979.
3. Hicks, R.M., Transonic wing design using potential flow codes - successes and failures. SAE-paper 810565, 1981.
4. Slooff, J.W., Computational Drag analysis and Minimization; Mission Impossible? AGARD-R-723, 1985.
5. Peifel, W.M., Optimization and design of three-dimensional aerodynamic configurations of arbitrary shape by a vortex lattice method. NASA SP 405, 1976.
6. Lamar, J.E., A vortex-lattice method for the mean camber shapes of trimmed non-planar planforms with minimum induced drag. NASA TN D-8090, 1976.
7. Kuhiman, J.M., Higher order farfield drag minimization for a subcritical wing design code. J. of Aircraft, Vol.17, No.9, 1980.
8. Kuhiman, J.M., Iterative optimal subcritical aerodynamic design code including profile drag. AIAA-83-0012, 1983.
9. Mason, W.M., Wing-canard aerodynamics at transonic speeds. Fundamental considerations on minimum drag spanloads. AIAA-82-0097, 1982.
10. Kroo, I., Propeller-wing integration for minimum induced loss. J. of Aircraft, Vol.23, No.7, July 1986.

11. Loth, J.L., Loth, F., Induced drag reduction with wing tip mounted propellers, AIAA-84-2149, 1984.
12. Prabhu, R.K., Tiwari, S.N., Studies on the interference of wings and propeller slipstreams, Report Old Dominion University, Ph.D. Thesis, 1984.
13. Vooren, J. v.d., Slooff, J.W., XFL022 NLR, a modified version of FL022, NLR IW-80-004 C, 1980.
14. Dam, R.F. van den, SAMID, an interactive system for aircraft drag minimization studies, NLR TR 88071, 1988.
15. Munk, M.M., The minimum induced drag of airfoils. NACA Report 121, 1921.
16. Lundry, J.L., A numerical solution for the minimum induced drag, and the corresponding loading, of nonplanar wings. NACA CR-1218, 1968.
17. Sweiger, J., Schneider, G., Sensberg, O., Löbert, G., Design of a forward swept wing fighter aircraft. ICAS-paper 84-09, 1984.

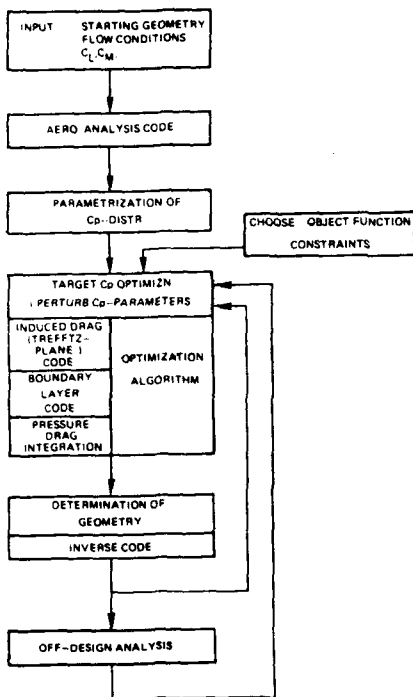


Fig. 1 Scheme for inverse numerical optimisation

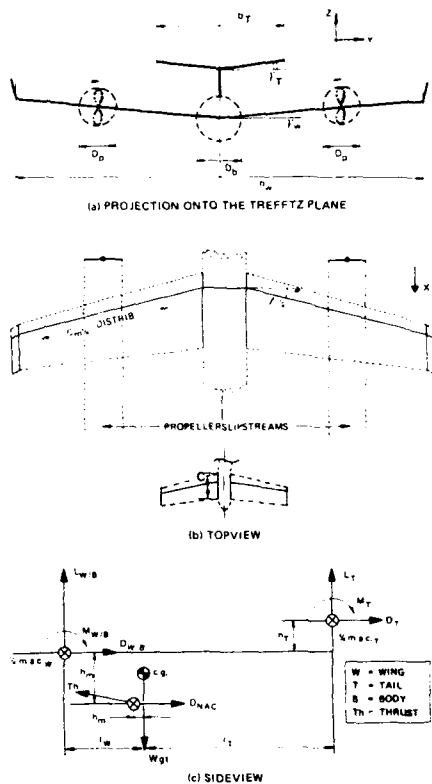


Fig. 2 Summary of input parameters for trimmed induced drag minimization

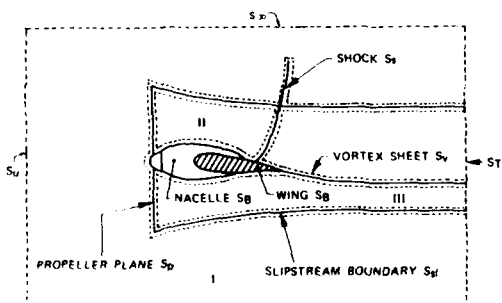


Fig. 3 Control volume for determination of (inviscid) drag through application of momentum theory

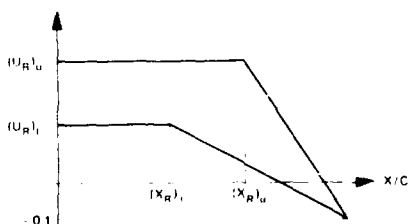


Fig. 4 Characteristic airfoil pressure distributions

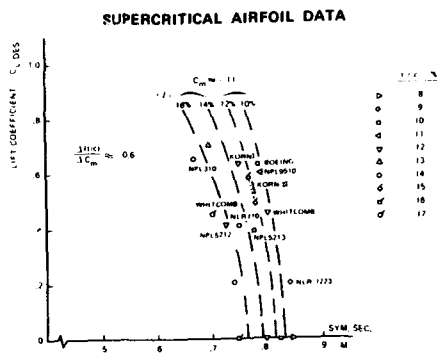


Fig. 5 Relation expressing limitations in design
 c_l , t/c , c_m and M
(Supercritical airfoil section data)

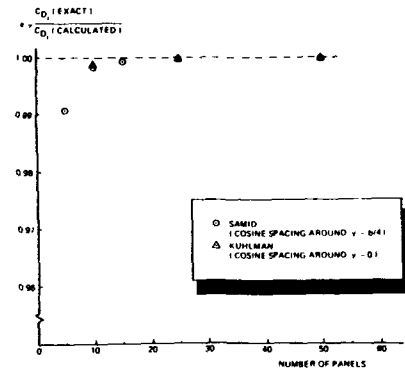


Fig. 6 Accuracy of the induced-drag computation
for a planar wing

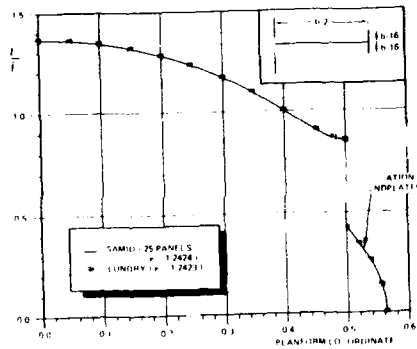


Fig. 7 Bound-circulation distributions of a wing
with end plates

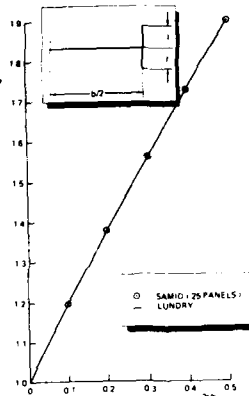
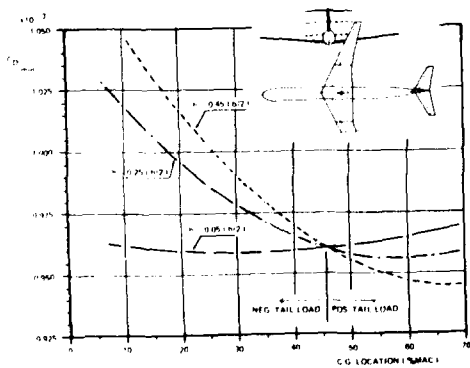
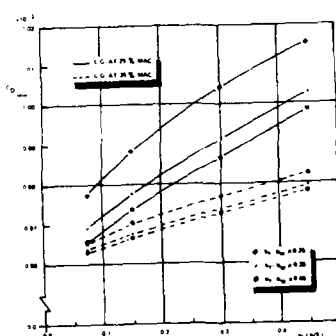


Fig. 8 Induced drag efficiency factor
for a wing with end plates



(a) Effects on the location of center-of-gravity
and the tail height relative to the wing on
the minimum trimmed induced-drag ($C_M(W/B) = -0.09$)



(b) Effects of the tail height and the tail-
to-wing span ratio on the minimum trimmed
induced-drag ($C_M(W/B) = -0.09$)

Fig. 9 Examples of trimmed induced-drag minimization studies

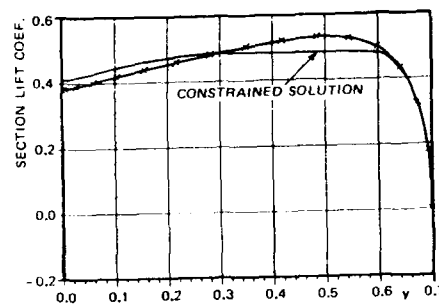


Fig. 10 The influence of C_l -constraints (for given x_R -distribution)

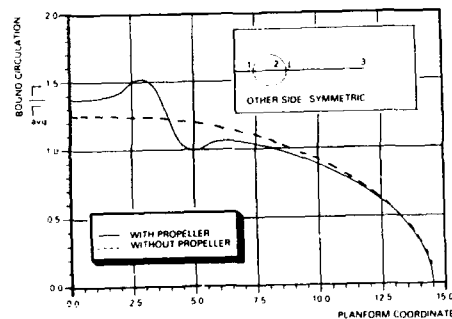
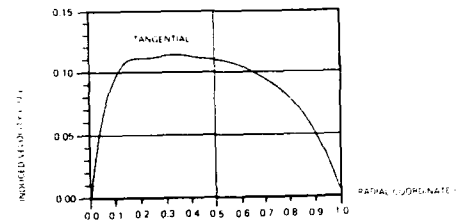
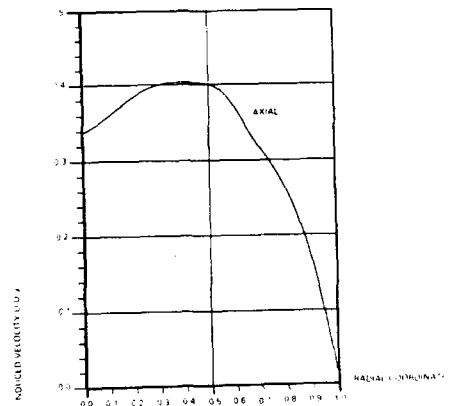


Fig. 12 Optimal bound circulation distribution for a wing with two up-inboard rotating propellers



(a) propeller-induced tangential velocity



(b) propeller-induced axial velocity

Fig. 11 Propeller-induced velocities

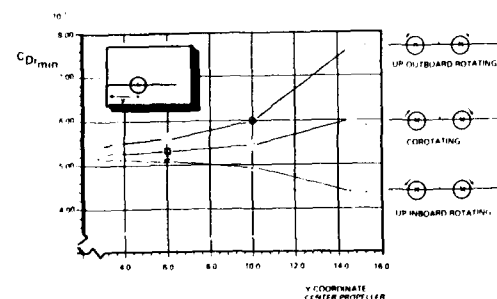


Fig. 13 Effects of the horizontal propeller location on the minimum induced drag

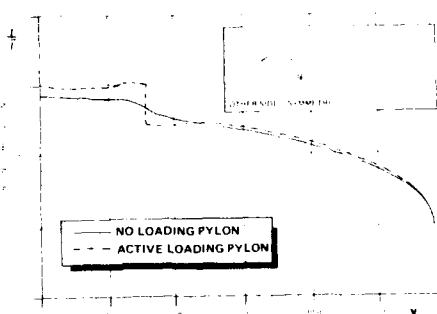


Fig. 14 Optimal bound-circulation distributions for configurations with "up-inboard" rotating propellers, with passive shaping and with "active" shaping of the pylon

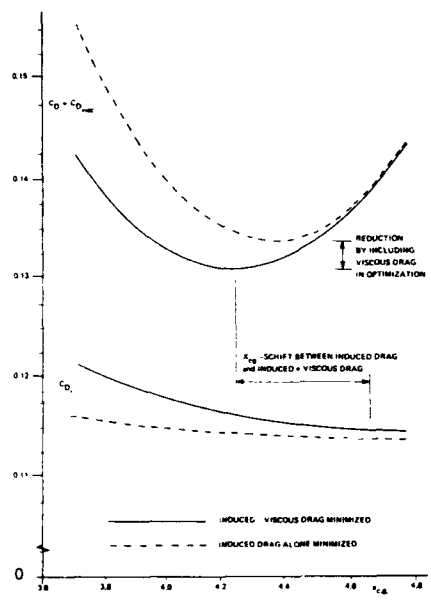


Fig. 15 "induced" drag minimization versus "induced + viscous" drag minimization

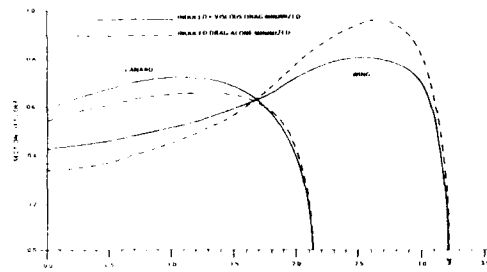


Fig. 16 Optimal C_L -distributions for minimum "induced" drag and minimum "induced+viscous" drag, resp.
($x_{c.g.}$ at minimum "induced+viscous" drag position)

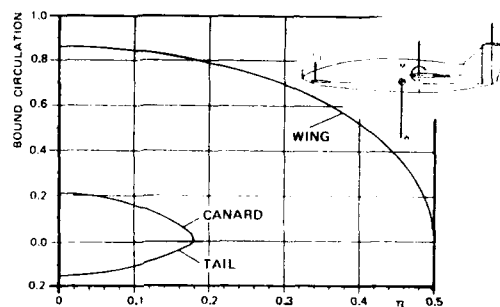


Fig. 17 Spanloads for minimum trimmed induced-drag
(three-surface aircraft)

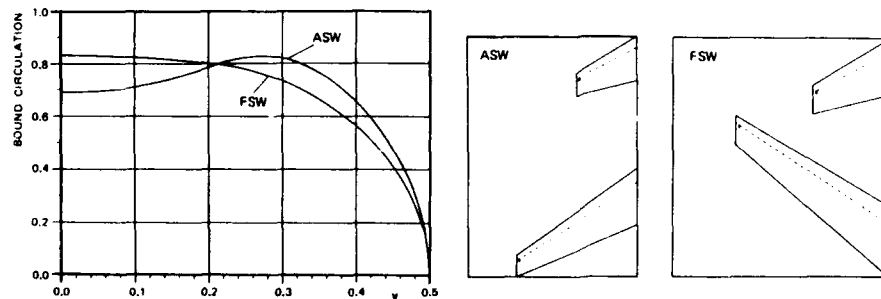


Fig. 18 Spanloads of forward and aft swept wing configurations

**AERODYNAMIC OPTIMIZATION BY SIMULTANEOUSLY UPDATING
FLOW VARIABLES AND DESIGN PARAMETERS**

M. H. Rizk
Sverdrup Technology, Inc./TEAS Group
P.O. Box 1935
 Eglin Air Force Base, Florida 32542-5000
U.S.A.

SUMMARY

The application of conventional optimization schemes to aerodynamic design problems leads to inner-outer iterative procedures that are very costly. In this paper, an alternative approach is presented based on the idea of updating the flow variable iterative solutions and the design parameter iterative solutions simultaneously. Several schemes based on this idea are applied to problems of optimizing advanced propeller designs and correcting wind tunnel wall interference. Computations are performed to test the schemes' efficiency, accuracy, and sensitivity to variations in the computational parameters.

SYMBOLS

c_1	incrementing factor for optimization scheme [see Equation (9)]	\hat{e}_l	unit vector along the P_l axis with components defined relative to the rotated design parameter coordinate system
c_2	decrementing factor for optimization scheme [see Equation (9)]	L	number of design parameters
C	positive constant for chord method [see Equation (7)]	L_e	measured model lift coefficient
C_p	power coefficient; also pressure coefficient	L_F	computed lift coefficient for model in free air
C_{po}	desired power coefficient	L_T	computed lift coefficient for model in wind tunnel
D	propeller diameter	M	Mach number; also number of problems solved in parallel by the optimization scheme
\hat{e}_l	unit vector along the P_l axis	n_c^a	number of iterations required for the convergence of the analysis problem's solution
E	objective function	n_c^o	number of iterations required for the convergence of the optimization problem's solution
f	constraint function	\vec{P}	vector of design parameters
\hat{g}	solution of the flow governing equations	\vec{P}_l	vector of design parameters relative to rotated coordinate system
G_l	l^{th} component of ∇f relative to rotated coordinate system	P_l	l^{th} component of design parameter vector
h	tunnel height	P_{l1}	l^{th} component of design parameter vector relative to rotated coordinate system
\hat{i}_l	unit vector along the P_l axis with components defined relative to the unrotated design parameter coordinate system	r	radial coordinate
		R_E	residual Euclidean norm
		R_{max}	maximum residual
		α	angle of attack
		$\beta_{03/4}$	$\beta_{3/4}$ which corresponds to the power coefficient C_{po}
		$\beta_{3/4}$	SR-3 blade angle at 75% blade span

β_0	unperturbed blade angle distribution
β^t	blade angle distribution perturbation
$\delta\vec{P}$	incremental vector used to update the vector of design parameters
δP_{max}	maximum incremental value allowed in updating the design parameters
ΔM	Mach number correction
ΔN	number of iterative steps at which \vec{P} is periodically updated
$\Delta\alpha$	angle-of-attack correction
ϵ	small positive incremental value used to perturb the design parameters
η	propeller efficiency
μ	parameter determining the allowable region in design parameter space for searching for the optimum solution [see Equation (26)]
ν	cost of solving an optimization problem/ cost of solving L analysis problems
σ	$= n_c^0 / n_c^a$
$\vec{\psi}$	flow iterative solution
Superscripts	
n	iteration number
$*$	optimum value
Subscripts	
c	measured tunnel condition
F	computed free-air condition
f	corrected condition
M	coordinate system rotated by the modified scheme
S	body surface
T	computed tunnel condition
∞	free-stream condition
$-$	rotated coordinate system

1. INTRODUCTION

Numerical optimization is one of the tools used in aerodynamic design. The solution of the optimization problem attempts to determine the vector of design parameters \vec{P} that minimizes the objective function $E(\vec{P}; \vec{q})$ subject to given constraints, where \vec{q} is the solution of the flow equations. In airfoil and wing design problems, \vec{P} contains the coefficients of the polynomials or the shape functions used to define the lifting surface, while E may be chosen to be the minimized drag, subject to the constraint of a minimum allowable lift value. The objective function E may also be chosen to be a measure of the difference between the pressure on the lifting surface and a desired pressure distribution.

Conventional optimization methods (e.g., the steepest descent method and the conjugate gradient method) are iterative procedures that determine a sequence of solutions $\vec{P}_1, \vec{P}_2, \dots$, that converges to the optimum solution \vec{P}^* . These methods require the evaluation of the objective function and constraint function many times before the optimum solution is determined. Since E is dependent on the solution \vec{q} , the flow governing equations must be solved each time E is evaluated. Therefore, any of the conventional optimization schemes become a two-cycle (inner-outer) iterative procedure. The inner iterative cycle solves the analysis problem for \vec{q} iteratively for a given iterative solution \vec{P} , while the outer iterative cycle determines the optimum \vec{P} iteratively. In the inner-outer iterative approach for solving the design problem (References 1-5), the usual procedure is to couple an existing analysis code (which solves the flow equations iteratively for a given \vec{P}) to an optimization code (which finds the optimum \vec{P} iteratively). The repetitive execution of time-consuming analysis codes is the source of the high cost of this approach.

An alternative to the costly conventional two-cycle approach is the single-cycle approach. This approach is based on the idea of updating the flow variable iterative solutions and the design parameter iterative solutions simultaneously. The iterative procedure for solving the flow governing equations (the analysis problem) is modified so that the solutions \vec{q} of the flow equations and the design parameters \vec{P} are updated simultaneously. This results in the successively improved approximations (\vec{q}^n, \vec{P}^n) , where $n = 1, 2, \dots$ that converge to the solution (\vec{q}^*, \vec{P}^*) , thus satisfying the optimization problem. With this approach, the need for the costly inner-outer iterative procedure is eliminated. Schemes based on this approach are presented below. The results of applying these schemes to aerodynamic problems are also presented.

2. OPTIMIZATION PROBLEM

In the optimization problems considered here, the optimum design parameter vector, \vec{P}^* , is determined so that

$$E(\vec{P}^*; \vec{g}) = \min_{\vec{P}} E(\vec{P}; \vec{g}) \quad (1)$$

subject to the constraint

$$f(\vec{P}; \vec{g}) = 0 \quad (2)$$

with the flow variable vector \vec{g} satisfying the flow governing equation

$$\vec{D}(\vec{g}) = 0 \quad (3)$$

subject to the boundary condition

$$\vec{B}(\vec{g}; \vec{P}) = 0 \quad (4)$$

The flow governing equation, Equation (3), may be the Navier-Stokes, Euler, potential flow equations or an approximation of any of these equations. The boundary conditions given by Equation (4) include boundary conditions applied at the body surface as well as far-field boundary conditions. Schemes are presented below for solving the single equality constraint problem defined by Equations (1)-(4). Extensions of these schemes to other constrained and unconstrained problems are also presented.

3. OPTIMIZATION APPROACHES

Different approaches may be used to solve the optimization problem defined by Equations (1)-(4). In this section, a discussion of several of these approaches is presented. The discussion is limited to the one-design-parameter problem, governed by Equations (1), (3), and (4) with the vector \vec{P} replaced by the scalar P . This special problem allows the use of graphical illustrations to complement the discussion and is chosen for that reason. However, many aspects of the discussion may be extended to the general problem defined by Equations (1)-(4).

The iterative procedure used to solve the flow governing equations determines a sequence of successive approximations, \vec{g}^n , where $n = 1, 2, \dots$. The flow solution therefore evolves gradually with n . It is possible to replace the n coordinate by a time-like coordinate t and to view the evolution of \vec{g} as a time dependent process. However, the time here is not real. The time coordinate t will be used interchangeably with the n coordinate in discussions given here. For example, \vec{g}^n which denotes the n^{th} iterative flow solution may be replaced by $\vec{g}(t)$, where $t = n$.

3.1 Graphical Approach

The point P^* at which E is a minimum can be

determined by choosing a set of closely spaced points, $P = P_m^g$, $m = 1, 2, \dots, M$, and evaluating the function E at these points. A curve showing the variation of E with P may then be plotted and the value of P^* at which E is a minimum, E_{min} , can be determined (see Figure 1). The objective function $E(P_m^g; \vec{g}_m)$ is dependent on the flow solution \vec{g}_m . To evaluate E for a given P_m^g it is therefore necessary to choose an initial iterative guess for \vec{g} , which is assumed to be the free stream flow, then the flow equations are solved iteratively so that \vec{g}_m evolves in time until convergence occurs. The iterative flow solutions are therefore evaluated along M paths as shown in Figure 2, with N iterative solutions evaluated at each path where N is a number large enough to allow the solutions on all paths to reach convergence. The iterative solutions $E(P_m^g; \vec{g}_m)$ along those paths define a valley shaped surface, S^g , as shown in Figure 3. The minimum value of the objective function is time dependent and is given by $E^{dg}(t)$. The path of this point is given by $P^{dg}(t)$. As the solution converges, $P^{dg}(t)$ and $E^{dg}(t)$ converge to P^* and E_{min} .

3.2 Steady-State Approach

This is the conventional approach to solving optimization problems. It is a two-cycle (inner-outer) iterative procedure. An optimization scheme is used to determine a sequence of successive approximations, P_m^{ss} , $m = 1, 2, \dots$, which converge to the optimum value P^* . This is the outer iterative process. Like the graphical approach, E is evaluated at different P values as shown in Figure 1, however, the use of an optimization scheme to choose these values leads to a significant reduction in the number of these evaluations in comparison to the graphical approach. For each P value ($P = P_m^{ss}$) the flow equations are solved iteratively (inner iterations) along $P = \text{constant}$ paths, similar to those shown in Figure 2. However, it is possible to reduce the number of iterative solutions obtained on a particular path by using the last converged outer iterative flow solution as an initial guess for the present outer iteration. The conventional approach is labeled here a steady-state approach because the design parameter, P , is held fixed while the flow solution evolves in time. It is updated only after the flow solution is converged to a steady state. In other words, P is updated on the basis of information obtained from the steady-state curve shown in Figure 1. Information from the surface shown in Figure 3 is not used in this process.

3.3 Time-Dependent Approach

In the time-dependent approach, the iterative procedure for solving the flow governing equations is modified so that \vec{g} and P are updated simultaneously. In this case the multiple iterative paths, $P = P_m^{ss}$, $m = 1, 2, \dots$, used in the steady-state approach are

replaced by a single time varying path $P = P^{ld}(t)$. The solution $E^{ld}(t)$ along this path is embedded in the surface S^{ld} given by $E^{lds}(t, P)$. It is defined by the iterative solutions along time-dependent paths parallel to $P^{ld}(t)$. These paths are given by $P = P^{ld}(t) + S_l$, $l = 1, 2, \dots$, where S_l is a constant for a given path. The minimum value of the objective function is time dependent and is given by $E^{old}(t)$. The path of this point is given by $P^{old}(t)$. As the solution converges, $P^{ld}(t)$, $P^{old}(t)$, $E^{ld}(t)$, $E^{old}(t)$, and $E^{lds}(t, P)$ converge respectively to P^* , P^* , E_{min} , E_{min} , and $E(P)$. This approach updates P as \vec{g} evolves in time. It is a single-cycle approach, since it eliminates the need for the two-cycle (inner-outer) iterative procedure.

Before developing a time-dependent scheme, it is important to recognize some of the main differences between the steady-state and the time-dependent formulations. In the steady-state formulation, the search is performed for a fixed target, P^* , for which $E(P^*)$ is the minimum of the fixed curve $E(P)$. In the time-dependent formulation, however, the search is performed for a moving target, $P^{old}(t)$, and the objective function $E^{lds}(t, P)$ is a continuously evolving function. While the use of higher order schemes which depend on information from a number of iterative solutions may be advantageous in the steady-state formulation, iterative schemes should be limited to lower order schemes in the time-dependent formulation, since different iterative solutions are not obtained at the same time t . Another important difference between both formulations is that the iterative \vec{g} and P solutions are noninteracting in the steady-state formulation, while they are mutually interacting in the time-dependent formulation. In the latter case, the path $P^{ld}(t)$ should be chosen so that the flow solution converges in a number of iterations comparable to that required for solving an analysis problem with P held fixed. Large corrections applied to P can cause the flow solution to be nonconvergent, while extremely small corrections applied to P can lead to a slow convergence of the optimization solutions. Figures 4a, 4b, and 4c show cases in which the corrections applied to P are too small, acceptable, and too large respectively. The actual path used in the computations is that given by $P^{ld}(t)$. Computations are not performed for the path $P^{old}(t)$; however, that path may be found if desired by computing surface S^{ld} .

4. TIME-DEPENDENT SCHEMES

The basic idea of updating both \vec{g} and \vec{P} simultaneously can be used to develop a family of efficient optimization schemes. Three of these schemes are presented here. The first, scheme I, is a general scheme which can be used to solve problems with different constraint conditions. The second and third schemes (II and III) are applicable to a limited class of problems. Nevertheless, including the last two

schemes here serves two purposes. They provide additional examples of schemes that update the design parameters and the flow variables simultaneously. Moreover, results obtained from applying these schemes to optimization problems provide additional sets of data for determining the effects of updating the design parameters while the flow solution is developing.

4.1 Scheme I (Parallel Scheme)

This scheme is first presented for the single equality constraint problem defined by Equations (1)-(4). It is then extended to other problems.

4.1.1 Single Equality Constraint

The goal of the optimization scheme is to determine the values of the design parameters that minimize the objective function, E , subject to an equality constraint. A search must therefore be conducted in the design parameter space \vec{P} for the optimum solution, \vec{P}^* . This optimization problem is most conveniently solved in the rotated design parameter space \vec{P} , with the \underline{P}_1 coordinate normal to the constraint surface and the \underline{P}_l coordinates, where $l = 2, 3, \dots, L$, parallel to the constraint surface. For fixed values of the components of \vec{P} , let

$$\vec{g}^{n+1} = \vec{\psi}(\vec{g}^n; \vec{P}), \quad n = 0, 1, 2, \dots \quad (5)$$

be the iterative solution for the analysis problem, where $\vec{\psi}$ denotes the solution obtained by applying the iterative scheme for solving the flow governing equations once using \vec{g}^n as an initial guess. As for the analysis solution, obtaining the optimization solution requires the repeated application of Equation (5) to update the flow field. While \vec{P} is held fixed in the former case, it is allowed to vary in the latter.

The vector of design parameters \vec{P} is updated every ΔN iterations. Therefore,

$$\vec{P}^{n+1} = \vec{P}^n + \delta \vec{P}^{n+1} \quad (6)$$

where

$$\delta \vec{P}^{n+1} = 0, \quad (n+1)/\Delta N \neq 1, 2, 3, \dots$$

In the iterative steps that satisfy the relation $(n+1)/\Delta N = 1, 2, 3, \dots$, the incremental values for the design parameters are given by

$$\delta \underline{P}_1^{n+1} = - \frac{f^n}{|f^n|} [\min(C |f^n|, \delta P_{max})] \quad (7)$$

$$\delta \underline{P}_l^{n+1} = \min \left(1, \frac{\delta P_{max}}{|\Delta \underline{P}_l^{n+1}|} \right) \Delta \underline{P}_l^{n+1}, \quad l = 2, 3, \dots, L \quad (8)$$

where

$$f^n = f(\vec{P}^n; \vec{g}^n)$$

$$\Delta P_l^{n+1} = \frac{1}{2} [c_1(\tau_l^{n+1} + 1) + c_2(\tau_l^{n+1} - 1)] \delta P_l^{n+1-\Delta N} \quad (9)$$

$$\tau_l^{n+1} = -\frac{\Delta E_l^n \delta P_l^{n+1-\Delta N}}{|\Delta E_l^n \delta P_l^{n+1-\Delta N}|} \quad (10)$$

The purpose of ΔE_l^n appearing in Equation (10) is to determine the sign of $\partial E / \partial P_l^n$, which in turn determines the sign of the new incremental step along the P_l^n direction.

The incremental displacement in the design parameter space introduced so that the constraint may be satisfied is taken in the direction normal to the constraint surface and is determined by the chord method in Equation (7). The constant δP_{max} sets an upper limit on the magnitude of this incremental displacement. The incremental displacements given by Equation (8) are introduced along the coordinate axes, which are parallel to the constraint surface with the purpose of reducing the value of the objective function. The sign of the incremental correction δP_l^{n+1} , where δP_l^{n+1} is the l^{th} component of the vector $\delta \vec{P}^{n+1}$, is chosen to be opposite to that of $\partial E / \partial P_l^n$. The magnitude of the increment δP_l^{n+1} is given by

$$|\delta P_l^{n+1}| = c |\delta P_l^{n+1-\Delta N}|$$

with an upper limit given by δP_{max} , where $c > 0$. If the signs of δP_l^{n+1} and $\delta P_l^{n+1-\Delta N}$ are in agreement, then the last two iterative solutions P_l^n and $P_l^{n-\Delta N}$ fall to one side of the point along the P_l direction at which E is a minimum. In this case, c is set equal to the constant c_1 , which is greater than 1. Increasing the magnitude of the step size in this manner accelerates the approach toward the point along the P_l direction at which E is a minimum. On the other hand, if the signs of δP_l^{n+1} and $\delta P_l^{n-\Delta N}$ are not in agreement, then P_l^n and $P_l^{n-\Delta N}$ fall on opposite sides of the point along the P_l direction at which E is a minimum. In this case, c is set equal to the constant c_2 , which is less than 1. Decreasing the magnitude of the step size in this manner is necessary for convergence to the point along the P_l direction at which E is a minimum.

The updated components of the design parameter vector \vec{P}^{n+1} are used to calculate the new flow iterative solution, \vec{g}^{n+1} , given by

$$\vec{g}^{n+1} = \vec{\psi}(\vec{g}^n; \vec{P}^{n+1}) \quad (11)$$

In addition to the main solution given by Equation (11), the perturbed solutions \vec{g}_l^{n+1} , $l = 1, 2, \dots, L$, given by

$$\vec{g}_l^{n+1} = \vec{\psi}(\vec{g}_l^n; \vec{P}^{n+1} + \epsilon \vec{i}_l^{n+1}) \quad (12)$$

are also computed. Here ϵ is a small positive constant and \vec{i}_l^{n+1} , $l = 1, 2, \dots, L$, are the set of orthogonal unit vectors along the axes of the rotated coordinate system $P_1^{n+1}, P_2^{n+1}, \dots, P_L^{n+1}$. In Equation (10) ΔE_l^n is given by

$$\Delta E_l^n = E(\vec{P}^n + \epsilon \vec{i}_l^n; \vec{g}_l^n) - E(\vec{P}^n; \vec{g}^n) \quad (13)$$

Scheme I is referred to as a parallel scheme because the sign of the incremental change δP_l^{n+1} of Equation (8) is chosen on the basis of comparing the main iterative solution $E(\vec{P}^n; \vec{g}^n)$ with a perturbed solution $E(\vec{P}^n + \epsilon \vec{i}_l^n; \vec{g}_l^n)$. The paths along which these solutions are computed in the \vec{P} - t plane are parallel to each other, as shown in Figure 5.

While the optimization procedure is most suitably conducted in terms of the transformed parameters P_l , $l = 1, 2, \dots, L$, the flow solution is computed in terms of the physical design parameters P_l , $l = 1, 2, \dots, L$. To express the transformed design parameters in Equations (11) and (12) in terms of the original design parameters, it is necessary to use the transformation equation, which relates these two sets of parameters.

$$\vec{P}^{n+1} = T^{n+1} \vec{P}^{n+1}$$

where the orthogonal transformation matrix T^{n+1} is given by

$$T^{n+1} = [\vec{i}_1^{n+1} \vec{i}_2^{n+1} \dots \vec{i}_L^{n+1}]$$

The unit vector \vec{i}_l^{n+1} is normal to the constraint surface at $\vec{P} = \vec{P}^n$ and is given by

$$\vec{i}_l^{n+1} = \nabla f(\vec{P}^n; \vec{g}^n) / |\nabla f(\vec{P}^n; \vec{g}^n)| \quad (14)$$

where an estimate for \underline{G}_l^n , the l^{th} component of ∇f , is given by

$$\underline{G}_l^n = [f(\vec{P}^n + \epsilon \vec{i}_l^n; \vec{g}_l^n) - f(\vec{P}^n; \vec{g}^n)]/\epsilon \quad (15)$$

The Gram-Schmidt orthogonalization process, which uses a set of L linearly independent vectors to construct a set of L orthonormal vectors, is used to construct the unit vectors \vec{i}_l^{n+1} , $l = 2, 3, \dots, L$, along the rotated axes P_l^{n+1} , $l = 2, 3, \dots, L$. The following equation is used for this purpose:

$$\vec{i}_l^{n+1} = \frac{\vec{i}_l^n}{|\vec{i}_l^n|}, \quad l = 2, 3, \dots, L$$

where

$$\vec{i}_l^{n+1} = \vec{i}_l^n - \sum_{k=1}^L \left(\vec{i}_l^n \cdot \vec{i}_k^{n+1} \right) \vec{i}_k^{n+1} \quad (16)$$

In the initial iterative step, the vectors \vec{i}_l are given by $\vec{i}_l = \vec{e}_l$, $l = 1, 2, \dots, L$, where \vec{e}_l , $l = 1, 2, \dots, L$,

is the set of orthogonal unit vectors along the axes of the coordinate system P_1, P_2, \dots, P_L . While the flow variable vector \vec{g} is updated each iterative step, the coordinate system in the design parameter space is rotated every ΔN iterations. The unit vectors \vec{i}_P , like the vector of design parameters \vec{P} , are updated only in the iterative steps that satisfy the relation $(n+1)/\Delta N = 1, 2, 3, \dots$

The optimization scheme described above requires that $L + 1$ iterative problems be solved in parallel. In addition to the main solution, L perturbed solutions are computed in which each of the design parameters in the transformed space P_1, P_2, \dots, P_L is perturbed. The computational costs and the computer memory requirements are therefore proportional to $L + 1$. A modification to this scheme requires that only L iterative solutions be obtained. In the modified procedure, the perturbation solution associated with the perturbed design parameter in the direction of the P_1 axis, normal to the constraint surface, is not computed. This solution was used in Equation (15) to compute $G_{1,n+1}^n$, which is required for the calculation of the vector \vec{i}_1^{n+1} , which determines the direction normal to the constraint surface in Equation (14). In the absence of this solution, a new procedure for rotating the design parameter space must be defined. The procedure is first explained for the case of a two-design-parameter problem, and then it is extended to the general multi-design-parameter problem.

Figure 6 shows the design parameter space for a two-design-parameter problem. In the figure, the constraint function values f_0^n, f_1^n, f_2^n are defined as follows:

$$\begin{aligned} f_0^n &= f(\vec{P}^n; \vec{g}^n) \\ f_1^n &= f(\vec{P}^n + \epsilon \vec{i}_1^n; \vec{g}^n) \\ f_2^n &= f(\vec{P}^n + \epsilon \vec{i}_2^n; \vec{g}^n) \end{aligned}$$

In the modified procedure, the chord method, used in Equation (7) to satisfy the constraint condition, is used to rotate the design parameter space. The rotation angle $\delta\theta_M^{n+1}$ given by

$$\delta\theta_M^{n+1} = \tan^{-1} \left(\frac{C(f_2^n - f_0^n)}{\epsilon} \right) \quad (17)$$

is used to rotate the coordinate system, where the subscript M indicates that the modified scheme is used. The angle $\delta\theta_M^{n+1}$ is now compared to the corresponding rotation angle $\delta\theta^{n+1}$ used in the original scheme and given by

$$\delta\theta^{n+1} = \tan^{-1} \left(\frac{f_2^n - f_0^n}{\epsilon} \frac{\epsilon}{f_1^n - f_0^n} \right) \quad (18)$$

This comparison shows that the term $f_2^n - f_0^n$ in the original scheme is replaced by ϵ/C in the modified

scheme. Therefore, the modified scheme may be viewed as the original scheme with the exception that the exact value for \vec{i}_1 is replaced by an approximate estimate in which the gradient of f in the direction of the P_1 axis, G_1 , is not calculated but is estimated using the same proportionality constant used in the chord method of Equation (7). Thus,

$$G_1 = \frac{1}{C} \quad (19)$$

This is applicable for both the two-design-parameter problem and the general multi-design-parameter problem.

In the optimization scheme developed here, corrective increments are applied to the design parameter solutions every few iterations of updating the flow solutions. For convergence to occur, the signs of the increments must be chosen correctly to allow the iterative solution to approach the desired solution. The magnitudes of the increments are dependent on the computational constants c_1, c_2 , and C . Because the design parameters are updated frequently during the iterative process, we are not concerned with determining the incremental step sizes that lead to the highest short-term convergence rate. In fact, this may be difficult to define, since the flow variable solutions are continuously changing during the iterative process. Our aim is to achieve design parameter convergence over a long term defined by the number of iterations required for the flow solution convergence. A wide range of incremental step sizes should produce the desired convergence properties over many iterations, even though convergence properties over a few iterations may differ. These comments apply to both of the schemes described above for determining the design parameter space rotation. The direct procedure for determining the design parameter space rotation in the original scheme is replaced by an iterative procedure in the modified scheme. Since this rotation is updated frequently during the iterative process, this replacement should have no substantial effect on the overall convergence of the solution.

A potential problem exists when the modified scheme is used for rotating the design parameter axes. In the first $\Delta N - 1$ iterative steps of solving the problem, the coordinate system in the design parameter space coincides with the original unrotated design parameter space P_1, P_2, \dots, P_L . At the ΔN^{th} iterative step, a new rotated coordinate system is determined. When Equation (15) for determining $G_{1,\Delta N-1}^n$ is used, we are guaranteed that the vector $\vec{i}_1^{\Delta N-1}$ points in the direction in which the constraint function increases. Consequently, the use of Equation (7) will cause the iterative solution to approach the constraint surface. When Equation (15) is replaced by Equation (19) for determining $G_1^{\Delta N-1}$, there is a possibility that the computed vector $\vec{i}_1^{\Delta N-1}$ will point in the direction in which the constraint function decreases. In this case, the assumption that C is positive is wrong, and using

it will cause the solution to diverge. This occurs if the vector \vec{e}_1 is nearly in the direction of $-\nabla f^{\Delta N-1}$; that is, if the quantity

$$-\frac{\nabla f^{\Delta N-1}}{|\nabla f^{\Delta N-1}|} \cdot \vec{e}_1$$

is close to unity. The probability of this occurring is approximately 1:4 in a two-design-parameter problem and is reduced further as the number of design parameters increases. There are two suggested approaches for overcoming this problem. In the first approach, the initial few iterations are performed using the original scheme for determining G_1^n by Equation (15) in order to determine the correct initial directions for the P_1 axis. This may then be updated using the modified scheme, Equation (19), in the rest of the computation. Realizing that the probability for the potential problem to occur is small, the second approach uses the modified scheme from the beginning of the computation. If divergence does occur, then the constraint function is redefined to be equal to the negative of the original constraint function, and the problem is solved again.

4.1.2. Extensions of Scheme I

Scheme I is applicable to optimization problems with a single equality constraint. However, this scheme may be extended to more general problems such as multiple constraint problems and problems with inequality constraints. These extensions are now briefly presented.

In the case of multiple constraints, the set of equations

$$f_k(\vec{P}; \vec{g}) = 0, k = 1, 2, \dots, K$$

replaces Equation (2), where K is the number of constraints. For this problem, Equation (7) is replaced by

$$\delta P_l^{n+1} = -\frac{f_l^n}{|f_l^n|} \left[\min(C|f_l^n|, \delta P_{max}) \right], \\ l = 1, 2, \dots, K$$

Equation (8) is applied for values of l given by $l = K+1, K+2, \dots, L$ and the unit vectors \vec{i}_l^{n+1} are given by

$$\vec{i}_l^{n+1} = \begin{cases} \nabla f_l(\vec{P}^n; \vec{g}^n) / |\nabla f_l(\vec{P}^n; \vec{g}^n)|, & l = 1 \\ \vec{Q}_l^{n+1} / |\vec{Q}_l^{n+1}|, & l = 2, 3, \dots, K \\ \vec{i}_l^n / |\vec{i}_l^n|, & l = K+1, K+2, \dots, L \end{cases}$$

where

$$\vec{Q}_l^{n+1} = \vec{N}_l^{n+1} - \sum_{r=1}^{l-1} (\vec{N}_l^{n+1} \cdot \vec{i}_r^{n+1}) \vec{i}_r^{n+1},$$

$$l = 2, 3, \dots, K$$

$$\vec{N}_l^{n+1} = \nabla f_l(\vec{P}^n; \vec{g}^n)$$

and \vec{i}_l^{n+1} was defined in Equation (16).

In the case of an unconstrained problem, the problem is solved in the original, unrotated design parameter space. In this case Equation (7) is not used and Equation (8) is applied for l values given by $l = 1, 2, \dots, L$.

In the case of a problem with inequality constraints, the solution procedure at a given iterative step is equivalent to that of an unconstrained problem, if none of the constraints are effective, and it is equivalent to that of a problem with K_e equality constraints, if K_e of the constraints are effective. For the problem with inequality constraints, Equation (2) is replaced by

$$f_k(\vec{P}; \vec{g}) \leq 0, k = 1, 2, \dots, K$$

At the iterative step $n + 1$, the k^{th} constraint is effective if either of the following conditions is satisfied:

$$f_k(\vec{P}^n; \vec{g}^n) \geq \delta$$

where δ is a small positive number, or

$$|f_k(\vec{P}^n; \vec{g}^n)| < \delta, \frac{\partial E(\vec{P}^n; \vec{g}^n)}{\partial P_k^n} < 0$$

Otherwise it is not effective.

4.2 Scheme II (Branch Scheme)

The perturbed solutions \vec{g}_l^n are used only once every ΔN iterative steps to compute the perturbed objective functions appearing in Equation (13). It is therefore possible to modify scheme I so that it becomes unnecessary to compute flow solutions along paths parallel to that of the main solution. In this modified scheme, Equation (13) is replaced by

$$\Delta E_l^n = E(\vec{P}^n + \epsilon \vec{i}_l^n; \vec{g}_l^{n+1}) - E(\vec{P}^n; \vec{g}_l^{n+1}) \quad (20)$$

where

$$\vec{g}_l^{n+1} = \vec{\psi}(\vec{g}^n; \vec{P}^n) \quad (21)$$

$$\vec{H}_l^{n+1} = \vec{\psi}(\vec{g}^n; \vec{P}^n + \epsilon \vec{i}_l^n) \quad (22)$$

In this formulation, Equation (12) is no longer used to calculate \vec{g}_l^{n+1} and Equations (21) and (22) are used to compute \vec{H}_l^{n+1} and \vec{H}_l^{n+1} only once every ΔN iterations. If ΔN is greater than or equal to five, substantial savings in computational costs may occur. The paths along which computations are performed are shown in Figure 7.

It should be noted that scheme II will be successful as long as the signs of ΔE_l^n predicted by Equations (13) and (20) are in agreement. The magnitudes of ΔE_l^n given by the two equations will not be in agreement, even as the flow solution converges. For that reason scheme II may not be used in general for solving constrained optimization problems. In these problems ∇f is used to determine the direction normal to the constraint surface. Correct results are obtained only if the computed ∇f converges to the exact ∇f . This does not occur for scheme II. The use of scheme II is therefore limited to unconstrained problems solved in the original (unrotated) design parameter space. An exception to that is the constrained problem in which the direction of the normal to the constraint is known (Reference 6). In this case the constrained problem is solved in the original (unrotated) design parameter space. Further discussions about scheme II are found in Reference 7.

A possible variation of scheme II is shown in Figure 8. It combines elements from both schemes I and II.

4.3 Scheme III (Special Scheme)

This scheme is applicable to a limited class of two-design-parameter problems with an equality constraint. The objective function is assumed to be of special form and the constraint line is assumed to be normal to the P_1 axis in design parameter space. Therefore, the solution is obtained in the original (unrotated) design parameter space.

The scheme was developed for application to a particular problem arising from a transonic wind tunnel wall interference correction procedure. In this procedure the free-air flowfield around the model is computed. The design parameters are the model angle of attack α_F and the free-air Mach number $M_{\infty F}$, so that $\vec{P} = (\alpha_F, M_{\infty F})$. Their optimum values are determined so that Equation (1) is satisfied with

$$E = \frac{\int (M_{FS} - M_{TS})^2 ds}{\int M_{TS}^2 ds} \quad (23)$$

subject to the constraint:

$$f = L_F - L_e = 0 \quad (24)$$

where M_{FS} is the computed Mach number distribution on the model surface in free-air and M_{TS} is the corresponding Mach number distribution in the wind tunnel. This is obtained from a wind tunnel flow computation which is performed prior to the free-air computation. The integrals in Equation (23) are taken over the model surface.

In scheme III a single solution given by Equation (11) is computed. To determine the sign of $\partial E^n / \partial P^n$ it is therefore necessary to use values of E at different iterative steps. In this scheme $\Delta N = 1$ and ΔE_2^n is

defined by

$$\Delta E_2^n = (E^n - E^{n-1})(e^n - e^{n-1})$$

where

$$\begin{aligned} E^n &= E(\vec{P}^n; \vec{g}^n) \\ e^n &= e(\vec{P}^n; \vec{g}^n) \\ e &= \frac{\int (M_{FS} - M_{TS}) ds}{\int M_{TS} ds} \end{aligned}$$

Because ΔE_2^n is evaluated at two different time steps the sign of ΔE_2^n may not always agree with that of $\partial E^n / \partial P^n$. As long as the frequency at which this disagreement occurs is below a certain limit the scheme converges to the correct solution. The coordinate system in design parameter space is not rotated. Therefore, the search for the minimum objective function is conducted along constant P_1 lines. In general, this will not lead to accurate determination of the optimum solution, however, in the particular problem considered here the constant P_1 lines are nearly parallel to the constraint curve. The resulting error is therefore negligible. Further discussions about scheme III are found in Reference 8.

5. RESULTS

The optimization procedures described above were applied to propeller design problems and wind tunnel wall interference problems. The computations were performed on the Cray X-MP computer. The results of these computations are presented below.

5.1 Propeller Design

The optimization procedure I described above, combined with the Euler analysis code developed by Yamamoto et al. (Reference 9), was used in Reference 10 to find the twist distribution for the blades of the eight-bladed SR-3 propeller with the objective of maximizing its efficiency under the constraint of a desired power coefficient given by $C_{po} = 1.7$. The computations were performed for a free-stream Mach number of 0.8 and an advance ratio of 3.06. Let $\beta_{o3/4}$ be the blade angle at the 75% blade span corresponding to the desired power coefficient. We take the blade angle distribution, $\beta_o(r)$, corresponding to this propeller as our base configuration. A perturbation, $\beta'(r)$, to the blade twist distribution, $\beta_o(r)$, was computed so that the propeller efficiency would be maximized subject to the power constraint. The perturbation twist distribution is given by

$$\beta'(r) = P_1 + P_2 \left(\frac{r - R/2}{R/2} \right) + 2P_3 \left\{ \left(\frac{r - R/2}{R/2} \right)^2 - \frac{1}{2} \right\} \quad (25)$$

where P_1 , P_2 , and P_3 are the components of the vector of design parameters \vec{P} and R is the propeller radius.

Experimentation with the propeller analysis code indicated that the flow iterative solution diverges when the blade tip angle exceeds a certain limit. To exclude the region leading to the divergence from our search in the design parameter space, the following redefinition of the objective function was introduced:

$$E = -\eta + \max \left\{ 0.0, 0.1 \left(\sqrt{P_2^2 + P_3^2} - \mu \right) \right\} \quad (26)$$

where μ determines the allowable search region. As the value of μ increases, the allowable search region also increases. The value of μ was taken to be equal to 5.0 unless otherwise specified.

The mesh used in the following computations consists of 45 points in the axial direction, 21 points in the radial direction, and 11 points between adjacent blades in the circumferential direction. Computations are initialized by the SR-3 flow solution, which corresponds to a 54.9° angle at the 75% blade span. This initial solution was intentionally chosen not to be a close approximation of the desired solution. In all of the following computations, the modified coordinate rotation scheme, which determines G_1 by Equation (19) instead of Equation (15), is used unless otherwise specified. Also, unless otherwise specified, the initial iterative guesses for the design parameters are set equal to zero and the computational parameters c_1 , c_2 , C , δP_2^0 , δP_3^0 , δP_{\max} , ϵ , and ΔN are given, respectively, by 1.2, 0.6, 3.0, 0.5, 0.5, 1.0, 0.0001, and 40.

The optimization procedure was applied to two-design-parameter problems and to three-design-parameter problems. For the two-design-parameter computations, the values of P_3 in Equations (25) and (26) are set equal to zero. Results for the two-design-parameter problem are presented, followed by those for the three-design-parameter problem. For the initial flow solution, which corresponds to a $\beta_{3/4}$ value of 54.9°, the value of C_p was 1.1. Also the value of $\beta_{3/4}$ was determined to be 58.067°. The design parameters predicted by the optimization scheme are given by $P_1^* = -2.83^\circ$, $P_2^* = 5.51^\circ$. The predicted solution does satisfy the power constraint. The value of C_p corresponding to this solution is 1.6999. The objective function, E , was reduced from the value -0.839 in the case of the original design, with $P_1 = P_2 = 0.0$, to the value -0.908 in the case of the optimized design. The value of the efficiency was increased from 0.839 for the original design to 0.910 for the optimized design.

The computed value of efficiency, which corresponds to the optimized design, is approximately 5% higher than expected. Towards the end of this study it was discovered that an approximate formulation used in the analysis code to integrate the aerodynamic forces near the blade base was the cause of this over-prediction. The main portion of the results presented here was obtained using the approximate formulation

for computing the performance. These results are presented first. They are then followed by results obtained by using an accurate formulation for computing the performance. While there may be no interest in the first set of solutions for the purpose of improving the propeller design, these results are valid for the purpose of testing the optimization scheme. In this case, $-\eta$ is viewed as an objective function without attaching a physical meaning to it. In the second set of results it was necessary to use an accurate formulation for computing the performance in order to show the required blade shape modification for improved performance and the corresponding increase in performance obtained by optimization.

The iterative histories of the design parameters are shown in Figure 9, while the iterative histories of the power and efficiency are shown in Figure 10. From these figures two distinct stages in the convergence process of the solution may be identified. In the first stage, relatively rapid changes in the values of \tilde{P} , C_p , and η occur as they approach the converged values of the solutions. At the end of this stage, these parameters are close to their final values. In the second stage, minor adjustments take place as the parameter solutions converge to their final values. The residual, R_E , is a measure of the convergence of the flow field solution. Figure 11 compares the residual history for the design problem, in which \tilde{g} is updated in addition to \tilde{P} , to the residual history for the regular analysis problem, in which \tilde{g} only is updated while \tilde{P} is held fixed. The figure indicates that modifying the propeller geometry in the design problem as the iterative solutions for the flow variables are updated does not negatively affect the rate of convergence of the flow field solution in comparison to the analysis problem. In fact, the following results of our computations show that the convergence of the flow field solution is accelerated when the design parameters are updated to satisfy the power constraint or to satisfy the conditions of the optimization problem. For a regular analysis problem with \tilde{P} set equal to \tilde{P}^* , the number of iterations required for convergence was 4710. Hereafter, convergence is assumed to be achieved when the magnitude of the residual, R_E , is reduced to the value of 10^{-7} . For a constrained solution in which the second component of the design parameter vector, P_2 , was set equal to the value P_2^* , while the first component was updated throughout the iterative process so that the constraint $C_p = C_{po}$ would be satisfied, convergence was attained after 4040 iterative steps, indicating an increased convergence rate relative to the regular analysis problem. For the design problem in which both P_1 and P_2 were updated in a manner that allows the constraint $C_p = C_{po}$ to be satisfied and the objective function E to be minimized, the number of iterative steps required for convergence was further reduced to 3250.

On the average, 0.972 cpu second was required for the iterative step in the design problem, while 0.403 cpu

second was required for the iterative step in the analysis problem. Therefore, the average design iterative step required slightly more than double the cpu requirements for the analysis iterative step. In the design problem, two analysis problems are solved in parallel. The additional cpu requirement for the design problem is mainly due to generating a new computational mesh whenever the design parameters are updated.

For a regular analysis problem, the computational mesh is generated only one time at the beginning of the computation. For a design problem, however, it is necessary to regenerate the computational mesh whenever the design parameters are updated. In the present computations, this was done once every 40 iterative steps. The cost of mesh generation relative to the cost of solving the flow equations was acceptably low. As the value of ΔN decreases, however, a point may be reached at which the cost of generating the mesh becomes excessively high, and it may represent a substantial fraction of the total computational cost. In this case, a possible alternative to regenerating new meshes, whenever the design parameters are updated, is the use of approximate meshes that are generated by linearly combining $L+1$ reference meshes. The reference meshes may be updated every $J \Delta N$ iterative steps, where $J > 1$. The need for making this approximation does not arise here, as the propeller analysis code used here has relatively slow convergence properties and, therefore, the appropriate ΔN value is relatively large. However, the use of accelerating schemes, such as the multigrid scheme, would allow the ΔN value to be sufficiently low to require the use of the mesh approximation discussed above.

We have performed a single computation using the exact formulation for calculating c_1 , as given by Equation (14), with G_1 computed by Equation (15). This formulation requires solving $L+1$ problems in parallel instead of L problems, in the case of the approximate formulation given by Equation (19). The average iterative step for this computation required 1.474 cpu second. The number of iterations required for convergence was 3425. Comparing these values to the corresponding values for the approximate formulation indicates that there is a strong advantage in using the approximate formulation over the exact formulation.

To verify that the computed solution is indeed the optimum solution, solutions were computed that were slightly perturbed from the optimum predicted solutions but that satisfied the power constraint. Table 1 compares the values of the objective function for the solution predicted by the optimization scheme, shown in the first row, to those for the perturbed solutions, shown in the second and third rows. It is apparent from the table that perturbing the design

parameters causes the value of the objective function to increase. Therefore, the design parameters predicted by the optimization scheme do indeed minimize the value of the objective function.

Table 1. The Objective Function at the Optimum Solution and Perturbed Solutions for the Two-Design-Parameter Problem

P_1	P_2	E
-2.83	5.51	-0.90773
-2.73	5.31	-0.90730
-2.93	5.71	-0.90728

The sensitivity of the scheme's convergence to the initial iterative guesses of the solution and to the computational parameters was tested by recomputing the problem defined above with perturbed initial conditions and computational parameters. Table 2 shows the number of iterative steps, n_c^0 , required for convergence when different values are used for the initial iterative solutions and the computational parameters. It is clear from the table that the convergence properties of the scheme are weakly sensitive to the values of the initial conditions and the computational parameters. Needless to say, there is an optimum set of values for these parameters that maximizes the convergence rate of the scheme for a given problem. However, within a relatively wide range of these parameter values, good convergence is achieved. This is due to the frequent updating of the design parameters in the course of solving the problem. The cpu requirement for the average iterative step is approximately the same for all the cases solved, except for the case in which $\Delta N = 25$.

Table 2. Effect of Perturbing the Initial Conditions and the Computational Parameters on the Scheme's Convergence, for the Two-Design Parameter Problem

P_1^0	P_2^0	ΔN	C	c_1	c_2	n_c^0
0.0	0.0	40	3.0	1.2	0.6	3250
3.0	-5.0	40	3.0	1.2	0.6	3690
0.0	0.0	25	3.0	1.2	0.6	3376
0.0	0.0	40	4.5	1.2	0.6	3252
0.0	0.0	40	6.0	1.2	0.6	3250
0.0	0.0	40	3.0	1.5	0.6	3333
0.0	0.0	40	3.0	1.2	0.4	3120
0.0	0.0	40	3.0	1.5	0.4	3281

The cpu requirement for the average iterative step in this case is given by 1.078 seconds, in comparison to

approximately 0.972 second for the other cases. This is due to the increased frequency of generating the computational mesh in the case with $\Delta N = 25$. Figures 12 through 14 show the iterative histories for P_1 , P_2 , η , C_p and R_E for the case in which the initial iterative guesses for the design parameters, P_1^0 and P_2^0 , were perturbed. Among all the perturbed computations, the rate of convergence for this case was affected the most.

The computations performed above for the two-design-parameter problem were performed with a value of 5.0 for μ . To perform computations that allow both parabolic and linear modifications to the blade angle distributions, it was necessary to reduce the value of μ to 4.0. The three-design-parameter optimization computations were solved using this value for μ . The main two-design-parameter computation was also repeated using this value for μ to allow a comparison between the two-design-parameter and the three-design-parameter results. The optimum values of the design parameters for the two-design-parameter problem with $\mu = 4.0$ were found to be given by $P_1^* = -2.35^\circ$ and $P_2^* = 4.56^\circ$. The value of C_p corresponding to this solution is 1.6999. The objective function E was reduced from the value -0.839 in the case of the original design, with $P_1 = P_2 = 0.0$, to the value -0.897 in the case of the optimized design. The value of η was increased from 0.839 for the original design to 0.900 for the optimized design. As expected, the magnitudes of both E and η determined with $\mu = 4.0$ are less than those determined with $\mu = 5.0$. As the value of μ decreases, the restriction on the allowable search region in the design parameter space increases. In the two-design-parameter problem, 3235 iterative steps were required for convergence. The cpu requirement per iterative step was 0.972 second. The optimum values of the design parameters for the three-design-parameter problem with $\mu = 4.0$ were found to be $P_1^* = -2.77^\circ$, $P_2^* = 4.50^\circ$, and $P_3^* = -1.20^\circ$. The corresponding values of C_p , E , and η are given by 1.6999, -0.900, and 0.905, respectively, indicating a superior design to that achieved by using only two design parameters. The number of iterative steps required for convergence was 3228, while the cpu requirement per iterative step was 1.459 seconds. The iterative histories for P_1 , P_2 , P_3 , η , C_p , and R_E are shown in Figures 15 through 17.

To verify the accuracy of the computed solution, several solutions were computed that were slightly perturbed from the optimum predicted solution but that satisfied the power constraint. Table 3 compares the values of the objective function for the solution predicted by the optimization scheme, shown in the first row, to those for the perturbed solutions shown in the following rows. It is apparent from the table that perturbing the design parameters causes the value of the objective function to increase. Therefore, the design parameters predicted by the optimization

scheme do indeed minimize the value of the objective function.

Table 3. The Objective Function at the Optimum Solution and Perturbed Solutions for the Three-Design Parameter Problem

P_1	P_2	P_3	E
-2.77	4.50	-1.20	-0.90026
-2.87	4.50	-1.45	-0.90011
-2.87	4.69	-1.20	-0.89986
-2.67	4.50	-0.93	-0.90012
-2.67	4.30	-1.20	-0.89988

Computations were performed using the accurate formulation for computing the propeller performance. In these computations it was found that η responds to changes in the design parameters at an iteratively much slower rate than that associated with the first set of computations. For that reason it was necessary to reduce the value of c_1 to 0.98. All other computational parameters were set equal to their same values used in the first set of computations. In this set of computations, it was determined that $\beta_{3/4} = 57.648^\circ$. The value of C_p for the initial flow solution, which corresponds to a $\beta_{3/4}$ value of 54.9°, was 1.2. By optimizing the blade shape for the two-design-parameter problem, the value of the efficiency was increased from 0.8229 for the original design to 0.8233 for the optimized design. For a regular analysis problem with P set equal to \bar{P}^* the number of iterations required for convergence was 4320. A comparison of this number with the number of iterations required to solve the optimization problem, 3260, shows that the cost of solving the optimization problem is approximately twice the cost of solving a regular analysis problem.

In the computations presented above, the effect of varying the linear term of Equation (25) on the propeller efficiency was investigated. To investigate the effect of varying the quadratic term in Equation (25) on the propeller efficiency, a computation was performed in which P_3 was allowed to vary while P_2 was set equal to zero. In this case, the design parameters predicted by the optimization scheme were given by $P_1^* = -0.79^\circ$, $P_3^* = -2.07^\circ$. The value of C_p corresponding to this solution was 1.7000, and the value of η was 0.82549. The number of iterations required for convergence was 3980. A comparison of the values of η for the two cases in which (P_1^*, P_2^*) and (P_1^*, P_3^*) were the design parameters shows that the introduction of a quadratic perturbation to the twist distribution is more effective in increasing the efficiency than the introduction of a linear perturbation.

Finally, the optimum values of the design parameters for the three-design-parameter problem were found to be $P_1^* = -3.34^\circ$, $P_2^* = 3.92^\circ$, and $P_3 = -3.23^\circ$. The corresponding values of C_p and η are given by 1.7000 and 0.83291, respectively. It is apparent that using a combination of linear and quadratic perturbations in the blade angle distribution is much more effective for improving the efficiency than using only one of these distributions. Relative to the original SR-3 design, using both perturbed distributions increased the propeller efficiency by 0.0100. This is compared to a value of 0.0026 for the quadratic distribution alone and a value of 0.0004 for the linear distribution alone. The number of iterative steps required for convergence was 4380 in comparison to 4460 for the regular analysis problem.

The iterative histories for \vec{P} , η , C_p , and R_E in the second set of computations, not presented here, are similar to those of the first set of computations (Figures 9 through 17), and may be found in Reference 11.

Figure 18 compares the optimum blade angle perturbations from the SR-3 baseline design predicted for the cases of linear, quadratic, and combined linear and quadratic shape functions. Curve C, which gives the blade angle perturbation distribution for maximum improvement in efficiency, shows that the efficiency of the SR-3 propeller can be improved by reducing the blade angle distribution both at the hub and at the tip. This explains the observed weak sensitivity of the propeller efficiency to linear variations in the blade angle distribution. The use of a linear shape function allows an increase in the blade angle at either the tip or the hub positions and a decrease in the blade angle at the other position. Therefore, the positive effect on efficiency resulting from the perturbed blade angle distribution at one of these positions tends to cancel the negative effect resulting from the perturbed blade angle distribution at the other position leading to the apparent insensitivity of the efficiency to linear variations in the blade angle distribution. The maximum improvement in efficiency obtained here resulted from the use of linear and quadratic shape functions. Further improvement may be obtained by using other shape functions.

5.2 Wind Tunnel Wall Interference Corrections

References 12 and 13 present a wall interference correction procedure which is divided into two main steps. In the first step the flow is computed around the model in the wind tunnel subject to measured boundary conditions at the tunnel walls. The model angle of attack, α_T , that causes the computed model lift, L_T , to match the measured lift, L_e , is determined by the chord method. The Mach number distribution on the model surface, M_{TS} , is also determined in this step. In the second step, which is formulated as an

optimization problem, the flow is computed around the model in free air. The design parameters P_1 and P_2 are the model angle of attack, α_F , and the free-stream Mach number, $M_{\infty F}$, respectively. They are determined so that the objective function given by Equation (23) is minimized subject to the constraint given by Equation (24). The Mach number correction, ΔM , and the angle-of-attack correction, $\Delta\alpha$, are given by

$$\Delta M = M_{\infty F} - M_{\infty e}; \Delta\alpha = \alpha_F - \alpha_T$$

and the corrected Mach number and angle of attack are then found from the relations

$$M_{\infty f} = M_{\infty e} + \Delta M; \alpha_f = \alpha_e + \Delta\alpha$$

The flow was assumed to be governed by the Euler equations. The flow solver used was based on a finite volume discretization. A multigrid strategy together with a multistage time-stepping scheme were used to advance the flow solution to a steady state as rapidly as possible. Details of the dissipative terms, the multistage scheme and the multigrid method are given in References 14-16. Some results of applying the optimization procedures to the wall interference problem in References 12 and 13 are presented below.

The correction procedure was applied to a wing/body combination consisting of an ONERA M6 wing, with a wing span and maximum chord of 2.4 and 0.6737 unit lengths, respectively, mounted on a cylindrical body of a 0.2-unit-length radius. The model was assumed to be tested in an open jet with zero pressure perturbations along its boundaries. The tunnel height and width considered were 2.0 and 4.0 unit lengths, respectively. The computational domain consisted of half the flow field by including the plane of symmetry as one of its boundaries. The computational parameters δP_2^0 , c_1 , c_2 , C , and δP_{max} were assigned the values 0.005, 1.2, 0.6, 0.3, and 0.2 respectively. The initial guess for the flow solution was set equal to free-stream conditions. A 72x24x12 mesh was used for the tunnel computation, while a 72x32x12 mesh was used for the free-air computation. The free-air mesh and the tunnel mesh were identical in a region bounded by the upper and lower tunnel walls and the wing tip. Beyond the wing tip, the meshes did not coincide. The experimental conditions were given by

$$M_{\infty e} = 0.84 \text{ and } L_e = 0.20.$$

In the first step of the correction procedure, the tunnel flow is computed and the angle of attack, α_T , is determined. It was found to be given by $\alpha_T = 2.777^\circ$. In the second step of the correction procedure, the free-air flow is computed and the parameters P_1 and P_2 are determined by using scheme III, where

$$P_1 = \alpha_F \text{ and } P_2 = M_{\infty F}.$$

Their values were found to be given by $\alpha_F = 2.468^\circ$ and $M_{\infty F} = 0.833$. The angle-of-attack and Mach number corrections are, therefore, given by $\Delta\alpha = -0.309^\circ$, and $\Delta M = -0.007$. Figure 19 shows the iterative histories for α_F and L_F , while the iterative history for $M_{\infty F}$ is shown in Figure 20. Figure 21 compares R_{max} for the second step in the correction procedure, in which \tilde{g} is updated in addition to α_F and $M_{\infty F}$, to R_{max} for the regular analysis solution, in which only \tilde{g} is updated while α_F and $M_{\infty F}$ are held fixed. The figure indicates that the convergence rates for the analysis and the correction schemes are comparable. The high-frequency oscillations apparent in the curve associated with the correction procedure are due to the introduction of perturbations in the flow field as $M_{\infty F}$ is updated. The computational requirements for the free-air correction scheme and the analysis scheme are essentially the same. The first of these computations required 153 cpu seconds, while the second required 150 cpu seconds. For the uncorrected free-air flow ($M_{\infty F} = 0.84$, $\alpha_F = 2.777^\circ$), the values of L_F and E are given by $L_F = 0.235$, $E = 5.2 \times 10^{-6}$. For the corrected free-air flow ($M_{\infty F} = 0.833$, $\alpha_F = 2.468^\circ$), these values are given by $L_F = 0.200$, $E = 6.92 \times 10^{-7}$. The corrections therefore achieved the goal of satisfying the lift constraint and of reducing the value of the objective function.

Scheme III was applied to different three-dimensional configurations with success. However, problems developed when applying it to two-dimensional configurations, as the supersonic bubble size increased beyond a certain limit. To demonstrate this problem the procedure is now applied to a NACA 0012 airfoil tested in an open jet of height $h = 3.6$. The airfoil is assumed to have a chord of unit length and to be located in the middle between the upper and lower boundaries. A 72x64 mesh is used for the tunnel simulation and a 72x96 mesh is used for the free-air simulation. The airfoil lift coefficient and the tunnel Mach number are given by $L_e = 0.35$ and $M_{\infty e} = 0.7$.

In the first step of the correction procedure, the wind tunnel flow is computed and the angle of attack α_T is determined. In the second step of the correction procedure, the free-air flow is computed and the parameters α_F and $M_{\infty F}$ are determined. The initial iterative values of α_F and $M_{\infty F}$ are chosen to be equal to α_T and $M_{\infty e}$, respectively. The initial flow field solution is set equal to free-stream conditions. The parameters δP_2^0 , c_1 , c_2 , C , δP_{max} , ΔN , and ϵ are given, respectively, by 0.005, 1.2, 0.6, 0.3, 0.2, 4, and 10^{-5} .

The iterative history of $M_{\infty F}$ resulting from using scheme I is shown in Figure 22a. In this figure, an initial stage of about 150 iterative steps is identified in which relatively rapid variations in the value of $M_{\infty F}$ take place. At the end of this stage, the value

of $M_{\infty F}$ is essentially converged. Only minor variations are observed in the value of $M_{\infty F}$ beyond the initial stage. The iterative history of $M_{\infty F}$ resulting from using scheme III is shown in Figure 22b. An initial stage of about 60 iterative steps of rapid variations is observed in this figure. The solution beyond this point seems to be essentially converged. However, at approximately the 80th and the 230th iterative steps, a rapid departure from the apparently converged solution takes place. Within about 25 iterative steps in both cases, an essentially converged solution is observed again. Many computations were performed using scheme III, for different test conditions. The appearance of local spike-shaped deviations is a common feature among these solutions. However, the size of these spikes and the frequency of their occurrence depends on the particular problem being solved. In scheme I, the incremental value δP_2 is determined by comparing two objective functions at the same time step. In scheme III, this value is determined by comparing two objective functions at different time steps. Scheme III functions properly as long as the dependence of the objective function on the parameter $M_{\infty F}$ is stronger than its dependence on time. As its dependence on time becomes comparable or stronger than its dependence on $M_{\infty F}$, the computed δP_2 values no longer lead to convergence to the optimum solution. The local divergence shown in Figure 22b is due to the solution's weak dependence on $M_{\infty F}$ as the values of δP_2 become small. As the local divergence occurs, the value of δP_2 increases, causing a stronger dependence on $M_{\infty F}$ and causing reconvergence. In other words, the process that takes place at the spikes is self-stabilizing. It is, therefore, possible to use scheme III to determine a solution by simply ignoring the local solutions at the spikes. However, as the supersonic region increases in size, the size of the spikes also increases. Eventually, it becomes no longer possible to use scheme III for determining valid solutions. Figure 22c shows the iterative history of $M_{\infty F}$ resulting from using scheme III in the same problem solved above, but with a value of $M_{\infty e}$ of 0.75 rather than 0.7. It is apparent that a converged solution in this figure is no longer identifiable. Therefore, scheme III is no longer useful in determining a solution.

Figure 23 shows the history for the maximum residual, R_{max} , for the three cases corresponding to Figure 22. While the effect of the spikes is seen to be local and limited to a few time steps in Figure 22b, the recovery to the pre-spike level is seen to take a relatively longer time interval in the case of the maximum residual, as indicated in Figure 23b, which shows that, beyond 300 time steps, the maximum residual oscillates about a fixed value. The computation was continued to 800 time steps, and the oscillatory behavior was found to continue. This behavior is due to the same process that leads to the local divergence observed above. As indicated above,

at certain stages of the computation, the signs and values of δP_2 are no longer chosen in a manner that causes $M_{\infty F}$ to approach its optimum value. If conditions are such that the sign of δP_2 remains unchanged for a large number of steps, then the local divergence observed above will occur. On the other hand, if the positive and negative signs of δP_2 are reasonably well balanced, then the oscillatory behavior observed in Figure 23b occurs. It should be noted that, even though the maximum residual may no longer converge, the level at which this occurs in Figure 23b does indicate that, for practical purposes, the solution is converged. The uncertainty caused by scheme III in this particular problem should be of no practical concern.

Table 4 compares the accuracy of the schemes I and III. The exact solution was obtained by solving a series of problems with different values of $M_{\infty F}$. In each problem the value of α_F , which satisfies the lift constraint, was determined by the chord method. In each of these problems, the objective function was computed. The exact solution is the solution that results in the minimum value for the objective function. It does appear from the table that the results obtained by each of the two schemes are accurate and the errors are within acceptable levels.

Table 4. A Comparison of the Accuracy of the Optimization Schemes

	exact	scheme I	scheme III
$\Delta\alpha$	-1.6000°	-1.5999°	-1.5981°
ΔM	-0.0062	0.0062	-0.0065
error in $\Delta\alpha$	0.0%	0.0%	0.1%
error in ΔM	0.0%	0.0%	-4.8%
E	8.97×10^{-4}	8.97×10^{-4}	8.98×10^{-4}

To compare the efficiency and relative costs of the two schemes, it is necessary to set a convergence criterion. The convergence criterion used here assumes that convergence is attained when $R_{max} = 10^{-4}$. At this value of the maximum residual, it is found that the values of $\Delta\alpha$, ΔM , and E are all essentially converged. Based on this convergence criterion, Table 5 compares the number of iterations and the computational time required for convergence for the different schemes and for a regular analysis solution. It is clear from the table that updating the angle of attack and the Mach number in addition to the flow variables resulted in reduced convergence rates relative to that of an analysis problem in which only the flow variables are updated. The table also indicates that the computational time per iteration required for scheme I is double that of

scheme III. This is due to the requirement of computing two solutions in parallel when scheme I is used. While scheme III updates α_F and $M_{\infty F}$ each iterative step, scheme I, through the parameter ΔN , allows the user to specify the frequency of updating these parameters. In the present computations, these parameters were updated every four iterative steps. We did not attempt to determine the value of ΔN that maximizes the rate of convergence. Therefore, there is a good possibility that the efficiency of scheme I can be improved over that indicated.

Table 5. A Comparison of the Efficiency of the Optimization Schemes

	analysis	scheme I	scheme III
Number of Iterations	92	268	174
CPU Seconds	23	137	44

The above computations were performed for a case in which scheme III functions properly to allow comparison between that scheme and scheme I in the range in which it is valid. Scheme I was applied successfully to cases at high Mach numbers (Reference 12) in the range where scheme III cannot be used. An example of these cases is defined by the test conditions $h = 4.6$, $M_{\infty e} = 0.8$ and $L_e = 0.35$. A 72x80 mesh was used for the tunnel simulation and a 72x112 mesh was used for the free-air simulation. The first step of the correction procedure determined an α_T value of 2.8296°. Figure 24 shows the iterative histories for $M_{\infty F}$, α_F , L_F and R_{max} in the second step of the correction procedure. This step determined an α_F value of 1.6488° and an $M_{\infty F}$ value of 0.7871. A comparison between the solution obtained in the second step and a regular analysis solution indicates that 246 iterations and 143 cpu seconds are required for the present solution to achieve convergence, while 66 iterations and 19 cpu seconds are required for the analysis solution to achieve convergence. The correction results are given by

$$\Delta\alpha = -1.1808^\circ, \Delta M = -0.0129, E_M = 3.54 \times 10^{-4}$$

These values are identical to the exact solution. Figure 25 presents a comparison between the pressure on the airfoil surface for the wind tunnel flow ($M_{\infty T} = 0.8$, $\alpha_T = 2.8296^\circ$), the free-air flow at the uncorrected conditions ($M_{\infty F} = 0.8$, $\alpha_F = 2.8296^\circ$) and the free-air flow at the corrected conditions ($M_{\infty F} = 0.7871$, $\alpha_F = 1.6488^\circ$). As indicated from the figure, the correction procedure does accomplish the goal of determining the free-air corrected conditions (α_F , $M_{\infty F}$) with aerodynamic properties nearly matching the corresponding properties for the

tunnel conditions (α_T , $M_\infty e$). The value of E is reduced from 384.36×10^{-4} for the free-air flow at the uncorrected conditions to 3.54×10^{-4} for the free-air flow at the corrected conditions.

Scheme III was applied in References 8 and 17 to the problem of wall interference correction. There, however, the transonic small disturbance equation was assumed to be the flow governing equation and the solution was obtained by successive line overrelaxation.

5.3 Efficiency of Optimization Schemes

Schemes I and II were applied in this paper (P) and in Reference 6 to propeller design problems (PD). Schemes I, II, and III were applied in this paper in References 7, 8, and 17 to wall interference correction problems (WIC). Scheme II was applied in Reference 18 to airfoil design problems (AD). In these applications the Euler equations, the potential flow equation and the transonic small disturbance (TSD) were assumed to be the flow governing equations. The potential flow and TSD equations were solved by successive line overrelaxation (SLOR), while the Euler equations were solved by method A, described in References 9, method B described in Reference 16, or the multigrid method C based on the schemes of References 14-16. One-, two-, and three-design-parameter problems were solved.

The effect of updating the design parameters while the iterative flow solutions evolve, on the convergence of the flow solution, is measured by the parameter σ given by

$$\sigma = \frac{n_c^0}{n_c^d}$$

where n_c^0 is the number of iterations required for convergence, when solving the optimization problem, and n_c^d is the corresponding number of iterations required for convergence, when solving the analysis problem. A σ value of one indicates that updating the design parameters while the iterative flow solution evolves has no effect on the convergence of the flow solution, while σ values which are less than one and greater than one indicate accelerating and decelerating convergence effects, respectively. To compare the efficiency of different schemes, it is convenient to define the parameter ν , which is the ratio of the cost of solving the optimization problem to the cost of solving L regular analysis problems. It is given by

$$\nu = \lambda\sigma$$

where

$$\lambda = \begin{cases} M/L \text{ for scheme I} \\ (\Delta N + L + Z) / (L\Delta N) \text{ for scheme II} \\ 1/L \text{ for scheme III} \end{cases}$$

M is the number of problems solved in parallel for scheme I; Z takes the values of 1 and 0 for unconstrained and constrained problems, respectively.

Table 6 compares the parameters ν and σ for different problems solved in this paper and in References 6, 7, 8, 17, and 18. All problems satisfy a single equality constraint, except those of References 7, 8, and 18, which are unconstrained. The table shows that good convergence rates for the flow iterative solutions are possible even if the design parameters are allowed to vary as the flow solutions evolve. The table also shows that it is possible to solve an L -design-parameter optimization problem at a cost equal to L times the cost of solving the analysis problem. It

Table 6. Efficiency of Solving Optimization Problems

Problem	Flow Eqs.	Method of Solution	Scheme	L	N	σ	ν	Ref.
PD	Euler	A	I	2	2	0.7-0.8	0.7-0.8	P
PD	Euler	A	I	2	3	0.7	1.1	P
PD	Euler	A	I	3	3	0.7-1.0	0.7-1.0	P
PD	Potential	SLOR	II	3	-	1.1	2.2	6
WIC	Euler	B	I	2	2	2.9-3.7	2.9-3.7	P
WIC	Euler	B	III	2	1	1.0-1.9	0.5-1.0	P
WIC	TSD	SLOR	II	1	-	0.7-0.8	1.1-1.2	7
WIC	TSD	SLOR	II	2	-	0.8-1.5	0.7-1.4	7
WIC	TSD	SLOR	II	3	-	1.4-1.6	0.9-1.1	7
WIC	TSD	SLOR	III	1	1	0.9-1.1	0.9-1.1	8
WIC	TSD	SLOR	III	2	1	0.9	0.5	17
AD	Euler	C	II	3	-	2.9	1.3	18

should be noted that the costs considered here do not include those for mesh generation and evaluation of the objective and constraint functions. These costs were minor in the problems presented here.

6. CONCLUSIONS

In this paper, an approach based on updating the flow variables and the design parameters simultaneously was presented. This approach is applicable to aerodynamic optimization problems in which the flow governing equations are nonlinear equations that are solved iteratively. Three schemes based on this approach were presented.

Scheme I is a general scheme. It was applied to two- and three-design-parameter problems with a single equality constraint. However, extensions of this scheme applicable to optimization problems with multiple equality and inequality constraints were presented. The results show that the scheme is highly accurate in determining the solution of constrained optimization problems. Schemes II and III also presented here are only applicable to a limited class of problems. The cost of solving the optimization problems presented here was within the range $(0.5L - 3.7L)$ times the cost of solving a regular analysis problem, where L is the number of design parameters. This wide range is a reflection of the different problems solved, the different procedures used in solving the flow governing equation, and the different degrees of accuracy to which the design parameters were determined. Tests performed on scheme I indicate that the convergence rate of the solution is weakly sensitive to variations in the computational parameters and the initial iterative guesses for the design parameters.

The three schemes presented here are only examples of schemes which update the flow variables and the design parameters simultaneously. Other schemes based on this approach may be developed. The results of the preliminary tests conducted indicate that the approach of updating the flow variables and the design parameters simultaneously is an attractive alternative to the costly inner-outer iterative procedure associated with the use of conventional optimization schemes. Further tests, however, are required to better evaluate this approach. Direct comparisons between the results of this approach to the results of conventional schemes are necessary. Applying this approach to problems with a larger number of design parameters than used here and investigating its performance in this case is also necessary for a better evaluation of this approach.

REFERENCES

1. Hicks, R. M., Murman, E. M., and Vanderplaats, G. N., "An Assessment of Airfoil Design by Numerical Optimization," NASA TM X-3092, July 1974.
2. Haney, H. P., Johnson, R. R., and Hicks, R. M., "Computational Optimization and Wind Tunnel Test of Transonic Wing Designs," *Journal of Aircraft*, Vol. 17, July 1980, pp. 457-463.
3. Hicks, R. M., "Transonic Wing Design Using Potential-Flow Codes - Successes and Failures," SAE Paper 810565, April 1981.
4. Cosentino, G. B., and Holst, T. L., "Numerical Optimization Design of Advanced Transonic Wing Configurations," AIAA Paper 85-0424, January 1985.
5. Davis, W., "TRO-2D: A Code for Rational Transonic Aero Optimization," AIAA Paper 85-0425, January 1985.
6. Rizk, M.H., and Jou, W.-H., "Propeller Design by Optimizatio," AIAA Paper 86-0081, January 1986.
7. Rizk, M.H., "The Single-Cycle Scheme: A New Approach to Numerical Optimization," *AIAA Journal*, Vol. 21, December 1983, pp. 1640-1647.
8. Rizk, M.H., "A New Approach to Optimization for Aerodynamic Applications," *Journal of Aircraft*, Vol. 20, January 1983, pp. 94-96.
9. Yamamoto, O., Barton, J. M., and Bober, L. J., "Improved Euler Analysis of Advanced Turboprop Propeller Flows," AIAA Paper 86-1521, June 1986.
10. Rizk, M.H., "Optimizing Advanced Propeller Designs by Simultaneously Updating Flow Variables and Design Parameters," *Journal of Aircraft*, Vol. 26, June 1989, pp. 515-522.
11. Rizk, M.H., "Aerodynamic Optimization by Simultaneously Updating Flow Variables and Design Parameters With Application to Advanced Propeller Designs," NASA CR-182181, July 1988.
12. Rizk, M.H., Lovell, D.R., and Baker, T.J., "Euler Procedure for Correcting Two-Dimensional Transonic Wind-Tunnel Wall Interference", *AIAA Journal*, Vol. 26, December 1988, pp. 1457-1466.
13. Rizk, M.H., Lovell, D.R., and Baker, T.J., "Euler Procedure for Three-Dimensional Transonic Wall Interference", *Journal of Aircraft*, Vol. 26, January 1989, pp. 48-55.

14. Jameson, A., and Baker, T.J., "Solution of the Euler Equations for Complex Configurations", AIAA Paper 83-1929, July 1983.
15. Jameson, A., and Baker, T.J., "Multigrid Solution of the Euler Equations for Aircraft Configurations," AIAA Paper 84-0093, January 1984.
16. Jameson, A., Schmidt, W., and Turkel, E., "Numerical Solutions of the Euler Equations by Finite Volume Methods Using Runge-Kutta Time-Stepping Schemes," AIAA Paper 81-1259, June 1981.
17. Rizk, M.H., and Murman, E.M., "Wind Tunnel Wall Interference Corrections for Aircraft Models in the Transonic Regime," *Journal of Aircraft*, Vol. 21, January 1984, pp. 54-61.
18. Rizk, M.H., "Application of the Single-Cycle Optimization Approach to Aerodynamic Design," *Journal of Aircraft*, Vol. 22, June 1985, pp. 509-515.

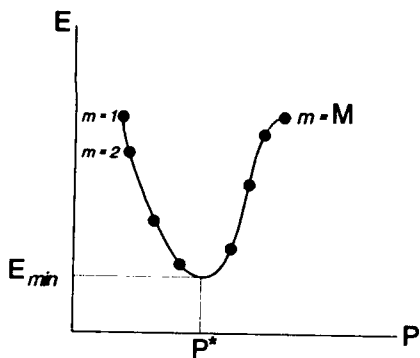


Figure 1. Objective Function.

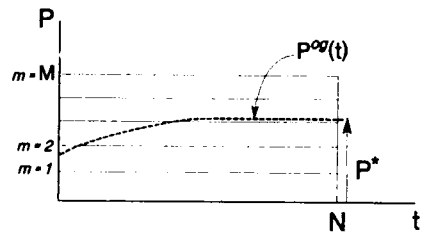


Figure 2. Path of Objective Function's Minimum Point (Graphical Approach).

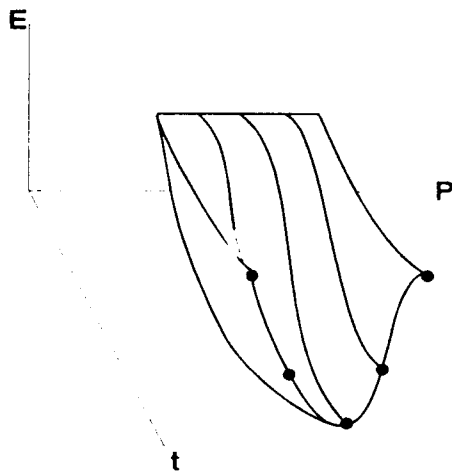


Figure 3. Objective Function's Time Evolution.

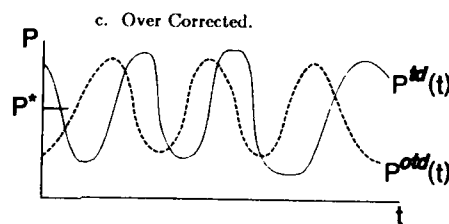
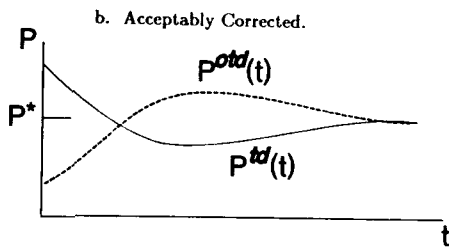
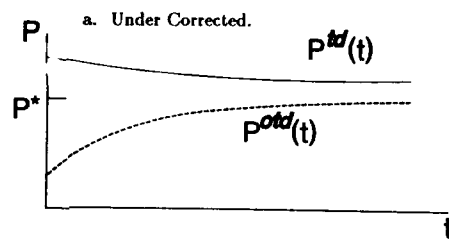


Figure 4. Design Parameter and Objective Function's Minimum Paths (Time-Dependent Approach).

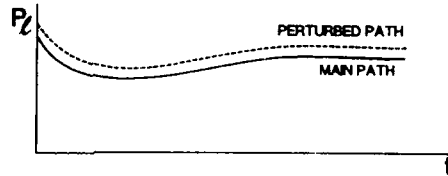


Figure 5. Parallel Scheme (I).

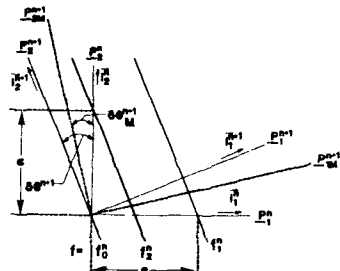


Figure 6. Two-Dimensional Design Parameter Space

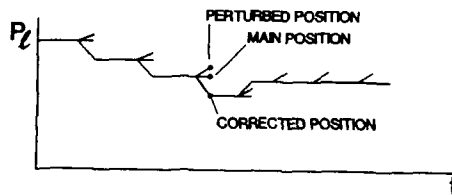


Figure 7. Branch Scheme (II).

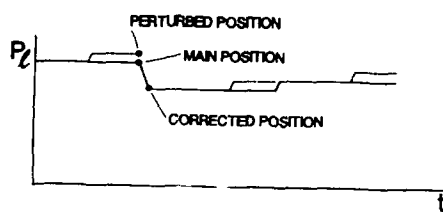


Figure 8. Combined Parallel-Branch Scheme.

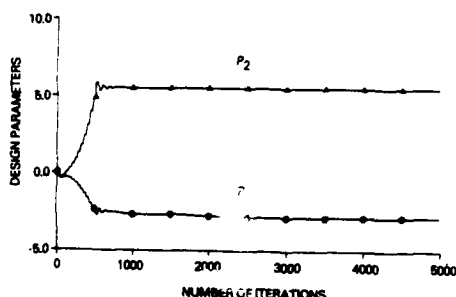


Figure 9. Design Parameter Iterative Histories for the Two-Design-Parameter Problem.

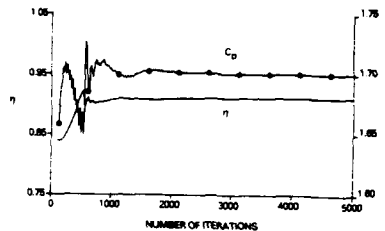


Figure 10. Power and Efficiency Iterative Histories for the Two-Design-Parameter Problem.

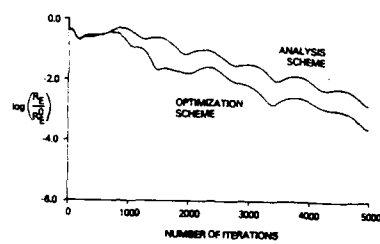


Figure 11. Residual Iterative Histories for the Analysis Problem and the Two-Design-Parameter Optimization Problem.

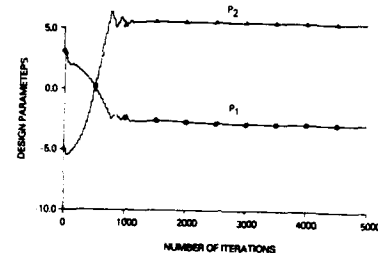


Figure 12. Design Parameter Iterative Histories for the Two-Design-Parameter Problem with Perturbed Initial Conditions.

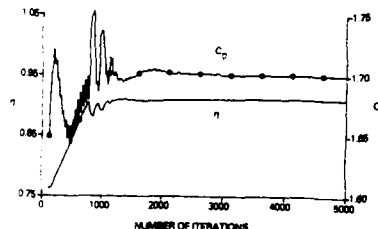


Figure 13. Power and Efficiency Iterative Histories for the Two-Design-Parameter Problem with Perturbed Initial Conditions.

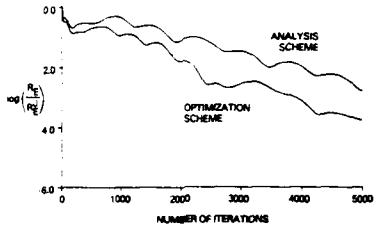


Figure 14. Residual Iterative Histories for the Analysis Problem and the Two-Design-Parameter Optimization Problem with Perturbed Initial Conditions.

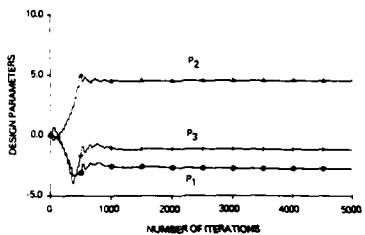


Figure 15. Design Parameter Iterative Histories for the Three-Design-Parameter Problem.

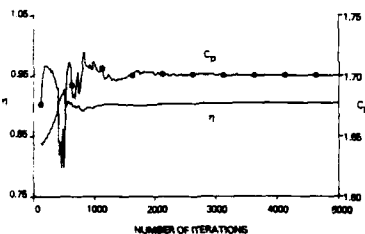


Figure 16. Power and Efficiency Iterative Histories for the Three-Design-Parameter Problem.

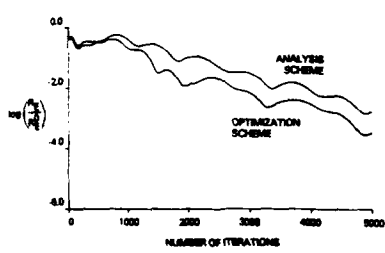


Figure 17. Residual Iterative Histories for the Analysis Problem and the Three-Design-Parameter Optimization Problem.

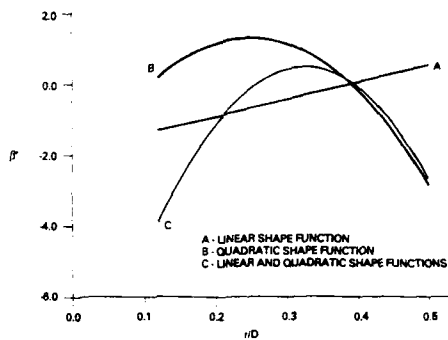


Figure 18. Optimum Blade Angle Perturbations.

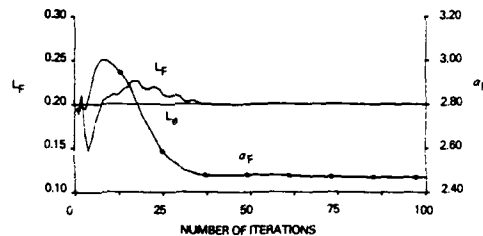


Figure 19. Iterative Histories for the Free-Air Solutions (Scheme III).

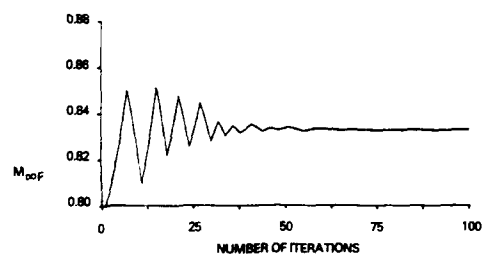


Figure 20. Iterative History for $M_{\infty F}$ (Scheme III).

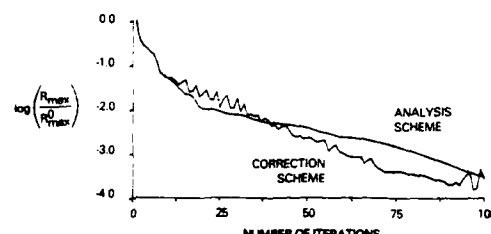


Figure 21. Residual Evolution Histories for the Correction Problem and the Analysis Problem in Free Air (Scheme III).

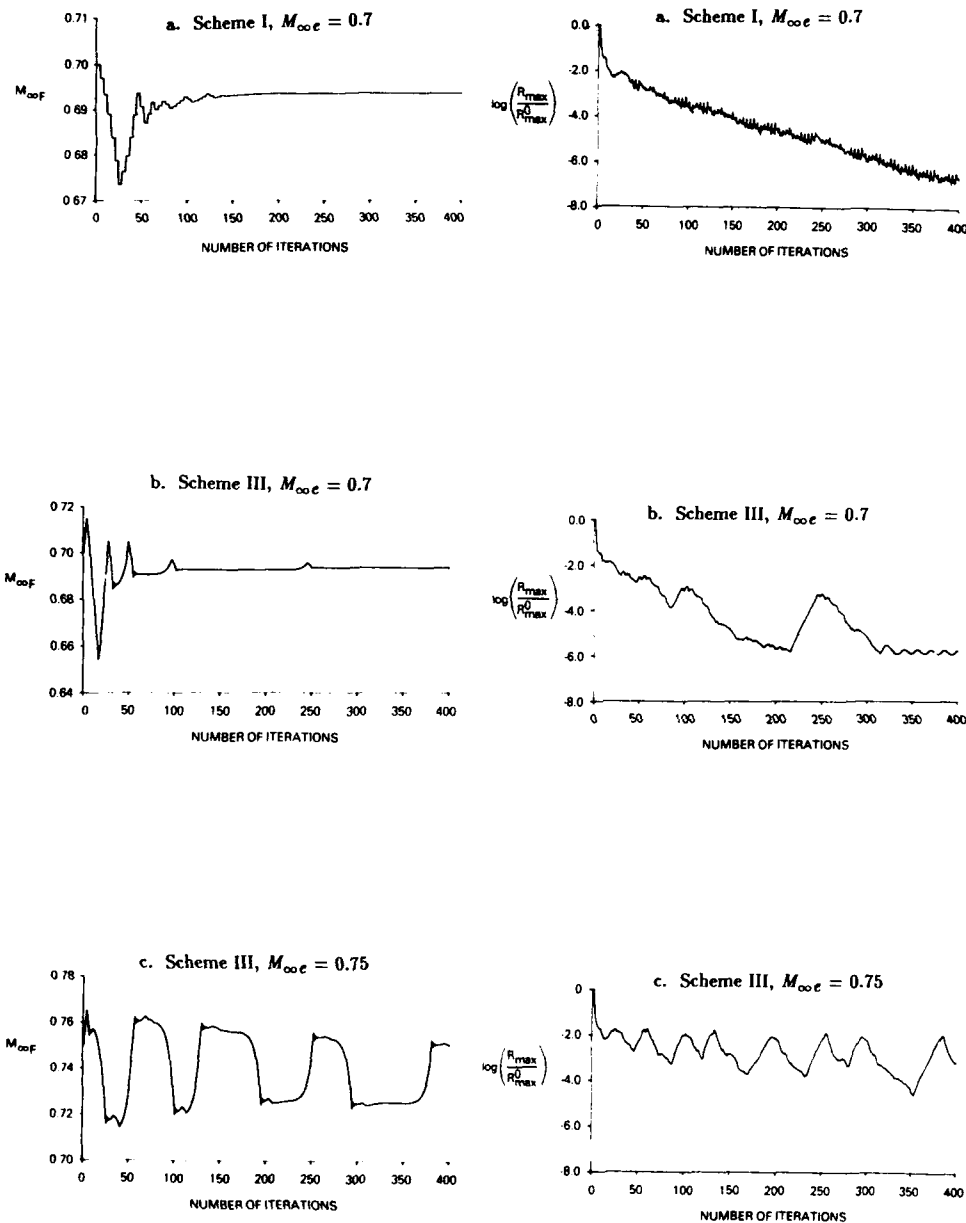


Figure 22. Iterative History for $M_{\infty}F$
($h = 3.6$, $L_e = 0.35$).

Figure 23. Maximum Residual Evolution History
($h = 3.6$, $L_e = 0.35$).

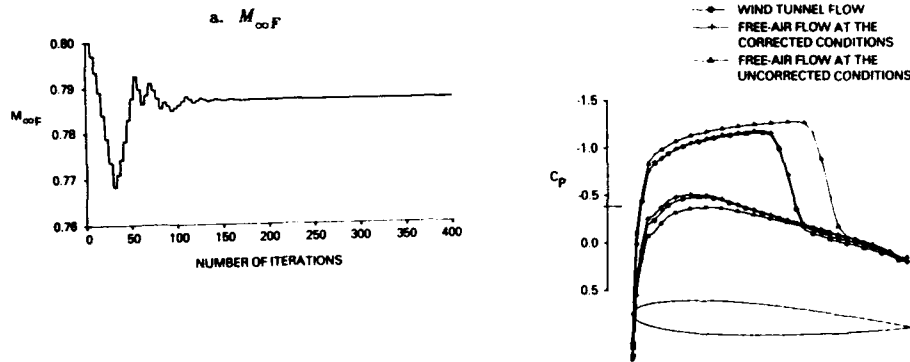


Figure 25. Pressure Distribution on the Airfoil Surface ($h = 4.6$, $M_{\infty e} = 0.8$, $L_e = 0.35$).

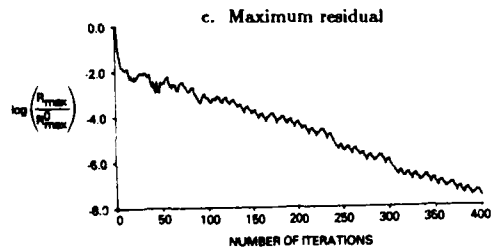
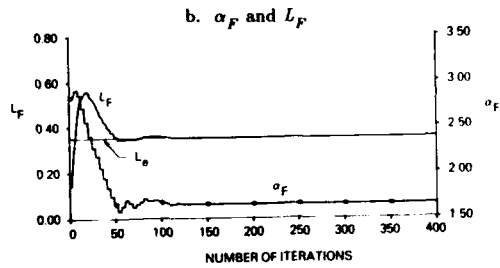


Figure 24. Iterative Histories for the Free-Air Solutions Using Scheme I ($h = 4.6$, $M_{\infty e} = 0.8$, $L_e = 0.35$).

REPORT DOCUMENTATION PAGE			
1. Recipient's Reference	2. Originator's Reference	3. Further Reference	4. Security Classification of Document
	AGARD-R-780	ISBN 92-835-0591-3	UNCLASSIFIED
5. Originator	Advisory Group for Aerospace Research and Development North Atlantic Treaty Organization 7 rue Ancelle, 92200 Neuilly sur Seine, France		
6. Title	INVERSE METHODS FOR AIRFOIL DESIGN FOR AERONAUTICAL AND TURBOMACHINERY APPLICATIONS		
7. Presented at			
8. Author(s)/Editor(s)			9. Date
Various			November 1990
10. Author's/Editor's Address			11. Pages
Various			258
12. Distribution Statement	This document is distributed in accordance with AGARD policies and regulations, which are outlined on the Outside Back Covers of all AGARD publications.		
13. Keywords/Descriptors	Airfoils Design Turbomachinery Aircraft Boundary layer Optimization Pressure distribution Iteration Applications of mathematics		
14. Abstract	<p>This lecture series is devoted to the major aspects of aerofoil design both for aeronautical and turbomachine application, as there are:</p> <ul style="list-style-type: none"> • optimisation of target pressure and velocity distribution. Both direct optimisation resulting from an inverse boundary layer calculation and an iterative optimisation of the losses are presented. • aerofoil design by means of inverse methods. This ranges from simple parametric definitions of two-dimensional cross sections to a detailed numerical definition of three dimensional shapes. <p>The methodology to account for a large number of constraints and off-design operation is also discussed and illustrated by a large number of applications.</p> <p>The material assembled in this book was prepared under the combined sponsorship of the Fluid Dynamics Panel, the von Kármán Institute and the Consultant and Exchange Program of AGARD and was presented as an AGARD Special Course at the von Kármán Institute, Rhode-Saint-Genèse, Belgium on 14th—18th May 1990.</p>		

<p>AGARD Report No.780 Advisory Group for Aerospace Research and Development, NATO INVERSE METHODS FOR AIRFOIL DESIGN FOR AERONAUTICAL AND TURBOMACHINERY APPLICATIONS Published November 1990 258 pages</p> <p>This lecture series is devoted to the major aspects of aerfoil design both for aeronautical and turbomachine application, as there are:</p> <ul style="list-style-type: none"> • optimisation of target pressure and velocity distribution. Both direct optimisation resulting from an inverse boundary layer calculation and an iterative optimisation of the losses are presented. <p>P.T.O.</p>	<p>AGARD-R-780</p> <p>Airfoils Design Turbomachinery Aircraft Boundary layer Optimization Pressure distribution Iteration Applications of mathematics</p> <p>This lecture series is devoted to the major aspects of aerfoil design both for aeronautical and turbomachine application, as there are:</p> <ul style="list-style-type: none"> • optimisation of target pressure and velocity distribution. Both direct optimisation resulting from an inverse boundary layer calculation and an iterative optimisation of the losses are presented. <p>P.T.O.</p>	<p>AGARD Report No.780 Advisory Group for Aerospace Research and Development, NATO INVERSE METHODS FOR AIRFOIL DESIGN FOR AERONAUTICAL AND TURBOMACHINERY APPLICATIONS Published November 1990 258 pages</p> <p>This lecture series is devoted to the major aspects of aerfoil design both for aeronautical and turbomachine application, as there are:</p> <ul style="list-style-type: none"> • optimisation of target pressure and velocity distribution. Both direct optimisation resulting from an inverse boundary layer calculation and an iterative optimisation of the losses are presented. <p>P.T.O.</p>
---	---	---

<p>• aerofoil design by means of inverse methods. This ranges from simple parametric definitions of two-dimensional cross sections to a detailed numerical definition of three dimensional shapes.</p> <p>The methodology to account for a large number of constraints and off-design operation is also discussed and illustrated by a large number of applications.</p> <p>The material assembled in this book was prepared under the combined sponsorship of the Fluid Dynamics Panel, the von Kármán Institute and the Consultant and Exchange Program of AGARD and was presented as an AGARD Special Course at the von Kármán Institute, Rhode-Saint-Genèse, Belgium on 14th–18th May 1990.</p> <p style="text-align: right;">ISBN 92-835-0591-3</p>	<ul style="list-style-type: none"> • aerofoil design by means of inverse methods. This ranges from simple parametric definitions of two-dimensional cross sections to a detailed numerical definition of three dimensional shapes. <p>The methodology to account for a large number of constraints and off-design operation is also discussed and illustrated by a large number of applications.</p> <p>The material assembled in this book was prepared under the combined sponsorship of the Fluid Dynamics Panel, the von Kármán Institute and the Consultant and Exchange Program of AGARD and was presented as an AGARD Special Course at the von Kármán Institute, Rhode-Saint-Genèse, Belgium on 14th–18th May 1990.</p> <p style="text-align: right;">ISBN 92-835-0591-3</p>
--	---

AGARD
NATO OTAN
7 RUE ANCELLE · 92200 NEUILLY-SUR-SEINE
FRANCE
Téléphone (1)47.38.57.00 · Telex 610 176

**DIFFUSION DES PUBLICATIONS
AGARD NON CLASSIFIEES**

L'AGARD ne détient pas de stocks de ses publications, dans un but de distribution générale à l'adresse ci-dessus. La diffusion initiale des publications de l'AGARD est effectuée auprès des pays membres de cette organisation par l'intermédiaire des Centres Nationaux de Distribution suivants. Ces Centres disposent parfois d'exemplaires additionnels; dans les cas contraire, on peut se procurer ces exemplaires sous forme de microfiches ou de microcopies auprès des Agences de Vente dont la liste suit.

CENTRES DE DIFFUSION NATIONAUX

ALLEMAGNE Fachinformationszentrum, Karlsruhe D-7514 Eggenstein-Leopoldshafen 2	ISLANDE Director of Aviation c/o Flugrad Reykjavik
BELGIQUE Coordonnateur AGARD-VSL Etat-Major de la Force Aérienne Quartier Reine Elisabeth Rue d'Evere, 1140 Bruxelles	ITALIE Aeronautica Militare Ufficio del Delegato Nazionale all'AGARD 3 Piazzale Adenauer 00144 Roma EUR
CANADA Directeur du Service des Renseignements Scientifiques Ministère de la Défense Nationale Ottawa, Ontario K1A 0K2	LUXEMBOURG <i>Voir Belgique</i>
DANEMARK Danish Defence Research Board Ved Idrætsparken 4 2100 Copenhagen Ø	NORVEGE Norwegian Defence Research Establishment Attn: Biblioteket P.O. Box 25 N-2007 Kjeller
ESPAGNE INTA (AGARD Publications) Pintor Rosales 34 28008 Madrid	PAYS-BAS Netherlands Delegation to AGARD National Aerospace Laboratory NLR Kluiverweg 1 2629 HS Delft
ETATS-UNIS National Aeronautics and Space Administration Langley Research Center M/S 180 Hampton, Virginia 23665	PORTUGAL Portuguese National Coordinator to AGARD Gabinete de Estudos e Programas CLAFIA Base de Alfragide Alfragide 2700 Amadora
FRANCE O.N.E.R.A. (Direction) 29, Avenue de la Division Leclerc 92320, Châtillon sous Bagneux	ROYAUME UNI Defence Research Information Centre Kentigern House 65 Brown Street Glasgow G2 8EX
GRECE Hellenic Air Force Air War College Scientific and Technical Library Dekelia Air Force Base Dekelia, Athens TGA 1010	TURQUIE Millî Savunma Bakanlığı (MSB) ARGE Daire Başkanlığı (ARGE) Ankara

LE CENTRE NATIONAL DE DISTRIBUTION DES ETATS-UNIS (NASA) NE DETIENT PAS DE STOCKS
DES PUBLICATIONS AGARD ET LES DEMANDES D'EXEMPLAIRES DOIVENT ETRE ADRESSEES DIRECTEMENT
AU SERVICE NATIONAL TECHNIQUE DE L'INFORMATION (NTIS) DONT L'ADRESSE SUIT.

AGENCES DE VENTE

National Technical Information Service (NTIS) 5285 Port Royal Road Springfield, Virginia 22161 Etats-Unis	ESA/Information Retrieval Service European Space Agency 10, rue Mario Nikis 75015 Paris France	The British Library Document Supply Division Boston Spa, Wetherby West Yorkshire LS23 7BQ Royaume Uni
---	--	---

Les demandes de microfiches ou de photocopies de documents AGARD doivent comporter le numéro de série AGARD, le titre, le nom de l'auteur ou du rédacteur-coordonnateur et la date de publication. Les demandes adressées au NTIS doivent comporter le numéro matricule NASA du rapport. Des références bibliographiques complètes ainsi que des résumés des publications AGARD figurent dans les journaux suivants:

Scientific and Technical Aerospace Reports (STAR)
publié par la NASA Scientific and Technical
Information Branch
NASA Headquarters (NIT-40)
Washington D.C. 20546
Etats-Unis

Government Reports Announcements (GRA)
publié par National Technical Information Services.
Springfield
Virginia 22161
Etats-Unis

*Imprimé par Specialised Printing Services Limited
40 Chigwell Lane, Loughton, Essex IG10 3TZ*